Evolution of deformation of the Himalayan prism: from imaging to modelling

---

Évolution de la déformation du prisme Himalayen: de l'imagerie à la modélisation

THÈSE DE DOCTORAT
présentée par

György HETÉNYI

Pour l'obtention du titre de Docteur de l'Université Paris XI
(Spécialité: Sciences de la Terre; École Doctorale 143)
Préparée au Laboratoire de Géologie de l'École Normale Supérieure

Soutenance le 29 Novembre 2007
Devant le jury composé de:

Mr. CATTIN, Rodolphe	MdC, École Normale Supérieure	Directeur de thèse
Mr. CONNOLLY, James	Senior Scientist, ETH Zürich	Rapporteur
Mr. HORVÁTH, Frank	Pr., Université Eötvös, Budapest	Invité
Mr. LE PICHON, Xavier	Pr., Collège de France	Examinateur
Mr. NÁBĚLEK, John	Pr., Oregon State University	Invité
Mr. VERGNE, Jérôme	MdC, École Normale Supérieure	Co-directeur de thèse
Mr. VIRIEUX, Jean	Pr., Université Joseph-Fourier	Rapporteur
Mr. ZEYEN, Hermann	Pr., Université Paris XI	Examinateur

Abstract

The Himalayas and the Tibetan Plateau are considered as the classical case of continental collision. In the meantime, some fundamental questions concerning the structure, rheology and physical processes influencing the evolution of the region's lithosphere are still pending.

The Hi-CLIMB seismology experiment deployed a large number (255) of broadband stations during three years on an 800 km profile along 85°E, across the Himalayas and the southern half of the Tibetan Plateau. The close station spacing ($\sim$4-9 km), the large amount of data (1.5 terabyte), the high-frequency receiver functions and the use of multiply converted waves result in a detailed image of lithospheric structures at all scales. These images allow to follow: (1) faults at shallow ($\sim$3-4 km) depth; (2) the Main Himalayan Thrust from its shallow part to its deep and ductile continuation; (3) shallow and localized low-velocity layers (previously referred to as "bright spots") in Tibet in correlation with grabens; and (4) underplating of the Indian lower crust beneath Lhasa block. Furthermore, our results show (5) that the Indian lower lithosphere advances northward to about the centre of the Tibetan Plateau, where it is opposed to the Eurasian lithospheric mantle; (6) that the main sutures at the surface have no pronounced signature at depth; and (7) that the upper mantle discontinuities at 410 and 670 km do not seem to be affected by the ongoing orogeny. The obtained information on geometries are then used in two applications.

Based on the improved knowledge on flexural geometry beneath the foreland basin, the rheology of the India plate is re-assessed. Thermomechanical modelling results reveal that the effective elastic thickness decreases from south to north due to decoupling, caused by flexural and thermal weakening. To explain the support of the Tibetan Plateau's topography as well as regional isostasy in the Himalayas, a strong upper mantle is required.

Combining the geometry of underplating with Bouguer anomaly data, localized densification of the Indian lower crust is shown to occur where it reaches its maximal depth. This effect is associated to eclogitization. Investigations of the thermal field and pressure–temperature–density relations assuming different hydration levels are performed using thermo-kinematic and petrological models, respectively. The results suggest that the Indian lower crust is partially hydrated, and that eclogitization is kinetically hindered compared to phase equilibria. Overstepping is explained by the absence of free water in the system, and subsists until dehydration reactions occur at higher P-T conditions.

In conclusion, constraints on geometry and internal properties, as well as evaluation of the importance of physical processes are necessary in order to better understand the build-up of the observed lithospheric structures and the evolution of their deformation.

Résumé

L'Himalaya et le Plateau Tibétain sont considérés comme l'exemple classique de collision continentale. Cependant, de nombreuses questions fondamentales sur la structure, la rhéologie et les processus physiques liés à l'évolution de la lithosphère de cette région restent ouvertes.

Dans le cadre de l'expérience sismologique Hi-CLIMB, un grand nombre de stations large-bande (255) a été déployé pendant trois ans sur un profil de 800 km, à travers l'Himalaya et la moitié sud du Plateau Tibétain. L'espacement serré des stations ($\sim$4-9 km), la quantité importante des données (1.5 téraoctets), et l'utilisation de méthodes comme les fonctions récepteurs haute-fréquence ainsi que les conversions multiples ont permis d'obtenir une image détaillée des structures lithosphériques à toute échelle. Ces images permettent un suivi: (1) des failles à faible profondeur ($\sim$3-4 km); (2) du chevauchement majeur (MHT) de sa partie superficielle jusqu'à sa continuité profonde et ductile; (3) des zones à vitesses lentes localisées et peu profondes ("bright spots") sous le Tibet en corrélation avec des grabens; (4) de la croûte inférieure indienne sous-plaquée au bloc Lhasa. De plus, nos résultats suggèrent que (5) la lithosphère inférieure indienne avance vers le nord jusqu'au centre du Plateau Tibétain, où elle est opposée au manteau lithosphérique de l'Eurasie; que (6) les sutures en surface n'ont pas de signature marquée en profondeur; et que (7) les discontinuités du manteau supérieur à 410 et 670 km ne sont pas affectées par l'orogenèse. Les informations obtenues sur les géométries sont ensuite utilisées dans deux applications.

La rhéologie de la plaque Inde est réévaluée en utilisant l'image améliorée de sa flexure sous le bassin avant-arc. Les résultats des modélisations thermomécaniques montrent que l'épaisseur élastique équivalente diminue du sud au nord dû au découplage lié à l'affaiblissement flexural et thermique. Le support de la topographie du Plateau Tibétain ainsi que l'isostasie régionale en Himalaya nécessitent un manteau résistant.

En combinant la géométrie du sous-plaquage avec des anomalies de Bouguer, une densification localisée de la croûte inférieure indienne est mise en évidence à l'endroit où elle atteint sa profondeur maximale. Cette densification est associée à l'éclogitisation. Des analyses du champ thermique et les relations pression–température–densité en supposant différents niveaux d'hydratation sont effectuées par des modélisations thermo-cinématiques et pétrologiques. Les résultats suggèrent que la croûte inférieure indienne est partiellement hydratée, et que l'éclogitisation subit un retard. Ce dernier effet est expliqué par l'absence d'eau libre dans le système, l'éclogitisation n'ayant pas lieu jusqu'à l'occurrence des réactions de déshydratation à des P-T plus élevées que les conditions d'équilibre.

En conclusion, cette thèse apporte de nouvelles contraintes sur la géométrie et les propriétés internes de la lithosphère, éléments clés pour mieux évaluer l'importance des différents processus physiques impliqués dans la mise en place des structures et l'évolution de la déformation en Himalaya-Tibet.

Összefoglaló

A Himalája és a Tibeti fennsík a kontinentális kollízió klasszikus példája, mégis több, ezzel kapcsolatos alapvető kérdéskör, úgy mint például a litoszféra szerkezete, reológiája, és deformációjának fejlődését befolyásoló fizikai folyamatok a mai napig vita tárgyai.

A Hi-CLIMB szeizmológiai kísérlet nagyszámú (255) szélessávú állomást helyezett el egy 800 km hosszú, 85°K mentén futó profilon, a Himaláján és a Tibeti fennsík déli részén keresztül. A sűrűn (∼4-9 km) kihelyezett állomások, a három év alatt gyűjtött nagy mennyiségű adat (1.5 terabájt), a magasfrekvenciás vevőfüggvények és a többszörösen átalakult hullámok lehetővé tették, hogy részletes képet nyerjünk a litoszféra kis- és nagyléptékű szerkezetéről. Ezek megmutatták: (1) felszínközeli (∼3-4 km) vetők helyzetét; (2) a Main Himalayan Thrust-öt, annak sekély részétől a mélyebb, képlékeny folytatásáig; (3) sekély, elszigetelt, alacsony sebességű zónák (ún. "bright spot"-ok) jelenlétét és extenziós medencékkel való összefüggésüket Tibetben; továbbá (4) hogy az indiai alsó kéreg Tibet déli része (a Lhasa blokk) alá lapul. Az eredmények továbbá arra utalnak, (5) hogy az indiai alsó litoszféra észak felé a Tibeti fennsík közepéig terjed, ahol is az eurázsiai köpeny-litoszférának feszül; (6) hogy a felszíni szuturák a mélyben nem észlelhetők; és (7) hogy a hegységképződés nincs hatással a felső köpenybeli diszkontinuitások (410 és 670 km) szerkezetére. A kimutatott szerkezeti formákat a továbbiakban két alkalmazásban hasznosítjuk.

Az előtéri medence alatt lehajló India lemez alakja alapján újraértékeljük ez utóbbi reológiáját. Termomechanikus modelleredmények szerint a csatolás a hajlítás és a növekvő hőmérséklet miatti meggyengülés következtében megszűnik, ezért az effektív elasztikus vastagság délről északra lecsökken. A Tibeti fennsík fenntartásához és a Himalájabeli regionális izosztáziához feltétlen szükséges a köpeny hosszútávú (tartó)ereje.

Az indiai alsó kéreg Tibet alá lapulásának alakját Bouguer anomália modellezéssel kiegészítve megállapítjuk, hogy az alsó kéreg legnagyobb mélységét elérve gyors sűrűség-növekedésen megy keresztül. Ezt a jelenséget eklogitizációként értelmezzük. Termo-kinematikai és kőzettani modelleket felhasználva feltérképezzük a hőmérsékleti teret, továbbá a különböző víztartalommal számolt nyomás–hőmérséklet–sűrűség összefüggéseket. Ezen számítások alapján arra lehet következtetni, hogy az indiai alsó kéreg részlegesen hidratált, és hogy az egyensúlyi viszonyokhoz képest az eklogitizáció kinetikailag késik. Ez a túllépés szabad vizet nem tartalmazó reakciókkal magyarázható. A jelenség addig áll fenn, amíg magasabb P-T körülmények mellett nem lépnek fel dehidratációs reakciók.

Végeredményben elmondható, hogy a szerkezeti formák és a belső tulajdonságok, valamint a fizikai folyamatok fontosságának feltérképezése alapvető feltétele annak, hogy megértsük a megfigyelt litoszférikus szerkezetek kialakulását és deformációjuk evolúcióját.

Remerciements / Acknowledgements / Köszönetnyilvánítások

Contents

Résumé étendu en français

"Le Tibet a toujours été un endroit mystérieux. Au 19ème siècle, des explorateurs aux yeux écarquillés ont décrit la région avec innocence (...) Outres les fortes variations de densité de population, liée à l'immensité de ce territoire, l'isolement des Tibétains est associé à la culture même de ces peuples (...) En conséquence nous avons très peu appris sur les caractéristiques géologiques élémentaires de cette région remarquable, et la plupart des tentatives de ces dernières années — ayant pour objectif de relier la structure tectonique du Tibet (et du reste de l'Asie Centrale) à la collision tectonique entre la péninsule indienne et l'Asie — se sont basées sur des déductions parfois hasardeuses faites à partir des objets topographiques."

C'est avec ces phrases que John Maddox, éditeur de la revue *Nature*[1], a présenté la série d'articles parue en 1984 concernant les premières expériences géophysiques au Tibet, menées dans le cadre d'une collaboration sino-française. Cette présentation est toujours d'actualité: la fascination pour cette région se nourrit toujours des récits des explorateurs et de vifs débats scientifiques. Mener des expériences géophysiques au Tibet reste difficile, c'est pourtant une des clés pour mieux comprendre les mécanismes actifs lors d'une orogenèse. Ma thèse s'inscrit dans ce contexte: après une présentation de l'état des connaissances au 19ème siècle, et un résumé des avancées faites principalement depuis l'avènement de la tectonique des plaques, je présente les outils et méthodes déployés pour améliorer l'image de la structure lithosphérique, ainsi que les implications concernant les processus physiques associés à l'orogenèse himalayenne et à l'évolution de la déformation.

---

[1]Nature, Vol. 307, 5 Janvier 1984, page 9.

Des explorateurs à la tectonique des plaques

L'arc Himalayen et le Plateau Tibétain ont toujours été un lieu de fascination, de crainte, et de mystère pour l'homme. Depuis des siècles, les habitants de ces régions associent les sommets inaccessibles à des dieux bouddhistes et hindous. Ils partent pour leurs pèlerinages à travers le Tibet afin d'effectuer le tour du Mont Kailash. Plus récemment, les visiteurs du monde occidental ont été attirés pour d'autres motifs, parfois louables: la curiosité de découvrir et mieux connaître cette région, ses religions, ses langues, son histoire, sa géologie; parfois peu avouable: la volonté d'imposer leur religion, et d'asseoir d'avantage le pouvoir de leurs gouvernements.

Figure 1: Lajos Lóczy (left) and Émile Argand (right)

Les explorateurs du passé, comme ceux du présent, devaient faire face à de nombreuses difficultés. Un défi que certains n'ont pas hésité à affronter à plusieurs reprises, parfois au péril de leur vie. Leurs expériences est présentée en Chapitre 1. La diversité des témoignages permet d'imaginer leur vision du Tibet il y a ~100-150 ans. Je me suis ensuite plus particulièrement attardé sur deux personnes dont les travaux ont marqué un tournant dans la compréhension de la géologie du Plateau Tibétain et de ses bordures. Mon premier choix s'est porté sur un compatriote, Lajos (von) LÓCZY. Ce choix est lié en partie au fait que ses travaux sont peu connus car difficilement accessibles, mais aussi car ceux-ci ont eu une portée importante, notamment concernant l'inversion du métamorphisme au Népal, la structure en nappe de l'avant-pays himalayen, l'existence d'une chaîne Transhimalayenne, et la géologie de la bordure est du plateau. Mon second choix est Émile ARGAND, auteur de *La tectonique de l'Asie*, qui représente pour moi l'ouvrage marquant le passage de la géologie traditionelle aux sciences de la Terre modernes. Bien qu'Émile Argand n'ait jamais mis les pieds au Tibet, et bien qu'il n'ait eu accès qu'à des observations géologiques (et pas géophysiques au sens propre du terme), sa manière d'interpréter les déformations dans un cadre physique a initié la façon dont nous travaillons encore aujourd'hui pour comprendre la géodynamique de cette région. J'ai choisi de résumer ses travaux sur *La tectonique de l'Asie* car plusieurs idées, comme la notion de sous-plaquage, m'ont paru intéressantes, notamment en comparaison avec les débats actuels sur la structure et le régime de déformation dans la région Himalaya-Tibet.

Himalaya-Tibet: vers une image plus fine des structures lithosphériques

Les idées d'Émile Argand n'ont trouvé un écho que bien après leurs parutions: suite à l'avènement de la tectonique des plaques. À partir de ce moment là, c'est un nouveau chapitre qui s'est ouvert en sciences de la Terre, qui a conduit à l'état actuel de nos connaissances sur cette région. Les grandes lignes de la géodynamique du sud-Tibet sont aujourd'hui bien connues, mais certains passages font l'objet d'âpres discussions, sans cesse alimentées par de nouvelles données. Mon Chapitre 2 résume ce "livre ouvert" de la collision Inde-Asie, en abordant:

- les informations bien contraintes, comme la trajectoire de l'Inde avant collision;

- les estimations plus incertaines, comme la quantité de raccourcissement depuis la phase de collision, ou l'évolution du soulèvement dans le temps;

- les thèmes débattus, comme le mécanisme prépondérant dans l'accommodation de la déformation (diffuse ou localisée?), l'évolution géodynamique du plateau (subduction? Épaississement diffus? Écoulement canalisé? Sous-plaquage?), ou la quantité et la nature des fluides dans la croûte (fusion partielle étendue dans la croûte? Fluides aqueux ou magmatiques sous les "points brillants"?).

(a) Subduction   (b) Épaississement diffus   (c) Écoulement canalisé   (d) Sous-plaquage
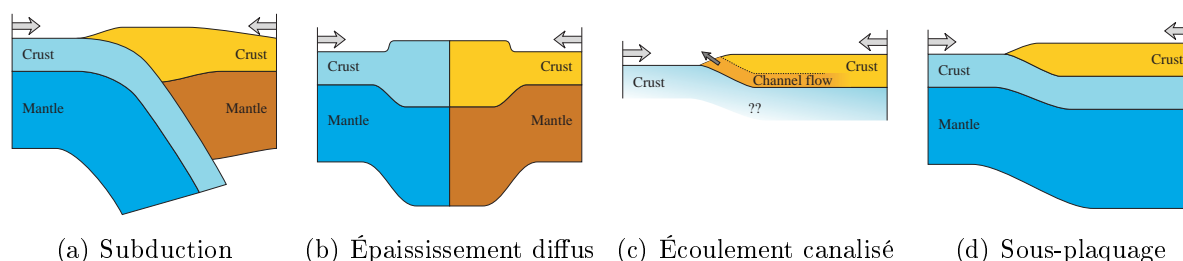
Figure 2: Représentation schématique des quatre principaux mécanismes expliquant la formation d'un plateau.

Cette présentation est basée sur les outils (notamment géophysiques) qui sont utilisés pour déduire ces informations. La représentation du domaine d'investigation dans un espace *temps–échelle spatiale–profondeur* de chacune des méthodes permet de mettre en avant le manque d'information dont nous disposons en profondeur, ce qui conduit à des images parcellaires et floues des structures lithosphériques.

Un des principal objectifs de cette thèse est d'améliorer l'imagerie de ces structures, basé sur l'analyse conjointe de nouvelles données sismologiques, de mesures gravimétriques existantes, et le développement de modèles numériques.

DATA – <u>D</u>onnées: <u>A</u>cquisition, <u>T</u>raitement et <u>A</u>ssimilation

La qualité d'une image dépend principalement de deux facteurs: la qualité des données, et un traitement approprié.

Les nouvelles données sur lesquelles se base cette thèse sont les données sismologiques large-bande, acquises dans le cadre de l'expérience internationale Hi-CLIMB. Pendant trois ans, 255 sites, équipés de sismomètres large-bande trois composantes et fonctionnant en acquisition continue, ont été installés tous les 4 à 9 km à travers le Népal et la moitié sud du Tibet. Plus de 1.5 téraoctets de donnée brutes ont été acquis. Afin de ne sélectionner que les données pertinentes pour un traitement par la méthode des fonctions récepteurs, outil principal utilisé tout au long de cette thèse, une suite de procédures de contrôle qualité ont été mises en place et calibrées. Le traitement en fonction récepteur est ensuite détaillé, aussi bien du point de vue théorique que pratique, à travers le choix de la méthode de déconvolution (itérative ou fréquentielle), des fréquences de coupure des filtres ou des paramètres de la migration, éléments influençant la qualité de l'image finale.

L'analyse des fonctions récepteurs est présentée sous plusieurs aspects dont:

– l'usage des conversions d'onde multiples lors de l'étape de migration, permettant de construire un modèle de vitesse 2-D, mais aussi de mieux cerner les phénomènes d'interférence, et comment ils affectent les images déduites des migrations;

– l'utilisation de la composante tangentielle des fonctions récepteurs, principalement dans le cadre de la détermination du pendage des interfaces;

– l'inversion des fonctions récepteurs, qui, bien que peu robuste pour déduire des vitesses absolues, permet quand même de préciser des variations de vitesse relatives aux interfaces;

– des questions relatives à la représentation d'image, comme l'influence du lissage horizontal et l'apport de la sommation non-linéaire.

Le deuxième type de données utilisé dans cette thèse est constitué d'une compilation de mesures d'anomalies de Bouguer couvrant tout le Plateau Tibétain. La construction de ce jeu de données est détaillée dans le Chapitre 3. La modélisation de ces anomalies est abordée notamment à travers quelques points théoriques et pratiques résumant des principes à respecter. Pour faciliter cette modélisation, un logiciel bénéficiant d'une interface graphique et interactive permettant de gérer les géométries et les différents paramètres du modèle a été développé au cours de cette thèse.
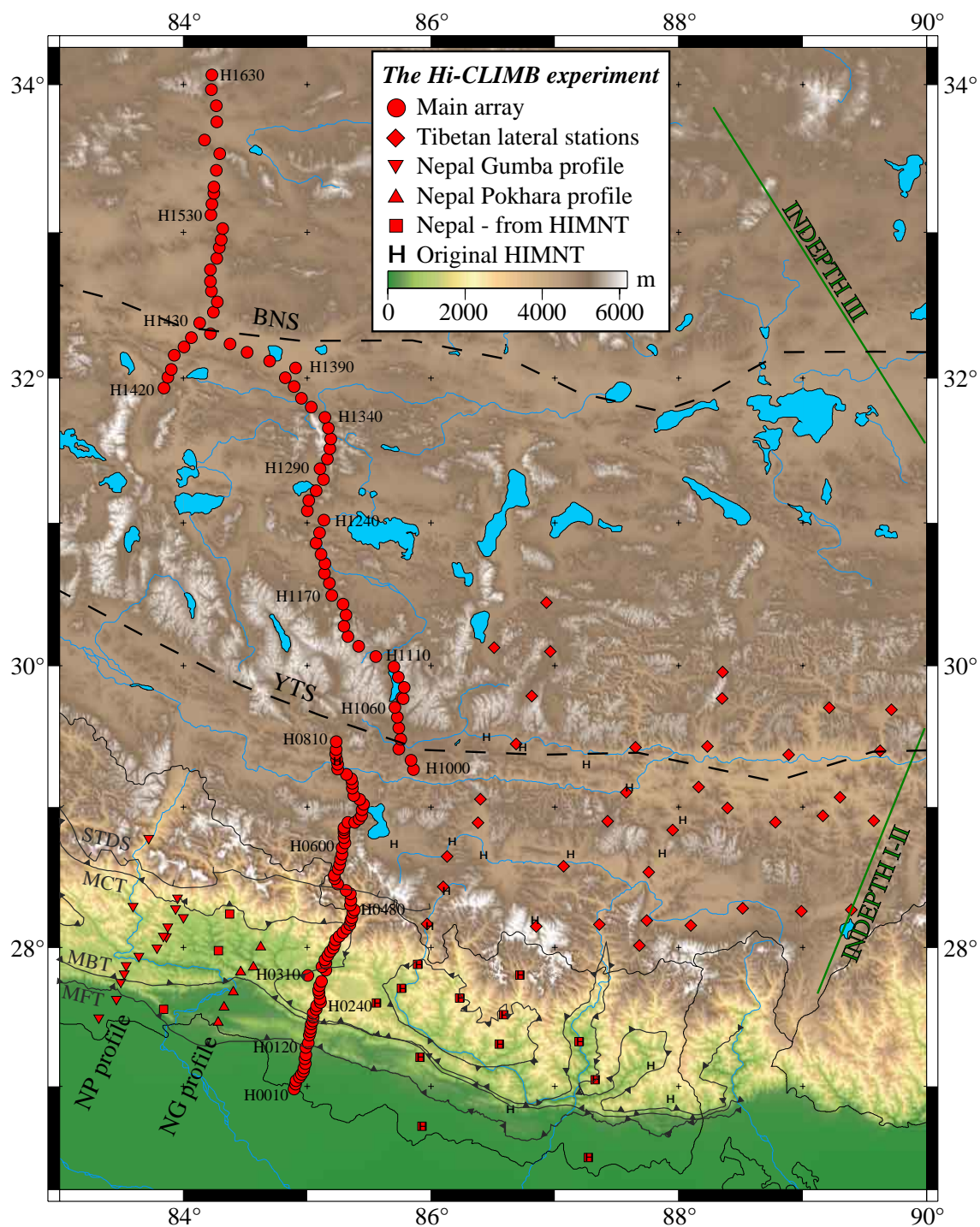
Figure 3: Stations de l'expérience Hi-CLIMB (symboles rouge), ainsi que la position d'autres expériences dans la région. Les sutures majeures sont celle de Yarlung Tsangpo (YTS) et de Banggong-Nujiang (BNS).
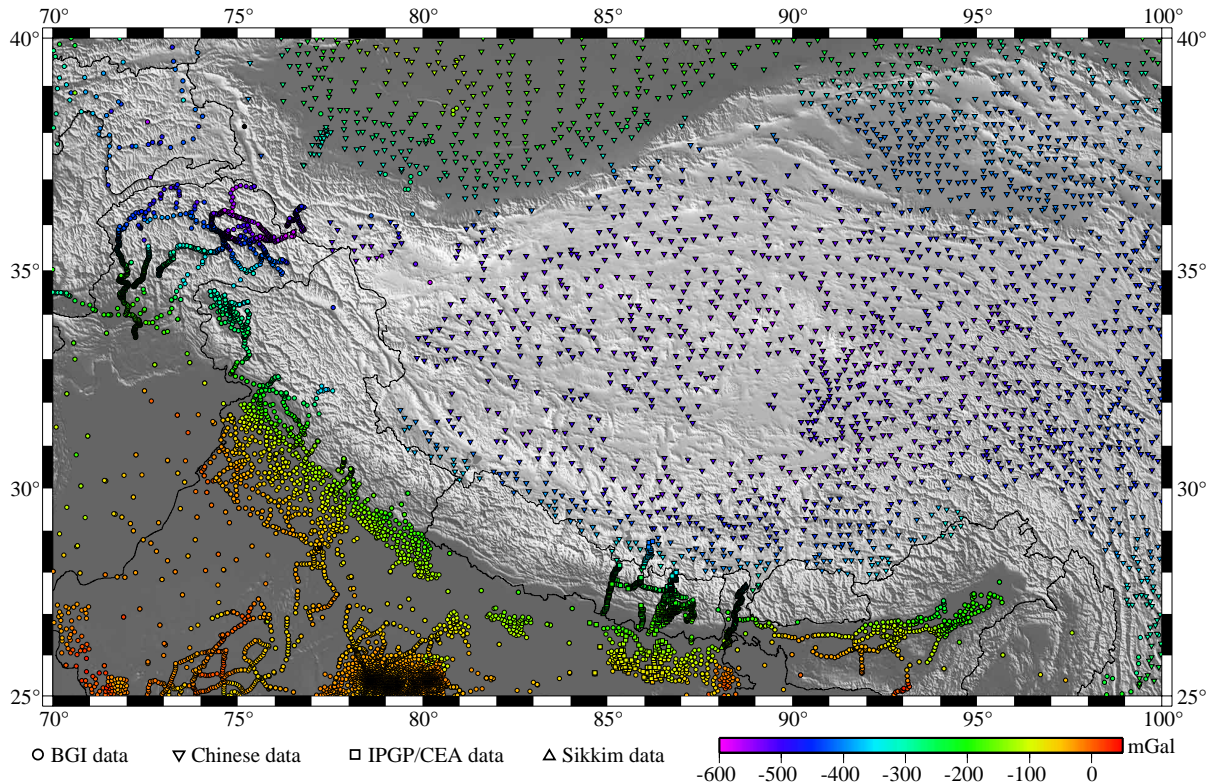
Figure 4: Données d'anomalie de Bouguer dans la région de l'Himalaya-Tibet.

Structures et fluides crustaux

Le Chapitre 4 étudie les structures de la croûte supérieure en allant des objets les plus petits et les plus superficiels vers les objets de plus grande taille, *via* une analyse des fonctions récepteurs à des fréquences décroissantes.

La première partie se focalise sur les premiers kilomètres, soit la gamme de profondeurs classiquement étudiée par la sismique réflexion. L'un des objectifs est l'imagerie fine de la structure interne du bassin flexural d'avant-arc associé au bassin du Gange. À l'aide de dix stations et d'inversions non-linéaires de fonctions récepteurs haute fréquence (∼2 Hz), la base du bassin est observée entre 4,5 et 5 km de profondeur. Sa structure interne fait apparaître un gradient de vitesse dans les séries sédimentaires Néogènes surmontées par une couche fine de quelques centaines de mètres d'alluvions récents présentant des vitesses extrêmement faibles. Au nord de ce bassin débutent les chevauchements liés à la déformation de l'avant-pays népalais. En analysant la variabilité des fonctions récepteurs en fonction de l'azimut d'arrivée des séismes, nous avons pu définir la localisation des failles chevauchantes dans les premiers kilomètres sous la surface. Le chevauchement

frontal (Main Frontal Thrust, MFT) a été imagé et modélisé plus en détail: son pendage de $\sim 25°$ à 3 km de profondeur, plus faible que son pendage en surface estimé par des études géologiques, suggère une géométrie listrique, et son enracinement sur le chevauchement majeur (Main Himalayan Thrust, MHT).

La deuxième partie vise à mieux contraindre la géométrie du MHT le long du profil principal Hi-CLIMB. Dans cette étude, la migration des fonctions récepteurs est complétée par une tomographie basée sur la corrélation de bruit ambiant entre couples de stations. Deux zones à vitesses lentes sont mises en évidence par ces deux méthodes: la première (LVZ1), sous le moyen-pays népalais, est presque parfaitement horizontale et se situe à 10 km de profondeur; la deuxième (LVZ2), située sous le Haut Himalaya est localisée vers 35 km de profondeur et présente un pendage important vers le nord. Cette géométrie est en accord avec la position du MHT proposée *via* d'autres approches. L'inversion conjointe des deux jeux de données contraint la diminution de vitesse au toit de la LVZ1 à plus de 20%. Ces deux zones à vitesse réduite, ainsi que les contraintes apportés par les observations magnétotelluriques et les modélisations thermo-cinématiques, sont interprétées en termes d'accumulation de fluides: aqueux au niveau du LVZ1, associés à la déshydratation des sédiments lors des réactions métamorphiques de bas degré; et magmatique (fusion partielle) au niveau du LVZ2. Ainsi le MHT est imagé de manière indirecte sur deux segments où deux types de fluides sont piégés au niveau de ce décollement. Des images produites sous les stations situées en dehors du profil principal révèlent d'autre part que la géométrie et les caractéristiques du MHT et de l'interface croûte-manteau, présentent des variations latérales non négligeables.

La troisième partie aborde le problème des fluides au niveau de la croûte Tibétaine, notamment en regard des points brillants ("bright spots") observés durant l'expérience INDEPTH et interprétés comme marquant le toit de zones à vitesse réduite. De telles zones sont bien observées le long de la partie tibétaine du profil Hi-CLIMB et présentent une signature similaire à celle de la zone à faible vitesse imagée sous le moyen pays himalayen. L'analyse des stations latérales indique que la position structurale de ces zones à faible vitesse est corrélée avec celle des grabens en extension, impliquant qu'elles n'occupent pas une surface significative sous le plateau et suggérant qu'elles sont la conséquence de processus de rifting à petite échelle. L'épaisseur de ces zones à faible vitesse est de l'ordre de quelques kilomètres seulement, et elles ne marquent pas le toit d'une croûte tibétaine partiellement fondue comme l'indique les valeurs peu élevées du rapport V_P/V_S moyen de la croûte tibétaine obtenu. La détermination des variations de ce rapport le long du profil principal permet d'autre part d'établir un modèle de vitesse à 2 dimensions et ainsi d'améliorer les migration à l'échelle lithosphérique.
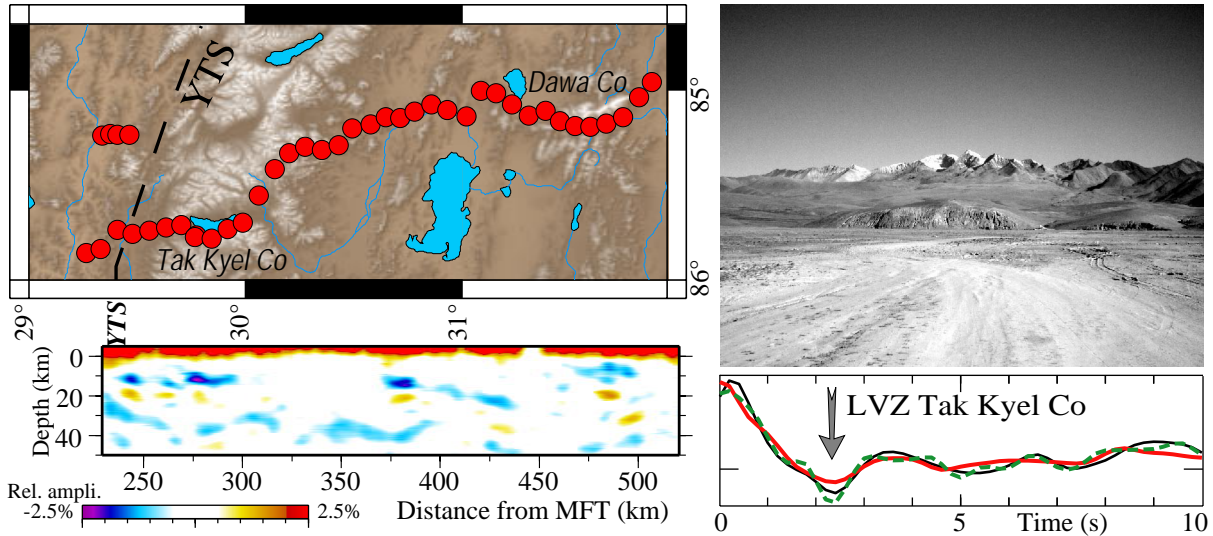
Figure 5: Brights spots et grabens: vue en carte, profil migré, sur le terrain, et par inversion des fonctions récepteurs.

Structures lithosphériques: jusqu'où l'Inde avance-t-elle sous le Tibet?

Le Chapitre 5 discute les structures à l'échelle lithosphérique, et en premier lieu la limite croûte-manteau. En utilisant les conversions multiples, et en étudiant les interactions possibles avec les conversions PS directes, une nouvelle image est produite. Elle permet de clarifier les ambiguïtés et interférences présentes sur l'image migrée obtenue uniquement à partir des phases PS directes. Ainsi l'interprétation devient plus aisée: le Moho se dessine à 40 km de profondeur sous le bassin du Gange, et s'approfondit sous le haut Himalaya, pour atteindre une profondeur maximale de ∼73 km au niveau de la suture du Yarlung Tsangpo (YTS). Même si la structure interne de la croûte se complexifie à ce niveau, cette suture ne semble pas affecter le Moho qui est imagé à une profondeur quasi-constante sur ∼200 km sous le bloc Lhasa. À ∼100 km au sud de la suture de Banggong-Nujiang (BNS), le signal du Moho s'affaiblit puis cette interface réapparaît plus nettement sous le bloc Qiangtang à une profondeur plus faible d'environ 10 km.

L'autre caractéristique majeure de l'image réside dans la présence d'une interface parallèle au Moho à une profondeur de ∼58 km sous le bloc Lhasa. La continuité de ces deux interfaces, l'épaisseur de ∼15 km de la couche qu'elles délimitent et l'amplitude des conversions associées sont autant d'argument permettant de suggérer que la croûte inférieure indienne est sous-plaquée sur plus de 200 km de distance horizontale sous le sud-Tibet, et qu'elle est soumis à des processus d'éclogitisation. La terminaison nord de ces deux interfaces — Moho et toit de la croûte inférieure indienne — se situe à ∼450 km au nord du

front de déformation actuel. Cette valeur est donc la borne inférieure de la pénétration de la lithosphère indienne sous l'Eurasie. Le découplage entre la croûte tibétaine et la croûte inférieure indienne sous-plaquée s'effectue le long de la partie profonde du MHT qui est matérialisée par une zone à faible vitesse observée de manière continue au-dessus de la croûte inférieure indienne.
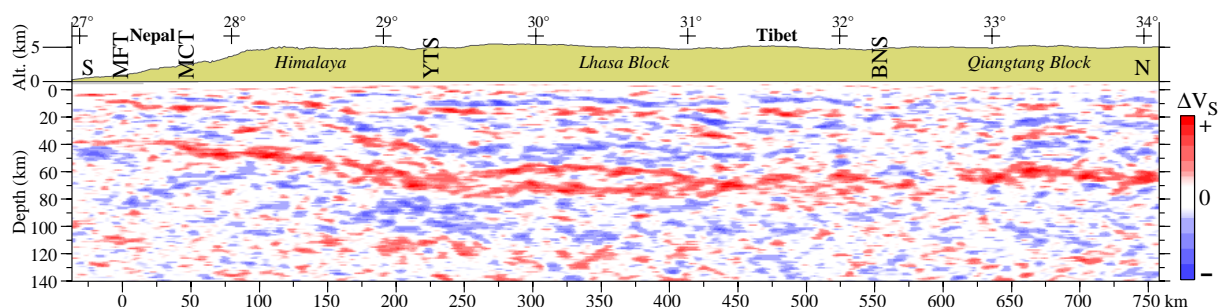
Figure 6: Sommation non-linéaire de trois migrations de fonctions récepteurs selon les phases converties directe et multiples.

L'absence d'un contraste marqué entre croûte et manteau plus au nord, dans la zone de la BNS, est expliquée par la présence d'une limite lithosphérique majeure entre l'Inde et l'Eurasie dans cette zone. Les fonctions récepteurs ne sont pas adaptées à imager des structures sub-verticales et des contrastes d'impédance faibles, donc la continuité de deux plaques. Cependant, d'autres observations aboutissent à des conclusions similaires concernant le sous-plaquage et la limite des deux lithosphères :

- Cette limite marque un changement dans la polarisation des conversions autour du Moho. Cette interface présente en effet un caractère anisotrope sans doute causé par un empilement de lambeaux de croûte inférieure à vergence nord sous le bloc Lhasa et à vergence sud sous le bloc Qiangtang et résultant de la contrainte cisaillante appliquée.

- Cette limite est également associée à un changement de vergence des linéations pentées observées dans le manteau supérieur dont l'orientation est semblable à ce qui est observé au niveau du Moho. Ces linéations indiquent que le manteau subit une déformation complexe avec plusieurs niveaux de découplage internes, expliquant, pour la partie supérieure cassante du manteau, les séismes profonds qui y sont observés.

Replacé dans le contexte des modèles d'évolution de la collision Inde-Asie, nos résultats sont en faveur d'un scénario basé sur le sous-plaquage. Cependant, il apparaît que ce mécanisme n'a pas pu fonctionner depuis le début de la collision continentale, mais

plutôt seulement depuis le Miocène inférieur. Cette époque marque peut-être le passage d'un régime de subduction à un régime de sous-plaquage suite à une délamination lithosphérique. Le rebond induit par un tel phénomène aurait entraîné un réchauffement du géotherme, la génération des leucogranites himalayens et le volcanisme sud-tibétain.

Enfin, les discontinuités mantelliques à 410 et à 670 km de profondeur sont quasi-horizontales sous le profil principal, et ne semblent donc pas être perturbées par l'orogenèse et les déformations actuelles associées.

Est-ce que la lithosphère indienne supporte l'Himalaya et le Sud Tibet?

L'épaisseur élastique équivalente (EET) est une mesure de résistance d'une plaque à des contraintes, et notamment à la flexure. Les estimations de l'EET de la plaque Inde sont aujourd'hui très dispersées, variant entre 36 et 110 km. La raison principale d'une telle dispersion est liée à une connaissance des géométries en profondeur qui n'est pas suffisamment précise.

Dans le Chapitre 6[2], l'EET de la plaque Inde est estimée à partir des nouvelles contraintes sismologiques obtenues dans les Chapitres 4 et 5: le pendage de la plaque Inde sous le bassin du Gange ($<1°$); l'épaisseur de la croûte indienne (35 km); ainsi que la profondeur du Moho sous le Tibet. Cette géométrie est complétée par des contraintes apportés par un forage, et des profils de sismique réflexion. L'utilisation de cette géométrie et la confrontation des résultats des modèles thermomécaniques aux données gravimétriques permettent d'aboutir à plusieurs conclusions:

- dû à des effets d'affaiblissement flexural et thermique, l'épaisseur élastique équivalente de la plaque Inde diminue fortement du sud au nord pendant sa descente sous l'Himalaya et le Tibet, où elle atteint $\sim$20-30 km;

- le seul niveau résistant de la lithosphère indienne sous le sud-Tibet est le manteau supérieur;

- le changement d'EET le plus abrupt est localisé $\sim$200 km au sud du front de déformation (le MFT), et il est associé au découplage progressif de la croûte et du manteau.

Nos résultats montrent clairement que des rhéologies avec un manteau peu résistant n'expliquent pas la géométrie des structures lithosphériques observées, et sont au contraire

---

en faveur des modèles rhéologiques dans lesquelles le manteau est résistant. Cependant, les contraintes géométriques actuelles ne permettent pas de déterminer si les croûtes supérieure et inférieure sont couplées ou découplées.
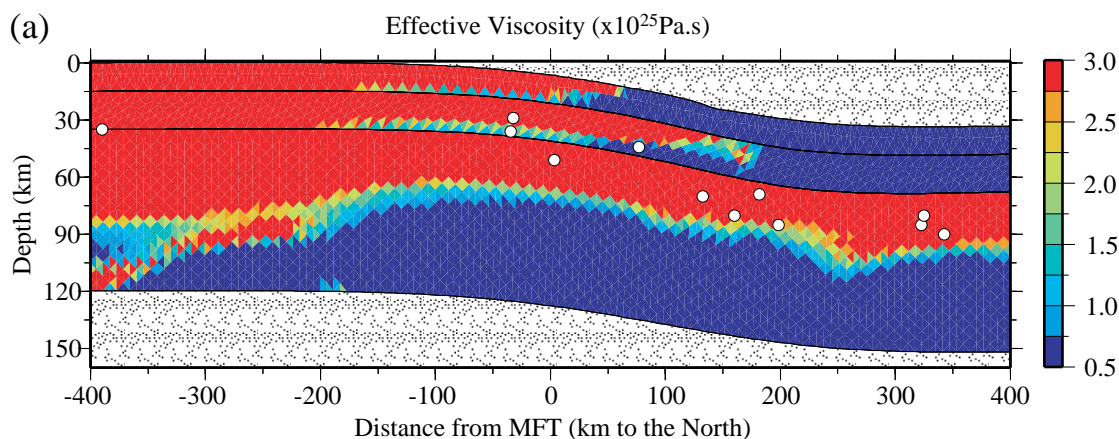
Figure 7: Profil de viscosité équivalente de la plaque Inde sous le poids de la croûte Tibétaine.

Rôle de l'eau dans les transformations minéralogiques dans la croûte inférieure

Dans le Chapitre 7[3], nous étudions les variations latérales des structures crustales sur la bordure sud du Plateau Tibétain, en compilant des données sismologiques de trois expériences (Hi-CLIMB, HIMNT, INDEPTH), ainsi que des données d'anomalie de Bouguer. La comparaison des profils suggère des variations latérales dans la pente et la localisation de la descente de la base de croûte indienne, mais peu de variations dans la profondeur maximale sous le Tibet. Un calcul simple montre que l'isostasie de type Airy ne peut pas être vérifiée, et que la présence d'une croûte inférieure plus dense sous le plateau Tibétain est nécessaire. Des modèles de densité multicouche révèlent que l'essentielle de la densification de la croûte inférieure doit être localisée à l'endroit où celle-ci atteint sa profondeur maximale.

Dans un second temps, l'utilisation de grilles pétrogénétiques (température–pression–densité) permet d'apporter de nouvelles contraintes sur les processus responsables de cette densification. En testant différents hypothèses sur le contenu en eau (sec, partiellement hydraté, ou saturé), nous obtenons des modèles de densité dont les anomalies de Bouguer

---

[3]Basé sur le papier: Hetényi, G., Cattin, R., Brunet, F., Bollinger, L., Vergne, J., Nábělek, J. L. et Diament, M. (2007). Density distribution of the India plate beneath the Tibetan Plateau: geophysical and petrological constraints on the kinetics of lower-crustal eclogitization. *Earth Planet. Sci. Lett.*, **264**, 226–244. doi: 10.1016/j.epsl.2007.09.036

associées sont confrontées aux observations. Nos résultats suggèrent que la distribution de densité dans la croûte inférieure soit associé à une composition mafique et partiellement hydratée (ca. 1 wt.% H$_2$O), dans laquelle le processus d'éclogitisation est retardé. Ce dernier effet n'est pas le ralentissement des cinétiques de réaction, mais un retard ("overstepping") des réactions métamorphiques dans lesquelles l'eau libre n'intervient pas, comme *albite* → *jadéite + quartz* dans notre cas. Le système peut rester hors équilibre jusqu'à atteindre des réactions de déshydratation, où le processus d'éclogitisation et donc de densification de la croûte inférieure se déroule rapidement. Ces résultats mettent en avant l'importance de l'eau libre dans des réactions métamorphiques, et, en conséquence, dans des processus géodynamiques.
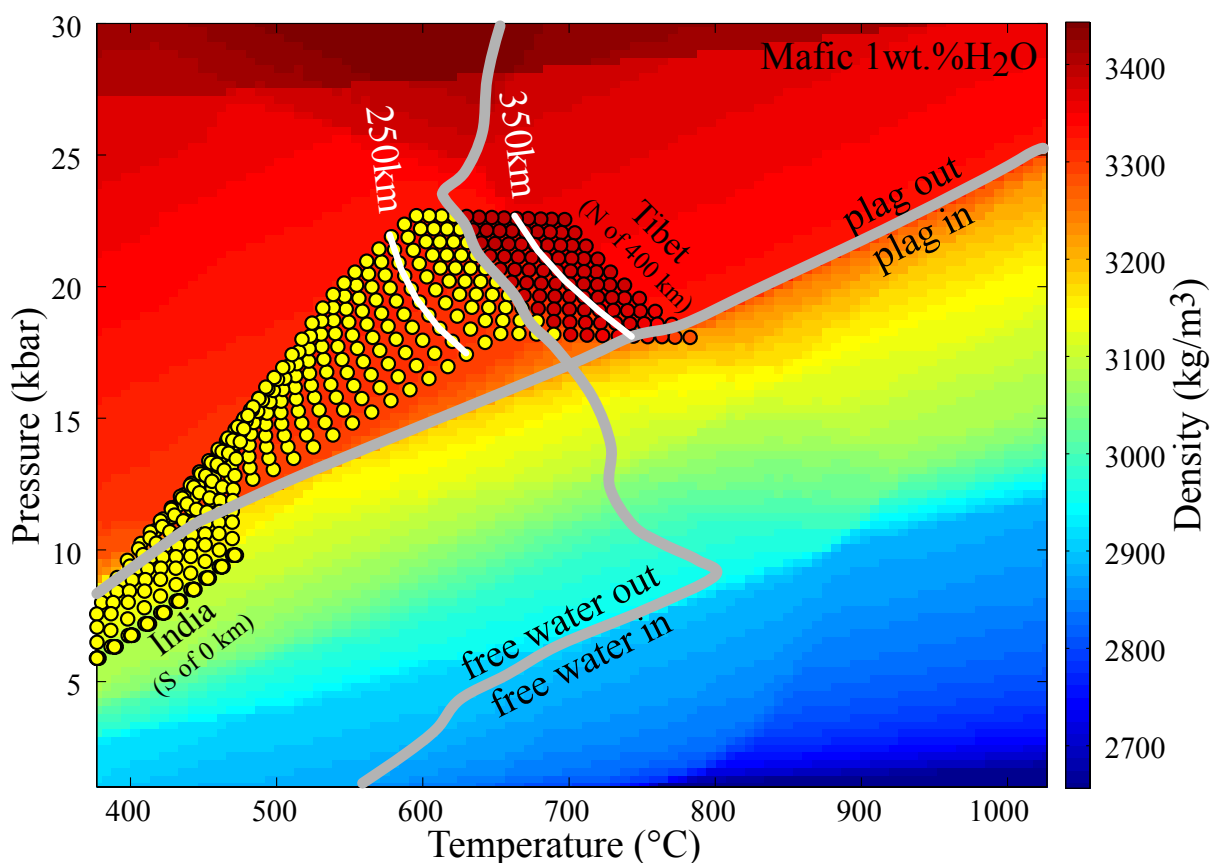
Figure 8: *Grille de densité pour une croûte inférieure de composition mafique et avec 1 wt.% d'eau. Les lignes grises délimitent le champ de stabilité des plagioclases et de l'eau libre dans le système, respectivement. Les points représentent la distribution des conditions P-T et de la densité dans la croûte inférieure indienne qui subit un retard à l'éclogitisation et donc à la densification.*

Études en cours et perspectives

Vers une meilleure prise en compte des variations de densité dans les modèles numériques. À la jonction des deux chapitres précédents, les études en cours créent un lien entre modélisation numérique et les changements de phases liés au métamorphisme. Actuellement, la relation entre ces deux approches n'est que partiellement implémentée dans les codes existants: la densité des éléments peut évoluer en fonction des faciès métamorphiques, mais d'un point de vue technique la densité des éléments varie indépendamment de leur volume, c'est-à-dire que les modèles ne respectent pas la conservation de la masse! Dans le type de modèle que nous développons (Chapitre 8), le but est d'appliquer des variations volumétriques correspondantes aux variations de densité. Pour réaliser ces variations, nous passons par la modification des contraintes internes du système. Les résultats préliminaires sur un modèle en raccourcissement avec une topographie pré-existante montrent que les changements de phase ont un rôle important dans l'évolution de la déformation: leur ampleur est comparable aux effets liés à l'érosion. Mais contrairement aux processus de surface, les changements de phase tentent à localiser la déformation à grande échelle.

Utilisation d'autres méthodes sismologiques. L'utilisation des fonctions récepteurs a permis d'obtenir une image détaillée des structures. Cependant, cette méthode n'est pas adaptée pour contraindre le champ de vitesse absolu. D'autres approches, comme la tomographie et les ondes de surface, ainsi que des inversions conjointes devraient être appliquées pour mieux contraindre les vitesses absolues en 2-D.

Variation gravimétrique et risque sismique. Song and Simons (2003) ont proposé d'utiliser les variations latérales de la topographie et des anomalies de gravité en zone de subduction pour évaluer le risque sismique. L'application de leur méthode à l'Himalaya est prometteuse. Cependant, tant que la couverture des données de gravimétrie reste incomplète, notamment dans l'ouest du Népal, le lien entre les variations latérales et le potentiel des séismes importants ne peut pas être discuté. Une mission gravimétriques de quelques semaines permettrait sans doute de finaliser cette étude.

Et à longue échéance... les variations latérales des structures à grande échelle, ainsi que les processus tridimensionnels (comme l'extrusion) ne peuvent pas être mieux contraints tant que les expériences géophysiques ont une couverture faible par rapport à la taille du Plateau Tibétain. Des efforts scientifiques et politiques doivent donc être poursuivis pour avancer vers une meilleure compréhension de l'évolution de la déformation de cette région.

Introduction

Why have the Himalayas and the Tibetan Plateau fascinated earthlings through history?

Prior to discussion of scientific themes, the first and most obvious answer is because of their prominent altitude. Since earliest times, inhabitants associated different Buddhist and Hindu Gods to the highest peaks, and thousands of pilgrims suffered across Tibet to walk or to crawl around Mount Kailash. In the past few centuries, numerous explorers from the western world attempted and succeeded in slowly discovering the vast surface of the plateau. In Chapter 1, I try to give an insight of what Tibet might resembled to some 100-150 years ago, and I choose to present two personalities in particular who make the connection between explorers and geoscientists. The first is LÓCZY, who has made valuable discoveries along the eastern border of the Tibetan Plateau: as accessing his results is difficult, I give a summary of his work concerning South-East Asia, and of his early findings on a few geological questions. The second person is ARGAND, who actually never put his feet in Tibet, but who compiled a great amount of information and addressed issues decades earlier than they became topical. Summarizing his thoughts on the evolution of the Himalaya-Tibet system (for example underplating) is particularly interesting in light of our current knowledge on deformation patterns.

As a result of centuries of investigations, first the topographic, then the geologic image of Tibet have crystallized, which are the surface expression of its history. On the contrarily, what interested people over the last four decades is what is *below* this vast region of high topography, and how it relates to the features observed at surface. This constitutes our above mentioned "current knowledge": principally those information that

were acquired with geophysical methods, and interpreted in the general frame of plate tectonics. In this context, the second answer to the above question is that the Himalaya-Tibet region fascinates people because it is found to be the most impressive example of continent-continent collision. Its first order and large scale characteristics are now well-known; however, several issues still remain controversial, especially concerning the structure and evolution of the lithosphere. Chapter 2 gives an overview of some of the accepted and debated topics, and shows that the a major reason of our incomplete knowledge is low data coverage, and a general decrease of resolution with depth.

In order to better understand the Himalaya-Tibet region, this thesis aims to focus the geophysical images and to improve their quality. Following the steps of a few predecessors, we can no further concentrate on topography or on large-scale processes alone. It is important to determine exactly what happens in front of, behind, and beneath the Himalayan Arc:

– What is the input to this collisional system? What are the structure, geometry and characteristics of the India plate south of the mountain range? What happens to it after passing beneath and beyond the orogen?

– Why and in what aspects the Tibetan Plateau is different from the Himalayas? Is the entire plateau homogeneous in terms of lithospheric structure? If not, where are the boundaries, and what characterizes the different blocks?

– What are the principal physical processes governing lithospheric evolution? How do they influence the support of topography? Are there fluids in the crust, and if yes, how much, where, and what kind? How does metamorphism influence orogeny and the evolution of deformation?

These are the main questions that motivate this work, and describe the interest and fascination of my directors, collaborators and myself concerning the Himalayas and the Tibetan Plateau.

Our observational and scientific tools in providing improved resolution images are primarily closely spaced, high-frequency and new seismological data from the Hi-CLIMB experiment, together with a compilation of gravity anomalies and numerical approaches. Chapter 3 overviews the different datasets, and details theoretical and practical aspects of the receiver function method. What is new in this work is that we use this same tool to obtain information throughout the lithosphere, from shallow and small features to deep interfaces and large scale processes. Shallow objects, such as faults and low-velocity zones are investigated in Chapter 4. The general image of the lithosphere is usually blurred by

interferences, but we use and benefit from multiple conversions that greatly clarify the picture (Chapter 5).

Then we take advantage of the seismological results and combine them with available datasets in numerical modelling studies. Chapter 6 analyzes the flexural behaviour of India, and aims to add new elements to the ongoing debate on the rheology of the lithosphere. Gravity anomalies provide complementary information on the interior of lithospheric units, and, using thermo-kinematic and petrological modelling, the role of metamorphic reactions and water content in the lower crust is investigated (Chapter 7). This way new seismological images of the lithosphere and insights into primary physical processes beneath the orogen are presented, which can be integrated into the evolutionary scenario of the India-Asia collision.
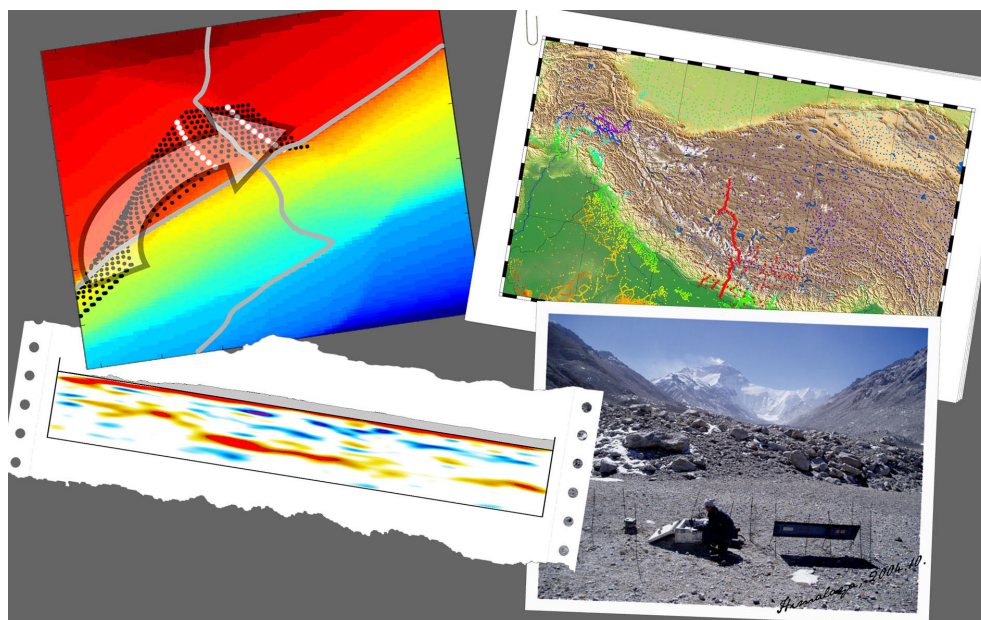
From explorers to plate tectonics

"During the classical exploration in the 19th and early 20th centuries, the ratio between facts and theories was 1:0.5. The application of plate tectonics to the Himalayas changed this ratio to 1:3 and with modern geophysics, including paleomagnetics, with geochemistry and detailed structural analysis, the ratio became 1:5."

A. Gansser, 1991

The exploration of the Himalayan-Tibetan region was a challenge in all historical times, and it still is today. Regardless of being a missionary in the Middle Ages, an explorer in the 19th century, or a scientific in the 21st, this region is different in many aspects from what the visitor is used to, including landscape, climate, customs (popular or religious), and every day life.

Preceding the scientific results of this thesis, this chapter commemorates a few Europeans related to Tibet from the late 19th and early 20th centuries, depicting their experiences. There was no intention to give an exhaustive list of all persons here, but rather to select those that have a particular link to the themes discussed later, or whose work is hardly accessible. The perspectives and findings — related to earth sciences or not, — are interesting to compare with what we know today: it gives an insight into some steps of the era where the above mentioned *"ratio between facts and theories"* evolved very much.

1.1   Some late explorers and early scientists

1.1.1   A non-exhaustive overview

As far as known, the first stranger to visit Tibet was Odoric de Pordenone, a Franciscan friar of a Czech family born in Italy. He left Europe in 1318, travelled to Asia by sea, visited most countries in South-East Asia, and returned to Europe by land, walking from Beijing to Constantinople. Unfortunately, he did not leave too much detail concerning his journey across Tibet.
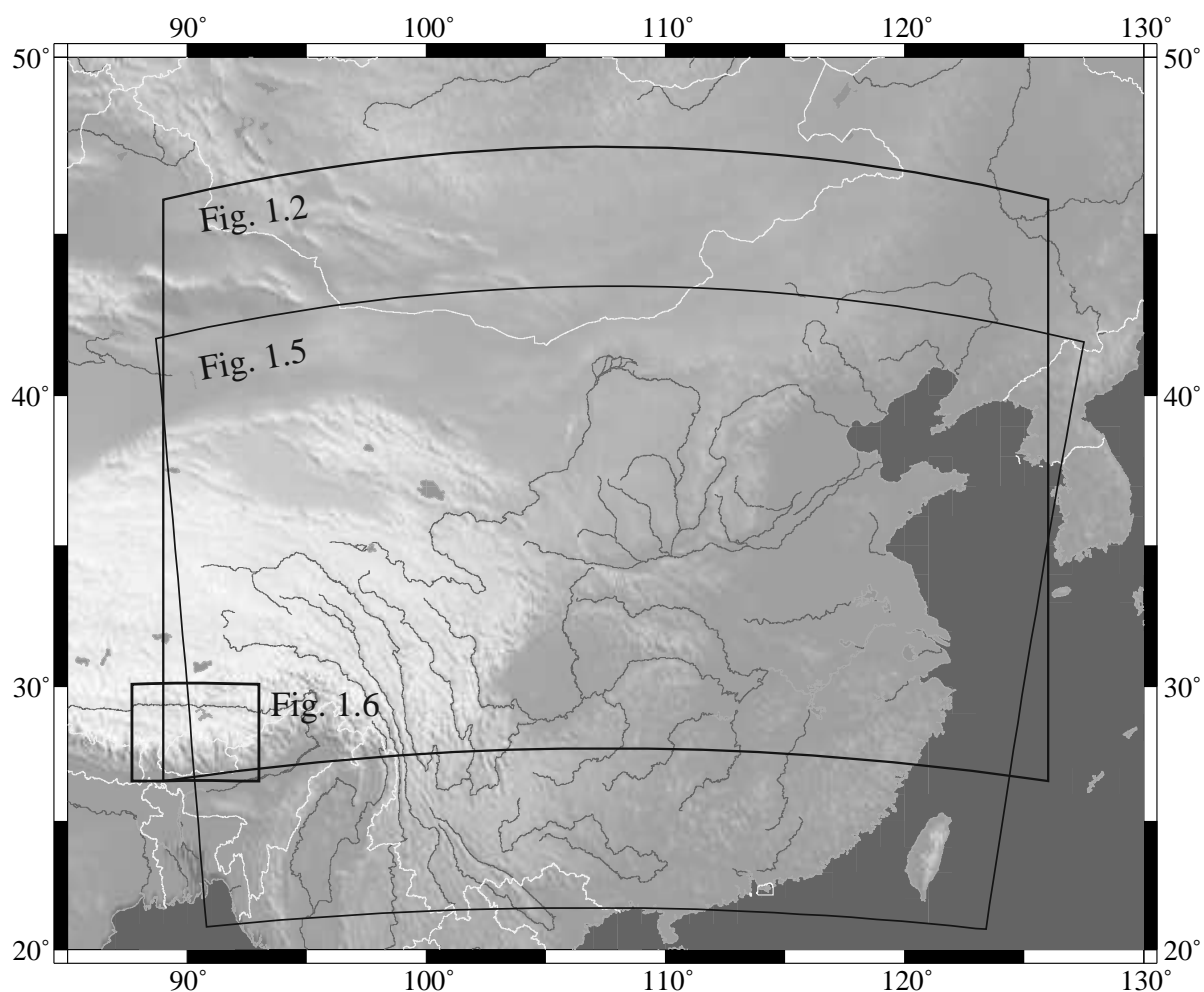
Figure 1.1: The approximate locations of the maps presented in this chapter

Several other missionaries and also some travellers followed him during the centuries, with religious convictions or other motivations. For example, Sándor (Alexander) Csoma de Kőrös from Transylvania, after several years of studies and with 13 spoken languages,

left in 1819 to the East in search for the origins of the Hungarian language and people. His long and lonely way brought him to the Zangla monastery in Zanskar, where he practically became and lived like a Buddhist monk. His growing knowledge of Tibetan language and culture resulted in several works, among them the founding pieces of Tibetology, and also *Essay towards a Dictionary Tibetan and English* and *A Grammar of the Tibetan Language in English*, two works that became classics and widely used. His original goal has changed and resulted in something different, but *"Csoma's glory is in that in pursuing a dream, he accomplished reality"* (W. W. Hunter). In 1842, he set his road toward Lhasa, but unfortunately died of malaria in Darjeeling, where his grave can still be visited.
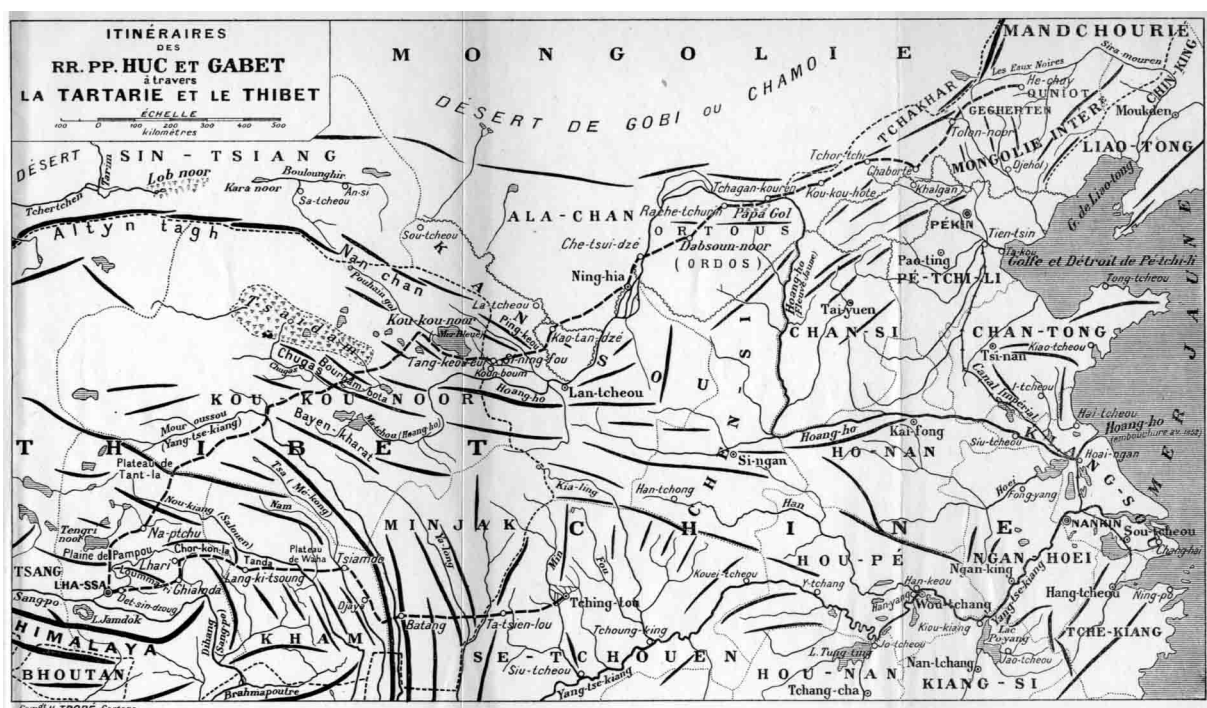
Figure 1.2: Huc's map showing their itinerary in dashed line, 1844-1846 (from Huc, 1854)

By this time, French Lazarist missionary friars Régis-Evariste Huc and Joseph Gabet were already on their long travel through Tartary, Tibet and China (Huc, 1854). Their journey in Tibet (Fig. 1.2) "began" with a several months rest in the Kun-bum (Kounboum) monastery, where they have had to wait the Chinese ambassador and its troop to join them on their way from Peking to Lhasa. It took about four months to reach the *"source of superstitions that dominate High Asia"* on foot (*i.e.* Lhasa). They passed near Kuku-Nor (Kou-kou-nor), Qaidam (Tsaïdam), across Bayan-Har (Bayan-Kharat), and arrived to the capital on the 29th of January 1846. They were probably the last people who reached Lhasa (Lha-Ssa) without facing diplomatic problems, but their welcome was ambivalent and

caused tensions between the Tibetan Regent and the head of the Chinese administration, the Amban. They were forced to leave Lhasa on the 15th of March 1846 towards the East, passing by Batang, Litang, Ta-tsien-lu, and leaving Tibet in June.

For many years afterwards, the exploration of Tibet was carried on by "pundits", disguised local people trained by the Indian Government who learned how to survey and draw maps, such as Nain-Singh or the mysterious "A—K".

To keep a chronological order, an important step in earth science history should be noted here. In 1855, royal astronomer George Biddell Airy published a short but pointed paper on the *"effect of the attraction of mountain masses"* (Airy, 1855), shortly after the much longer discussion of John

Figure 1.3: The way Pratt (left) and Airy (right) imagined isostasy (from Airy, 1855)

Henry Pratt (1855). Airy's paper includes only two small figures (Fig. 1.3), but these summarize well how he and Pratt imagined the support of mountains such as the Himalayas from below, or more commonly isostasy. For more details about isostasy and gravity anomalies, we refer to Chapters 6 and 7.
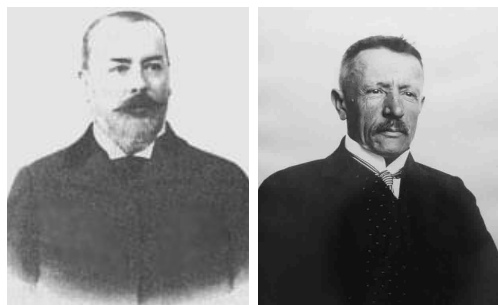
Figure 1.4: Count Béla Széchenyi (left) and Lajos Lóczy (right)

One of the longest expeditions to explore Tibet was financed by Count Széchenyi (Fig. 1.4a), between 1877 and 1880. He was accompanied by Lajos Lóczy[1] (Fig. 1.4b), to carry out geological and geographical observations, and Officer Gustav Krenner for the cartographic surveying. They travelled all over China, along the Hoang-ho river, to the Gobi desert, the Xining-fu (Si-ning-fou in Huc, 1854) basin, Kuku-Nor[2], Nan-Shan[3], Sichuan Basin (Sse-Tchouen in Huc, 1854), and the Irrawaddy River, totalling a distance of 7816 km on foot, horse and boat, for 300 days in China[4] (Fig. 1.5). Their demand for a permit to enter Tibet and Lhasa was refused, but despite this great disappointment, they accomplished a long journey and a great work. Lóczy collected

---

[1] Also mentioned as Ludwig von Lóczy or Louis (de) Lóczy in German or French publications, respectively.

[2] Nor = lake in Mongolian

[3] Shan = mountain in Chinese

[4] ~ 26 km/day

geological, paleontological, botanical and other samples that made up 19 boxes weighting more than 700 kg by the end of the expedition. Their classification and the publication of the journey's description and results lasted for two decades. These publications cover a wide range of themes: geography, geology, detailed maps, description of new minerals, fossils and species, etc...
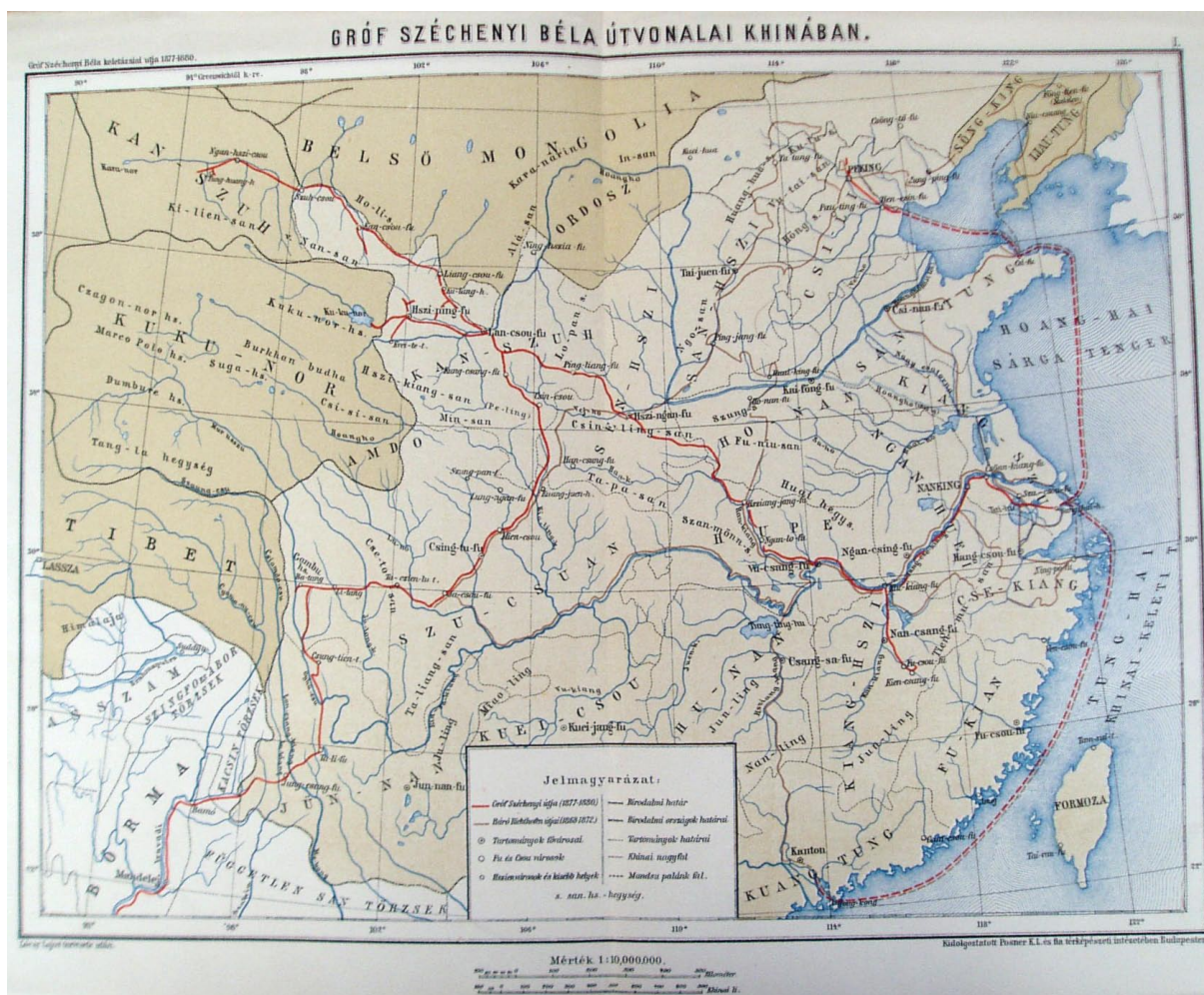
Figure 1.5: *The itinerary of Count Széchenyi's expedition, 1877-1880 (from Lóczy, 1886)*

Upon finishing, *"German, French, British, Russian and Japanese reviews acknowledged greatly the improvement of knowledge of Inner Asia's and Western China's geomorphology and scientific fundament"*. Baron Ferdinand Richthoffen, professor in Berlin, qualified it *"a masterpiece of geological work"*. The works *"describe the interweaving high mountain ranges on the eastern border of Inner Asia; provide tips for travellers; correct previous maps; and present a journey with multi-faceted descriptions"*. The more than

twenty related publications have worth several prices from German, French and Hungarian Institutes (Lóczy, 1898; Lóczy, 1919).

Some of Lóczy's works are summarized in Section 1.2, with more focus on results concerning the geology of the Himalayas and the Tibetan Plateau.
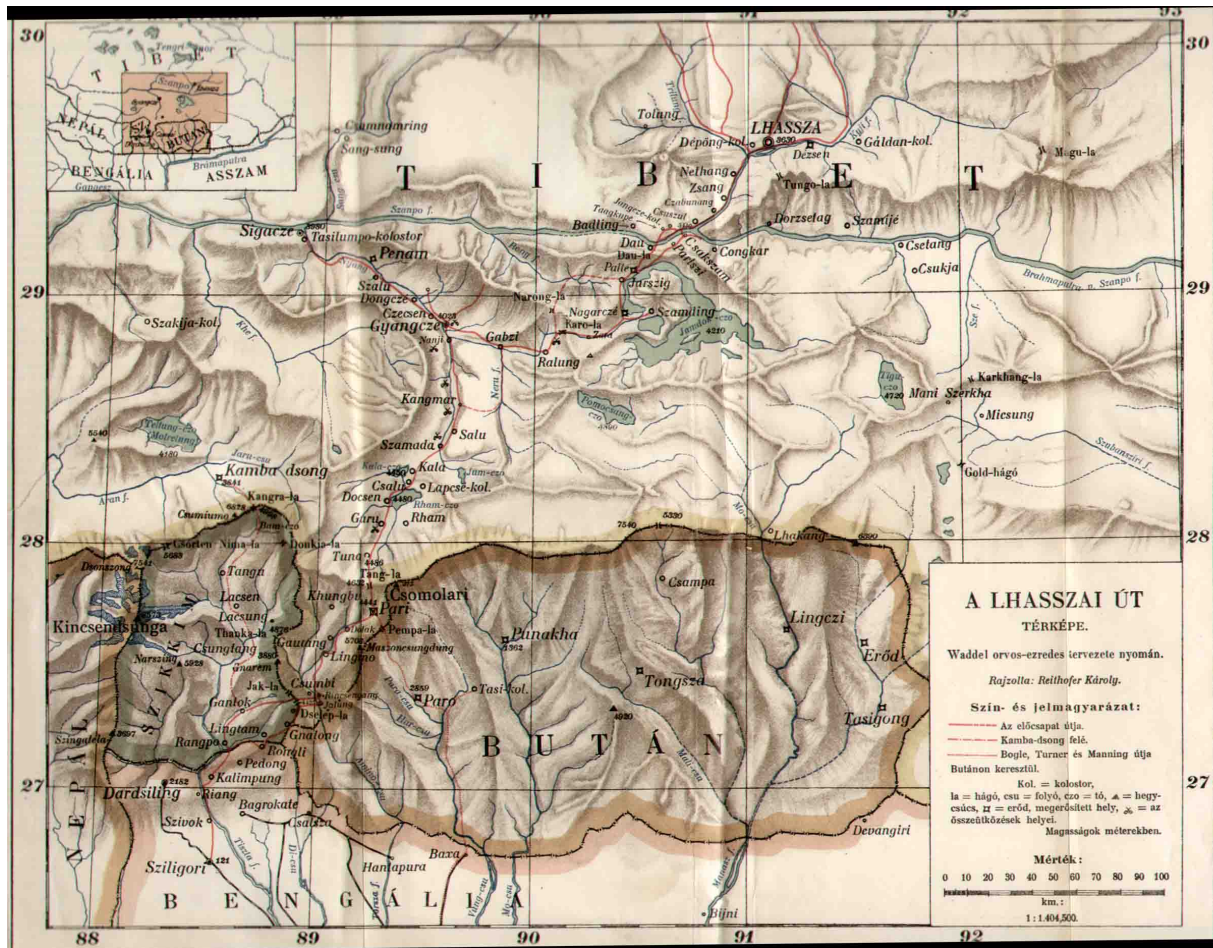
Figure 1.6: The itinerary of the British Army in Tibet, 1903-1904 (from Waddell, 1910)

The road to Lhasa did not open for other great explorers either, such as Prjevalsky, Dutreuil de Rhins, or Hedin. A light chance to change the situation was the "armed expedition" of the British Army to Lhasa, in 1903-04, "to boost the Tibetan-Indian trade". The story can be reconstructed following the work of the army's doctor, Austine L. Waddell (Waddell, 1910). Like Huc and Gabet, they travelled during the winter and thus in severe weather conditions, leaving on the 6th of November 1903 from Siligori (Sikkim, India), south of and close to Darjeeling. They climbed to the Dselep-La[5], and continued across

---

[5]La = pass in Tibetan

Pari[6], Kangmar, Gyangtse, next to Yamdok-Tso[7], and finally Lhasa (Fig. 1.6). Due to the great difference in the technical level of the British and the Tibetan army, the battles were short and without severe losses for the British. It seems that the main factors controlling the advance of the army were weather conditions and food supplies. Once in Lhasa, in August 1904, the signature of the Peace Treaty was quickly achieved, and the army returned on the same way between September and early 1905. The account ends with some lofty paragraphs about the opening of trading routes and free access to Tibet, but the 1910 translation's editor notes that the revision of the Peace Treaty, followed by an exchange of letters between Russians, Chinese and British, closed again the doors of Lhasa...

Another long-ago but interesting scientific paper to mention is by R. D. Oldham in 1914, who studied "deflections of the plumb-line" on a smaller scale than Airy (Oldham, 1914). His results in the Ganges basin show the need to take into account *"invisible underground topography"*, or density-variations in depth. Despite that only few measurements were available, Oldham gave rather accurate estimations on rock densities and basin depth. For more details on this topic, we refer to Chapters 6 and 7.

Figure 1.7: Emile Argand

A person and a work that definitely mark a milestone are Emile Argand (Fig. 1.7) and his *La tectonique de l'Asie* (Argand, 1924). Argand was born in Geneva, and have got in touch with medicine and architecture, in Paris and Lausanne, before arriving to geology and to Neuchâtel. His first works focused on the structure of the Alps, but soon his interest turned to the entire Alp-Himalayan system. He gathered information from many different sources, including other papers and field observations of Swiss petroleum geologists, but Argand himself has never put a foot in Asia. This did not prevent him from giving a first and general overview of orogeny and the tectonic history of "Asia", as it is mentioned in the title of his work, or rather global plate tectonics, as it is in reality. His work was first presented during the 1922 International Geological Congress in Brussels: his day-long speech was fast and hardly comprehensible, the map being the summary and the basis of his work was barely visible, but nonetheless it was a success. The writing of the actual (200-page long) paper was a difficult task, and according to Carozzi (1977), acknowledgements concerning its existence go to Mrs. Lugeon, Argand's professor's wife. She saved piles of papers knead by Argand and ready to be burned, while he was "forced" to write the manuscript during all his "leisure time" ("forced" included free access to the vine cellar,

---

[6]Also figuring as Pagri, Phari, Pali on different maps

[7]Tso = lake in Tibetan

cigars, and Mrs. Lugeon's good food). Finally the document was completed, and with the work of Wegener, it is regarded as the first signs of plate tectonics.

Some notes on this paper will conclude this retrospective chapter.

1.1.2   Geographical names and data

In second half of the nineteenth century, the exploration of continents approached to its end. One of the last regions to map was the Tibetan Plateau, due to its large size and to the difficult access. Central Tibet was practically unexplored, and the Himalayas were surveyed in the mid-19th century only, when Sir George Everest named the world's highest mountain "Peak XV". The knowledge of Tibet's geography at the turn of the 19th to 20th century was probably equal to its geophysical coverage at the turn of the 20th to 21st century.
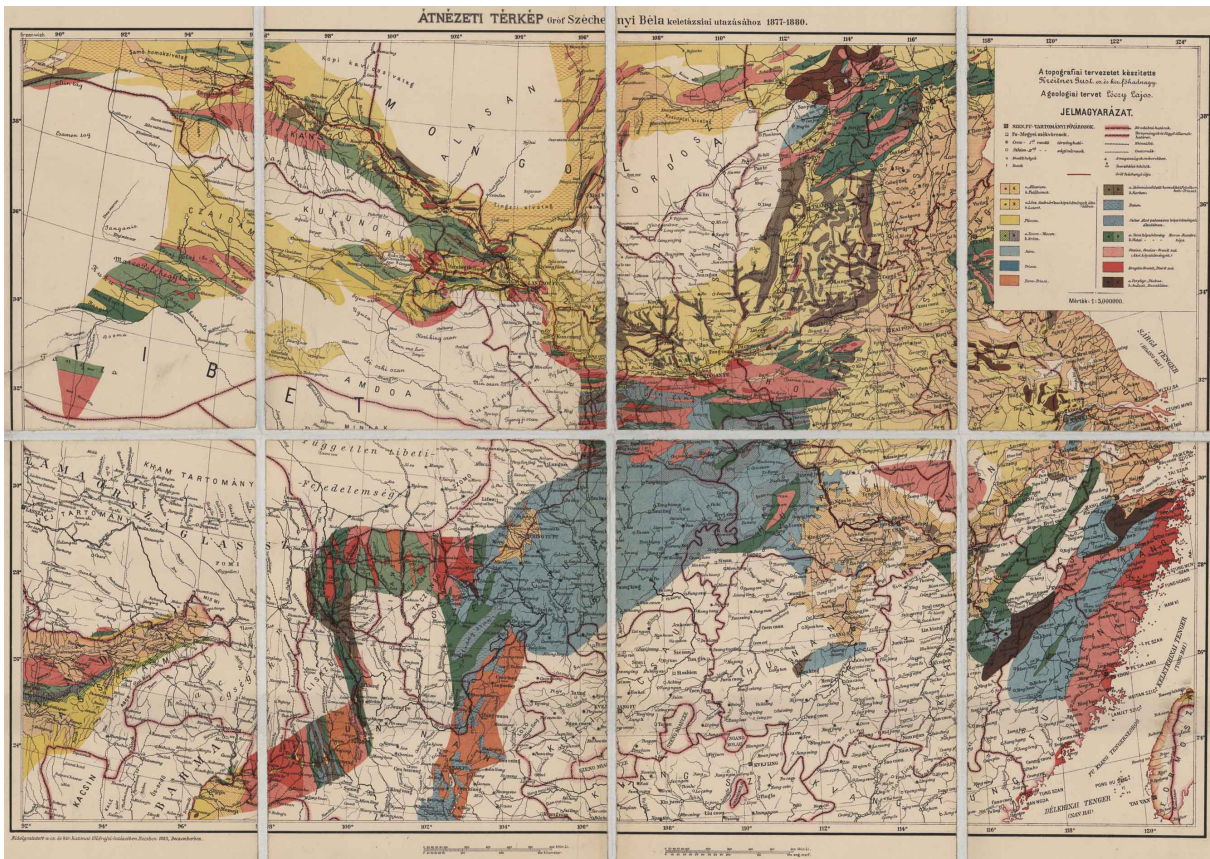
Figure 1.8: The geological map compiled by Lóczy after the expedition (Museum of the Geological Institute of Hungary)

The explorers' challenge was probably heightened by the quality and the resolution of the maps they have used. Huc and Gabet had an Andriveau-Goujon map which was published several years before their travel, but based on observations that dated from several decades earlier. Waddell — or rather the British army — probably ameliorated the available maps of the region. Count Széchenyi's expedition left with and navigated on a 1:750'000 scale map, counted distance using a pedometer and a compass, reported new geographic coordinates using different astronomical tools, and measured altitudes using aneroid barometer, Mariotte–Gay-Lussac type short barometer (or boiling-thermometer) and triangulation (Fig. 1.8).

In this context, it is interesting to compare the different altitude data mentioned in the different sources in time, and to compare with what is known today (Table 1.1). The values published more than a century ago are sometimes very close to present-day values, however, differences of several hundreds of metres occur, too. It is difficult to assess if the accurate measures were obtained only by chance, or because of the correct calibration of different tools prior to measuring.

The difficulty of this comparison is that the appellation of mountains, regions and villages are transcribed phonetically using the author's language, thus vowels are rarely the same, and the voiced and unvoiced consonants are often commuted (see also the first column of Table 1.1). For example, the name of the main tributary of the Brahmaputra, southern Tibet's major river can be composed in many different ways:

Ya	r			g		Z			g		
	l	u	n	–			a	n	–	p	o
	rl	ou	–			Ts		–		b	

where one line from each column should be selected.

Tibet földjén át vetett metszet Indiától Szibiriáig.
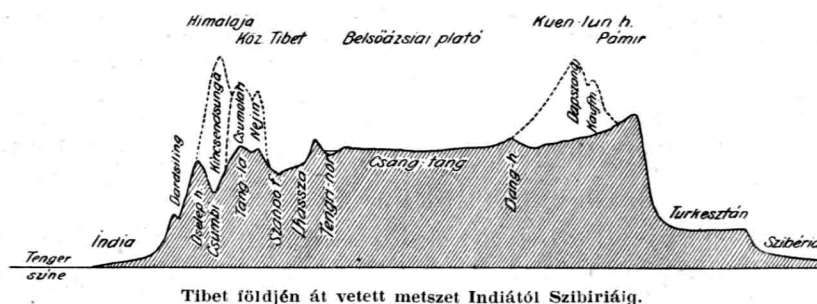
Figure 1.9: An early example of topographic section from Waddell (1910): "A section thrown through Tibet's land from India to Siberia"

		Waddell (1904)	Waddell's map (1910)	Lóczy (1880-1898)	Today
Bhutan-Sikkim-Tibet border		4426		4390	
Bidan-Tso	lake	4018-4100		4185	
Darjeeling	city		2182	2200	2134
Dauladiri / Daulaghiri / Dhaulagiri	peak			8176	8172-8201
Donkia-La	pass			5516	5516-5608
Dselep La / Jelap La	pass	4358		4423	4373-4572
Everest / Tchomokankar	peak		8882	8840	8848
G(h)ora-La	pass			5455	∼5000
Gyangze / Gyantse	city		4023		3990
Mustagh-Ata / Tagarma	peak			7731	7546
Kalimpung	city			1200	1219 - 1247
Kamba-La/Gamba-La/Khampa-La	pass	5120			4794
Kathmandu	city			1230	1299 - 1317
Khan Tengri (Lord of Spirits)	peak			7300	7010
Kinj[e/i]ndsunga/ Kan(g)chenjunga	peak	8579	8573	8550-8583	8598
Kongra-La	pass			4988	∼5300-5486
Kuku Nor / Qinghai Lake	lake			3347	3205
Leh	city			3439	3650
Lhasa	city		3630	3628	3650-3680
888 K.2 / K2	peak		8616		8611
Naku-La	pass			5555	5270-∼5300
Nam Tso / Tengri Nor (Sky Lake)	lake			4630	4718
Ninchentangla/Nyenchen Tanglha/ Nyainqêntanglha	peak			7114-7370	7162
Nojin Kangsang / Nojin Kangtsang	peak	6320			7191
Padim (south of Kanchenjunga)	peak			6689	6691
Pangong-Tso	lake			4247	4250
Ralung	village	4423			∼4500
Sigatse / Xigaze	city		3980		3836-3860
Siligori / Siliguri	city			120	122
Tingri / Dingri	city			4224	4340-4342
Tchumolari/Jomo Lhari/Chomo Lhari	peak	7015	7373	7298	7000-7327
Tuna / Dusna / Duna	village	4575			∼4800
Yamdrok Tso/Jamdok-Tso (/Palti?)	lake	4834	4210	4100	4408-4490
Yatung	village			3200	2987

Table 1.1: Comparison of altitude data between different sources and current measurements

Finally, to give some idea on the distances to travel and the necessary time some 150 years ago, here is a list of journeys, starting from Lhasa, collected by Lóczy:

- to Ta-tsien-lu, with a caravan: 2810 km in 57 days;

- to Xining-fu, with a caravan: 1500-1600 km in 52-53 days;

- to Leh, on foot: 1762 km in 101 days;

- to Gartok, travellers counted 58 days for 1300 km;

- the Chinese courier on horse took 136 days to go to Beijing.

1.1.3 Personal experiences in Tibet

The travelling experiences of Huc and Gabet were probably the most difficult, as their journey, lasting from October to January, meant severe climatic conditions. Several people of the ambassador's troop were abandoned along the road because they have frozen overnight, and friar Gabet almost had the same fate. Friar Huc himself (Fig. 1.10) seems to be a tough person and did not become sick; moreover, the nomads thought him to be a brave warrior because of his beard and moustache. On their way, the friars experienced altitude sickness, met dangerous nomad bandits (kolos), and drank melted snow. Compared to these difficulties, it seems that having to eat "tsamba" (or "tsampa", roasted barley flour, usually mixed with salty butter tea), did not cause a major problem, although it is mentioned that they also ate garlic to be *"protected against poisonous steams released by the mountains"*.

The travelling conditions of Dr. Waddell were by far the most comfortable. Being the doctor of the army, he travelled by train to Siligori, and probably did not carry heavy loads. The army counted a couple of thousands people, mostly of Indian and Nepali origin, as well as British officers. The supplies were brought continuously by carts on newly built or ameliorated roads, and even a telegram line was constructed that allowed to communicate with London in less than one hour! They brought good tents, collapsible boats and carts, installed stores along their road, etc. Despite the technical advances of the army, Dr. Waddell complained about the weather: heavy snowing and raining, sand-storms, temperatures lower than −30°C, and snow-blindness of soldiers who have lost their greenish glasses. The numerous photos (!) in the book also prove that the conditions were the best possible for the time.

Figure 1.10: Friar Huc in Chinese costume (from Huc, 1854)

A common feature in the experiences of Huc and Waddell is their delight upon their arrival to Lhasa. Beyond taking a rest at their destination, they rejoiced in seeing many

white houses and people, as well as the numerous poplar and alder trees; the vegetation that they were missing along their path is still characterizing the Tibetan capital.

Count Széchenyi and Lóczy travelled mostly in regions where Europeans have not passed before, and due to this, their experience during their journey varied from place to place. They were sometimes received by Chinese officials with big parade and gunfire in their honour, and sometimes "received" by lamas with hostility and rocks thrown on them. They travelled, rarely, on ship in all comfort, but advanced mostly on horseback or on foot, sometimes following deep valleys on dangerous, narrow paths. They did not escape from altitude sickness, tsamba (of which the *"first cup was welcome to warm them up after a cold day outside, but the second one was not for their stomach"*), cold nights and sandstorms. Altogether, the countless novelties of the journey made that the expedition was a great experience.

One interesting aspect of Huc's, Waddell's and Lóczy's image of their journey is that they often compare what they see to what they have seen before. Waddell saw a resemblance between the castles of Gyangtse and Edinburgh. Lóczy, during his excursion to the Dselep-La, compares the foothills of the Himalayas to some landscapes that he has seen in the Pannonian Basin. However, there is one exceptional thing they cannot really compare to anything, and thus they spend several pages on: the yak.

1.1.4   Writing styles

Huc's *Souvenirs of a journey in Thibet* is a rather open minded work written in a free style, considering that the author is a religious person. Of course, he discusses the history of Buddhism, religious rituals and clothes as well as cultural habits, and often finds similarities between Lamaism and Catholicism. But most of the time the text is a description of what they have lived and experienced day by day during their travel, including fine details that are unexpected from a religious author. For example, he details very much the use of "argol" (yak excrement): how it is collected, and how it is classified into four groups based on heat- and smoke-production. He also mentioned how fascinating it was to slip down on a glacier on their bottom. The "missionary goal" sums up to not more than a couple of remarks, such as the good opportunity for Christianity to expand into Tibet by bringing in vaccinations.

Dr. Waddell was not only a doctor engaged in the army, but also a natural scientist and a learned person. For the first reason, it looks that he was obliged to write about the army's advance, success, strategy and every day life, but most of the book is about observations in the nature, discussion on Buddhism and monks. It starts with an overview

of earlier travellers in Tibet and religious history, includes a complete table of Tibetan ranks and hierarchy, and ends with two chapters describing Lhasa where he visited several monasteries and discussed with many chief lamas. Just like Huc, he regularly makes interesting or funny remarks: for example, *"the Tibetan language uses a majority of consonants in order to prevent people from opening their mouth in the cold"*. At several points, he brings examples to the contradiction that he finds between Buddhist principles and the behaviour of the lamas, concerning fighting and killing, and also about eating or not eating meat: one caste of lamas is not supposed to kill animals or accept butchers in their order, but they have their own non-lama butchers to get and prepare meat. (This is very similar to the experience of Huc in Kun-bum monastery, where the servants of the lamas brought them rabbit meat every day, which made the friars happy but also caused a dispute with the lamas.) In summary, except the fact that the doctor travelled with the British army, his journey seems to have been as pleasant as that of any traveller.

Lóczy's works are written in a fluent style, which sometimes turns into storytelling, and rarely to verbose. The scientific descriptions tend to be as accurate as possible, and even if they become long due to the incorporation of more and more details, the author makes an effort to locate them in a broader frame. There are evidences that Lóczy followed the results of other researchers and explorers: there are references in his works related to the expedition in Asia, and he also published reviews on different themes such as *The earthquake* (Lóczy, 1880b), and translated works from German (*e.g. The formation of the Alps*, from Eduard Suess (Lóczy, 1876); see section 1.2.4 for these two reviews).

The topics discussed by Lóczy may change rapidly within the same work or chapter, from the description of the landscape, flora and fauna, precipitation, to that of the population, society, traditions, political relations, and back. The more "scientific" parts focus on geology (minerals, rocks, formations, structures, and tectonics), geography (landscapes, geomorphology, and also infrastructure, economy), meteorology (precipitation and rainfall curves), biology (new species of butterflies, plants), etc. The line of narration is kept interesting by adding personal experiences and stories, so the general image gives a good overview of a traveller's experience.

Argand's work is a scientific paper, which could actually be a complete book[8]. As he never visited the Himalayas or other mountains in Asia, *La tectonique de l'Asie* is rather a compilation of all facts known at the time and their close interpretation. For this reason, it is sometimes difficult to follow, as the theme of the discussion may change rapidly and

---

[8]The only aspect that is different from current papers or reviews is the almost complete lack of citations. It is clear that Argand used a lot of sources, but only a few names are mentioned explicitly in the text, such as Suess, Richthoffen, Lóczy, Wegener, etc. . .
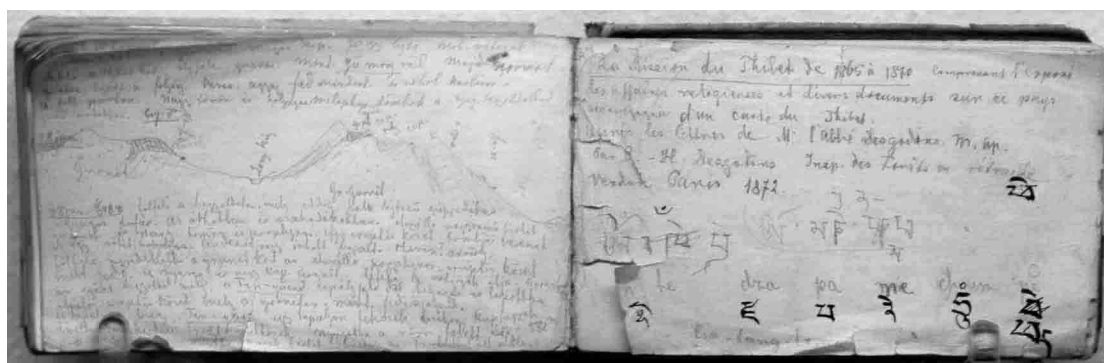
Figure 1.11: The notebook of Lóczy during the expedition. On the left page, the a sketch of a geological section; on the right, bibliographic notes and Chinese characters. (Museum of the Geological Institute of Hungary)

can go deep even in one paragraph. On the other hand, the principle ideas come back from time to time and make the reading somewhat pedagogic.

The best guideline is to read the rich analytical index, which helps to follow the main thread of the text. The work was translated to English by A. V. Carozzi, who says the followings about Argand's style: *"To read and understand Argand requires a long and sustained intellectual effort, which is however rewarded by the enjoyment of a masterpiece that continually reveals unexpected facts of its perfection. (...) In fact, there is no redundancy in Argand; everything is concision. Any attempt at simplification might lead to a complete misunderstanding of his thinking."*

1.1.5   Scientific notes

The notes of Huc concerning geology are rather limited. He remarks the presence of carbonic acid in the gases emanating at Borhan-Bota, between Qaidam and Bayan-Har; and on their return way from Lhasa, he mentions the occurrence of cinnabar (HgS) near Batang.

Dr. Waddell appears with many more faces: as a sociologist describing the population of Lhasa, or as a map surveyor presenting precise map of the capital. His natural scientist face is expressed in several short paragraphs or notes throughout his book, some of them based on learnt facts, but mostly on observations along the road.

Among the notes reflecting his *a priori* knowledge, the only one concerning geophysics is the following: "close to such high mountain ranges, the extra mass above sea-level perturbs the gravitational field of the Earth and increases the level of the sea, so that the sea-level in Calcutta is higher than the average". There also is a short and rather correct

discussion on the geology and the folding of the Himalayas and its recent uplift.

His other notes are field observations along the army's way: rocks (*e.g.* granite near Kangmar), medicinal plants, the size of lakes compared to what is represented on their maps. He finds that the extent of glaciers is smaller than described by previous travellers, and also that many terraces are present near the shores of Yamdok-Tso. He notes that the fortification of Pari is tumble-down but not destroyed, which is an indicator of low earthquake activity, coherent with the souvenirs of local people. Waddell records several hot springs and measures their temperature: 55.55°C 20 km east of Pari; 40.8°C (water) and 20.4°C (air) in Kangmar (compared to 30.5 and 13°C measured by captain Turner about a century earlier) with sulphurous smell but without precipitated sulphur. This is coherent with a much recent map showing hot springs over 40°C temperature, including this region (Gansser, 1991). Along the Yarlung Tsangpo[9], Waddell describes sand-dunes with 6-7 m high crests, and old granites resembling to conglomerates with limestones and shales. The temperature of the river in July was 4.44°C, and Waddell's analysis showed out some traces of gold by sieving.

An insight to Lóczy's and Argand's scientific results is given in the following two sections.

1.2   A selection of Lóczy's scientific results

Lajos Lóczy (1849-1920) was born in Bratislava, raised in Transylvania, and he studied in Switzerland, with Escher von der Linth and Albert Heim. At the age of 28, while he was an assistant of the Mineralogical and Paleontological Collection of the Hungarian National Museum, he was chosen by Count Béla Széchenyi — on the recommendation of Suess in Vienna — to accompany him on his expedition to Asia. The expedition lasted almost three years, and the processing of Lóczy's observations lasted 20 years. On his return to Budapest, Lóczy taught at the Technical University, than at the University of Sciences, and later became the head of the Royal Geological Institute. During his carrier, he concentrated on — beyond publishing the Asian expedition's results and teaching — important works throughout the Pannonian basin: compilation of the famous monograph on Lake Balaton, works carried out in Serbia, the denomination of the Tisia block (SE Hungary and W-Romania), etc. He excelled among the contemporary researchers with his breadth of view and with his own observations; his publications and vulgarisation notes (*e.g. Geography and geology*; Lóczy, 1880a) count more than 140 opera (Telegdi-Roth,

---

[9]Tsangpo = river in Tibetan

1949).

1.2.1   The expedition's itinerary

The expedition left Trieste on boat on the 3rd of December 1877, and mostly sailed until Han-Kou. On the way, they crossed and visited India, South China, Japan, and Lóczy even went to Java while the administration work in China was completed. They left from Shanghai on the 4th of November, 1878, for a fourteen-month journey in Inner China. The permit to enter Tibet itself was refused by both the Chinese government, and by the hostility of the lamas, so the expedition contoured Tibet on the NE, E and SE sides, following an approximate arc enclosed between latitudes 40°N and 23°N and longitudes 96°E and 106°E (Fig. 1.5). They made several excursions from Xining-fu to explore Kuku-Nor and to go along the Qilian Shan (Khilian Shan). On their way to the south, they crossed the Sichuan Basin, the city of Ta-tsien-lu, then arrived to Batang through Litang. During their excursions in the borderland of the Tibetan Plateau, the Chinese Government refused to provide anyone to accompany them, but they have found a Roman Catholic Chinese guide with whom they discussed in Latin (!). They left the region of Batang and returned to Chinese territories at the end of 1879, headed south to Yunnan, and then crossed the Indo-Chinese range to the West to arrive in today's Myanmar. They sailed back to Europe and arrived to Trieste on the 1st of May, 1880 (Lóczy, 1880c; Lóczy, 1886; Lóczy, 1898).

1.2.2   On two books related to the expedition

Description of natural relations and countries of the Chinese Empire

This book (Lóczy, 1886) is a very extensive description of China's geography, including the Tibetan Plateau. In the first part, after a review of earlier travellers' findings, there is a systematic description of mountain ranges, rivers, lakes, and geology. As the inner parts of Tibet were still *terra incognita*, some of the results are rather relevant, concerning the existence of saline lakes and endorheic regions. Despite the lack of maps in the eastern syntax of the Himalayas, the Yarlung Tsangpo is thought to be the Tibetan branch of the Brahmaputra, and not of the Irrawaddy. The main structures of the Qilian-Shan strike WNW-ESE, with at least 7-10 parallel ranges. The Indo-Malay rivers were known downstream, with main directions of NNW-SSE, but the expedition verified the upstream continuity of this structure south-west of the Sichuan Basin. Lóczy notes that Tibet is a high flat-land geographically only, but geologically it is very much folded. The geological history of northern-China, southern-China and India is recapitulated in the following table:

	NORTH CHINA		SOUTH CHINA		INDIA	
	Sediments	Eruptive rocks and structural factors	Sediments	Eruptive rocks and structural factors		
Present Era	Shifting sand; Aerial settling of deserts. Watercourse change of the Hoang-ho (Yellow River)	Thermal sources. Uplift especially on the coasts	The Yangtze builds it delta. Incision on canyons on the eastern border of the Tibetan Plateau.	Thermal sources. Sub-sidence of the coasts, uplift in the west.	Shifting sand. Fluvial deposits. Lower laterite. Former alluvia of the Ganges. Sediments of lakes. High gravel-beds;	Post-Tertiary and Present Era sediments
Post Tertiary	Loess	Basalt, dolerite	Laterite. Greater and deeper extent of ice-flows.	Basalt, andesite		
Pliocene	Kve-te series (with mammals). Lacustrine sediments (loess?)		Sediments of high-laying endorheic lakes on the Yunnan Plateau		Upper laterite. Kattivar miliolite. Siwalik series in western Tibet. Mammal-containing layers in Assam and Burma	Pliocene
U. Creta-ceous	---		Upper Cretaceous near Lhasa in Tibet	The end of wrinkling in the Indo-Chinese meridional mountain ranges.	Deccan trapp. Sparse Cretaceous and Jurassic layers. Upper Gondwana layers.	Cretaceous, Jurassic
Lower Jurassic (Dogger, Lias)	Sediments of large sweetwater endorheic lakes. Sandstone, marl, conglomerate. With Mesozoic type plant remnants.	Porphyre	Layers of the great red basin (in Sichouan) and of other sweetwater lakes. Sandstone, marl, conglomerate.		Cretaceous, Jurassic, Triassic and Rhätian in W and NW Himalaya.	Triassic, Rhätian
Triassic	---		Middle Triassic, in Yunnan (marine formation)			
Triassic, Permian, partly Carboni-ferous	Sandstone series above lime (horizontally)	Porphyre, diabase	Sandstone and slate layer-series (folded) in Yunnan and Sichuan		Upper layer of Saltrange. Lower Gondwana: Pan-czet Samuela. Damuda layers in Sikkim, Bhutan. Moulmen group in Burma	Triassic, Permian, Carboni-ferous (N China)
Carboni-ferous	Lime (marine formation)	Young granite conti nent in entire N and NW China	Lime, Devonian, Silurian: with remnants of bonelesses (e.g. molluscs) at many places, the extension of the two lower is never big	Diabase melaphyre and porphyre eruptions	Talc(?). Lower layers of Saltrange. Carboniferous and Silurian in the W and NW Himalayas.	Carboni-ferous, Devonian, Silurian
Devonian Silurian						
Sinian system	Globulite limestone (with Trilo-bites), diatomaceous lime-stone, red sandstones and shales. Mass quartz in N China horizontally; in the sys-tem of the Kuen-lun (folded).	Wrinkling in the Kuen-lun moun-tain system	Half-metamorphic slates, limes, layers with serpentine in western Yunnan.		Salty mud in Punjab. Gneiss in Ladakh-Zanskar. Silok(?)-series in Assam. Mergui group in Burma.	Cambrian group
Wutaian system	Crystalline slates. Quartzite sandstoe. Amphibole slate. Coarse conglomerates, and green schists, the main mass of the Nan-shan (Ki-lien-shan = Kuen-lun)	End of wrinkling. Appearance of korea-granite pegmatite and quartz-porphyre in N China	Shales with phyllites, sandstones. Conglomerates.	Granite quartz porphyre.	Vindhian series, submetamorphic formations, Arvali range, Behar-Sillok	Huronian group.
Archaic layer group	Amphiblole-gneiss, Chlorite-gneiss	Diorite	Gneiss, mica-schist		Gneiss with granite. Gneiss crystalline slates. Central gneiss.	Laurentian group.
	Ancient/primary gneiss and granite		Central gneiss massifs on the eastern border of the Tibetan highland. The coastal gneiss granite and porphyre.			

The second part of this book is the *Detailed description of the Chinese Empire's countries*, and the third one focuses on its "supplementary countries" such as Manchuria, Mongolia, Dzungaria, eastern Turkestan, and finally Tibet on more than 100 pages. This latter could be a separate book, as the description covers the history of Tibet, its relation with China, its administration system, its physical geography and resources, infrastructure, climate, population, the way of living, traditions, Buddhism, language, etc. that will not be detailed here. Concerning geology, the investigations and known facts are summarized shortly, and it is pointed out that due to the enormous size of the undiscovered territory, it is very difficult to make a synthesis. However, some relevant questions to answer are asked, and there are more than one of them to which there is no clear answer as of today (*e.g.* the timing of uplift of the plateau; the evolution of the relationship between the altitude of Tibet, the precipitation and the extent of ice covering it; etc.).

Finally, Lóczy advances a hypothesis of the Transhimalayas: *"North of the Himalayan range, there is a first big valley, extending from Leh in Ladakh, along the Satleds River, to the town of Tingri and the Arun and Kosi Rivers. Behind, there is a second mountain range, south of the big rivers of the Yarlung, which reaches high altitudes, and merges to a third mountain range at Mount Kailash, at the source of the Indus, Ganges, Yarlung Tsangpo and the Satleds. The relationship of this third mountain range with other structures is not mapped yet"*. This description is based on some earlier and spotty observations by explorers and pundits. However, the *"third mountain range"*, the Transhimalayas itself, a 2500 km long plutonic belt North of and parallel to the Yarlung Tsangpo were first explored — on Lóczy's advice — by Sven Hedin, during his third travel in 1906-1908.

The description of geological observations and their results from Count Béla Széchenyi's East-Asian travel 1877-1880

This book (Lóczy, 1890) is an excerpt of the *Scientific results of Count Béla Széchenyi's travel in East Asia*. The first part deals with China's coasts and relatively low lands, the second with the Kunlun range, the third with the Indo-Chinese range, and the fourth with Inner Asia's highlands.

This fourth part begins with a detailed description of the observed formations, from older to younger ages, and their structural relationship. From these descriptions, it turns out that the identification of the different formations were based on either European, either Russian examples, which is not illogical considering that they are on the same tectonic mega-plate, but the real reason was probably that these regions were the most studied and published at the time. The description of the Mesozoic and Cenozoic formations is relatively

correct, and there is an increasing amount of uncertainties on older geological ages. However, the Wutaian formations is identified as Archaic (compared to early Proterozoic today; Xi, 1985), and the trace of the Sinian mountains (on the NE border of the Yangtze Craton, Cambrian according to Lóczy, considered as late Proterozoic today; Xi, 1985) is recognized despite the fact that their topography has been overwritten by younger processes.

On the tectonics of the eastern border of the Tibetan Plateau, the observations of the time remain clearly local, with major white areas on both the geographical, and even more on the geological maps. A recurrent problem is the presence of folds of different scales that are perpendicular to the main structures. However, there are several statements that are accurate, concerning: the folded mountain chains bordering the plateau; the geometry of the Himalayas' eastern syntax and the Indo-Chinese ranges; a certain plastic behaviour of the crust (a concept of Heim and Suess, also applied by Argand), etc. Lóczy also sees that what these interpretations lack is a physical and mechanical basis, and that *"any critics on the observations and their interpretations will help to advance the understanding of the processes"*. Towards the end of the chapter, one can read the following: *"While the land of Indian Gondwana aligned the southward propagating accumulating earthwaves into parallel wrinkles up to the Gobi Basin, the same waves have spread towards the East into a quadrant"*. This is not very far from collision and extrusion tectonics!

The last chapter deals with recent processes. The Himalayan and Indo-Birman region seemed to be active until the Pliocene at least. During the Quaternary, the main phenomena characterizing the actual landscape were:

- decreasing lake levels and their increasing salinity, apparition and increase in size of endorheic regions;

- river incision and terraces;

- formation of loess;

- desertification of the Gobi;

- several ice-ages; and

- gradual retreat of the ice-sheet.

1.2.3   Structures and metamorphism in the Himalayas: a question that is still topical today

The widespread reversed metamorphism on the southern flank of the Himalayas was first described and interpreted by Lóczy in 1878. He suggested large recumbent folds (nappes) as a possible reason, even before the discovery of similar nappes in the Alps (Gansser, 1991). Unfortunately, the German publication came to light only 30 years later, but this issue was studied all along the 20th century and even today (Heim and Gansser, 1939; Pêcher, 1978; Bollinger *et al.*, 2004). The next two sections present the original Hungarian publication of these results in 1883, followed by the extended version published in 1907 with a short German summary.

On the excursion made in the Eastern Himalayas

This short note (Lóczy, 1883) was read in the Academy in 1883, and is a summary of the field observations made during a 25-day excursion from Darjeeling to the Tibetan border (Dselep-La). Lóczy notes the Terai alluvial cones, the extreme steepness of the Himalayas in Sikkim, and the structural division of the mountain range into Sub- (mostly Tertiary), Lower- and Central Himalayas. He mentions the geological formations such as shales, micaschists, amphibolitic shales dipping to the North, all overlaid by granites-gneisses. Lóczy re-interprets the point of view and the map of Mallett (1875), and proposes large-scale (at least 25 km) thrusting, and a tectonic window in the valley.

Observations in the Eastern Himalayas

This paper (Lóczy, 1907) is the complete version of Lóczy's excursion to Sikkim and the Dselep-La in February 1878, and was published with a German summary (Fig. 1.12). It includes many observations on flora and fauna, political situation and others. The geological results are 10 pages long, and appear at the end of the paper.

The excursion's route is later followed by Waddell, but at the time, instead a 20-hour train ride, in 1903, it was considered as a "small expedition". Nepal and Bhutan were allied to the Chinese, and the only way to Tibet was across Sikkim. The description starts with geomorphologic observations. *"South of the Siwaliks, there is no elevation at all: from the Ganges basin to Siligori, there is about 100 m climb for a distance of 400 km. (. . .) In the Kanchenjunga mountains, the actual limit of glaciers is 3100 m, the geologically visible one is 2400 m."*

Among the geological observations, the first is the presence of an "alluvial cone"

122   LITERATUR.

(2.) v. Lóczy, Dr. Ludwig. *Megfigyelések a Keleti Himalájában.* Föld-
rajzi Közlemények XXXV. köt. 6—7. füzet. (*Beobachtungen im öst-
lichen Himalaya.* Abrégé Bd. XXXV, Heft 6—7.)

Als Mitglied der Széchenyischen Expedition verbrachte v. Lóczy 1878
zehn Tage im östlichen Himalaya. Über diesen Ausflug berichtet die obige Ab-

LITERATUR.   123

handlung, in der über die geographischen und geologischen Originalbeobach-
tungen des Verfassers berichtet wird. Für uns ist nun zunächst der vierte Teil
der Studie von Interesse, in welchem v. Lóczy seine geologischen und tek-
tonischen Beobachtungen zusammenfaßt. Nach seinen Ermittelungen sind die
höchsten Erhebungen der Erde vom Fuße des Himalaya über Sikkim bis zum
Hochland von Tibet (mit den ältesten beginnend) aus folgenden Bildungen
aufgebaut:

1. *Die Gneis-Granitgruppe* erstreckt sich in S—N-licher Richtung in
120 km Breite; es ist dies von Kursiong über Dardschiling und den Singalila-
Kamm und von Kalimpung über den Cola-Kamm eine zusammenhängende
Masse bis zum orographischen Hauptkamm des Himalaya und der Tibeter
Wasserscheide des Tistaflusses.

2. Die groben Quarzite, phyllitischen, kupfererzführenden Schiefertone
der *paläozoischen oder kambrischen Daling-Schichtenfolge* und endlich Phyl-
lite die stellenweise in Glimmerschiefer übergehen.

3. In der *triassischen Damuda-Schichtengruppe* kommen in der Um-
gebung von Punkabarri, am Fuße des Dardschilinger Himalaya, Sandsteine.
kohliger Tonschiefer, Konglomerate und dünne Kupferlager vor.

4. Die am Fuße des Butaner Himalaya auftretende Baxa-Schichtengruppe
berührt das Gebiet des Dardschiling nur mit ihrem W-Ende. Das Hauptglied
dieser Gruppe ist ein mächtiger Dolomit, dem sich bunte Tonschiefer und
weiße Quarzitlager anschließen.

5. Tertiäre Schichten folgen dem Fuße des Himalaya an beiden Ufern
des Tistaflusses in weiter Verbreitung. Hierher sind weiche Sandsteine mit
dünnen Braunkohlenflözen zu stellen. Die am Fuße des Himalaya entwickelte
Gruppe der Siwalik-Schichten ist miozän und terrestrisch (Süßwasserbildung).

Sehr verschieden von all diesen Gesteinen ist die jenseits der Granit-
riesen des Himalaya sich erstreckende Schichtengruppe, d. i. das Tibetaner
Hochland, die aus marinen (karbonischen, permischen, triassischen, juras-
sischen, kretazischen und eozänen) fossilienreichen Gesteinen aufgebaut er-
scheint, während die Gesteine der am Fuße des Himalaya auftretenden Gruppe
größtenteils, metamorph, fossilleer und ihre triassischen und tertiären Sedi-
mente kontinentalen Ursprungs sind.

Demnach können also im östlichen Himalaya zwei Fazies unterschieden
werden, u. z.: 1. diejenige am Fuße des Himalaya, d. i. die der Indischen
Halbinsel; 2. die Tibetaner Transgression.

E-lich vom Tistaflusse gelangt die indische terrestrische Fazies in die
Nachbarschaft der Tibetaner marinen Fazies.

Die Hauptperiode der großen Faltung des Himalaya und der hinter-
indischen Gebirgsketten wird durch die durch das SE-liche Asien dahin-
ziehende mezozoische Flyschzone bezeichnet.

Die 1878 vom Verfasser gemachte Beobachtung, wonach die Tektonik
nur durch eine riesige Schichtenüberschiebung, d. i. eine überkippte Anti-
klinale zu erklären sei, wobei der Gneis in einer Breite von 25 km jüngere
Schichten bedeckt — wie er dies auch in der Fachsitzung der Ungar. Geolo-

124   LITERATUR.

gischen Gesellschaft am 2. Mai 1883 vorgetragen hat[1] — wurde durch die
seither bewerkstelligten Untersuchungen im vollen Maße gerechtfertigt, indem
es heute außer Zweifel steht, daß der Gneis von Sikkim in einer Breite von
65—75 km den jüngeren metamorphen Schiefern von Daling aufgelagert ist.

Dies wären in großen Zügen die hauptsächlichsten geologischen Ergeb-
nisse der Studien v. Lóczys. Die Abhandlung ist mit einigen guten Profilen,
einer geologischen Kartenskizze und einer — leider sehr schlecht reprodu-
zierten — farbigen geologischen Karte des zwischen den Dardschiling. Butan,
Sikkim und Tibet entfallenden Grenzenwinkels im Maßstabe 1 : 250.000 versehen.

— s.

Figure 1.12: The German summary of Lóczy's 1907 paper

formation in Terai (called Bhaver), which overlays the Siwaliks. Then follow phyllites, amphibole- and mica-schists, augen-gneisses, green-schists, quartzites, sometimes containing graphite. The metamorphic ages are grouped into Precambrian, Vindhyan and Cudda-pakian. The series from south to north (also from older to younger ages), from the feet of the Himalayas across Sikkim to Tibet are listed as follows:

- granites and gneiss, on about 120 km, until the watershed;

- Palaeozoic-Cambrian Daling series: quartzite, sandstone, phyllite with some copper, and mica schist;

- Triassic Damuda sandstone, schists with coal, conglomerates;

- Baxa dolomites, shales, quartzites;

- Tertiary formations along the Tista[10] River, sandstone, lignite, with a 35°dip to the N-NNW.

Lóczy then differentiates two "facies". The one in Tibet is composed of marine sediments, associated to a long transgression (Carboniferous-Permian-Jurassic-Cretaceous-Eocene). The other, in the Lower Himalayas, is mainly composed of metamorphic rocks of continental origin (Triassic and Tertiary), without any fossils.

Lóczy discusses in detail the relationship between the granite-gneiss and phyllites. First of all, he declares identical two groups of gneisses that were considered to be different by Mallet. Structurally, these gneisses can be found over the younger metamorphic Daling phyllites and schists, along at least 25 km (as stated in 1883), but potentially along more than 65-70 km, as confirmed by later studies. Lóczy concluded as early as 1883 the presence of a nappe; in 1907, he says: *"The inverse order of series and the case of an overfolded anticline is so clear, that it cannot be imagined more evident"*, as it is well illustrated on Figure 1.13. He describes the valley of the Tista River as *"a window, which is nothing else, but a region of metamorphic shales, surrounded by gneiss and gneiss-granite peaks from everywhere"*. He observes that phyllites dip a little to the N, but the overlying gneisses are sub-horizontal. According to Medlicott, the situation is similar in the region of Simla and in the Valley of Satleds. They together believe that folding initiated in Mesozoic times, but the paroxysm is located in Miocene times. *"The forces acting on the mountain range and originating from the change of isostasy are probably still active today (...) but erosion should not be neglected either."* Nor *"incision of the Tista River, and post-glacial uplift"*, ends the discussion, which shows the appearance — even if qualitatively only — of newer

---

[10]Also figuring as Teesta.

concepts in earth sciences around the turn of the century. Lóczy emphasizes that *"detailed geophysical measurements are wanted"* in order to open deeper discussion of the region.
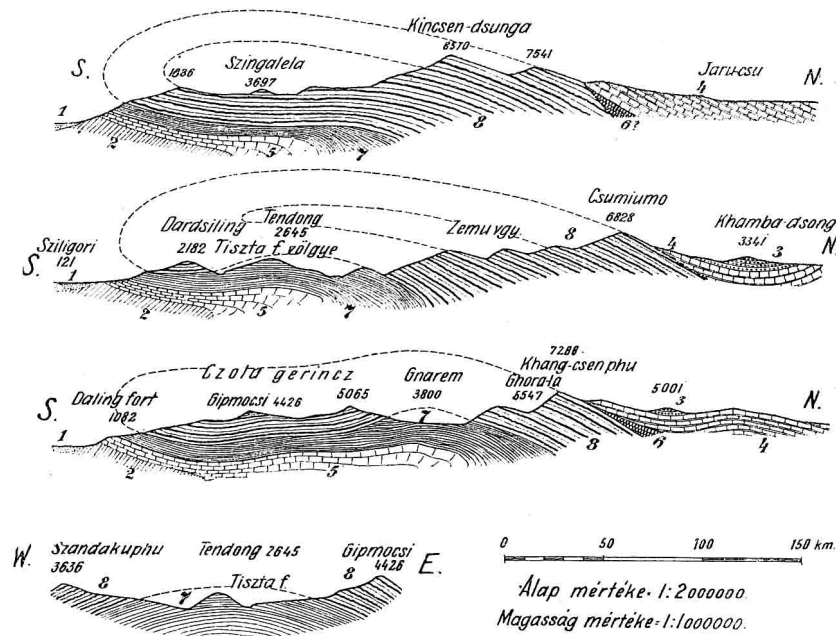
Figure 1.13: Profiles along the western watershed of the Tista River (top), along its valley (second), along its eastern watershed (third), and across its valley (bottom). 1: Alluvium, Diluvium, etc. 2: Siwalik layers. 3: Tertiary and Cretaceous in Tibet. 4: Jurassic in Tibet. 5: Permian and Triassic layers at the base of the Himalayas. 6: Triassic in Tibet. 7: Palaeozoic layers. 8: Gneiss, granite, etc.

1.2.4 Two reviews

The birth of the Alps

Soon after its publication, Lóczy gives a review of Eduard Suess's book, *Die Entstehung der Alpen* (Suess, 1875). This work (Lóczy, 1876) not only deals with the Alps, but also with the principles of mountain building in general, as seen 130 years ago. Even if some concepts of the time are not precise or correct, the asymmetry and uneven shortening of the Carpathians, the Jura and the Himalayas is observed. The role of horizontal forces is emphasized (50 years before Argand, see section 1.3.1), and the role of rigidity of layers is recognized in the size and direction of folds. Mountains are classified into three groups: rifts and volcanoes (Czech Ore-mountains, Balkan), folded and underthrust mountains (Appenines, Carpathians, Alps), and folded-only mountains (Jura).

About the earthquake

The year of his return from the Asian expedition, Lóczy publishes a summary of what has been known about the earthquake with only 30 years of observations and basically no instruments (Lóczy, 1880b).

There were already several known concepts (such as epicentrum, homoseista, isoseista), and the propagation of elastic waves following a shock in the Earth's interior is described. The danger of surface waves following big earthquakes was observed, as well as site effects due to soil types and building conditions. The tsunami is mentioned briefly, and volcanic sources are classified as of second order compared to the majority of earthquakes.

The quantitative estimates are of course mostly inaccurate, mainly due to the low accuracy measuremeants of relatively short times. The speed of waves in wet sand is estimated to 251.5 m·s^{-1} , in weathered granite to 398.0 m·s^{-1} , and in compact granite to 507.5 m·s^{-1} . However, the time delay between the source of the Lisbon earthquake and its observation in Germany resulted in an estimate of 4.5 miles per second, which yields a rather correct value depending on which mile is used. A tsunami's propagation speed is said to be 200-400 miles per hour, which is also an acceptable result. A shake map of an 1872 German earthquake is presented, where the estimate of the source's depth is 19850 m. Concerning the temporal aspects, *"the main shock lasts between a few seconds and one minute, but the aftershocks may last months. (...) There is at least one felt quake per day on the globe"*.

The accompanying effects of an earthquake are listed as follows: hum, variation in the magnetic field, change of temperature and outflow of thermal sources, landslides, mud cones, emanation of sulphurous gases. As of the areal distributions, earthquakes are rare in shields, river deltas, and occur principally in mountain belts. A catalogue describing "historical" earthquakes in the World and in Hungary is presented, and an early zonation of earthquake hazard is given for the Alp-Carpathian zone and the Pannonian Basin.

Finally, it is noted that earthquakes are related to mountain building, as marine sediments must have risen from the abysses to the mountains through non-equilibrium stages. *"The earthquake is the only phenomenon, which makes sensible the continuous change in the Earth's crust equilibrium."*

1.3   Argand's *La tectonique de l'Asie*

The main work of Argand, just like that of Wegener, came very early in the history of Earth sciences. This caused that the general ideas were not unanimously nor immediately

accepted. After a first wave, the level of interest towards his studies increased from a low level and slowly.

Today, plate tectonics and associated phenomena are widely accepted, and Wegener and Argand are considered some sort of pioneers. Reading *La tectonique de l'Asie* gives the impression of an advanced contemporary textbook; but in the light of what have been know at the time of its writing, it is much more impressive. It reveals the steps of how Argand deduced his conclusions and displays more completely his view of different processes and geographical regions.

The following sections depict some of Argand's observations and ideas which seemed to be worth to mention before passing on to more recent studies and the results of this thesis.

1.3.1 Physics and Argand's physical view of natural phenomena

Argand follows a very systematic and organized way to describe and classify his observations (for example virgations into those of first or of second order, simple or double ones). Similarly, the descriptions are detailed for many geographical zones, showing that he used several sources to assess the Alp-Himalayan system, the Circum-Pacific region, Indochina, Tarim, Siberia, etc. There are several paragraphs which prove that Argand was in the possession of precise maps, and that he had excellent vision in three dimensions: without one or the other, it is hard to follow the steps of his description.

In *La tectonique de l'Asie*, there is not a single equation, but this does not prevent Argand from giving a very precise and physical framework. It is said very early, that one- or two-dimensional argumentations are occasional, and that there is no synthesis without a continuous view (of deformation) in 3-D. He repeats at several points that in tectonics, the principal forces are horizontal, and the vertical movements are consequences. Isostasy is an accepted concept, seen as a re-adaptation of altitude towards equilibrium. Argand draws the attention to the fact that physical parameters cannot be regarded as constants: compressive forces vary with time and also from one segment of a mountain range to another; the deformation of continents is very heterogeneous with depth and with materials.

Argand's view of the tectonic movements and deformation is also very broad. Early in his work, he says that on tectonic scales, tabular mechanics is an approach, and that the reality is plastic flow[11]. This is also very well represented on a figure showing Asia's

---

[11]Later in the paper, Argand says that in collision zones, the deformation may be accommodated in two different ways: at the surface by clean-cut thrusts, at depth by more plastic conformations.

plasticity, or the deformation regime of Asia during the alpine cycle. Reasoning in terms of energy and drawing a quick energy balance[12], he shows that the role of faults can be falsely overestimated compared to the deformation of the continuum: *"Tectonics should be the visualization, then the science of deformations, before being that of dislocations: this is a necessity inherent to the process itself."* Viscosity is a clear concept for him, as well as absorption: *"none of the continuums allow the complete and instantaneous transmission of forces and stresses to large distances"* due to imperfect rigidity and friction inside a mass. Even on short distances, some time is required to transmit forces, and events can be considered as synchronous only within the error-bars of the stratigraphic scale. He states that in the media involved in tectonics, there is never compression without (ex-)tension, and supports this by bringing the example of glaciers and crevasses. Finally, Argand describes and characterizes two deformation regimes, which were much later labelled "thin-skinned" and "thick-skinned".

1.3.2 New concepts and their relation to other domains

According to Carozzi (1977), Argand's contribution rests on two fundamental concepts of Wegener's: continental rafts of sial[13] flowing and drifting on the sima[14], and the plastic behaviour of all crustal materials under long-continued stresses. The consequent tectonic deformations are thus related to differences in relative plasticity. There are four major ways by means of which the plastic continental rafts develop zones of folding (listed in decreasing order of magnitude):

- basement folds (*"plis de fond"*[15]) express the large-scale doming of continents through friction at the base of the drifting crust. This type of deformation consumes the greatest amount of energy, and involves large volumes of reactivated old material[16];

- marginal folds (*"chaînes marginales"*) are generated at the bow of drifting continents, where the less plastic mass of the continent is folded by almost paradoxical

---

[12]Energy estimations are assessed later in the work as well, *e.g.* the energy/unit length of a subduction zone is less than that of a collision; there are big difference between a pure collision and a homogeneous subduction in terms of energy variations, too.

[13]Sial is for the upper layer of the crust, or continental crust, as it is made of rocks rich in silicates and aluminous minerals.

[14]Similarly, the lower layer of the Earth's crust, or oceanic crust, containing silicates and magnesium-bearing minerals.

[15]The energy $\times$ surface balance yields that *"the energetic preponderance belongs, with much greater dimensions, to basement folding, which represents not only the specific reaction of continents to tangential effort but also the major expression of folding on this planet"*.

[16]The nuclei of particularly old massifs being formed of Precambrian material, having approximately the same average plasticity, are hard to deform internally.

"resistance" of the more plastic substratum;

– geosynclinal folds (*"chaînes géosynclincales"*): the result of plastic behaviour under tension followed in time by compression

– sedimentary covers of cratonic masses fold disharmonically over their substratum by décollement generating cover folding (*"plissements de couverture"*).

All along Argand's work, examples are brought and classified in the above categories. He anticipates that the comparison of different mountain ranges being in different states can be assembled into one general, evolutionary history. In this way, he concludes to (but already anticipates it in the first pages) the description of an entire orogenic cycle, of which the temporal limits are not clear yet, but which can be directly linked to the (later named) Wilson cycle.

Argand's view of Bouguer anomalies are very close to the current one, especially on a large scale. They are *"related to the variations of the thickness of a lighter material, sial, on a denser material, sima"*. The inferred *"lenses of deep-seated sial are more or less imperfect negatives of the main visible intumescences"*. Argand states that Bouguer anomalies are useful where the masses affected by basement folding are great and the effects of secondary modifications small. Argand warns that beyond the lack of data, care is needed with regard to the interaction with isostasy, tectonic or external forces, and deformation. The terms over-/under-compensations are clear, and he even talks about an *interdependent compensation"* due to the lateral intervention of elastic or semi-rigid effects (regional isostasy).

Concerning Asia, Argand says that a denser network of gravity stations is wanted: *"In this respect, most of the segment of (central) Asia remains temporarily unknown, but its gravimetric exploration will certainly disclose important facts."* He probably read some works similar to that of Oldham (1914), as he thought that *"it is superfluous to recall data pertaining to the Himalayas and to the Indo-Gangetic foredeep, which are classical regions with respect to the history of gravimetry."*

1.3.3 The Himalayas and the Alp-Himalayan system

The region of the Himalayas was not very well known at this time, and all that Argand could do was to interpolate local observations. The so-called Himalayan zone was known to be an overfolding to the south, and Precambrian fragments of Peninsular India, as well as Nummulitic (Palaeogene) synclines north of the Everest region were observed. Jurassic and Cretaceous sediments of the Tethys were extending to the north, and this belt,

including granitoids and Cenozoic lavas, formed the main structure between the source of the Indus and along the Brahmaputra until the 88th meridian.

On the scale of the India-Eurasia collision, Argand divides the space into three parts: Indo-Serindian zone (actual Himalayas and Tibet), Serindian zone (Tarim basin), and Serindo-Siberian zone (actual Tien Shan). Serindia has a strong influence on the deformation of the two other parts, but its structure need more exploration as it is located deeper, covered by sediments.

Extending this collision zone along the parallels, Argand divides Eurasia to old Europe in the west and to the land of Angara (or old Asia) in the east. He says that the collision between Eurasia and Indo-Africa is very similar in its eastern and western part; but, in lack of energy, the displacements in the west are much smaller (*"Europe is an unfinished Asia"*). On a north-south comparison, Argand delineates two geosynclinal folds (*"plissements géosynclinaux"*): the one in the south includes the Atlas, the Apennines, the Dinarides, the Taurides, the Zagros and the Himalayas; the one in the north is formed by the Alps, the Carpathians, the Balkan, the Kopet Dag, the Karakoram, the Kunlun, and can be then continued in a *"deep flux to the northeast"* (similar to nowadays' extrusion tectonics).

Argand's reflection on Tibet ends with the summary of three observations. First, the Serindian massif is the common buttress of the Kunlun and the Tien Shan pushed in opposite directions. Second, the Kunlun Mountains represent older ages compared to the Himalayas. Third, along the 2600 km long Himalayan front, from Peshawar to Assam, India advances to the NNE-NE[17]. The gathered evidences show that the Indian massif has undergone a great displacement, and lead Argand to the question of mobility of the continents.

1.3.4   The dawn of plate tectonics

In the first two thirds of *La tectonique de l'Asie*, there are paragraphs on observations that can be related to today's plate tectonics, but there is no real discussion *on* and *of* a global scale. The Hebridian and Laurentian massifs were known, and Argand describes a large pre-Atlantic geosyncline, across which the double-American bloc and the Old World were connected before by orogenic structures. Hence, in his view, today's Atlantic is a second Atlantic. Concerning the Tethys, its closing between Indo-Africa and the old Eurasia is clear in his eyes.

---

[17]This angle is equal to a direction of $\sim$N34°E, comparable with present-day motion seen by GPS.

Towards the end of this part, the question of energy source to basement folding becomes boiling: *"Basement folding is the main aspect of a fundamental process that overtops and commands the basement folding itself and, consequently, the deformation of new chains and cover folds."* On the following pages, he mentions *"deep-seated tectonics"*, *"infra-tectonics"*, *"total tectonics"* and *"geoid"*, stating that the issue is complicated. He does not want to extend the discussion to this larger scale, where he estimates that the vertical forces have a major role, and wants to keep the gravity anomalies to explain plastic deformations and tectonics only, where the main forces are horizontal.

1.3.5 Fixism versus mobilism

After a more than 100-page long preparation, Argand arrives to the discussion of the problem between fixism and mobilism, and very rapidly he says that the already presented facts reconcile better with the latter one. He recapitulates all geographic zones in the light of mobilism and fixism, their evolution in time and the main directions of movement, as well as the questions the controversy creates. The conclusion is that *"fixism is not a theory but a negative element common to several theories"*. Argand is more negative on fixism than positive on mobilism. He is convinced that his observations and the basic principles laid down by Wegener are correct, but he is also aware of that *"the validity of a theory is nothing else than its capability of accounting for all the known facts at the time it is presented"*.

In the detailed arguments of the above debate, Argand shows, for example, that fixism is not compatible with isostasy. Also, the fixist point of view implies variations of power and not resistance (as does mobilism), and as *"a statistic law has a physical reason in the inorganic world"*, mobilism has more ease to explain these variations.

One of the surest points in linking Argand's text to his figures is the parallel drawn between the Himalayan and the Mediterranean region in light of mobilism (Fig. 1.14). He compares the Mediterranean to a 3-D puzzle (of which he presents the solution on a series of cartoons depicting its Cenozoic evolution), which is smaller, but more complicated than the Himalayas in every aspect. Central Europe, the Alp-Carpathian zone is like a small India, which, rather than descending, overruns the northern plate. Baltica, the Bohemian Massif and a piece of Gondwanaland are the miniature copies of Siberia, Serindia and India. Additional complications include *"distensional behaviours, which seem to have accentuated the almond-shaped configuration of the Pannonic depression and to have contributed to the establishment of the infra-tectonic complication of that region, where the areas of thinned sial, risen sima, and positive anomaly predominate"*.
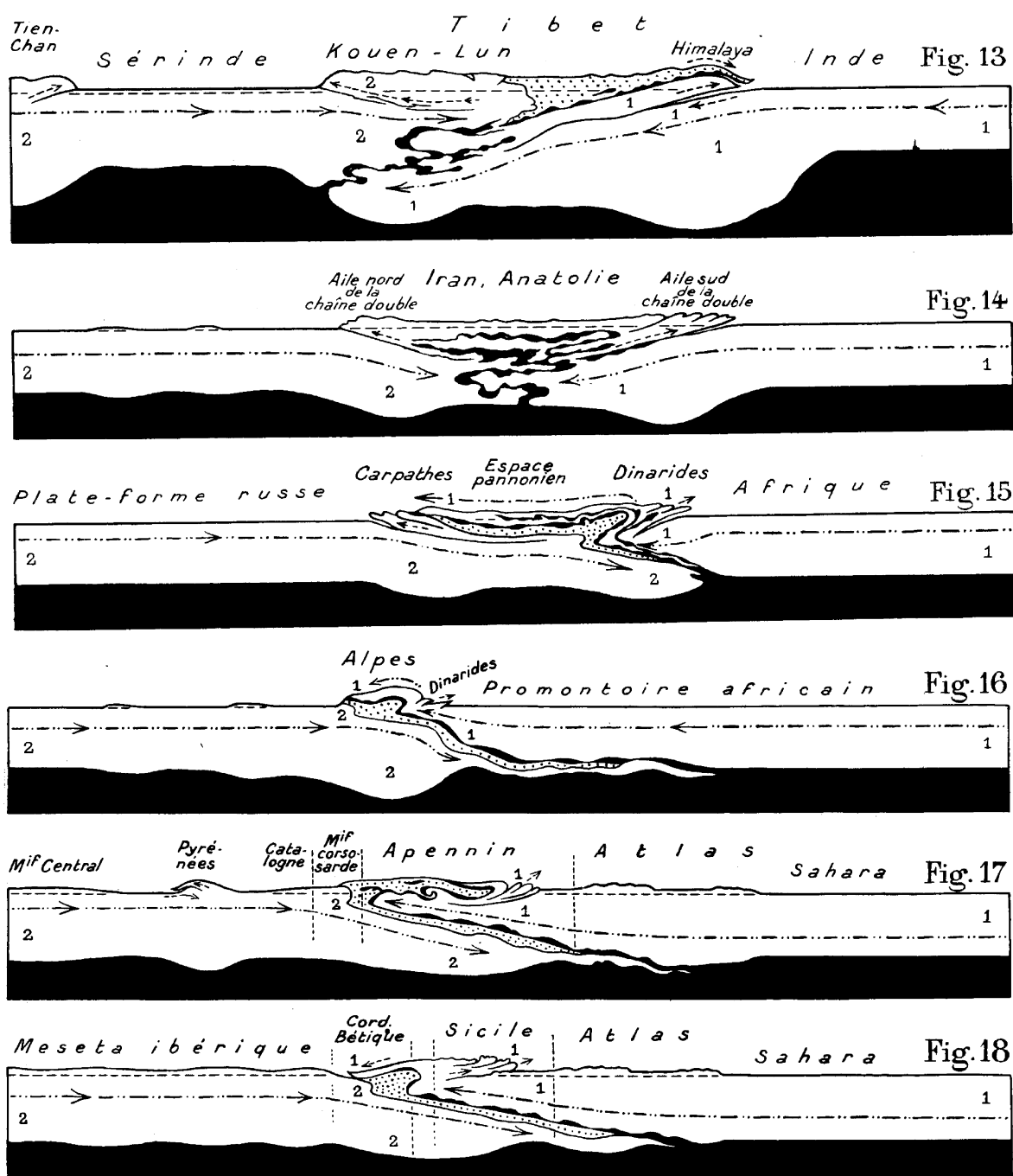
Figure 1.14: A series of N-S cross-sections through the Alp-Himalayan orogen, from east to west (Argand, 1924). Note the underplating of India beneath Tibet, and compare the geometry with those in the following Chapters.

1.3.6 Conclusions

Once the question of fixism versus mobilism elucidated, Argand makes a last tour around the globe and describes it in light of the mobilist frame of ideas. The conclusions are those of today's plate tectonics. *"The Mid-Atlantic Ridge, similar to a wreck of sial tossed around and deformed in the sima, seems to be the heritage of the time in which the New World was beginning to separate from the Old*[18] *(. . .) "The basement fold of the Himalayan zone was definitively initiated in the old sial of Gondwana, by its collision with the old sial of Angara; both influenced each other, first in an indirect manner across the sial of the Tethys reworked into marine deposits, then in a direct manner by the substratum of the Tibetan intumescence"*. The story of separation from Africa of Australia and Antarctica, Madagascar and India is also described. The collisional front between Eurasia and Indo-Africa is estimated to a length of 9-11'000 km, and the India-Eurasia shortening to 2000 km (compare with 3000 km according to Wegener, and with estimates in Chapter 2).

On the final pages, Argand warns that the presented theory and consequences are nothing more that a non-unique solution, explaining all observed facts at the time. Other sources of deformation should not be neglected: *"It is superfluous to cite all the deformations attributed to isostasy. The lateral push derived from the filling, from the accumulation of the deposits in a furrow that subsides, can play a certain role on cover foldings of a certain thickness, as it does in incipient and not too broad geosynclines. The changes of volume due to recrystallization, and those generated by the evolution of deep-seated magmas, cannot be correctly estimated at present, but it would be dangerous to underestimate them."* Finally, Argand attracts attention that mobilism still has to find a source of energy to cover expenses of translations and deformations. But this is another story. . .

---
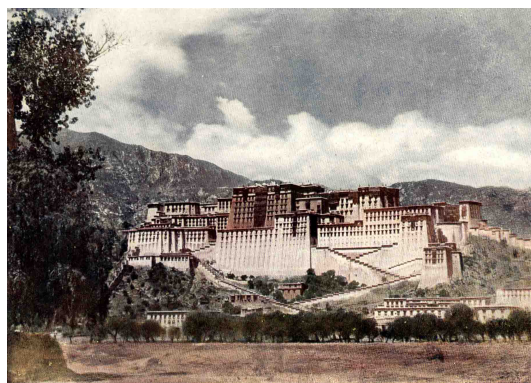
[18]It seems that the first acoustic sounding were known at that time, including the region of the Azores, and together with temperature measurements of the ocean.

Himalaya–Tibet: an image always blurred at depth?

From one day to another, // The valley became mountain,
The mountain collapsed, became a trough, // It was washed by water, became a valley.
Which point of this // Moving world is unvarying?
From one day to another, // The sea dried out, became a desert,
The desert was flooded, became a lake, // The plain buckled, became a hill.
Manas (Kyrgyz mythology)[1]

Introduction

This chapter aims to introduce the scientific frame of this thesis. It briefly presents the Himalayan-Tibetan region, and then gives an overview of a few concepts: first, those that are widely accepted, and then those that are highly debated. Some of these debates, such as models of plateau evolution, are ongoing since almost a century; others, like the strength of the continental lithosphere, were born within the last two decades. A link is made between open questions and the work presented in the following chapters, including the applied tools: how can we provide improved resolution images of the lithosphere? What kind of supports exist to maintain a plateau in elevation? What is the role of precise petrological modelling in geophysics? The results of these analyses bring new constraints

---

[1]English translation by G. Báger

on the above questions and move forward the debates towards a more accurate image of geodynamic processes.

2.1 The geography of the Tibetan Plateau

The Tibetan Plateau (Fig. 2.1) lies in at least five countries, depending on the definition of the boundaries and the limits of the plateau. With over 3.5 million km^2 of surface area at an average elevation of 5023 m (Fielding *et al.*, 1994), it is the largest and highest plateau on Earth. On its southern border, it is bounded by the ∼2500 km long Himalayan arc, which is often defined as the mountains lying between two peaks forming its western and eastern syntaxes: Nanga Parbat (8125 m) and Namche Barwa (7782 m). The Himalayas form a rain shadow of the Tibetan Plateau which thus receives limited amount of precipitation. A part of this goes into the endorheic region with salty and freshwater lakes, another goes into major rivers draining the plateau. All the main Himalayan and Transhimalayan rivers originate from the holy Mount Kailash (6638 m) (Gansser, 1964); the other group of rivers drain the plateau on its southeastern and eastern side. On its northeast and northwest side, the Tibetan Plateau is separated from the Gobi and Taklamakan Desert — located in the Tarim Basin — by the Qilian and Kunlun Ranges, respectively. Finally, at the Pamir Mountains, the junction of the Kunlun Range and the westward extension of the Himalaya, the Karakoram, closes the loop around the Tibetan Plateau.

2.2 The origin and deformation of the plateau

The structure and evolution of the Tibetan Plateau were investigated by a large number of approaches. Figure 2.2 represents a few of these in a bi-dimensional *time–characteristic scale* space, and shows that none of them allows to reconstruct the entire geological record at both small and large scales. Hence the different research methods are often combined to provide better constrained, more robust results. The problem is, however, that the confidence level of the studies is different, and/or that coupled approaches hinge on assumptions on which not everyone agrees, giving rise to a certain number of debates. Nonetheless, even if the number of questioned issues is large, there are several groups of observations which are rather well constrained, and more or less widely accepted.
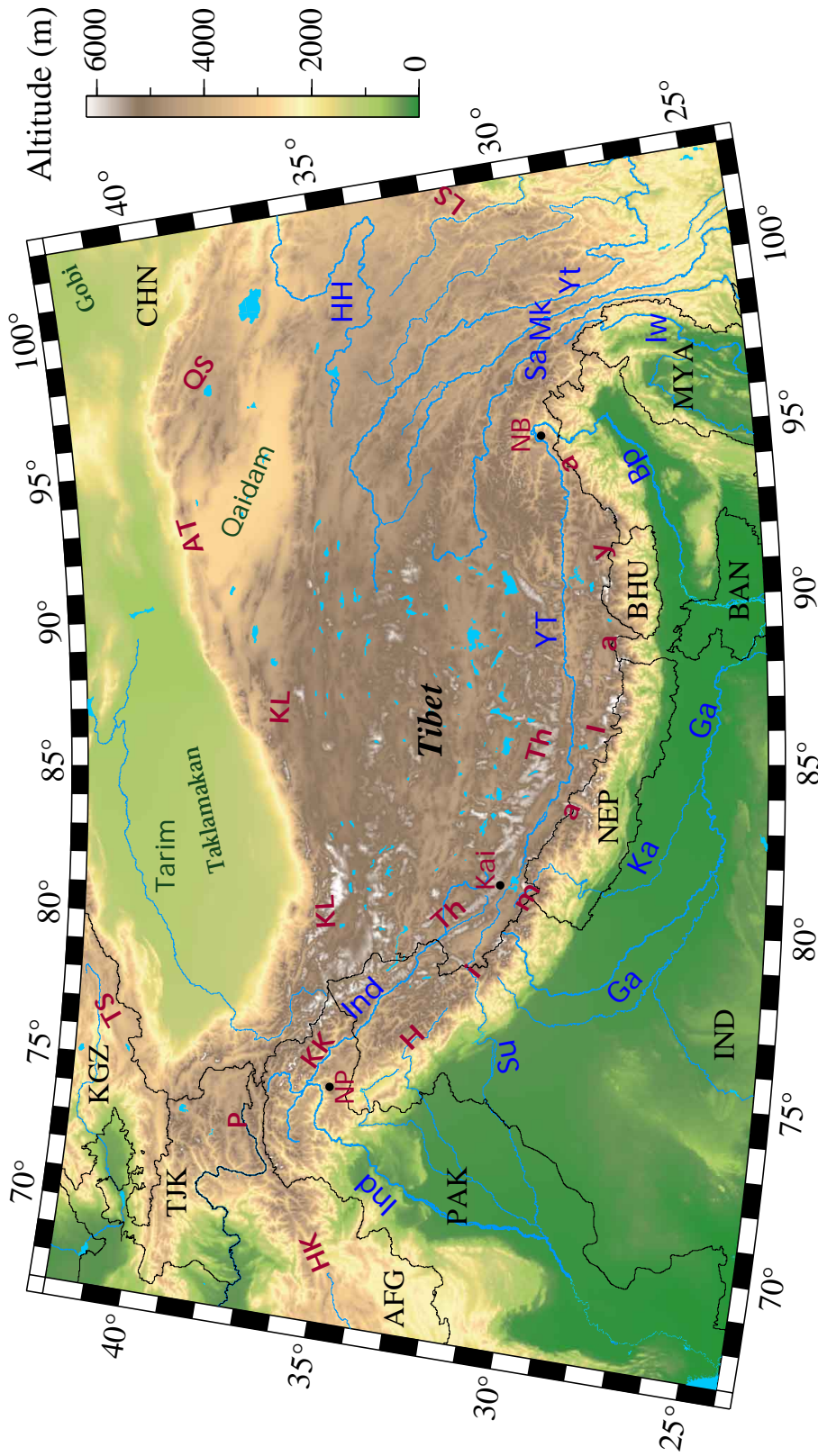
Figure 2.1: *Physical geography of the Himalayan-Tibetan region. Mountain ranges in purple are Th (Transhimalaya), LS (Longmen Shan), QS (Qilian Shan), AT (Altyn Tagh), KL (Kunlun Range), KK (Karakorum), P (Pamir), HK (Hindu Kush), and TS (Tien Shan). Peaks in purple are NP (Nanga Parbat), Kai (Kailash), and NB (Namche Barwa). Major rivers in blue are Ind (Indus), Su (Sutlej), Ga (Ganges), Ka (Karnali), Bp (Brahmaputra) and its upper course YT (Yarlung Tsangpo), Iw (Irrawaddy), Sa (Salween, or Nu Jiang), Mk (Mekong), Yt (Yangtze, or Chang Jiang), and HH (Huang He, or Yellow River). Main basins adjacent to the Tibetan Plateau are the Ganges basin in the south, the Tarim in the north, and the Qaidam basin in the northeast. Countries are noted using their Olympic abbreviations.*

Figure 2.2: Schematic representation of observations in the Himalaya-Tibet region in the time–scale space. The ellipses outline the approximate coverage of a few approaches noted in the corresponding colours. Note that seismology and gravity, even if they measure current structures, can also provide temporal information that have been accumulated in the past few million years (i.e. shear-wave splitting and mantle deformation).
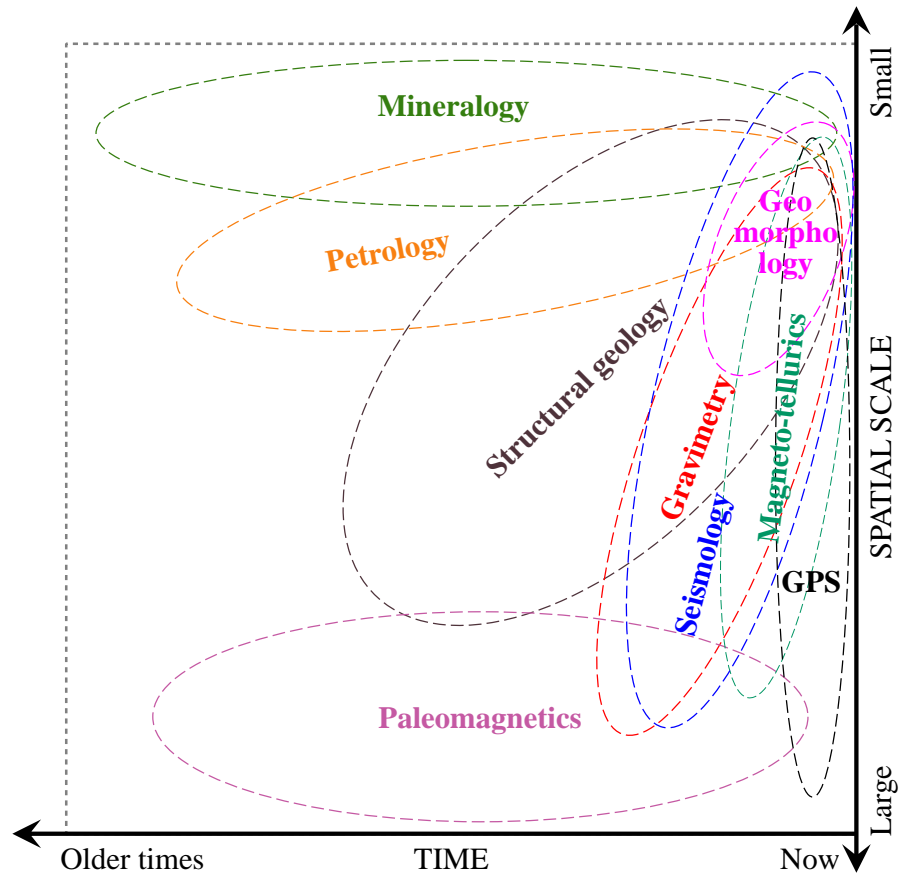
2.2.1   Plate tectonics

If we look at the Tibetan Plateau on the scale of plate tectonics, — thus on a large scale ($\sim$1000 km), and back in time ($\sim 10^7$ years), — we find that it is a mosaic of small continental blocks accreted to the Eurasian continent from the south since the Paleozoic (Allègre *et al.*, 1984; Tapponnier *et al.*, 2001), now separated by clearly marked sutures (Fig. 2.3). We know that the final collision took place with the arrival of the India plate in the early Cenozoic, with arguments based on paleomagnetic data on the slowdown of India plate motion (Patriat and Achache, 1984; Besse *et al.*, 1984; Besse and Courtillot, 1988), biostratigraphy (Beck *et al.*, 1995), and field studies of ophiolites (Mahéo *et al.*, 2006), among others.

However, a date which would be more precise than the Paleocene to mid-Eocene (66-45 Ma) range proposed for the onset of continental collision is largely debated. This is partly due to the west-to-east evolution of the Tethys Ocean ocean's final closure, but also to the simplifications and inherent errors of the different methods. Some authors even
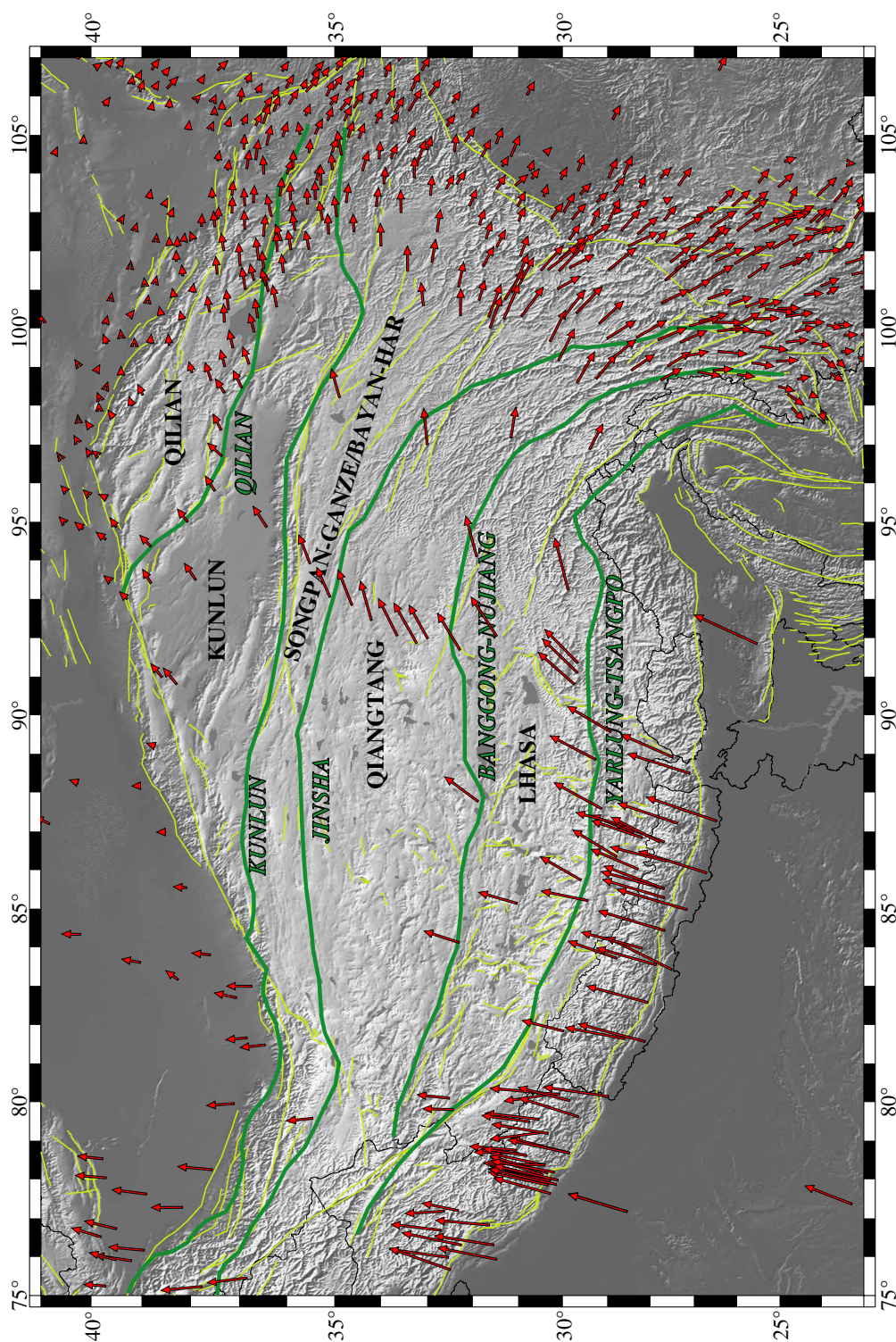
Figure 2.3: Geological and current deformation of the Tibetan Plateau at the surface. Geological deformation: thick green lines denote major sutures of Lower Paleozoic (Qilian), Paleozoic (Kunlun), Triassic (Jinsha), Late Jurassic (Banggong-Nujiang) and Early Tertiary (Yarlung Tsangpo) age (Tapponnier et al., 2001), separating continental blocks marked in black. Current deformation: fault activity (light-green) and surface deformation (red arrows) are both evidences of ongoing deformation of the region. GPS velocity field with respect to stable Eurasia from Zhang et al. (2004).

suggest a different timing, and, on the basis of new field evidences, put the beginning date of the continental collision to the Eocene-Oligocene boundary, at $\sim$ 34 Ma (Wang *et al.*, 2002; Aitchison *et al.*, 2007).

Furthermore, the plate tectonic interpretations become more difficult to make when one wants to reconstruct Greater India plate, for example. The size of India prior to collision, and the amount of shortening since closure of the Tethys Ocean, are still debated (see below), and seismic tomography studies that seem to find the missing parts of India (*e.g.* Van der Voo *et al.*, 1999) are not widely accepted. This points to an important issue concerning the different research approaches (Fig. 2.2): they are not only dissimilar in the time- and characteristic scale-domain, but also have a very different depth sensitivity.

2.2.2   The *depth—resolution* relation

Figure 2.4 shows the depth range of different research methods in the *time–scale–depth* space: Figure 2.2 is redrawn on top of the cube, and the ellipse coverages are extended downward. For example paleomagnetics still covers the large-wavelength and geological-time domain at surface, but its penetration in depth, represented by a cone, is limited. On the other hand, seismology and gravity methods, beyond having a large coverage on top of the cube, also extend downward in a narrowing but deep and oblique cone. This makes that while they are applied for sub-surface investigations, they also yield most of our observations on the Earth's large scale deep structure.

Figure 2.4 also shows the boundary of well-constrained observables and features (light-green subspace), which allows to discuss the issue of resolution and its limits. If we look at current processes (right side of the cube), it is evident that we have to take a middle course between images of high resolution and images at depth. Going towards larger scales, the depth sensitivity increases: in geomorphology, for example, the evolution of erosion will depend on the surrounding lithology, the average precipitation, and the uplift of an orogen (Godard, 2006). Then, the further we try to image in depth, further our images become less well-defined. For example, in Tibet, there is a general agreement on the fact that the crust is thickened to 80 km or less, but estimates vary with the methods and 10 km or larger differences in Moho depth are not uncommon, even at the same geographical position. The imaging of secondary discontinuities, such as the Conrad or the 520-km, is even more uncertain.
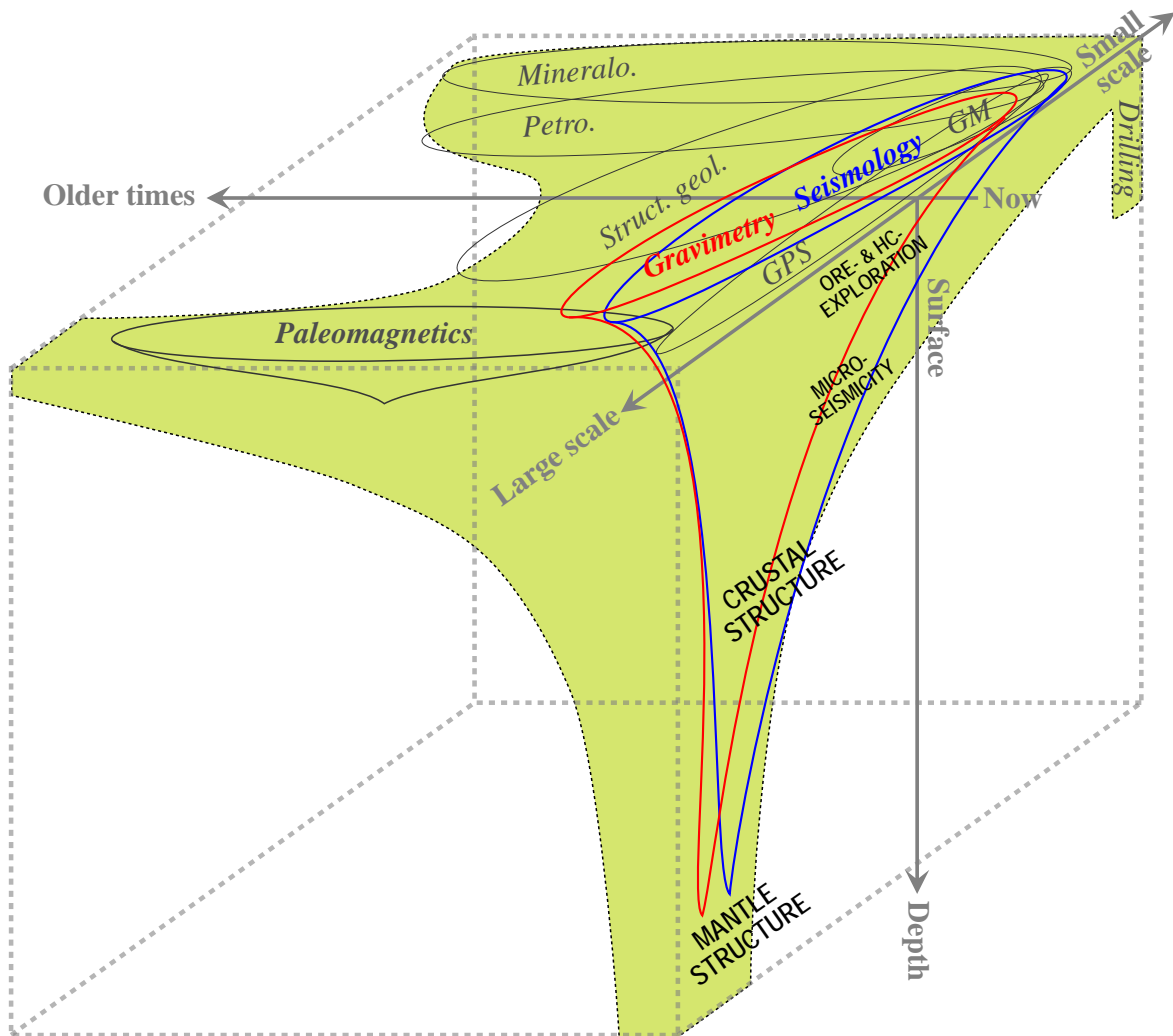
Figure 2.4: Observations in the time–scale–depth space. The approaches presented on Figure 2.2 are reported on top of the cube, and their depth sensitivity is illustrated by cones (for three methods only, to keep the figure readable). The light-green colour approximates the well-constrained subspace enveloping all cones. For example, in very early geological times (left side of the cube), only paleomagnetic and mineralogical information are available, and only at surface. At small scales (back of the cube), mineralogy and petrology provide most of our knowledge, completed by deep wells for very local measurements. The depth—resolution relation (right side of the cube) is discussed in the text. Keywords in black capital letters show a few targets for seismologic and gravimetric applications. (Abbreviations: GM – geomorphology; HC – hydrocarbon.)

2.2.3   Recent deformation patterns

On the closest corner and edge of the *time–scale–depth* cube (Fig. 2.4), we can locate those geophysical measurements that are relatively the most accurate. This is due to the

increasing precision of technical tools, that are able to detect very small signals in both time and displacement. These signals allow us to characterize those regions of the Earth that are deforming at a higher rate than the resolution of these tools. In the Himalayan-Tibetan region, this is clearly the case, as it is indicated by both Global Positioning System (GPS) and seismicity data.

Current deformation at surface is best measured using GPS data. Its acquisition in the region has started in 1991 (Jackson and Bilham, 1994), and has been continuous since then (*e.g.* Jouanne *et al.*, 1999; Larson *et al.*, 1999; Paul *et al.*, 2001; Chen *et al.*, 2004; Zhang *et al.*, 2004; Bettinelli *et al.*, 2006; Gan *et al.*, 2007). Figure 2.3 shows the GPS data compilation of Zhang *et al.* (2004) with respect to stable Eurasia. Despite the uneven spatial coverage, it shows that the current deformation pattern seen by this technique is complex: the movement of India plate is attenuated but transmitted in a straight line in the western part of the plateau, while the velocity vectors are deviated further east and point radially out on its eastern and southeastern border. This deformation pattern represents well that, along with the approximately N-S collision-compression, the Tibetan Plateau is in roughly E-W extension today. This is also documented by N-S trending grabens, located mostly in the southern half of Tibet (Armijo *et al.*, 1986). Further north, the E-W extension is also accommodated along strike-slip faults, such as the NE/NW striking left-/right-slip conjugate fault systems in the vicinity of the Banggong-Nujiang Suture. Here, the surface displacement field estimated from synthetic aperture radar interferometry (InSAR) shows 30-60 km wide zones of concentrated shear, coinciding with active fault traces, suggesting that faulting is the dominant mode of deformation (Taylor and Peltzer, 2006). However, extrapolating current slip rates back in time shows some discrepancies with geochronologic constraints on fault initiation. This not only puts more importance on plateau-bounding structures in absorbing the India-Asia convergence, but also gives place to speculation on diffuse deformation within the plateau. Hence the localized vs. diffuse deformation pattern in Tibet is still a debated issue (see Sections 2.3 as well as Note C).

In Nepal, the main deformation is accommodated across the Main Frontal Thrust (MFT), with a current and Holocene convergence rate estimate of 19±2.5 and 21±1.5 mm·yr^{-1} , respectively (Bettinelli *et al.*, 2006; Lavé and Avouac, 2000). The MFT is the surface expression of the Main Himalayan Thrust (MHT), the main detachment separating the India and Eurasia plates. North of the MFT, other, previously active thrust faults, such as the Main Boundary Thrust (MBT) and the Main Central Thrust (MCT), document the in-sequence propagation of deformation with time (see Figure 4.1 for a detailed map and a schematic cross-section).

Instrumentally measured seismicity is another tool the assess current deformation
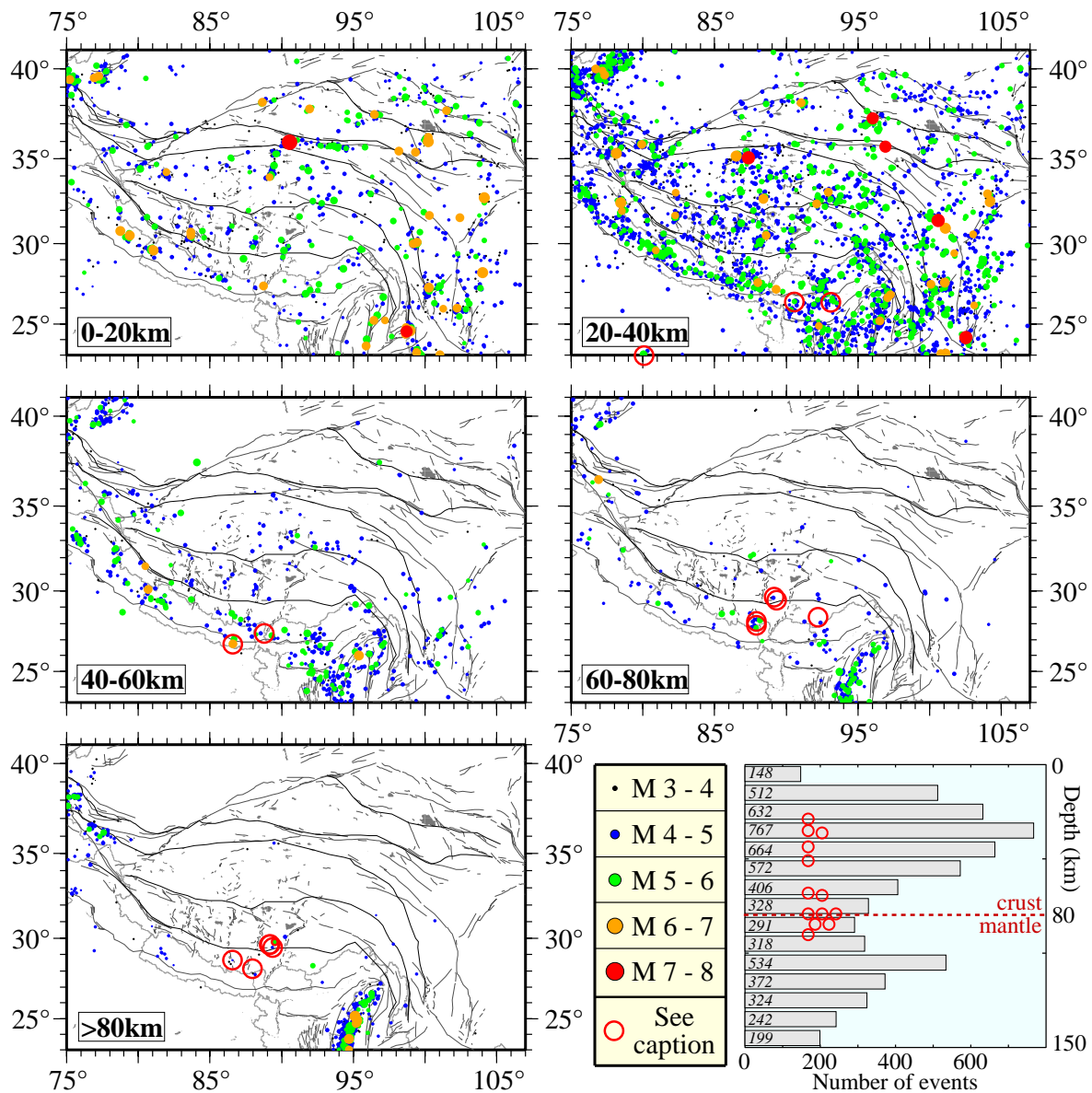
Figure 2.5: Maps: seismicity of $M \geq 3$ in the Himalayan-Tibetan region by 20 km depth ranges (between 1962 and 2007). Full circles are sized proportionally to magnitude and coloured by range of magnitude. Empty red circles are earthquakes analyzed by Chen and Yang (2004) and Maggi et al.(2000) by waveform inversion (the 80 km deep events are reported on both the 60–80 km and >80 km maps). Sutures, faults, lakes, and political boundaries are marked in background for information. Data are from the ANSS composite earthquake catalogue (http://www.ncedc.org/anss/). Histogram: depth distribution of the 8604 earthquakes of the ANSS catalogue by 10 km depth ranges. Events located automatically to 10 and 33 km depth were excluded from the histogram. The empty red circles are as on the maps, and emphasize the occurrence of earthquakes in the upper mantle.

of the lithosphere, and to better localize it at depth. Figure 2.5 represents the seismicity of the region with emphasis on its depth distribution. A large part of the events occur on or close to strike-slip faults or graben-bounding normal faults, and most of the earthquake activity takes place between 20 and 40 km depth. However, a part of the events occur where no faults are observed at surface. Also, the deep seismicity is not negligible, especially in the southern half of the plateau. Events at more than 80 km depth are most representative of brittle mantle deformation, constrained by waveform modelling (*e.g.* Maggi *et al.*, 2000; Chen and Yang, 2004), or subduction zones near both syntaxes of the Himalayas.

2.2.4 Interpretations on the cube

The previous three sections gave an overview of usually acquired geophysical and geological *measurements*. However, these data are *interpreted* by the authors using different (numerical, analogue, and/or imaginary) models, which, in general, lead them to less well-constrained parts of the cube on Figure 2.4. Most often, these interpretations are oriented along one axis of the cube (*e.g.* inferring mantle dynamics from surface measurements; extrapolating an isotopic signature of a set of minerals to the entire region), and sometimes oriented diagonally (*e.g.* guess the temporal evolution of a mountain range from a couple of mineral cooling age determinations).

It seems to me that both measurements and interpretation are equally important: on one hand, adequate and accurate data are the basis of a well founded research study; on the other hand, developing state of the art techniques to analyse and model the acquired data is crucial in order to infer relevant conclusions.

The next section will deal with the dynamic models that have been proposed on retracing the evolution of the Himalayan-Tibetan region from current measurements at all scales: their similarities and differences, the arguments that support and contradict them.

2.3 Evolution models and lithospheric structure

Evolutionary models of the Tibetan Plateau are numerous and diverse, and often represent competing schools of thought. However, they can be classified into four major groups, based on the main lithospheric process that governs them. These are subduction, diffuse thickening, channel flow, and underplating (Fig. 2.6). The four groups are discussed in this section along with their supporting arguments, which, we will see, sometimes show incomplete or blurred geophysical images of the lithosphere, and are not always conclusive. Two of the more important arguments that should be reproduced by evolutionary models

(a) Subduction

(b) Diffuse crustal thickening

(c) Channel flow

(d) Underplating
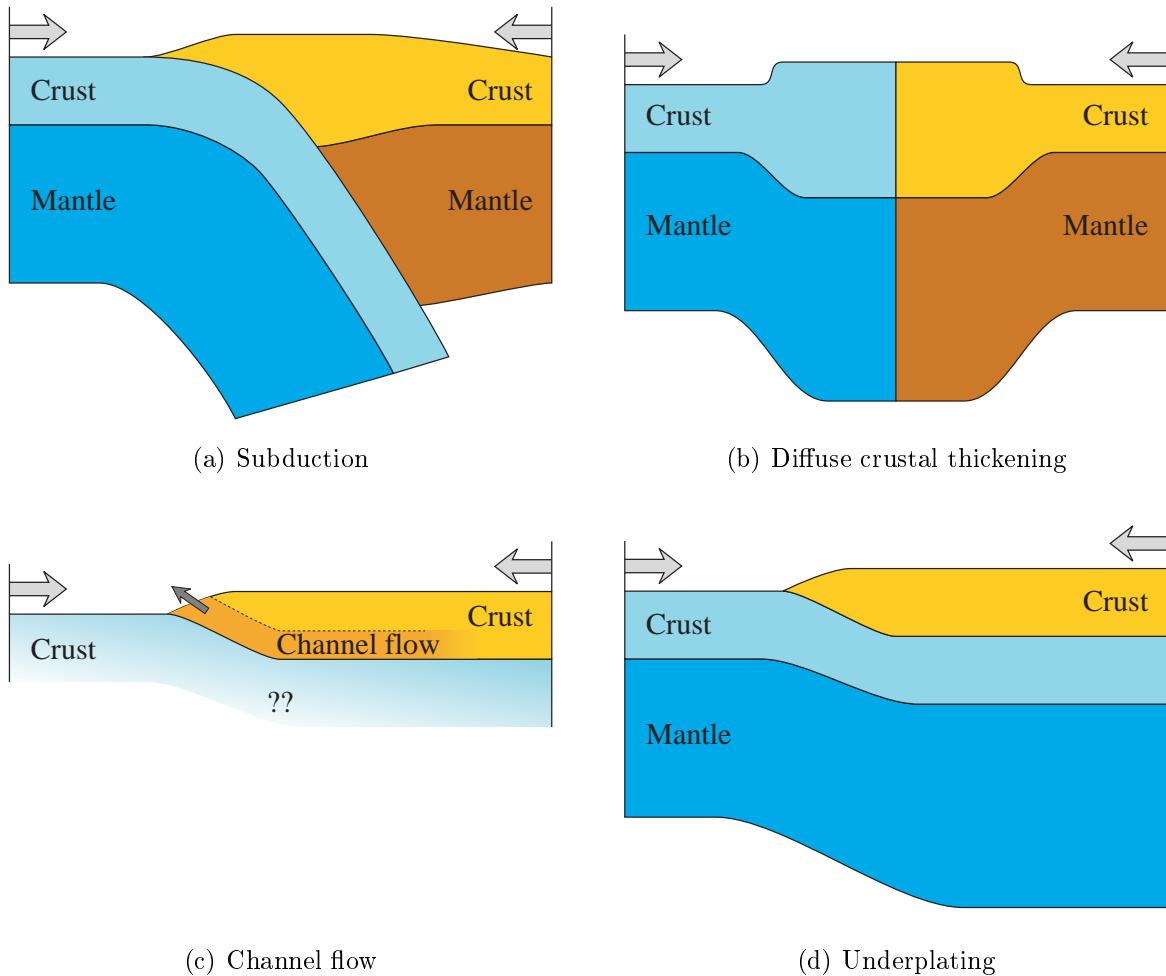
Figure 2.6: Schematic representation of four main mechanisms that may be responsible for plateau growth. Blue and yellow-brown colours mark the lithosphere of two different tectonic plates, with lighter tones for the crust and darker ones for the mantle. See text for discussion.

are the amount of convergence during the collision, and the timing of the Tibetan Plateau's uplift. However, as it is illustrated in Notes A and B, it seems to be difficult to provide precise estimates for these processes. Convergence could be understood as purely the amount of shortening since closure of the Tethys Ocean, but should also account for intracontinental thrusting, internal deformation and lateral escape of mass. Furthermore, the amount of convergence may exhibit significant lateral variations along the ~2500 km long Himalayan arc. Determining plateau uplift is even more difficult, due to the huge surface of Tibet and the available time period during which uplift can be distributed. Estimates are often based on local measurements that cannot be always extended, or isotopic signatures that may

be biased or overwritten by other processes. Hence the evolutionary models, beyond their specific assumptions on dynamic processes governing deformation, are not easy to test in lack of precise estimates of convergence and/or uplift. I think, anyhow, that imaging the current state of the lithosphere at high resolution is crucial in our understanding, as it solidifies one of the elements on which evolutionary models are based, and thus it reduces the existing ambiguities.

Note A

CONVERGENCE AND PLATEAU UPLIFT (1.)

Constraining precisely the timing of the Tibetan Plateau uplift, and the amount of convergence between India and Eurasia would allow provide supplemental arguments for the understanding of how this broad region deformed in the last 50 Myr. However, as it is shown on Figures A and B, the estimates for these two quantities vary significantly, depending on the used method, on the studied sub-region, and on the working hypothesis of different authors.

Figure A: Convergence estimates in km according to sources cited on the abscissa (non-exhaustive list): M75 (Molnar and Tapponnier, 1975); P84 (Patriat and Achache, 1984); B84 (Besse et al., 1984) 550 km in the suture + 400 in intracontinental thrusting; K85 (Klootwijk et al., 1985) 650 km underplating since Early Miocene + 2000 km before; Z99 (Zaman and Torii, 1999); Y00 (Yin and Harrison, 2000); J02 (Johnson, 2002) estimates in the Western, Central, and Eastern part; R04 (Replumaz et al., 2004); A07 (Aitchison et al., 2007) Greater India's maximum extension prior to collision in the central part of the Himalayan Arc.

Note B

Convergence and plateau uplift (2.)

Uplift rate and its timing is important to determine as they reflect ongoing deep processes of the lithosphere. This topic is an interdisciplinary study area between geological, geophysical and atmospheric sciences, as high mountain ranges and broad, dry plateaus affect the climate both on local and global scale. Furthermore, the effect of climate on orogeny is also essential. The relation between climate and mountain building is emphasized by part of the results shown below, which were obtained using records of former climates in sediments, oxygen isotopes, numerical models of climate and monsoon, among others.

Figure B: Estimates in time on the uplift of the Tibetan Plateau according to sources cited on the abscissa (non-exhaustive list): Co90 (Copeland and Harrison, 1990) episodic uplift; Mo93 (Molnar et al., 1993); T93 (Turner et al., 1993); H95 (Harrison et al., 1995); W95 (Westaway, 1995) once at 17 Ma, and smoothly since 11Ma; Fi96 (Fielding, 1996); Fo96 (Fort, 1996) half of the uplift before 8 Ma; Ch98 (Chung et al., 1998) diachronous between West and East; R01 (Rowley et al., 2001); Z01 (Zhisheng et al., 2001); Ma02 (Mahéo et al., 2002); Mu06 (Mugnier and Huyghe, 2006).

2.3.1 Subduction

Before images of the subsurface were available, a large number of people regarded the Indus–Yarlung Tsangpo Suture as the boundary between the original Eurasian and

Indian continental masses (Miyashiro, 1982). As there was no occurrence of Indian affinity rock north of this line, and as the suture is marked by an ophiolite zone, the easiest way to explain the northward movement of the India plate was to assume continental subduction (Fig. 2.6a).

When seismology and gravity measurements started to provide information on the structure beneath the plateau, several models were drawn, which contained north-vergent, south-vergent, or both type of subductions. Furthermore, the northern/southern extent of the India/Eurasia plate were put at different latitudes. The model of Jin *et al.* (1996) based on gravity anomalies represents the Indian lithosphere plunging beneath the Asian one, with a mantle suture in depth located near the YTS. At the same time, Makovsky *et al.*(1996b)[2] imaged the Indian crust beneath the Himalayas with a northward dip, but could not conclude whether the continuation of the Moho was horizontal, with the same dip as observed, or with a dip at even higher angle. A tomography study, conducted by Van der Voo *et al.* (1999) showed a series of northward subductions and slab-breakoffs through the Mesozoic and the Cenozoic, but the resolution of their model was aimed at imaging the mantle and not the lithosphere. With the use of P-to-S and S-to-P converted waves (receiver functions), facing subductions were imaged, with the Indian lithosphere descending north of, but close to the YTS, and the Asian lithosphere plunging close to the Jinsha suture (Kosarev *et al.*, 1999; Kumar *et al.*, 2006)[3]. The southward subduction of the Asian plate was seen by Kind *et al.* (2002) at the same position, further south by Shi *et al.* (2004) — interestingly, both on INDEPTH III profile, — and on the border of the Tarim basin in NW Tibet by Wittlinger *et al.* (2004). This last subduction was also observed in gravity anomalies (Jiang *et al.*, 2004). Finally, finite element numerical models reproduced the subduction of the India plate (Toussaint *et al.*, 2004), as well as that of the Asia plate (Willett and Beaumont, 1994), followed by considerable slab retreat.

The main arguments at surface for the subduction model are summarized in Tapponnier *et al.* (2001). Magmatism, Cenozoic deformation and the successive north-northeast growth and uplift of the Tibetan Plateau are related to several south-verging subductions of the decoupled Asian mantle at the main sutures, and one north-verging subduction of the Indian mantle at the YTS. As the subductions were oblique, the process was accompanied by active strike-slip faulting, which thus took a major role in the deformation of the plateau (see also Note C).

---

[2]INDEPTH (INternational DEep Profiling of Tibet and the Himalayas) I experiment

[3]Mainly INDEPTH II and INDEPTH III data, respectively

2.3.2 Diffuse thickening

A second class of model concerning plateau evolution is known as diffuse crustal thickening (England and Houseman, 1986). The studies that belong here mostly perform numerical models using a thin viscous sheet, in order to reproduce two physical fields: velocity and strain rate. Surface velocity observations are usually taken from GPS measurements, and strain rates are mostly estimated from the spatial distribution of earthquake moment tensors.

As it can be seen on Figure 2.6b, the principal deformation evolution regime of the entire lithosphere is thickening. However, England and Houseman (1989) showed that the model is also able to explain the observed E-W extension in Tibet. After considerable thickening, convective instability removes the thickened boundary layer, and it is replaced by hot asthenosphere. The rapid uplift and raise of gravitational potential energy then drives extrusion. This type of modelling approach was completed by adding strains from plate tectonic forces (Holt *et al.*, 1995), and then by including Quaternary fault slip rates in strain rate calculations (Holt *et al.*, 2000).

The use of a viscous model seems to be justified when we observe that the axes of principal horizontal compressional strain align with topographic gradients (England and Molnar, 2005). However, there are major critics that the diffuse thickening model owns.

The first is the lack of convincing argument in lithospheric structure beneath the surface. A convective instability could be easily confused with an observed subduction, and does not provide sufficient support. An argument would be to clearly observe the intra-crustal structure coherent with the model's assumptions. Seismic reflection results near the Yarlung Tsangpo Suture show crustal imbrications, which could be explained by doubling both the upper and lower crust's thickness separately, and thus producing something similar to Figure 2.6b. However, it is inferred from the same dataset that the Moho is not smooth beneath the High Himalaya, and there may be a vertical step of as much as 20 km across the YTS and the BNS, along with undulations of the crust-mantle interface in Lhasa block (Hirn *et al.*, 1984a; Hirn *et al.*, 1984b; Hirn and Sapin, 1984). The importance of block tectonics, with sharply varying Moho depth between them, was pointed out in the NE part of the plateau as well (Vergne *et al.*, 2002).

The second group of critics concerning thin viscous sheet modelling is the neglect of faults; this aspect is developed in Note C. In summary, while the viscous models reproduce well surface velocities and strain measurements, they usually do not take into account structural constraints at depth.

Note C

Between plate and fault tectonics

Sections 2.3.1 and 2.3.2 point to an important issue in continental deformation kinematics. On one hand, emphasis is put on faults (Tapponnier *et al.*, 2001), on the other hand, on a continuum view averaged over 300 km (England and Molnar, 2005). Some people tried to resolve this problem by including several small, rigid blocks in their numerical model. The number of block varies upon the authors and the area of the studied region: 8 (Shen *et al.*, 2005), 11 (Thatcher, 2007) (Fig. C), 17 (Meade, 2007), 42 (Holt *et al.*, 2000). This approach probably reaches a temporary agreement with the surface deformation pattern, but the block contours should possibly be reconsidered after $\sim 10^6$ years. Also, the relation between these blocks at depth needs to be clarified. Finally, as Figure 2.3 illustrates, the current GPS data distribution is inhomogeneous and insufficient in many regions of the Tibetan Plateau, even in the most recently published papers (*e.g.* Gan *et al.*, 2007). A much better spatial coverage would certainly help to step forward in this debate.

Figure C: An example of block model with fault slip rates (modified from Thatcher, 2007)

2.3.3 Channel flow

A class of model is the so-called "channel flow" model (Fig. 2.6c), describing the development of a relatively low viscosity layer within the crust (*e.g.* Royden, 1996). Numerical models including a low-viscosity layer explain the outward growth of the Tibetan Plateau

and produce a dynamic topography along its borders; they also create ductile extrusion of the Greater Himalayan sequence, and approximate the main features of Himalayan meta-morphism (Clark and Royden, 2000; Shen *et al.*, 2001; Beaumont *et al.*, 2001; Jamieson *et al.*, 2004; Clark *et al.*, 2005).

Arguments for the channel flow are manifold. The uniform altitude of the plateau, and the low flexural rigidity of the flanks of central and south Tibetan grabens suggest a shallow isostatic compensation depth, which could indicate a viscous layer (Masek *et al.*, 1994). However, the authors mention lower crustal flow and viscosities less than 10^{22} Pa·s . Eastward removal of lower crustal material by lateral escape, likely *via* ductile flow, was also proposed, by comparing Tibetan *seismic velocity–depth* functions to global averages (Haines *et al.*, 2003). The high heat flow values measured in Tibet are also an important argument — 146 and 91 mW·m^{-2} in two Himalayan lakes, associated to the recent em-placement of plutonic bodies at <25 km depth (Francheteau *et al.*, 1984). However, one should not forget that these data are extremely local compared to the size of the Tibetan Plateau, where the data coverage is extremely sparse, and that the measured values are spatially variable (Hu *et al.*, 2000).

In conclusion, channel flow models are produced by numerical models, but there is no general consensus if this process occurs in the upper, middle, or lower crust. As-sumptions generally include a relatively hot geothermal gradient, and viscosity reduction due to supposed partial melt (see "bright spots" in subsection 2.4.2) (Beaumont *et al.*, 2004). The used viscosities are between 10^{17} and 10^{19} Pa·s , and some models show that these low-viscosity channels attain a thickness of 15 km with an average flow speed of 80 mm·yr^{-1} (Clark *et al.*, 2005). Le Pichon (2007) pointed out that even though uncertainties exist concerning the thermal field and the rheology of the lithosphere, the values cur-rently used/obtained by channel flow models for viscosity/temperature are very low/high, respectively, and that the input horizontal velocities are often overestimated.

There is also another question mark concerning an issue that channel flow models do not discuss. As it is emphasized on Figure 2.6c, it is not clear what happens *beneath* the Tibetan crust and the flowing channel. In the presented models (*e.g.* Beaumont *et al.*, 2001), the base of the Tibetan crust is drawn with a horizontal line, and the underlying zones are either not discussed in detail, or are supposed to be Indian lower crust underlying Tibet horizontally. Hence, as channel flow models focus only on part of Tibet's thickened crust, they do not explain the entire lithosphere's deformation regime, which reduces the number of large-scale models to three (subduction, viscous thickening, underplating). Fi-nally, similarly to the diffuse thickening case, channel flow modelling basically neglects imaged interfaces at depth, which makes the modelling much more easier compared to

models with structural constraints.

2.3.4 Underplating

Underplating models of the Tibetan Plateau evolution originate from Argand's hypothesis (see Chapter 1 and Figure 1.14), and suppose that the descending lithosphere comes back to a horizontal position immediately beneath the crust of the overlying plate (Fig. 2.6d). The models belonging to this group differ in the extent of horizontal advance, and the fate of the underplated lithosphere: stopping horizontally, or descending at some point. Nevertheless, all models show underplating of India beneath Asia, and never the contrary.

Argand (1924)'s model was reintroduced first by Gansser (1964) and then by Powell and Conaghan (1973), who propose a slab-breakoff at 45 Ma, followed by underplating of India until it meets the first southward subducting Asian mantle subduction. The first seismological measurements supporting this type of model were provided by Barazangi and Ni (1982) and Ni and Barazangi (1983). They observed high Pn and Sn propagation rates beneath the southern part of the plateau, and poor propagation of these waves in the northern part. In their interpretation the limit of the two zones corresponds to the northern extent of the India plate which underthrust Tibet after a subduction and slab detachment in the Miocene. Further support for the presence of underplated material beneath Tibet was the focal depth determination and fault plane solution for an event occurring at 85 km depth by Molnar and Chen (1983), followed by other similar studies. As stated previously, the INDEPTH I experiment imaged the descending Moho across the Himalayas, but could not elucidate its position further north nor confirm the proposed underthrusting (Zhao *et al.*, 1993).

Due to the north-south contrast in Pn wave propagation observed by Barazangi and Ni (1982), and similar studies and contrasts for Pn, Sn, Pg, and Pnl velocity, as well as anisotropy (McNamara *et al.*, 1994; McNamara *et al.*, 1995; McNamara *et al.*, 1997; Rodgers and Schwartz, 1997), more studies have focused on the region of the BNS in the last decade. Using S-to-P receiver functions, Owens and Zandt (1997) found a 20 km thinning of the crust across the Banggong-Nujiang Suture, with normal Poisson's ratios to its south, and high values to the north. Their interpretation shows underplating of the Indian lithosphere — with decreasing amount of crust — until the BNS, possibly continued in subduction of oceanic lithosphere. Seismic polarization anisotropy revealed a major increase in shear-wave splitting in Qiangtang block and isotropic structure beneath Lhasa block, emphasizing the importance of the BNS (Huang *et al.*, 2000). However, in the in-

terpretation, the authors draw the end of the underthrust Indian lithosphere vertically, without further subduction. A tomographic image from the same INDEPTH III dataset shows a high-velocity zone at depths of 100-400 km beneath the BNS, and the authors draw vertical down-welling of the underthrust Indian lithosphere (Tilmann *et al.*, 2003). Unfortunately, this tomography result does not include the upper 80-100 km, which would be the most interesting regarding the thickened Tibetan crust. The north-south contrast close to the BNS was also observed in surface wave dispersion (Rapine *et al.*, 2003) and in the thickness of the electrically resistive upper crust (Solon *et al.*, 2005), although the authors of the latter study interpret their observations in terms of preexisting geological structures, rather than the northern limit of underthrusting. Finally, similarly to the subduction models, global tomographic images do not provide sufficient resolution that would allow to infer pertinent conclusions on the question (*e.g.* Replumaz *et al.*, 2004; Huang and Zhao, 2006).

2.4 How it feels within the lithosphere?

The first discoveries of the Earth's internal structure revealed the existence of discontinuities, such as the one found between the crust and the mantle by Mohorovičić. This is no surprise, as it easier to detect first order variations (the boundaries) of an anomalous region, than to map its internal structure. The previous section mainly discussed the boundaries of subducted, underplated, or thickened parts of the lithosphere; the current section will focus more on what concerns their interior.

2.4.1 Strong or weak?

There is a physical parameter that describes the apparent strength of a lithospheric plate, called effective elastic thickness (EET). As discussed later in this thesis, there is a controversy concerning its value in continental areas. In the Himalayan-Tibetan region, the current estimates range between 36.5 km (Jackson, 2002) and 100 km (Lyon-Caen and Molnar, 1983). Beyond the quantitative discrepancy, there are major differences in the approach on how to estimate the EET. This is due not only to the different ideas on what the EET means, but also on the weak constraints on the rheology of the lithospheric rocks, their water content, and the corresponding temperature field. The issue of weak vs. strong lithosphere rheology is discussed in Chapter 6 in more detail.

2.4.2   Wet or dry?

The different phases of the INDEPTH project provide today the most widely held views about the internal properties of the crust in the Himalayan-Tibetan region. According to these, there is significant amount of partial melt and/or water in the crust. The INDEPTH I seismic reflection studies report so called "bright spots", or highly reflective zones in the middle crust beneath southern Tibet, associating them to partially melted granites in the thickened crust (Nelson *et al.*, 1996; Brown *et al.*, 1996). These granitic magmas can be accompanied by a free aqueous fluid phase, possibly brine water (Makovsky *et al.*, 1996a; Makovsky and Klemperer, 1999). Magnetotelluric studies show that fluids (both melt and aqueous) in Lhasa block are at shallower depths (15-20 km) compared to Qiangtang block (mostly melt at mid-crustal levels of 30-40 km) (Wei *et al.*, 2001). The fluids are better localized in the south and are rather widespread in the north (Haines *et al.*, 2003). However, there is still a *fluid content–bright spot thickness* offset between the results of different geophysical methods and petrologically viable conditions; thus Li *et al.* (2003) estimated quantitatively, using magnetotelluric data and modelling, the amount of aqueous fluid and partial melt in south Tibet, and came up with 100-200 m and >10 km, respectively. Compared to the mostly N-S oriented INDEPTH data, and E-W comparison of magnetotelluric study results, although based on a small number of profiles, show interconnected fluids at the southern border of the plateau at about 30-50 km depth (Unsworth *et al.*, 2005).

However, not all studies agree on the fluid content and the depth of the fluids in the crust of the Tibetan Plateau. For example, the inversion of Rayleigh wave dispersion curves indicate a dry crust in northern Tibet and melt in its southern part (Rapine *et al.*, 2003). Mechie *et al.* (2004) drew the attention to the role of the α-β quartz transition which can occur at shallow depth in the warm Tibetan crust and may generate significant signal in reflectivity and resistivity data.

Finally, the presence of fluids was also suggested based on magnetotelluric conductivities in Nepal, along the Main Himalayan Thrust at shallow depths, where metamorphic reactions would release free water during the underthrusting of sediments, and cause microseismicity (Lemonnier *et al.*, 1999).

The view that significant amounts of fluids are present in the Tibetan crust is widespread, despite the fact that (1) the location of (mostly MT) data is much more restricted than that of the seismic data; and (2) the published results are not all consistent. The results of this thesis concerning fluids in the Tibetan crust are described in Chapter 4.

2.4.3 Interview with a finite element

Numerical modelling is often used in geosciences to reproduce observed data using a physical model. When dealing with mountain building, finite element models are used in most of the cases. The physics describing the model include laws of mechanics (*e.g.* elastic, viscous, and/or plastic behaviour), thermodynamics (*e.g.* heat conduction and sources), and several boundary and initial conditions (*e.g.* convergence, erosion laws). The lithosphere is divided into domains, constituted of thousands of elements, and the above conditions as well as material properties are varied in order reproduce an observed structure in depth, or to match a physical field measured at the surface (*e.g.* strain, gravity, exhumation rate, cooling age). Then it is supposed that zones further away from constrained interfaces or regions are still relevant of the real situation.

Through this approach, finite elements are used in many different goals in the Himalayan-Tibetan region, for example, to:

- assess the role of erosion in mountain building (Avouac and Burov, 1996);

- investigate the origin of granite belts (Harrison *et al.*, 1997);

- estimate the strength of the lithosphere (Burov and Diament, 1995; Cattin *et al.*, 2001);

- reproduce exhumation ages and metamorphic peak temperatures (Bollinger *et al.*, 2006);

- model the evolution of the plateau based on different principles (see Section 2.3).

This list is not exhaustive, and could be continued. Numerical models are a powerful tool, but they should be used with a certain caution. The inputs of the models are sometimes based on very weak constraints, such as the thermal field at depth, or the rheology of different parts of the lithosphere. The boundary conditions, such as the timing and amount of convergence (see Note A) are not always well determined. Finally, the results of numerical models need to be compared to — and should approximately reproduce — real observations, such as exhumation rates, topography, deposited sediment balance, and the geometry of lithospheric and crustal structures.

2.5 Extending the cube

This introductory chapter presented the Himalayan-Tibetan region and some of the research topics, debates, and results concerning its geodynamics. The descriptions were not

aimed to be exhaustive, and focused mainly on questions that are discussed in the frame of this thesis.

The work presented in the following is located on the right side of the *time–scale–depth* cube (Fig. 2.4). The envelope of the well constrained observations shows that it is impossible to achieve both high-resolution and deep images. Small scale observations mainly come from mineralogy and petrology, but the used methods, such as geochemistry or isotopic dating, provide local constraints, and only on samples that have been exhumed. Hence obtaining information at depth is based on assumptions and interpretations. Drilling deep (and expensive) wells provide some localized images, but on a very limited vertical wavelength and depth penetration. Geophysical imaging methods, such as seismology and gravity, are needed to give insights at depth and to cover large areas. However, the interpretation of their results relies strongly on mineralogy and petrology.

In this thesis, we combine seismology and gravity observations and methods in the Himalayan-Tibetan region, and make an attempt to extend the subspace that is considered as well-constrained on the right side of the cube (Fig. 2.7). This extension aims to attain higher resolution in imaging crustal and lithospheric structures. Receiver functions are used to construct a clear and well-resolved image along a S-N profile across the Himalayas and the southern half of the Tibetan Plateau. The resolution is guaranteed by the closely spaced field deployment, as well as the high frequency applications to map shallow features close to the surface and in the upper crust. The clearness of the images is greatly improved by the use of multiple conversions within the lithosphere, and by deciphering (those numerous) zones where direct converted waves and multiples interfere and blur the image. Removing these interferences provides more robust information on many key locations, such as major sutures or tectonic blocks. This way, the crust-mantle interface, the bright spots in the upper crust, the near-surface trace of thrust faults, and the geometry of the boundary between India and Asia at depth can be clearly determined. Furthermore, with the obtained results along the main profile, providing a solid base to characterize the mentioned crustal and lithospheric features, the lateral variations can be easily discussed, and interpretations from previous experiments can be completed or modified.

The seismological approach draws the contours of our refined image of continental collision. It also proposes colours one should take to fill the interior of the bodies. Coupling the seismological results with gravity anomaly approach gives strong constraints on these colours, and helps to interpret the imaged structures in terms of density. The combined results then open the door to several applications and discussions. An example is the mechanical properties of the different structures, and their strength and behaviour in the support of the Tibetan Plateau's weight. Is it the mantle, the upper crust or the lower
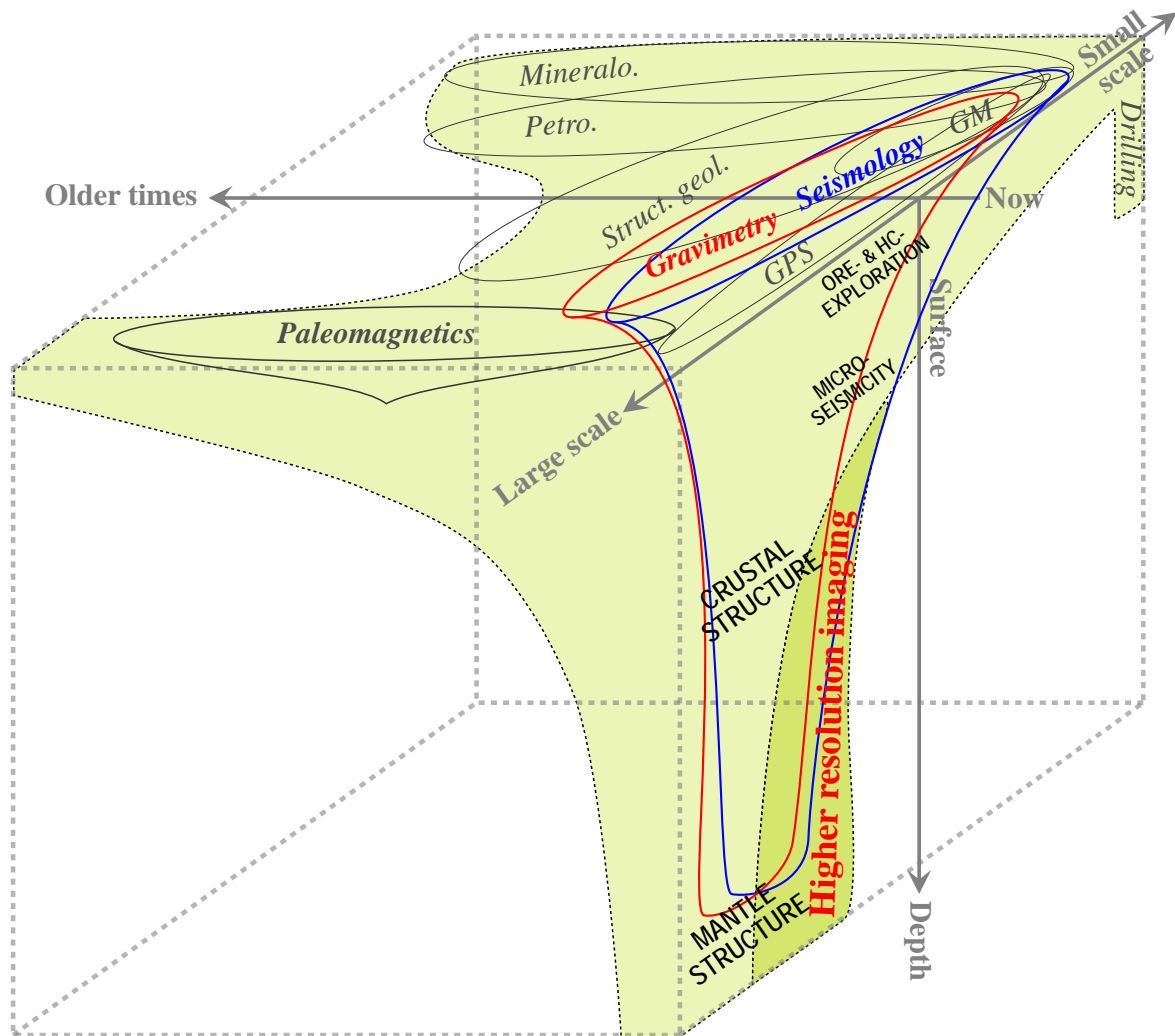
Figure 2.7: Extension of the well-constrained subspace of the time–scale–depth *space presented in Figure 2.4. High-resolution imaging of the crust and the lithospheric mantle by both seismologic and gravimetric approaches is one of the main aspects of this thesis.*

crust that plays the primary role in this task? Adding petrological models to gravity modelling details another interesting topic: the metamorphic transformations occurring in the lower crust. At what extent does water content influence this process, and how large is its implication on density and topography?

The main goals are to characterize the geometry of the current structures, to constrain their physical properties, to describe first-order physical processes that occur in the lithosphere, and, in light of all our observations and modelling results, to retrace the evolution of deformation that rules the collision zone.

CHAPTER 3

DATA – $\underline{D}$ata $\underline{A}$cquisition, $\underline{T}$reatment and $\underline{A}$ssimilation

---

"Geology is a science of the past; the future is geophysics."
E. Argand, 1919

3.1 Introduction

A typical feature of geophysical studies is the loss of resolution with depth. However, with improving technical tools and analysis methods, the sharpness and continuity of crustal and lithospheric images become better. One of the major goals of this thesis is to obtain increased resolution images of the Tibetan Plateau's internal structure: to determine discontinuities and to contour structural elements. The first and basic step towards this goal is high-resolution, continuous, and good-quality data; the second is its detailed processing and assimilation into imaging and geodynamic questions.

This chapter presents both the seismological and gravity field data: their provenance, quality, and quantity. The seismological data used in this thesis are unpublished, thus their acquisition is also discussed. The gravity data are compiled from existing datasets, so their internal consistency needs to be verified.

Data processing methods are described for both types of data. For the seismological part, a short overview of the receiver function method is presented, followed by practical and technical aspects of the specific treatment applied to the Hi-CLIMB dataset. For gravity data, Bouguer anomalies and modelling issues are summarized.
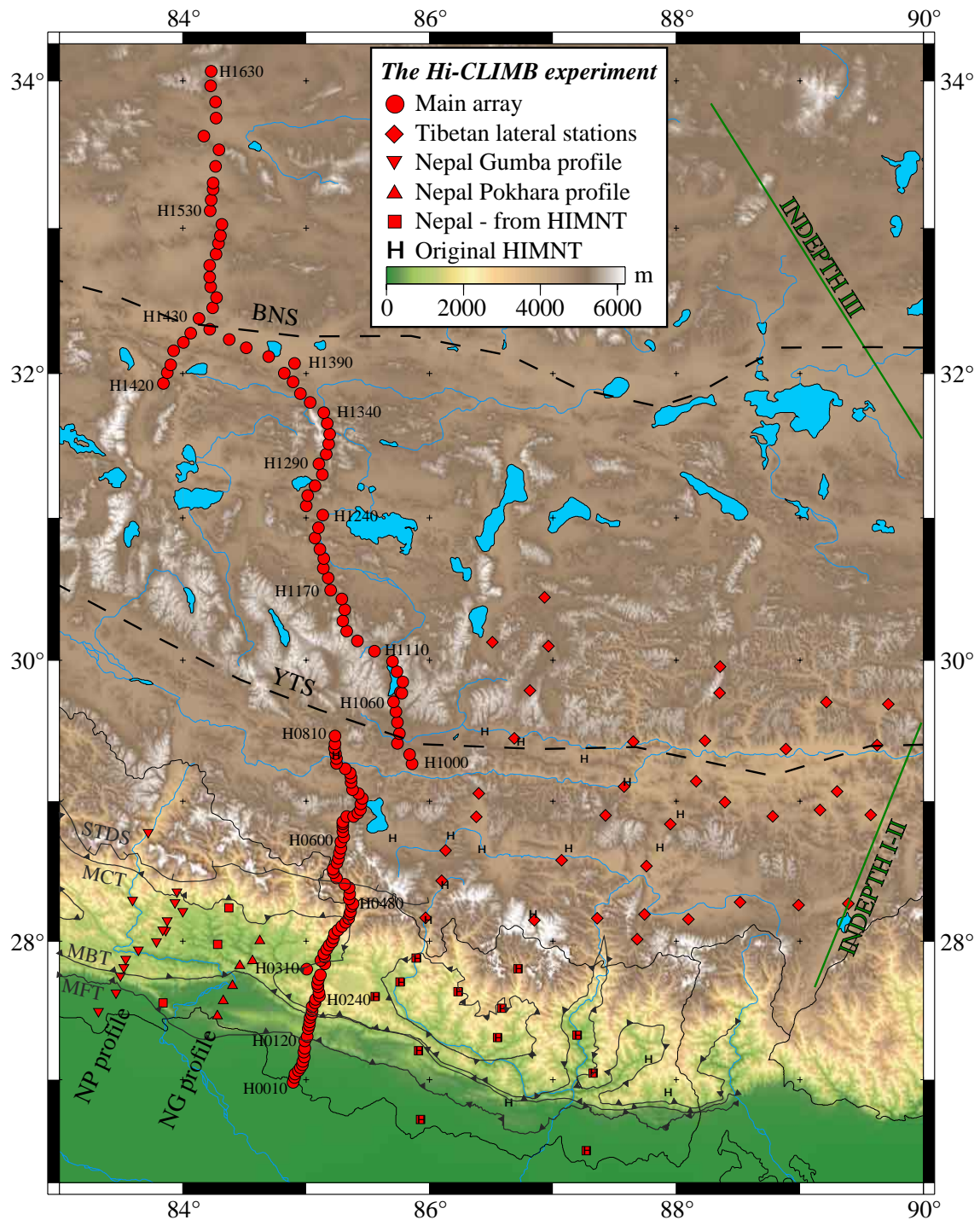
Figure 3.1: Stations of the Hi-CLIMB experiment. Red symbols mark the different groups of Hi-CLIMB stations, also summarized in Table 3.1. For better readability, only a few stations are identified along the main array. Complete station information is available in Appendix B. HIMNT station locations are noted for reference. HIMNT is "Himalayan Nepal Tibet earthquake seismic experiment" (see e.g. Schulte-Pelkum et al., 2005). Major sutures (YTS: Yarlung Tsangpo Suture, BNS: Banggong-Nujiang Suture) and faults, as well as the approximate lines of the INDEPTH experiments are drawn for reference.

3.2 Seismological data: the Hi-CLIMB experiment

3.2.1 Project Hi-CLIMB

Hi-CLIMB is an abbreviation for "Himalayan-Tibetan Continental Lithosphere during Mountain Building"[1]. It is a broadband seismology experiment whose aim is to investigate continent-continent collision across the entire thickness of the lithosphere, from its non-deformed foreland (Ganges Basin), through its most deforming and highest range (Himalayas), up to the centre of its back-arc highland (Tibetan Plateau)(Fig. 3.1) As of today, the Hi-CLIMB experience holds several records concerning the amount of collected data, station spacing, and others; some of these are mentioned below.

Group	Station names	Number of stations	With no data	Number of RFs
Main array	H0010–H1630	152	1	160'754
●Phase1	H0010–H0770	76	0	79'286
●Phase2	H0780–H1630	76	1	81'468
Nepal Pokhara line	NP010–NP100	15	0	3769
Nepal Gumba line	NG010–NG060	6	0	1745
Nepal from HIMNT	N+4 letters	15	1	2884
Tibet laterals	T0010–T0380	37	3	25'381
In Kathmandu	NK+3 letters	30		
Total Hi-CLIMB	5 characters	255		194'533
HIMNT experiment	4 letters	29	1	8108
GSN stations	LSA, KMI	2	0	6007
Total available		286		
Total for RFs		256	5	208'648

Table 3.1: An overview of deployed stations during the Hi-CLIMB experiment. The main focus of this thesis is the main array, but insights are given to 3-D variations using the lateral sites. The 30 stations in Kathmandu were deployed to investigate the Kathmandu basin and site effects, and are not discussed. The last two columns show the number of stations where no three-component record was recoverable for receiver function purposes, and the number of receiver functions calculated, respectively. GSN is Global Seismographic Network (http://www.iris.edu/about/GSN/).

---

[1]Hi-CLIMB is funded by the Continental Dynamics Program of the National Science Foundation, with Principal Investigators John Nábělek (Oregon State University) and Wang-Pin Chen (University of Illinois). For more details: http://quakes.oce.orst.edu/Nabelek/Hiclimb/index.html

3.2.2   Distribution of stations

There were exceptional efforts put into data acquisition. For a duration of 3 years, 255 sites were occupied by three-component, broadband seismometers (See Table 3.1 for a short overview, and Appendix B for station names, co-ordinates, and sensor types). The centrepiece of the project is a linear profile of 152, closely spaced stations along ∼85°E, deployed in two phases of ∼1.5 years each: Phase1 in the south, and Phase2 in the north. In Nepal, this main array was paralleled by two short profiles in the West (NP and NG sites), and half of the stations were recovered from the HIMNT experiment in the East. In Tibet, at the same time as Phase2, 37 lateral stations were deployed to the east, covering the zone between the Hi-CLIMB main array and the INDEPTH I and II experiments.

3.2.3   Data quantity and quality

The deployment of different stations and phases is depicted on Figure 3.2. For every station (on the ordinate), there is a black pixel at the earthquakes (on the abscissa) that provided a complete, three-component record. During the three year acquisition period, more than 1.5 terabyte of raw[2] data were collected for the Hi-CLIMB experiment.

Data acquisition was continuous at a sampling rate of 50 samples per seconds, but some lateral stations in Tibet worked at 40 samples per second during the winter in order to not to saturate the disks too early. During the entire experiment, only two stations were stolen, and a relatively low number of stations (1 in the main array, 3 in the Tibetan laterals) failed to work completely, due to decreased pressure at high altitudes[3] or other errors, and provided no data at all.

3.2.4   Noise sources

The acquired data's noise characteristics are out of the scope of this thesis; however, based on observed waveforms in general, the followings can be said: stations in Nepal show significantly more background noise compared to stations in Tibet, and even within Nepal, a decrease in noise level from south to north can be identified (de la Torre and Sheehan, 2005; Burtin *et al.*, 2007; Fig. 3.3). This is due not only to the fact that noise sources — primarily human, but also natural, — are more present in Nepal, but also that they are more fluctuating. Population density is obviously higher in Nepal. Daily and seasonal

---

[2]1.5 Tb in compact *mseed* format. This is equivalent to ∼40 DLT tapes, or ∼2000 CDs.

[3]Altitude of the different sites range from 12 to 5479 m above sea-level.
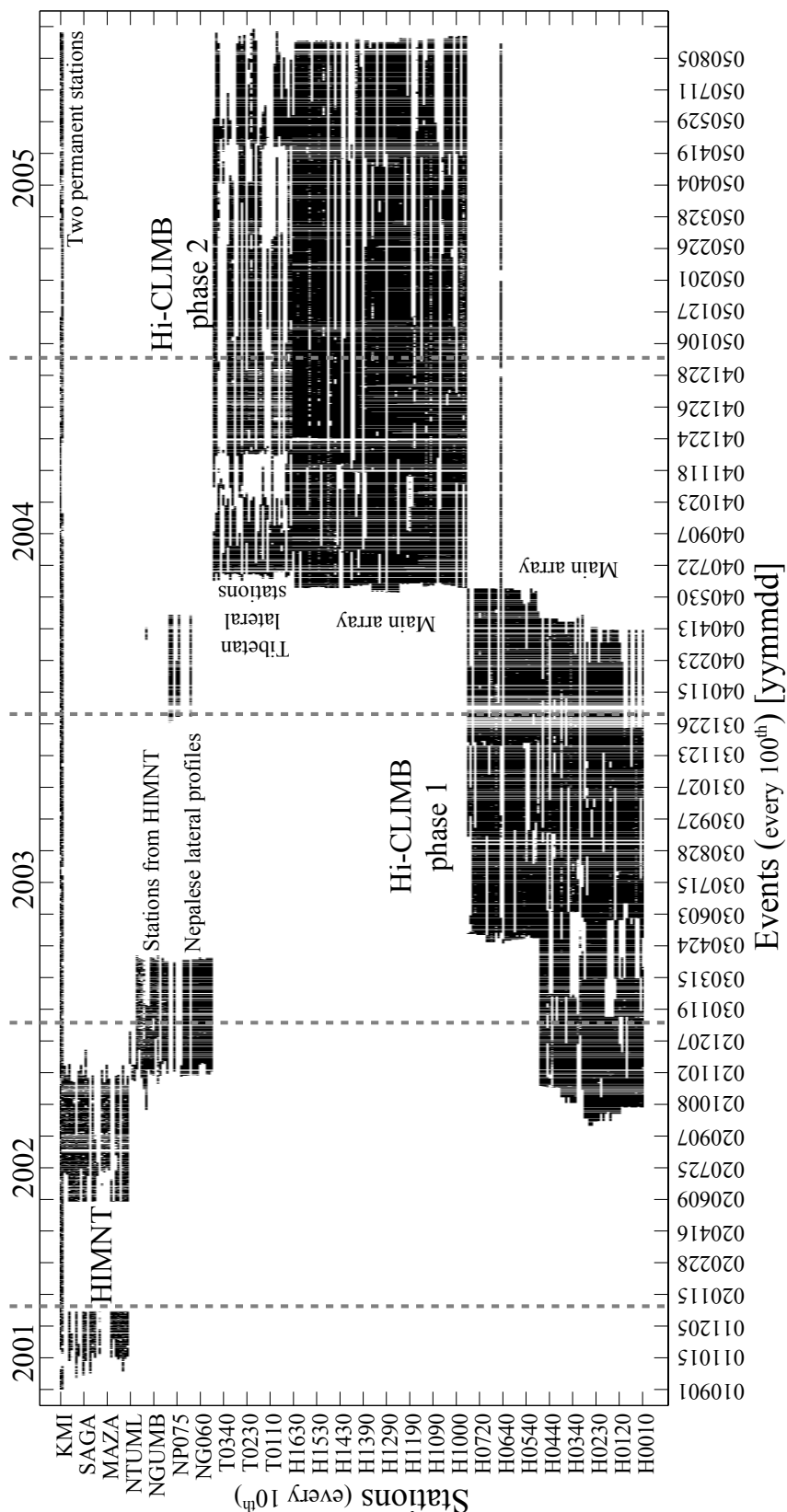
Figure 3.2: An overview of station deployment and data acquisition with time. In this 251×4293 matrix, every black pixel notes a three-component record collected for receiver function calculation. Horizontal gaps mean that a station experienced an acquisition error (typically: no battery, a missing component). Vertical gaps are likely when an earthquake occurs within suitable epicentral distances (see Section 3.3.1) for the GSN stations, but not for a group of Hi-CLIMB stations. Station names and statistics are summarized in Table 3.1 and detailed in Appendix B.

variations in river discharge (Burtin *et al.*, 2007), as well as temperature[4], humidity, and water-table level variations reach higher levels south of the Himalayas. Another important contaminating factor is the reverberations generated beneath rapidly varying topography (see stations H0220 and H0230 in Appendix C).
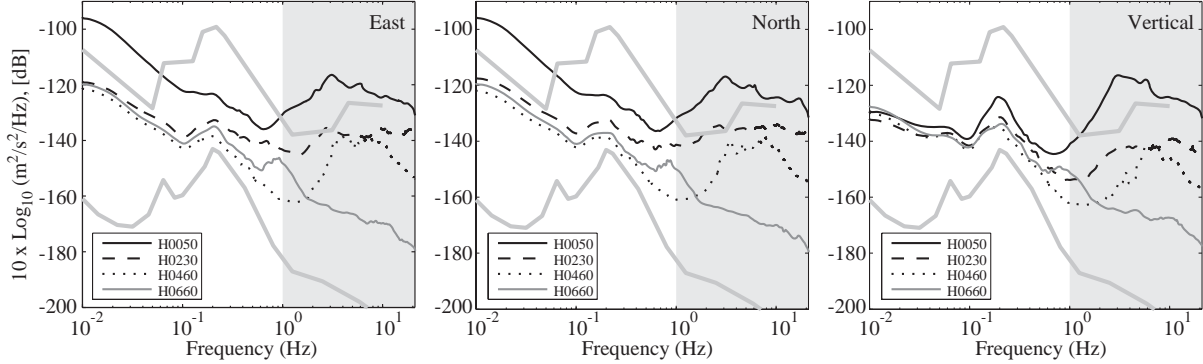
Figure 3.3: Mean annual (2003) Power Spectral Densities estimated for four stations (H0050, H0230, H0460 and H0660) from south to north, respectively, of the east, north and vertical components. Wide gray lines are the New High Noise Model (NHNM) and New Low Noise Model (NLNM) of Peterson (1993). The amplitudes are given in decibel [dB] relative to velocity $\left(10 \times \log_{10}\left[(m/s)^2/Hz\right]\right)$. Gray shaded area indicates the frequency band (1 – 20 Hz) discussed in Burtin et al.(2007). (From Burtin et al., 2007.)

3.2.5   High resolution and focused features

The 152 broadband sites of the main array were deployed to achieve unprecedented resolution, and to focus on some "features of interest". Among these, the most important are the continuous imaging of the Moho on several hundreds of kilometres, including its geometry at the Yarlung Tsangpo Suture (YTS), in Lhasa block, and north of the Banggong-Nujiang Suture (BNS), and the construction of a complete image of the Main Himalayan Thrust (MHT) which was previously imaged at different places and on different lengths. The lateral sites aimed to identify the interfaces recognized beneath the main profile, and to investigate their lateral variations.

In Phase1, the average station spacing was 3-5 km. Ten stations were deployed in the Ganges Basin, which allowed to construct an early image of the flexure of the India plate and to estimate its strength (see Chapter 6). In Nepal, the profile crosses all major

---

[4]Temperature variations were estimated using the relatively low accuracy (1°C) thermometers of the seismological stations. Average daily temperature variations for Phase1 are between 10 and 12°C, while they range between 6 and 8°C in Tibet.

thrust faults, namely the Main Frontal, Boundary, and Central Thrusts (see map on Fig. 3.1 and Fig. 4.1 for a geological cross-section through Nepal). Crossing the Nepal-Tibet border in the Trisuli River valley, Phase1 crosses the South Tibetan Detachment System (STDS) and continues up to the YTS.

Phase2 starts east of Phase1, and crosses the YTS again. The mean stations spacing was 8-10 km, with higher values far from sutures, and increased station density at the Banggong-Nujiang Suture (BNS), for example. Phase2 spans up to the centre of Qiangtang block. Station health was particularly important in Phase2, as the minimum, mean, and maximum elevation of the stations were 4485, 4901, and 5479 m above sea-level, respectively.

The above inter-station distances illustrate well the efforts that were put into deployment in order to gather high-resolution data. Most figures concerning the main profile are projected on a 800 km south-north transect along 85°E, which translates into a (projected) average inter-station distance of 5.3 km.

3.3   Receiver functions in theory

The receiver function method have been introduced about three decades ago (Langston, 1977a; Langston, 1977b). For the following two decades, it remained a relatively secluded tool, but in the last ten years, its popularity in imaging lithospheric structures have been continuously increasing. Its applications are now numerous and have spread to all tectonic plates where it was possible to place a seismometer (Fig. 3.4). Beyond studying crustal structure, research targets include subduction zones, passive margins, plumes, lithosphere-asthenosphere boundary (LAB), the thickness of the mantle transition zone, Moho zone thickness, sedimentary structure, and geothermal areas (Table 3.2). Also, the RF method is often coupled to other geophysical methods, such as surface waves, seismic refraction or electromagnetic surveys. Although receiver function applications are mostly local (one-station studies) and regional (arrays, or many stations), there are a couple of global compilations, for example on the composition of the continental crust depending on its age and origin (Zandt and Ammon, 1995), Finally, beyond the more widely applied P-to-S receiver functions, S-to-P conversions are also used to investigate the lithosphere, yielding lower frequency, but multiple-free images (see *e.g.* Wittlinger *et al.*, 2004 and Kumar *et al.*, 2006 for studies on the Tibetan Plateau).

Table 3.2: A non-exhaustive list of RF applications around the world. See Figure 3.4 for study locations and depths of interest. LAB: lithosphere-asthenosphere boundary.

#	Reference	Region	Theme
1	Bannister *et al.* (2003)	Antarctica	crustal structure
2	Benoit *et al.* (2003)	Arabian shield	transition zone
3	Budweg *et al.* (2006)	W-Europe	Eifel plume
4	Calkins *et al.* (2006)	Argentina	RF with local events
5	Clitheroe *et al.* (2000)	Australia	sediments
6	Endrun *et al.* (2004)	Greece	subduction
7	Ferris *et al.* (2003)	Alaska	subduction
8	Helffrich *et al.* (2003)	North Sea	transition zone
9	Hofstetter and Bock (2004)	Sinai sub-plate	crustal structure
10	James *et al.* (2003)	S-Africa	Moho thickness
11	Julià *et al.* (2005)	Tanzania	RF + surface waves
12	Li *et al.* (2004)	Hawaii	plume
13	Nicholson *et al.* (2005)	N-Cascadia	subduction
14	Oreshin *et al.* (2002)	Tien Shan	LAB
15	Owens (1987)	New York State	RF + seismic refraction
16	Özalaybey *et al.* (1997)	Basin and Range	RF + surface waves
17	Rychert *et al.* (2005)	NE-America	LAB
18	Savage *et al.* (2007)	New Zealand	subduction
19	Tiberi *et al.* (2007)	Oman	passive margin
20	Vergne *et al.* (2002)	NE-Tibet	Moho steps
21	Wilson *et al.* (2003)	California	geothermal zone
22	Zheng *et al.* (2005)	China	sediments

With reference to the above context, my work presented here investigates the southern half of the Tibetan Plateau and its border with Nepal, the Himalayas. The depth target
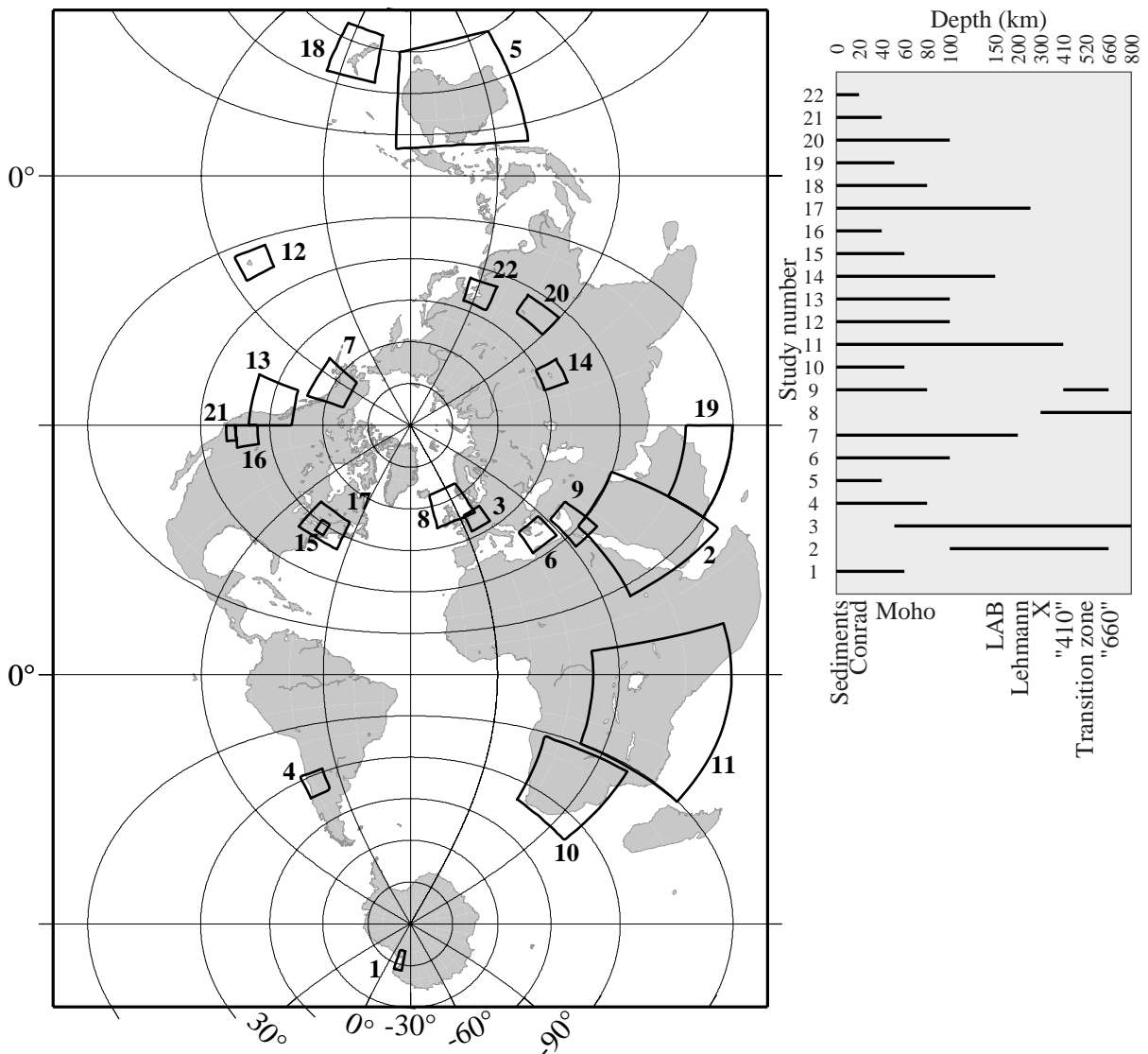
Figure 3.4: Location of receiver function applications around the world and distributed in depth (non-exhaustive list). The references corresponding to the numbers are listed in Table 3.2.

of this thesis is wide: fine scale structure of sediments, near-surface trace of faults, shallow bright-spots, an intra-crustal décollement zone, the Conrad discontinuity, the crust-mantle boundary, the uppermost mantle and its discontinuities, as presented in Chapters 4 and 5.

This section overviews briefly the physics and generalities concerning receiver functions: the generation of converted waves, their enhancing by signal processing, their representation in depth, and their inversion.

3.3.1   Why do we observe receiver functions?

In receiver function methods, we mostly use natural earthquakes as sources. The direct waves propagating through the Earth and arriving at a seismological station are easily observable. In the meantime, the impinging waves that undergo a phase conversion at a discontinuity are also visible, if this conversion occurs below and relatively close to the receiver station; hence the name *receiver function*. This term usually refers to P-to-S converted waves, but S-to-P converted waves are also used. In this thesis, — unless otherwise noted, — receiver functions will mean P-to-S conversions.

When analyzing the above paragraph, some of the employed terms need to be precised:

– A wave conversion occurs only if the impinging wave hits the discontinuity with an angle different from perpendicular. However, due to epicentral distance of teleseismic sources (usually 30-90°), the incidence angles are constrained to low values (see Fig. 5.7). Also, this distance to the receiver implies a certain magnitude for the event in order to be observable at the station (generally M≥5-5.5).

– The term "interface" or "discontinuity" means a more-or-less sharp variation in the material properties of the Earth that causes a wave conversion. We usually understand a change in compressional- and/or shear-wave velocity, but it is more correct to define a "discontinuity" by a contrast in impedance: $Z = \rho \cdot v$, where ρ is the density and v is velocity.

– As the compressional-wave velocity V_P is always greater than that of the shear-wave V_S , a P-to-S conversion means a peak in the waveform that arrives after the direct P arrival (Fig. 3.5).

– Furthermore, when a P-to-S conversion is observable, it is usually accompanied by so-called multiples. These are wave phases that travel an additional two-way trajectory between the surface and the discontinuity, and arrive later compared to the PS conversion (Fig. 3.5; Note D). The role of these multiples is important, as they provide additional information on the velocity structure above the interface (see Section 3.4.4 and Chapter 5).

Note D

ARRIVAL TIME OF CONVERTED PHASES

The theoretical arrival time of converted waves (in a tabular case) can be calculated easily from the Snell-Descartes law and geometrical considerations (Fig. 3.5). Let t_P and t_S be the travel-time of P and S wave between the surface and the converter, and t_m and t'_m the delay of the PS and PpS phase with respect to the P wave at the interface. Thus the arrival time of the different phases can be written as:

$$
\begin{aligned}
t_{PS} &= t_S + t_m - t_P \ , \\
t_{PpS} &= t_S + t_P - t_{m'} \ , \\
t_{PsS} &= t_{PS} + t_{PpS} \ .
\end{aligned}
\tag{3.1}
$$

The arrival times are a function of the depth to the impedance contrast H, the average velocity structure above it (V_P and V_S), and the ray parameter p:

$$
\begin{aligned}
t_{PS} &= H \left[\sqrt{\frac{1}{V_S^2} - p^2} - \sqrt{\frac{1}{V_P^2} - p^2} \right] , \\
t_{PpS} &= H \left[\sqrt{\frac{1}{V_S^2} - p^2} + \sqrt{\frac{1}{V_P^2} - p^2} \right] , \\
t_{PsS} &= 2 \cdot H \cdot \sqrt{\frac{1}{V_S^2} - p^2} .
\end{aligned}
\tag{3.2}
$$

Note in Equation 3.1 that the arrival time of the PsS phase is the sum of the delays of the PS and PpS phases, which can help in the identification of this converted phase.

3.3.2 How to obtain receiver functions?

We can compose a regular seismogram as a combination of the source time function of the incident wave $S(t)$, the Earth's structure impulse response $E(t)$, and the instrument's impulse response $I(t)$. For a three component seismogram, this can be written for the vertical, radial and tangential components, respectively, as:

$$
\begin{aligned}
Z(t) &= S(t) * E_Z(t) * I(t), \\
R(t) &= S(t) * E_R(t) * I(t), \\
T(t) &= S(t) * E_T(t) * I(t),
\end{aligned}
\tag{3.3}
$$
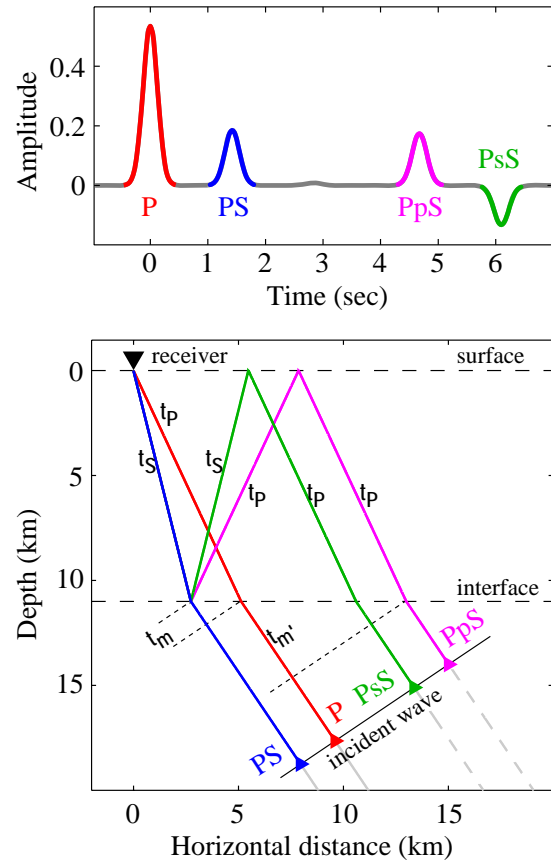
Figure 3.5: Top: A synthetic receiver function showing the direct P wave and the converted phases (PS, and multiples PpS and PsS) in case of a positive impedance contrast (increase with depth) at an interface below the station. Bottom: the path of the different phases from one incident wave. Capital and lower case letters note upward and downward propagating legs, respectively. Propagation times t_P, t_S, t_m and $t_{m'}$ help to calculate the arrival times of the different phases.

where $*$ denotes convolution. In a first approximation, we can suppose that the vertical component is the convolution of a pulse-like time function with the instrument's response (Burdick and Helmberger, 1974):

$$S(t) * I(t) \simeq Z(t). \tag{3.4}$$

Assuming that the instrument's response is the same for all components, we can deconvolve Equation 3.4 from Equation 3.3 to obtain the Earth's radial and tangential structure $E_R(t)$ and $E_T(t)$. Deconvolution is a complex mathematical operation. In RF techniques, although other approaches exist (*e.g.* multi-taper spectral correlation; Park and Levin, 2000) two methods became widespread: the spectral (frequency domain) and the iterative (time domain) deconvolution, discussed in the next section.

It is important to note that Equation 3.4 is an approximation, and that the result of the deconvolution gives the radial and tangential Earth response relative to the vertical one, $E_R(t)/E_Z(t)$ and $E_T(t)/E_Z(t)$. Hence these do not include the Earth's complete radial and tangential response, but only those wave-fields that end their path in an S-leg. Attempts

to extract the complete wave-field, and thus include P-ending legs as well, were performed on array deployments with varying structure beneath individual stations (Li and Nabelek, 1999).

Spectral (frequential) deconvolution

Convolution and deconvolution are more easily performed in the frequency domain, using Fourier-transforms:

$$
\begin{aligned}
E_R(f) &= \frac{R(f)}{I(f) \cdot S(f)} \simeq \frac{R(f)}{Z(f)}, \\
E_T(f) &= \frac{T(f)}{I(f) \cdot S(f)} \simeq \frac{T(f)}{Z(f)},
\end{aligned}
\tag{3.5}
$$

where f is frequency. $E_R(f)$ and $E_T(f)$ are then inverse Fourier transformed into the time-domain. Unfortunately, due to the limited bandwidth of the signals as well as random noise, the procedure in Equation 3.5 is numerically unstable (Langston, 1979). Clayton and Wiggins (1976) proposed to fill the troughs of the above spectral division to a minimum "water-level":

$$
E_{R,T}(f) = \frac{R,T(f) \cdot Z^{\diamond}(f)}{\phi(f)},
\tag{3.6}
$$

where f is frequency and $\diamond$ denotes complex conjugate, and

$$
\phi(f) = \max \left[\, Z(f) \cdot Z^{\diamond}(f) \, , \; c \cdot \max \left[Z(f) \cdot Z^{\diamond}(f) \right] \, \right].
\tag{3.7}
$$

The constant c is the water-level, and its value is usually 10^{-4}. Filtering is achieved by a Gaussian filter in the frequency domain applied to the result of the spectral division.

Iterative time domain deconvolution

It can be read from the above equations that a receiver function is a time series that, when convolved with the vertical component, reproduces the horizontal (radial or tangential) seismogram. Based on this formulation, Ligorría and Ammon (1999) presented an alternative deconvolution technique.

The method determines by cross-correlation of the vertical component and the original (residual) horizontal signal the location and amplitude of the first (next) spike. It then generates a predicted horizontal signal by the convolution of this iteratively updated series of spikes with the vertical signal. The difference between this predicted and the observed

horizontal seismogram is minimized in the least squares sense. At the end of the iteration, the series of spikes represent the best transfer function between the vertical and horizontal signals, thus the receiver function. In this method, filtering of the initial data is required, and the final RF is obtained by a Gaussian convolution in the time domain.

Comparison

The main difference between the two methods is in the recovery of broad velocity gradient zones — low spatial-frequency variations — with depth. These correspond to large peaks in the receiver function. The frequential deconvolution inherently reproduces these features. However, the RFs are often more noisy and ringing, due to the use of the water-level. As of the iterative deconvolution, creating a large peak means that a high number of iterations have to be performed, which is possible but expensive in time. On the other hand, on high-frequency data, the iterative method generally yields higher signal-to-noise ratio RFs compared to the frequential one. Taking into account the above advantages and disadvantages, low and high frequency images in this thesis are produced with frequentially and iteratively deconvolved RFs during migration, respectively (see Chapters 4 and 5). The limit between the two has been established empirically at 0.5 Hz, where the same set of traces deconvolved by the two methods resemble the most. An example of both deconvolutions applied to the same trace is shown on Figure 3.6.

3.3.3   Radial and tangential RF

Radial and tangential components, by definition, are oriented parallel and perpendicular, respectively, to the direction of the incident wave. Thus, in case of a tabular and isotropic structure, the generated receiver function does not show any back-azimuthal dependence, and the tangential RF does not produce any signal (Fig. 3.7a).

However, the structure of the Earth includes both dipping interfaces and anisotropic zones. The behaviour of receiver functions in these cases has been investigated thoroughly (*e.g.* Cassidy, 1992; Levin and Park, 1997; Savage, 1998). In case of a dipping interface, the peaks in the radial RF will have significant variation in arrival-time showing 2π periodicity following back-azimuth (Fig. 3.7b). Also, both radial and tangential RF peaks will have amplitude variations and polarity changes of the same periodicity. The back-azimuths where the tangential RF shows no signal correspond to the direction of the dipping interfaces gradient.

In case of transverse anisotropy, the variations in the RFs arrival time are generally smaller, and there are also amplitude variations in the radial RF, as well as polarity changes
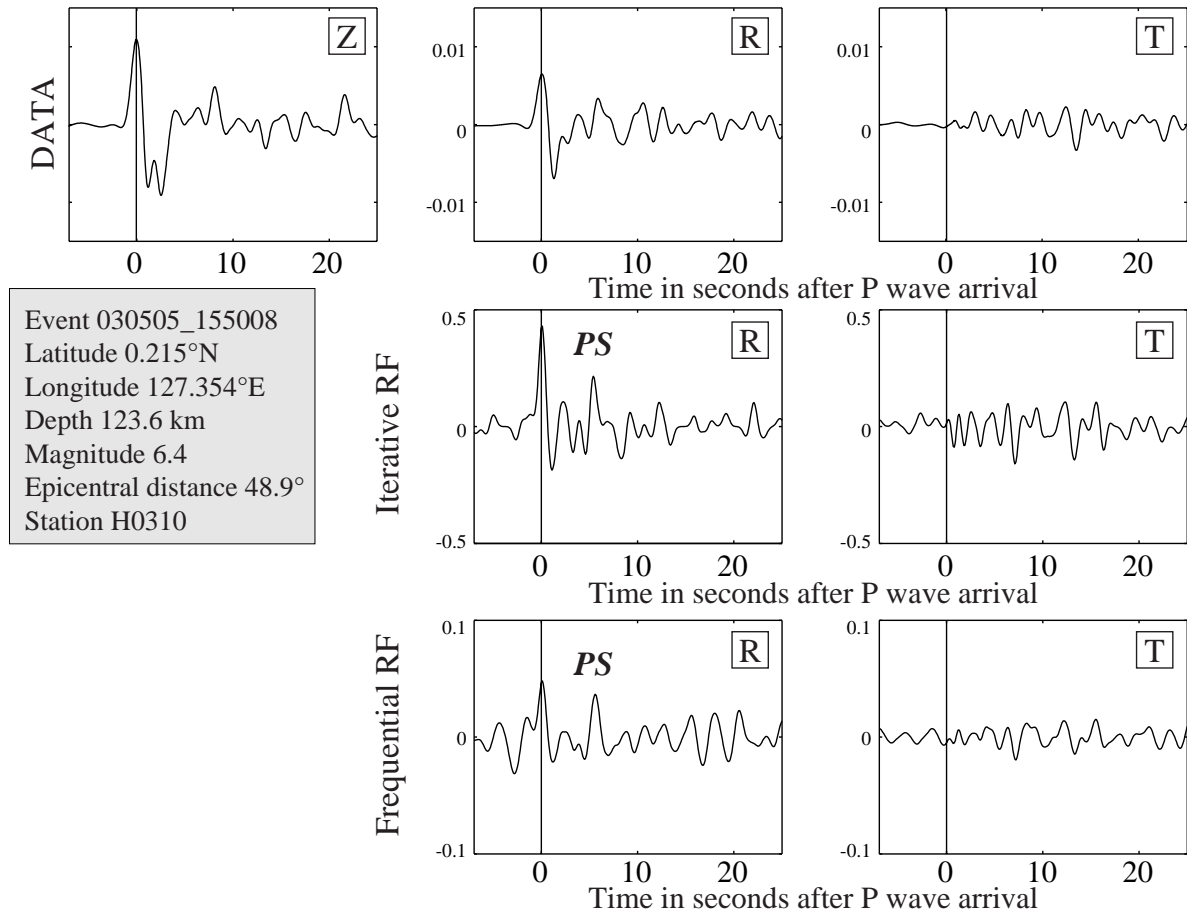
Figure 3.6: An example of three component data after a subduction earthquake in Indonesia. Top panels show original data band-pass filtered between 0.05 and 0.5 Hz. Second and third rows show receiver functions obtained using the iterative and frequential deconvolution methods, respectively. Note the enhanced amplitude of the PS phase on the radial RFs. See the legend for source and receiver details.

in the tangential RF. These variations have π periodicity with back-azimuth when the axis of anisotropy is sub-horizontal (Fig. 3.7c), but 2π periodicity when it dips at a higher angle (Fig. 3.7d). Due to the fact that observed seismograms contain noise, and that the back-azimuthal coverage is rarely perfect, it is not unambiguous to resolve whether receiver functions were generated by a dipping interface, anisotropic layer(s), or both. However, when several stations are used, continuously dipping (and thus deepening) interfaces can be followed on stacked migrated images, while anisotropy is cancelled out.
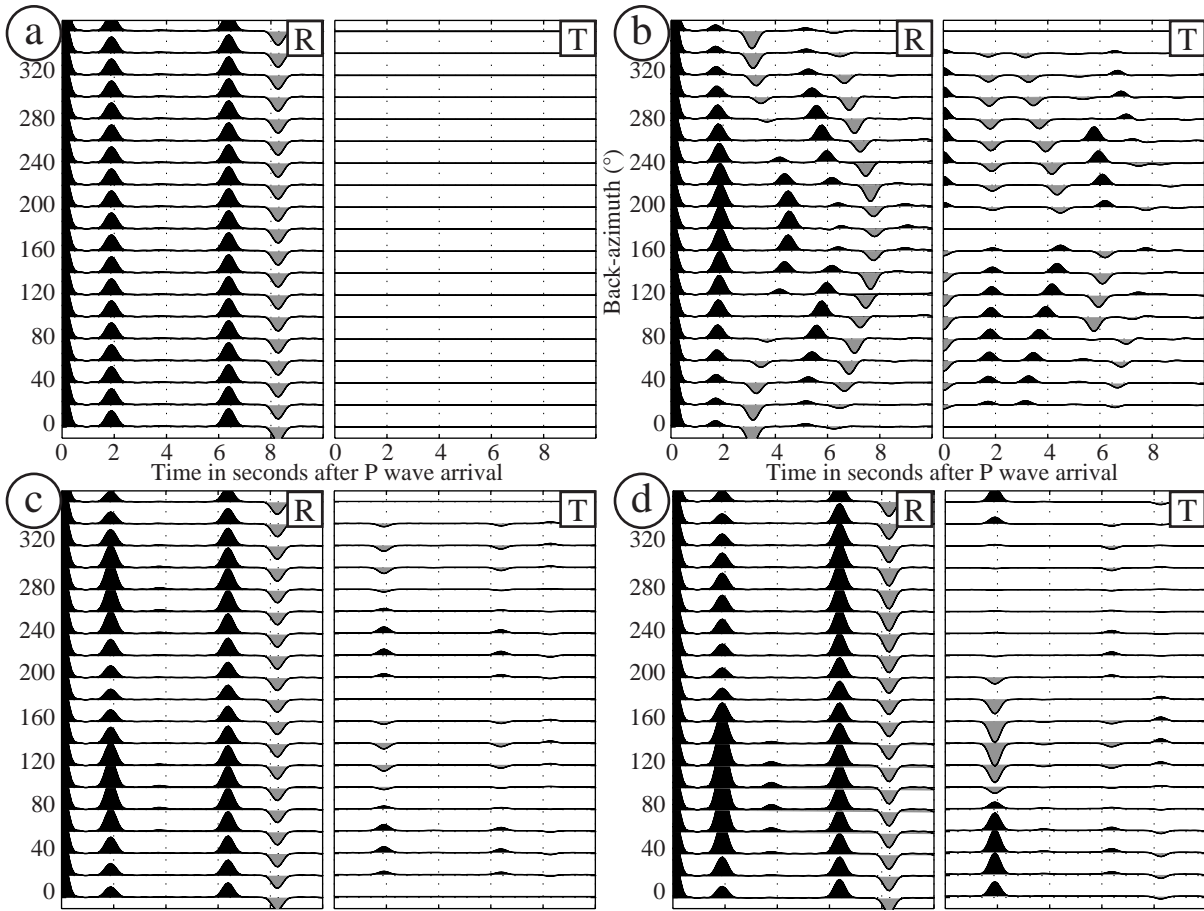
Figure 3.7: Synthetic radial (R) and tangential (T) RFs illustrating the effect of a dipping layer and anisotropy, as a function of back-azimuth. (a) Tabular, isotropic structure with one discontinuity at 15 km depth. (b) The interface dips 20° to the south; note the 2π periodicity. (c) The lower half-space has 15% horizontal transverse anisotropy (0° dip) oriented east; π periodicity. (d) Same as (c) but dipping at 45° to the east; 2π periodicity. In all models, V_P and V_P/V_S are 6.2 km·s^{-1} and 1.75 above the discontinuity, and 8.1 km·s^{-1} and 1.8 below, respectively. Ray parameter is 0.06 sec·km^{-1}, water-level is 10^{-4}, Gaussian filter width is 3.5.

3.3.4   Stacking and migration

"Stacking is everything"

P. Shearer, 2005

Individual receiver functions (or *traces*) are often contaminated by noise. Fortunately, in most of the cases, noise is incoherent from one trace to another. The simplest but very efficient way of suppressing noise is adding or averaging traces, by regrouping traces of similar ray-parameter, similar epicentral distance, or by ranges of back-azimuth.

Another way to represent large number of RFs is to perform a time-to-depth migration, which makes the interpretation easier. A commonly used method is the Common Conversion Point migration (CCP; Zhu, 2000). In this technique, the path of each receiver function is computed between the receiver station and the earthquake source assuming a constant ray-parameter. Then, using a gridded velocity model, the time samples of the receiver function are back-propagated along the ray-path, and the amplitude of the time samples are put into the corresponding grid cases (Fig. 3.8). Finally, after back-propagation of all traces, each grid cell is averaged using the number of rays crossing it, which yields the final migrated receiver function profile.

Migrating teleseismic receiver functions using the wave-equation was proposed by Chen *et al.* (2005). Their method includes a screen propagator taking into account the effect of diffraction, scattering, and travel time alternation caused by lateral heterogeneities, which makes it useful for imaging complex structures. However, their post-stack procedure suppresses part of the information compared to the pre-stack migration applied here; thus I did not adapt and used their method.
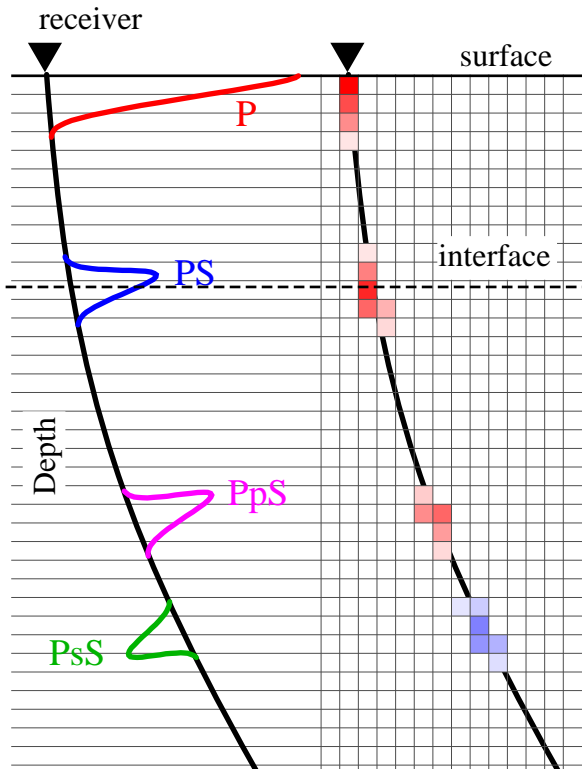
Figure 3.8: Schematic representation of receiver function CCP migration. The computed RF trace is laid along its theoretical path (left), and its amplitudes (red: positive, blue: negative) are gridded using a mesh (right).

3.3.5   Inversion techniques

The inversion of receiver functions is a complex problem. The amplitude and arrival time of different phases depend in a non-linear way on the depth of the interfaces and the velocity structure above them. Furthermore, as the observed variable is *time*, there is a strong trade-off between *depth* and *average velocity*. Also, as receiver functions are most sensitive to rapid variations, inversions recover the velocity *contrasts* usually well, but not the *absolute* values. To resolve the above trade-off and to obtain absolute velocities in complex zones, joint inversions with other types of data (*e.g.* surface waves; Julià *et al.*, 2005) are the best choice.

The research methods assigned within the Hi-CLIMB working group did not give us the opportunity to perform joint inversions. Consequently, here I only summarize two widespread methods for the inversion of receiver functions alone. Later in this thesis, I present results based on both methods applied to the Hi-CLIMB dataset (see Chapter 4 and Appendix D).

Semilinearized method

Linearizing the RF inversion problem comes back to write the difference between the observed (R^{obs}) and modelled ($R^{mod}(p_k)$) RFs as an expansion to Taylor series, up to its first order derivative with respect to the model parameters p_k:

$$dR_i = R_i^{obs} - R_i^{mod}(p_k) = \sum_{k=1}^{N} \frac{\partial R_i^{mod}}{\partial p_k} dp_k, \tag{3.8}$$

and to minimize this value in the least squares sense (Owens *et al.*, 1984). However, this technique is only valid if the initial model is close to the true model, which is not an obvious choice to make. To deal with this problem, one can begin the inversion with a range of initial models, and then find a linear relation between model and data (Ammon *et al.*, 1990). When applying this technique in practice, the modelled structure is divided into layers of constant thickness and V_P/V_S , thus the only parameter to search is V_S . These approximations are rather strong: in reality, the V_P/V_S -ratio significantly affects the depth of the interfaces and the amplitude of the conversions. At the same time, the number of parameters to invert is not reduced by this assumption, as they serve to divide the model into further layers. The stability characteristics of this technique make that it is considered robust only when a healthy guess on the initial velocity model can be made.

Neighbourhood algorithm

The Neighbourhood Algorithm (NA; Sambridge, 1999a) is a stochastic inversion method that was developed using the receiver function problem. The method's goal is to find an ensemble of models that preferentially sample the good data-fitting regions of a multidimensional parameter space. It takes advantage of so-called Voronoi cells (Fig. 3.9) to derive the direct search, and uses the rank of the data fit criterion rather than their absolute value. In the first step, the whole parameter space is divided into cells, using
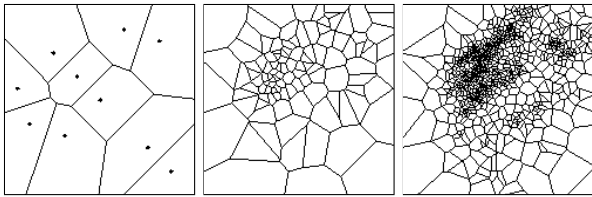
Figure 3.9: Steps of the NA: Voronoi cells around 10, 100 and 1000 points (from Sambridge, 1999a).

nearest neighbour regions, and the rank is established by computing the misfit function between observed and modelled data. Then the best n percent of the models are kept, and their original cells are re-sampled by tighter Voronoi cells. This self-adaptive scheme is repeated until the maximum number of iterations are reached. In practice, the NA allows for varying V_P/V_S and performs the inversion for layer thickness as well. It is an ideal tool to invert a large number of models in a non-linear problem, but is considerably slower than the semi-linearized approach. Also, as the best-fitting models are selected automatically within one round of inversion, interpretation of the results may call for new round(s) of inversion.

Applicability

The main issue in RF inversion is the choice of the initial model. For the semi-linearized method, the iterations will diverge rapidly if the initial model parameters are distant from the real case. The NA is less sensitive on this choice, however, *a priori* data on the depth of the interfaces, as well as on the velocity structure, are needed to ensure robust results. Beyond the choice of the initial model, the main difficulties of RF inversion are not related to the methods, but to the conditions. Both inversion methods assume tabular, plane interfaces with homogeneous velocities, and no attenuation. In reality, this is rarely the case: both dipping boundaries and anisotropy are present. Furthermore, attenuation causes smaller amplitudes than expected from theoretical calculations, thus inversion methods looking to reproduce the amplitude of the signal are generally biased. From this point of view, migration is more efficient, as it is based on arrival times and not amplitudes,

and thus produces a more suitable image for interpretation.

Finally, as mentioned above, the inversion of RFs alone does not allow to obtain absolute velocities, basically because the amplitude of the conversions carrying this information are modified, for example by attenuation. Joint approaches should be used on Hi-CLIMB data in order to corroborate the available results (see Chapters 4 and 5).

3.4 Receiver functions in practice
Application to the Hi-CLIMB data

Elements of the receiver function theory were presented in the previous section. However, their application comes only when there is available data, and after that these are put into the correct format to be processed. Data preparation is an important step, and may consume as much — if not more — time as the real, scientific computation.

This section focuses first on data formatting details. Then specific features of RF migration performed on the Hi-CLIMB dataset are discussed in order to prepare the presentation and interpretation of the results in the following chapters. Finally, a few image processing issues are raised to show how the interpretations may be biased by different representation modes of the same picture.
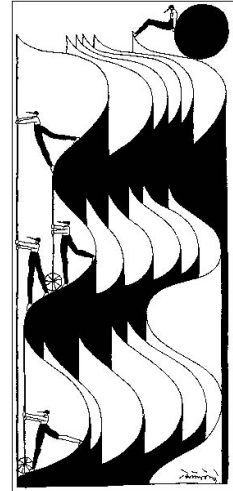
Figure 3.10: "Measuring receiver functions." Cartoon of B. Tettamanti ©

3.4.1 Signal processing and quality control

From the seismometer to the laboratory

The path from acquisition to a usable format is often long, and data usually transits through at least two formats and several storage devices. For example, a station acquires three months of data that are first saved to a laptop in the field, in *ref* format (in case of a *REF TEK* acquisition system). Then, the data from several stations are gathered on a DLT disk, sent to the laboratory by regular mail. There, they are transferred to a computer where they are converted to *mseed* format, and organized by sampling rate and acquisition date. At this stage, one file corresponds to ∼1 hour of continuous acquisition on one component of one station. In order to compute receiver functions in this thesis, the *mseed* files were converted to *SAC* format, and hourly files were merged in order to extract continuous data corresponding to each event.

The field surveys were performed by several persons in a quasi-continuous way. Data tapes were collected by John Nábělek, who organized all the dataset on several external disks on the same computer, and linked them in order to provide access to the entire dataset from one folder structure. Personally, I have participated to one field survey, and

then extracted and converted all events suitable to study RFs from the entire dataset to *SAC* format. Taking into account the updating of the scripts, the multiple data arrivals from the field, and the rearrangement of the extracted dataset, this took about 2-3 months.

The above process may contain and cause several errors, which will not be discussed in detail, only mentioned below:

– There may be different problems due to the deployment of a station. It happens rarely that the sensor is not oriented correctly to the north, causing problems with the horizontal components. This can be rectified if the error of orientation is recovered.

– Another problem related to data acquisition is if one of the sensor's components is not working, or if one of the recording channels experiences problems. As receiver function computation requires three components, these errors cannot be repaired.

– An observed error is that neighbouring, hourly recordings still miss time samples between the end of a file and the beginning of the following. These data gaps can be very short or rather long, but in any case, they should be eliminated. In the Hi-CLIMB dataset, this type of error affected 1635 traces (of 208'648).

– Finally, an error which is frequent but does not affect receiver function computation is the issue of time. The GPS devices at each station sometimes fail to lock on satellites, and while running on their internal clock, they accumulate more and more error. These time shifts are important when doing tomography or other techniques requiring exact timing, but receiver functions work with a relative time compared to the P wave arrival, and thus does not depend on absolute time measurements.

Data quantity

At the end of the field-to-laboratory path, more than 1.5 Terabyte of raw data were collected. For receiver function purposes, all $M \geq 5.0$ events from the ANSS catalogue were chosen, and the corresponding three-component records were extracted for earthquakes occurred within an epicentral distance range of 30 to 95° degrees. The duration of the Hi-CLIMB project, the number of stations, and the suitable epicentral distance of the Japanese and Sumatran subduction zones make that the resulting number of records, and thus RFs, amounts to $\sim$200'000 (Table 3.1).

To ensure a certain quality for the results, one has to make sure of the acceptable quality of the used records. Due to the amount of data, it is impossible to perform "visual inspection" of the entire dataset. An automatic selection process is required to select higher

quality records. This, in turn, can take advantage of the fact that the data were acquired along an array, and that nearby stations should provide more or less similar traces.

The quality controls presented below, including filtering and elimination of overlapping events, required calibration. Testing these parameters on a partial and then on the complete dataset, as well as selecting their appropriate values took about 1.5 months.

First quality control: ZNE

The first quality control process concerns the original three-component (Z-N-E) data. Traces are cut 30 seconds before and 135 seconds after the P wave arrival, and filtered in the frequency band that will be used for the computation of the RFs. Then the following values are calculated, for each trace (Fig. 3.11):

- *rmsall* – root-mean-square (*rms*) of the entire trace;
- *rmsbg* – *rms* of the background signal, between 30 and 5 seconds before the P arrival;
- *maxbg* – maximum of the background;
- *maxpk* – maximum of the peak, between -5 and 20 seconds of the P arrival;

The quality of a trace is measured using four control parameters, C1 to C4. A trace is of good quality, if:

- it resembles to other traces acquired at other stations for the same event:

$$median \cdot C1 \geq rmsall \geq median/C2; \qquad (3.9)$$

(where the median is calculated over traces at all stations for one event);

- it has a high signal-to-noise ratio in amplitude:

$$maxpk \geq maxbg \cdot C3; \qquad (3.10)$$

- it has a high signal-to-noise ratio compared to the background noise, too:

$$maxpk \geq rmsbg \cdot \sqrt{2} \cdot C4. \qquad (3.11)$$

While the first criterion is checked on all three components, the others are performed on the vertical component only. The sensitivity of the parameters is the following: when the value of C1 and C2 increases, they narrow the range of acceptable traces. Contrarily, when
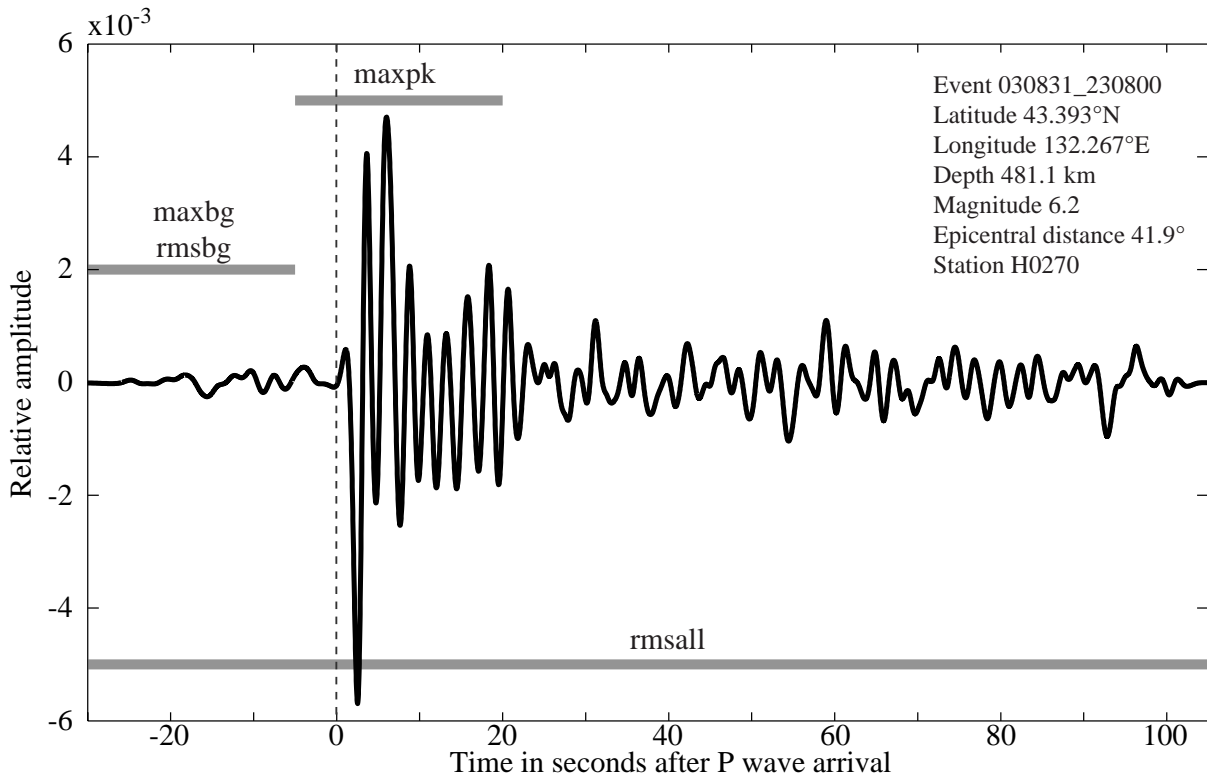
Figure 3.11: An example of acquired data, with gray bands showing where the different values serving for the raw data quality control are measured. See text for more details. (The trace is a vertical component data after a deep earthquake beneath E-Russia.)

C3 and C4 are decreased, they allow more traces to be included in a selection. Based on different tests and histograms calculated on the data, six empirical parameter sets (lists) were defined to create more or less restrictive selections of traces (Table 3.3).

Second quality control: RF

It is not uncommon that signals are weak (for example for distant, low magnitude earthquakes), or are contaminated by noise at several stations, and thus still pass the first quality control criteria, which is based on separate events. Due to these factors, and/or other problems during signal processing, low quality receiver functions are produced. One can establish a second set of criteria that allows to select and drop these RFs. A preliminary selection of RFs was performed based on the characteristics of the P wave arrival (Fig. 3.12) on iterative receiver functions. The position of the maximum absolute amplitude sample

List name		C1	C2	C3	C4	QC1	(%)	QC2	$^{QC2}/_{QC1}$ (%)
M≥5.5	all					56982	100		
Weak 1	W1	100	100	1	1	51'662	90.7	36'727	71.1
Weak 2	W2	15	15	2	2	41'766	73.3	33'836	81.0
Weak 3	W3	10	10	2	15	21'491	37.7	19'352	90.0
Strong 3	S3	5	5	3	30	12'805	22.5	11'803	92.2
Strong 2	S2	3	3	3	30	12'401	21.8	11'522	92.9
Strong 1	S1	2	2	5	30	11'008	19.3	10'356	94.1
M ≥5.0	all					194'533	100		
Weak 1	W1	100	100	1	1	162'079	83.3	78'204	48.3

Table 3.3: Statistics on the restrictiveness and efficiency of the quality control procedures. List W1 through S1 are increasingly restrictive selections computed using the C1–C4 parameter sets in the first quality control procedure (on ZNE data). The number of traces kept using this selection is written in the QC1 column. The QC2 column lists the number of traces left after applying the second quality control criteria. The last column is the ratio of QC2/QC1, and shows increasing percentages for the more restrictive lists. Statistics based on ZNE data filtered between 0.05 and 0.5 Hz.
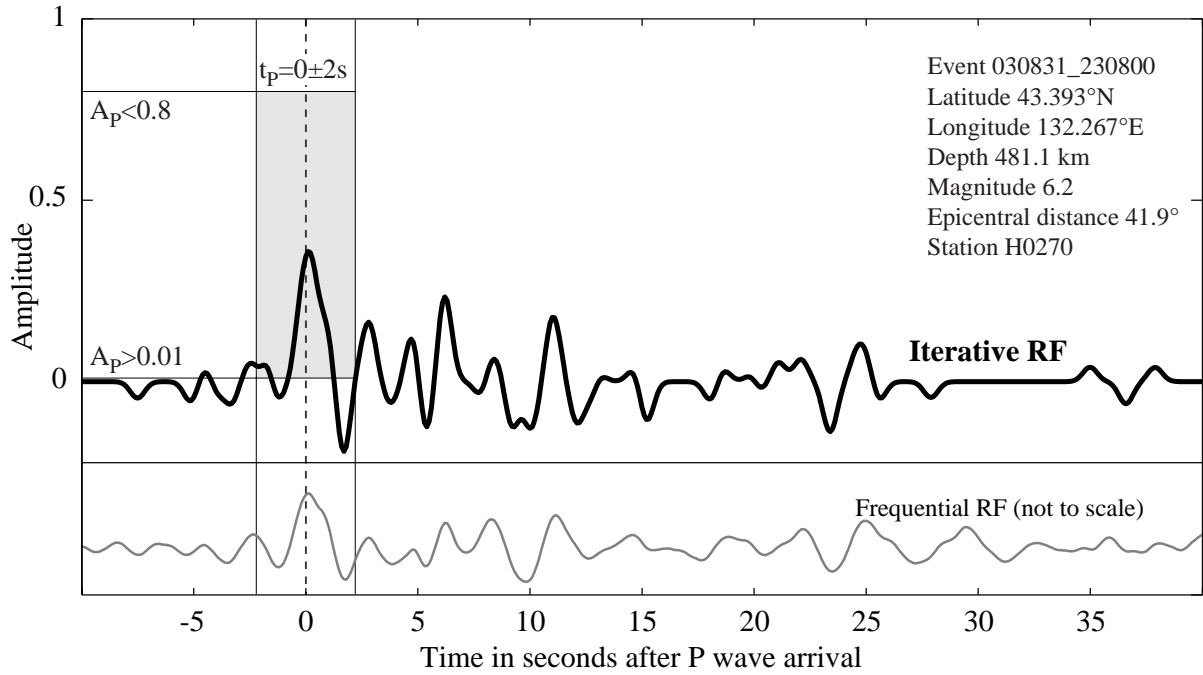
Figure 3.12: The iterative radial RF corresponding to the trace on Figure 3.11, band-pass filtered between 0.05 and 0.5 Hz. The second quality control aims to constrain the arrival time and amplitude of the P wave. The frequential RRF is shown for comparison.

is chosen (t_P) along with its amplitude (A_P), and these should satisfy:

$$|t_P| \leq 2 \ sec$$
$$0.01 \leq A_P \leq 0.8. \tag{3.12}$$

The first criterion eliminates traces with the most current problems: where the P wave does not emerge from the background, and where there are timing problems (*e.g.* between components). The amplitude limits included in the second criterion are determined empirically: a positive amplitude is expected, together with a theoretical limit of $A_P \leq 1.0$, but traces with $A_P \geq 0.8$ are often ringing, and do not provide clear converted phases. A high A_P value can easily result from an incorrect gain on one component of the seismometer.

The effectiveness of the second quality control is shown in Table 3.3: with increasing restrictivity of the first quality control, the second eliminates less and less data, and hence confirms the first QC. Further selections of RFs, for example based on their *rms*-value, are applied during migration (see Section 3.4.2).

Filtering

Filtering the seismological data allows to focus on different features of the lithosphere, and eliminates noise from frequency bands that are cut by the filter. This step of the data processing is applied between the two quality control steps (see previous sections). Filtering during the RF calculations depends on the type of deconvolution used.

For the frequential (spectral) deconvolution method, there is the possibility of filtering by simply multiplying Equation 3.6 by a Gaussian function. The width of a low-pass Gaussian centred at 0 Hz should be $f_{max}/\sqrt{2}$, where f_{max} is the cut-off frequency. In application to the Hi-CLIMB dataset, traces were first cut to –30 to 150 seconds with respect to P wave arrival, then the mean level of each trace was removed, and a 15 s wide Hanning window was applied on both ends to apodise traces prior to frequential deconvolution. For data storage purposes, traces were decimated to 10 samples per seconds, and only the –20-120 s range was kept for the computed RFs.

For the iterative (time domain) deconvolution, the procedure was to remove the mean level of each trace, apodise using a 15 s wide Hanning window, and to pad the trace with zeroes until the second next power of 2 in order to prevent eventual phase wraparound during filtering. Band-pass filtering was then performed using zero-phase, two-way, second order, Butterworth digital filter eliminating very low (<0.01 Hz) and very high (>4 Hz) frequencies. Then the traces were cut to the –20-120 s range, and the time domain

deconvolution method using 100 iterations was performed. This number was chosen as over 100 iterations the resemblance between the original and the iterated traces did not progress significantly, and also because of computation time issues. The obtained series of spikes were stored, and RFs corresponding to different bandwidth were obtained using Gaussian convolution, equivalent to a low-pass filter, where the width of the Gaussian is $1/(2\pi f_{max})$ and $f_{max} < 4Hz$.

The filter's corner frequencies are set with regard to the target of the final image and the thickness of the velocity gradients. Higher frequencies ($f_{max} > 0.5Hz$) are useful when aiming sharp velocity contrasts with depth, while low frequencies ($f_{max} \sim 0.2Hz$) are used to investigate smoother velocity variations, occuring across several kilometre thick zones. More examples are given in Chapters 4 and 5.

Overlapping events

As mentioned above, the Himalayan-Tibetan region lies within a favourable distance from the West Pacific and Sumatran subduction zones. This makes that earthquakes may occur and produce signal at a station within short intervals: the signal of the second earthquake, which is not always an aftershock, arrives within the coda of the first one.

In order to recover non-overlapping data, aftershocks and nearly coincidental earthquakes are eliminated according to the following scheme. First, as data are abundant, only $M \geq 5.5$ events were considered. Second, after each event, a given amount of clearing time was considered, depending on the events magnitude:

Magnitude above:	5.5	7	7.5	8	8.5	8.9
Clearing time:	42 min	97 min	3 h 43	8 h 33	19 h 41	1 day 21 h 18

This is a logarithmic relation between time and magnitude, except for low magnitudes where a threshold time level was maintained, and for the 2004 Sumatra earthquake, where the decaying was exceptionally long. Any event occurring within the given time lapse was discarded from RF migration.

3.4.2 CCP migration characteristics

The principle of Common Conversion Point migration was presented in section 3.3.4 and on Figure 3.8. Here I focus on technical details, and describe the generally used migration parameters applied to the Hi-CLIMB dataset. In one sentence: the receiver functions were subjected to pre-stack 2-D depth migration including altitude correction and back-azimuthal equalization.

Pre-stack. Migrating prior to stacking is a more timely procedure, however it provides a much more correct image compared to the post-stack approach. Pre-stack migration allows each trace to be laid along its own raypath and to place the RF amplitudes corresponding to their true lateral position.

2-D depth migration means that the arrival times on the RF are spread according to a velocity model so that the final image's vertical scale becomes depth. However, using a 2-D velocity model is not a common way to proceed. Here we propose a direct way to construct a 2-D velocity from receiver functions using multiples (Note E). The 2-D velocity model was applied to the main array only, which was the primary focus of this study.

Altitude correction is important to take into account, as the altitude range of the deployed Hi-CLIMB stations exceed 5 km. As one of the aims is to obtain a better resolution for the shallow structures and the Moho, the constructed 2-D velocity includes the true elevation of all stations, which allows higher precision and easier interpretation compared to a choice of a fixed reference level. This way all migrated images presented in this theses have a depth axis with reference to sea-level, and ~5 km should be added when discussing crustal or lithospheric thickness, for example.

Back-azimuthal equalization. There is probably only a few places on Earth where the azimuthal distribution of natural earthquake sources is close to homogeneous. The Himalayan-Tibetan region lies within favourable distance (30-95°) from the West Pacific and Sumatran subduction zones (Fig. 3.13a), but there are only a few events that provide azimuthal coverage from the other half of the globe (Fig. 3.13b). In order to provide equal illumination of the structures, the migrated RFs are first stacked either by quadrants (N, E, S, W or NE, SE, SW, NW), or by 20° back-azimuth ranges, and then the 4 or 18 images are averaged.

Back-azimuthal analysis of RFs is also a powerful tool to investigate the presence of anisotropy and/or dipping structures (see Section 3.3.3). Stacking the traces by narrow ranges of back-azimuth allows easier identification of arrival time and/or peak amplitude variations. Examples from the Hi-CLIMB dataset are presented in Chapters 4 and 5. Note that stacking traces by epicentral distace is not very important in the analysis of crustal features, as the corresponding signals are close to the P wave arrival and do not have significant move-out curves.

Finally, the last selection of receiver functions is performed during the migration process. It has been observed that the distribution of the filtered RFs' *rms* shows a small group of traces with much higher values (Fig. 3.14), which would possibly be overweighed during stacking. In order to provide sufficient representation of smaller *rms*-traces, RFs in the highest 5% of the *rms*-distribution were not taken into account.

Note E

CREATING A 2-D VELOCITY MODEL

Two-dimensional velocity models are essential when migrating in laterally varying media. For receiver functions, this task can be performed for example by using one of the multiple conversions. First, a regular RF migration is performed using a 1D velocity model (V_P^0 and V_S^0), (*e.g. iasp91* Kennett and Engdahl, 1991). This will locate the PS conversion to depth z_{PS}, and, using an apparent velocity, the PpS conversion to depth z_{PpS}. The relationship between z_{PS} and z_{PpS} indicates if the true average V_P/V_S -ratio above a discontinuity (usually the Moho) is the same, higher, or lower than the V_P/V_S of the initial velocity model (Fig. E). To calculate the true value of V_P/V_S , we can use the observed (O) arrival times

$$t_{PS}^O = \frac{z_{PS}}{V_P^0} \left(V_P^0 / V_S^0 - 1 \right), \qquad t_{PpS}^O = \frac{z_{PpS}}{V_P^0} \left(V_P^0 / V_S^0 + 1 \right). \qquad (3.13)$$

Taking advantage of the formulae for theoretical arrival times (Eq. 3.2), the true depth of the converter H and the average V_P/V_S above it are:

$$H = \frac{t_{PpS} - t_{PS}}{2} \cdot \frac{1}{V_P}, \qquad V_P/V_S = \frac{t_{PpS} + t_{PS}}{t_{PpS} - t_{PS}}. \qquad (3.14)$$

Then, assuming an initial P wave velocity model, division of V_P by V_P/V_S yields the 2-D shear-wave velocity model. The error of this model is a combination the precision in picking z_{PS} and z_{PpS}, and the accuracy of the initial P wave velocity model (see Section 4.4.3).
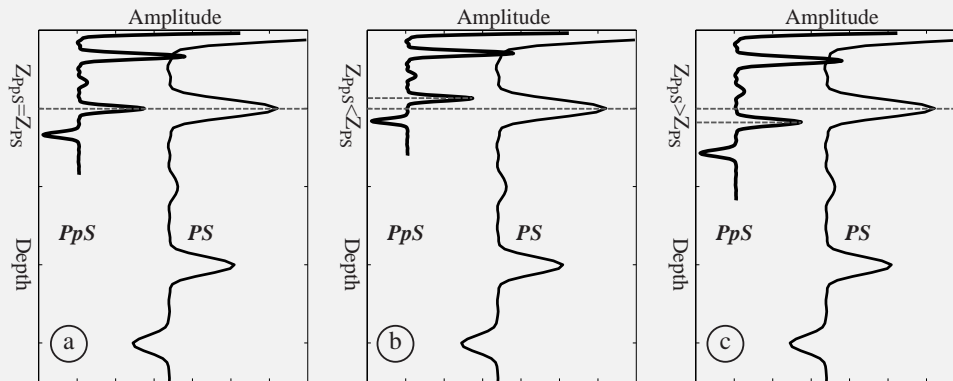
Figure E: The relationship between migrated PS and PpS phases and average V_P/V_S -ratio above an interface. (a) The depth of the two migrated phases are equal, the V_P/V_S -ratio is as in the initial model. (b) and (c) The PpS phase is shallower (deeper), the V_P/V_S -ratio should be increased (decreased) compared to the value in the initial model.
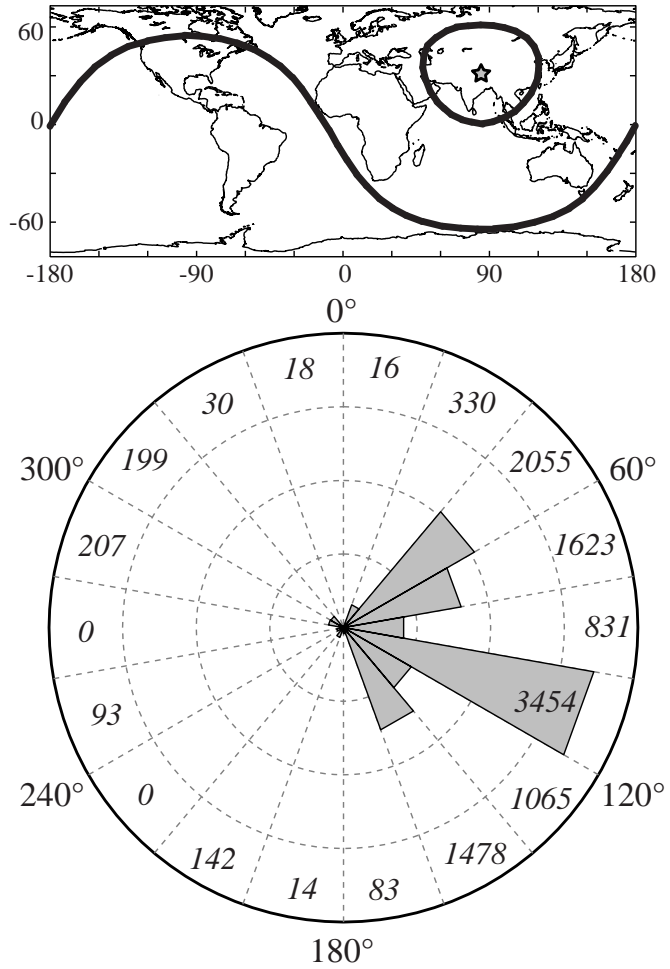
Figure 3.13: Top: iso-epicentral distance lines at 30 and 95° from the centre of the Hi-CLIMB main array (star). Earthquakes within this range are suitable to produce RFs. Bottom: back-azimuthal statistics of a selection of traces used for migration along the main profile (W3 list after second quality control).

Figure 3.14: An example of rms distribution of migrated traces showing that the top 5% of the traces have more than twice the amplitude of the other traces (W3 list after second quality control, iterative RFs, Gaussian filter with $f_{max}=0.5$ Hz)
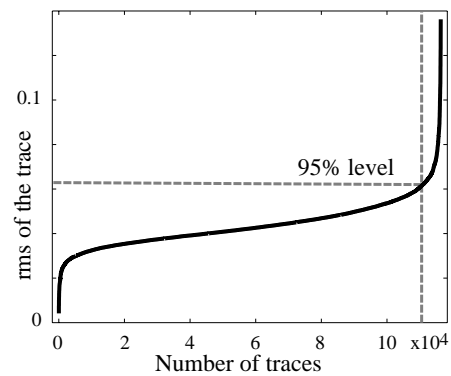
Computation time. The above calculation steps determine the time required to produce one migrated image. The two factors with the greatest influence are the size of the migration grid and the dimension of the velocity model. In a usual example for the main profile, with about 10'000 traces and a mesh of 1×1 km cell size, the migration is performed within 15 minutes down to 150 km depth using a 1-D velocity model[5]. However, the more accurate 2-D velocity model multiplies the needed time by a factor of ~ 10. Other processing steps require a rather constant amount of time: 5-10 minutes for filtering all traces, 10-30 seconds for smoothing one image, 30-60 seconds for representing another phase, such as PpS or PsS, and 10-30 seconds to export towards an *xyz*-grid usable by GMT (Wessel and Smith, 1991). All codes for receiver function processing are written in MATLAB. They are partially based on earlier codes by Jérôme Vergne, and were developped (for example for the 2-D migration) during this thesis.

3.4.3 Representation modes

Migration is the next to last step in receiver functions processing. The remaining task, the mode of representation, may be considered more of an artistic issue rather than scientific; however, it greatly affects the interpretation of the image by different persons. The first group of topic is colour tones and saturation levels (Note F): the goal here is not to detail the physical aspects why the eye is more attracted by hot colours or strong contrasts, but to show a few examples. The second group of topics are based on physical concepts: how to render horizontally coherent structures more visible, and how to strengthen information that are common to several images at the same time.

Smoothing

A popular operator applied to migrated images is horizontal smoothing. The reason for this is not only the Earth's lithospheric structure being mostly horizontal, but also (and mainly) the width of the Fresnel zone within which waves sample (and average) a particular interface.

Centred to each pixel, the smoothing operator averages over a given number of neighbouring pixels using a Gaussian curve, and thus enhances horizontally continuous features. Figure 3.15 shows a synthetic example and the effect of different smoothing widths on elements of different size, amplitude and dipping angle.

---

[5]Computation times are representative for a single processor of an Intel$^{\circledR}$ Xeon$^{\text{TM}}$3.20 GHz computer and using 2 GByte RAM.

Note F

COLOUR SCALE AND SATURATION

Conventionally used **colours** in seismological imaging (*e.g.* tomography) are cold-to-cold and hot-to-hot: that is to assign blue colours to fast zones, and red to slow ones. However, the receiver function images show the contour of zones, or impedance contrasts, and authors usually use red to mark a positive, and blue for a negative change of impedance with depth. In the meantime, the linearity between red and blue varies from one study to another, and attempts are made to introduce other colour tones. Figure F shows two columns of synthetic images using a classic (blue-to-red) and a modified colour scale including yellow and magenta.

Beyond the choice of the colour scale, the amplitude of the colours — the **saturation** level — has to be chosen as well. Figure F shows three saturation levels, going from low to high amplitudes. In this synthetic example, it is easy to identify that the top and bottom images are over-/under-saturated, respectively. However, in between these two extrema, most people do not choose the same saturation level as the optimal one.
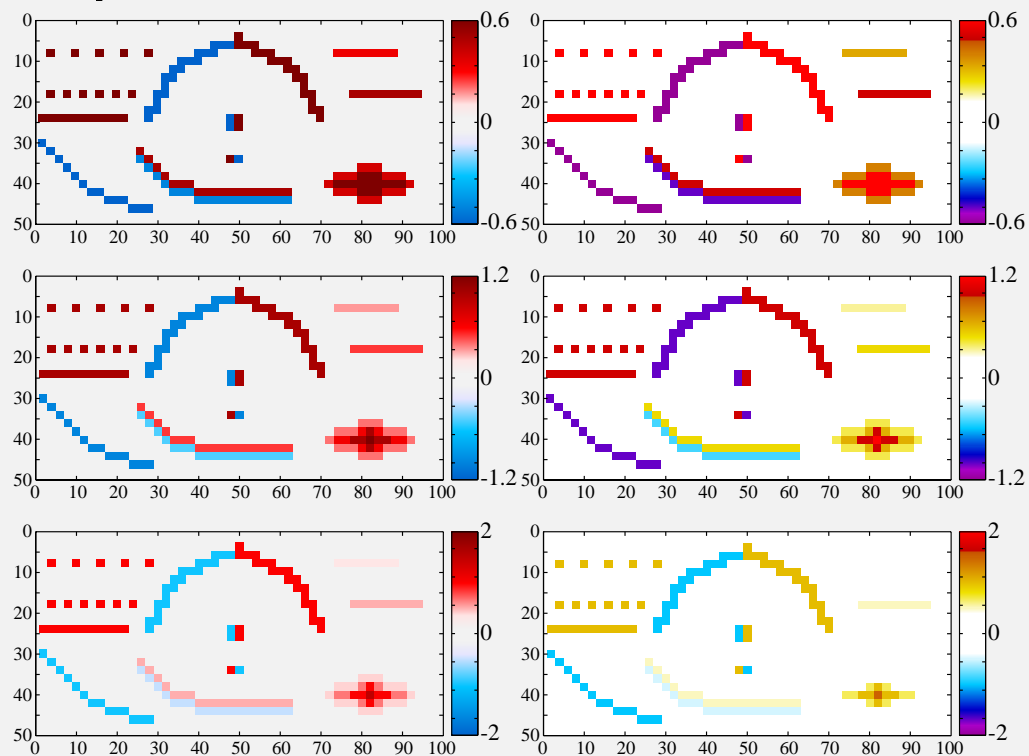
Figure F: A synthetic image using two different colour scales: conventional blue-to-red (left column), and a modified including other tones (right). The three rows correspond to three amplitude levels, showing the effect of saturation.
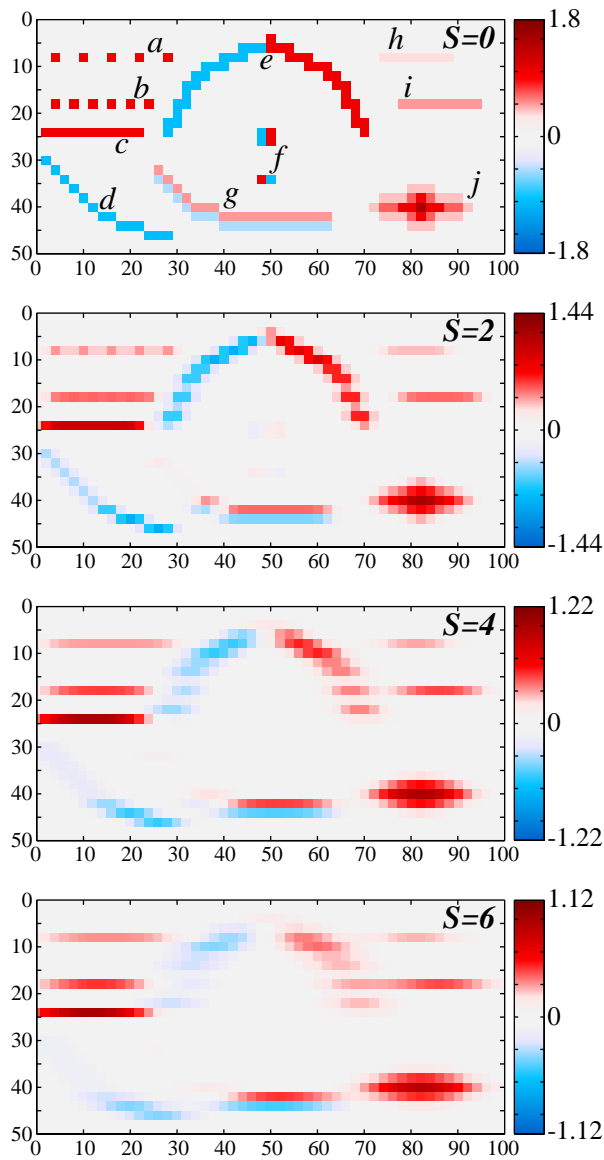
Figure 3.15: A synthetic image of 50×100 size with 2×2 size elements. The four rows correspond, from top to bottom, to no, 1, 2 and 3 neighbouring element horizontal smoothing. Amplitudes are scaled to 1.2 times the maximum value of the smoothed image. With increasing smoothing, horizontal elements are enhanced (a,b,c,g,h,i,j). However, the amplitudes remain high only if the original amplitudes were high and the feature was continuous (c,j). At high smoothing values, no difference can be made between the original continuous, but low-amplitude elements (h,i) and the point-like, but high-amplitude elements (a,b). Horizontal dipole-like (f), and small elements (on top of e) disappear. Dipping structures (d) vanish more rapidly on their steeper part compared to their relatively flat part, and even more rapidly in case of a dipole structure (left part of g).

Non-linear stacking

Taking several sets of information and averaging them in a non-linear way to enhance common features was introduced by Kanasewich (1973) in application to velocity models. His numerical formulation can be used to receiver function images (Wilson and Aster, 2005). The main idea here is to perform RF migration three times (Fig. 3.16a):

- First, with the regular velocities, migrating the PS phase correctly (m_{PS});

- Second, with apparent velocities, to migrate the PpS phase to the depth of the discontinuity (m_{PpS});

Figure 3.16: (a) Migration of the PS, PpS and PsS phases. The PsS image's polarity is flipped in order to have a positive peak at the wanted interface. (b) Simple sum of the multiple (MU) phases. (c) Non-linear stacking of the PS, PpS and flipped PsS images, using N=4 and 8. See text for more details.
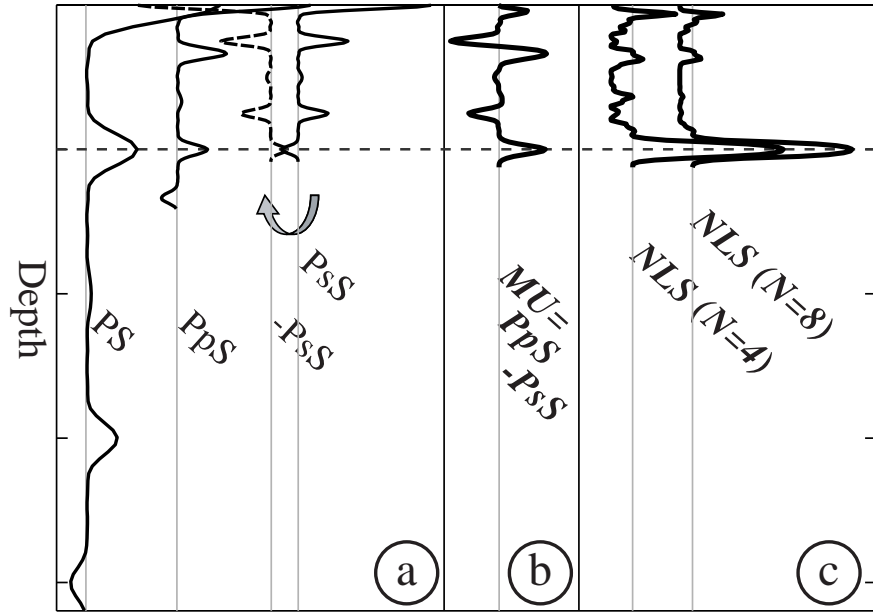
– Third, other apparent velocities, migrating the PsS phase (m_{PsS}).

The three migrations are performed on grids of the same size. Figure 3.16a implies two important things.

    – First: it is clear, that, due to the "vertical compression" or "distortion" of the image in PpS and PsS phase migrations, these phases will produce much narrower peaks. In order to obtain three images which have similar migrated — thus spatial — wavelengths, the PS and multiple phases should be filtered using

$$f_{max}^{PS} \approx 3 \cdot f_{max}^{PpS,PsS}.$$ (3.15)

    – Second: it is also clear that when PpS or PsS phase are migrated, the peaks before their arrival (the PS phase in the first case, the PS and the PpS phases in the second) will be "mismigrated" to shallower depths. This artefact should not be forgotten when interpreting migrated images of multiples, especially when several interfaces may be present.

Once the three migrated images m_{PS}, m_{PpS} and m_{PsS} are produced, one can look at the sum of the multiple phases (3.16b), or apply the non-linear stacking scheme:

$$m_{NLS} = ab^N$$ (3.16)

where

$$a = \frac{3|median(m_{PS} + m_{PpS} - m_{PsS})|}{(|m_{PS}| + |m_{PpS}| + |m_{PsS}|)} \tag{3.17}$$

$$b = \frac{|m_{PS} + m_{PpS} - m_{PsS}|}{(|m_{PS}| + |m_{PpS}| + |m_{PsS}|)}. \tag{3.18}$$

The a factor is a measure of the relative amplitude of the three images, and will be maximized when the three images have the same polarity and amplitude. The b^N factor is exclusively a nonlinear measure of polarity consistence. In regions where all three images have consistent polarity, b^N will have a (maximum) value of 1. The parameter N controls the degree of nonlinear scaling applied to the summed images. As $n \to \infty$, the summed images are multiplied by 1 where they all have the same polarity, and multiplied by 0 where they do not (Wilson and Aster, 2005). The choice of N will depend on the characteristics of a particular dataset; Figure 3.16c shows two synthetic examples for $N = 4$ and 8.

Non-linear stacking, as its name suggests, does not preserve true amplitudes. Figure 3.17 demonstrates the behaviour of the method as a function of the amplitude of the three components. A signal is produced only if the signs of all three phases are the same, independently of their amplitude (cases a, b, c), or when the amplitude of one phase is large and the two others are small but non-zero (d). In case of large-amplitude peaks of opposite sign, and in the presence of a zero component, non-linear stacking does not produce any output (e, f, g). Note that non-linear stacking behaves symmetrically for negative values.
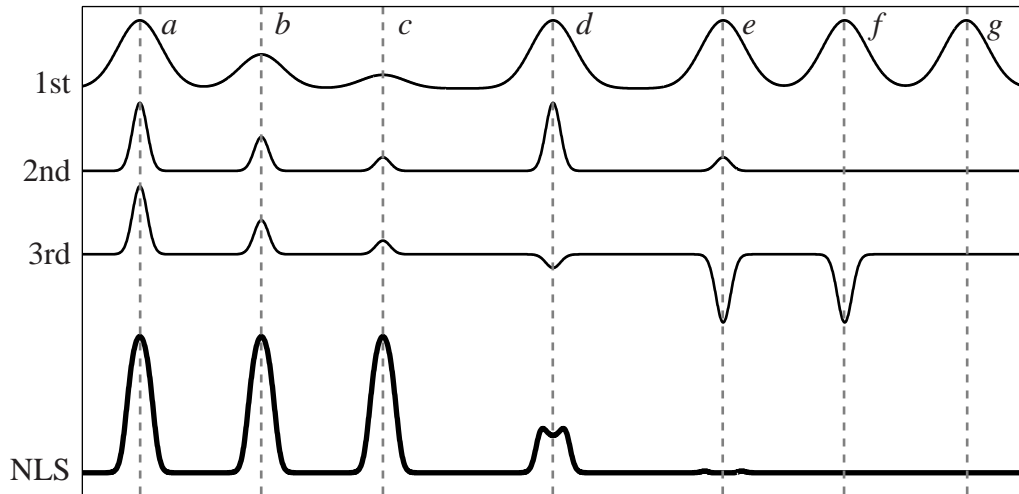
Figure 3.17: The behaviour of non-linear stacking in the presence of peaks of different amplitudes and with the first component being positive. See the text details.

3.4.4   On the importance of multiples

The previous section and Figure 3.16 presented the possibility to migrate the acquired traces with apparent velocities. This located the PpS or the PsS phase to the depth of the discontinuity, which allowed non-linear stacking. This operation is extremely useful in deciphering accurate crustal structure, as multiples from shallower interfaces, interfering with the Moho, for example, are eliminated. Thus the multiples of the Moho provide new constraints on its depth and structure. Similarly, if we migrate the PS phase to the theoretical depth of the PpS or PsS multiple, we can locate those zones where the multiple conversions of shallower features may interfere with the Moho, or where multiples of the Moho may interfere with upper mantle structure. Migrating multiples as PS, and PS as multiple phases is thus a very beneficial operation; its usefulness is illustrated in Chapter 5.

3.4.5   Summary to prepare the interpretations

Chapters 4 and 5 present the seismological results of this thesis, based on the receiver function techniques discussed here. The primary imaging tool is migration, with higher frequencies aiming to image shallower structures, and lower frequencies deeper ones, together with the respective deconvolution methods (iterative and frequential). Along the main profile, a 2-D velocity model is developed and used, while the lateral variations are investigated by using a 1-D model. Horizontal smoothing is chosen as a function of the Fresnel zone's width, and is never exaggerated, in order to avoid unnecessary blurring. Multiple phases are widely used to better constrain the structure of the lithosphere. The effect of non-linear stacking is also presented. Finally, inversion of receiver functions provide first order results on the presence or absence of pronounced low velocity zones in the crust. The processing parameters for each application and image are precised in Chapters 4 and 5.

3.5 Gravity data compilation

The gravity anomaly data used in this thesis were compiled from several published or public sources. The effective work here was to compare the different datasets, to convert them into a common reference and units, and to verify their spatial consistency. The final compilation is presented on Figure 3.18. The compiled dataset is then regarded as homogeneous, and no differentiation upon data provenance is made.

3.5.1 Compiled datasets

BGI data

The International Gravimetric Bureau (BGI[6]) provides worldwide gravity anomaly data upon request. It is itself a repository of numerous field surveys. Data are available as Bouguer anomalies, using a reduction density of 2670 kg·m^{-3} , but no terrain correction. They cover mostly India and the eastern half of Nepal. As this is the largest — and also a compiled — dataset, it is regarded as the reference for our compilation.

Chinese data

Bouguer anomaly data over China is published on a 5×5 *arcmin* grid (Sun, 1989). However, spatial sampling of the original measurements is uneven, as it was shown on a 2100·1100 pixel .`jpeg` image covering the 75-110°E and 25-40.5°N region. In order to overcome interpolation artefacts in the published gravity data, the grid was re-sampled at the location of the measurements that were digitalized using an automated process. Errors of positioning are due to the pixel-to-coordinate transformation, and are estimated to 3 km. The Mercator-to-latitude conversion of the digitalization induces up to 15 km of error but these are mostly corrected using the overlapping points between the BGI and the Chinese datasets. From this dataset, only those points were integrated to our compilation which were measured in inland China. This and all the following datasets include a reduction density of 2670 kg·m^{-3} , and terrain corrections up to 167 km.

---

[6]BGI: Bureau Gravimétrique International; http://bgi.cnes.fr
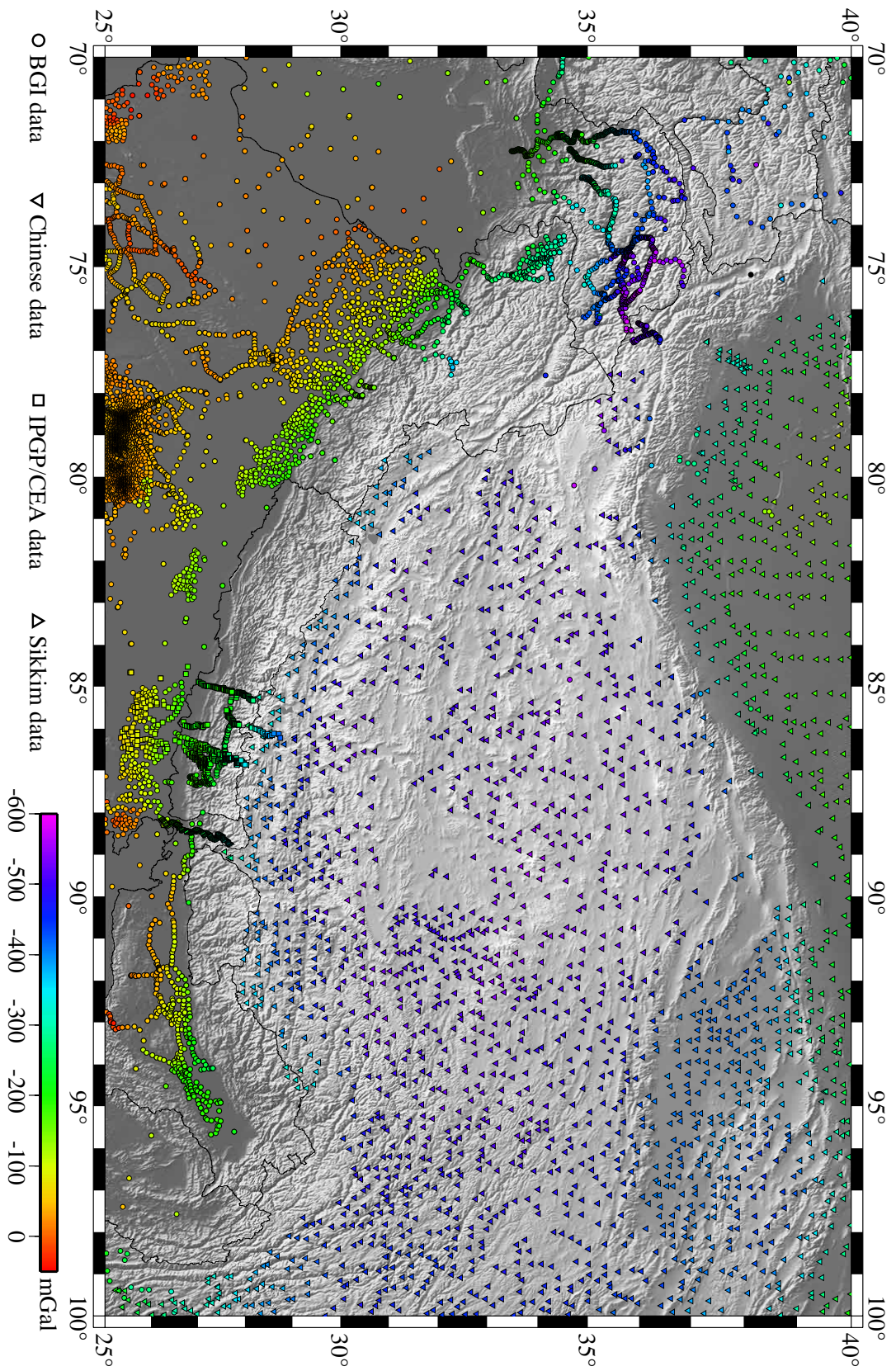
Figure 3.18: Bouguer anomaly data in the Himalayan-Tibetan region. See text for details about the compilation.

Data in Nepal

Joint French[7]-Nepali surveys, measured three profiles perpendicular to the Himalayan arc in Nepal and South Tibet (Cattin *et al.*, 2001; Martelet *et al.*, 2001). The western profile follows the same route as the Hi-CLIMB experiment's seismological stations, and provides an excellent base of comparison. The eastern profile runs close to the projected line of the HIMNT experiment. This dataset can be directly taken into account in the data compilation.

Sikkim data

A recent study (Tiwari *et al.*, 2006) published new gravity data across the Sikkim Himalayas, in the continuation of the INDEPTH I experiment's line. The main issue concerning this dataset is the unavailability of the raw data. The only way to proceed was to scan the published colour coded Bouguer anomaly map and to digitalize both the position of each data point as well as its value using red-green-blue component identification of the colours. This process includes a 0.5 km error in positioning, and ± 5 mGal error related to the colour scale's intervals.

3.5.2   Other datasets

Two other terrestrial datasets have been found that cover the Tibetan Plateau. One is issued from the research project *On the 1×1 degree mean gravity value for public use*, supported by the Chinese National Foundation for Surveying and Mapping. The second is 50 mGal contour map by the Chinese Academy of Geological Sciences. Unfortunately, the spatial frequency and the anomaly resolution of these two maps, respectively, are significantly less than those of our compilation.

In Nepal, additional data were kindly made available by the GETECH Group plc[8]. The 5 × 5 *arcmin* grid data cover the SE corner of the country, and regional gravity station locations with principal anomaly values were provided as well. However, as the spatial coverage of this dataset was found to be small, and some data points showed outlier values compared to the general trend of the consistency check profiles (see below), we chose to not to include it in our compilation.

---

[7]Supported by IPGP (Institut de Physique du Globe de Paris) and CEA (Commissariat à l'Énergie Atomique)

[8]GETECH, School of Earth Sciences, University of Leeds, Leeds, LS2 9JT UK. Tel: +44 113 343 5240; Fax: +44 113 242 9234; email: info@getech.com; website: http://www.getech.com/

The most accurate satellite gravity data are issued from the GRACE[9] experiment. The available datasets in 2006 were "complete to a degree and order 360" of the spherical harmonics. This means that the resolution of the model is 1°, or about 100 km, which made the use of satellite gravity data pointless for our purposes. The first application computing large wave-length Moho depth variations beneath the entire Tibetan Plateau from gravity data using an earlier model have also reached a similar spatial resolution (Shin *et al.*, 2007).

3.5.3   Consistency of the used datasets

Gravity anomaly data are relative measurements, which means that the relative differences within a dataset are relevant, but differences between different datasets should be referenced to the same level. Hence the consistency of the different datasets was verified along several projected profiles, perpendicular to the Himalayan arc, going from India to Tibet. These profiles covered the BGI and Chinese datasets, as well as the IPGP/CEA or the Sikkim data, depending on the profile (Fig. 3.19). The smoothness of the profiles was satisfactory in Nepal, but a –66 mGal shift of the Sikkim dataset was found to be necessary. Furthermore, these analyses showed that the average deviation compared to the general trend of the profile is ±10 mGal, excepting some smaller zones with ± 50mGal.
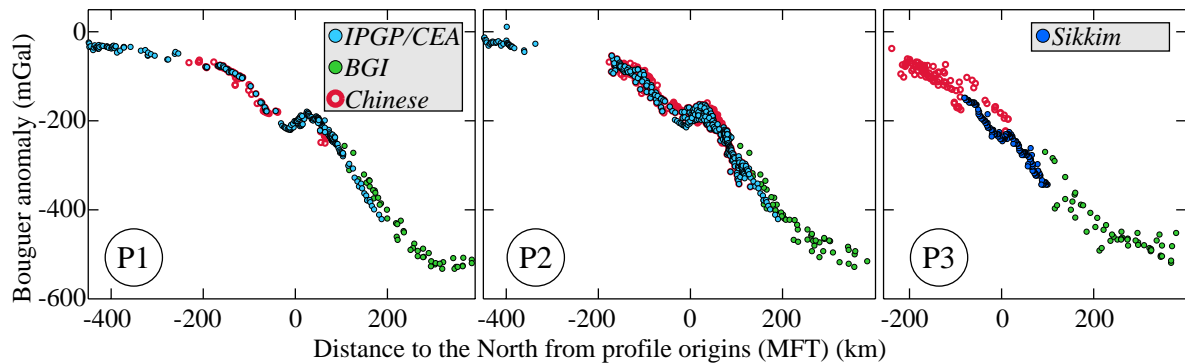
Figure 3.19: Three profiles perpendicular to the Himalayan arc along which different gravity datasets were projected and verified for consistency. Panels (a), (b) and (c) show three profiles, with their origin located at the MFT (centres and projection angles): 27.2829°N, 84.9885°E, N14°E; 26.873°N, 86.517°E, N17.8°E; and 26.8°N, 88.5°E, N25°E.

---

[9]GRACE: Gravity   Recovery   And   Climate   Experiment   Mission;   http://www.gfz-potsdam.de/pb1/op/grace/index_GRACE.html

3.6   Gravity anomaly modelling

The compiled Bouguer anomaly dataset completes very well the available seismo-
logical data along the south-central border of the Tibetan Plateau. As in our study the
receiver function profiles provide the contours of lithospheric bodies, gravity modelling can
focus on finding the correct densities to match the observed Bouguer anomalies. Using
this approach, not only the lateral variation of crustal structures are be mapped, but min-
eralogical phase changes in the Indian lower crust are investigated (see Chapter 7). This
section briefly describes the technical details of synthetic Bouguer anomaly calculations.

3.6.1   Principle of Bouguer anomaly

Bouguer anomaly is an expression of deficit or excess mass below the surface com-
pared to a reference level. To obtain its value, one has to substract the theoretical gravity
(computed for the latitude and corrected for the elevation of the measurement) from the
observed gravity, — yielding the free air anomaly, — and then removing the effect of
terrain attraction between the measurement point and the sea-level using a reference den-
sity, usually 2670 kg·m^{-3} . All these computational steps were performed for the compiled
dataset, thus the modelling of gravity anomalies here aims to directly calculate the syn-
thetic Bouguer anomaly of a density model and a given distribution of stations.

3.6.2   Modelling Bouguer anomaly in theory

A classic paper by Talwani *et al.* (1959) presents a method for the computation
of the gravitational attraction of an *n*-sided polygon. Their approach is convenient to
model two-dimensional problems, as any 2-D structure can be approximated by a polygon,
and any 2-D density distribution can be modeled using a set of constant density bodies.
Furthermore, the efficiency of computation was highly increased by the development of
an algorithm described in Won and Bevis (1987). This paper includes all the necessary
formulae, which will not be detailed here.

Although the south-central part of the Tibetan Plateau is well covered by gravity
data, seismological constraints are available along three main lines. Hence we choose to
model gravity anomalies in two dimensions along three arc-perpendicular profiles, and to
map lateral variations by comparing neighbouring modelling results.

3.6.3   Modelling Bouguer anomaly in practice

A gravity (and magnetic) anomaly modelling software, Hypermag, was published and made available by Saltus and Blakely (1995). However, this code worked on Sun microstations, which became less used due to higher calculation capacities of other type of processors. This brought us to develop a easily accessible, user-friendly tool to handle gravity anomaly data: GRANOM.

GRANOM is an interactive tool under MATLAB that I have developed to work with gravity anomalies. It calculates the anomalies associated to the provided geometries and density contrasts, and compares synthetic and measured data through a graphic interface. A guide presenting how to use GRANOM can be found in Appendix E. The software and the guide are also freely available[10] and can be distributed.

Here we present a validation test for the software compared to Hypermag as well as to an analytical formula. We simulate a cylinder of $R = 1$ km radius whose centre is located at $Z = 4$ km depth at horizontal distance $x = 0$, with a density anomaly of $\Delta\rho = 2900$ kg·m^{-3} . According to Turcotte and Schubert (1982), the induced vertical gravity anomaly Δg_z is:

$$\Delta g_z = \frac{2\pi G R^2 \Delta\rho Z}{(x^2 + Z^2)} \tag{3.19}$$

where G is the universal gravitational constant ($G = 6.67 \cdot 10^{-11}\ m^3 kg^{-1} s^{-2}$). In GRANOM and Hypermag, we simulate the cylinder by a body with a 40-sided polygonal cross-section. The synthetic gravity anomalies are shown on Figure 3.20. Both methods reproduce closely the result yielded by the analytical formula (Eq. 3.19). The deviations in the order of ∼0.1 mGal are related to the polygonal approximation of the cylinder.

---

[10]http://www.geologie.ens.fr/∼hetenyi/docudata.html
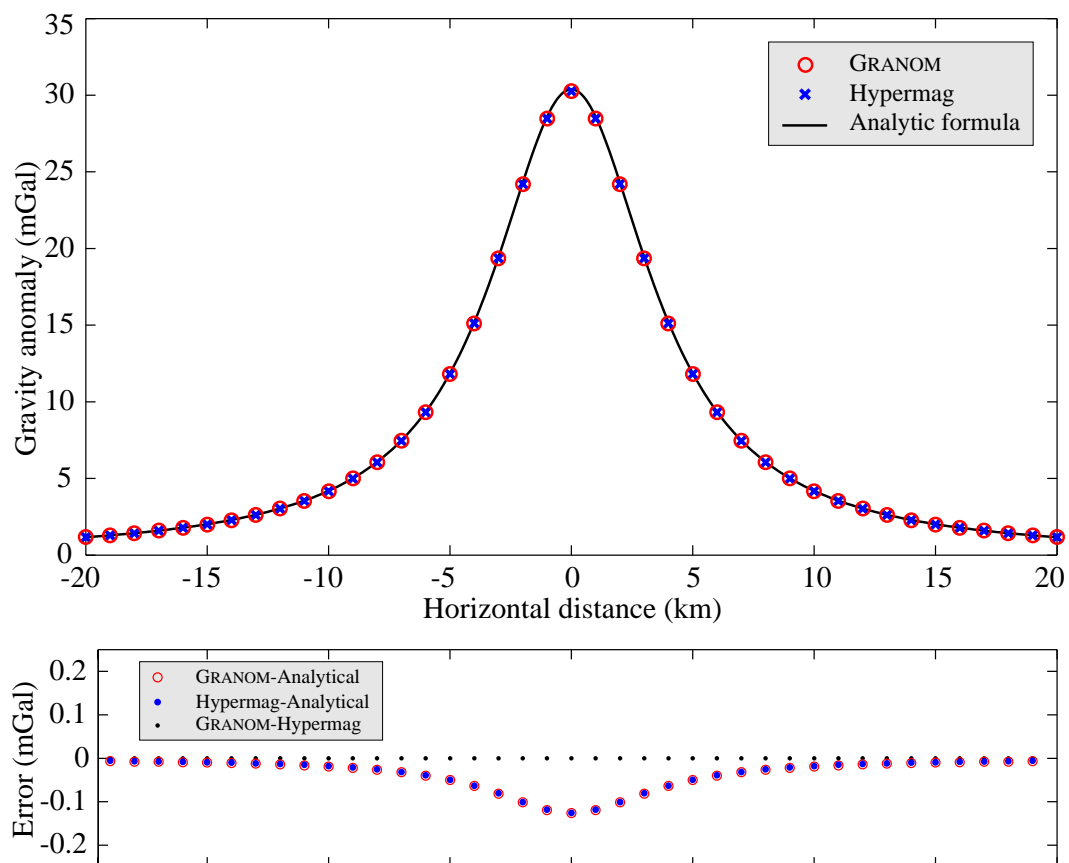
Figure 3.20: Validation of GRANOM compared to Hypermag and the analytical formula in case of a cylinder. The errors between the analytical and synthetic gravity anomalies result from the approximation of the cylinder's cross-section by a 40-sided polygon.

CHAPTER 4

Near-surface receiver functions and crustal fluids

"Imaging:
Writing computer programs to improve
the quality of collected images,
or to construct images which merge
information from multiple sources."
Webster dictionary

4.1   Introduction

Increasing resolution while imaging intra-crustal features is one of the goals of this thesis, as it was presented on Figure 2.7. The most commonly used seismological tools to explore the interior of the crust are tomography for velocity anomalies, and active seismic reflection and refraction for interfaces, which are also the target here. The latter methods were applied first in hydrocarbon exploration from the beginning of the 20th century, mostly in sedimentary basins, and were later used for academic purposes in many other contexts as well. On the other hand, with the advent of converted wave studies in the last few decades, the receiver function method now provides an alternative to characterize the crust. Both methods have their own advantages and disadvantages, which also makes them somewhat complementary.

Most of the differences originate from the source of the energy. In active seismics,

the source is usually an explosive detonated beneath the surface. This not only causes environmental damage, but also implies high costs. The generated waves provide information on P wave velocity primarily, and the receivers (geophones) are mostly one component instruments. The major imaging problem is the limited vertical penetration of the wave-field. This is especially important in Tibet, where the crust has a double thickness compared to the average. That's why the conducted seismic experiments usually imaged well the Main Himalayan Thrust and the shallower bright spots, but were unable to clearly follow the Moho and its variations at depth (*e.g.* Hirn *et al.*, 1984; Brown *et al.*, 1996). At greater depths, to explore the mantle, passive methods, such as tomography, are needed.

In receiver function studies, the sources are teleseismic earthquakes. This eliminates the penetration problem mentioned above, as the structures are illuminated from below. However, the frequency content of the wave-field is lower compared to seismics, thus the vertical resolution is also poorer. An advantage of the RF method is that the receivers have usually three components, which allows to study back-azimuthal variations related to dipping structures and/or anisotropy. Finally, the RFs are sensitive to S wave velocity, but the inversions recover mainly its relative variations.

The gap lying between seismic exploration and receiver functions was starting to get filled by approaching the two methods and also applying them at the same time and location. In NE Tibet, explosion seismology investigated the crustal thickening, mainly focusing the image on the upper crust (Galvé *et al.*, 2002a), while receiver functions provided a better image on the Moho (Vergne *et al.*, 2002). In southern Tibet, the Moho was imaged by simultaneously applying the receiver function and the wide angle reflection and refraction methods (Galvé *et al.*, 2002b). The reason for that these studies remained at a lithospheric scale is the sparse station spacing: the rays used to image the structures do not cross at shallow depths and hence do not provide information on the uppermost crust. The stations of the Hi-CLIMB experiment were deployed at short intervals that makes them suitable for imaging shallow structures. And, at the same time, they also allow to increase the maximum frequency used to image the Moho ($\sim$0.5 Hz), which is a step forward in approaching the resolution of active seismics and that of the RF method.

This chapter focuses on relatively small scale objects compared to the size of the lithosphere, located at uppermost- to mid-crustal depths. Topics cover single station fault imaging using tangential component RFs, sedimentary basin characterization using high-frequency data, and the presence of fluids in the crust constrained by V_P/V_S -ratios. This latter tool also allows to construct the 2-D velocity model that is used in Chapter 5.

4.2 Near-surface imaging

Stations located in Nepal provide data that allow to closely follow the effect of near-surface features on receiver functions. Near-surface means that their signal is visible shortly after the P wave arrival ($\sim$0-2 s). This, in turn, implies that a high frequency content is necessary to distinguish the different peaks related to converted phases. However, while achieving a good resolution, the maximum frequency cannot really exceed $\sim$2 Hz, as the teleseismic sources bring practically no information beyond that range. Also, the use of higher frequencies, if it was possible with some other type of source, would also require a station spacing that is smaller than that of the Hi-CLIMB experiment in order to cross rays and information beneath the receivers.

The 0-2 s delay time range usually corresponds to waves converted by structures lying between 0 and $\sim$15-20 km depth. As the Siwalik formations, filling the Ganges Basin and forming the foothills in Nepal, are relatively young sediments, their lower average velocity broadens the beginning of the RF signal and implies shallower (up to $\sim$10 km maximum) converters for the same delay time. Using high frequency ($f \sim$2 Hz) data in low velocity ($v_S \sim$2 km·s^{-1}) media, the vertical resolution of the structures that we can distinguish is theoretically $\lambda/4$, where $\lambda = v_S/f$ is the characteristic wavelength. This yields $\sim$250 m at best, but higher velocities and lower frequencies, together with a more realistic estimate of $\lambda/2$ for the resolution, makes <1 km. The horizontal extent of the investigated structures is larger than the width of the Fresnel zone ($\sim$1-1.5 km). The discussed features are shown on a map and on an interpreted geological cross-section along the Hi-CLIMB profile (Fig. 4.1).

4.2.1 Ganges basin

The southernmost 10 stations of the Hi-CLIMB experiment were deployed in the undeformed Ganges Basin. The basin is filled with relatively young (Mid-Miocene and younger) sediments, the Siwalik series, and has been investigated by seismic reflection studies and a deep well reaching the basement. This location was suitable to perform high-resolution RF analyses in order to determine the depth to the base of the basin and to the Moho. By estimating the dip of these interfaces, we constrained the flexural geometry, and then — by numerical modelling — the effective elastic thickness of the India plate. This study is detailed in Chapter 6.

Here I would like to briefly emphasize some aspects of the RF image (see Fig. 6.3). The data were filtered up to high frequencies (2 Hz), which allowed precise identification
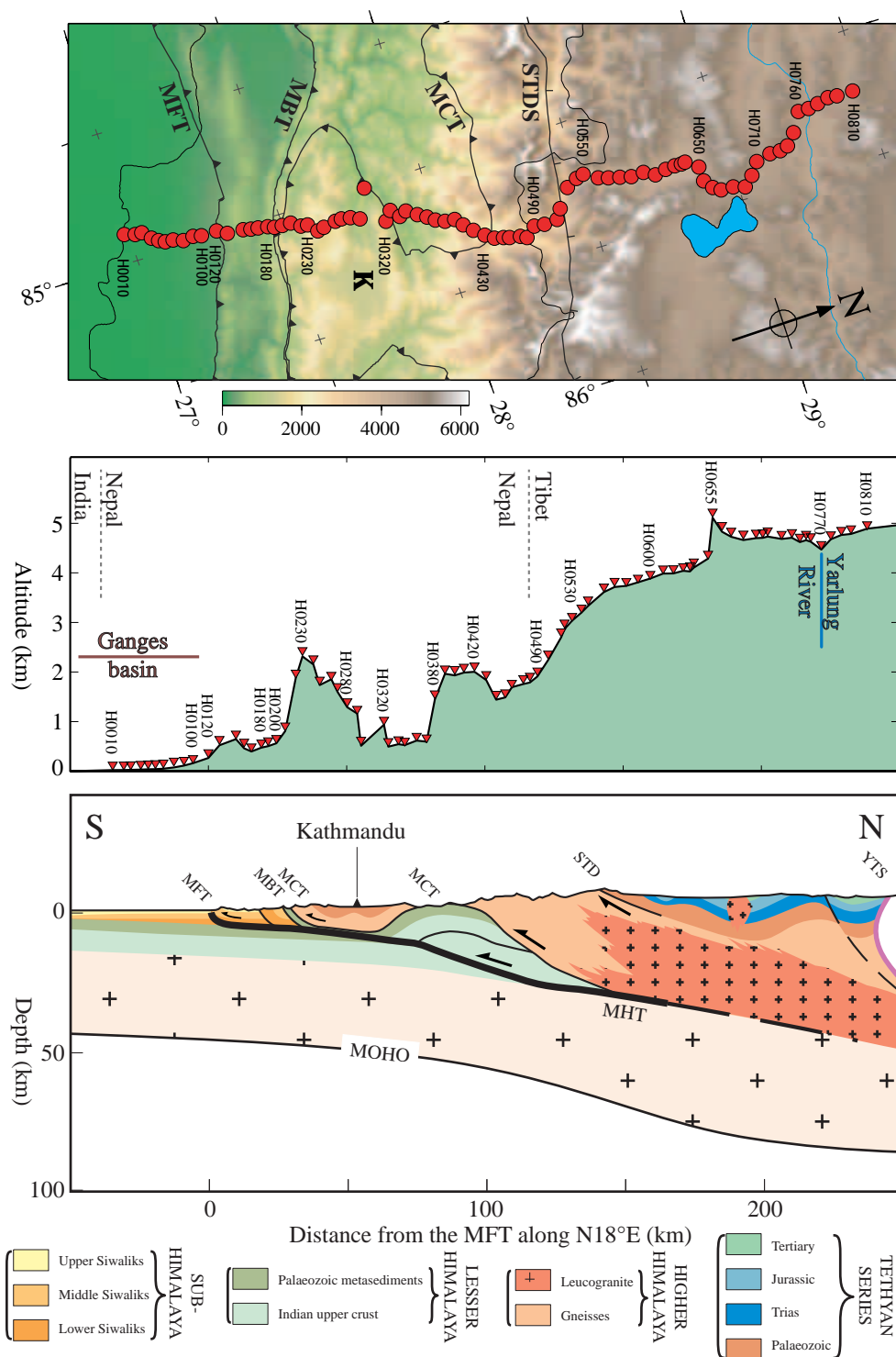
Figure 4.1: Structures and stations along a N18°E oriented profile in central Nepal: the southern part of the Hi-CLIMB main array (top) and a topographic profile drawn through the altitude of the stations (middle). Bottom: interpreted geological cross-section and main faults. (From Avouac, 2003.)

of the base of the basin at ∼2 s delay time. This boundary produces the largest peak on the RFs, because

- of the important impedance contrast;

- of the lack of direct P wave, due to the sub-vertical arrival at surface in a very low velocity medium;

- the Moho's amplitude is lowered by interfering negative multiples from the base of the basin.

Furthermore, the small amplitude, but coherent positive phase around ∼0.5-1 s (Fig. 6.3) was identified as the limit between the Siwalik series, and the more recently deposited, unconsolidated alluvial layer. Even if this layer is very thin (few hundred metres) and exceptionally low velocity, it was possible to constrain it by non-linear inversion and *a priori* information.

The characterization of these kinds of interfaces is classically carried out by seismic reflection profiling rather than receiver functions. Here the resolution of RF imaging was extended. The use of high-frequency data and the relatively low velocities make that the detailed image of the sedimentary basin have been produced from only 2 seconds of data. Beyond the depth and internal structure of the basin, the close station spacing contributed to the estimate of the dip at its base, which allowed to connect this analysis to the flexure and the strength of the India plate.

4.2.2   Imaging faults

The MFT

The northern end of the Ganges Basin is marked by the Main Frontal Thrust (MFT), the southernmost and currently active thrust of the Himalayan system. This fault cuts through the entire Siwalik series starting at a steep (∼50°) angle at surface, and it is modelled to merge to the Main Himalayan Thrust at depth (Lavé and Avouac, 2000). Station H0120 was located close to the surface trace of the MFT. Compared to the stations in the Ganges Basin, the main peaks on the radial RF are not at ∼2 s, and there are significant energies on the tangential component. As mentioned in Section 3.3.3, coherent peaks on the tangential RF are produced either by dipping interfaces (2π periodicity with back-azimuth), or by anisotropy (π periodicity for sub-horizontal or sub-vertical axis, 2π periodicity for ∼45° dipping axis).

The observed RFs at station H0120 are shown on Figure 4.2. Both the radial and the tangential RFs show two series of peaks, at ∼0 and ∼0.8 s. On the radial RF, the
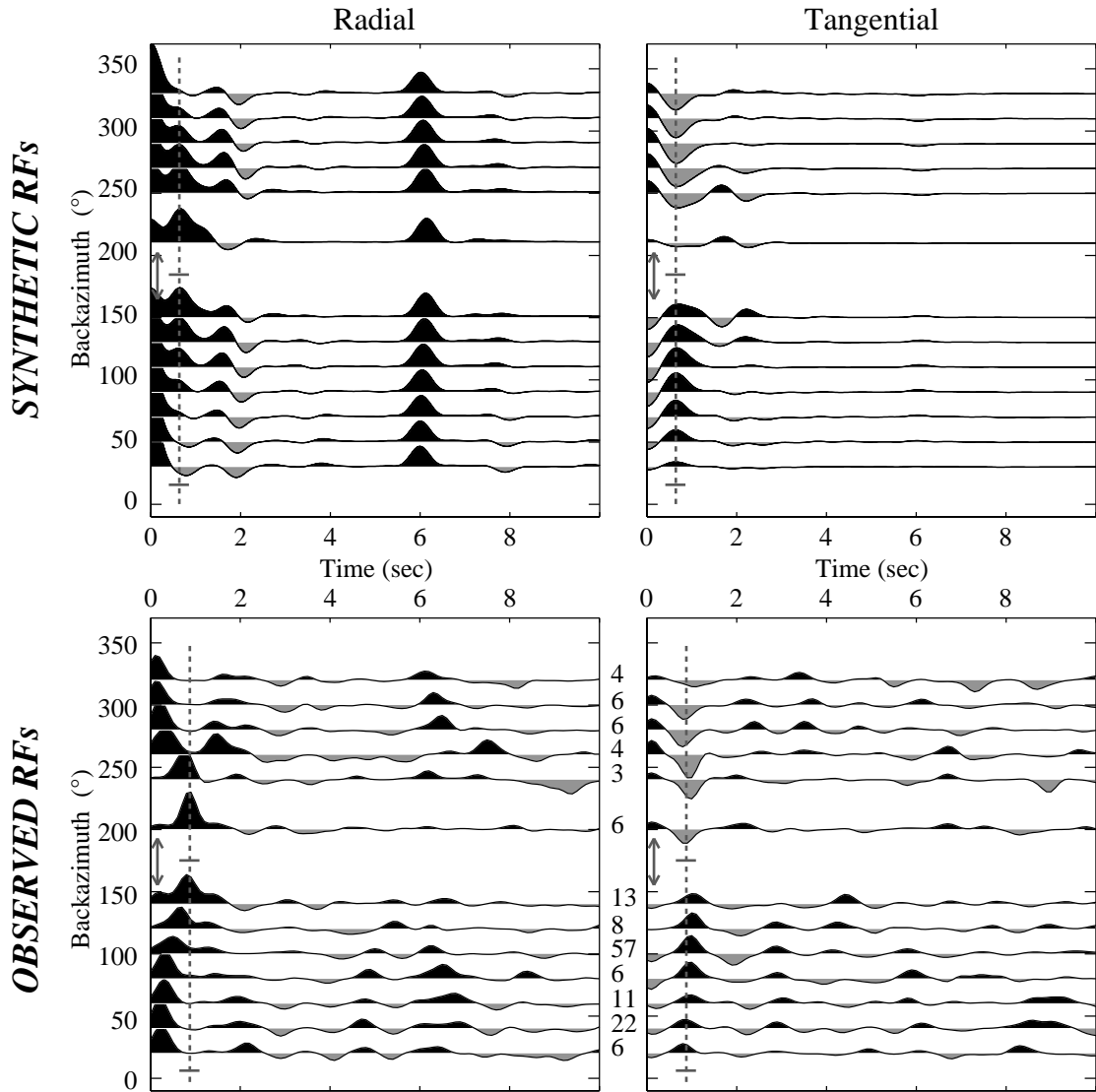
Figure 4.2: Observed (bottom) and synthetic (top) radial (left) and tangential (right) receiver functions at station H0120, using iterative deconvolution and 1Hz cut-off frequency. The observed data are stacked using 20° wide back-azimuth ranges (the number of traces per stack is indicated in the middle) with no overlap. The dashed lines and the arrow highlight the features indicating the presence of a dipping boundary.

maximum of the amplitude is reached for events located close to the south/north directions, respectively. On the tangential RF, the two series negative/positive polarities for waves coming from the east, and opposite, positive/negative ones from the west, respectively. The range of polarity change is located at ∼180-200°, suggesting that the plunge of the dipping boundary, or the axis of anisotropy is oriented ∼N20°E. However, the polarity change at 0

s delay time on the TRF, and the clear 2π periodicity of the amplitude variations is typical of a dipping interface (Savage, 1998). For this, and also because of the geological context, we choose a simple dipping layer model to produce synthetic radial and tangential RFs.
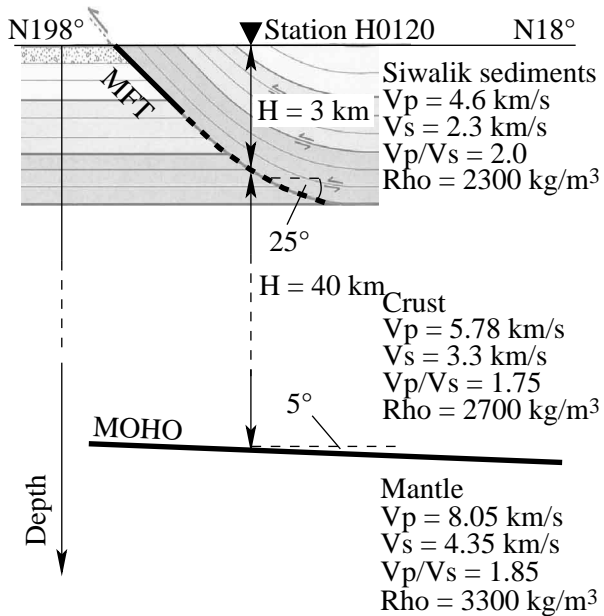
Figure 4.3: The synthetic model beneath the station above the MFT (H0120) over the image from Lavé and Avouac (2000). The model parameters were varied as indicated in the text to yield the synthetic radial and tangential RFs matching the observations. The final model parameters are precised on the figure.

The characteristics of the model are shown on Figure 4.3, over the scheme of Lavé and Avouac (2000). The two layers represent the thrust Siwalik sediments and the crust, over the half-space of the mantle. The varied parameters were the thickness and the velocity of the sediments, as well as the dip and orientation of the thrust fault. These parameters were tuned in order to match the observed 2π back-azimuthal variations of the radial and tangential RFs. The final model parameters and the synthetic RFs are shown on Figures 4.3 and 4.2, respectively. The synthetic RFs reproduce closely the amplitude variation of the RRF, as well as the polarity changes on the TRF, clearly modelling a dipping interface.

The main result here concerns the dip of the thrust fault. From the synthetic RF modelling, it is constrained to dip at about 25° at ∼3 km depth. This value is half of its dip at surface, suggesting a decreasing dip along the continuation of the MFT, hence a listric geometry. This is in agreement with what has been suggested based on geological studies. If the density of the stations was further increased, a high-frequency, continuous image of the MFT's descent could have been performed with the receiver function method.

The MBT, the MCT, and other features

Similarly to the above case with station H0120 detecting the shallow structure of the MFT, a single-station RF analysis was performed at all stations of Hi-CLIMB Phase1

(Fig. 4.1) to follow the effect of near-surface features on receiver functions.

Among the analyzed stations, several radial RFs showed 2π periodicity variations of amplitudes with back-azimuth. The maximum amplitude of the delayed peak usually occurred at around 200°. Furthermore, the tangential RFs showed polarity changes, with the angle of cancellation at the same back-azimuth (examples are shown on Fig. 4.4). These indicate a situation similar to that at station H0120: a shallow, N-dipping impedance contrast. Locating these stations on Figure 4.1, we find that the most prominently varying RF signals are associated to stations located close to other major thrust faults. Stations H0180, H0190 and H0200 (Fig. 4.4) lie in proximity of the surface trace of the MBT and the MCT, cutting through, again, the Siwalik series.
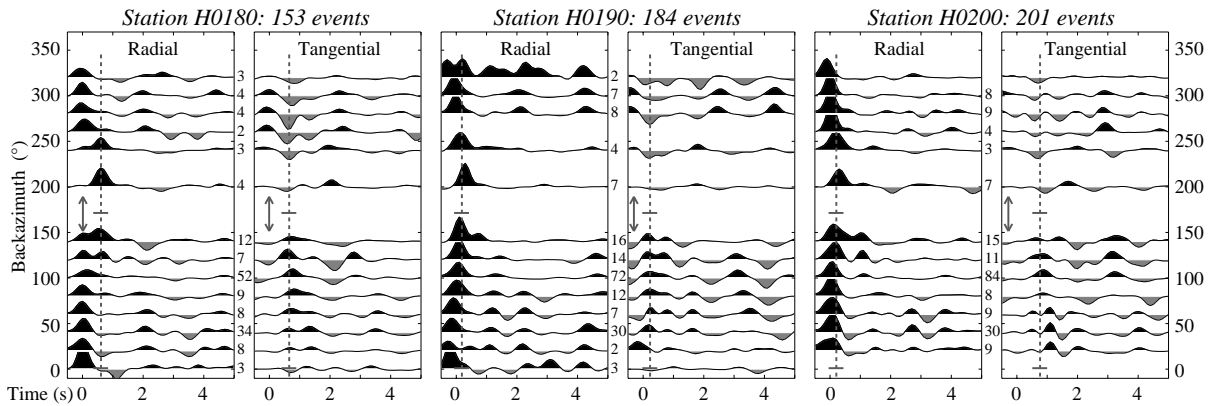
Figure 4.4: Radial and tangential RFs observed at stations near the surface trace of the MBT and the MCT. Back-azimuthal stacking was performed by 20° ranges, as for station H0120. The number of traces per range is indicated in the middle. The 2π periodicity of variations in arrival time and polarity (dashed lines and arrows) indicates north dipping structures related to the MBT and the MCT.

According to the geological cross section, there are three other occurrences of faults' surface trace further north: the MCT curves around and meets the profile again between stations H0320-H0330 and H0420-H0430, and the STDS is supposed to lie between H0520-H0530. The RFs computed at these stations were analyzed in search for effects of near-surface variations of arrival time and polarity with back-azimuth (see Appendix C). The signs of dipping structures, if visible, are less evident compared to the faults that cut through the sediments in the south. This may be due to two effects. First, the faults at these locations run either within the same geological unit, either between formations that does not significantly differ in terms of impedance contrast; thus no wave conversion with significant amplitude occurs. Second: both faults are rather fault zones, encompassing regions of a few kilometres wide, which would transform a sharper impedance contrast to a

more gradual change. Back-azimuthal variations of RFs, even if at a lesser extent, are also present at stations H0240, H0280, H0290, and H0380. These are relatively distant from the major thrust faults discussed above, but in an active mountain range, there are certainly smaller faults and/or dipping layers as well.

Similarly to the MFT, the MBT and the frontal MCT are also listric and merge the MHT, as shown on the geological cross section (Fig. 4.1). This single décollement in the upper crust is a primary, large scale structure, which can be imaged using several stations at the same time. Hence migrating RFs at high frequencies seems a suitable way to study it in the next section.

4.3 Do we see the MHT?

4.3.1 Setting

The Main Himalayan Thrust is a key issue in the understanding of Himalayan geo-dynamics and in evaluating earthquake hazard of the region: it is the major limit between the underthrusting India plate and the overriding Asian-Tibetan crust, and it gives place to all the major (M>8) earthquakes that have ruptured on hundreds of kilometres. Hence this mega-thrust has been the subject of numerous field campaigns and modelling studies.

Balanced and restored cross sections across Nepal gave birth to hypotheses on the structure of the MHT (*e.g.* Pêcher, 1978; Brunel, 1986; Schelling and Arita, 1991), usually including a flat part followed by a ramp further north beneath Nepal. Then the mega-thrust has been imaged by reflection seismics during the INDEPTH experiment (Brown *et al.*, 1996; Hauck *et al.*, 1998), which revealed a north dipping structure beneath the Himalayas. A magnetotelluric study in Nepal agreed with the geological results and, based on a conductive feature beneath the front of the Higher Himalaya, also suggested a *flat–ramp* structure (Lemonnier *et al.*, 1999).

The deformation pattern related to the MHT was modelled numerically along with mountain building processes and the seismic cycle (Cattin and Avouac, 2000), strain and stress build-up (Vergne *et al.*, 2001; Bollinger *et al.*, 2004), and geodetic shortening rate (Bettinelli *et al.*, 2006). Finally, RF imaging in eastern Nepal (Schulte-Pelkum *et al.*, 2005) imaged a smoothly deepening MHT between 100 and 200 km north of the MFT, and argued for the development of anisotropy while explaining back-azimuthal variations of RFs.

4.3.2 Receiver functions and ambient noise tomography

It is in the above context that findings on the MHT are presented[1]. In comparison with section 4.2, the target of the imaging here is the upper crust, hence the first few seconds (∼5 s after the P wave arrival) of the signal are used for migration. The typical frequencies are 0.5-2 Hz, yielding a vertical resolution of ∼1-2 km. The Main Himalayan Thrust lies at a depth where rays to different stations cross already, thus we expect to image it by migration all along Phase1.

A migrated receiver function profile was created using iteratively deconvolved data filtered at high frequencies (2 Hz), and gridded on a fine mesh ($dx = 0.5$ km ×

---

[1]Section 4.3.2 is based on: Vergne, J., Nábělek, J. L., Hetényi, G., and the Hi-CLIMB team (**in prep.**): Geometry and Characteristics of the Main Himalayan Thrust Revealed by the Hi-CLIMB Seismological Experiment

$dz = 0.25$ km). The W2 list was used to select RFs, yielding 8984 traces along the Phase1 profile, oriented N15°E. Stations H0220 and H0230 were excluded due to low signal-to-noise ratio. The migration was performed using the following velocity model (velocities in km·s^{-1}):

Depth (km)	Ganges Basin		MFT to MCT		Further north	
	V_P	V_S	V_P	V_S	V_P	V_S
0–5	3.6	1.6	4.5	2.5	5.6	3.2
5–23			5.6	3.2		
23–45			6.5	3.69		
45–			8.04	4.48		

We performed 4 migrations with traces arriving from the four cardinal directions, and then stacked the 4 images together with a 2 km wide horizontal smoothing filter. The final image is shown on Figure 4.5a.

Besides the Moho, lying at ∼40 km depth beneath Nepal, the strongest and most continuous signal is a *blue-over-red* feature in the upper crust, which corresponds to a velocity decrease at ∼10 km depth followed by a velocity increase at ∼15 km depth. It indicates the presence of a sub-horizontal, ∼70 km long, low velocity zone (LVZ1; Fig. 4.5c) expanding approximately between the surface position of the MBT and the front of the Higher Himalayas. The depth and the extension of the LVZ1 corresponds well to the inferred flat part of the MHT mentioned above.

A similar low velocity zone (*blue-over-red* signature) is also observed at ∼30 km depth under the High Himalayas, but exhibits a ∼10° dip to the north (LVZ2; Fig. 4.5c). The dip, depth and position of this LVZ2 is similar to that of the strong reflector imaged by the INDEPTH experiment. Thus, although we do not see a clear continuity between LVZ1 and LVZ2 on the migrated cross section, both fall within the previously inferred position of the MHT. To better understand the ongoing processes, we need information on the absolute velocities and to quantify the amount of velocity decrease. In order to obtain these, the inversion of the receiver functions needs to be stabilized by another method to yield robust results.

Ambient noise tomography is a recent method to deduce fundamental Rayleigh mode dispersion curves from cross-correlation of long enough noise records (Shapiro and Campillo, 2004). This is especially helpful in our case, as the small extent and the shallowness of the MHT in a strongly heterogeneous crust precludes to perform a regional surface wave tomography. We apply this method to the stations deployed during Phase1 of the Hi-CLIMB experiment. For each pair of stations separated by at least 30 km, up

to 1.5 year of noise record on the vertical component are cross-correlated. The obtained 1250 dispersion curves are then inverted between 8 and 35 s periods to produce a Rayleigh group velocity map under the network (Fig. 4.5b), with increasing periods sampling deeper structures.

In the southern part of the profile, up to the surface trace of the Main Boundary Thrust, the ∼5 km thick low velocity Siwalik sediments and recent unconsolidated alluvium induce the very low velocities observed at all periods up to 25 s. More striking is the low velocity zone centred on 16 s and visible north of the MBT. The extension of this zone corresponds well to the LVZ1 deduced from receiver functions. Another low velocity zone is observed under the High Himalayas at the highest sampled periods (25–30 s). Although the resolution is lower at these periods, the southern onset of this patch is consistent with that of the LVZ2.

Joint inversion of RFs and the obtained dispersion curves allowed to quantify the decrease of velocity at the LVZ1. The inversion procedure follows the one by Julià *et al.* (2000), except that the dispersion curves are produced by correlation of ambient noise rather than from other classical methods. Figure 4.6 summarizes the inversion characteristics. The results show a sharp, ∼20% decrease of shear-wave velocity at 10 km depth, a few km thick zone of low velocities, and a less sharp recovery of V_S with increasing depth.

The interpretation of LVZ1 is the presence of aqueous fluids, generated during the dewatering of the sediments underthrust beneath the MHT. Thermo-kinematic modelling shows that the temperature of this zone lies between ∼150°C and 300°C (Bollinger *et al.*, 2006). Hence the lower part of the Siwalik series, as well as the underlying sedimentary formations are subjected to low-grade metamorphic reactions and dehydration. The presence of fluids is consistent with the high conductivity zone and the microseismic activity mentioned above.

The LVZ1's signature stops abruptly at the topographic front of the High Himalayas. In terms of receiver functions, this means that there is not enough impedance contrast to produce significant converted waves. The fluids inferred to the south are not present in this zone. The MHT passes through geologic units which have similar, or slowly varying velocities and densities. As it has been discussed for the case of the surface trace of the MCT and the STD, we cannot expect to clearly image a fault in these conditions.

As of the LVZ2, interpreted as the continuation of the MHT, its position corresponds to the onset of a high conductivity zone, and the modelled temperature is ∼600°C (Bollinger *et al.*, 2006). These observations point to the presence of fluids, which are — considering the high temperatures — mainly partial melt. The onset of the LVZ2 is located around 160-170 km in-line distance, and its vertical extension is about 10 km. This zone of partial
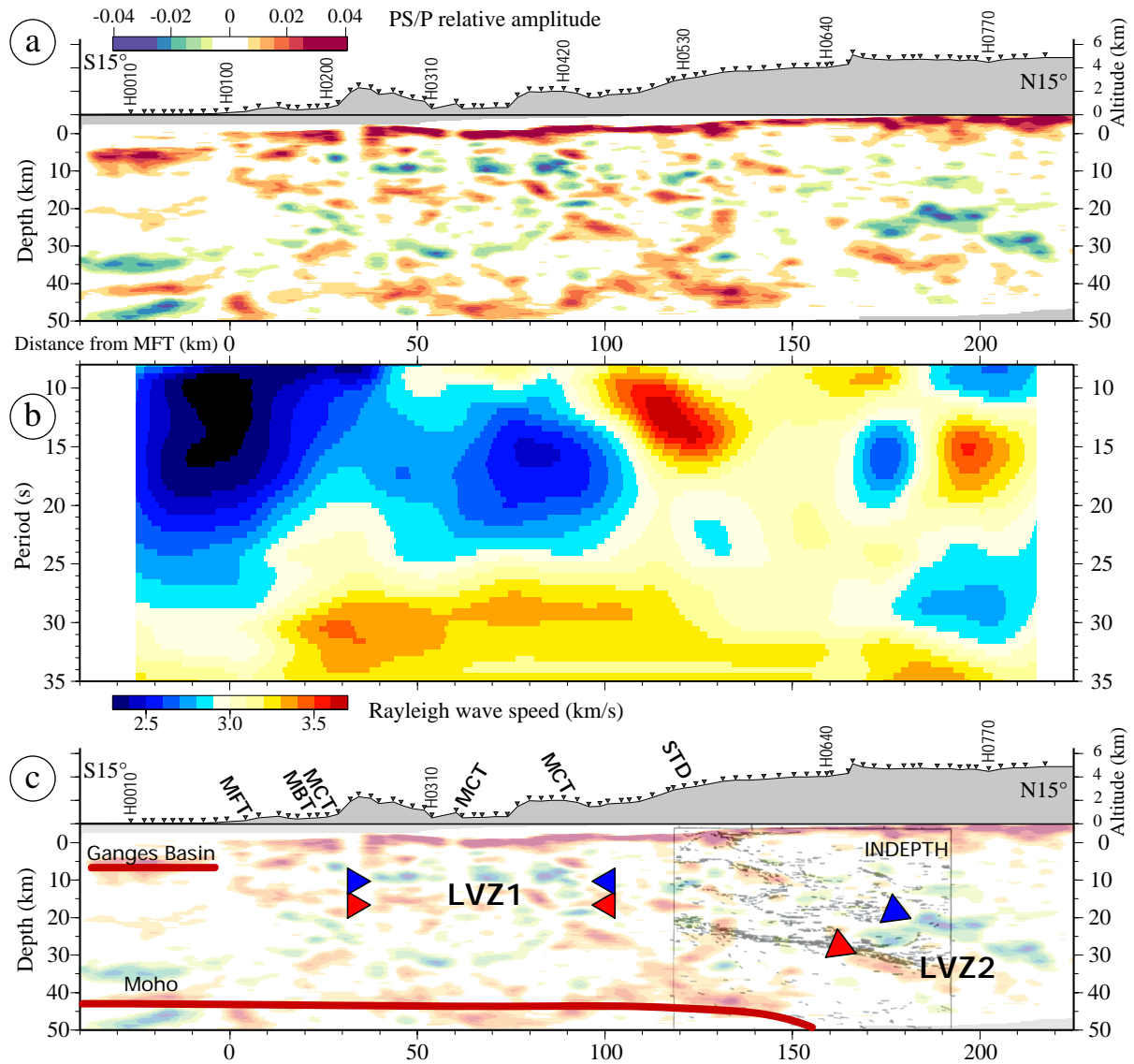
Figure 4.5: Imaging the MHT along a N15°E profile. (a) Migrated receiver function profile. (b) Tomography-like image based on dispersion curves using cross-correlation of ambient noise (From J. Vergne) (c) Highlighting of observed features and low velocity zones along the MHT. See text for discussion.
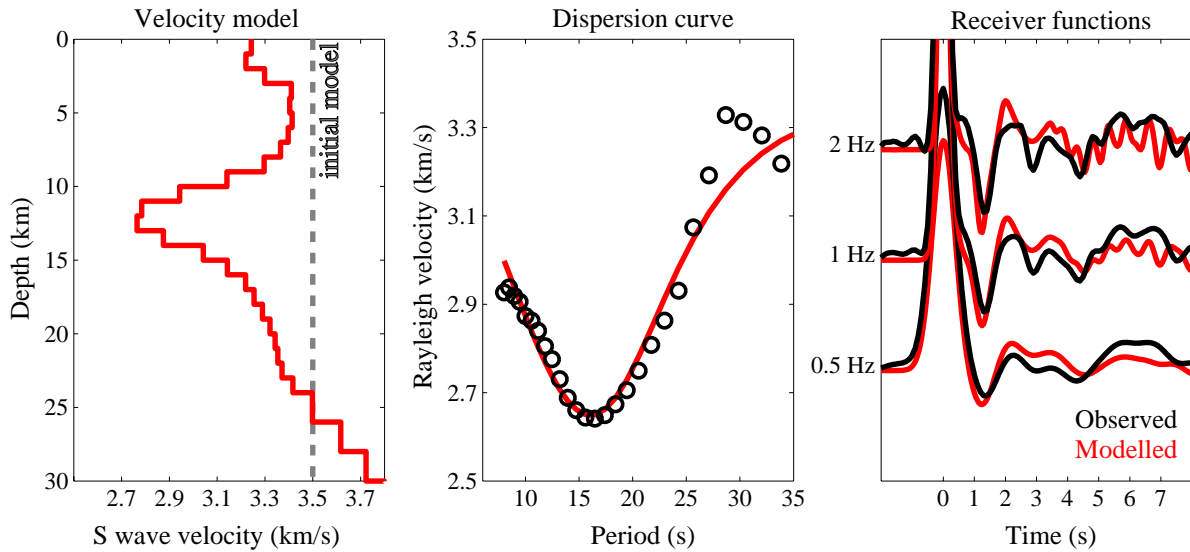
Figure 4.6: Summary of the joint inversion of RFs and dispersion curves obtained by ambient noise tomography. On the right, the observed (black) receiver functions at three different frequencies are well matched by the synthetic (red) results, and there is a similarly good agreement for the dispersion curve (centre). The left panel shows the final velocity model, which was found to be stable over a range of different initial models.

melt may potentially feed the Himalayan leucogranites. Both the LVZ1 and the LVZ2 indicate that we are able to see the MHT in an indirect manner only: the mega-thrust does not produce a significant impedance contrast and remains invisible, unless there are fluids associated to it.

Whether partial melt is present in southern Tibet as well, and if it is widespread or only locally present, is investigated in Section 4.4, after a lateral comparison of the results in Nepal.

4.3.3 Lateral variations beneath Nepal

Comparison with the HIMNT RF results

The HIMNT experiment's RF study (Schulte-Pelkum *et al.*, 2005) presents a 300 km long profile, which averages data from stations spanning 300 km laterally as well. (Fig.4.7). The seismological results show the crustal structure of the India plate beneath Nepal and the Himalayas (Fig.4.7b). Based on a differential image of events arriving from south and north (Fig.4.7c), the authors argue that as much as 20% of anisotropy may be present at shallow depths. An example of station SIND illustrates this effect (Fig. 4.8). Finally, on

the interpretation figure (Fig.4.7d), the shallow décollement zone related to the MHT is continued in a ductile zone, also anisotropic.
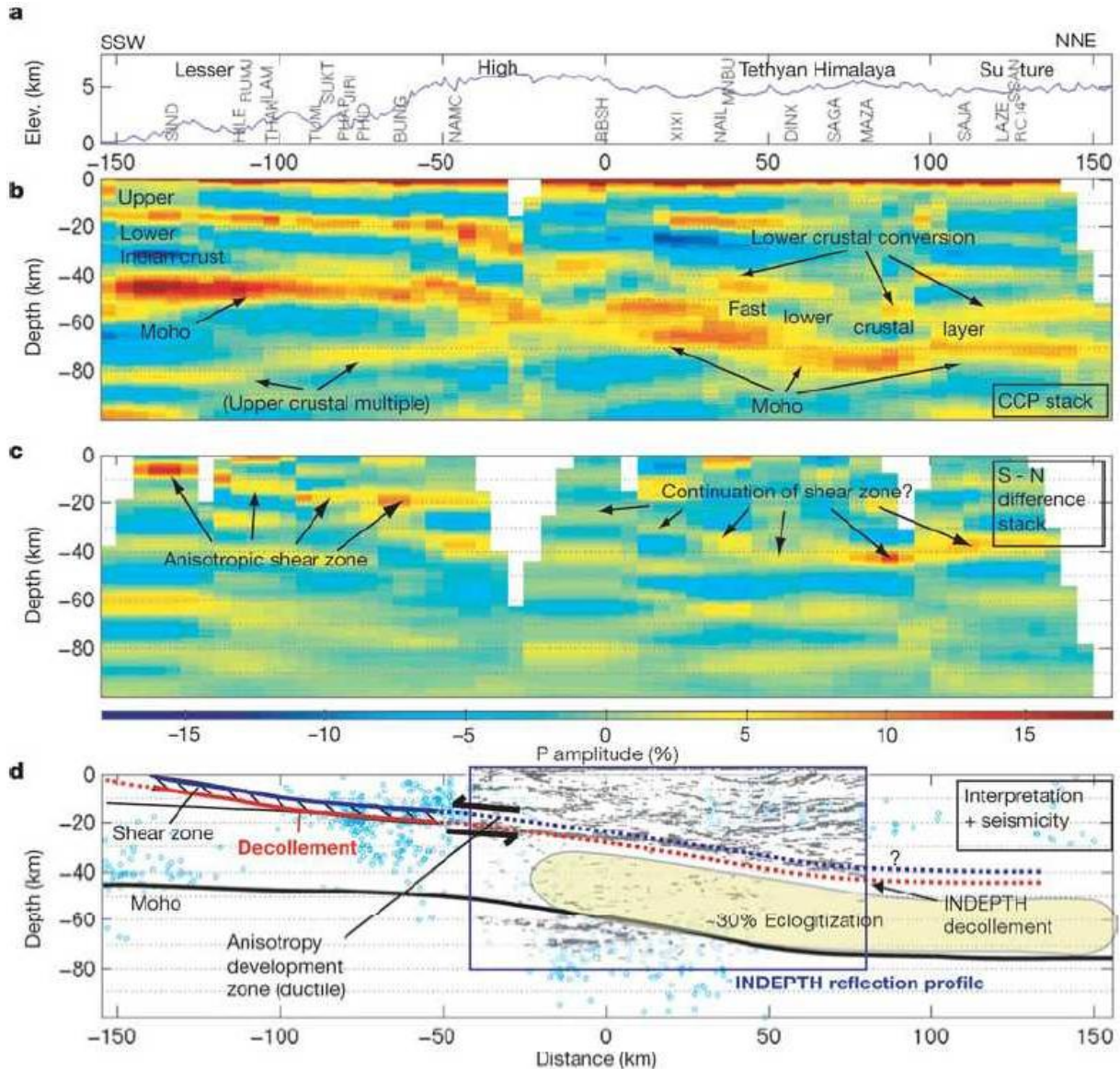
Figure 4.7: Receiver function migration from the HIMNT experiment (from Schulte-Pelkum et al., 2005). (a) Topography and stations along N18°E profile. (b) RF migration using 5 km wide bins and 30 km horizontal smoothing. White gaps are areas with no data coverage. Colour scale is proportional to relative amplitude. (c) South-minus-north azimuthal differ- ence migration to allow imaging of arrivals that change polarity over back-azimuth, with lateral smoothing of 10 km. (d) Interpretation.

I find that interpreting the variations in arrival time on the radial RF and the polarity

Figure 4.8: Below: observed and synthetic data showing anisotropic shear zone beneath station SIND of the HIMNT experiment (from Schulte-Pelkum et al., 2005). Radial (left) and transverse (right) receiver functions are averaged by 15° wide bins with 5° overlap (no duplication in count on right). Above: Similar processing for the same station but using a 2-year long dataset (1 year HIMNT (SIND0), 1 year Hi-CLIMB (NSIND); trace count now includes overlap). There are clear variations of arrival time with back-azimuth on the radial RF (dashed lines), in particular in the ranges where the HIMNT dataset has a lower number of traces (∼180-270°). This puts a question mark on the interpretation of the data as an anisotropic layer.
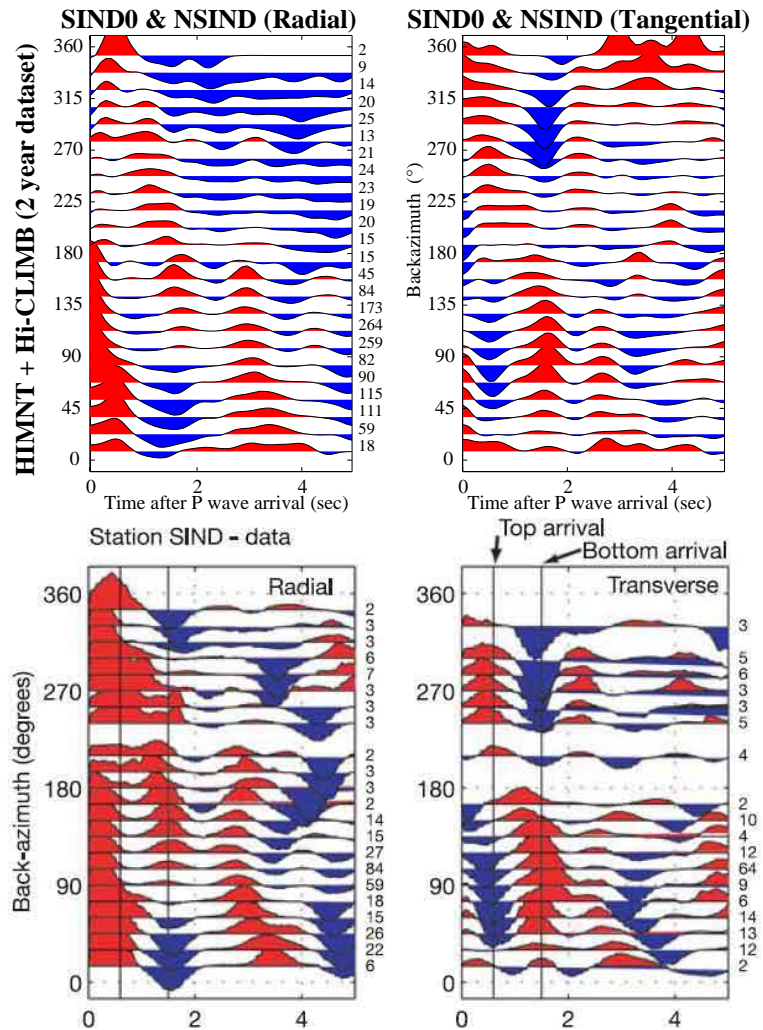
variations on the TRF in terms of anisotropy is not unambiguous. On the *south-minus-north* differential image (Fig. 4.7c), it can be clearly seen that the most prominent signal is related to station SIND, and that the amplitudes are less significant at other stations. The continuity of the interfaces is partly due to the very large horizontal smoothing (30 and 10 km, respectively, on the two profiles). The top of the proposed shear zone is unclear between −40 and +30 in-line distance, which makes it difficult to connect the southern and northern part of the image. Concerning the interpretation, ductile deformation is effective at higher temperatures, — thus at greater depths, — so another mechanism must be responsible for the development of tangential RF amplitudes at shallower depths.

As the Hi-CLIMB experiment collected further data at the site of station SIND, we have processed the 2-year long dataset and compared the receiver functions to the HIMNT results (Fig. 4.8). The completed dataset covers back-azimuth ranges where the smaller

dataset did not have enough traces. The results show a similar signature to those observed at station H0180, for example: two series of peaks with small arrival time difference, and clear 2π periodicity in the amplitude/polarity variations of the different peaks on the radial and tangential components. Station SIND lies close to the surface trace of the MBT and the MCT, as the stations discussed previously, thus the young sediments may have been deformed relatively easily, and they could have stacked up in many duplexes, producing north-dipping impedance contrasts. In this position, the presence of dipping faults cannot be neglected in modelling RFs, as it was the case for station H0120. Although there might be difficulties in the differentiation of narrow, anisotropic layers and multiply stacked, thin dipping structures, I believe that the role of dipping layers is more important than the role of anisotropy, especially in zones of brittle deformation. Here, too, a denser field deployment, together with a more homogeneous back-azimuthal coverage, would guarantee an improvement.

Hi-CLIMB short profiles in Nepal

The deployment of the Hi-CLIMB experiment in Nepal (Fig. 3.1) allows to image lateral variations in crustal structure. However, as the Pokhara (NP) and Gumba (NG) profiles were performed with much less stations and larger spacing, we cannot expect to reproduce the resolution of the main array's image. These two profiles run west of the main array from basically the MFT to the front of the High Himalayas. A third profile, to the east of the main array, and in the same line as the HIMNT experiment's projected profile, is studied using the 15 stations available over eastern Nepal. The processing of receiver functions for these three profiles was exactly the same as for the main array and Figure 4.5, with the exception that the colour scale's amplitude is halved for better saturation of the image. The origin of the profiles is about the MFT.

The resulting migrated sections are shown on Figure 4.9. The Ganges Basin is not covered enough to infer new information, although station NP010 shows the bottom of the sedimentary basin. As regards to the faults, a few stations located close to major thrust faults show polarity changes on the tangential RF (see for example NP030 and NP035 in Appendix C).

Concerning the low velocity zones, the only place where a *blue-over-red* pattern can be seen is beneath stations NP080, NP082 and NP085. However, further south, the LVZ seems to be absent. Similarly, there is no sign of significant velocity decrease along the NG profile. The situation is the same along the third profile, even if there are several stations that are projected to 40-50 km in-line distance from clearly different geographical positions.
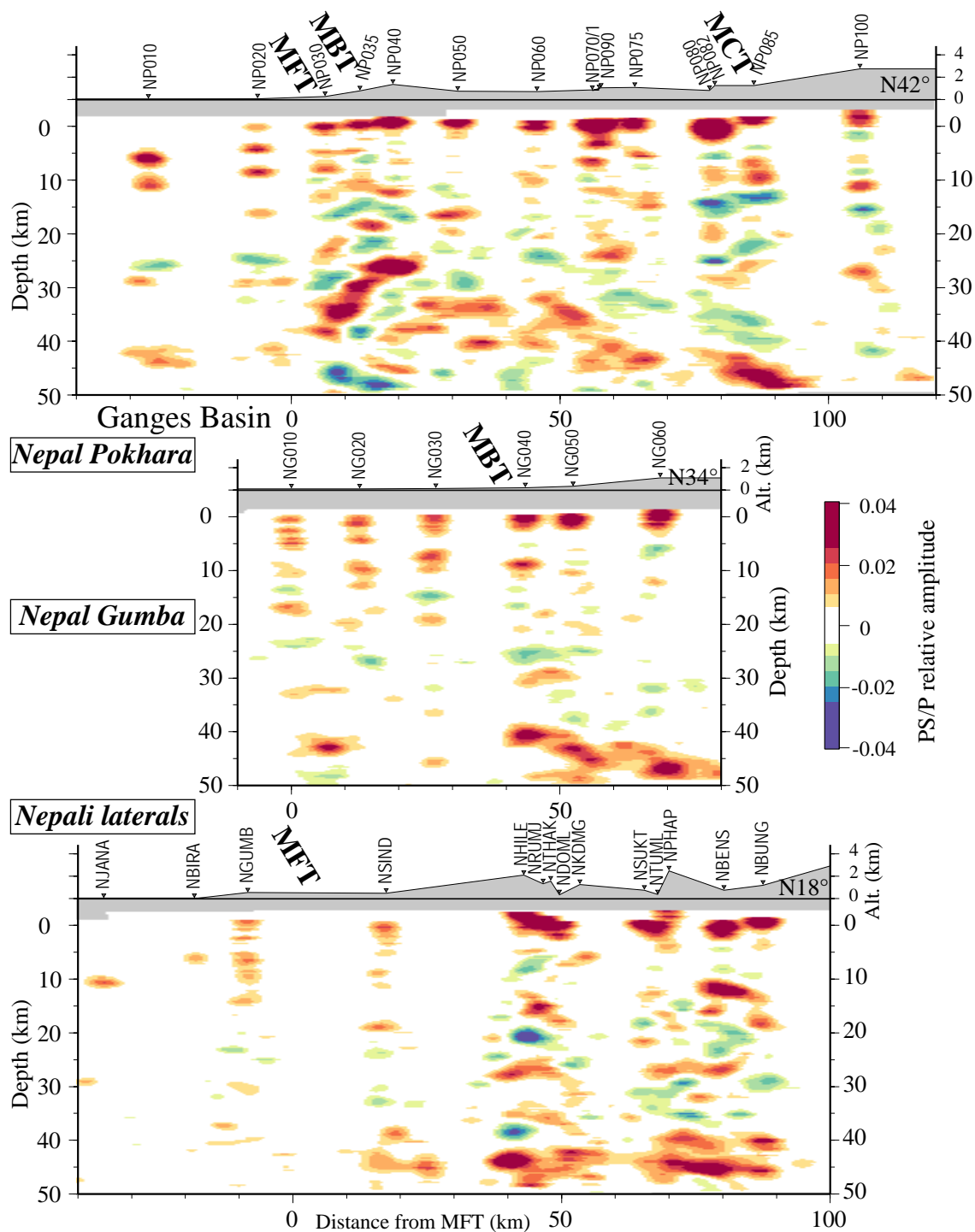
Figure 4.9: Crustal structure of Nepal beneath three short, more sparsely covered profiles. See text for discussion. The number of traces, as well as the projection parameters for three profiles are the following: NP: 612 traces, centred at [27.6889° N, 83.4784° E], oriented N42° E. NG: 314 tr., c: [27.4614° N, 84.2799° E], azi: N34° E. Eastern lateral: 374 tr., c: [26.873° N, 86.517° E], azi: N18° E.

A common feature of the three profiles is the Moho at ∼40-45 km average depth, similarly to its position on the main array profile. Imaging its deepening is limited by the extent of the arrays, but it seems to occur at ∼100 km on the NP, and at ∼80 km on the NG profile. (The third profile averages over significant lateral distances, thus its interpretation is pointless. However, it looks different from the HIMNT profile because of the 2 km wide horizontal smoothing, compared to 30 km in Schulte-Pelkum *et al.* (2005), and also due to the lower number of stations.)

In summary, the images beneath the short profiles in Nepal suggest that the lateral extension of the low velocity zone — observed beneath the main profile — is limited, and also that the descent of the Moho exhibits lateral variations. Along the main profile, the Moho is flat, and the LVZ is associated to fluids accumulated along the MHT. The hypothesis of dehydration during metamorphic reactions is supported by the presence of microseismicity, and by magnetotelluric measurements that relate the conductive zones to dewatering. Both the flat geometry of the underlying Moho, and the accumulation of fluids favour a lower effective friction coefficient (μ_{eff}) on the MHT. On the other hand, beneath the lateral arrays, the LVZ is absent, and the Moho plunges further south. This implies a higher μ_{eff} on the MHT. These differences may also explain why the Kathmandu klippe is preserved, and why this type of structural element is not present along the NG and NP profiles, for example.

The existence of the MHT, or a mega-thrust of any name beneath the entire Himalayan arc is without doubt. An issue to resolve here is to further explore and delimit the zones where fluid accumulation occurs. Do these zones correlate with the shape of the Moho and/or microseismicity? Is the hypothesis that there is a link between fluid bearing zones and the surface geometry of faults, as it is the case of the Kathmandu klippe, true? What is the role and behaviour of fluids in the seismic cycle? Is it possible to estimate precisely the amount of fluid from the underthrust sediment and dehydration balance?

These questions are examples of issues arising from observations at a few profiles perpendicular to the Himalayas. To answer them is a great puzzle, and the time of a thesis is enough to bring only a few elements to the whole. The above discussed profiles are located within 80-100 km from each other, and although their resolution is different, we cannot say that the intra-crustal structure is homogeneous. Here I would like to emphasize that in complex zones, such as active mountain ranges, important lateral variations may occur within horizontal distances that are clearly less than thought.

4.4 Crustal fluids and V_P/V_S

4.4.1 Bright spots in Tibet

I recall from Section 2.4.2 that the view that there are significant amounts of fluid in the Tibetan crust relies on the observations of "bright spots" by the INDEPTH I and II seismic experiments (Brown *et al.*, 1996; Makovsky *et al.*, 1996a). These bright spots appear as locally anomalous amplitudes on seismic reflection profiles (sensitive to V_P), and the coincident negative polarities indicate the presence of fluids. The authors associate the observed features to granitic melt, sometimes accompanied by smaller amounts of free aqueous fluid. However, there are disagreements concerning the amount of fluid present, the thickness and the depth of the partially melted zones. This is mainly because the above methods detect the top of the low velocity zones related to the bright spots, but not the bottom. Here we investigate the presence of fluids along the Hi-CLIMB main array, as well as beneath lateral stations in Tibet.

Main array

Similarly to the procedure after which low velocity zones along the MHT were observed, we perform a RF migration along the main array of the Hi-CLIMB experiment, and focus on the crustal structure beneath Phase2 (Fig. 4.10). Iteratively deconvolved RFs are migrated to 50 km depth to search *negative-over-positive* signatures for low velocity zones, or simply high amplitude negative zones for bright spots in the upper crust. To obtain a high-resolution image, and to get an idea of the spatial definition of the structures, two migrations are performed using 1 Hz and 0.5 Hz as the higher corner-frequency of the filter (Fig. 4.10).

On both migrated profiles, we recognize the low velocity zones imaged in Nepal; LVZ1 between 30 and 100 km in-line, and the onset of LVZ 2 from ∼170 km. North of the Yarlung Tsangpo Suture, several high amplitude patches can be observed at relatively shallow depths. The most pronounced negative (violet) zones are generally on top of positive (yellow) zones (see letters from *a* to *h* on Fig. 4.10), corresponding to a rapid decrease and then increase of velocity with depth. This is similar to the low velocity zones in Nepal, including the thicknesses; however, the amplitude of the patches is clearly lower.

We identify the described features as bright spots in the Tibetan crust for two reasons. First, they are located at depths that match those described by the INDEPTH experiment. Second, we suppose that the bright spots have a low velocity signature in V_S similar to that in V_P . The presence of clear low velocity zones at the stations above the
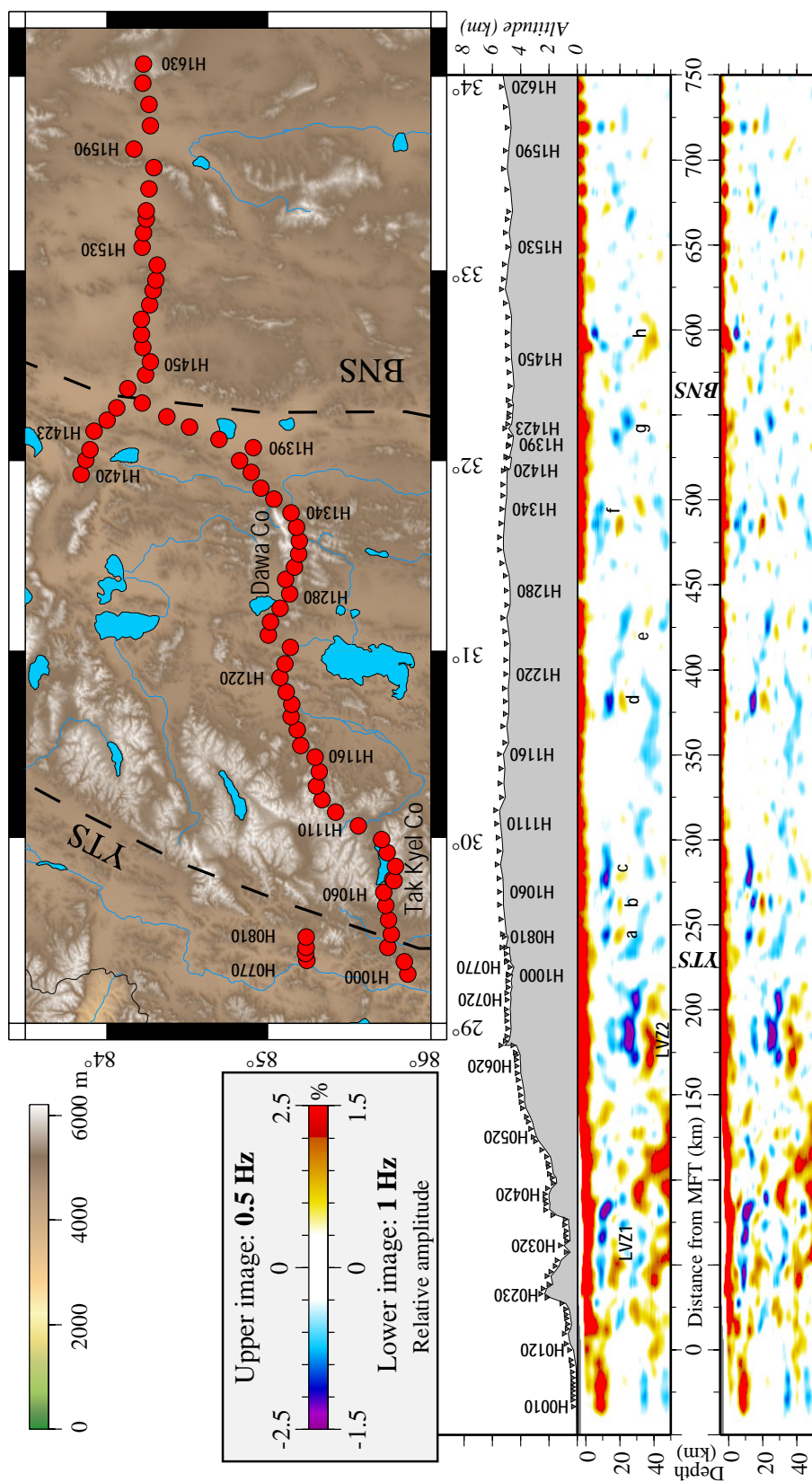
Figure 4.10: Top: Phase2 of the Hi-CLIMB experiment spanning from south of the Yarlung Tsangpo Suture (YTS), across Lhasa block, and north of the Banggong-Nujiang Suture (BNS). Bottom: migrated RF profiles with 0.5 and 1 Hz higher corner-frequencies, respectively. Letters **a** to **h** mark the features that we associate to bright spots. The W3 list was used to produce 10883 traces on the main profile, projected along 85°E and gridded onto a dx = 1 km × dz = 0.5 km mesh. Back-azimuthal equalizing by 20° ranges, and horizontal smoothing on 2 km.

described bright spots is also confirmed by the inversion of the RFs (see below, Note G, and Appendix D). Some of the patches appear to be grouped (*a-b-c* and *d-e* zone), although it is not clear if they are really connected or not. Even if they are connected, the horizontal extent of the bright spots does not exceed ∼50 km beneath the Hi-CLIMB main array, and their thickness is estimated to ∼10 km. While the horizontal extent is well constrained by the close spacing of the stations, the thickness estimate is certainly not that precise. Nevertheless, it gives a lower limit to the vertical extension of the bright spots, an estimate that is often unavailable from active seismic reflection or magnetotelluric data. The spatial definition of these structures is relatively sharp, as their contour is clearly visible even on the high frequency (1 Hz) migrated image. Finally, based on our profile, it seems that the bright spots are more frequent beneath Lhasa block compared to Qiangtang block.

Bright spots and grabens

Figure 4.10 aligns the presented migrated profiles and the topographic map along Phase2 of the Hi-CLIMB experiment. An important observation is that the elongated bright spots can be found beneath South Tibetan grabens. The surface location of the bright spots **a-b-c** lying beneath stations H1060-H1100 fits very well the Tak Kyel Co[2] graben crossing the Transhimalayas (or Gangdese Belt). Also, the reflective zone between stations H1300-H1350 (labelled **f**) lies beneath the graben north of a small lake, Dawa Co[3], in northern Lhasa block. The issue if there is a correlation or not between reflective zones in the upper crust and grabens in southern Tibet can be investigated using the Tibetan lateral sites of the Hi-CLIMB experiment (Fig. 4.11).

The more sparse deployment of stations east of the main array (35 km distance to the closest station in average) does not allow to produce high-frequency, continuous migrated profiles of the upper crust. To map the intra-crustal structure, we perform semi-linearized inversions of high quality receiver functions stacked for each station. (More details about the inversion procedure are given in Note G and Appendix D). However, as the inversion of receiver functions alone is not a stable procedure, we only look at the first order features of the obtained *velocity–depth* curves.

Among the Tibetan lateral sites, 25 inversions resulted in shear-wave velocity profiles where the presence of an intra-crustal velocity decrease could be elucidated. In the frame of the supposed relationship between grabens and bright spots, the locations of the station sites were classified into three categories (Fig. 4.12, Table 4.1):

---

[2]Or Daggyai Co, according to GoogleEarth.

[3]Name from GoogleEarth; no name from a published map was found.
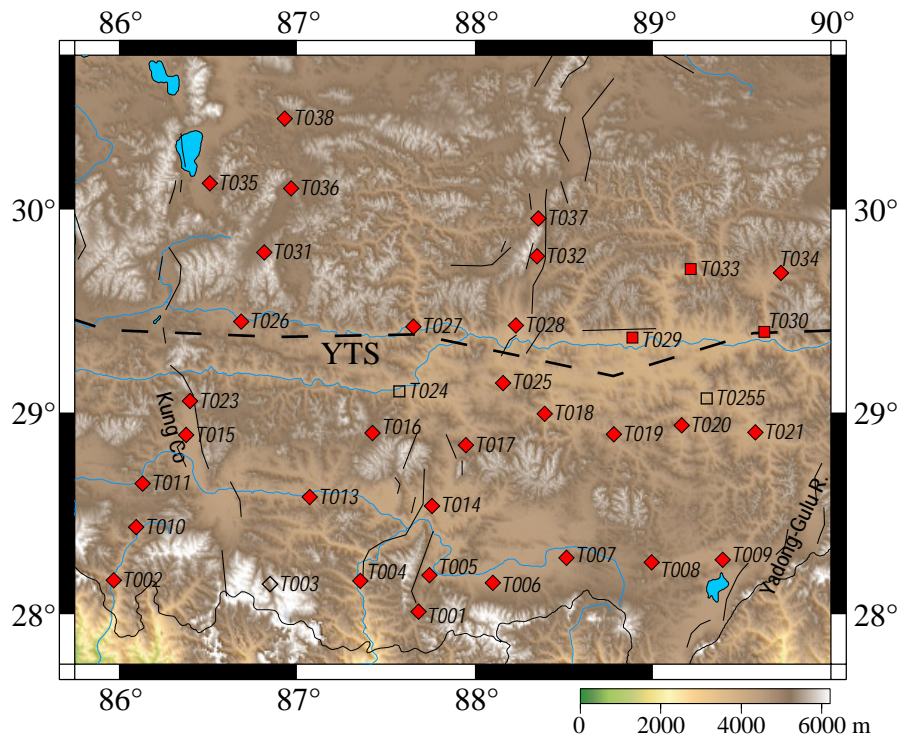
Figure 4.11: Topographic map showing the deployed Tibetan lateral sites and some of the active faults. The last character of the station name was omitted when it was "0" for better readability. Squares mark stations with 2Hz-sensors. Stations with no colour fill did not produce suitable data for RF computation.

– grabens, usually large, N-S trending, flat-bottom zones filled with sediments;

– valleys, mostly narrow, usually with an active watercourse;

– mountainous or other sites.

The classification is based partly on topographic map, and partly on field experience.

Table 4.1 shows the distribution of inversion results concerning the presence of a low velocity zone in the crust in relationship with the site classification. Mathematically, the presented matrix is "diagonally dominant", which means that low velocity zones are present mostly beneath grabens, and their occurrence is rare beneath other type of sites. This correlation aligns well with what has been observed along the main array. Also, it is coherent with the INDEPTH results, as the bright spots were detected in the Yadong-Gulu rift (Fig. 4.11).

The correlation between extension and the underlying high temperatures implies mechanisms that go in the current understanding of geodynamical processes. If *active*

In Kung Co graben, towards station T0230 (view to the North)

In Kung Co graben at station T0150 with Logan Mitchell

On the valley road to station T0040 (view to the East)

The valley becomes larger at station T0040 (view to the South)

A mountainous site at station T0250 with Dane Sherstad
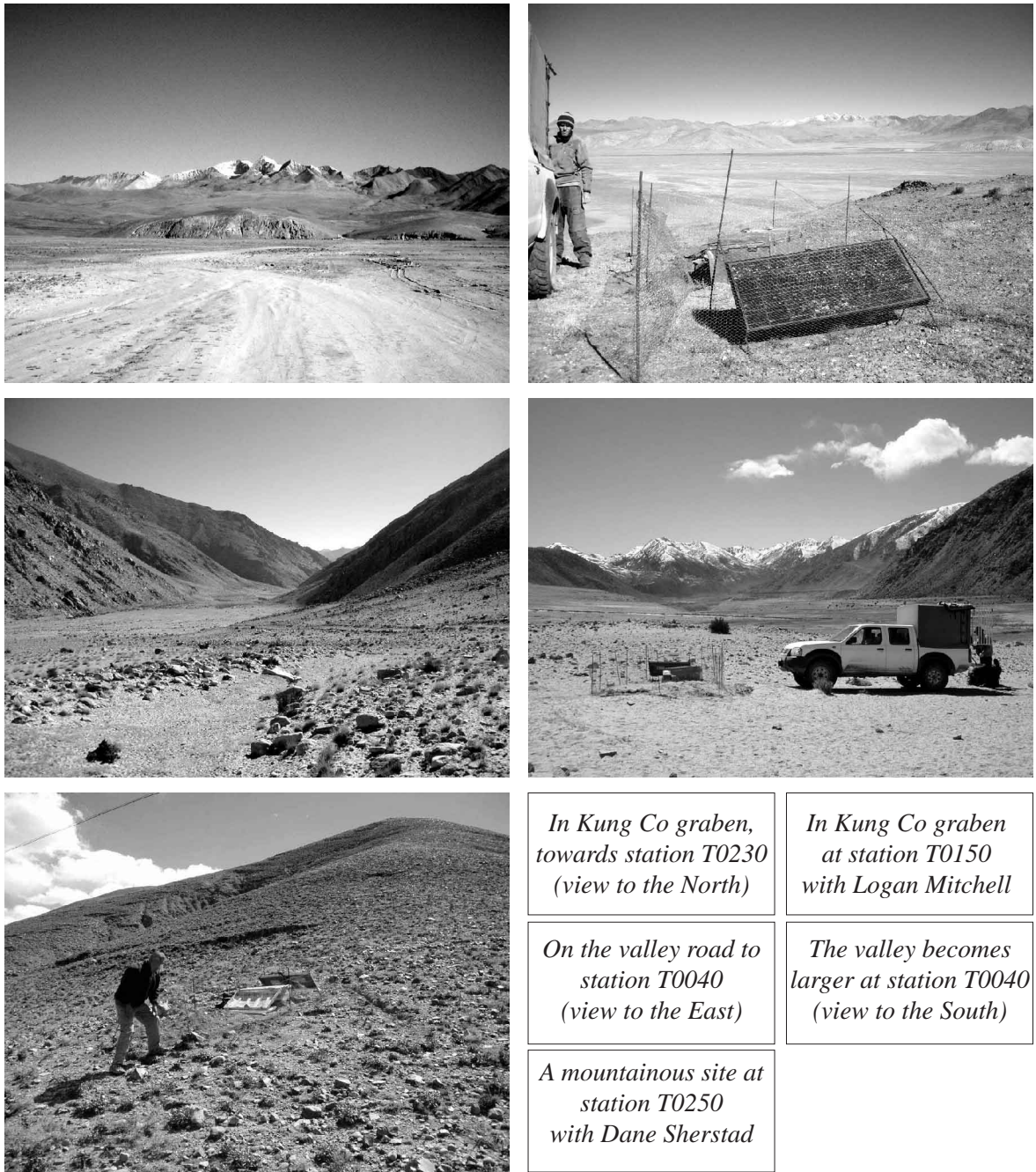
Figure 4.12: Picturing the classification of lateral seismological sites in southern Tibet.

rifting is responsible for this correlation, then an increase of temperature has contributed to localized rifting in South Tibet, and caused the appearance of extensional grabens. If rifting was *passive*, then the grabens opened first, and the rise of temperature in the

Location of	Number of	Low velocity zone is		
stations		Pronounced	Not clear	Absent
Graben	10	9	1	0
Valley	7	1	5	1
Mountain	8	1	2	5

Table 4.1: Observed relationship between site location and the presence of low velocity zones in RF inversion results. Stations are classified as the following (last "0" character is omitted);   Graben: T001, T015, T023, T028, T031, T032, T035, T036, T037, T038;   Valley: T002, T004, T010, T013, T026, T027, T034;   Mountain: T011, T014, T016, T018, T019, T020, T021, T025.

crust has followed after. With our current knowledge of the Tibetan Plateau, it would be difficult to lean towards one interpretation or the other. A much better coverage of heat flow measurements across the entire plateau, together with an increased knowledge on crustal radiogenic heat production and its variations, may help to interpret this correlation in terms of active or passive rifting, and would bring new arguments for either one of the models.

However, I would like to point out that the widespread view on large amounts of fluids relied on INDEPTH data that were acquired in grabens, primarily for logistic reasons. The results presented here agree with earlier observations, but show, using data acquired elsewhere than grabens, that bright spots are limited in horizontal size and in thickness as well. This, along with their limited occurrence, suggests that the amount of fluid in form of bright spots, hence partial melt, cannot be large in the Tibetan crust, and cannot affect vast zones or regions. It seems more probable that accumulation of partial melt and aqueous fluid occurs rather locally, as it is the case for the LVZ2 beneath Nepal, or the shallow bright spots in Tibet.

Note G
INVERSION OF HI-CLIMB RFs

During this thesis, the opportunity to process Hi-CLIMB data was opened to me by the receiver function method, hence I have performed RF inversions alone, even though there are more stable and robust procedures. The semi-linearized scheme was applied to all stations, and the NA for some selected stations. In order to stabilize the inversions, I have set up a step-like resolution procedure, starting from low frequencies and thick layer velocity models, and ending at high frequencies and thin layers (see Appendix D for details). This way, a certain coherency was ensured from low to high frequencies. Finally, the last, thus the finest velocity-model was used to produce a low-frequency RF, which was compared the data filtered at the same frequency band. This, and the similarity of the velocity models obtained at different steps of the inversion procedure, allowed to estimate the relative robustness of the results.

As the RFs were inverted in large amounts, in a semi-automatic way, the resulting V_S models do not always resemble between low and high frequencies, and/or between the semi-linearized scheme and the NA. Only at least partially coherent results were used for the interpretation beneath the Tibetan lateral stations. A few examples of RF inversion results, together with the parametrization of the inverse problem, are presented in Appendix D. Here an example of a station with a pronounced upper crustal LVZ (bright spot) beneath a graben is shown, with another example where this feature is clearly absent.
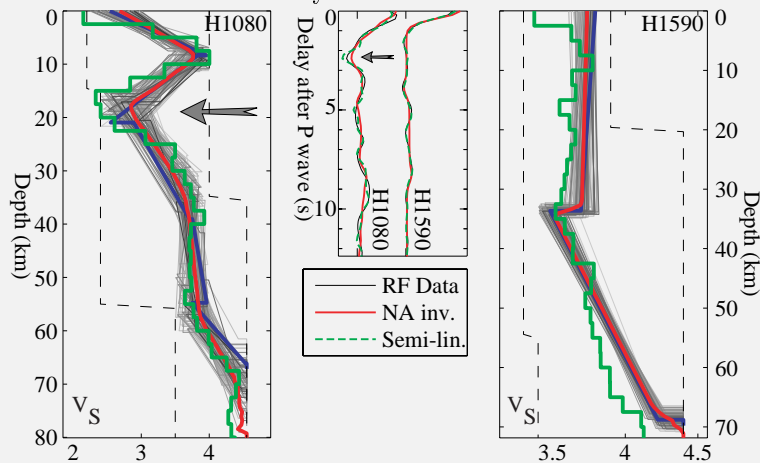
Figure G: Examples for (left): the clear presence of an upper crustal low velocity zone (arrow) on both the inversion result and the original RF (centre), in Tak Kyel Co graben; and (right): another station where this feature is absent, in Qiangtang block. The blue, gray and red curves are the best model, the best 1% of all tested models, and the average velocity model of these latters from the NA, respectively. The green line is from the semi-linearized method. V_S is in $km \cdot s^{-1}$.

4.4.2 Fluids and crustal V_P/V_S

Another way to investigate the amount of fluid in the Tibetan crust is to calculate the average crustal V_P/V_S . This ratio is representative of the bulk crustal composition (Zandt and Ammon, 1995), and can also indicate the presence of fluids. The average value for V_P/V_S is 1.73, but this number increases/decreases with decreasing/increasing SiO_2 content. The V_P/V_S signature of fluids is described by Watanabe (1993) (Fig. 4.13). Partial melt increases the V_P/V_S rapidly, while the presence of water causes a slight decrease until 10 vol.% and then an increase, but the value is never very different from 1.7-1.8.
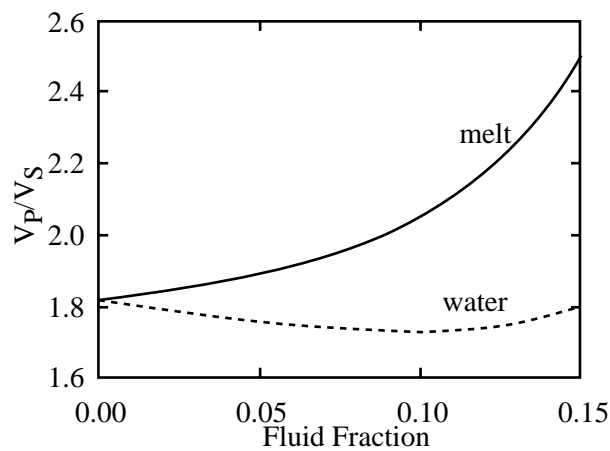
Figure 4.13: The variation of V_P/V_S with increasing amount of water or silicate melt. (From Watanabe, 1993.)

Computation of the average V_P/V_S -ratio based on the migrated depth of PS and PpS phases using a 1-D velocity model has been illustrated in Chapter 3. Here we focus on the results (Fig. 4.14), showing the average crustal V_P/V_S -ratio, and the calculated Moho depth discussed in Chapter 5.

The average value of V_P/V_S along the Hi-CLIMB main array can be separated into three major parts. In the region of Nepal, there are strong variations from south to north. The high values, typical of a crust with thick sedimentary cover (Clitheroe *et al.*, 2000), are related to the formations that are exposed at surface in the Ganges Basin, and which are underthrust beneath the Siwalik foothills. Further north, after a short section of regular V_P/V_S -values, we observe a $\sim$100 km long low V_P/V_S region (<1.7), which roughly matches the position of the High Himalayan range. Such a low value is typical for felsic rocks, thus the leucogranites present in the crust would provide an explanation. We note that the neighbouring HIMNT experiment also observed low values at the same in-line position[4].

---

[4]A. Sheehan, *Earthquakes and Crustal Structure of the Himalayas from the Himalayan Nepal Tibet Seismic Experiment (HIMNT)*. International Workshop on Seismology and Seismic Hazard in the Himalaya, Kathmandu, 2006.
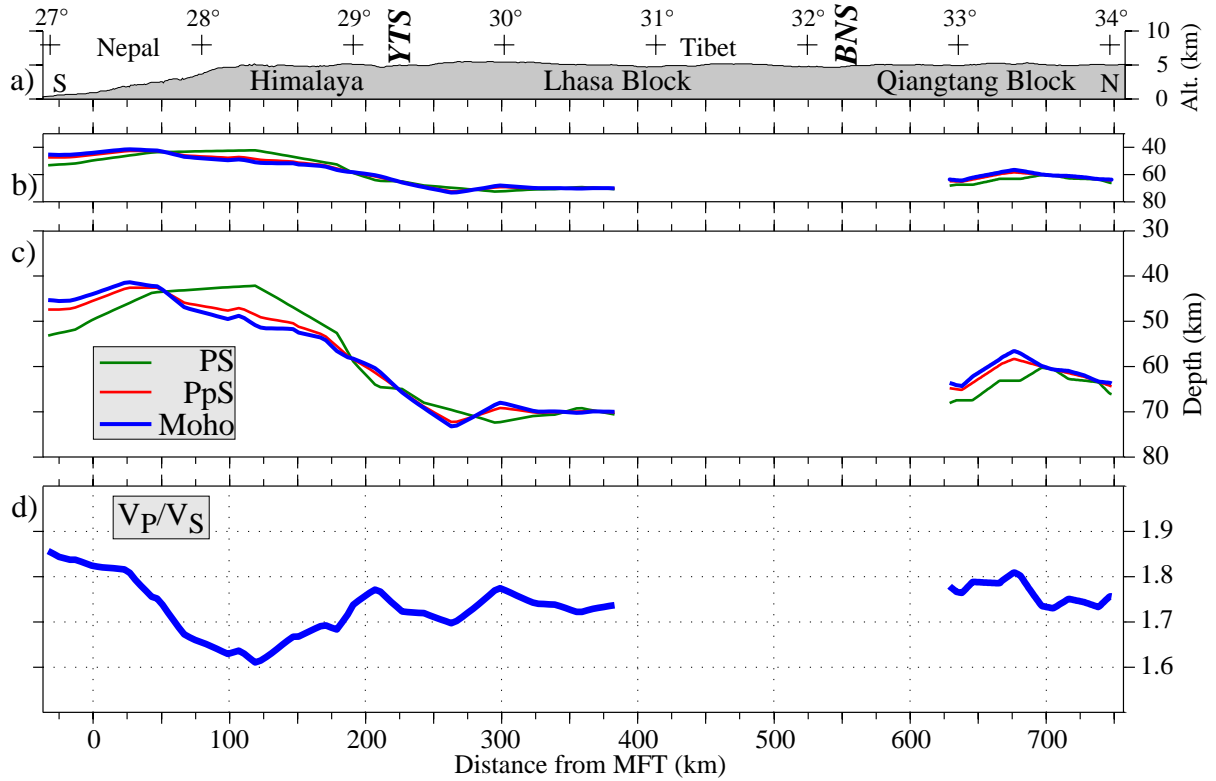
Figure 4.14: (a) Topography along longitude 85°E. (b) and (c) Depth of PS and PpS phases picked on 1-D migrated images, and the calculated depth of the Moho. The curves are in two parts, corresponding to the zones where both phases show coherent signal, allowing clear identification and picking of the phases. (b) is without vertical exaggeration. (d) Derived average crustal V_P/V_S -ratio. See text for discussion.

The second and third portions of the V_P/V_S curves correspond to Lhasa and Qiangtang blocks, respectively. Although there are small variations, the values here are always within the 1.7-1.8 range, suggesting a usual crustal composition. More important: the regular value of V_P/V_S excludes the possibility of widespread partial melt in the crust. A short calculation shows that if only one third of the crust would include 6 vol.% of melt, while the other two thirds would have a regular V_P/V_S of 1.75, then the average crustal V_P/V_S would exceed 1.8. These constraints do not contradict our previous findings, and still allow local accumulation of partial melt and/or aqueous fluid in the crust.

4.4.3 The final 2-D shear-wave velocity model

The last step in the analysis of wave propagation characteristics is the computation of the 2-D V_S model. As the variation of the average crustal V_P/V_S along the profile is

available, this step can easily be performed given an initial P wave velocity model. This is mostly accessible from seismic reflection results, or local earthquake analysis. For the Hi-CLIMB main array, the used V_P is constructed from three 1-D velocity models (Table 4.2). In Nepal, P wave velocity data is available from the Department of Mines and Geology. For Lhasa and Qiangtang blocks, we take the V_P models published by Haines *et al.* (2003). Then the 1-D velocity models are interpolated by horizontal, linear transitions between 120 and 160 in-line km between Nepal and Lhasa block, and between 400 and 600 km between Lhasa and Qiangtang blocks, respectively. The ∼5 km deep sedimentary basin at $V_P =$3.6 km·s^{-1} is added for the Ganges Basin, with a linear transition to upper crustal velocities between the MFT and the MCT. Vertically, the true altitude of the stations is included, and the bottom layer is extended to the depth of the Moho. Finally, this V_P model, as well as the obtained V_P/V_S values were gridded and then divided to yield the 2-D shear-wave velocity model. Velocities beneath the Moho were taken from *iasp91* (Kennett and Engdahl, 1991). The compiled V_P , V_S and V_P/V_S models are presented on Figure 4.15.

Nepal		Lhasa block		Qiangtang block	
H	V_P	H	V_P	H	V_P
23	5.60	20	6.00	17.2	5.70
32	6.50	15	6.25	15.3	6.10
	8.10	10	6.50	10	6.65
		10	6.73	10	6.85
		10	7.10	7.5	7.10
			8.00		8.00

Table 4.2: Initial 1-D P wave velocity models for Nepal (from DMG), Lhasa block and Qiangtang block (from Haines et al., 2003). H is layer thickness in km, V_P is in km·s^{-1} .

The application of a two dimensional velocity model is crucial when imaging in complex, laterally heterogeneous zones, such as the Himalayan-Tibetan region. The difference between 1-D and 2-D migrated depths could have already been estimated from the curves on Figure 4.14. Here I present an additional example on the effect of using a simplified, easily available, 1-D velocity model, and a more complex, adapted, 2-D one. Figure 4.16 shows 1-D versus 2-D migrations in the southernmost part of the Hi-CLIMB profile, in the Ganges Basin. Here the average V_P/V_S is elevated, and the sediments close to the surface exhibit very low velocities (see Chapter 6). The difference between the migrated depths is striking: when a 1-D model is used, the sediments in the basin are imaged at more than double thickness, and the Moho lies ∼15 km deeper than on the 2-D migration.
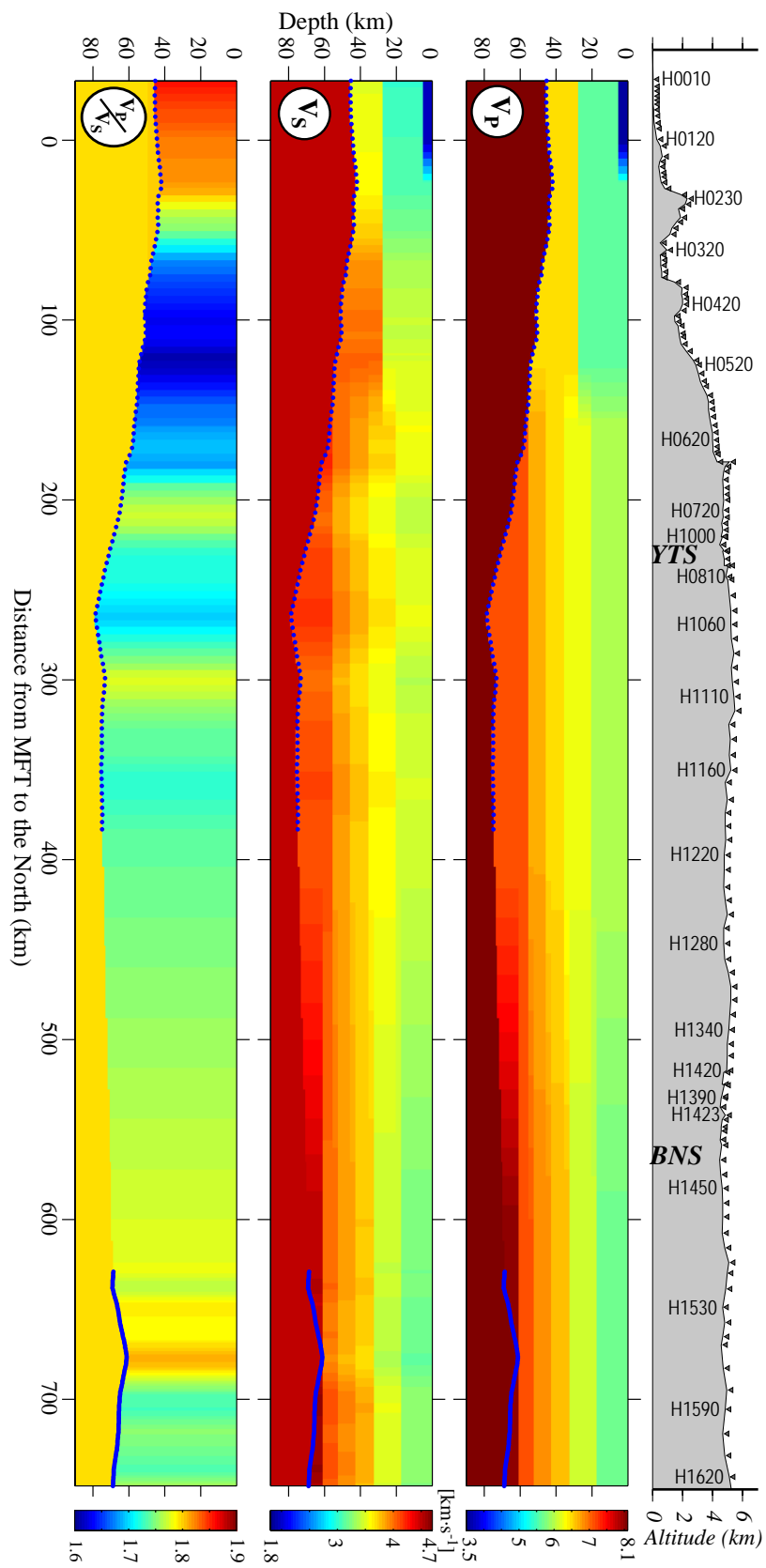
Figure 4.15: Final crustal 2-D V_P, V_S and V_P/V_S models derived as described in the text. Velocities below the Moho (blue dotted lines where its determination was accurate) are from iasp91. Depth is, exceptionally, with reference to the surface and not sea-level. V_P and V_S are in km·s^{-1}.
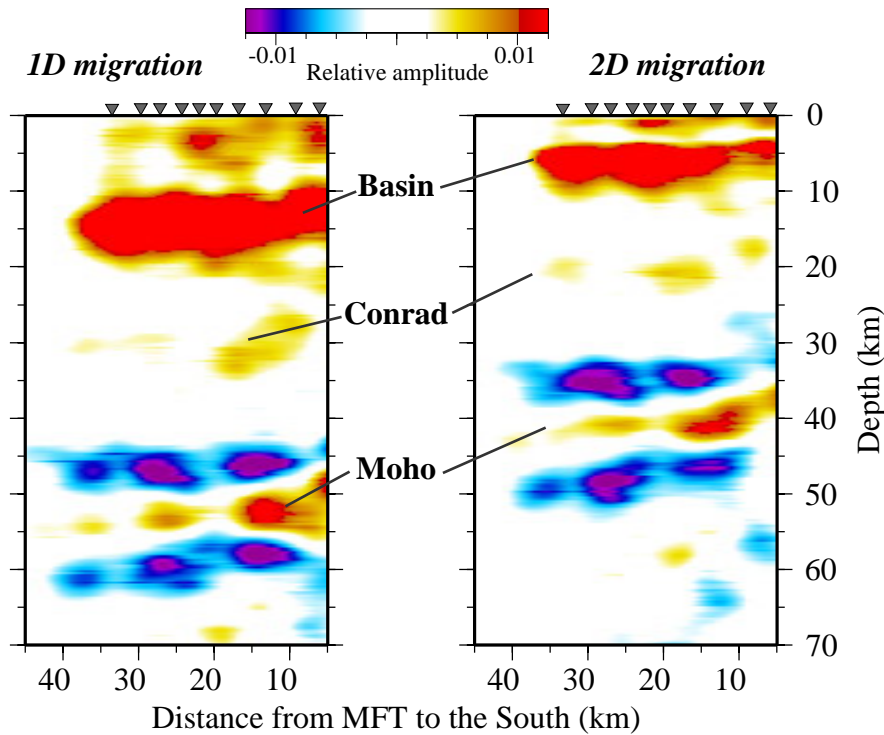
Figure 4.16: The Ganges Basin as an example illustrating the importance of using 2-D velocity models. The left and right images are migrations performed using a 1-D and 2-D velocity model, respectively. The difference in migrated depths for all interfaces is significant, due to the very low velocity sediments.

Error analysis in velocity determination

Sources of inaccuracy in the 2-D shear-wave velocity determination are twofold. First, the precision of picking a depth on a migrated image includes an error depending on the width of the signal, thus frequency content. In the presented case, I estimate the accuracy of picking to $\pm$ 2-3 km. Second, the quality of the results rely strongly on the supposed P wave structure, which is needed in the computation of the final 2-D V_S model from the derived V_P/V_S -ratio. Only the first source affects the precision of the V_P/V_S determination; if both the PS and the PpS picks have an error of 3 km, the V_P/V_S value will differ by ± 0.09. This level of precision may not seem extremely accurate, but even in the case of maximum errors, the observed V_P/V_S values are against models of widespread partial melting in the Tibetan crust.

Focusing the image in depth: Where and what the India plate hides?

"C'est une question ouverte de savoir
si le gros d'un continent,
dans toute sa hauteur,
peut s'engager sous le gros d'un autre,
dans toute sa hauteur."[1]
E. Argand, 1924

5.1   Introduction

Some of the main reasons for the lack of conclusive findings on the structure and dynamics of the lithosphere in Tibet are (1) its very large extension, (2) the low data coverage at uneven resolution, and (3) the insufficient knowledge and control of geodynamic processes based on these data (see Chapter 2). This chapter brings together available data and new elements concerning the main lithospheric boundaries inferred from the Hi-CLIMB experiment, and presents their geodynamical consequences. The main focus is the high resolution image beneath the main array and 3-D variations in southern Tibet. The features of the major tectonic blocks are discussed together with insights into the upper mantle structure. The primary goal is to characterize variations along 85°E, to draw the

---

[1]It is an open question to know if the bulk of a continent, in all its height, can get under the bulk of another, in all its height.

167

limits of the India plate, and to evaluate the proposed evolution models of the lithosphere.

The applied imaging method is receiver function migration, with some specific processing methods to differentiate direct and multiple conversions, and to enhance weak signals in order to clear up the lithospheric image. The foci are oriented on large scale structures, mainly interfaces but also the internal properties of bodies, that are continuous over significant distances. As the boundary of these objects is a potentially more smoothly varying velocity contrast, and because they are located at greater depth compared to upper-crustal features discussed in Chapter 4, we decrease the maximum frequency content to typically ∼0.5 Hz at the Moho, and less for the upper mantle. This allows to better image and investigate the lithospheric features, with a vertical resolution of ∼2 km. The horizontal resolution is also larger than previously, due to broadening the Fresnel zone, hence we choose a corresponding horizontal smoothing filter for our images, which is still less than the average station spacing along the main array.

5.2   Lithospheric structure across Tibet

5.2.1   The direct PS converted image

The use of PS converted phases is the classic way of receiver function imaging. First we used data from the W3 quality control list, which is not a very restrictive selection (see Note H). We filtered the data up to 0.5 Hz to perform a migration with the 2-D velocity model described in Section 4.4.3. The final image (Fig. 5.1) contains 10'875 traces and has a grid size of 1×1 km, with a horizontal smoothing of 3 km.

In the southernmost end of the profile, the Moho is imaged beneath the Ganges Basin at 40 km depth. Immediately to the north of this location, beneath most of Nepal (0–150 km distance), the image is difficult to interpret as the Moho does not appear clearly: two interfaces emerge at the same in-line location, at ∼40 and ∼55 km depth, respectively. Further north, from 150 km horizontal distance, the main interface becomes more clear, and the progressive deepening of the Moho can be followed at a gentle angle beneath the Himalaya, reaching its maximum, ∼73 km depth at the Yarlung Tsangpo Suture (YTS). The Moho can be followed without doubt beneath the YTS and north of this point. It does not seem to be interrupted at the latitude of the suture, as suggested earlier (*e.g.* Hirn *et al.*, 1984a), but crosses this point in a smooth way. Further north, beneath Lhasa block, the Moho is surprisingly flat along more than 200 km horizontal distance, until ∼100 km south of the Banggong-Nujiang Suture, where it becomes less well defined. It reappears in a clear way north of the BNS, beneath Qiangtang block, at a shallower depth of ∼65 km.
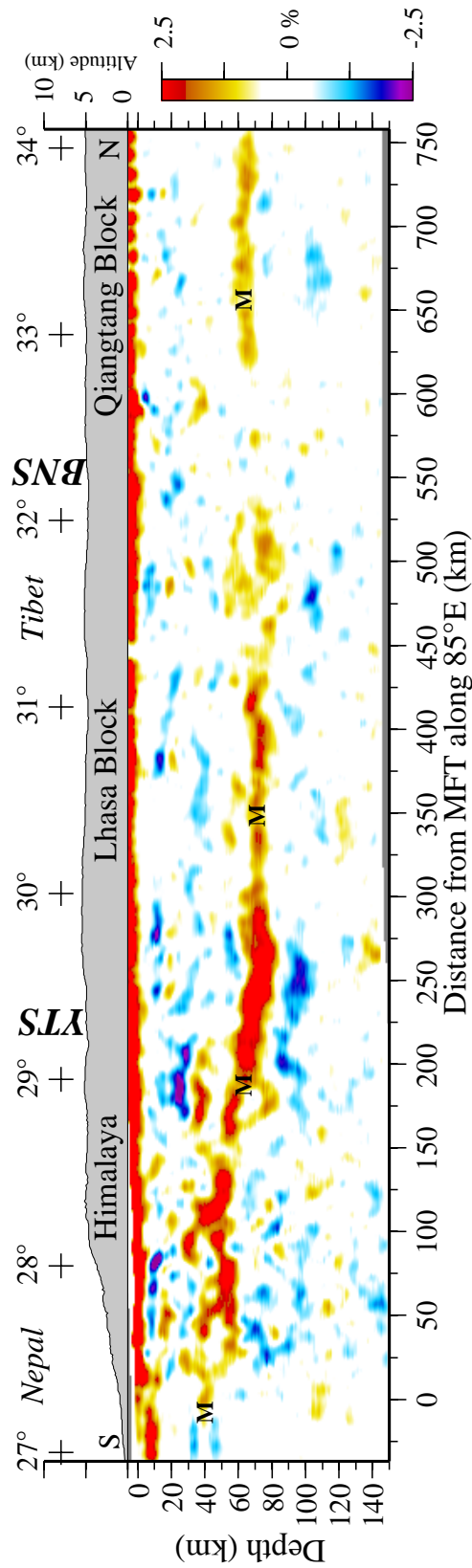
Figure 5.1: Receiver function migration along the main profile projected to 85°E. Colour scale is relative amplitude of PS converted phases to direct P arrival. No vertical exaggeration for the migrated image. The Moho is emphasized by letter "M". Stations H0220, H0230 and H1280 were excluded due to low signal-to-noise ratio and acquisition problems, respectively. On top: mean topography averaged over 100 km on both sides of the profile (vertically exaggerated). YTS and BNS mark the location of the Yarlung Tsangpo and Banggong-Nujiang Sutures, respectively.

Note H

Coherence of the migration — The effect of quality control

The quality of both raw data and computed RFs has been controlled during data processing (Chapter 3). It was an automated way to eliminate low quality recordings and to ensure that the selected dataset is consistent. Namely, several lists were established according to more or less strict parameter sets, suitable for inversion and stacking purposes, respectively. Here we ensure that this selection process does not bias the final image of the lithosphere. Figure H shows two PS migrations performed using the W3 (more strict) and W2 (less strict) selection lists with approximately $1 \cdot 10^4$ and $2 \cdot 10^4$ traces, respectively, as well as the difference of the two images. What we can deduce is that there are negligible differences in amplitudes all over the profile, except for the Ganges Basin where the number of traces differs the most, probably due the different noise level for data acquired in the sedimentary basin. Otherwise, we conclude that the presented RF migration images are consistent, and that they are not biased by the quality control process.
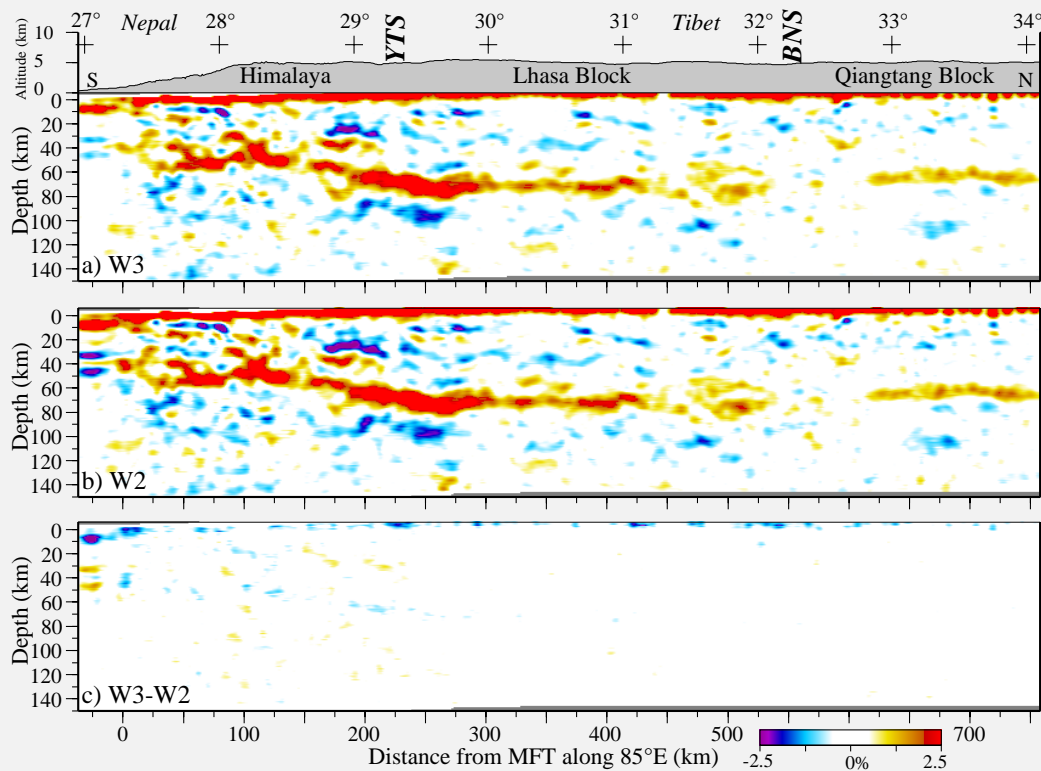
Figure H: Comparison of migrated images using W3 (a) and W2 (b) selection lists from the quality control process. All other parameters were identical. The differential image (c) proves that the presented profiles are unaffected by the data selection procedure.

The fact that the Moho is not evident to point beneath Nepal is somewhat embarrassing. Based on the simple structure beneath the Indian Shield (*e.g.* Saul *et al.*, 2000; Kumar *et al.*, 2001) and the Ganges Basin (see Sections 4.2 and 6.3), as well as the smooth topographic change, one would expect a clear image of the crust-mantle boundary beneath Nepal. This is clearly not the case: the observed two positive interfaces at ∼40 and ∼55 km depth, respectively, put a doubt on the clarity and validity of the PS converted image. Is the crustal structure really complicated, or is the image contaminated by multiple conversions of shallower impedance contrasts? If it is the latter case, do contaminations occur elsewhere in the profile, too? The use of multiples is, again, a valuable tool that helps to elucidate this issue.

5.2.2 Contamination by intra-crustal structures

It has been presented in Section 3.4.4 and on Figure 3.16, that multiply converted phases can be migrated to the correct depth using apparent velocities, which comes back to a vertical "shrinking" of the image. Similarly, the direct PS conversions can also be migrated to the theoretical depth of the PpS or PsS multiples, which means a vertical "stretching" of the original image[2]. This way, it is possible to point the zones where multiples of shallower, intra-crustal structures, may interfere with the PS conversion of the Moho.

Figure 5.2b shows the sum of the "stretched" images calculated for the PpS and PsS multiple along the main profile. The most prominent amplitudes are induced by the shallow low velocity zones. In Nepal, for example, the combination of multiples from the top and the bottom of the LVZ1 (see Note I) produce a positive peak at ∼55 km and correspond very well to the lower one of the questioned interfaces on the PS converted image (Fig. 5.1). Thus, the true position of the Moho beneath Nepal is rather the upper interface at ∼40 km depth. Further north, the LVZ2 seen on the PS image is not visible on the "PS-as-MUltiple" migration, as its deeper location after "stretching" falls below the lower boundary of the image.

Beneath Lhasa block, the multiples of the bright spots (negative-over positive amplitudes on the PS image) cause an interesting effect, yielding negative-positive-negative series of peaks with depth (see Note I for the illustration). The positive peak in the centre falls about the depth of the Moho on the PS migration, and enhances its amplitude, as it can be seen between ∼250-300 km and around 400 km in-line distance. Similarly, a little south of the BNS, part of the signal observed on the PS image may come from positive,

---

[2]These "shrinking" and "stretching" operations are non-linear, as the velocity is not constant with depth.
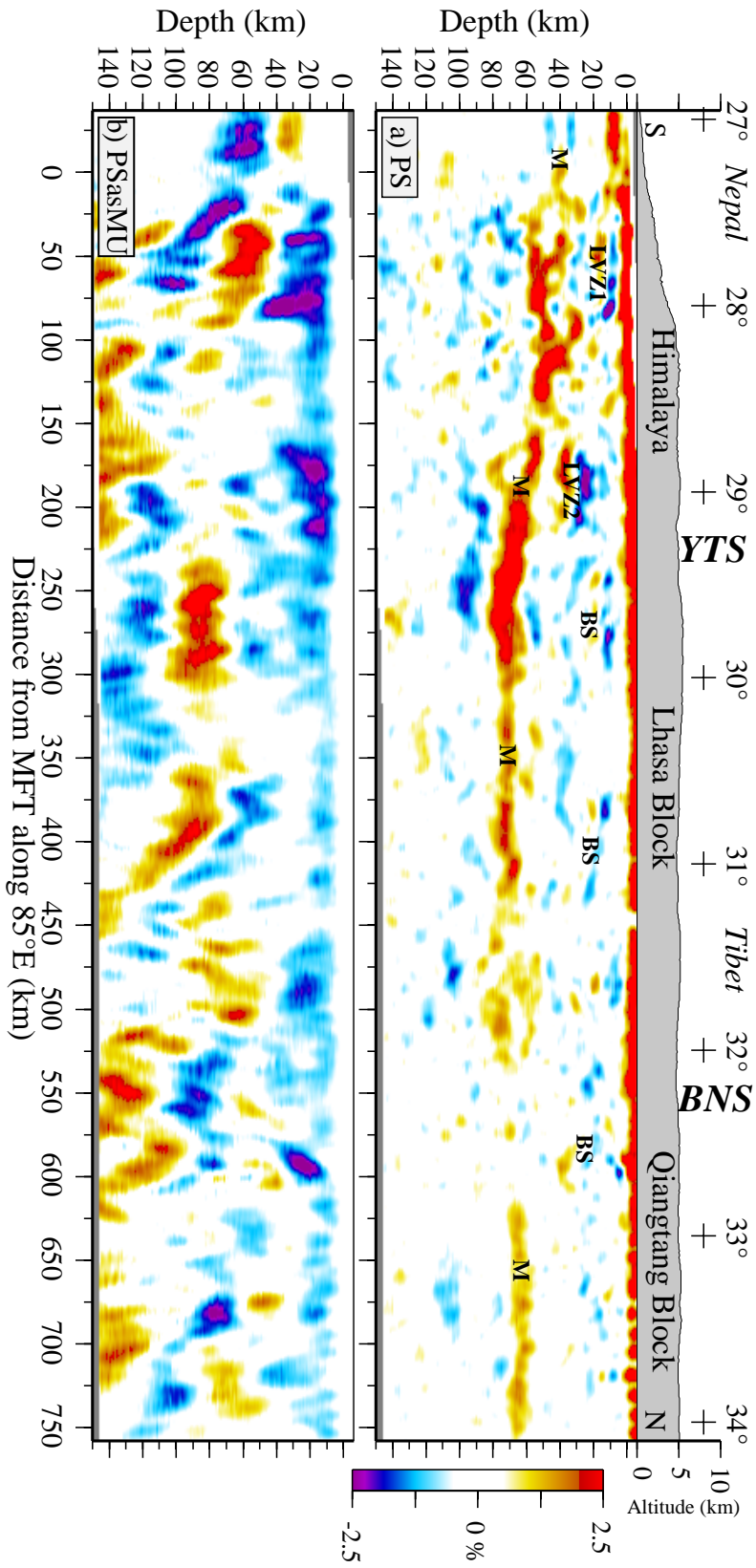
Figure 5.2: (a) Receiver function migration of the PS converted phase from Figure 5.1, serving as a reference. (b) RF migration of the PS phase to the theoretical depth of its multiples, corresponding to a vertical "stretching" of the original migration. This operation helps to outline zones where multiples of shallower structures interfere with the PS phase.

but lower amplitude multiples of shallower features. Beneath Qiangtang block, there seems to be no major interference, as the negative spot on the "stretched" image at 700 km falls beneath the Moho of the PS migration.

In conclusion, migrating the PS conversions as multiple phases helps to decipher the PS image and to locate areas where multiples of shallower discontinuities may interfere with the direct conversion of deeper ones. Although this operation is very sensitive to the accuracy of the velocity model at shallow depths, and thus exact depth estimates are difficult to provide, the potentially interfering zones can be outlined. The discussed and observed interference points to the problem of using PS converted phases only, which does not provide an optimal base for the interpretation of lithospheric structures.

Note I

THE EFFECT OF LVZ ON THE MIGRATION OF PS PHASE AS MULTIPLES

The shallow low velocity zones (LVZs) corresponding to bright spots in the Tibetan upper crust exhibit a negative-over-positive signature on the PS image. According to the "stretching" outlined previously for the migration of the PS phase as a multiple, we first migrate the LVZs as a PpS phase, and then as a PsS phase (Fig. I). In our case, this operation locates the positive peaks of the two multiples approximately to the same depth. Summing the two images thus results in a negative-positive-negative pattern, which is clearly visible on Figure 5.2b.

Figure I: Migrating a low-velocity zone signature to the theoretical depth of the PpS and PsS multiples. As the PsS image is flipped, the positive amplitudes from the two "stretched" images stack coherently, and yield a prominent positive peak between two negative ones, recognizable on Figure 5.2b.

5.2.3   Clearing the image using multiple conversions

At this point, we would like to produce an image that is — as much as possible — free from interferences between the multiples of shallower features and direct PS conversions. Thus we migrate the image with apparent velocities that place the multiples to the depth of the PS conversions, as explained in Section 3.4.4. This way, the image is "shrunk", and the multiple phases bring additional constraints on the structure of the crust-mantle boundary. Due to the vertical "shrinking" at the same frequency content, the width of the signal is decreased, yielding finer structures on the image. However, the upper ∼20 km of the image cannot be interpreted as it includes the PS conversions migrated to a shallower, "false" depth. The main drawback of this method is the possibility of deeper interfaces with a strong impedance contrast, that can be "shrunk" and placed to the depth of the Moho, causing false interpretations. However, the main mantle discontinuities represent clearly smaller velocity contrasts compared to the Moho. Furthermore, we have verified the expected depth of the 410 and 670 km discontinuities when migrating multiple phases: the corresponding signals fall at ∼120-140 and ∼200-220 km depth, respectively. Hence the Moho is unaffected by these interfaces on our images.

Figure 5.3a shows the migration of the multiple phases. The Moho is now well defined beneath Nepal (little less beneath the Ganges Basin), as the interferences from shallower structures were successfully suppressed. Although the image seems to be a little more complicated beneath the YTS, it reveals the new and most essential result beneath Lhasa block: a double interface, located at ∼73 km depth and ∼15 km above it. Both interfaces can be followed at a nearly constant depth on at least 200 km horizontal distance. The upper interface exhibits higher amplitudes, but in our interpretation, this does not necessarily mean that it is the Moho, for the following reasons:

1. Interpreting the shallower feature as the Moho would put a hardly removable question mark on the deeper interface. This would mean that there is a second significant velocity increase **in the upper mantle**, located immediately beneath the Moho, which is unlikely.

2. If we identify the shallower interface as the Moho, and calculate the **average** crustal V_P/V_S using its depth, we obtain a value **of ∼2.05**, corresponding to more than 10% melt (see Fig. 4.13) for the entire Tibetan crust. This is also implausible.

3. Finally, the southward **continuity** of both interfaces gives a logical clue to their identification. The lower interface joins the Moho of the India plate at the YTS, and can be followed along its smooth deepening beneath the Himalaya, arriving at
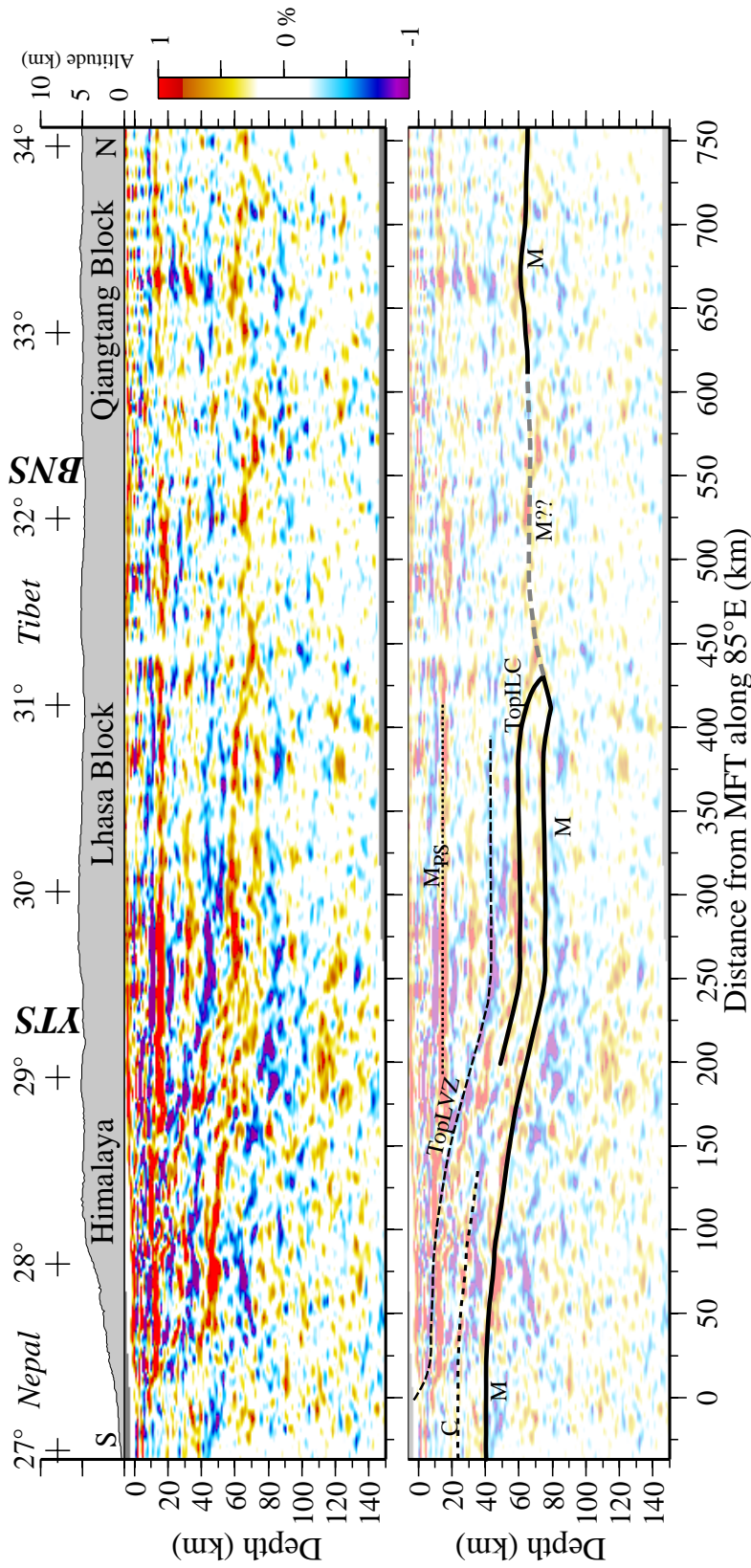
Figure 5.3: (a) Migrating the multiple phases to the depth of the PS phase by "shrinking" the image. This operation eliminates the discussed interferences from shallower structures and bring precisions to the PS image. Horizontal smoothing is restricted to 3 km also, to allow detailed interpretation. (b) Interpretation of the observed interfaces in (a). While the Moho (M) is well observed beneath the entire profile with the exception of the BNS zone (M??), the Conrad discontinuity (C) is weak beneath Nepal, but becomes stronger than the Moho beneath Lhasa block, where it marks the top of the Indian lower crust (TopILC). The top of the low velocity zones (TopLVZ; see Chapter 4 for more details) draws the Main Himalayan Thrust (MHT), the LVZ2 being continued in a negative interface beneath Lhasa block. Finally, the shallow part of the image should not be interpreted directly, as the direct PS conversion of the Moho (M_{PS}) is now "shrunk" and located at ~15 km depth.

40 km depth beneath the Ganges Basin (see also the PS image, Figure 5.1). The upper interface beneath Lhasa block is accompanied by a negative zone above it, which joins the Main Himalayan Thrust, imaged at the LVZ2 characterized by the negative-over-positive signature (see Fig. 5.2a for location and Chapter 4 for more details on LVZ2). The amplitude of the positive interface itself decreases beneath the Himalayas, but reappears locally ~15 km above the Moho further south, in Nepal.

In summary, the layer between ~58 and ~73 km depth beneath Lhasa block is above the Indian plate's Moho and below the Main Himalayan Thrust, thus we identify it as the Indian Lower Crust (ILC). According to our images, the ILC is underplated beneath the southern half of the Tibetan Plateau. Its ~15 km thickness corresponds well to the thickness of the lower crust beneath the Ganges Basin (Fig. 4.16), and further south beneath the Indian Shield (see station BLSP in Kumar *et al.*, 2001). The nature of the ILC is discussed in Section 5.3.

Towards to northern end of Lhasa block, south of the Banggong-Nujiang Suture (BNS), the top and bottom of the ILC merge on the image issued from migrating multiple phases. This also corresponds to the point where the amplitude of the Moho clearly decreases on the PS image. At this stage, we can identify the advance of the Indian lithosphere (except its upper crust) beneath Tibet until 450 km horizontal distance from the MFT along the Hi-CLIMB profile, which corresponds to latitude 31.3°N at longitude 85°E.

Beneath the zone of the Banggong-Nujiang Suture, the signal located at the expected depth of the Moho is not continuous on the migration of multiple phases. However, it is still stronger than on the PS image, where there seems to be a real gap, indicating the absence of a sharp impedance contrast. The different depths of the patches between ~500 and ~600 km in-line seen by the multiple phases suggest a complex structure beneath the BNS.

Further north, beneath Qiangtang block, the conversions imaged by the multiples form a more consistent line at 60-65 km depth. This matches well with the imaged Moho depth on the PS migration. Unlike Lhasa block, a second, shallower impedance contrast is clearly absent. This indicates a more simple, classic crustal structure.

Figure 5.3 emphasizes the importance of multiple phases, as they have helped to clear up the image and the interpretations as well. The double-interface structure beneath Lhasa block was invisible on the PS converted image, and this was not only due to the applied frequencies. The main reason for that the PS migration has failed to image both interfaces is that upper crustal multiples (mainly from bright spots) basically hided the top of the Indian lower crust. In the zones where bright spots are not present (for example

between ~300-360 km horizontal distance), the top of the ILC is visible even by the direct PS conversions (Fig. 5.2).

5.2.4   Non-linear stacking

We presented in Section 3.4.3 the idea of stacking images in a non-linear way in order to amplify coherent and to suppress incoherent zones. Here we apply this scheme to the PS, PpS and PsS migrations. As it was shown on Figures 5.1 and 5.3, the thickness of the signal on the PS and multiple images is different if we perform the migration at the same maximum frequency. In order to produce similar signal widths suitable for non-linear stacking, a signal ratio of ~3 should be respected (Wilson and Aster, 2005), for example 1 Hz for the PS and 0.3 Hz for the multiple phases (Fig. 5.4a, b, c). Then the non-linear stacking scheme was applied, producing the image on Figure 5.4d. As the non-linear stacking distorts the relative amplitudes, we use a more conventional colour scale.

The advantage of the non-linearly stacked image is that the main characteristics of the PS and the multiple migrations can be seen at the same time without most of the interfering artefacts. This synthetic image shows (see the corresponding letters):

(a) an equally clear Moho beneath the Ganges Basin and Nepal, where the doubtful second interface at ~55 km is now suppressed. The smooth deepening from 40 km beneath India to 73 km at the YTS is also evident;

(b) that the low-velocity zones (blue-over-red) observed in Nepal and associated to the Main Himalayan Thrust, are now continuous: they clearly connect shallow and deep structures on the same image, and extend until 450 km north of the MFT;

(c) the Indian Lower Crust beneath Lhasa block, lying between the continuity of the two previous interfaces, up to latitude 31.3°N. The Conrad discontinuity south of Lhasa block, due to its weak amplitudes, does not show a prominent signal;

(d) a relatively weaker signal beneath the BNS zone (mainly from the PpS and PsS image);

(e) coherent Moho signature at ~65 km depth beneath Qiangtang block;

(f) that some local interferences still occur, for example as the direct conversion of the Moho on the multiple images, "shrunk" to ~15 km depth, overlaps with (and enhances) some of the bright spots.
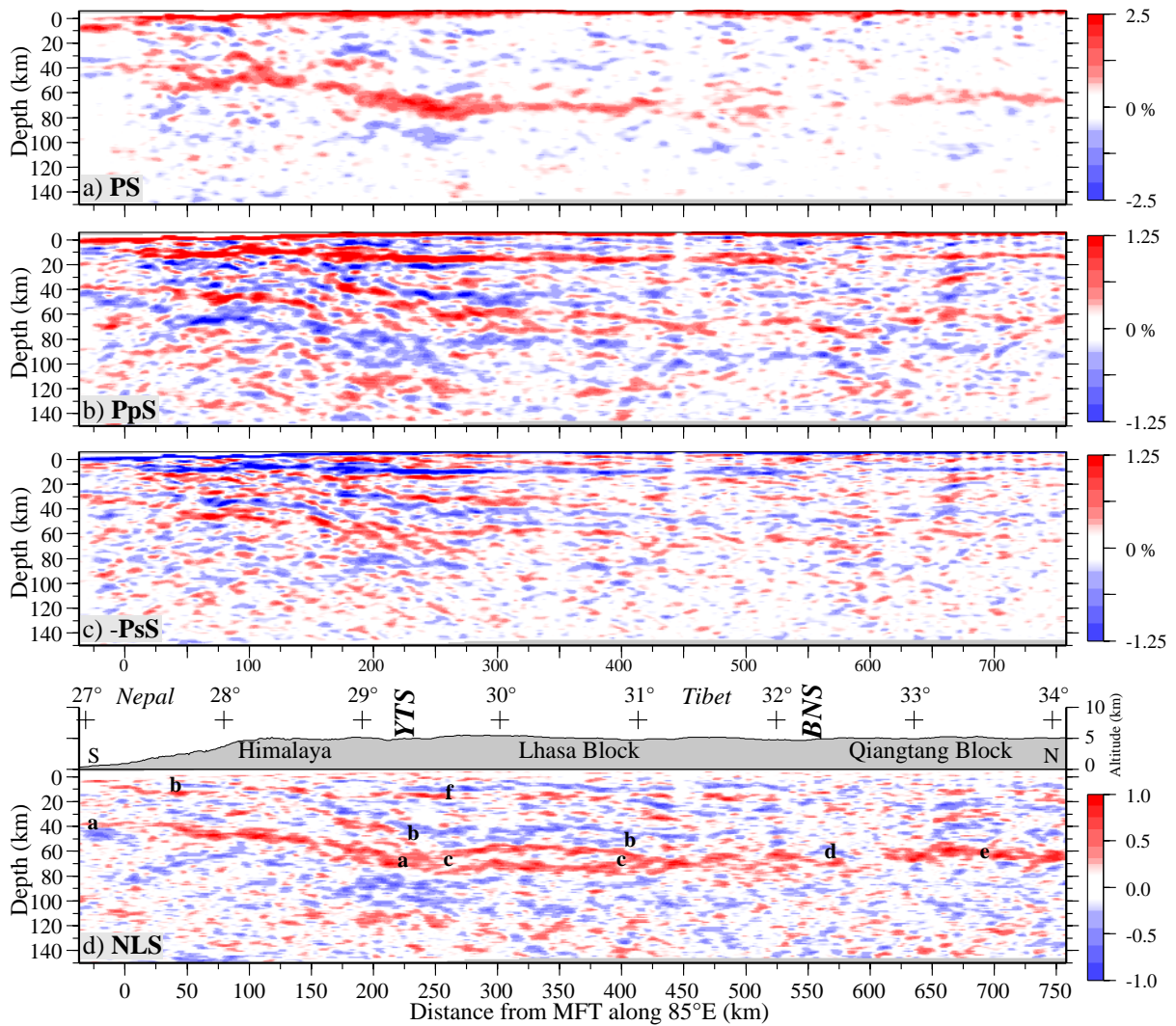
Figure 5.4: Applying the non-linear stacking scheme: (a) PS migration at 1 Hz maximum frequency. (b) PpS migration and 0.3 Hz. (c) The inverse of PsS migration at 0.3 Hz. (d) Non-linear stacking of the three above images, with $N = 8$ (see Section 3.4.3 for the meaning of this parameter). All images have been horizontally smoothed over 3 km after processing.

5.3   Eclogites beneath Lhasa block

Geologically, Lhasa block is limited by the YTS on the south and by the BNS on the north. Its upper-crustal structure beneath the Hi-CLIMB profile has been discussed in Chapter 4. Here we focus primarily on the lower crust, as the receiver function migrations reveal two parallel interfaces under almost the entire block. In our interpretation, this corresponds to the lower crust of the India plate (ILC), underthrust on more than 200 km horizontal distance north of the YTS. One important observation is that the amplitude of the conversion on top of the ILC is clearly stronger than at its bottom. The presence of a low velocity zone alone, with recovering velocities with depth just above the ILC, would not explain entirely this high amplitude. An additional effect may be due to velocity increase and/or to density change in the Indian lower crust. This would not only increase/decrease the impedance contrast at the top/bottom of the ILC, but would also explain the weaker signal of the Moho beneath Lhasa block compared to Nepal.

A potential candidate for higher velocity and/or density material is eclogite (Christensen and Mooney, 1995). Its presence beneath Lhasa block inferred by the seismological image and gravity anomalies is discussed in Chapter 7, together with petrological modelling. Here we take advantage of the complementarity of gravity data and seismological observations. In general, we can distinguish three main cases for the relative sensitivity of these two methods:

- In case of a shallow feature, gravity anomalies may provide more information compared to a low-frequency seismological image (*e.g.* receiver function and not active seismic reflection), both in terms of density and geometry (for example a granite intrusion; Cattin *et al.*, 2001);

- In case of a deep anomaly, for example in the mantle, gravimetry becomes insensitive, but seismology brings information on the amplitude of the anomalies and their location at depth;

- Finally, our case is in between the previous ones: seismology provides accurate geometrical constraints and thus draws the contours of different lithospheric bodies; hence the task of gravity modelling is made easier, and can focus on finding the correct densities, which are less well constrained from receiver functions.

In this section, even if the densities are better constrained by the more sensitive gravity anomalies, I present several seismological arguments to show that the methods are complementary and the results are coherent.

5.3.1   Relative amplitudes

The migration of multiples clearly reveals a higher amplitude on top of the Indian Lower Crust beneath Lhasa block compared to its bottom. In a simple isotropic synthetic test aiming to reproduce this effect, two layers over a half space are used to model receiver functions. The P wave velocity of the lower layer is varied in steps between the V_P -values of the upper layer and of the half space. The synthetic RFs are represented on Figure 5.5 and focus on the amplitude variation of the PS conversions occurring at the two interfaces (the observed features are also valid for the multiple phases). The effect of relative velocity differences is linear: the discontinuity where the jump in velocity is greater produces the higher amplitude conversion. Thus the first option to reproduce the observed relation of amplitudes is to have an Indian lower crust whose velocity is closer to the underlying mantle than to the overlying crust. As the overlying crust may have low velocities (see the LVZs on the migrated image), this may imply a V_P between 7 and 7.5 km·s^{-1} for the lower crust.

Figure 5.5: Synthetic RFs induced by an isotropic velocity model in which V_P of the lower layer is varied. The ratio of converted amplitudes (here PS) is proportional to the ratio of velocity jumps across the two discontinuities. The thick line at $V_P = 7.3$ km·s^{-1} is halfway between the velocities of the upper and lower media, and exhibits equal amplitudes. (V_P/V_S is 1.80 in all layers. Ray parameter = 0.06 s · km^{-1}, water-level = 10^{-4}, Gaussian width = 3.5, densities are derived from Equation 5.1.)

VELOCITY MODEL	Layer	Thickness (km)	V_P (km/s)
	Upper	65	6.5
	Lower	15	varied as above
	Mantle		8.1
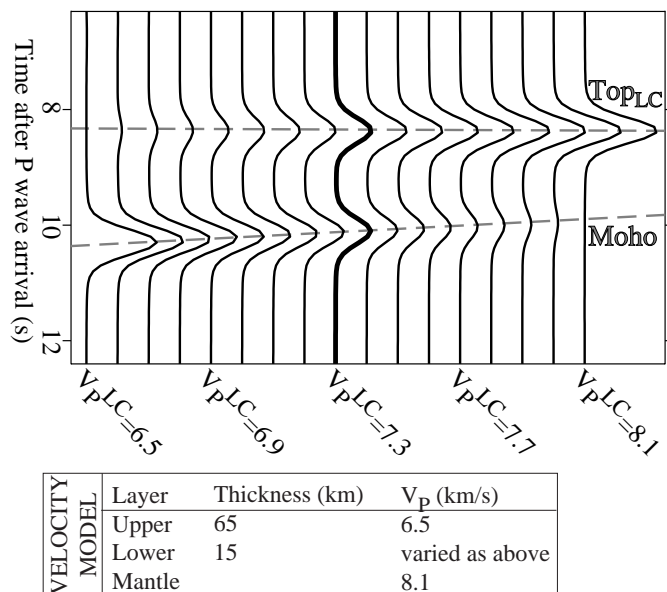
Impedance vs. velocity

Usually, we tend to argue in terms of velocity and relative velocities, although it would be more correct to discuss impedances. In seismics and seismology, impedance (Z) is the product of density (ρ) and velocity (v). The reason for the above simplification is

that these quantities change in a similar way in the range of geophysical problems[3]. Their relation between ρ and v is most often described by Birch's law (Birch, 1961):

$$\rho = 0.32 \cdot V_P + 770, \tag{5.1}$$

(where ρ and V_P are in SI units), or by other rules, such as the quadratic law commonly used in synthetic RF calculation[4]:

$$\rho = 2350 + 3.6 \cdot 10^{-5} \cdot (V_P - 3000)^2. \tag{5.2}$$

The above equations are usually used to approximate the observed v—ρ relationship for a wide range of rocks. However, if we report these laws and measured velocity and density (or acoustic impedance) values on a same graph (Fig. 5.6; Guéguen and Palciauskas, 1992), one can see that some groups of rocks, and especially eclogites, are the most off of the above equations, equivalent to errors of 250 kg·m^{-3} and more. The main reason for this is that Birch's law (Eq. 5.1) is calculated for a constant mean atomic weight, which remains valid for most minerals, but eclogite contains significant amounts of garnet whose mean atomic weight is higher due to the *Fe*-content (Anderson, 1989). In terms of seismological modelling, this deviation should be taken into account and densities should be estimated independently from velocity in case of eclogitic bodies. Let us take a more precise example for the Indian Lower Crust beneath Lhasa block (Table 5.1). A velocity that is little closer to the V_P of the crust, together with a density close or equal to the ρ of the mantle, still produces a higher impedance contrast — and thus RF amplitude — on top of the ILC, in agreement with the observations.

Based on laboratory measurements of natural eclogite samples, their reflection co-efficient was estimated by Bascou *et al.* (2001). Based on the results, an *eclogite/crust* interface is found to be a generally good reflector, whereas an *eclogite/mantle* boundary is less easily detectable. This is in agreement with the findings presented in the previous sections.

---

[3]This is, however, a puzzle, as in rock mechanics velocity is inversely proportional to density: $v = \sqrt{\dfrac{\mu}{\rho}}$, where μ is the corresponding elastic parameter. The observed relationships are hence due to the proportionality of velocity and the elastic parameters, rather than density.

[4]M. Sambridge's code, http://wwwrses.anu.edu.au/~malcolm/na/

Figure 5.6: Measured acoustic impedances and P wave velocities of principal volcanic and metamorphic rocks, together with a linear relationship (solid black line). Redrawn from Guéguen and Palciauskas (1992). In gray, a linear and a parabolic approximation of density from velocity (Eq. 5.1 solid line, Eq. 5.2 dashed line).
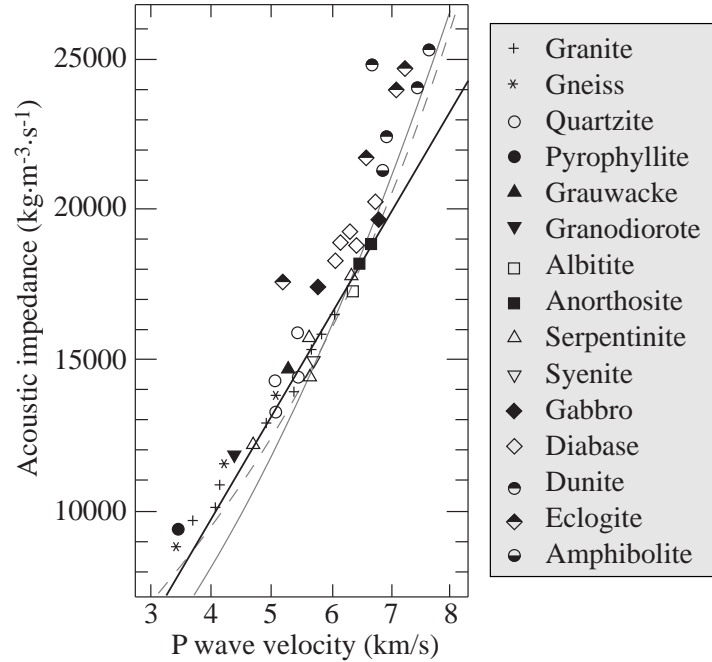
Layer	V_P (km·s^{-1})	ρ (kg·m^{-3})	Z ($kg \cdot m^{-2} \cdot s^{-1}$)
Upper crust	6.5-6.8	2900	18850-19720
Eclogitized ILC	7.0-7.5	3300	23100-24750
Mantle	8.0-8.1	3300	26400-26730

Table 5.1: Estimates of impedance Z for the Indian lower crust and neighbouring layers beneath Lhasa block, as a function of velocity and density. For eclogites, the higher density values compared to Birch's law can easily compensate a lower velocity, resulting a higher impedance contrast on top of the ILC than at its bottom (3380-5900 and 1650-3630 kg · $m^{-2} \cdot s^{-1}$, respectively).

5.4 The extent of the India plate

5.4.1 Partial summary

The receiver function migrations presented in Section 5.2 revealed the position of the Moho at a high resolution. The continuity of this interface from beneath the Ganges Basin and across the Yarlung Tsangpo Suture is hardly questionable. Despite the fact that the northernmost rocks of Indian affinity at surface can be found near and south of the YTS, most of the lithosphere (the lower crust and the mantle) of the India plate advances at least 200 km further north at depth.

These results constrain the position of the Indian lower crust along 85°E and up to latitude 31.3°N. But what happens North of this point? Is it possible to trace further the Indian lithosphere? Why is the signal of the Moho weak beneath the Banggong-Nujiang Suture? Are there lateral variations in the thickness of the Tibetan crust? The following sections examine these questions and give elements to answer them.

5.4.2 The polarity of the Moho

The generation of converted wave phases is subject to several conditions. One of these is that the incident wave should arrive at a high angle from perpendicular. This is well represented by the transmission coefficient T_{PS} curve for a simple discontinuity as a function of incidence angle α (Fig. 5.7a). Exactly perpendicular incident waves do not produce conversions. At increasing incidence angles, the transmission coefficient also increases, but the amplitude of P-to-S converted waves is limited by the epicentral distance of teleseismic earthquakes (typically ~30-90°). For α over ~40°, the transmission coefficient would further increase, but teleseismic waves are unlikely to hit the Moho at these angles, with one important exception. This case is when the waves are arriving at the usual angles from the vertical (β), but the impedance contrast is not horizontal (Fig. 5.7c). In this case, the incidence angle should be corrected by the dip of the interface, and T_{PS} will have a back-azimuthal dependence for waves arriving at the same β.

The described behaviour of converted waves resembles to polarizing filters that let through waves from parallelly oriented vibrations and stop those that are orthogonal. This method can be applied to the RF migration scheme. Traces are regrouped into four sectors according to their back-azimuth values, corresponding to the four cardinal directions ±45°. Then the migration and stacking are performed as usual. The results for the northern and southern quadrants, focusing on the Moho, are shown on Figure 5.8.

The difference between Lhasa and Qiangtang blocks is striking. The former is clearly

Figure 5.7: (a) Transmission coefficient T_{PS} as a function of incidence angle α for an incident P wave ($V_P = 8.1 km \cdot s^{-1}$) converted to an S wave ($V_S = 3.75 km \cdot s^{-1}$). (b) For a horizontal impedance contrast, α is also the angle from the vertical (β), and T_{PS} depends on α only. (c) In case of a dipping interface, $\alpha \neq \beta$. The transmission may be important, provided the wave comes from the down-dip direction (right), but may be zero if they come from the opposite side and hit the interface perpendicularly (left).
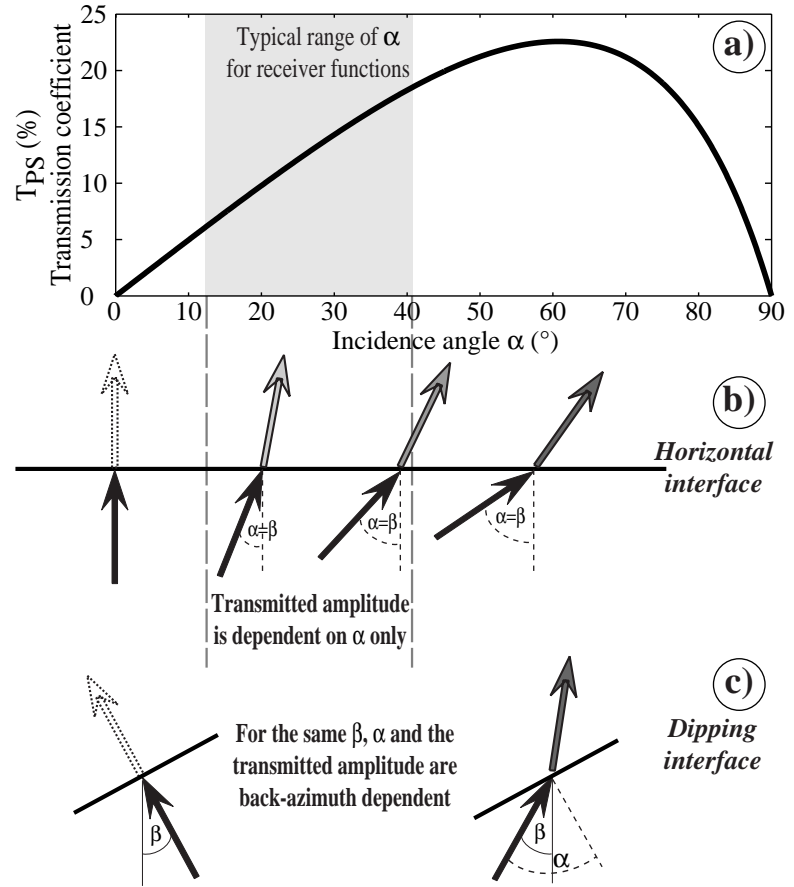
seen by the traces arriving from the north, but shows a less coherent, fitful image from the south. The Moho beneath the latter is invisible for events located to the north, and is image by those located to the south, together with some signal in the BNS zone. In light of the presented characteristics of RF polarization, we interpret this as the following. For that the crust-mantle boundary beneath Lhasa/Qiangtang block become invisible from the south/north, respectively, their internal structure should be close to perpendicular to the arriving waves. This polarity reveals that the internal structure of Lhasa block is rather dipping to the north, and that of Qiangtang block is dipping to the south.

A similar conclusion comes from the observation of tangential RF amplitudes beneath the two tectonic blocks. Both components of iterative RFs were filtered at 0.25 Hz and stacked by 10° wide back-azimuth ranges from stations located in Lhasa and Qiangtang blocks, to construct two respective average RFs. Then we superposed the radial and tangential components for each block, and analyzed the amplitude of the TRF around the time of the Moho conversion on the RRF (Fig. 5.9). In the eastern back-azimuths, where the number of events is large, the sign of the TRF is opposite between Lhasa and Qiang-
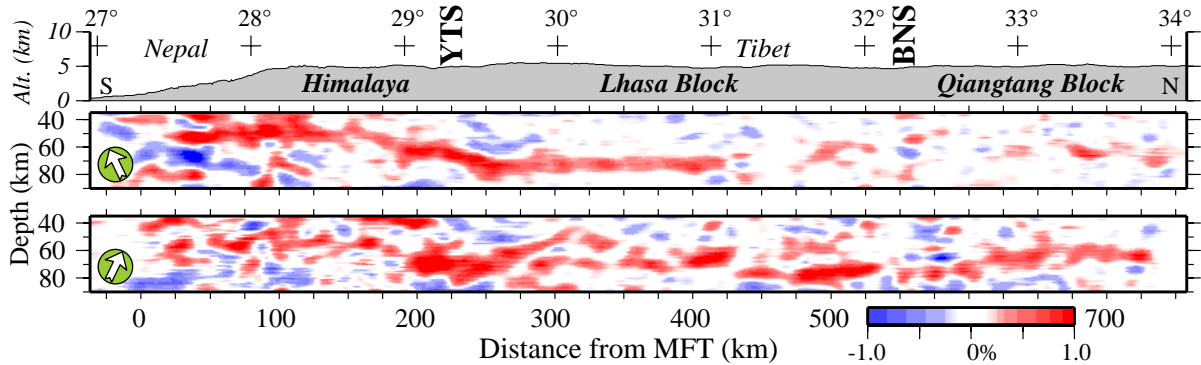
Figure 5.8: Polarized images of the Moho beneath Lhasa and Qiangtang blocks, seen from the north and the south as marked by the arrows on the left. No vertical exaggeration. See text for discussion.

tang blocks: it is always negative beneath the former, and positive beneath the latter. The uneven back-azimuthal coverage does not allow to determine the complete curves of amplitude variations, and to clearly decide whether it is caused by anisotropy, dipping interfaces or a combination of the two, but the constrained points suggest an opposite orientation of the causing effect.

Both of the above observations can be interpreted in the same frame. The internal structure observed by the polarized images is either "pure" anisotropy, either smaller or larger imbrications around the crust-mantle boundary, a sort of macro-anisotropy; or a combination of both effects. Their axis beneath Lhasa and Qiangtang blocks is dipping roughly to the north and the south, respectively. Using the polarity crossing between the two curves of the tangential RF amplitudes (Fig. 5.9), occurring at ∼30° and between 190-220° back-azimuth, the orientation of the structures can be constrained to the N-NE, sub-parallel to the direction of India plate's motion with respect to Eurasia. The clear presence of oriented internal structures is the product of the compression that accompanies the continental collision, and the shear stresses that develop between the underthrusting and overriding plates. Their orientation provides an additional support for the northward extent of the Indian lithosphere beneath Lhasa block. Compared to the stacked migrations which provide a static image of the collision zone's structure, here we find evidence for the dynamics beneath the Tibetan Plateau from back-azimuthal variations of receiver functions. The imaged deformation pattern must have developed during the past million years, and, similarly to shear-wave splitting analysis, provide important temporal information on the development of the present structure.
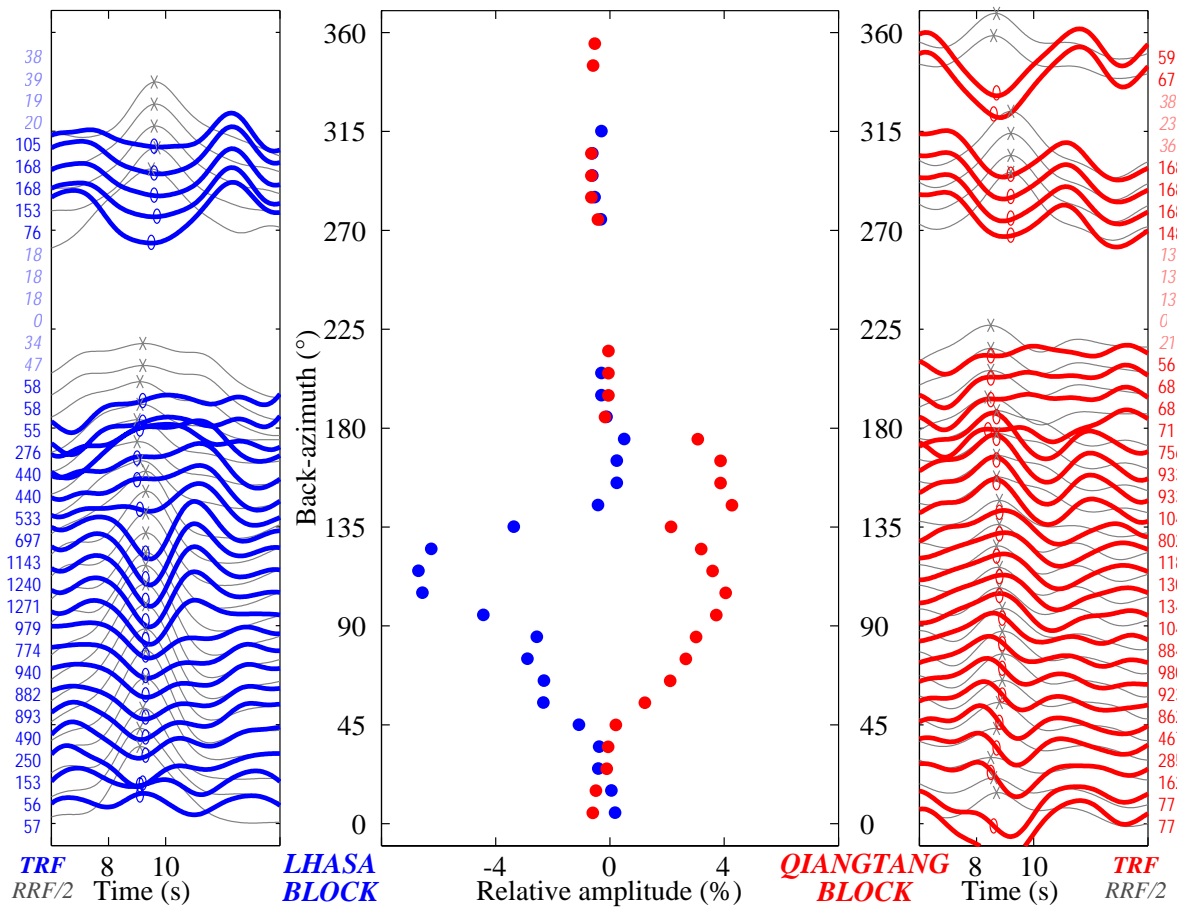
Figure 5.9: Amplitude variations of TRFs related to the Moho beneath Lhasa and Qiangtang blocks. Left and right: comparison of the radial (gray) and tangential (colour) component RFs, averaged at stations H1000-H1200 (Lhasa) and H1450-H1630 (Qiangtang), respectively. Back-azimuthal stacking by 10° wide, 20° overlapping intervals. The crosses mark the maximum amplitude on the RRF, and the ellipses the corresponding time sample on the TRF. The amplitude of the TRF was averaged over ±0.4 seconds and reported in the central graph. Trace count on both sides, stacks with less than 50 traces are not shown. The amplitude of the RRFs is halved for better readability. Centre: Back-azimuthal variation of average TRF amplitude at the Moho's delay time. The amplitudes of the two blocks are clearly opposed in the well constrained, eastern back-azimuthal ranges, and suggest an opposing dipping axis of their cause.

5.4.3 What happens at the BNS?

Or why we do not see anything there?

The zone of the Banggong-Nujiang Suture remains a relatively light spot on the migrated images, and thus a dark spot in the interpretation. The lack of strong signal on

the PS migrations suggests a very smooth velocity increase with depth. North and south of the BNS, the Moho signature is clear on both the PS and the multiple migration images, and can be directly linked to Eurasian and Indian lithosphere, respectively. These observations demand for a solution concerning the continuity of the India plate after underplating Tibet up to 31.3°N. Three possibilities can be proposed:

- The India plate plunges steeply north of this point, at an angle close to the vertical. In this case, we cannot image it, as the receiver function method is unable to detect vertical impedance contrasts. Also, a material that is dense enough to sink into the mantle will not exhibit any (significant) impedance contrast, and thus it will not generate converted waves.

- The India plate enters into a subduction-type geometry, and descends at a shallower angle beneath Qiangtang block. In this case, if there remains an impedance contrast, teleseismic waves arriving from the North may potentially produce detectable converted waves. Upon this assumption, we first performed migrations keeping only high magnitude, and then only deep events that usually provide clear signal. Then we examined receiver functions from 44 individual, high magnitude and deep events without migration. No convincing signal for northward subduction of the India plate was detected.

- The India plate stops at latitude 31.3°N. What we see is its northernmost tip, about 100 km south of the surface trace of the BNS.

Further interpretation of the structure and processes around the Banggong-Nujiang Suture zone is presented in Section 5.6.2, together with constraints from other experiments' results, and discussion on the possible evolution scenarios of the collision zone.

5.4.4 Lateral variations in southern Tibet

The depth of the Moho beneath Nepal, prior to its plunging beneath the Himalayas, is quite homogeneous, but lateral variations of the in-line position of its plunge exist (see Section 4.3.3 and Figure 4.9). Beneath the Tethyan Himalayas and southern Lhasa block, the deployed lateral stations already enabled to investigate the presence of bright spots east of the main profile (see Section 4.4). The relatively sparser station spacing did not allow to produce high-resolution, continuous migrated profiles for the upper crust. For the lithospheric structure, and mainly the crust-mantle boundary, due to the applied lower frequencies and the wider Fresnel zone, the impinging waves sample a larger area beneath

the stations. This does not completely fill the gaps between the stations, but with a 10 km horizontal smoothing the Moho can be followed more easily.

Figure 5.10: Location of the 9 short profiles composed of the Tibetan lateral stations, located to the East of the main array (see Fig. 3.1). The last character of the station name was omitted when it was "0" for better readability. Squares are 2Hz-sensors, not really suitable for low frequency analysis. Stations with no colour fill did not produce suitable data for RF computation.
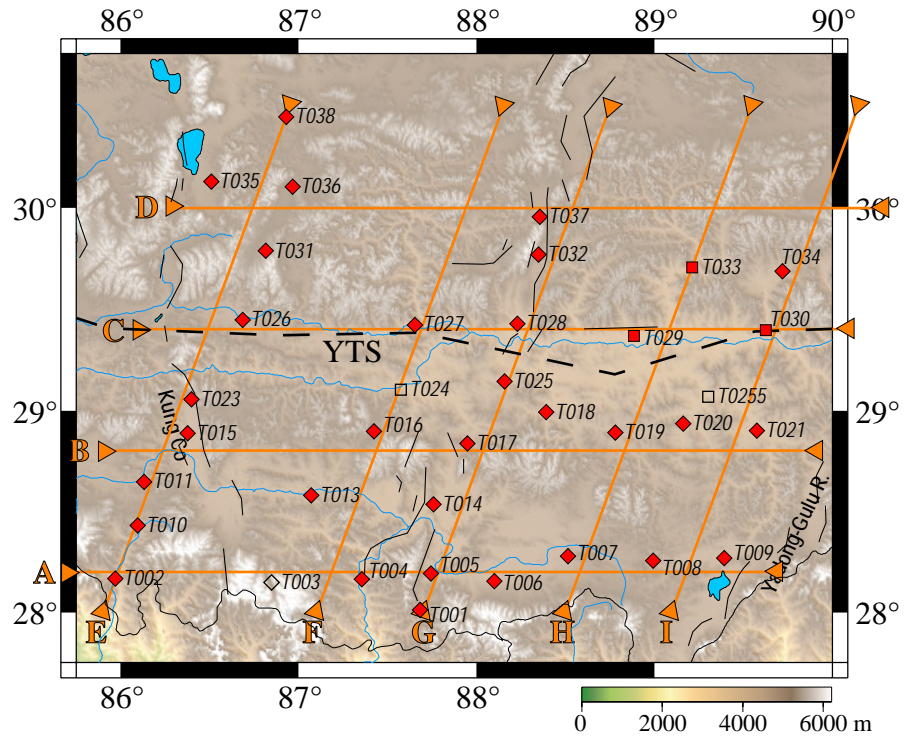
The geometry of the station network was designed to allow the construction of short, near-perpendicular profiles: four oriented E-W, and five oriented N20°E (Fig. 5.10). Migration of iterative RFs from the W3 list filtered at 0.5 Hz was performed using a 1-D velocity model, based on *iasp91* (Kennett and Engdahl, 1991), but with the crust-mantle velocity increase at 80 km depth. The migration mesh size was 1×1 km, and back-azimuthal averaging was performed by 20° ranges. As the stations deployed at the lateral sites were provided by different institutes, there were more heterogeneity in the used sensors and data acquisition systems (see Appendix B). This caused relatively more malfunctioning due to temperature and altitude. Also, the 2Hz-sensors either did not produce RF data at all, or yielded only a very limited number of traces (see stations T0290, T0300 and T0330 on the migrated profiles). This is due to their lowest resonance frequency, located around 2 Hz, hence not very sensitive to teleseismic signals, carrying information up to the ∼1 Hz frequency range.

Figures 5.11 and 5.12 present the result of the migrations in southern Tibet. Perpendicular to the main array, profiles A and especially B provide the most continuous image of the Moho. From west to east, the crust-mantle boundary deepens from ∼50 to ∼70 km,

Figure 5.11: Migrated E-W profiles in south Tibet. See Figure 5.10 for profile locations.
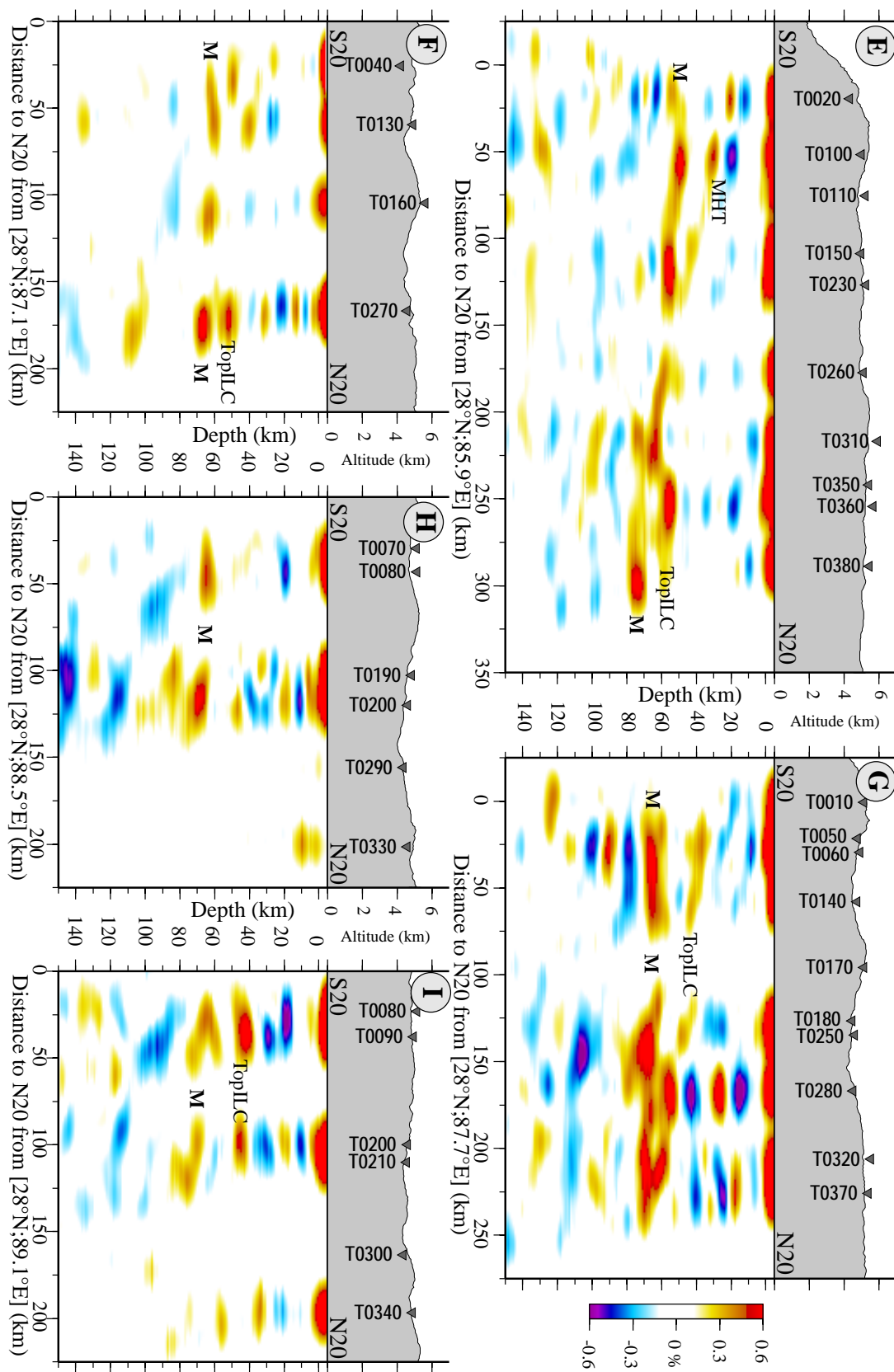
Figure 5.12: Migrated N20°E profiles in south Tibet. See Figure 5.10 for profile locations.

and from ∼55 to ∼70 km on profiles A and B, respectively, over a horizontal distance of ∼350 km. The position of the Moho 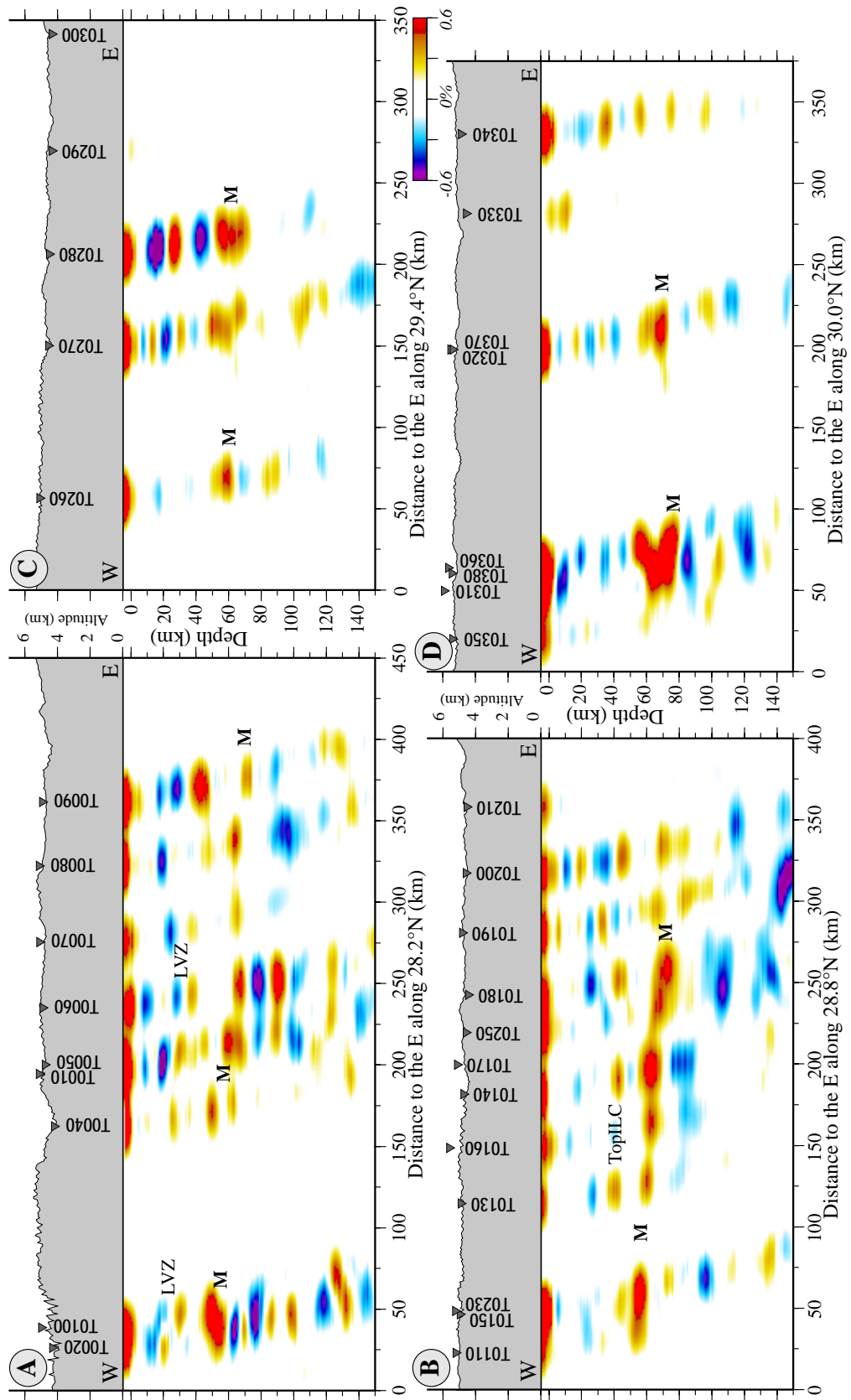on profiles C and D is not clear enough to support the 15-20 km deepening towards the east. Despite the sparser station spacing, there are improvements in the image beneath the lateral network compared to the main array. This is due to the lower number of bright spots, which produced embarrassing multiples hiding the lower crust along the main array. Here these multiples are less frequent, thus the top of the Indian lower crust can be clearly pointed on the PS image, for example on profile B. Also, the low-velocity zone associated to the MHT is clearly visible on profile A between the ∼20-30 km depth range.

The profiles that are parallel to the main array all start from latitude 28°N, and are a little shorter compared to the perpendiculars. Profiles E and G show a great similarity with the image of the principal array. On profile E, the Moho deepens from ∼50 to over 70 km depth at about the same geometry as the main array, reaching its maximal depth close to the YTS and crossing the suture's line. As mentioned above, the local lack of strong upper crustal features is useful in that they do not produce multiples hiding the lower crust. This way, the LVZ around the MHT can be guessed from ∼20 km in the south to ∼55 km in the north, accompanied by the increasing positive amplitude induced by the top of the Indian lower crust, still ∼15 km above the Moho. The same structures are all visible on profile G as well, however, the converters are located a little deeper. The Moho on the southern end of this profile is already at 65 km depth, suggesting that its deepening from Nepal occurs further south. Profile F resembles to profile G, showing both the Moho and the top of the Indian lower crust, and profile H images mainly the Moho at 65 km depth. Finally, profile I shows again the two impedance contrasts associated to the top and the bottom of the Indian Lower Crust, at 45-50 and 65-70 km depths, respectively.

In summary, using the observation of the main array, the migrations beneath the lateral profiles are easily interpreted in terms of Moho, MHT, and Indian lower crust structure. It is important to note that the interpretation of the PS converted images was facilitated by the relative absence of multiples from upper crustal features, that have hidden part of the information along the main array.

To visualize the lateral variations beneath southern Tibet in three dimensions, the imaged depths of the MHT and of the Moho were picked on the migrated profiles (Fig. 5.13). The region basically covers the zone between the Hi-CLIMB and the INDEPTH experiments over more than 2 latitude degrees. The view from the NE allows to follow the first order variations of both surfaces. The deepening of the Moho from south to north mimics the shape observed along the Hi-CLIMB main array. At the same time, the Moho's ∼20 km deepening to the east is also imaged, suggesting that the south-to-north deepening
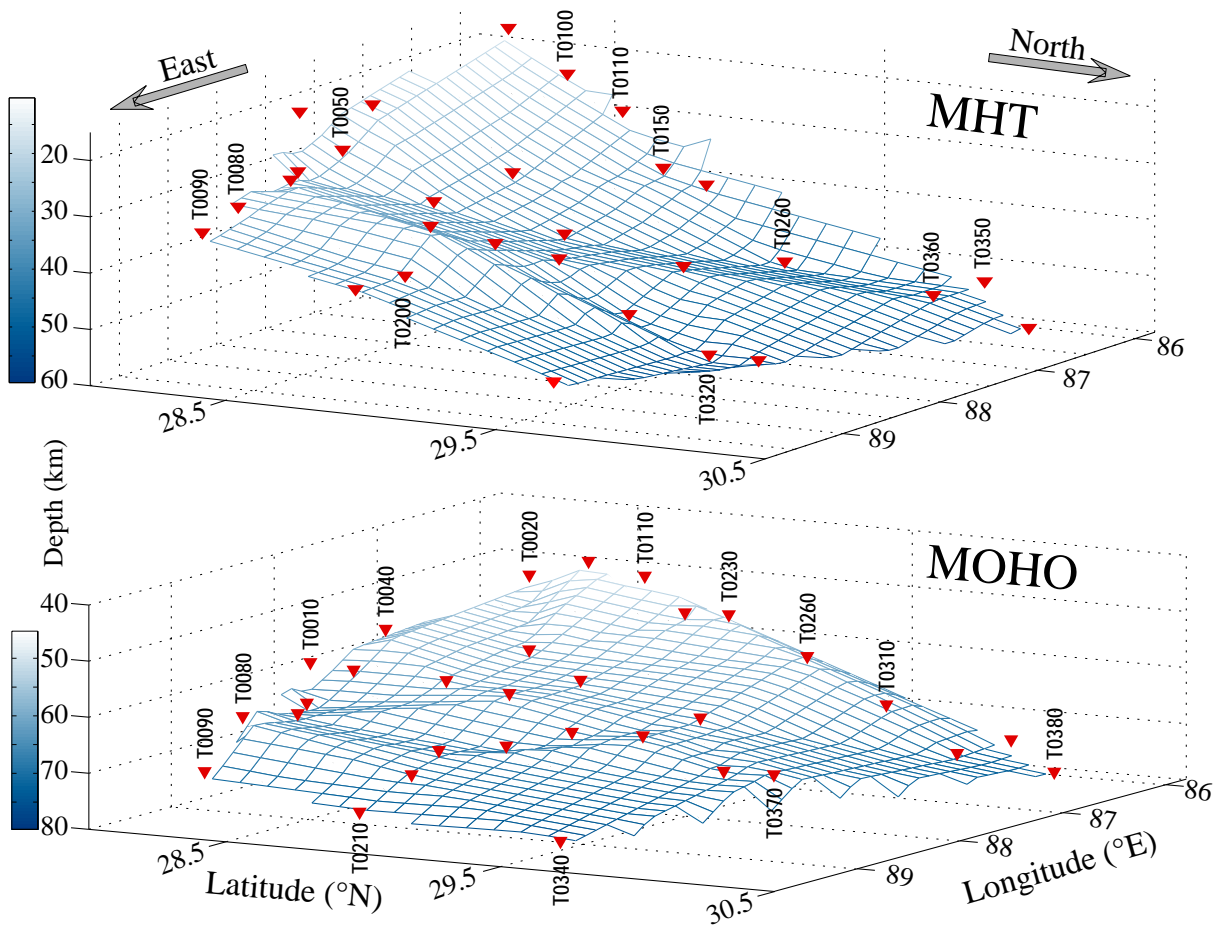
Figure 5.13: Mapping the Moho beneath southern Tibet. Interpolation from minima and maxima Moho depth estimates picked on the migrations of Figures 5.11 and 5.12 beneath the stations (red triangles). The deviation of minima and maxima values deviation from the average estimate varies between ±3 and ±9 km. Distances are not to scale.

occurs closer the MFT as we go eastward along the Himalayas. This is in agreement with the constraints on Moho depth from both the HIMNT and the INDEPTH experiments (Fig. 5.14), located approximately in line with profile F and I, respectively. The crust-mantle boundary reaches the same depth beneath Tibet, but the deepening on the southern border seems to be more related to the position of the topographic front than to the distance from the MFT. The differences in density structure along the profiles of the three seismological experiments are studied in Chapter 7.

The MHT, already imaged along ∼400 km horizontal distance on the main profile, keeps its low-velocity signature laterally. This extends the assumptions of aqueous fluid and partial melt accumulation to the east of the Hi-CLIMB experiment's main array, locating

zones of brittle and ductile deformation (see Section 4.3). Concerning the shape of the MHT beneath the lateral network (Fig. 5.13), the considerations discussed above for the Moho for the northward and eastward deepenings remain valid, with an additional factor. This is due to the absolute step in depth of the MHT between the south and the north, which, due to the connection of upper and lower crustal structures, is larger than the step of the Moho. As a consequence, the average steepness of the MHT's surface is higher than that of the Moho on Figure 5.13. Hence the thickness of the Indian crust beneath the central and eastern part of the Himalayas should decrease from south, where it is complete, to north, where only the lower crust is present.
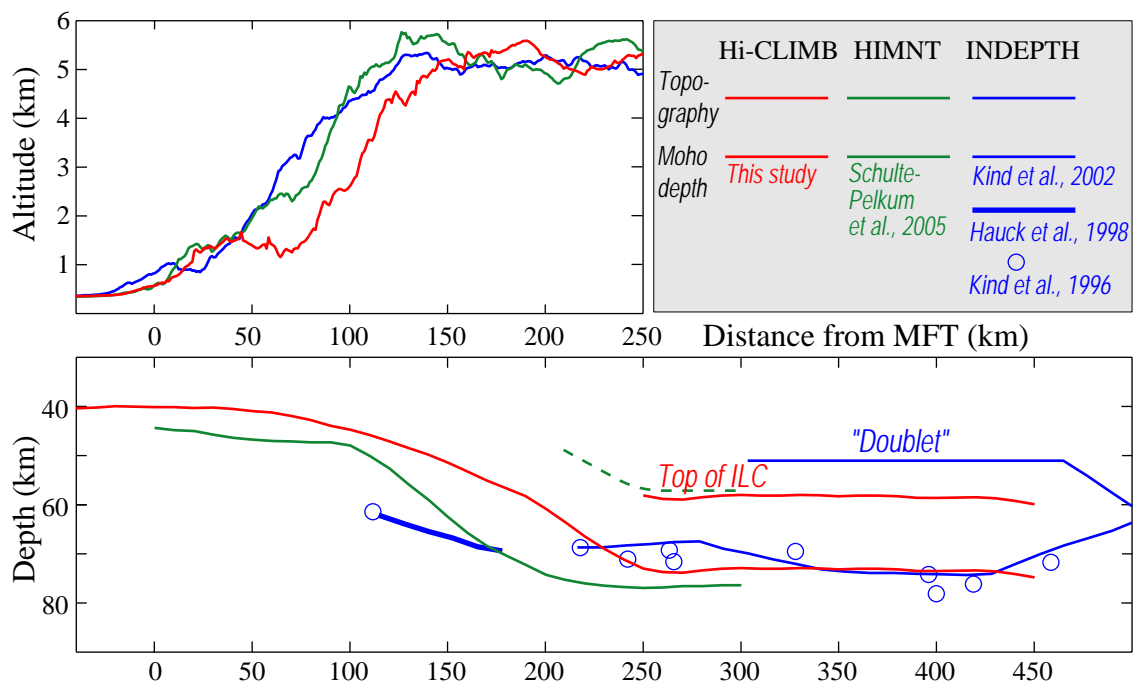
Figure 5.14: Lateral variation of Moho depth (bottom) and topography (top) along the main seismological experiments across the southern border of the Tibetan Plateau. The origin of the profiles correspond to the location of the Main Frontal Thrust. Both Moho deepening and the topographic step occur closer to the MFT towards the east, although their in-line location is offset and the horizontal differences are larger between the Moho estimates. The top of the Indian lower crust is noted for the Hi-CLIMB (Top of ILC), the HIMNT (dashed green line) and the INDEPTH experiments ("Doublet"). Altitudes averaged over 50 km on both sides of the profiles. Exact profile positions are in Chapter 7.

5.5   Upper mantle structure

5.5.1   The phase transition discontinuities

After having studied the structure of the lithosphere and its lateral variations, we continue the downward travel beneath the main array. The upper mantle discontinuities beneath Tibet are sampled by the stations of the Hi-CLIMB main array over a large zone to the east, as most of the M$\geq$5.5 events are located in this direction and the piercing point of the rays fall beneath the plateau. The migration revealing the deep structure is presented on Figure 5.15 at two different frequencies. The larger and smaller figures were produced using data filtered a 0.5 Hz (2 sec) and 0.125 Hz (8 sec) maximum frequency, respectively. The migration mesh was 2×2 km, and back-azimuthal equalizing as well as horizontal smoothing were applied. The width of the smoothing window was 25 km in order to average a 3-D structure over the Fresnel zone, but to avoid oversmoothing and related artefacts of the image.

The Moho appears in saturated colours in the upper part of the image, again with a lack of signal beneath the BNS. Between 150-250 and 200-320 km depth, are the PpS (positive) and PsS (negative) multiples of the Moho, respectively. They reproduce its geometry by exaggerating its dip beneath the Himalayas and the depth difference across the BNS.

The 410 and 670 km discontinuities show up clearly and horizontally. Their image is net even at higher frequencies, suggesting that the velocity increase across both transition zones is not broad. The interfaces show very little undulations, their average depth is 405.5 ± 2.5 and 670.5 ± 3.0 km, respectively. On the migrated images, there is no clear sign of a horizontal interface at 520 km depth, although some lower amplitude patches exist between $\sim$450 and 550 km (observed on oversaturated images, not shown here). In conclusion: based on the RF image of the 410 and 670 km discontinuities, the upper mantle transition zone is seemingly unaffected by the ongoing orogeny in Tibet.

5.5.2   An observation from below the Moho

Receiver functions are known to map relatively sharp variations of velocity, such as the Moho or the upper mantle discontinuities. However, there are at least 300 km between the crust-mantle boundary and the 410-discontinuity on which we have basically no information. This is due to the fact that the impedance contrasts in this zone are very weak, and they are further disturbed by the presence of the crustal multiples, as illustrated in the previous section for the Moho, its multiples occupying the 200-320 km depth range beneath
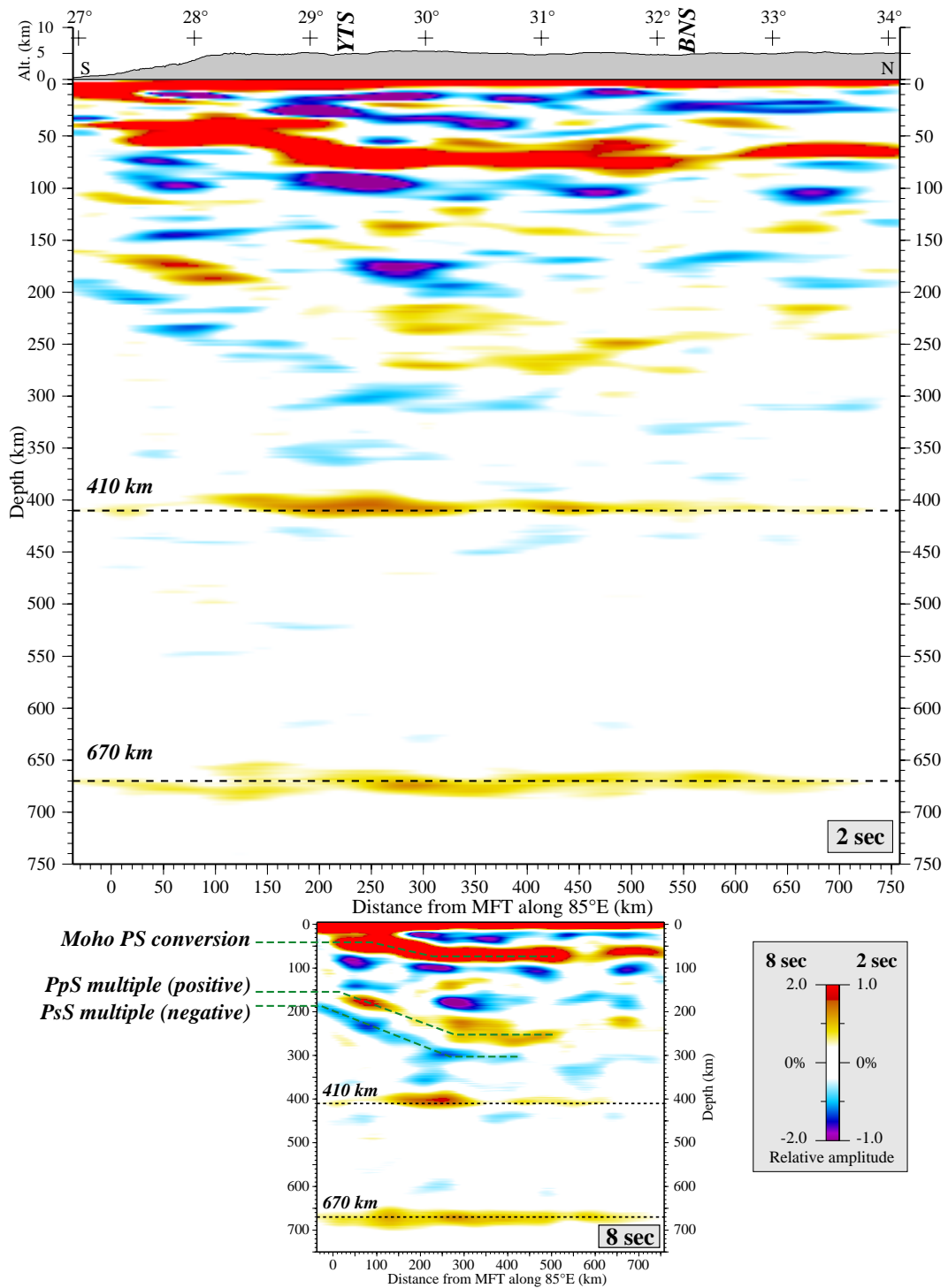
Figure 5.15: Upper mantle discontinuities beneath the Hi-CLIMB main array with 25 km horizontal smoothing. The 410 and 670 km boundaries are clearly visible both at 2 sec (0.5 Hz) and 8 sec (0.125 Hz) maximum frequency content.

Tibet (Fig. 5.15), Nevertheless, we have taken a look into the uppermost mantle (80-200 km) to see if any information can be inferred concerning the India plate or the processes beneath the Banggong-Nujiang Suture. To avoid interference from intra-crustal multiples, we migrated both multiple phases, and saturated the image to enhance the signals related to weak contrasts. Then, in our particular and not very robust approach, we analyzed the positive, and then the negative conversions separately. The latter one is shown on Figure 5.16, where the positive values of a regular image, like to Moho, become white, and gray represents negative conversions only. The resulting image was observed independently by several persons, who attempted to search and draw lineations, representative of the uppermost mantle's deformation history. As the direct PS conversions of the 410- and 670-discontinuities are potentially included in this image as horizontal boundaries, the persons preferentially looked for dipping interfaces.
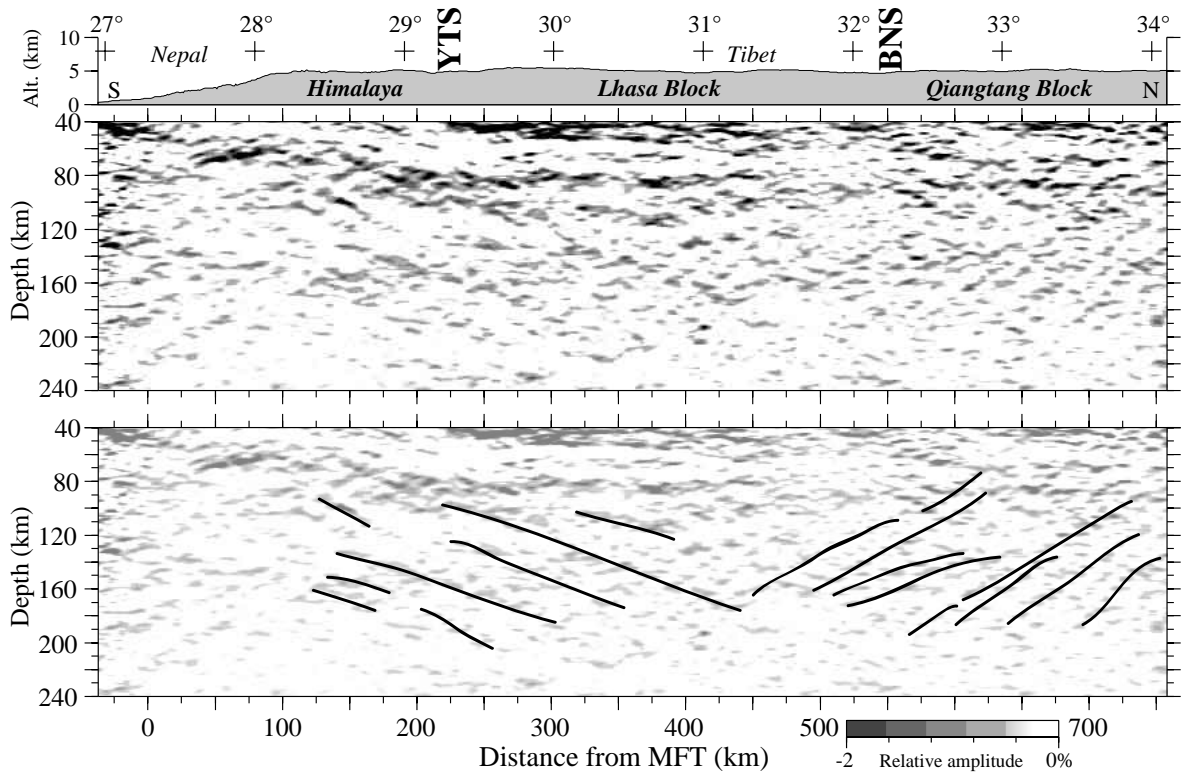
Figure 5.16: Top: multiple conversion migrations along the main array, representing the negative conversions of a regular PpS–PsS image, in search for uppermost mantle structure. Bottom: line-drawing of dipping structures over the shaded migration image. The observations suggest dipping in coherence with lithospheric movement of India and Eurasia, but the interpretation needs support from more robust methods.

The coherent parts of the line-drawing are represented on the shaded image (Fig.

5.16). The lines lie between 80 and 200 km depth, and dip ~20° to the north beneath Lhasa block, and ~35° to the south beneath Qiangtang block. The orientation of these plunging axes coincide with the directions of imbrications seen by the polarized image of the Moho, and meet between 400 and 500 km in-line distance, south of the location of the BNS. The interpretation of the line-drawing is upper mantle fabric that has been deformed and aligned by the main tectonic forces acting in the collision zone. Northward dipping lines would represent the uppermost mantle of India, and southward dipping mantle structures north of 31°N would be remnants from present and/or past, south-directed subductions of Eurasia.

This observation is clearly not robust. However, it coincides with the S-SE dipping converters located at the same tectonic position, imaged to the east of our profile (Shi *et al.*, 2004), also by receiver function imaging. This supports the southward descent of the Eurasian lithosphere in central Tibet. In the meantime, the hypothesis of Indian lithospheric mantle structure beneath Lhasa block and its northward dip must be strengthened by results based on more suitable methods. One of these would be S-to-P receiver functions, that are free from multiples, and yield information on the geometry of the structures. Another approach would be shear-wave splitting, which would provide information on the recent deformation regime (mantle flow), but without the constraints on geometry. These computations need to be performed on the Hi-CLIMB dataset.

At this point, we can state that while the Indian lower crust is underthrust horizontally beneath most of Lhasa block, there are signs pointing to the possibly complicated deformation pattern in the lithospheric mantle, with N-dipping lineations. These seem to be homogeneously distributed along our profile, without any evidence of localization of deformation, such as subduction or wholescale delamination.

5.6   Interpretation and implications on evolution models

5.6.1   Interpretation of the seismological observations

Here we summarize and interpret the main structures and deformation of the lithosphere based on the presented seismological results, with Figure 5.17 providing a support to follow the discussion.

The **Moho** is clearly followed along the main array and beneath the major tectonic blocks. Its depth varies smoothly from 40 km beneath the flexural Ganges Basin to 73 km beneath Lhasa block that it underlies horizontally on more than 200 km. While the Moho is continuous across the Yarlung Tsangpo Suture, it is rather undefined south of and beneath the Banggong-Nujiang Suture. North of this point, in Qiangtang block, its signal is strong again, located at a ∼10 km shallower depth than in Lhasa block. Lateral sites in southern Tibet reveal that the shape of the Moho's descent is similar, but occurs further south and closer to the MFT as we go eastward along the arc of the Himalayas.

The multiply converted phases allow to clarify the image and to reveal a **double impedance contrast** beneath most of Lhasa block. Gravity anomalies (Chapter 7) and modelling, as well as the amplitude of the conversions suggest that the ∼15 km thick zone between the two interfaces corresponds to eclogite facies rocks. Based on the geometry of the Moho and the Main Himalayan Thrust, this is interpreted as the **underplating of the Indian lower crust** beneath Tibet and its **eclogitization** beneath Lhasa block.

The **Main Himalayan Thrust**, the main boundary along which the India plate descends beneath the Himalayas, was imaged by receiver functions and tomography based on ambient noise correlation. The observed low velocity zones image in an *indirect* manner the fluids associated to the Main Himalayan Thrust: aqueous fluid and partial melt at the flat and ramp section of the mega-thrust, respectively. Further north, the MHT merges into a zone of generally low velocity above the eclogitized lower crust, which further explains the observed impedance contrast on top of the eclogites. With this northward continuation of the MHT, we are able to follow this mega-thrust on more than 450 km distance, from its surface expression to lower crustal depths. The deeper part of the MHT is a presumably low viscosity ductile detachment, which can accommodate new material allowing the underplated region to rise in elevation.

The MHT's flat, lower mid-crustal low-velocity zone beneath Lhasa block appears to take up the relative motion between India and Eurasia, according to the **polarized image** of the zone above the Moho. Both differences between illuminations from north and south, and the amplitude variation of the tangential receiver functions suggest the north-dipping
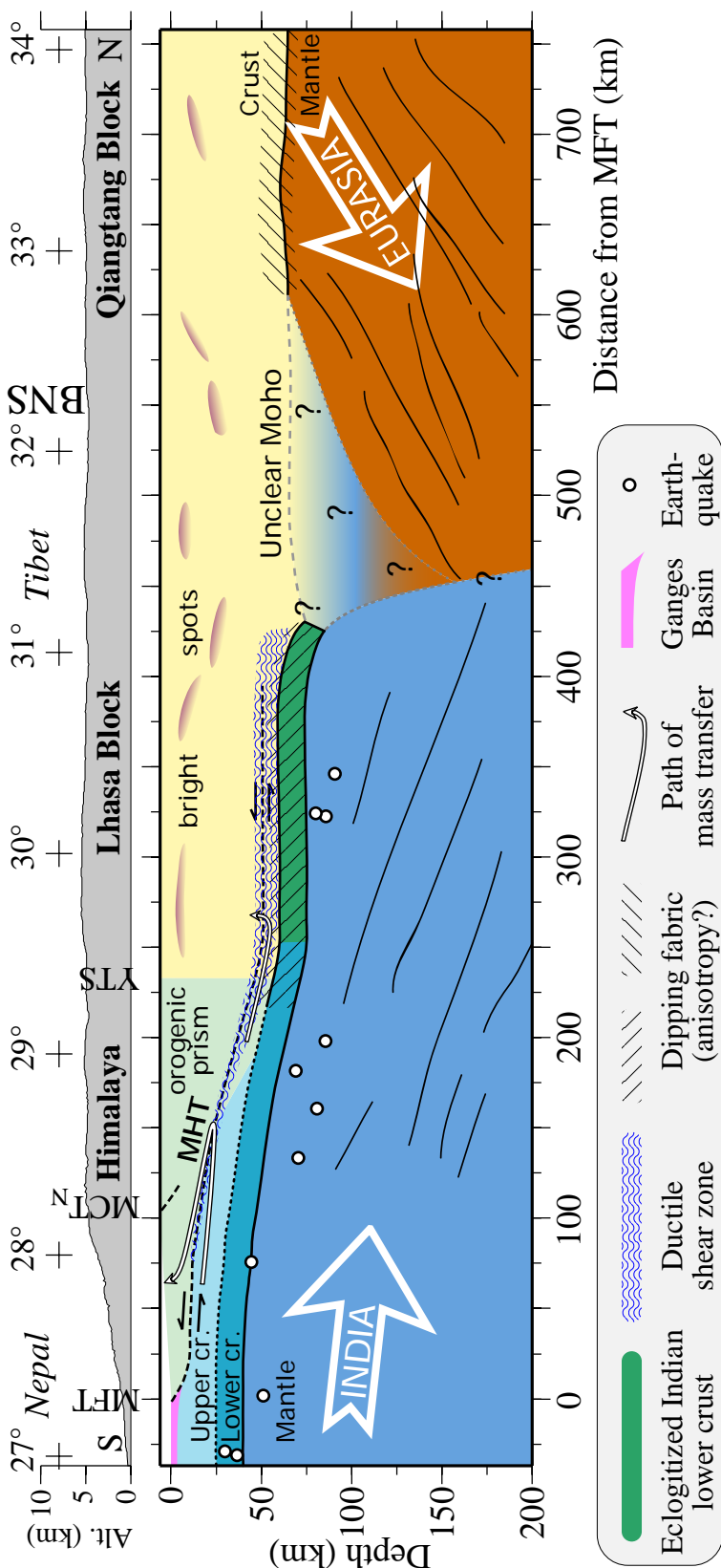
Figure 5.17: Interpretative scheme of the India-Eurasia collision zone as seen by the Hi-CLIMB experiment. The Indian lithosphere underplates the Tibetan Plateau on ∼450 km, including its lower crust which undergoes eclogitization. The Main Himalayan Thrust (MHT), already ductile beneath the Himalayas, merges to a mid-crustal low-velocity zone in Lhasa block and accommodates the convergence. It also allows upper crustal material to build the Himalayas as well as Lhasa block by crustal thickening from below. The Moho beneath Qiangtang block is ∼10 km shallower than beneath Lhasa block. Upper crustal bright spots are observed in both southern and northern Tibet. The polarity of both the Moho and the lower lithosphere reflects the different tectonic origin and evolution of the Indian and Eurasian lithospheric blocks. The main boundary between them is located south of the BNS and is marked with an unclear crust-mantle boundary. Earthquakes (from Chen and Yang, 2004) suggest currently active deformation within the uppermost mantle. MFT: Main Frontal Thrust. MCT$_N$: northern expression of the Main Central Thrust.

imbricate structure above the Moho, in agreement with a top-to-S-SW—bottom-to-N-NE shear zone. The same feature is observed beneath Qiangtang block, but in the opposite direction, constraining a shear zone that accommodates the relative motion between the crust and the southward moving Eurasian mantle. According to S-to-P receiver functions, this shear zone is located above the Moho (G. Wittlinger, personal communication). The crust of Qiangtang block appears to be more simple compared to Lhasa block: it is unaffected by the India plate, and it contains less bright spots in the upper crust.

Underplating material to Lhasa block from below in a ductile manner does not imply that most of the crust is partially melted. On the contrary, the deduced average V_P/V_S -ratio of the Tibetan Plateau's crust shows a regular composition, with **no presence of significant amount of fluid at large scale**. Furthermore, low velocity zones — more commonly known by their reflective top as "bright spots" — in the upper crust were detected and delimited. Their position is highly correlated to extensional grabens, and their extension is local, never exceeding $\sim$50 km in length and $\sim$10 km in thickness. The observations suggest local occurrence of limited amounts of fluid, probably with a majority of aqueous fluids, as that much melt would increase the above discussed V_P/V_S -ratio.

The **northward extent of the India plate**'s lower crust and mantle is determined by combining the above observations along a longitude 85°E profile. The main receiver function image reveals a continuous Moho up to latitude 31.3°N. The top of the underplated Indian lower crust, the second interface on the multiple migration image, runs parallel to the Moho and stops at the same latitude. The polarized nature of the zone above the Moho extends to the same range of distance. In conclusion, most of India plate, as seen by the receiver functions, underplates Tibet on 450 km horizontal distance from the MFT.

The **main lithospheric boundary** zone is located south of and beneath the Banggong-Nujiang Suture. The northward extent of India, the observed opposition of polarities between the Lhasa and Qiangtang blocks, as well as the possible existence of upper mantle lineations all lead to this conclusion. Both the Indian and the Eurasian lithosphere should either stop or plunge in the vicinity of this zone. Mixing of crustal and mantle materials and their downward transport may make this boundary horizontally wide and structurally complex. This also explains the lack of clear Moho signal on the receiver function images, suggesting a broad velocity transition with depth from the crust to the mantle.

Finally, the difference between the horizontally underplated Indian lower crust, and the potentially internally deforming lithospheric mantle suggest that these units are not fully coupled. The current deep earthquake activity, located beneath India and Lhasa block (Chen and Yang, 2004), supports the presence of brittle deformation in the uppermost part

of the mantle. Both features are reproduced by thermomechanical modelling (Chapter 6) constrained by gravity anomalies and flexural geometry, requiring a rheology in which the underlying mantle can deform viscously, producing the observed lineations beneath the southern half of the profile.

5.6.2 Conclusions with regard to earlier studies

The **northward extent of the India plate** is a question that remained open for long. The question now seems to find an appropriate answer: the India plate's crust is well constrained by the Hi-CLIMB experiment's results, and this knowledge can be used to more easily interpret earlier results. The India plate's lower crust, already discernible beneath Nepal, and exhibiting high velocities beneath the Himalayas at longitude 86°E (Schulte-Pelkum *et al.*, 2005; Monsalve *et al.*, 2006), undergoes metamorphic transformation into eclogite. This causes the characteristic double impedance contrast observed beneath Lhasa block, which provides an important attribute to identify the plate laterally, beneath the Hi-CLIMB network and further away (see Fig. 5.18 for a map and the mentioned profiles):

– To the east, the INDEPTH experiment observed a "doublet" above the Moho up to more than 30°N using P-to-S converted waves, and on two different profiles (Kind *et al.*, 2002).

– On the same dataset, S-to-P receiver functions show the descent of India, its maximal depth reached at around the YTS, and its flattening beneath Lhasa block. On the western profile, a clear change in the signature of the Moho (from a double to a simple interface) occurs close to the BNS, similarly to the P-to-S image. On the eastern profile, there is also an increase in the amplitude of the Moho signal from south to north (Wittlinger *et al.*, 2004b).

– To the west, P-to-S RFs across the Kunlun range also image a part of the lithosphere with a double crust, stopping at the BNS (Wittlinger *et al.*, 2004a).

These constraints in the western, central, and eastern part of the Tibetan Plateau clearly draw the northern extent of the Indian lower crust (Fig. 5.18): it is located parallelly to the Himalayan arc, and about ∼450 km north of the Main Frontal Thrust. In the meantime, the comparison of six images along four profiles show, that while the location where the Indian crust reaches its maximal depth can be approximately related to the Yarlung Tsangpo Suture, the position of the Banggong-Nujiang Suture with respect to the northern extent of the Indian lower crust is variable, with horizontal distances ranging between 0 and 150 km.

Figure 5.18: The northward extent of India. The Hi-CLIMB experiment's results help to interpret profiles of earlier seismological experiments (in purple lines) with less data at lower spatial resolution. The migrated profiles (right) constrain the position of the northern edge of India beneath the Tibetan Plateau (yellow dashed line).
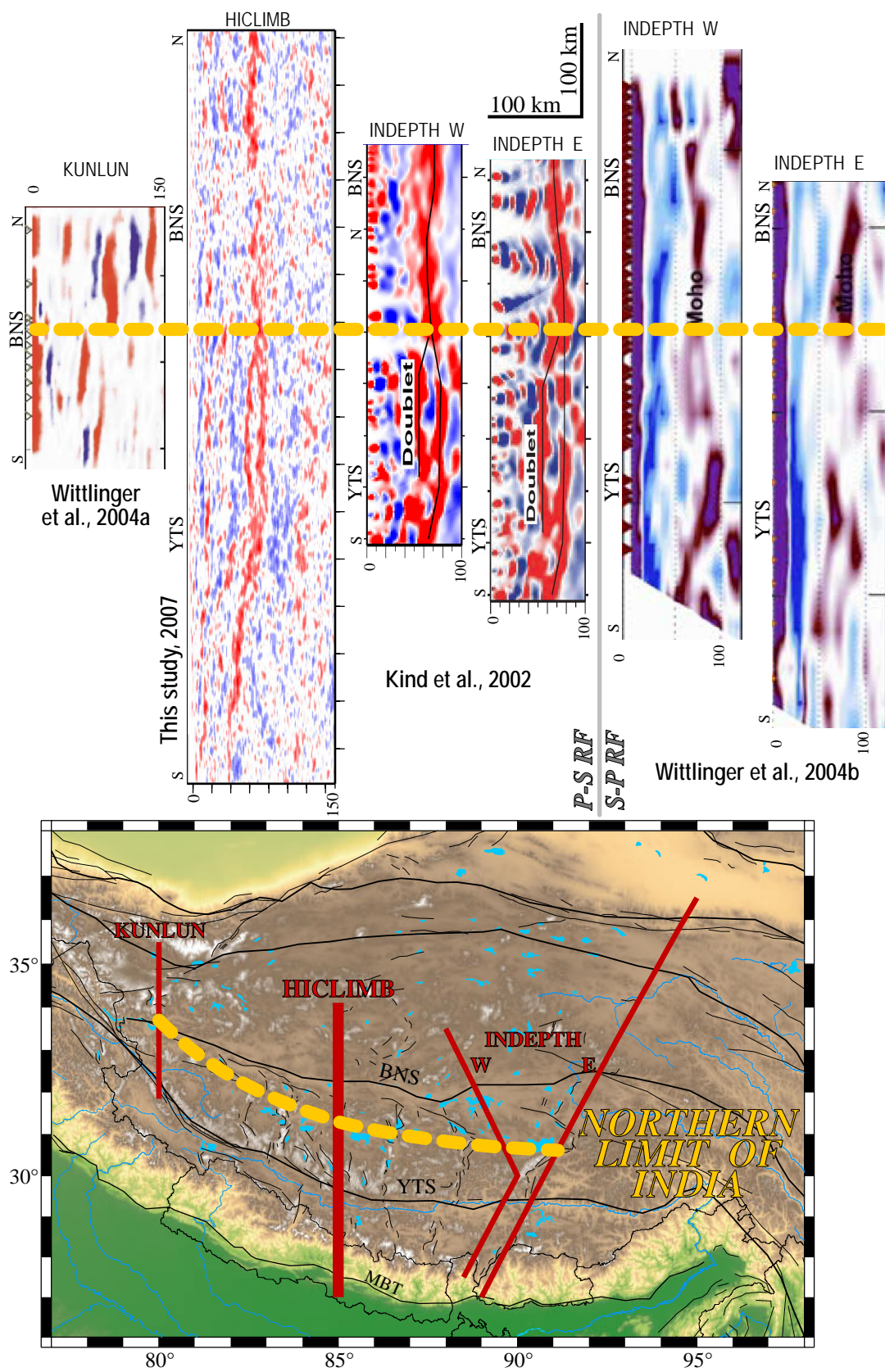
The **main lithospheric boundary** between India and Eurasia at depth is located north of latitude 31.3°N according the Hi-CLIMB experiment. The role of the Banggong-Nujiang Suture itself is unclear, as the boundary zone is not centred beneath but located south of the suture. However, a primary boundary south of the BNS is not a unique observation. A line separating domains of different Pn and Sn wave propagation properties was recognized south of the BNS already a quarter of a century ago (Barazangi and Ni, 1982). The presence of shear-wave splitting also appears a little south compared to the BNS (Huang *et al.*, 2000). In central Tibet, tomography around the zone of the BNS shows a sub-vertical boundary between 100 and 400 km depth with relatively fast and slow zones south and north of the suture, respectively (Tilmann *et al.*, 2003; Fig. 5.19). The authors interpret these as the downwelling of the Indian mantle lithosphere to the south, and the upwelling counterflow to the north, explaining the warm mantle beneath Qiangtang block. However, according to the RF results of the Hi-CLIMB experiment, the downwelling does not seem to cross the 410 (nor the 670) km phase transition zone, contrary to the arguments of Kosarev *et al.* (1999). If downwelling occurs, it either does not reach these discontinuities, or they are thermally rapidly reset and the material transfer is imperceptible.
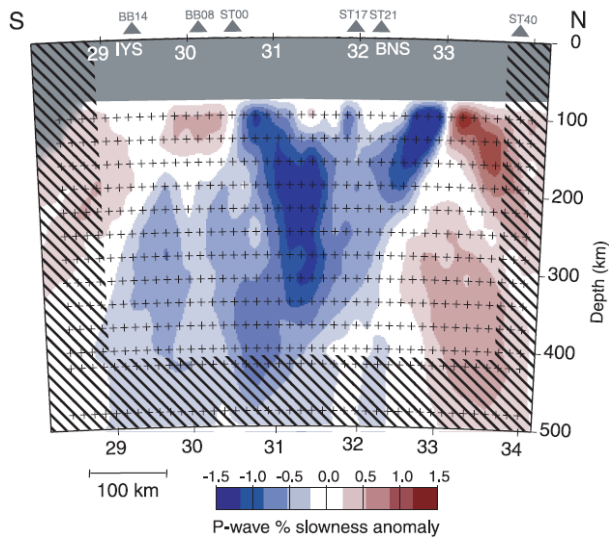
Figure 5.19: Seismic tomography beneath the INDEPTH III experiment in central Tibet (from Tilmann et al., *2003).*

5.6.3   Evolution models

Subduction

Drawing a parallel between a subduction zone and a continent-continent collision is a classic idea, and the process of subduction was proposed for nearly every major suture in

the Himalayan-Tibetan system (*e.g.* Tapponnier *et al.*, 2001). The Hi-CLIMB experiment's line crosses two of them: the Yarlung Tsangpo and the Banggong-Nujiang Sutures.

The fate of the India plate at the YTS was debated, and different scenarios, such as underplating, constant dip subduction, and deepening subduction, were proposed (Makovsky *et al.*, 1996b). The tight station spacing of the Hi-CLIMB experiment allowed to follow closely the shape of the Moho, and to exclude the possibility of disruption in the crust-mantle boundary beneath the YTS. Thus investigations based on assumed continental subduction of the Indian crust YTS, or on Moho step across the suture, are not supported by our results.
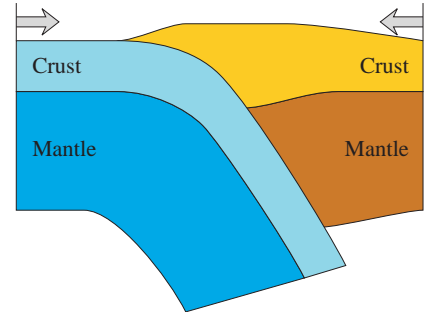
The Moho beneath the BNS is not clear, as it has been discussed above. There might be a subduction invisible to the RF method, if the impedance contrast with the mantle vanishes rapidly along the slab. However, based on tomography and on our observations of upper mantle lineations, there is no subduction of one plate's lithosphere nor lithospheric mantle beneath that of the other. The main boundary between India and Eurasia at depth, located south of the BNS at longitude 85°E, is close to vertical.

Diffuse crustal thickening

Numerical models using viscous thin sheets assume a build-up of the plateau in which the horizontal limit of the entire crust lies at the same position, and in which deformation occurs inside the different media. The style of deformation seen by the Hi-CLIMB experiment does not confirm these hypotheses. The limit between India and Eurasia at surface lies at the YTS, however, at depth, the lower crust advances at least 200 km further north. Moreover, upper crustal material seems to enter the ductile zone at lower mid-crustal depths in Lhasa block, and to contribute to plateau building from below. The amount and style of deformation is clearly different for the upper and lower crust of the India plate.
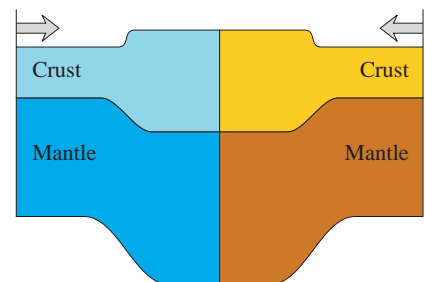
Channel flow

There are numerical models that include a thick channel (up to 15-25 km) of very low viscosity ($2 \cdot 10^{18}$Pa·s) and high temperature (>700°C at the Moho, 900°C in the lower crust) flowing at a high speed (80 mm·yr^{-1}) (Jamieson *et al.*, 2002; Clark *et al.*, 2005). Based on these characteristics, one would expect to observe a low velocity zone on the seismological image with a considerable thickness. There is actually a candidate for a such zone in our results: the ductile shear zone in the continuation of the Main Himalayan Thrust beneath Lhasa block. However, the observed low velocity is not conclusive in the identification of this zone, and other arguments should be considered:
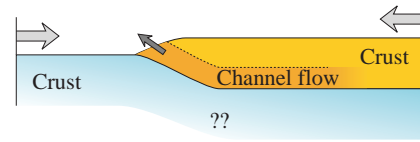
- In case of channelized flow, one may expect a symmetric and parabolic flow profile with zero velocities on the sides and maximum velocities close to the centre. This type of flow, however, would not produce unidirectional dipping structure/anisotropy, as it was observed by the polarized images.

- The polarized images localize the shearing near the underthrust Indian lower crust, and not at mid-crustal depths within Tibetan crust, as drawn in Beaumont *et al.* (2001), for example.

- The regular value of the average crustal V_P/V_S -ratio indicates that widespread partial melt, which could give place to a thick, high-temperature, ductile zone, is unlikely. The thickness of the observed low velocity zone does not seem to reach the 15-25 km range, and the corresponding thermal model (Chapter 7) is at least 100°C colder than the values cited above.

- There seems to be no relationship between the low velocity zone along the MHT beneath Lhasa block, and the occurrence of shallow bright spots, both features being localized in depth and thickness. The bright spots seem to be limited horizontally and related to E-W extensional grabens, rather than to the MHT or widespread partial melt. In case of channel flow, the low viscosity layer would be located at mid-crustal depths, clearly deeper than bright spots, and shallower than imaged depth of the MHT.

- Finally, if the channel flow model was true, the upward continuation of the MHT's deep section should arrive at surface north of the Main Central Thrust and south of the South Tibetan Detachment System. However, our images suggest that the deep,

ductile part of the shear-zone continues in a shallow, brittle section beneath Nepal (Fig. 5.17).

I do not argue that channel flow does not exist in nature; it might, under certain conditions. The primary condition is temperature, which is amongst the less well constrained variables at depth, and which is up to now not confirmed by slow anomalies of seismic tomography studies, for example. The other parameter is rheology, also poorly constrained, mainly due to its dependence on water content but also due to compositional variations. If channel flow exists in other regions, its thickness and flow speed should be better explained by observed geophysical data.

Underplating

It is now time to revisit Argand and the question *"if the bulk of a continent, in all its height, can get under the bulk of another, in all its height"*.

Based on the receiver function images, the actual mode of deformation beneath the southern half of the Tibetan Plateau is underplating. However, only the lower crust of the India plate gets under the plateau, *in all its height* of about 15 km, and, accompanied by — but not fully coupled to — the mantle, advances ∼450 km north of the MFT. The upper crust seems to (1) cross the MHT below the High Himalayas and to accrete the Himalayan prism (*e.g.* Bollinger *et al.*, 2006), and to (2) enter the low velocity, low viscosity zone beneath Lhasa block and to thicken the Tibetan Plateau from below.

In this way, Argand's image is almost correct, and, together with Powell and Conaghan (1973), is closer to reality than many other models. Part of the *sial* but all of the *sima* underthrusts the plateau, not entirely, but halfway through.

5.6.4   New elements in the evolutionary scenario

The observations made along the main array of the Hi-CLIMB experiment were summarized and interpreted on Figure 5.17. Based on these results, constraining the present structure beneath the central Tibetan Plateau, the following new elements can be introduced to the evolutionary scenario of the India-Asia collision zone. Due to the south-north orientation of the new dataset, the results and implications are in two dimensions, and does not allow to discuss the evolution in 3-D (*e.g.* extrusion).
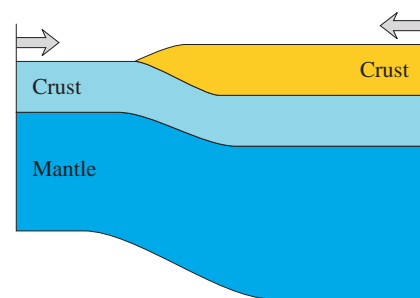
Subduction-underplating transition. Subduction of India beneath Asia characterized the early evolution of the collision. First the oceanic crust, then part of the continental lithosphere have descended south of the Yarlung Tsangpo Suture. However, the current image of the lithosphere shows horizontal underplating of Indian lower crust beneath Lhasa block. A plausible explanation for the transition from subduction to underplating is delamination of the lower lithosphere. Seismic tomography observing relatively fast, isolated zones beneath today's peninsular India (Van der Voo *et al.*, 1999) strengthens this hypothesis, together with structural, stratigraphic, tectonic and metamorphic arguments (Powell and Conaghan, 1973; Guillot *et al.*, 2003). After delamination, the northern end of the India plate, freed of considerable weight, have rebound by buoyancy. This caused relatively rapid uplift of the topography, and increased the geotherm in Tibet (see below).

Timing of the above transition can be estimated in different ways.

First, if we assume an underthrusting rate similar to the current estimate (17 mm·yr^{-1} ; Bollinger *et al.*, 2006), the required time to underplate ∼200 km horizontal distance is ∼12 Myr. However, the error estimates should take into account varying (probably decreasing) underplating velocities with time, the uncertainty on the initial position of underplating, and internal shortening (see below).

Another way to constrain the transition is the age distribution of partial melt and volcanism, triggered by the increased temperatures. The age of Himalayan leucogranites ranges from ∼24 to 12 Ma, and their middle-crustal origin south of the Yarlung Tsangpo Suture, together with an overthrusting rate (close to the actual) of 4-5 mm·yr^{-1} also explain the location of the older/younger leucogranites in the south/north, respectively. Further north, in Lhasa block, potassic volcanism appears to have been active between ∼20-16 and ∼10 Ma (Turner *et al.*, 1996). The above date estimates suggest a northward propagating thermal anomaly causing an increase in temperatures, that were maintained by continued conductive heating for ∼10 Myr.

The close temporal relationship between the beginning of underplating and rapid uplift in the Himalayas was proposed by Powell and Conaghan (1973). Hence a third way to constrain the subduction-underplating transition would be to compile precise estimates of uplift at an increased spatial coverage across the plateau. However, as discussed in Section 2.3, estimates of plateau uplift are not homogeneous, neither in time nor in space.

Based on the above arguments, the transition from subduction to underplating can be estimated to have occurred at the beginning of Miocene. I would like to emphasize the primary importance of lithospheric delamination in the evolution of the Himalayan-Tibetan region, as it allowed the deformation regime to switch from collision to underthrusting.

Evolution of underplating   after the rebound of the lower crust and lithospheric mantle was forced by the continuing northward movement of India. The relatively flat geometry of the lower crust is what we observe today beneath Lhasa block. This process also dragged part of the upper crust, and, at the same time, have developed the Main Himalayan Thrust further at depth. While the lower crust advanced towards the north, the orogenic prism (the Himalaya) was still fed by the Indian upper crust south of the Yarlung Tsangpo Suture. Underplating was probably slowed down by the Eurasian lithospheric mantle, which, divested from its buoyant crust, was able to start to sink gravitationally. The opposition of the two lithospheres caused "jamming" of India's front in the north compared to its southern part, causing partial decoupling between the Indian lower crust and the upper mantle. These two units evolved differently in response to the northward push of India, which allows to resolve the discrepancy between the time necessary to produce $\sim$200 km of underplating ($\sim$12 Myr) and the time since the Lower Miocene ($\sim$20 Myr).

The lower crust, still horizontal beneath Lhasa block, have developed internal imbrications, observed by the polarized images and the tangential component receiver functions. It may also have thickened by up to 20%, still keeping its $\sim$15 km thickness *via* compensation by its volume decrease due to densification in the eclogite facies ($>$10%), and by the error-bar of its thickness estimate (10%). With the shortening and thickening of the lower crust, the onset time estimated to $\sim$12 Ma based on horizontal underthrusting rate only can be largely increased, hence becoming more coherent with Lower Miocene age.

The top of the lithospheric mantle may have remained sub-horizontal, and behaved in a brittle manner, as reproduced by thermomechanical modelling in Chapter 6. Below, the ductile part of the lithospheric mantle started to deform all over beneath Lhasa block and the Yarlung Tsangpo Suture, similarly to an in-sequence jump of subduction zone, but without localizing deformation, due to the viscous rheology. This is only suggested by the observed descending upper mantle lineations in our results, but similar features were also imaged around the YTS beneath the INDEPTH profile (Kosarev *et al.*, 1999; Kumar *et al.*, 2006). Finally, a strong argument for the current and active deformation of the lithosphere all over beneath India, the Himalaya, and Lhasa block, are the deep earthquakes located in the uppermost mantle (Chen and Yang, 2004).

CHAPTER 6

Can the India plate support the Himalayas and South Tibet?

Foreword

This chapter presents the first multidisciplinary study using seismological data from the Hi-CLIMB experiment. Here we investigate the question of the elastic thickness of the India plate, an issue and a location which are often taken as an example in the debate on the rheology of the lithosphere. The receiver functions in the undeformed Ganges Basin provide new, valuable constraints on the flexural geometry of the plate, which serve both as an input and, together with gravity anomalies, as a set of control parameters for thermo-mechanical modelling. The results of numerical models show that decoupling of the crust and the mantle occur and make the effective elastic thickness drop south of the Himalayan range. The different tests accounting for various rheologies emphasize the importance of the strength of the mantle in supporting the load of Tibetan crust.

Before the beginning of this study, I would like to present an analogue for the "effective elastic thickness" (EET) of a plate in flexure. The reason for this is that, in my opinion, the clearly different quantitative estimates on the EET root in the different concepts or pictures concerning the physical meaning of the EET. The analogue, which have been used for centuries, is the shock absorber by leaf spring in vehicles, pictured on carriages on Figure 6.1. The use of several thin plates, separated by oil, makes that the system mechanically damps sudden impulses by flexure. Using more and thinner plates, it becomes easier to bend the system. If only one plate of the total thickness is used

with the same force, there is hardly any bending. Flexure of the lithosphere is somewhat similar. If the layers are coupled, then it is difficult to bend them. If they are decoupled by viscous layers (equivalent of the oil in the above example), then the effective elastic resistance decreases and flexure occurs more easily. The equation of flexure, as well as the relationship between the effective and individual thicknesses of the layers are described in the following study, which has been published in Geophysical Journal International.

Figure 6.1: Analogy for the effective elastic thickness: leaf spring shock absorbing system of carriages. Pictures are from the Carriage Museums of Keszthely (left) and Chaumont-sur-Loire (right).

The effective elastic thickness of the India Plate from receiver function imaging, gravity anomalies and thermomechanical modelling

György Hetényi,[1] Rodolphe Cattin,[1] Jérôme Vergne[1] and John L. Nábělek[2]

[1] *Laboratoire de Géologie, ENS Paris, 24 rue Lhomond, 75005 Paris, France. E-mail: hetenyi@geologie.ens.fr*
[2] *College of Oceanic and Atmospheric Sciences, Oregon State University, Corvallis, OR 97331, USA*

Summary

The range and the meaning of the effective elastic thickness (EET) in continental areas have been subject to controversy over the last two decades. Here we take advantage of the new data set from the Hi-CLIMB seismological experiment to re-estimate the EET of the India Plate along a south-north profile extending from the Ganges basin to central Tibet. Receiver functions give a high-resolution image of the base of the foreland basin at ∼5 km depth and constrain the crustal thickness, which increases northwards from ∼35 km beneath the Indo-Gangetic plain to ∼70 km in southern Tibet. Together with available data sets including seismic profiles, seismological images from both INDEPTH and HIMNT experiments, deep well measurements and Bouguer anomaly profiles, we interpret this new image with 2-D thermomechanical modelling solutions, using different type of crustal and mantle rheologies. We find that (1) the EET of the India Plate decreases northwards from 60-80 to 20-30 km as it is flexed down beneath Himalayas and Tibet, due to thermal and flexural weakening; (2) the only resistant layer of the India Plate beneath southern Tibet is the upper mantle, which serves as a support for the topographic load and (3) the most abrupt drop in the EET, located around 200 km south of the MFT, is associated with a gradual decoupling between the crust and the mantle. We show that our geometrical constraints do not allow to determine if the upper and lower crust are coupled or not. Our results clearly reveal that a rheology with a weak mantle is unable to explain the geometry of the lithosphere in this region, and they are in favour of a rheology in which the mantle is strong.

6.1   Introduction

The effective elastic thickness (EET) is a concept related to the apparent strength of a plate. Its value over oceanic lithospheres is often associated with the 600 °C isotherm (Burov and Diament, 1995; Watts and Zhong, 2000). Over continental plates, the estimate of the EET has been subject to controversy and to some more detailed discussion over the last two decades. One of the most discussed regions, despite the extensive studies and large available data sets, is the northern edge of the India–Australia plate (India Plate hereinafter) across the Himalayan belt and Tibet.

EET(km)	Method or concept	Authors
80-100	Elastic plate, Bouguer anomaly	Lyon-Caen and Molnar (1983), Karner and Watts (1983)
90 India, 30-45 Tibet	Bouguer anomaly , variable EET	Jin *et al.* (1996)
42	Free-air anomaly and topography coherence	McKenzie and Fairhead (1997)
40-50 India, 30 Tibet	Thermomechanical modelling, viscoelastoplastic rheology	Cattin *et al.* (2001)
36.5	Seismogenic and elastic thickness similarity ('crème brûlée')	Jackson (2002), based also on Maggi *et al.* (2000)
60-70	Integrated brittle, elastic and ductile strength ('jelly sandwich')	Watts and Burov (2003), Burov and Watts (2006)

Table 6.1: Summary of the previous estimates of the EET in the Himalayan-Tibetan region by different methods and authors

Table 6.1 summarizes the estimates of the EET in the Himalayan-Tibetan region. The first approach was based on the physical equations describing the flexure of a completely elastic beam (Hetényi, 1946). As more geophysical data became available (such as gravity anomaly, seismicity, etc.), and more sophisticated modelling tools were developed, the complexity of the models evolved, and several different values have been published for the EET. In the last five years, the debate on the EET concentrated around two school of thoughts with different views of the rheology: one with a weak mantle and a strong crust (also dubbed 'crème brûlée' by Burov and Watts, 2006), and one with a strong mantle and

a strong upper crust (also dubbed 'jelly sandwich' by Jackson, 2002).

One reason for these uncertainties in the estimate of the EET of the India plate is the lack of continuous information on the shape of its flexure from India to Tibet. In order to investigate the geometry of the lithospheric structures in this area, several seismological experiments were performed, including the HIMNT experiment in Nepal and southern Tibet (Schulte-Pelkum *et al.*, 2005) and the INDEPTH experiment in Tibet (*e.g.* Zhao *et al.*, 1993; Nelson *et al.*, 1996; Hauck *et al.*, 1998; Alsdorf *et al.*, 1998). However, due to the long distance ($\sim$ 250 km) between HIMNT and INDEPTH experiments, data from these previous results cannot be easily combined. Moreover, these experiments do not extend into the Ganges basin, where a good estimate of the basin and Moho depth are of great importance to evaluate the EET. Here, we take advantage of the new data set from the Hi-CLIMB broad-band seismological experiment, which provides the first detailed and continuous lithospheric profile across the Himalayan range, from the Ganges basin to central Tibet (Nábělek *et al.*, 2005).

In a first part, we constrain the geometry of the lithospheric structures at two different scales. Using the receiver function method, we image the geometry of the flexural sedimentary foreland basin from a subset of the new, high-resolution seismological Hi-CLIMB data (Fig. 6.2 inset). As receiver functions observed in young sedimentary basins have particular properties, we describe our proceedings in detail. At larger scale, we combine the profile up to central Tibet, obtained from more Hi-CLIMB data (Nábělek *et al.*, 2005), with previous results from seismic reflection (Zhao *et al.*, 1993; Alsdorf *et al.*, 1998), receiver function (Hauck *et al.*, 1998; Kumar *et al.*, 2001; Schulte-Pelkum *et al.*, 2005) and gravity anomaly data (Cattin *et al.*, 2001).

These sets of information are used in the second part of this study, which focuses on thermomechanical modelling of the flexure of the India Plate under a load representing the Tibetan crust. A large number of parameters are varied, and the results are evaluated upon the aforementioned geometrical criteria. The aim of this study is to demonstrate the consistency of all available geophysical observations, and to re-estimate of the EET and its variation along a profile perpendicular to the mountain range. The validity of the obtained models is tested by calculating the corresponding Bouguer anomaly , and by comparing it with the observations in the same area (Fig. 6.2; Cattin *et al.*, 2001). At the end of this paper, special emphasis is given to the analysis of the time-dependence of the EET.
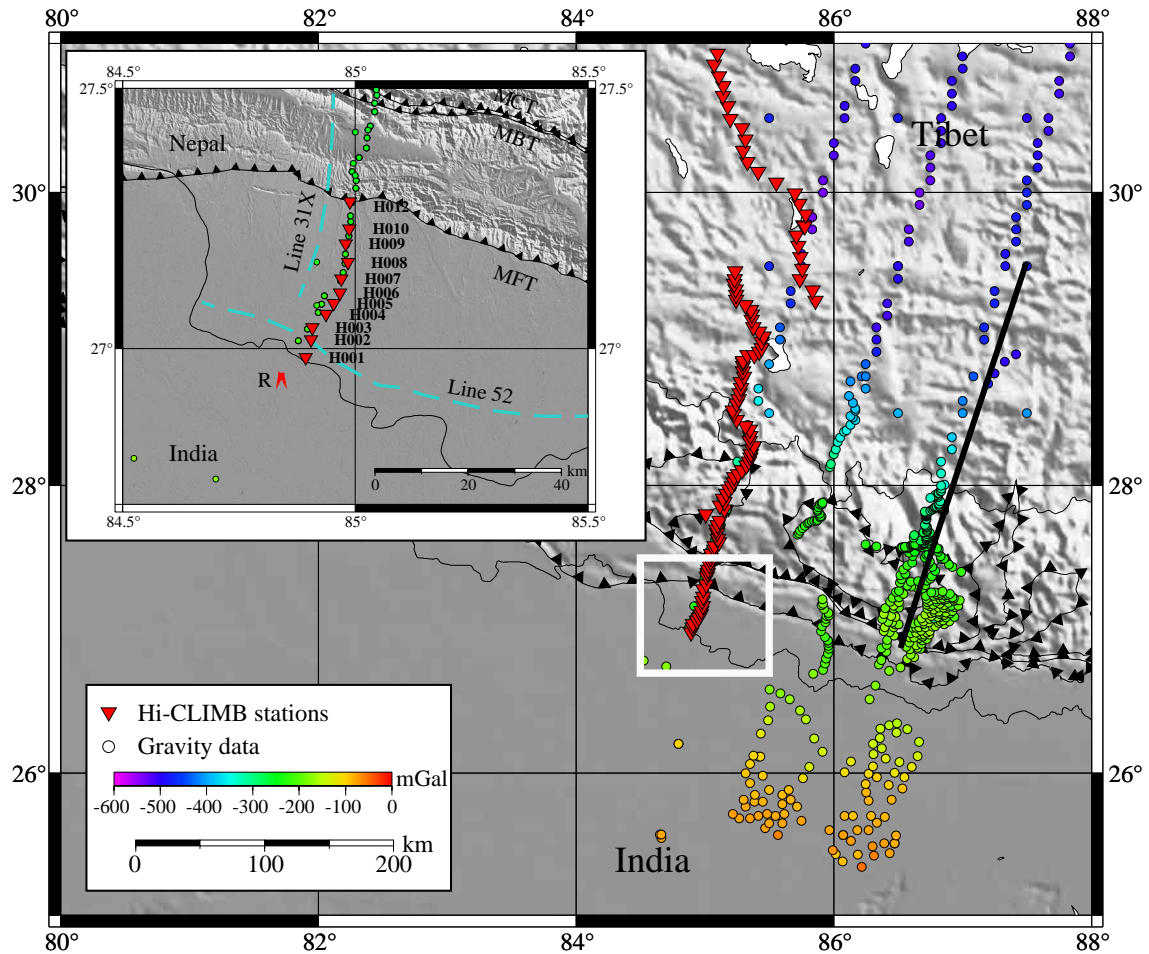
Figure 6.2: The study-area in northern India, central Nepal and southern Tibet, showing the location of seismological stations (red triangles), gravity measurements (circles) and major thrust-faults. Thick line represents the profile of Schulte-Pelkum et al.(2005). Inset: close-up on the northern edge of the Ganges basin and the seismological stations used in this study. Thrust-faults from north to south are the Main Central Thrust (MCT), the Main Boundary Thrust (MBT) and the Main Frontal Thrust (MFT), respectively. 'R' represents deep well data location at Raxaul. Lines 31X and 52 give the location of the seismic reflection profiles mentioned in this study.

6.2   Geodynamic setting and constraints on the geometry of the Ganges basin

The important amount of shortening that occurred over the last tens of million years (*e.g.* Lyon-Caen and Molnar, 1983; Armijo *et al.*, 1986 and continues today (Larson *et al.*, 1999; Chen and Yang, 2004) between India and Eurasia is mainly accommodated along

major thrust faults such as the Main Central Thrust (MCT), the Main Boundary Thrust (MBT) and the Main Frontal Thrust (MFT) (Fig. 1, inset; *e.g.* Avouac, 2003). These faults are thought to root along the Main Himalayan Thrust (MHT), imaged at a depth of 25 to 40 km from the INDEPTH experiment (Zhao *et al.*, 1993; Alsdorf *et al.*, 1998), which is considered as the plate interface. The MFT is probably the major active fault at present in the Himalayas of central Nepal (Lavé and Avouac, 2000). This fault separates the deformed foothills to the north from the undeformed foreland basin of the Ganges River to the south. The Raxaul deep well (Fig. 6.2 inset) reveals the local stratigraphy of the basin showing recent alluvial layers over the molassic Siwaliks Group formation with a total thickness of 4.1 km (Sastri *et al.*, 1971). The Siwaliks have three lithostratigraphic units, corresponding to the change in facies from distal mudstone and clay to proximal conglomerate and breccia (Schelling, 1992; Métivier *et al.*, 1999). The thickness of the alluvial layer may reach up to 1 km and is characterized by very low velocities due to its recent formation and small compaction (Raiverman *et al.*, 1983). Seismic reflection profiles designed for commercial exploration are also available (DMG, 1990) and, although being of poor quality, provide additional information about the subsurface structures. They seem to indicate that the base of the Ganges basin is essentially flat, both parallel (line 52, Fig. 6.2 inset) and perpendicular to the Himalayan front (line 31X). The fact that the available profiles are not depth-converted using a laterally varying velocity model precludes more precise dip estimates. Other dip estimates based on gravity anomaly measurements (*e.g.* Lyon-Caen and Molnar, 1983; Cattin *et al.*, 2001), on the interpretation of another seismic profile (Lavé and Avouac, 2000), and on an aeromagnetic survey (Agocs, 1957), rather show a gentle northward deepening of this surface, with dip values ranging between 1.5 and 4°.

A better constrained estimate of the dip of the base of the basin is important, as it is a good indicator of the shape of the flexure of the India Plate, which is dependent of its EET. Measurements of the depth and dip of the base of the basin can thus help to better constrain the EET: a more rigid plate will have a smaller dip, and a less rigid plate a steeper dip.

6.3   Geometry of the structures

6.3.1   The Ganges foreland basin

Seismological data processing

This study is among the firsts that images shallow structures by the mean of high-frequency receiver functions, originally designed to image deeper lithospheric structures (see also Wilson *et al.* (2003) and Zheng *et al.* (2005) for other examples). This technique is aimed to isolate P-to-S converted waves and multiple reflections/conversions from interfaces associated with an impedance contrast. For the principles, we refer to the works of Langston (1979), (Ammon *et al.*, 1990) and (Ammon, 1991). Receiver functions obtained at stations located above young sedimentary cover usually exhibit a very different shape than those located on bedrock, due to contamination by multiple reverberations inside the basin. However, detailed examination and modelling of these receiver functions at high frequency can provide valuable information about the basin structure. Obtaining the correct depth–velocity structure of the basin is also very important to get an accurate estimate of the Moho depth in this region. Neglecting the effect of the basin would lead to an error of several kilometres on the Moho depth.

Here we use 11 three-component broad-band seismological stations of the Hi-CLIMB experiment located in the northern part of the Ganges basin. With the use of receiver functions, we obtain a high-resolution image of the basin structure and an estimate of the Moho depth. The stations were placed at slightly elevated areas above the water table. As insurance from flooding during the monsoon, the seismometers were placed in sealed drums, but there was no indication that the water table ever reached as high as the vault. All the sites in this area were much noisier at high frequencies than stations further north due to the presence of the low-velocity sediments and strong anthropogenic activity, which resulted in less usable data for these stations.

Data were acquired for a period of 1 year, during which a total of 458 teleseismic earthquakes were recorded with suitable epicentral distances (20-90°) and magnitudes greater than 5.2. Events with low quality signal are excluded, including small magnitude and distant events, low signal-to-noise ratio traces, and most aftershocks. The selection process keeps an average of 150 events per station. The selected three-component data are first rotated to the theoretical wave-arrival direction (back-azimuth). After applying a bandpass filter between 0.05 and 2 Hz, deconvolution of the vertical trace from the radial and tangential ones is performed using the iterative time-domain method of Ligorría and Ammon (1999). The process is stopped after 50 iterations, or earlier if more than 95 per
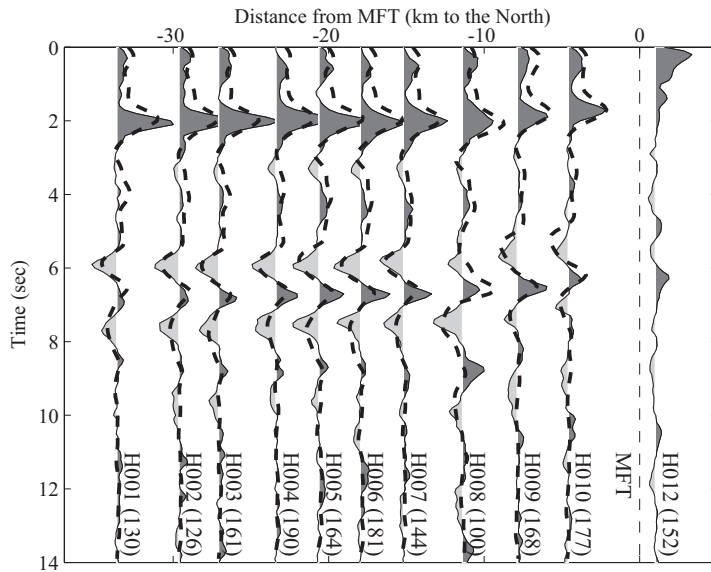
Figure 6.3: Stacked receiver function results (dark and light gray filled curves) in the Ganges basin. Station name is followed by the number of traces in stack (in parentheses). Superposed thicker dash lines at stations H001-H010 represent the average of 50 inverted traces at each station with the lowest misfit. Thin dashed line shows the location of the MFT.

cent of the radial component signal is fit. Finally, we convolve the resulting spiky receiver functions with a Gaussian of a width corresponding to the maximum frequency (2 Hz).

Receiver function results

The obtained P-to-S radial receiver functions do not show significant variations with the back-azimuth and are thus stacked at each station (Fig. 6.3). Moreover, the receiver functions calculated for the transverse component (not shown) do not show coherent energetic arrivals, which indicates the absence of both anisotropy and strongly dipping layers. We thus consider that the stacked radial receiver functions are representative of the structure beneath each station. In general, the waveforms are similar between stations H001 and H010, all located in the Ganges basin. A common feature of these mean receiver functions is the lack of the P-wave arrival at 0 s, indicative of very low velocities close to the surface (*e.g.* (Sheehan *et al.*, 1995) that polarizes the direct P-wave almost vertically. The most energetic arrival is a prominent positive peak at around 2 s of delay compared to the P-wave reference time. Other coherent peaks on all traces are a negative-positive-negative sequence at around 6, 7 and 8 s, respectively, and secondary peaks at around 0.5-1 s delay. Small variations in arrival times and amplitudes can be observed along profile, such as the $\sim$10 per cent decrease in the amplitude of the 2 s-peak towards the north, or the $\sim$0.2 s earlier arrival of the 6-7-8 s sequence towards the north.

The waveform at station H012 is simpler compared to the others. This is mainly due to the fact that it is located right at the MFT, where the low-velocity alluvial layer is

absent, and where the MFT brought more compacted, higher velocity sediments close to the surface (Lavé and Avouac, 2000).

Waveform inversion procedure

In order to determine the detailed structure of the basin, we proceed to find velocity models that adequately match our observations at each station in the basin. This inverse problem being far from linear, we use the neighbourhood algorithm (NA; Sambridge, 1999a, a stochastic inversion method based on partially guided exploration of the parameter space. Starting from a random distribution of parameter sets and establishing a rank of the corresponding cost functions, this method will preferentially sample the good data-fitting regions of the parameter space.

The application of the NA to the inversion of the receiver function problem is described by Sambridge (1999b), and we follow his procedure. Our process inverts traces for all 10 stations separately, and iterations are stopped after 10100 tested models. The best 50 models at each station are selected based on the lowest cost function values and are then averaged, as we ensure that they all belong to only one class of model.

An important question is the choice of the cost function. Mellman (1980) states that the best error-function in trying to match interacting waveforms is the L2-norm. However, as the $\mathcal{L}$2-norm tries to minimize the difference between each time-sample, it is likely that secondary peaks with smaller amplitudes will be de-emphasized. Frederiksen (2000) proposes a cross-correlation based cost function, as it places less emphasis on amplitudes than on traveltimes, which are more robustly recovered features of receiver functions. The finally presented results in this study include two series of inversions, using one type of cost function each.

Our common starting model includes four layers: a thin low-velocity alluvial layer, a basin-filling sedimentary layer, crust, and mantle. It is clear that *a priori* information is necessary to better constrain the inversion results and to reduce the depth–velocity ambiguity, a common feature of receiver function non-uniqueness (Ammon *et al.*, 1990). For this reason, the velocity of P-waves in the mantle is fixed to 8.1 km·s^{-1} with a V_P/V_S -ratio of 1.85, and the crustal shear-wave speed varies from 3.31 to 3.66 km·s^{-1} from top to bottom with a V_P/V_S -ratio of 1.75. This value is consistent with previous estimates for the Indian crust (Kumar *et al.*, 2001). As the porosities of the different Siwalik formations are different (Raiverman *et al.*, 1983), we consider that the two upper layers are young enough that compaction may vary significantly with depth. Thus, we allow velocity to vary independently at the top and at the bottom of both layers, forming a linear velocity
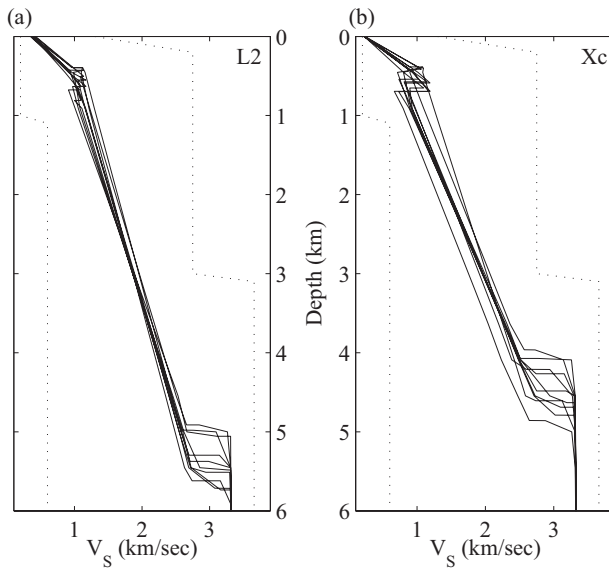
Figure 6.4: Inversion results for S-wave velocity in the sedimentary basin using a $\mathcal{L}$2-norm (a) and a cross-correlation based error function (b). Each line represents the average of the 50 best velocity models at one station. Dotted lines are the allowed minima and maxima for the velocity values during inversion. The results show very low velocities in the alluvial layer, and a velocity-gradient in both the Siwaliks Group formation and the alluvial layer.

gradient. The remaining nine parameters to invert are summarized in Table 6.2.

	Depth (km)	Velocity at the top (km·s^{-1})	Velocity at the bottom (kmPs)	V_P/V_S -ratio
Alluvial layer	0.2-1	0.2-1.3	0.2-1.3	1.75-2.3
Sedimentary layer	3-6.5	0.6-2.75	0.6-2.75	1.75-2.1
Crust	32-39	3.31 (fixed)	3.66 (fixed)	1.75 (fixed)

Table 6.2: The nine parameters to invert with the Neighbourhood Algorithm with the allowed limits (based on a priori information).

Inversion results and interpretation

The inverted receiver function traces using the cross-correlation cost function at each station are represented in Fig. 6.3 (thick dashed lines). They reproduce properly both the arrival time and the amplitude of major peaks of the observed traces. However, secondary features are sometimes not as well reproduced. For example, the fit at station H008 is of lower quality probably because of less data available. Stations H001 to H010 represent very similar structural features. (Station H012, not inverted, makes an exception as it is located just above of the MFT). There is a slight difference between the profiles obtained with the two tested cost functions, which is that the cross-correlation method shows slightly shallower interfaces compared to the $\mathcal{L}$2-norm.

The shear-wave velocity–depth profiles in the basin obtained by both cost-function inversions are shown in Figures 6.4(a and b). All models show a very low speed of 0.2 km·s^{-1}

close to the surface, in the alluvial layer, which confirms the absence of a major peak at 0 s corresponding to the direct P-wave. This top layer exhibits very high V_P/V_S -ratio ($\sim$2.1), consistent with the unconsolidated nature of the sediments (Clitheroe *et al.*, 2000), and a strong velocity gradient with depth of 1.3-1.55 s^{-1}, mainly due to the rapid compaction. The small velocity decrease at the base of the alluvial layer is not a robust feature of the NA-inversion results, and the amplitude of the corresponding negative receiver function peak is probably indistinguishable from noise.

The Siwaliks sedimentary layers show a mean velocity gradient of 0.3-0.45 s^{-1}, again consistent with an increase of compaction and a decrease of porosity with depth, with an average V_P/V_S -ratio of 2. The interface corresponding to the base of the basin is imaged at a depth of 4.75$\pm$0.25 km depending on the used cost function. It marks an important increase of S-wave velocity of 25 per cent, that produces a strong P-to-S conversion corresponding to the peak observed at $\sim$2 s on the receiver functions. This interface also induces several high-amplitude reverberations inside the basin, such as the negative arrivals at $\sim$6 and $\sim$8 s.

Fig. 6.5 shows synthetic receiver functions that demonstrate the sensitivity of the waveform on basin depth. We have tested three basin depths (2.75, 4.75, 6.75 km) using the velocity variations obtained during the inversion (Fig. 6.5e) and keeping the crust-mantle boundary at 40 km depth. The synthetic receiver functions (Figs 6.5a–c) show how sensitive the arrival time of the P-to-S conversion at the base of the basin is to the depth of this interface: a shallower or a deeper basin is unambiguously incoherent with the observations, and the value of 4.75 km is preferred.

The Moho is recovered at a depth of 40 ± 0.5 km, depending on the cost-function. It corresponds to the positive peak seen on the receiver functions at $\sim$7 s, as it is shown by the synthetic tests in Figs 6.5b and d. This depth value indicates that the thickness of the Indian crust, sediments excepted, is $\sim$35 km. Beyond the effect of the cost-function, the 1σ standard deviation of the best 50 inverted models gives an uncertainty of $\pm$300 m and $\pm$1 km on the depth of the basin and of the Moho, respectively. Moreover, analyses of the spread of the selected models show that there is a small remaining trade-off between the depth to an interface and the average velocity above it. All these uncertainties combined were taken into account for the geometrical constraints (Figs 6.6 and 6.8).

Inspection of the inversion results from south to north show that both the bottom of the basin and the Moho are sub-horizontal, very gently dipping to the north. The estimated dip beneath this part of the basin is $\sim$0.7°. This value is smaller than all estimates obtained from previous studies,which suggests a rather rigid India Plate. This new image of the Ganges foreland basin and the underlying crust is used as a geometrical constraint in the
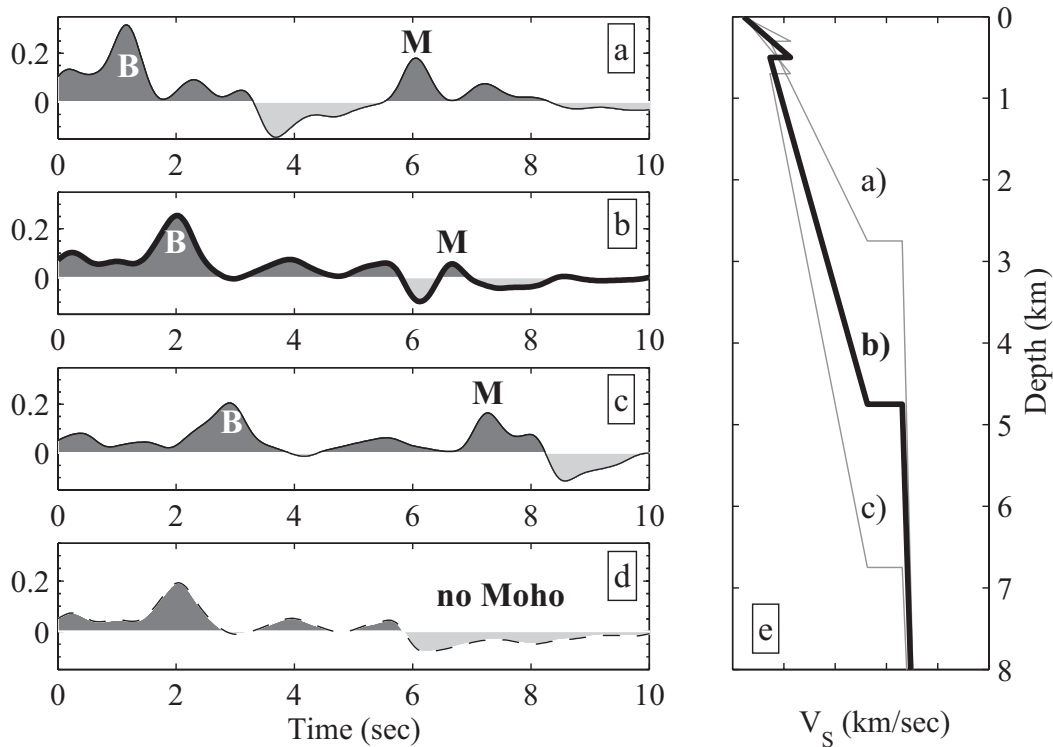
Figure 6.5: Synthetic receiver functions for sedimentary layers of different thickness, and the corresponding velocity models. (a)-(c): Comparison of receiver functions above a 2.75 km (a); a 4.75 km (b) and a 6.75 km; (c) deep basin. 'B' and 'M' give the arrival time of the P-to-S conversion at the base of the basin and at the Moho, respectively. The Moho is at 40 km depth in all cases; (d) is the same as (b) except that there is no Moho in the model; (e) Velocity model. The alluvial layer's thickness is 0.5 km, and shear-wave velocity is linearly increasing from 0.22 to 1.13 km·s^{-1} . The velocity of the sedimentary layer increases from 0.73 to 2.63 km·s^{-1} .

following part of this paper.

6.3.2   Moho depth from Ganges basin to central Tibet

At larger scale, the main crustal structures have been described in detail by many authors (*e.g.* Hirn *et al.*, 1984; Schelling and Arita, 1991; Zhao *et al.*, 1993; Avouac, 2003). Here, we summarize the estimates of the Moho depth from the Indo-Gangetic plain to central Tibet, which is the main geometric constraint on the flexural behaviour of the India Plate. Kumar *et al.* (2001) give a 33-39 km thick crust for the south Indian shield from teleseismic receiver functions. This thickness is consistent with our estimate of 35 km beneath the Ganges basin. Our results on the Ganges basin, seismological experiment
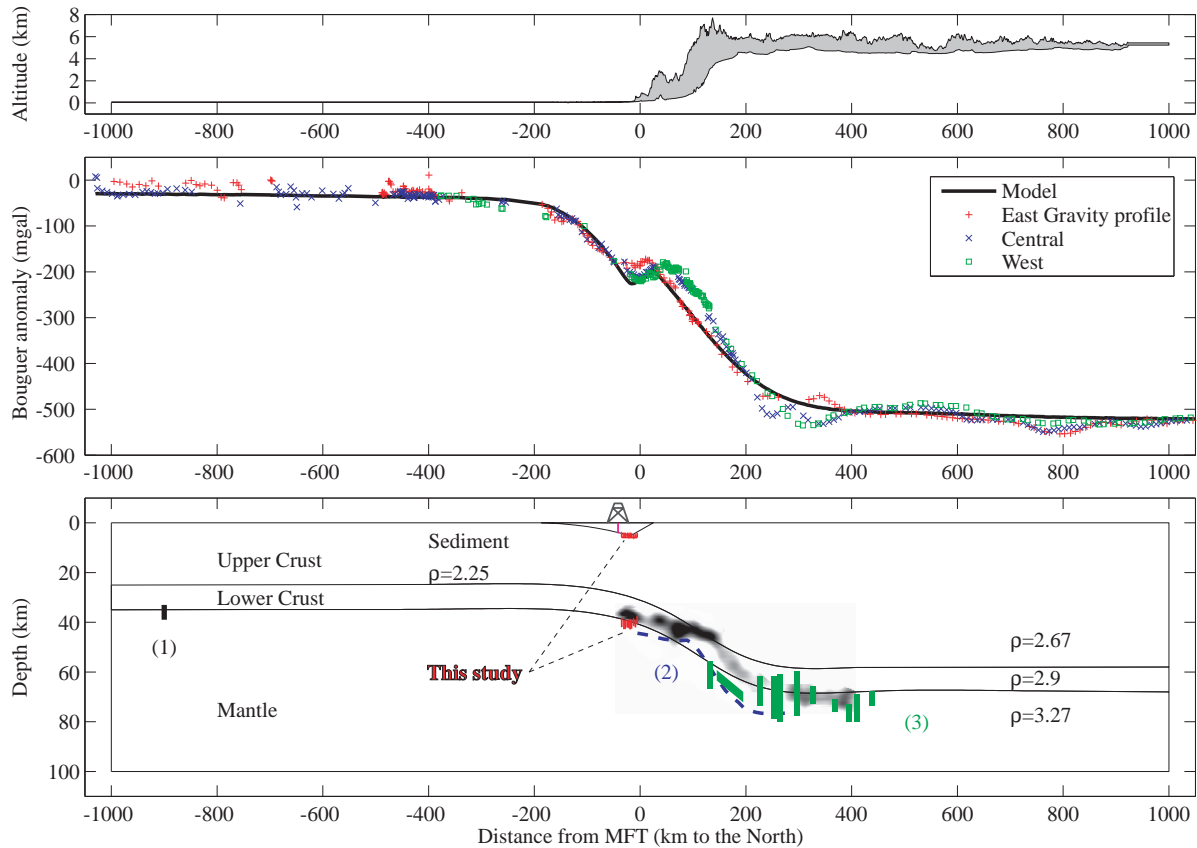
Figure 6.6: Data, model and results on a large scale profile. Top: minimum and maximum elevation averaged within 50 km on either side of the profile. Middle: data of the three gravity-measurement profiles (red +, blue X, green □, see Fig. 6.2 for location), and the calculated gravity anomaly (thick line). Bottom: the three-layer thermomechanical model with the sedimentary basin (densities are in g.cm³). In colour: different geometrical constraints: sedimentary basin and Moho depth from receiver functions (red error bars, this study); the Raxaul deep well's depth (magenta, Sastri et al., 1971); India Plate thickness from receiver functions (black error bar (1), Kumar et al.. 2001); Moho geometry (blue dashed line (2), Schulte-Pelkum et al., 2005, depth datum is local surface elevation); Moho depth and dip of INDEPTH (green, (3) for receiver function error bars (Hauck et al., 1998) and Moho dip from migrated reflection profiles (green, Alsdorf et al., 1998), depth datum is sea level); and the shape of the Moho from receiver functions of the Hi-CLIMB experiment (background image patches, Nábělek et al., 2005, depth datum is sea level). Results from other experiments were projected with reference to major thrust faults.

(Schulte-Pelkum *et al.*, 2005) and gravity measurements (Cattin *et al.*, 2001) all reveal that the Indian plate dips gently northwards. Both the HIMNT (Schulte-Pelkum *et al.*, 2005) and the Hi-CLIMB (Nábělek *et al.*, 2005) seismological experiments show a large

deepening of the Moho beneath the front of the High Himalayas over a distance of 200-250 km, in agreement with the steep gradient of the Bouguer anomaly . In southern Tibet, all available seismological studies suggest a crustal thickness of the order of 70-80 km, consistent with isostatic support of the Tibetan Plateau (Lyon-Caen and Molnar, 1985; Cattin *et al.*, 2001). All these features are summarized in the synthesis section shown in Fig. 6.6.

6.4 Modelling the flexure

6.4.1 Thermomechanical modelling

Following (Cattin *et al.*, 2001), our model is based on a N18°cross-section perpendicular to the range, extending from India to the Tibetan Plateau (Fig. 6.7).We use a 2-D finite element model (Hassani *et al.*, 1997) in a reference fixed to the India Plate. The Indian lithosphere is modelled by three bodies: the upper and lower crust and the mantle.

One of the main assumptions is that the model simulates the flexure of the India Plate only. Faults and mineral phase changes are not included. The load of the Himalayas, the Tibetan Plateau and crust are modelled by a vertical pressure $P(x,t)$, proportional to the average elevation and crustal thickness along the profile, which excludes shear forces. The horizontal convergence rate of 15 mm·yr^{-1} is simulated by the southward propagation of $P(x,t)$ with time. Similarly, the $\Delta P(x,t)$ accounts for the sedimentary infill of the foredeep. Sedimentation is assumed to maintain a flat foreland at a constant elevation (sea level) south of the MFT. The model accounts for the mechanical layering of the crust and the non-Newtonian viscous rheology of rocks as a function of temperature and pressure. The rheologies are dependent on temperature, which is calculated from Royden (1993)'s formulation using a constant surface heat flow that corresponds to a reduced mantle heat flow of 15 mW·m^{-2} , 273°K for the surface temperature and 2.5 μW·m^{-3} for the upper crustal heat production. The entire model is submitted to gravitational forces ($g = 9.81$ m·s^{-2}) and is supported at its base by hydrostatic pressure. Free vertical displacements are allowed at both ends of the model. Several tests, including model size, number of elements and time steps, are performed in order to avoid numerical instabilities related to the method and the boundary conditions, and to define characteristic parameters of our experiments. In further runs, the models have a length of 1500 km, include 9000 triangular elements, are ran for 10 Ma and each run is divided into 50'000 time steps.

During the exploration of the parameter space, 90 experiments are run altogether. The varied parameters are the following (between the limits shown in brackets): Young's
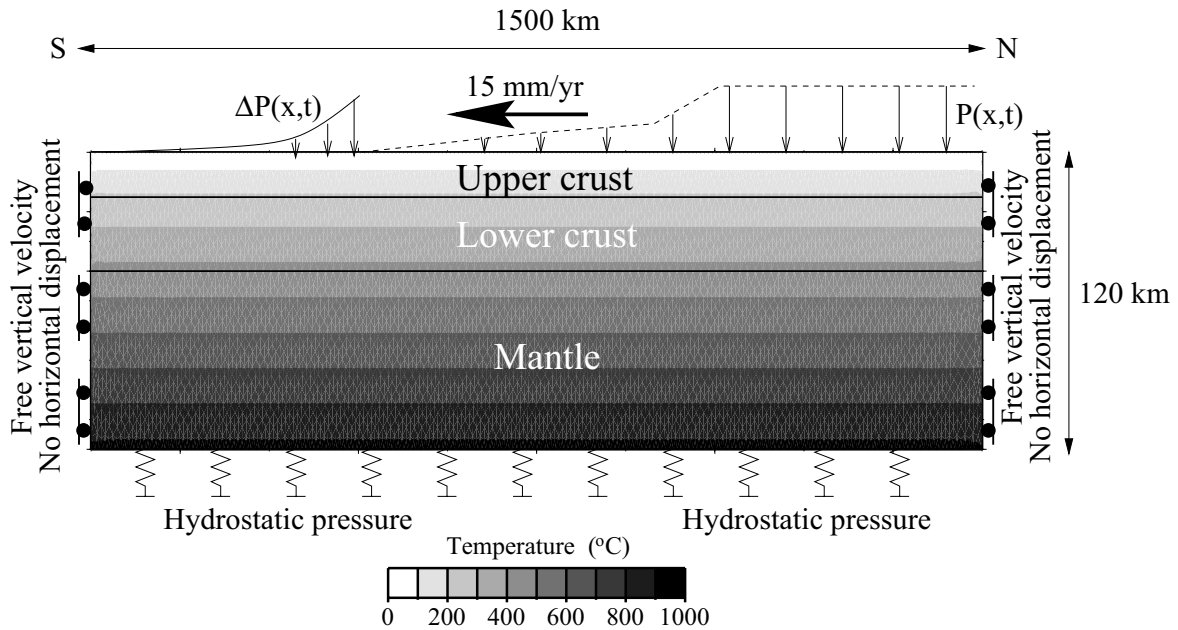
Figure 6.7: Initial stage of the thermomechanical model used in this study along a S-N profile. The mantle, the lower and upper crust are represented by three layers with different rheologies (Table 6.3). Vertical loads model the weight of the sediments (ΔP) and the crust Himalayas and Tibet (P). The load P moves southward at a rate of 15 mm·yr^{-1} to simulate the Tibet-India convergence. Temperature varies with depth, and the gravitational force is 9.81 m.s^{-2}. Free vertical displacements are allowed at both ends of the model, which is supported at its base by hydrostatic pressure. See text for more details.

modulus E [50-120 GPa], sediment density ρ_S [2250-2450 kg·m^{-3}], crustal thickness Z_M [34-38 km], initial depth of the boundary between the upper and the lower crust (the Conrad discontinuity) Z_M [10-25 km], upper crustal density ρ_{UC} [2600-2900 kg·m^{-3}] and Poisson's ratio η [0.25-0.29] of the India Plate.

Some of the above parameters with very small influence on flexure geometry are fixed in the following, such as the upper crustal density to 2670 kg·m^{-3} , Poisson's ratio to 0.25 and crustal thickness to 35 km. Table 6.3 summarizes a set of rheological parameters used for a 'strong-mantle' model composed of quartz, diabase and dunite. 'Weak-mantle' type yield stress envelopes — with several rheologies similar to the ones in Jackson (2002) — are also used to test the flexural behaviour of this type of lithosphere, while keeping all other boundary conditions the same. The results of all these experiments are compared to geometrical constraints, such as — primarily — the geometry of the basin (Fig. 6.8), and — secondarily — the geometry of the Moho along the profile (Fig. 6.6).

	Dry quartzite (upper crust)	Diabase (lower crust)	Wet dunite (upper mantle)
ρ kg·m^{-3}	2670	2900	3270
η	0.25	0.25	0.25
c (MPa)	10	10	10
Φ	30°	30°	30°
γ_0 $(MPa^n.s^{-1})$	$1.585 \cdot 10^7$	$6.31 \cdot 10^2$	398
n	2.9	3.05	4.5
E_a $(kJ.mol^{-1})$	149	276	498

Table 6.3: Rheological parameters used for a thermomechanical model with a strong mantle: ρ, density; η, Poisson's ratio; c, cohesion; Φ, internal friction angle; γ_0, power-law strain rate; n, power-law exponent and E_a, power-law activation energy. For exact equations, we refer to Cattin et al., (2001). Material properties are from laboratory measurements. The values are taken from the compilation of Le Pichon and Chamot-Rooke (1991).

6.4.2 Results and interpretation

Comparison with seismic images and limitations of the approach

The large number of performed test-runs shows that the geometry of the flexure is strongly influenced by the thickness of the upper crust, Z_C: the thicker it is, the smaller the curvature of the plate will be. This effect can be compensated or amplified by different sediment densities, Young's moduli, and by changing the rheology of the mantle. Geometrical constraints suggest a Young's modulus of 60-100 GPa, and we use $\rho_S = 2250$ kg·m^{-3} for sediment density, a value most consistent with geological observations. Two endmembers, with $Z_C = 15$ km and $Z_C = 25$ km will be analyzed in more detail in the next section.

Considering the above influences, a set of dozen solutions was found to best fit the geometrical constraints, and their geometry is represented at both small (Fig. 6.8) and large scale (Fig. 6.6). We emphasize that the obtained geometries are the result of modelling flexural support of the topography only. The observations related to both faults and mineral phase changes (*e.g.* eclogitization) are not included, thus cannot be reproduced. For example, uplifted recent alluvial sediments south of the MFT suggest the presence of a blind thrust fault underneath the Ganges basin (Schelling, 1992), which would slightly perturb the structure beneath stations H009 and H010, and thus explain the partly low quality fit of the model (Fig. 6.8). Other limitation of our modelling is being 2-D. Our calculations are consistent with data sets close to our study profile (gravity measurements, Hi-CLIMB profile, seismic reflection and the deep well data). However, our simple 2-D approach cannot reproduce lateral variations of the Moho shape imaged by the HIMNT
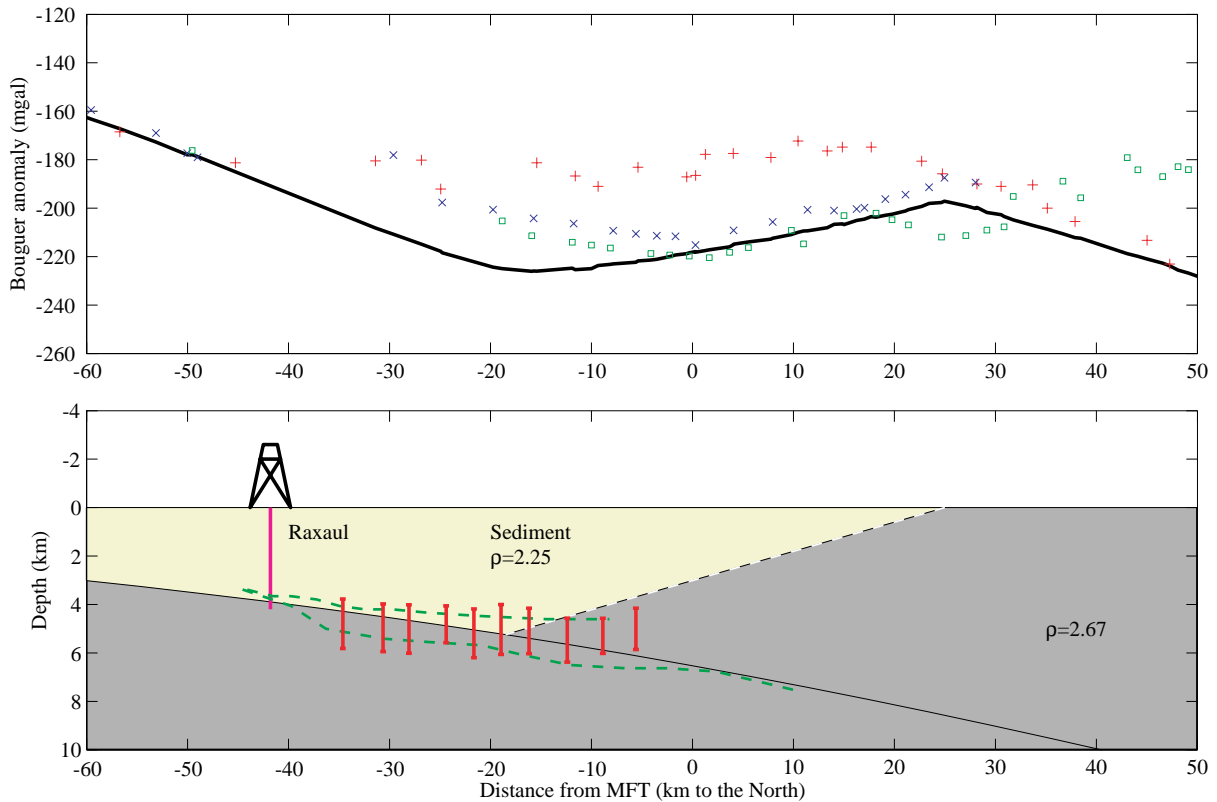
Figure 6.8: Data, model and results on a smaller scale profile. Top: measured and modelled small wavelength gravity anomaly (same legend as on Fig. 6.6). Bottom: flexural geometry of the final model with sedimentary infill (densities are in g.cm^{-3}). The basin ends with a straight ramp (black-white dashed line) in order to take into account density variations. In magenta: depth extent of the Raxaul deep well (Sastri et al., 1971), base of the basin imaged by receiver functions (red error bars, this study), and probable depth of the basin based on geological studies and seismic profiles (green dashed lines; DMG, 1990).

and INDEPTH profile, which are 160 and 400 km away from our study profile, respectively.

Comparison with Bouguer anomaly

To validate the set of obtained solutions, we calculate the Bouguer anomaly associated to the final geometry of the modelled bodies, including the Tibetan crust with a constant density of 2670 kg·m^{-3} . The calculations are performed using the USGS Hypermag software (Saltus and Blakely, 1995), which is based on the Ewing-Talwani lineintegral method. The calculated anomalies are then compared to several gravity data sets merged Cattin *et al.*, 2001 to construct a 2000 km long profile, which is close to our seismological network (Fig. 6.2).

Figures 6.8 and 6.6 show the obtained geometries by numerical modelling, and the calculated Bouguer anomalies superposed to the observed data at both small (foreland basin) and large (from India to central Tibet) scales, respectively. At large wavelengths (Fig. 6.6), the calculated anomalies are in very good agreement with the measurements. As previously proposed by Cattin *et al.* (2001), we interpret the discrepancy observed at 300 km in terms of eclogitization of the lowermost crust beneath southern Tibet. At a smaller scale (Fig. 6.8), our results are consistent with the general trend of the observations, showing a local minimum and maximum over a distance of ∼40 km. However, the residual gravity anomalies reveal two major disagreements: first, an offset of ∼15 km in horizontal distance, and second, a difference of ∼20 mGal in the amplitude. We interpret these disagreements as the joint effect of the followings.

1. The oversimplified geometry used for the northern end of the Ganges basin. We kept the entire geometry issued from the numerical model and added only a straight line (black-white dashed ramp), to add the fewest parameters possible, to model the northern end of the basin.

2. Local density contrasts due to both compaction and lithological variations.

3. Lateral variations of the observations.

Such refined modelling, which requires to take into account geological features such as the MFT, MBT and Palung granites, is out of the scope of this paper. More detailed explanation of the gravity anomalies north of the foreland basin can be found in Cattin *et al.* (2001).

Despite these local discrepancies between observed and calculated Bouguer anomalies, our thermomechanical approach explains most of available geophysical data, and thus demonstrates the internal consistency of the used data sets and its compatibility with current understanding of the support of the topographic load in the Himalayan border of the Tibetan Plateau.

Effective elastic thickness

The advantage of numerical thermomechanical modelling is an access to a great number of calculated physical parameters of the model, such as the effective viscosity

$$\eta = \frac{\sigma}{\dot{\varepsilon}} \tag{6.1}$$

where σ and $\dot{\varepsilon}$ are stress and strain rate, respectively. We use this parameter to assess the EET in our depth-varying rheology models. For a plate decoupled into n layers, the EET is given by (*e.g.* Burov and Diament, 1992)

$$EET = \left(\sum_{i=1}^{n} h_i^3 \right)^{1/3} \tag{6.2}$$

where h_i is the elastic thickness of the ith layer. For each layer, h_i is the thickness of the elastic core, where relaxation time of the material is at least twice as long as the time of the experiment. The relaxation time τ is defined as

$$\tau = \frac{\eta}{E} \tag{6.3}$$

with E being Young's modulus. The elastic part of a layer will be the region where η is larger than $\eta_{max} \sim$2-3·10^{25} $Pa\cdot s$ for a modelled deformation age of 10 Ma and Young's modulus between 60 and 100 GPa.

Figs 6.9(a and b) show the effective viscosity profile with $Z_C = 15$ and 25 km, respectively. Both of these models are in agreement with the geometries of the data sets and with the earthquake distribution obtained by Maggi *et al.* (2000) and Chen and Yang (2004). This suggests that it is not possible to determine from geometrical constraints if there is intra-crustal coupling or decoupling within the central Indian shield. In both cases, the flexural rigidity of crustal layers decreases northwards due to thermal and flexural weakening, resulting in a very thin elastic core of the India Plate beneath the High Himalayas, and in no elastic core of the Indian crust beneath Tibet. In the mantle, even if the more viscous zone becomes thinner northwards, the uppermost mantle remains well above the threshold value η_{max}. The mean depth of the elastic core of the India Plate is about 80-85 km beneath the surface of the Tibetan Plateau.

Fig. 6.10 gives the associated EET of the India Plate and the elastic thickness of each layer of the model along our study profile. Both cases show that there is a large decrease of the EET from south to north. In the south, beneath the central Indian Shield, the EET reaches a value as high as 70-80 km, which is consistent with its thermotectonic age (Burov and Watts, 2006). Decoupling of all layers from adjacent ones happens in a zone 200 km south of the MFT in both cases. Due to the cubic-mean employed in the calculation of the effective elastic thickness (Eq. 6.2), this leads to a sudden drop of the EET, down to the 30-40 km range. It can also be seen that the elastic thickness of the mantle is larger than the crustal EET, even when the upper and lower crust are coupled. This reveals clearly the main role played by the upper mantle in the strength of the India
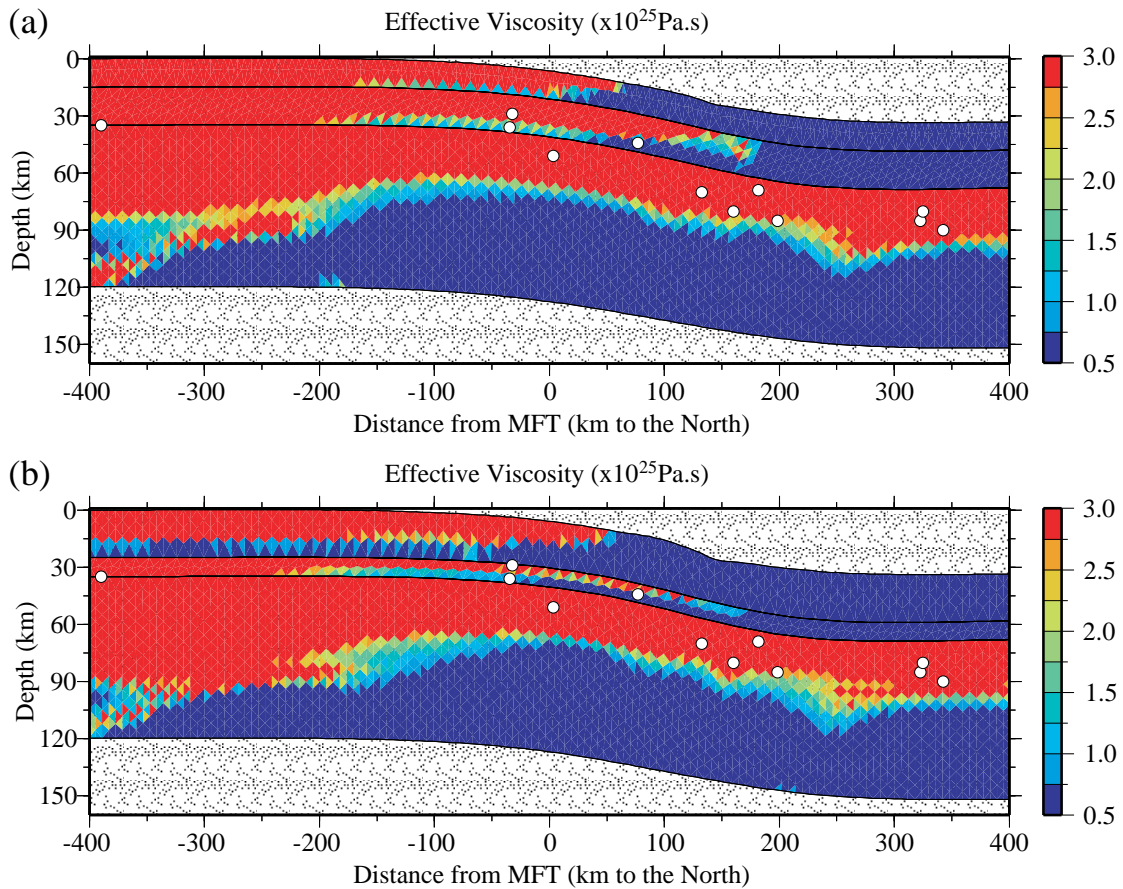
Figure 6.9: Effective viscosity profiles of the India Plate under a load simulating the Tibetan crust. (a) Completely coupled case under the Indian continent. (b) Decoupling at the upper crust-lower crust interface. White circles mark earthquakes discussed by Maggi et al., (2000) and by Chen and Yang (2004) as earthquakes occurring in the lower crust or in the upper mantle. Red areas are the strong, blue areas are the weak, ductile parts of the Indian lithosphere. In both cases, the mean depth of the elastic core of the India Plate is about 80-85 km beneath the Tibetan Plateau. Lightly dotted areas, outside of the plate, are not modelled.

Plate. North of the MFT, both the upper and lower crust loose their strength under the effect of flexure and temperature, while the elastic thickness of the mantle decreases only slightly. Here the EET of the Indian lithosphere ranges between 20 and 30 km, which is consistent with the value previously proposed by Jin et al. (1996). The main (and only) contribution to the strength of the Indian lithosphere comes from the mantle, as previously suggested by Lyon-Caen and Molnar (1983). This is true for all cases throughout the entire northern part of the profile, under the Himalayas and the Tibetan Plateau, which are thus mainly held up by a strong uppermost mantle. We note that if a real Tibetan crust was

present in the model, or eclogitization could be modelled, the EET might have a higher value in this region, but the strength of the Indian upper mantle and its role would remain the same.
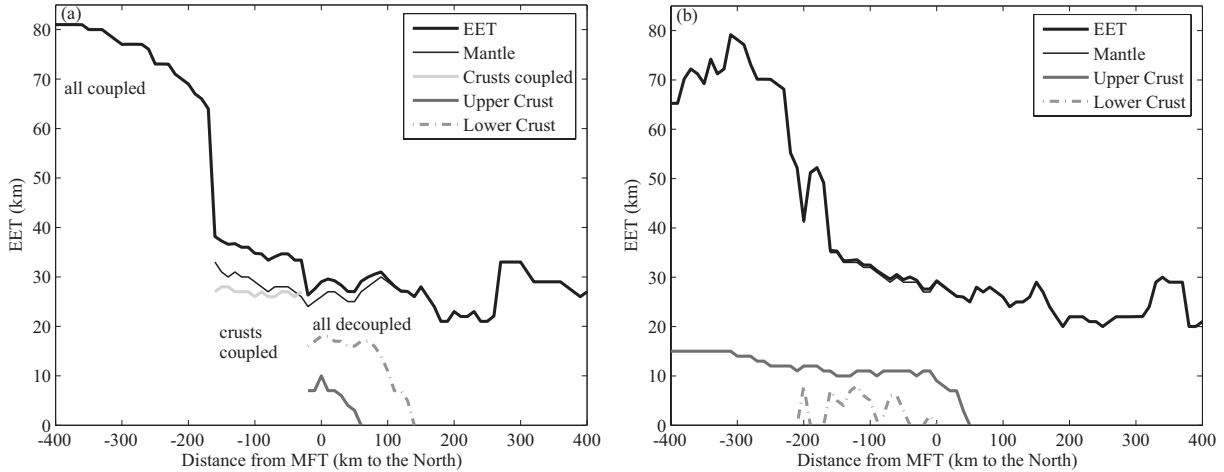
Figure 6.10: Effective elastic thickness of the different layers and of the entire Indian lithosphere, corresponding to Fig. 6.9(a) Completely coupled case under the Indian continent. Text inside the figure refers to ranges of distances with different coupling conditions between layers. (b) Decoupling at the upper crust–lower crust interface. In both cases, decoupling of the layers happens about 150-200 km south of the MFT, and the mantle remains the strongest part of the lithosphere north of this point.

Comparison with previous studies

The new seismological constraints on Moho and basin depths, together with existing data, have been used to constrain the output of numerical models, which allowed us to re-estimate the EET of the India Plate from India to central Tibet. Here we discuss the difference of our results with previous studies.

Our EET-estimate is consistent with the first studies based on analytical solutions of the flexure of a 2-D thin plate under both the weight of topography and sediments and the effect of additional bending moments (Lyon-Caen and Molnar, 1983; Jin *et al.*, 1996). The main difference compared to these studies is the better constraint on the depth of the basin, the modelling method (viscoelastoplastic behaviour, which includes thermal information, instead of elastic flexure with additional bending moment), and the larger amount of gravity-anomaly data used. As previously mentioned by Lyon-Caen and Molnar (1983), our results suggest a near-constant value of the EET in the region located ~150

km north of the MFT, and its low value is associated with the loss of the strength of the Indian crust beneath southern Tibet.

Our estimated EET value of 60-80 km in India and 20-30 km beneath the Tibetan Plateau is also consistent with the recent result of Jordan and Watts (2005) and Burov and Watts (2006), which suggest an EET of 40-100 and 70 km, respectively. However, a detailed comparison of our results with a section of the EET-map of Jordan and Watts (2005) along our profile shows that their maximum value obtained is higher by 20-30 km, and that the drop in the value of the EET occurs further to the north. The method of Jordan and Watts (2005) has some difficulties resolving high EET values based on gravity modelling, because there is little change in flexure and, hence, gravity anomaly for EET-values over ∼70 km (Tony Watts, personal communication, 2006). As of the difference in the position of the EET-drop, the coupled or decoupled state of the lithospheric layers is very sensitive to the assumed rheology and thermal regime, which are the less well controlled parameters in our modelling. The use of a slightly colder regime and/or a more viscous rheology (*e.g.* more mafic composition of the lower crust) would cause coupling of the layers further north and, hence, a better agreement.

In contrast, our results do not agree with the estimates of McKenzie and Fairhead (1997) and Jackson (2002), who give a constant EET of ∼40 km south of the MFT. Following Jackson (2002), we test several yield stress envelopes with a strong crust and a weak mantle using different viscous mantle and crustal rheologies in our thermomechanical modelling in order to check the 'weak-mantle' rheology. Most of the tests end with viscous or plastic instability, similarly to the results of Burov and Watts (2006). In the successfully finished tests, the obtained geometry is clearly inconsistent with the observations: the flexural geometry has its bulge at the location of the 4-km deep sedimentary basin, meaning that the wavelength of the flexure is much smaller than the real case (Fig. 6.11). We draw the attention to the gravity anomaly profile presented in Jackson (2002), which does not extend north of the MFT, and so it ranges between +20 and –60 mGal only, excluding the larger amplitudes (–550 mGal under Tibet in our profile). The limited extent of their profile may explain some of differences in the value of the EET. Moreover, our new seismological images of the Himalayan foreland suggest shallower structures than in earlier studies, so the reassessed earthquakes of Maggi *et al.* (2000) have occurred in the mantle (Fig. 6.9a).

Cattin *et al.* (2001) have previously performed thermomechanical modelling in this region and found a lower EET of 40-50 km in the Himalayan foreland. The difference from their study to the present paper is the new seismological data that helps to constrain the depth and shape of the Moho as well as the geometry of the Ganges basin. Our re-evaluated Indian crustal thickness is 35 km, compared to the assumed 40 km in Cattin *et al.* (2001).

Figure 6.11:   Flexural geometries   obtained   by 'strong-mantle' and 'weak-mantle'   type   rheologies. Dark gray error bars repre-sent the base of the basin imaged by receiver func-tions (this study), light gray line shows the depth of the Raxaul deep well (Sastri et al., 1971).
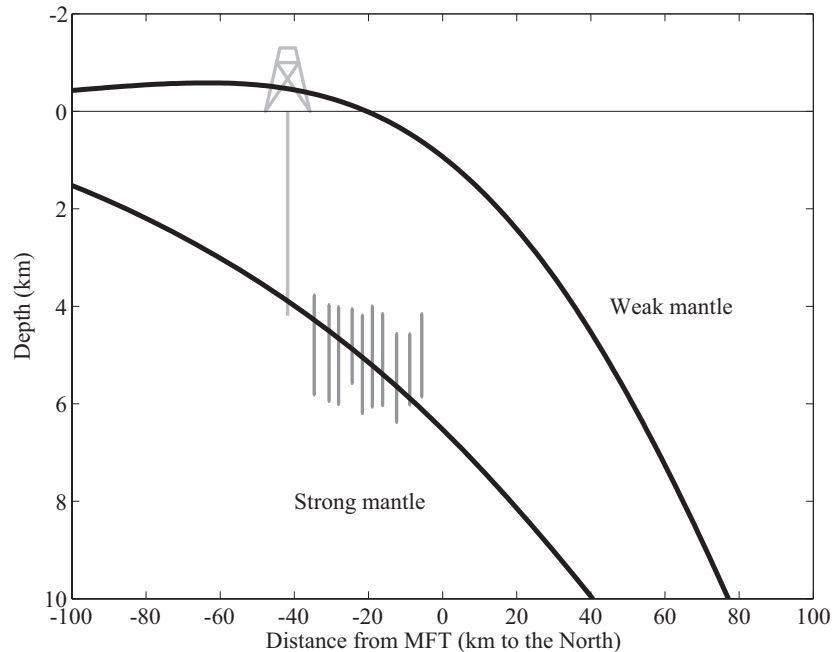
The use of this lower value resulted in the coupling of the mantle and the lower crust south of the MFT in our study, while they were decoupled in (Cattin *et al.*, 2001), yielding lower EET-values of about 20-30 km.

Dependence on relaxation time

The main feature of the presented EET-profile across the Himalayas is the general northward weakening of the lithosphere, and the sudden drop of the EET at 150-200 km south of the MFT due to the decoupling of the crust and the mantle. This EET-profile was calculated using a constant relaxation time of 10 Ma. However, it is clear that age of the deformation is not constant along the profile: it can be as high as 50 Ma in the Himalayas, and as low as a couple of millions of years in the foreland, as it is suggested by the age of the sediments. Fig. 6.12 represents a smoothed EET-map as a function of distance from the MFT and characteristic relaxation time, for both the coupled and decoupled case. The previous calculation with a relaxation time of 10 Ma corresponds to the abscissa. In order to take account for the variable age of deformation along a transect perpendicular to the mountain range, oblique sections-such as the 20 or 50 mm·yr^{-1} examples-should be considered. The use of these more realistic sections emphasizes the more important feature of the EET-profiles: a northward decrease from a value as high as 90 km to as low as 20 km is possible within a distance of 600 km. The transition is somewhat smoother in the coupled case (a) than in the decoupled one (b). This emphasizes the importance

of the uncertainties on the estimated EET, which clearly depends on parameters still unconstrained as the rheology of both crust and upper mantle, the thickness of the upper crust or the detailed timing of the deformation across the Himalayas. Based on our set of numerical tests we estimate that EET values obtained in this study should be handled with a 5-10 km error bar.
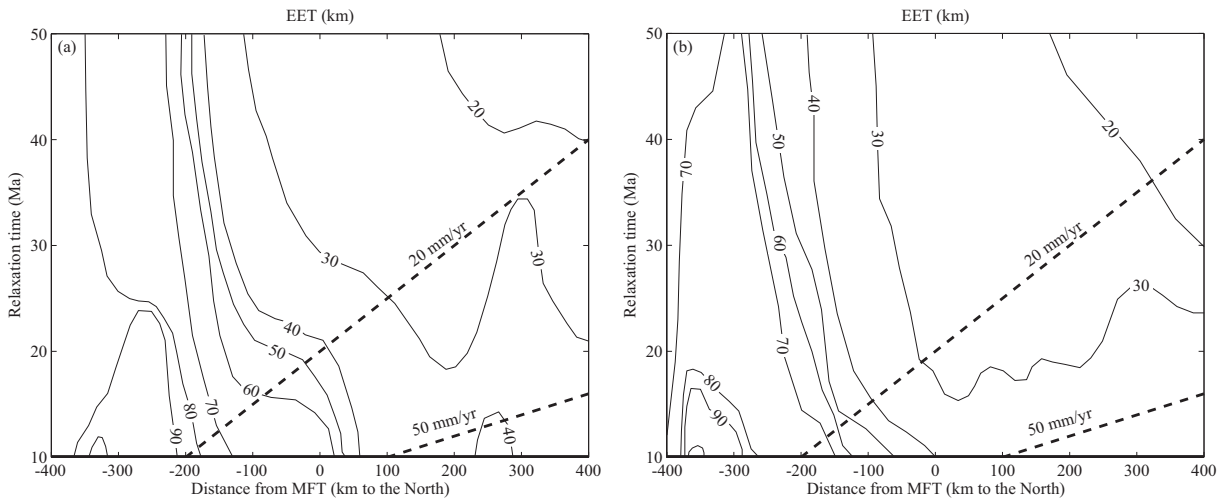
Figure 6.12: Map view of effective elastic thickness as a function of relaxation time and distance from the MFT. (a) and (b) represent the same cases as on Figs 6.9 and 6.10. The figures were drawn by calculating several EET-profiles with different effective viscosity threshold values corresponding to different deformation ages. The values on the abscissa (thick solid line), corresponding to 10 Ma of deformation age, are the values represented in Figs 6.9 and 6.10. An EET-profile associated to a higher deformation age is a section of this map along a horizontal line. Taking into account the difference in the age of the deformation under the Himalayas and of the foreland, oblique EET-profiles should be considered such as the dashed lines corresponding to different convergence rates. The main features of the EET-profiles (high values in the south, low values in the north) remain similar.

6.5   Conclusions

We re-evaluate the EET of the India Plate by using new seismological data of the Hi-CLIMB experiment, and by determining the geometry of the interfaces beneath the Ganges basin. Depths to the base of the sedimentary basin and to the Moho are found to be 5 and 40 km, respectively, with both interfaces dipping at a very shallow angle ($< 1.5°$). These, together with available geometrical constraints as well as the large-scale Hi-CLIMB image, are used in a three-layer thermomechanical model, in order to study the flexure

of the Indian lithosphere. We simulate the effect of the Tibetan Plateau using a vertical load.We neglect the effect of the EET of the Eurasian crust, associated with the elastic core of the upper and lower crust, and the decoupling of the shear zone, associated with the MHT. Thus, we favour a simple approach with no shear stress at the top of the India Plate.

Based on these assumptions, physical properties of the model then permit to calculate the effective elastic thickness along the entire profile. The results show that the EET of the India Plate:

1. Is high under the Indian continent ($>$ 60-70 km) due to the coupling between crust and mantle.

2. Drops to a value of 30-40 km in a transitional zone at 150-200 km south of the MFT because of gradual decoupling.

3. Reaches a value as low as 20-30 km north of the MFT due to the loss of the crustal strength. The elastic core in this region resides in the mantle of the India Plate, which implies that it is the main support of the Himalayan-Tibetan load.

The characteristics of the obtained EET-profile are even more emphasized if we take into account the age of deformation of each region. The resulting geometry and the densities associated to the layers allow calculating the gravity anomalies along the same profile, which are consistent with the observed gravity anomalies. The large disagreement in the value of the EET presented by earlier studies is probably due to the facts that either the model was too simple, either the data set did not cover the entire collision zone, or that the study was based on fewer types of data. Our results clearly show that rheologies with a weak mantle are not possible in this region, as the resulting flexural geometry is inconsistent with the observations.

Acknowledgements

Afterword

The presented study marks a new point in the debate on the rheology of the lithosphere. The principal improvement compared to previous studies is the exact geometry of the India plate's flexure, that became available with the Hi-CLIMB experiment.

Beyond the presented study, the results also serve in the interpretation of the receiver function migration of the main profile (see Chapter 5). The flatness of the Indian lower crust, underplated beneath Lhasa block, was much better constrained than the lineations in the lithospheric mantle. The fact that, in the numerical models, the crust and the mantle may decouple easily, suggests that the lower crust and the upper mantle may deform differently with regard to the compressive boundary conditions of the India plate.

Here the flexural geometry was modelled along one profile. However, as it was suggested by the seismological results in Chapter 4 and 5, lateral variations exist. These are reflected on Figure 6.6 where gravity anomalies along three different profiles differ as well. If the gravity anomaly variations are purely caused by differences in geometry, or if there are density inhomogeneities as well along the southern border of the Tibetan Plateau, is investigated by detailed Bouguer anomaly modelling density contrasts in the next chapter.

Mineralogical transformations and water in the lower crust

Foreword

In the previous chapter, we investigated the physics of the topography's support on the southern border of the Tibetan Plateau. Here we mainly focus on the mechanisms related to metamorphic facies and density changes in the lower crust, by extending the seismological results towards petrology and gravity anomalies. First of all, as it was presented in the previous Chapters (Fig. 5.14 and 6.6), lateral variations exist in the lithospheric image, both in Moho depth and in Bouguer anomalies. This study combines the new geometrical constraints with detailed gravity anomaly modelling, in the goal of determining where the main density transformations occur within the crust. The more important of these is the transformation of the lower crust into eclogite. The idea of eclogitization occurring further north than expected was already existing (*e.g.* Henry *et al.*, 1997; Cattin *et al.*, 2001), but these models were built on a very small number of constrained points at depth. Here the models are revisited and improved. First: the geometries are now much better known, and thus Bouguer anomaly modelling is reduced to finding densities within already contoured bodies. Second: petrological modelling provides accurate petrogenetical

(here density ρ as a function of temperature T and pressure P) grids that complete the set of tools applied to this issue. These grids point out the fundamental role of water content: this latter not only determines the possible density range of the lower crust *via* the dependence of stable mineral phases on the level of hydration, but also allows to account for kinetic delays of eclogite facies metamorphism.

7.0.1 Local isostasy

The study presented in this chapter has been accepted for publication in Earth and Planetary Science Letters. As an opening, here the first step of our analysis is developed. This consists of testing a local isostatic model for the structure beneath the Tibetan Plateau compared to India (Fig. 7.1a). In local isostatic compensation, the thickness of the crustal root derives from the extra weight of the topography (see Eq. 7.1), that we take along three profiles (Fig. 7.2). Assuming a simple crust-and-mantle model with homogeneous densities within each, we calculate synthetic gravity anomalies for a wide range of a crustal densities ρ_C and density contrasts across the Moho $\Delta\rho = \rho_M - \rho_C$. Then we calculate the misfit χ^2 between these synthetic and the observed anomalies (see Eq. 7.2).
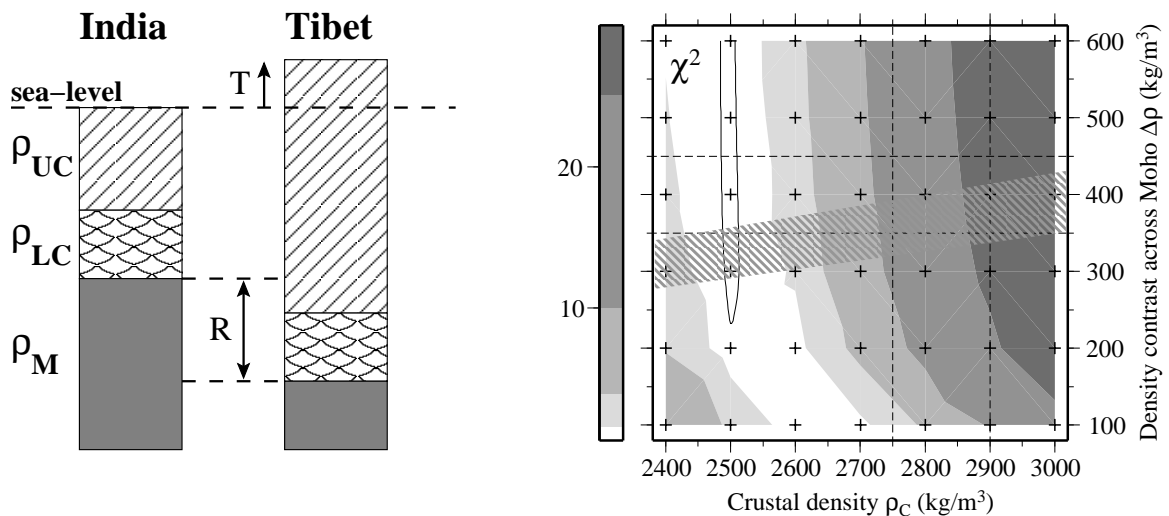
Figure 7.1: Left: a simple isostatic model with a mantle, a lower crust of constant thickness, and an upper crust thickened by crustal root **R** *due to topography* **T**. *Right: misfit between isostatic models and observed anomalies as a function of the density of the crust ρ_C and density contrast across the Moho $\Delta\rho$. The dashed zone is outlined by the ratio of the observed crustal root and topography from Equation 7.1. The dashed lines delimit the normal range for both ρ_C and $\Delta\rho$. See text for discussion.*

Figure 7.1b gives the misfit distribution in case of local isostasy in Tibet (the zone

more than 300 km north of the MFT) as a function of ρ_C and $\Delta\rho$. The best fit is obtained when the absolute value of the density is low (2500 kg·m^{-3} for the crust, 2800-3100 kg·m^{-3} for the mantle). Using an R/T ratio of 7-8.5 in Equation 7.1 (dashed zone on Fig. 7.1b) as inferred from seismological observations, the best-fitting model is obtained for $\rho_C =$ 2450-2550 and $\Delta\rho = $ 350-400 kg·m^{-3} . The density contrast between crust and mantle is in the normal range, but absolute densities are inconsistent with the known values. Thus we conclude that the observed Bouguer anomalies cannot be compatible with a simple isostatic model, and hence the depth of the primary density contrast should be located shallower than the seismological Moho.

Density distribution of the India plate beneath the Tibetan Plateau: geophysical and petrological constraints on the kinetics of lower-crustal eclogitization

György Hetényi [a], Rodolphe Cattin [a], Fabrice Brunet [a], Laurent Bollinger [b], Jérôme Vergne [a], John L. Nábělek [c], Michel Diament [d]

[a] *Laboratoire de Géologie, Ecole Normale Supérieure, CNRS – UMR 8538, 24 rue Lhomond, 75005 Paris, France*
[b] *Laboratoire de Détection et de Géophysique, CEA, BP12, 91680 Bruyères-le-Châtel, France*
[c] *College of Oceanic and Atmospheric Sciences, Oregon State University, Corvallis, OR 97331, USA*
[d] *Institut de Physique du Globe de Paris, 4 place Jussieu, 75252 Paris, France*

Editor: C. P. Jaupart

Abstract

We combine seismological and Bouguer anomaly data with thermo-kinematic and petrological modelling to constrain the extent and kinetics of the eclogitization process in the Indian lower crust underthrusting Tibet. Based on Airy-type isostasy gravity modelling, we show that the presence of denser material (eclogites) is required beneath the Tibetan Plateau. Using the geometries of main crustal interfaces constrained by seismological experiments along three profiles perpendicular to the Himalayan arc, multilayer density-models suggest that eclogitization of the Indian lower crust is completed where the maximal depth of its descent is reached.

In an integrated geophysical and petrological approach, the temperature field of the studied area is determined and realistic pressure–temperature–density grids are calculated assuming different hydration levels for the Indian lower crust. The derived density profiles are used to forward model Bouguer anomalies and to compare them to the observations. It appears that eclogitization of the Indian lower crust is delayed compared to where it

is expected to occur from phase equilibria. The results show that neither dry nor fully hydrated (free water in excess) lower-crust models are satisfactory. A hydration level of ca. 1 wt.% H_2O, consistent with a lower crust having experienced amphibolitic conditions, is more realistic and yields better results. On this basis, the densification delay of the Indian lower crust can be accounted for by a kinetic hindrance (overstepping) of the consumption of the plagioclase component (garnet and clinopyroxene forming reactions), which does not release water. Densification proceeds relatively rapidly (within 6 Myr) at higher pressure and temperature (at least 100°C above equilibrium), when dehydration reactions start releasing water.

These results emphasize the key role of free water in metamorphic reaction kinetics and, consequently, on geodynamical processes.

7.1   Introduction

The southern border of the Tibetan Plateau is the scene of continental collision since 50 Ma (Patriat and Achache, 1984). Over the last three decades this region has been extensively studied to understand both its building and its structure from various methods, including structural geology, petrologic observations, thermo-chronological data, GPS measurements and seismological experiments (*e.g.* LeFort, 1986; Zhao *et al.*, 1993; Jackson and Bilham, 1994; Lavé and Avouac, 2000; Bollinger *et al.*, 2004; Bettinelli *et al.*, 2006). The convergence across the Himalayas is mainly accommodated along major thrust faults, including the Main Central Thrust, the Main Boundary Thrust and the Main Frontal Thrust (Fig. 7.2)(*e.g.* Cattin and Avouac, 2000; Avouac, 2003). They all root to the Main Himalayan Thrust, which is imaged by the INDEPTH experiment between Sikkim and Lhasa (Nelson *et al.*, 1996; Hauck *et al.*, 1998) and by the Hi-CLIMB experiment in central Nepal (Vergne *et al.*, 2005). Indian crustal material is brought along this detachment to depths exceeding 50 km and at temperatures greater than 500°C. In these pressure–temperature conditions major metamorphic reactions take place in the Indian lower crust (ILC). Previous studies have shown that eclogitization of the lower crust is a key process in the support of high topographic elevation of both Himalayas and Tibet (Bousquet *et al.*, 1997; Henry *et al.*, 1997; Cattin *et al.*, 2001; Tiwari *et al.*, 2006).

However, the pressure–temperature path of the underthrust lower crust is still poorly constrained. Based on a receiver function profile and observed fast lower-crustal P-wave velocities, Schulte-Pelkum *et al.* (2005) argue that the lower crust is partially (∼30%) eclogitized just South of the Yarlung Tsangpo Suture (YTS), and that the eclogitization process is governed by water availability. This implies that the lower-crustal material reaches the eclogite facies via granulite facies conditions, as shown in Le Pichon *et al.* (1997) for geotherms established after more than ∼20 Myr of relaxation. However the latter study also shows that the geotherm may follow an amphibolite–eclogite and even a blueschist–eclogite path for shorter relaxation times between ∼10-20 Myr and less than ∼10 Myr, respectively.

The major shortcoming of these previous studies is the lack of accurate crustal geometries and thicknesses. Here we take advantage of the recent Hi-CLIMB seismic experiment, which imaged the main lithospheric structures from the Siwaliks to central Tibet (Nábělek *et al.*, 2005; Hetényi *et al.*, 2006). Along with the INDEPTH and the HIMNT experiments (Zhao *et al.*, 1993; Schulte-Pelkum *et al.*, 2005), these seismological profiles crossing the southern border of the Tibetan Plateau are used with gravity data to study both lateral variations and eclogitization of the Indian lower crust. First we discuss the
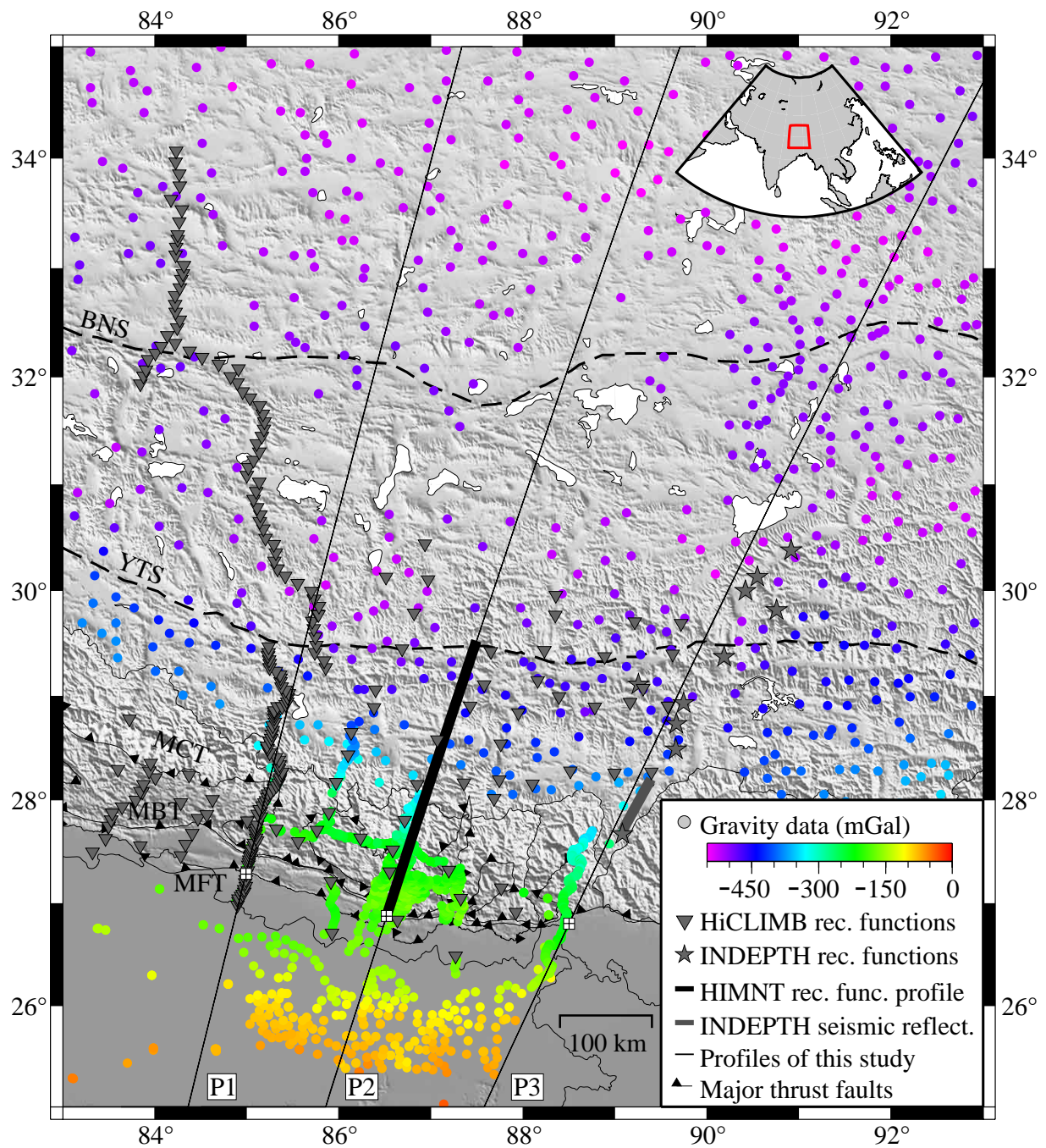
Figure 7.2: Topographic map showing the area of interest, the location of the compiled seismological and gravity data, and the profiles used in this study. The crosses indicate the origin of profiles with the following co-ordinates and orientations: P1 (27.2829° N, 84.9885° E, N14° E); P2 (26.873° N, 86.517° E, N17.8° E); and P3 (26.8° N, 88.5° E, N25° E). YTS and BNS are the approximate locations of the Yarlung Tsangpo Suture and the Banggong-Nujiang Suture, respectively. MCT, MBT and MFT are the Main Central, Boundary and Frontal Thrusts, respectively. Data points less than 100 km away from each profile are projected and constitute the constraints on the depth of crustal structures as well as the gravity anomalies to fit for each profile. Topography data are from the SRTM30 database (Rodriguez et al., 2005). All depths in this study are referenced to sea-level.

compensation of Tibetan Plateau in terms of Airy isostasy. Next, using both gravity anomalies and geometrical constraints we estimate density variation in the India lower crust. To better constrain the P–T path of the Indian lower crust, we calculate density distributions from thermo-kinematic modelling and accurate petrogenetic grids. These modellings yield a multitude of density distributions, which we evaluate by comparing their synthetic gravity anomalies to observed ones. Finally, introduction of reaction kinetics to the model is appraised and interpreted, together with the path of the Indian lower crust in the pressure–temperature space.

7.2   Seismological and gravity anomaly datasets

Previous studies have used seismological or gravity observations to image the main structures of the Himalayas and southern Tibet. The HIMNT experiment (Schulte-Pelkum *et al.*, 2005) reveals a descending Moho beneath the Himalayas and its flattening South of the YTS, which is the northern extent of surface occurrences of Indian-affinity rocks. However, the Moho's geometry further North remains unknown because the YTS marks the northern extension of this experiment. More recently the Hi-CLIMB project gave a higher-resolution crustal image from the Ganges Basin to the North of the Banggong-Nujiang Suture (BNS) along ∼85°E (Nábělek *et al.*, 2005; Hetényi *et al.*, 2006). Along this profile the descent of the India plate is clearly visible. The Indian lower crust smoothly crosses the YTS at depth, and underthrusts the southern part of the Tibetan Plateau almost until the BNS. This suture is known to be a major lithospheric limit: South of the BNS (Lhasa block), the crust is thicker and colder (Owens and Zandt, 1997), and shows better refracted wave propagation properties (Barazangi and Ni, 1982; Ni and Barazangi, 1983) than to its North (Qiangtang block). Analysis of Bouguer anomalies in the southern border of and across Tibet (Lyon-Caen and Molnar, 1983; Jin *et al.*, 1996) shows gravity anomalies as low as –500 mGal (1 mGal = 10^{-5} m·s^{-2}) and confirms a thickened crust all over the plateau.

To achieve good spatial coverage and study lateral variations on the southern border of the Tibetan Plateau, we gathered seismological and gravity anomaly data from several sources along three profiles associated with the INDEPTH, HIMNT and Hi-CLIMB seismological experiments (Figs. 7.2 and 7.3).

7.2.1   Seismological data

The seismological data come from three major experiments (Fig. 7.2). Phase 1 (South) of the Hi-CLIMB main array defines the line of profile P1 (Nábělek *et al.*, 2005). Profile P2 passes along the HIMNT experiment line (Schulte-Pelkum *et al.*, 2005). The southern path of the INDEPTH experiment through the Himalayas defines profile P3 (Nelson *et al.*, 1996; Hauck *et al.*, 1998). The obtained geometries of the main crustal boundaries are compared on Figure 7.3.
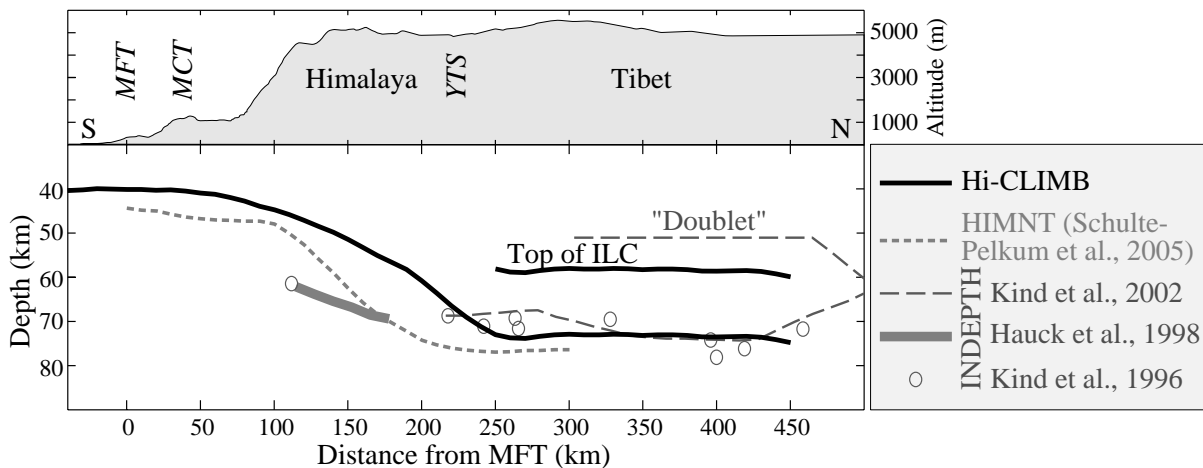
Figure 7.3: Above: mean topography along profile P1. Below: geometry of the Moho constrained by three seismological experiments along profiles P1 (Hi-CLIMB), P2 (HIMNT) and P3 (INDEPTH). The top of the Indian lower crust (ILC) imaged along profile P1, and the equivalent "doublet" along profile P3, are also represented. Vertical exaggeration is 3:1.

The depth-constraints of crustal interfaces for the Hi-CLIMB experiment (triangles on Fig. 7.2) come from receiver function calculations. We computed the receiver functions using the iterative time-domain deconvolution method of Ligorría and Ammon (1999) using a band-pass filter between 0.01 Hz and 0.5 Hz corner frequencies and 100 iterations. Along the main array, the calculated receiver functions are migrated using the Common Conversion Point method (Zhu, 2000), including altitude corrections and with a 2-D velocity-model constrained by calculating average V_P/V_S -ratios using multiples (Nábělek *et al.*, 2005). Using the P-to-S conversion image along with the stacked images of the multiples, we pick the depth of the Moho. The top of the Indian lower crust is well imaged beneath southern Tibet (Lhasa block). It is located 15 km above the Moho and exhibits a seismic signature generally stronger than that of the Moho, indicating a major increase in density and velocity. This 15 km lower crust is present beneath the Indian shield, but its upper limit has a smaller impedance contrast. For the lateral stations in Tibet (to the east of

the main array), the depth of the Moho and its error-bar are estimated by using the H$-\kappa$ stacking method (Zhu and Kanamori, 2000), and verified on sections migrated similarly as above.

The depth of the Moho along profile P2 comes directly from the interpretation of a migrated receiver function image of the HIMNT experiment (Schulte-Pelkum *et al.*, 2005). We report this as the Moho depth, and use our interpretation of the HIMNT raw migration image (located at a little shallower depth) as an estimate for the error-bar.

The geometry of the Moho along profile P3 comes from several interpretations of the INDEPTH dataset. First, we use the Moho depth interpreted from the INDEPTH I and II seismic reflection profile (Hauck *et al.*, 1998). We also use ten broadband stations (stars on Fig. 7.2) where the depth of the Moho has been estimated by individual receiver function inversions (Kind *et al.*, 1996). On the migrated receiver function profile by Kind *et al.* (2002), one can note a double seismic discontinuity at $\sim$55 km and $\sim$70-75 km depth, similarly to what is observed in the Hi-CLIMB experiment (see above). Again, we interpret this double discontinuity as the contour of the underthrust Indian lower crust; its disappearance occurs close to the BNS and marks a transition toward the North where the entire lithosphere is of Eurasian affinity.

7.2.2   Bouguer anomaly data

The gravity data used in this study are compiled from four sources. The largest dataset comes from the International Gravimetric Bureau (Bureau Gravimétrique International, BGI, http://bgi.cnes.fr). These gravity data are gathered from different experiments, and are provided as processed Bouguer anomalies covering well India and southern Nepal. Three arc-perpendicular profiles in Nepal were measured by joint French experiments (Cattin *et al.*, 2001; Martelet *et al.*, 2001). The eastern and the western of these profiles closely follow profiles P1 and P2, respectively. A study by Tiwari *et al.* (2006) provides new gravity data across the Sikkim Himalayas, which is in the continuation of the INDEPTH line corresponding to profile P3. Finally, we add the 5×5 *arcmin* gridded Bouguer anomalies over China (Sun, 1989), re-sampled at the locations of the measurements to overcome the smoothing processes. All these Bouguer anomalies were calculated using a reduction density of 2670 kg·m^{-3} , and all datasets except BGI include terrain corrections up to 167 km (Cattin *et al.*, 2001).

As gravity surveys yield relative measurements only, shifting of different datasets is allowed and required in order to obtain a homogeneous compilation. We use the BGI dataset as the reference, and check the consistency of the other datasets by comparing

values at geographically close measurements, and by looking at profiles perpendicular to the Himalayas containing data from several datasets. The data by Tiwari *et al.* (2006) need to be shifted by –66 mGal; the data by Cattin *et al.* (2001) and Sun (1989) are consistent with the BGI reference.

The gravity data projected along the three 2000 km long profiles give similar trends with a ∼500 mGal Bouguer anomaly decrease from the Ganges plain to the Tibetan Plateau. The average deviation on this general trend is on the order of ±10 mGal, with some smaller regions showing greater deviations of ±50 mGal.

7.3 Forward modelling: the isostatic case

The support of the Tibetan Plateau is often associated with crustal thickening in terms of local Airy isostasy (*e.g.* Jin *et al.*, 1996; Cattin *et al.*, 2001). Here we test this assumption using both gravity measurements and variations of crustal thickness inferred from seismological constraints along profile P1, where the best resolved and longest continuous dataset is available.

7.3.1 Calculations

Our method to calculate the 2D synthetic gravity anomalies is the following. First, we define the shape of the Moho on each profile from the seismological data described above. Based on observations along the Hi-CLIMB profile, where the Indian lower crust underthrusts the entire Lhasa block, we fix the lower-crustal thickness to 15 km. Similar value is used in the study of Tiwari *et al.* (2006), and is observed on INDEPTH data along profile P3. The Moho and the top of the Indian lower crust separate the model into three areas, to which we associate reference densities: ρ_M for the mantle, ρ_{LC} for the ILC, and ρ_{UC} for the upper crust. The model is extended at both ends: to the North at a constant depth corresponding to the northernmost observations, and to the South at 35 km Moho depth, as observed beneath the Indian shield (*e.g.* Saul *et al.*, 2000). Finally, our approach includes a sedimentary domain corresponding to the foreland basin, with a density of ρ_S = 2250 kg·m^{-3} and a geometry of the basement following Hetényi *et al.* (2006) for profiles P1 and P2, and Tiwari *et al.* (2006) for profile P3.

Then we use the algorithm of Won and Bevis (1987), based on the method of Talwani *et al.* (1959), to calculate the gravitational attraction of the defined polygons at the altitude of the observed data locations. The obtained anomaly curve is then shifted to the same

level as the observations in the southern part of the profile, where the mean level of the gravity anomalies does not differ significantly from zero.

We estimate the sensitivity of our modelling by vertically shifting the Moho depth beneath Tibet by ± 3 km, which is the average error-bar on the seismological image. The greatest deviation is ± 49 mGal, which is the same magnitude as the misfit between modelled and observed anomalies, and as the maximum extent of data dispersion along the profile.

7.3.2   Constraints on isostasy

In order to explain the observed gravity anomalies, we first test models assuming local isostatic compensation (Airy, 1855) of the Tibetan Plateau (the zone located beyond 300 km north of the MFT). These tests are performed using the topography and gravity data along profile P1, and with the simplification that the entire crust has a uniform density ($\rho_C = \rho_{LC} = \rho_{UC}$). In this case, the crustal root R (the deepening of the Moho) derives simply from topography as:

$$R = \frac{T \cdot \rho_C}{\Delta \rho}, \tag{7.1}$$

where $\Delta \rho = \rho_M - \rho_C$ is the density contrast across the Moho, and T is the average topography. Then the agreement of the observed (Obs_i) and calculated (Cal_i) gravity data is measured by the misfit function

$$\chi^2 = \frac{\sum_{i=1}^{N} \left((Obs_i - Cal_i) / \sigma_i \right)^2}{N}, \tag{7.2}$$

where N is the number of data samples, and σ is an estimate of data dispersion, defined in 40 equidistant intervals along the entire profile as half of the difference between the highest and lowest data value.

The value of the misfit, calculated for a wide range of ρ_C and $\Delta \rho$, shows that local isostatic compensation would occur if the density of the crust and the mantle were low (2500 kg·m^{-3} and 2800-3100 kg·m^{-3} , respectively). Even though the density contrast across the Moho is consistent with previous studies (Jin *et al.*, 1996; Cattin *et al.*, 2001), the absolute values of density are inconsistent with those known for a typical mantle and an average crust (*e.g.* Turcotte and Schubert, 1982; Christensen and Mooney, 1995; Szafián and Horváth, 2006). Thus we conclude that the observed Bouguer anomalies are not compatible with a simple isostatic model, and that the primary density contrast beneath Tibet should be introduced at shallower depth. In order to explain the anomalies, we construct more

realistic density models (see the next section), in which the used geometries already take into account regional isostatic effects due to the weight of the Tibetan Plateau and the flexure of the India plate (Hetényi *et al.*, 2006).

7.4 Density variations beneath Tibet

To better approach the real composition of the lithosphere, we take into account the density variations of the Indian lower crust due to eclogitization (see *e.g.* Henry *et al.*, 1997; Cattin *et al.*, 2001). In this metamorphic transformation process, the density of the lower crust increases to reach a value that is close to that of the mantle (Bousquet *et al.*, 1997; Jull and Kelemen, 2001). Bousquet *et al.* (1997) determined simplified petrogenetic grids, which show that the density of eclogites depends on the initial composition of the rock as well as on the P–T conditions, and ranges between 3080 and 3630 kg·m^{-3} . Based on these grids and on thermo-kinematic modelling, Henry *et al.* (1997) proposed that the high altitude of the Himalayas is related to the absence of eclogites beneath the mountain range, due to the fast rates of underthrusting of relatively cold material. Furthermore, based on gravity data combined with numerical modelling, Cattin *et al.* (2001) showed that eclogitization does not take place under the High Himalayan range as expected from a steady-state local equilibrium assumption, but further North beneath the Tibetan Plateau. More recently, Tiwari *et al.* (2006) showed that gravity and magnetic anomalies across Sikkim can be explained with a model in which the crust beneath Tibet (between 56 and 72 km depth) is eclogitized ∼100 km north of the YTS.

To explore the effect of density variation within the lower crust and to constrain its spatial extent, we first test two end-members models without and with densification, respectively, using the geometries of profile P1. Next we propose a gradual density variation that is consistent with the observed gravity anomalies for the three studied profiles.

7.4.1 Tests of densification of the Indian lower crust beneath Tibet

In the first test (Model 1), we suppose that Tibetan crust becomes denser with depth but we assume no density variation within the Indian lower crust (Fig. 7.4a). The calculated Bouguer anomaly is roughly consistent with the observed one between the Ganges plain and the High Himalayas. However in southern and central Tibet, the calculated anomaly is systematically lower than — and thus inconsistent with — the observed one. The misfit reaches up to 250 mGal in central Tibet, which implies that the primary density contrast is located deeper than necessary (undercompensation).
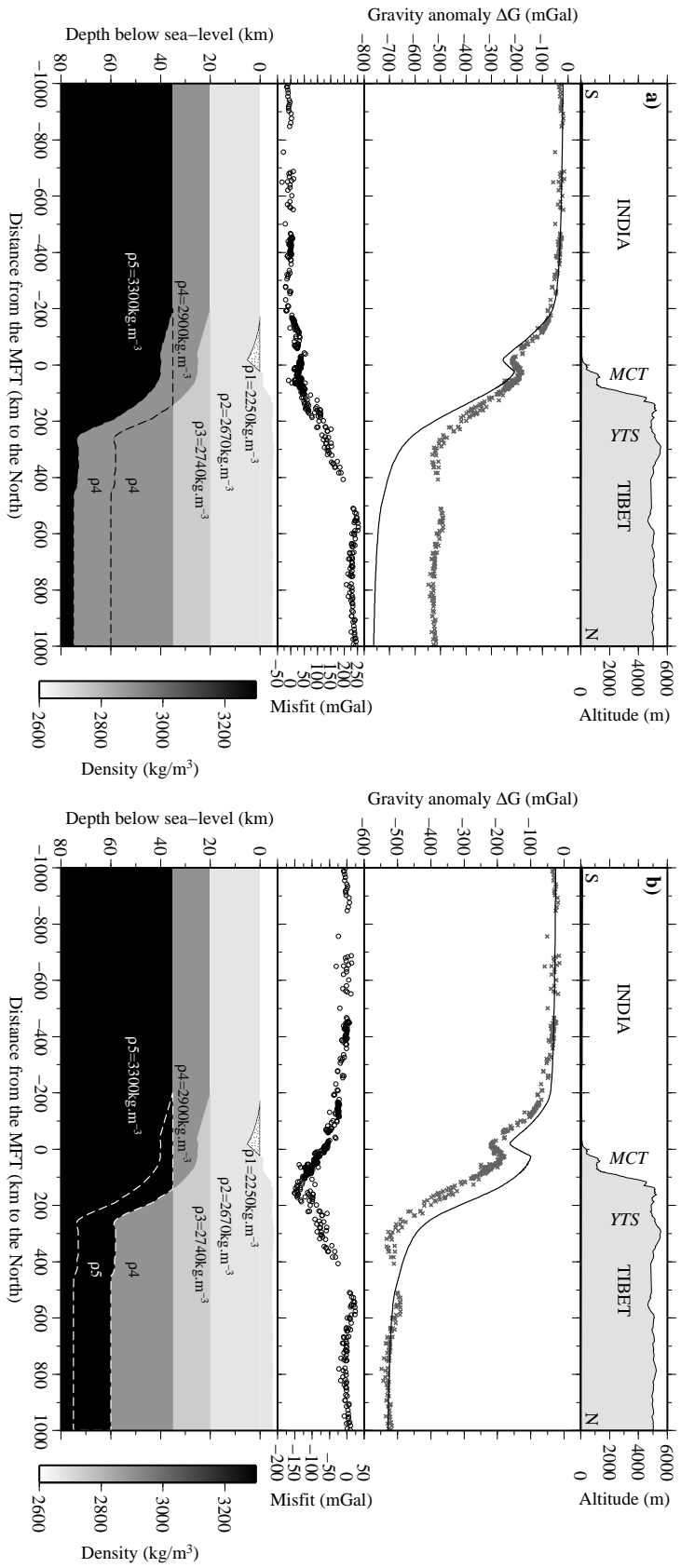
Figure 7.4: Two end-member tests without and with densification of the Indian lower crust. Top: Topography. Below: Observed (crosses) and calculated (solid line) Bouguer anomalies along the profile, and their difference (below). Bottom: Geometry and density of the bodies. The dashed line contours the underthrust ILC. (a) Model 1: no density variation within the Indian lower crust: while the differences between the model and the observations are small along most of the southern part of the profile, a clear divergence appears north of 100 km. (b) Model 2: sudden density increase of the entire Indian lower crust beneath 35 km depth: the misfit is small on both ends of the profile, but there is a clear difference between -200 and 500 km.

In the second test (Model 2), we assume a density increase of 400 kg·m^{-3} for the entire underthrust part of the ILC (beneath 35 km, Fig. 7.4b), thus its density contrast with the mantle is close to zero as suggested by Henry *et al.* (1997). However, we assume that the underthrust part remains lighter than the mantle and we do not address the question of delamination. The Bouguer anomaly corresponding to Model 2 presents a step of ∼500 mGal between India and central Tibet, in agreement with the observed anomaly. Nevertheless, the calculated anomaly is systematically higher than the observed one between −200 and 500 km distance, beneath the foreland basin and the Himalayan range, with a maximum deviation of ∼150 mGal, implying overcompensation in this zone.

The deviations between the calculated and observed anomalies in these two models represent end-members, and suggest a progressive density variation of the Indian lower crust. These changes occur between the foreland basin and southern Tibet, 500 km north from the MFT, where the density of the lower crust reaches the density of the mantle. We performed similar tests on profiles P2 and P3 and obtained identical results.

7.4.2 Gradual density variation of the ILC along profile and lateral comparisons

To model a gradual change of the Indian lower-crustal density from 2900 to 3300 kg·m^{-3} , we divide the zone between −200 and 500 km into 100 km long segments and vary their densities manually and stepwise. Numerous models have been tested to simulate northward densification, using linear density gradients on varying length as well as non-linear density changes, in order to minimize χ^2 in Equation 7.2. We similarly processed all three profiles; our results (Figures 7.5a–c) show many similarities but also some differences.

The similarities of the results lie in the fact that, in the very first order, the geometry of the Moho is quite similar along each profile: it starts at 35 km depth in the South and ends at about 75 km depth beneath the Tibetan Plateau. The density values show that the major change in density of the Indian lower crust occurs once it reaches its maximum depth. Also, a slow gradual change from lower to higher values takes place in the descending part.

The differences between the three profiles are also linked to the geometries: the steepness and the localisation of the lower crust's descent are particular to each profile. Between profile P1 and P2, the differences are small: profile P2 shows a somewhat steeper dip, located closer to the front of the range compared to profile P1, but both profiles reach their maximum depth in one ramp. This is not the case for profile P3: there is a flat part in the descent of the lower crust between two ramps, and constraints on the geometry (even
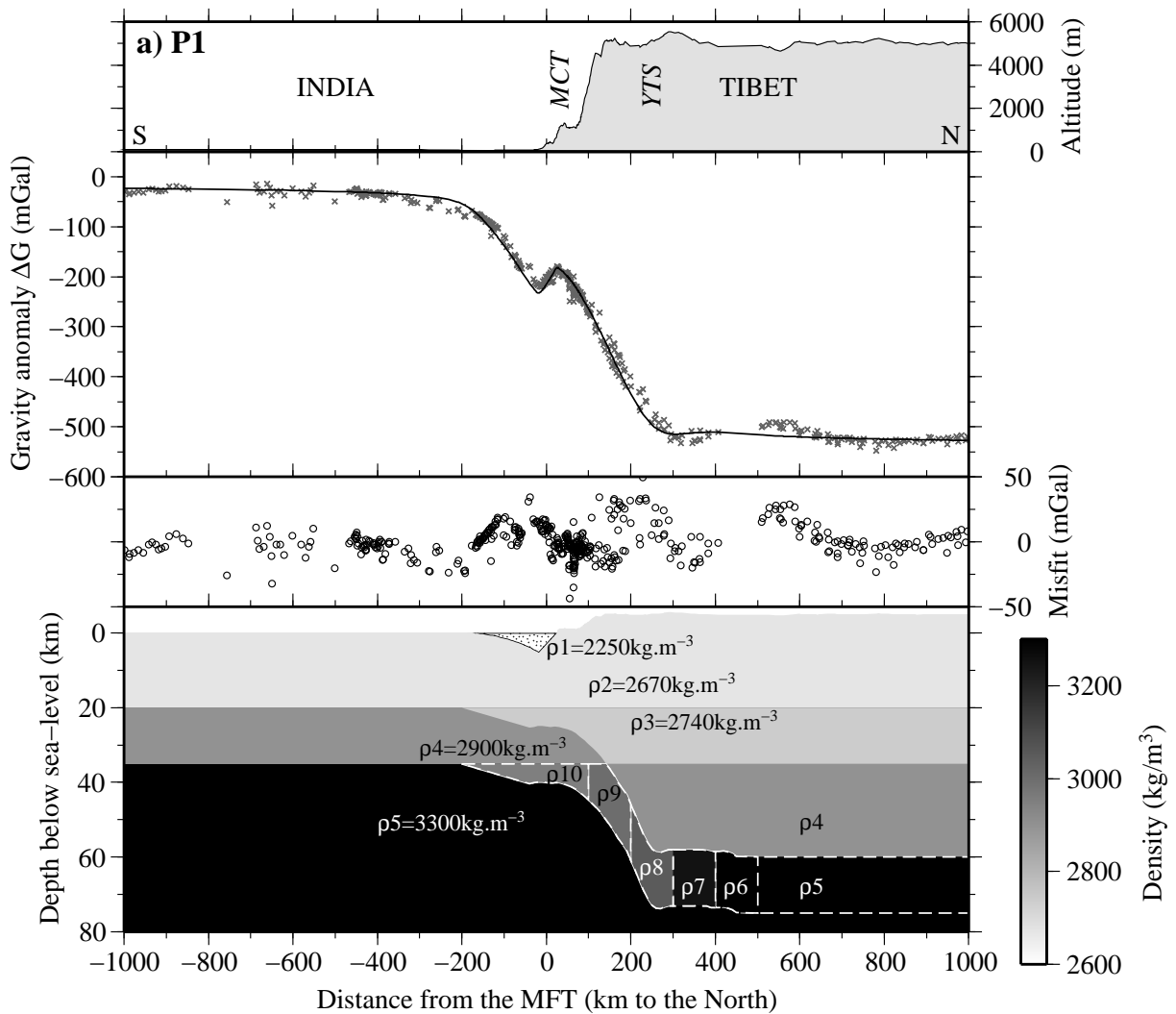
Figure 7.5: (a)–(c) Three models corresponding to the best fit solutions at profiles P1, P2 and P3 (graphs as on Fig. 7.4, b and c are on the next page). The imaged geometry of the Moho is assumed for all profiles with an Indian lower-crustal thickness of 15 km. The descending lower crust is divided into 100 km long bodies and their densities are varied independently to fit the observed Bouguer anomalies. These best models show that the major density jump occurs when the ILC reaches its maximum depth, what we interpret as the completion of the eclogitization process. The density-contrast between the crust and the mantle remains significant during the descent of the lower crust. White dots on the bottom graph of Figure 7.5b represent lower-crustal microseismicity relocalized by Monsalve et al.(2006). The white solid lines on the bottom graph of Figure 7.5c show the shear-wave velocity models obtained by inversion of receiver function data at individual broadband stations of the INDEPTH experiment (Kind et al., 1996), the overlying scale representing $1 \ km \cdot s^{-1}$ steps per tick in V_S . Density values that are not noted on the figures are the following: (a) $\rho_6 = 3300$, $\rho_7 = 3250$, $\rho_8 = 3050$, $\rho_9 = 3000$, and $\rho_{10} = 2950 \ kg \cdot m^{-3}$. (b) $\rho_6 = 3300$, $\rho_7 = 3100$, and $\rho_8 = 3050 \ kg \cdot m^{-3}$. (c) $\rho_6 = 3200$, $\rho_7 = 3100$, and $\rho_8 = 3000 \ kg \cdot m^{-3}$.
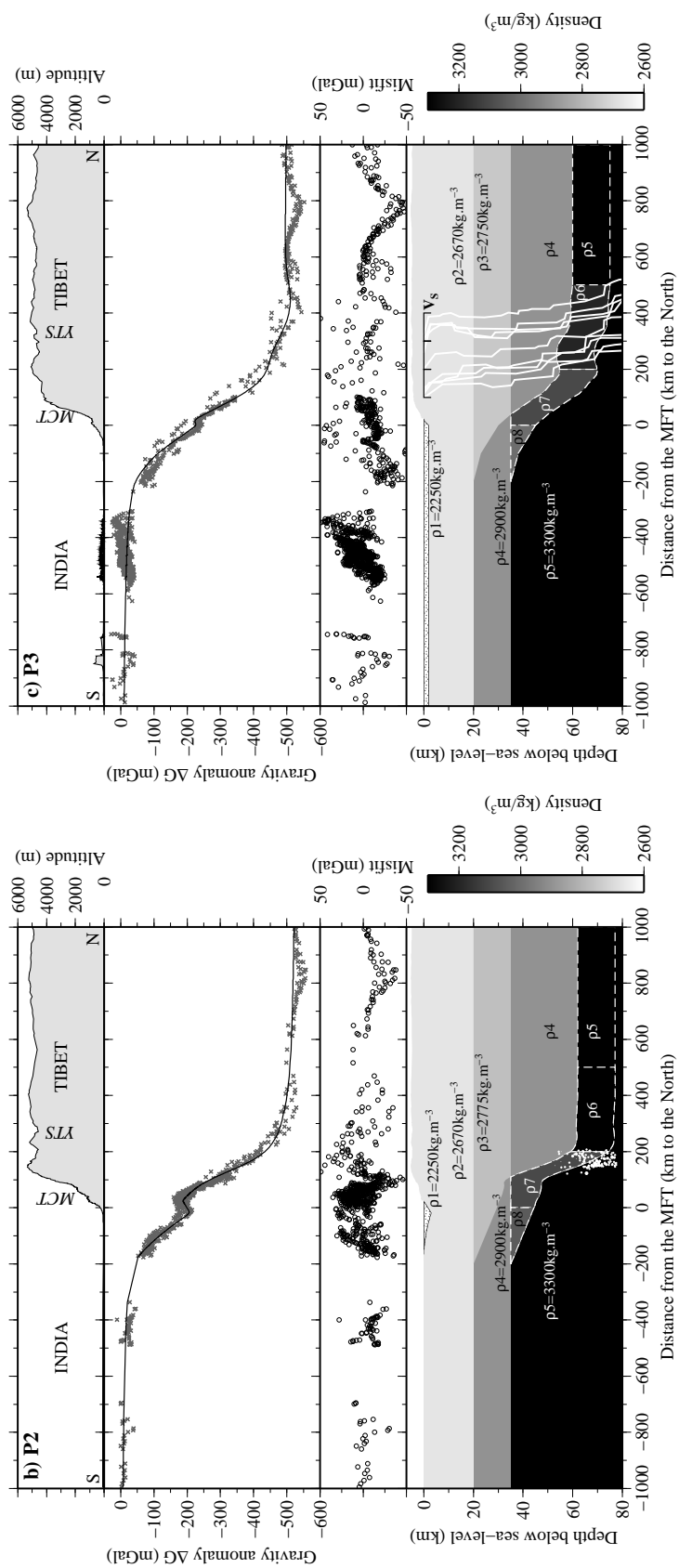
Figure 7.5b and 7.5c. See part 7.5a for caption.

if they are less tight) suggest that it plunges at a lower angle and on a longer distance than profiles P1 and P2. Thus the gradual change of density also takes place on a larger distance. One additional difference is the geometry of the foreland basin: while data are well explained by a flexural form at profiles P1 and P2, it is better represented with a shallower, flat-bottom basin at profile P3, as previously mentioned by Tiwari *et al.* (2006).

These results are also consistent with the detailed seismological image. The inverted receiver functions at individual stations of the INDEPTH experiment (Kind *et al.*, 1996) show a two-step transition in shear-wave velocity between the lower crust and the mantle in southern Tibet (white lines on Fig. 7.5c). These receiver functions are located in a zone where the density of the Indian lower crust is constant, but lower than that of the mantle. The same features are visible at Hi-CLIMB stations in Lhasa block (Nábĕlek *et al.*, 2005), and high lower-crustal velocities are observed in the northern part of the HIMNT experiment (Schulte-Pelkum *et al.*, 2005). This two-step transition can be explained by the high density of eclogites relative to their P-wave velocity (Guéguen and Palciauskas, 1992), which leads to two impedance-contrasts: one between the bottom of Tibetan crust and the top of the eclogitized Indian lower crust, and the second between the bottom of the ILC and the top of the lithospheric mantle. (More quantitatively, following Hacker and Abers (2004), at a pressure of 20 kbar and a temperature range of 600-700°C, we obtain a P-wave velocity of 7.5 ± 0.1 km·s^{-1} and a mantle density value of 3350 ± 30 kg·m^{-3} , the error-bars accounting for compositional variations of eclogite.)

Our findings confirm the results of Henry *et al.* (1997), which suggest that the extreme altitude of the Himalayas, in a zone between 100 and 200 km north of the front, can be explained by the absence of eclogites beneath them. Due to the fast subduction rate and the relatively cold temperatures, the eclogitization process is completed further North, at $\sim$300 km from the MFT (Henry *et al.*, 1997).

7.4.3   Limitations of this approach: towards a coupled petrological modelling

The ILC density at depth is estimated by taking into account large-scale observations only. This first-order approach, neglecting the presence of local geological features, appears to be reasonable. The limited spatial extent and second-order density contrast of these features contribute to gravity anomalies only within the dispersion of the data (tens of mGals).

Also, we neglect here density variations resulting from thermal expansion and compressibility. Furthermore, the petrological relevance of the gradual density change occurring

in the ILC, which is inferred from geophysical data, has not been evaluated. This evaluation requires the modelling of metamorphic transformations, in particular eclogitization at depth. This is only possible if the pressure and temperature distributions beneath Tibet are accurately established. In the next section we overcome these limitations and we combine thermo-kinematic modelling and petrogenetic grids to evaluate the petrological relevance of the density models retrieved above.

7.5 Integrated geophysical and petrological approach: modelling

The density of the Indian lower crust beneath the Tibetan Plateau can be determined from the temperature field at depth (thermo-kinematic model) and from phase equilibria calculation (petrological modelling) for a given lower-crustal composition.

The comparison between the density distribution derived from geophysical data (see above) and that predicted by combining petrological and thermo-kinematic modelling provides an indirect way to probe the phase transformations occurring within the Indian lower crust.

7.5.1 Thermo-kinematic modelling

We use a finite-element thermo-kinematic model (FEAP, Finite Element Analysis Program) which solves the heat advection–diffusion equation in transient state (Zienkiewicz and Taylor, 1989) to obtain the temperature field beneath the Himalayas and southern Tibet; including thermal expansion and compressibility. Using this modelling approach, Bollinger *et al.* (2006) reproduced the inverse metamorphic gradient, peak temperatures and exhumation ages, constrained by dense field observations across the Himalayan range in central Nepal.

Our model is similar to the one presented by Bollinger *et al.* (2006) and is shown on Figure 7.6. It includes a single thrust zone (MHT) with an accretion window, five layers of uniform physical properties within each, steady-state topography, and a convergence rate across the range of 21 mm·yr^{-1} , matching the Holocene shortening rate (Lavé and Avouac, 2000). For more details, we refer to Bollinger *et al.* (2006) and references therein.

As our model focuses on the lower Indian crust, we update the previously used geometry according to seismological observations: the Moho beneath India is located at 35 km, the lower crust has a constant thickness of 15 km, and the descent of the plate is
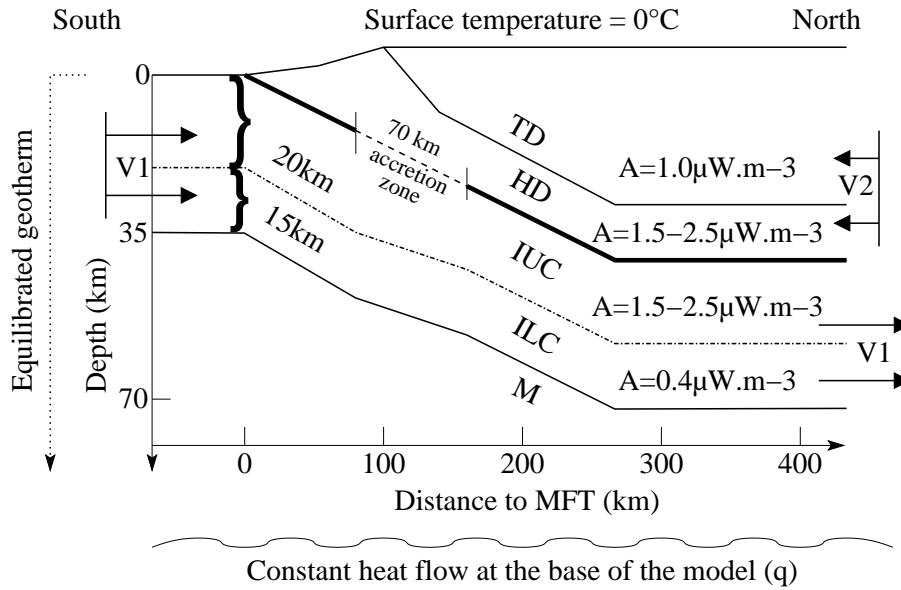
Figure 7.6: Geometry, thermal parameters and boundary conditions of the thermo-kinematic model, after Bollinger et al.*(2006): M: mantle; ILC: Indian Lower Crust; IUC: Indian Upper Crust; HD: Himalayan Domain; TD: Tethyan Domain. The thick solid line denotes the Main Himalayan Thrust, along which India underthrusts Tibet. The velocities of the two blocks are kept constant (underthrusting rate of V1 = 17 mm·yr^{-1} , overthrusting rate of V2 = -4 mm·yr^{-1}), such as the radioactive heat production of the lower crust (0.4 $\mu W·m^{-3}$; Pinet* et al.*, 1991) and of the Tethyan Domain (1.0 $\mu W·m^{-3}$). The varied parameters are the basal heat flow and the radiogenic heat production in the HD and the IUC.*

continued until the Moho reaches a depth of 73 km.

Following previous studies (Henry *et al.*, 1997; Bollinger *et al.*, 2006), we test the effect of two thermal parameters: upper crustal radiogenic heat production A, and basal heat flow of the model q. The latter parameter is varied between 15 mW·m^{-2} (Pinet *et al.*, 1991; Gupta, 1993) and 30 mW·m^{-2} (Rao *et al.*, 1976) by steps of 2.5 mW·m^{-2} . Since the radiogenic heat production of the Indian upper crust beneath the Himalayas, of the Lesser Himalayas and of the overlying High Himalayan Crystalline are still largely unconstrained, locally ranging between 0.7 and 5 μW·m^{-3} (Menon *et al.*, 2003), we have considered that 1.5 and 2.5 μW·m^{-3} represent mean low and high values in these regions and adopted these end-members for A. These values appear to be consistent with the few heterogeneous local estimates of the High Himalayan crystalline radiogenic heat production (England *et al.*, 1992). Aside from the above parameters, the model follows the one in Bollinger *et al.* (2006) including the granodioritic composition of the Himalayan and Tethyan domain, as well as of the Indian upper crust. The composition of the Indian lower crust is discussed in the

following section.

7.5.2 Petrological modelling

To assess the gravity anomalies produced by a density-distribution based on a thermo-kinematic model, one needs to know the dependence of density as a function of temperature and pressure.

We calculated mineral compositions and modes for an average lower crust composition as a function of pressure and temperature using Perple_X (Connolly, 2005). For a given composition and a set of solution phases, Gibbs energy is minimized to map the phase relations on that composition. Then, physical properties, such as density, are derived. A high density resolution (in the P–T space) and a high accuracy level can be achieved with this software since mineral compositional variations with P and T are taken into account along with thermal expansion and compressibility for individual phases. In all cases, density models derived from Perple_X assume thermo-chemical equilibrium at all scales.

We use an average lower-crustal composition based on Rudnick and Fountain (1995) and Rudnick and Gao (2003) with eight major oxide components (including water; see Table 7.1). The selected solid-solution data and the corresponding thermodynamic sources are listed in Table 7.2. Actually, we have considered three different lower crust compositions differing only in their water content.

- MW (Mafic and Wet) is a fully hydrated lower crust. Full hydration means that the water content in MW corresponds to the minimum water content required to stabilize all the hydrous phases (and in the same proportion) as in a water-saturated system under greenschist/blueschist facies conditions, *i.e.* conditions at which the Indian lower crust enters the Himalayan subduction. This hydration level is derived from the Perple_X output (5.54 wt.%).

- MD (Mafic and Dry) is a completely dry lower crust without any hydrated mineral. We suppose here that the Indian Lower Crust experienced granulitic P–T conditions without being rehydrated before entering the Himalayan subduction.

- MPH (Mafic and Partially Hydrated) is a partially hydrated lower crust (1 wt.% H_2O). This simulates a scenario where the Indian Lower Crust first experienced amphibolitic conditions (with no subsequent hydration event) and then re-equilibrated under greenschist/blueschist conditions prior to underthrusting.

Model Name:	MW (Wet)	MD (Dry)	MPH (1% water)
SiO_2	53.961	53.961	53.422
Al_2O_3	17.078	17.078	16.907
FeO_x	8.660	8.660	8.573
MgO	7.316	7.316	7.243
CaO	9.691	9.691	9.594
Na_2O	2.678	2.678	2.651
K_2O	0.616	0.616	0.610
H_2O	0.0-5.54⋆	0.0	1.0
TOTAL	100.00	100.00	100.00
Hydration	Full	None	Partial

Table 7.1: *Petrological model parameters, with composition of the lower crust in weight percent (Rudnick and Fountain, 1995; Rudnick and Gao, 2003). ⋆For the MW model, the H_2O component is in excess (i.e. fully hydrated assumption). This corresponds to a hydration level for the ILC (amount of water contained in hydrous minerals) comprised between 0.24 wt.% and 5.11 wt.% H_2O depending on the P–T conditions along the P–T path derived here. The hydration level of the ILC before it is underthrust amounts to ca. 3 wt.% H_2O.*

7.6   Results and discussion: constraints on eclogitization of the Indian lower crust

For the sake of simplicity, the following sections are structured in a way that the parameters of the ILC density model based on thermo-kinematic and petrologic constraints which fits better the geophysical data, called "best fit model" hereinafter, are presented first. Then the sensitivity of these parameters is discussed in detail, and the various constraints on the thermo-kinematic and petrologic modelling are addressed. Finally, we show how this combined approach can provide new constraints on the eclogitization kinetics of the ILC.

7.6.1   The best fit model

Figure 7.7 shows the best fit model solution of this study. It yields gravity anomalies in very good agreement with measurements, leading to a misfit lower than 50 mGal, and in many cases lower than 25 mGal, which corresponds to the estimated error of our dataset. This result clearly confirms the major role of eclogitization in the support of Tibet. The density distribution of this model is obtained by using a temperature field calculated with $A = 2.5~\mu W \cdot m^{-3}$ and $q = 15~mW \cdot m^{-2}$, an amphibolitic crust (MPH model) and a delay in

Phase	Formula	Source
biotite	$K[Mg_xFe_yMn_{1-x-y}]_{3-w}Al_{1+2w}Si_{3-w}O_{10}(OH)_2$, $x+y \leq 1$	Powell and Holland, 1999
orthopyroxene	$[Mg_xFe_{1-x}]_{2-y}Al_{2y}Si_{2-y}O_6$	Holland and Powell, 1996
clinopyroxene	$Na_{1-y}Ca_yMg_{xy}Fe_{(1-x)y}Al_{1-y}Si_2O_6$	Holland and Powell, 1996
muscovite	$K_xNa_{1-x}Mg_yFe_zAl_{3-2(y+z)}Si_{3+y+z}O_{10}(OH)_2$	Holland and Powell, 1998
clinoamphibole	$Ca_{2-2w}Na_{z+2w}[Mg_xFe_{1-x}]_{3+2y+z}Al_{3-3y-w}Si_{7+w+y}O_{22}(OH)_2$, $w+y+z \leq 1$	Wei and Powell, 2003; White et al., 2003
garnet	$Fe_{3x}Ca_{3y}Mg_{3z}Mn_{3(1-x-y-z)}Al_2Si_3O_{12}$, $x+y+z \leq 1$	Holland and Powell, 1998
feldspar	$K_yNa_xCa_{1-x-y}Al_{2-x-y}Si_{2+x+y}O_8$, $x+y \leq 1$	Fuhrman and Lindsley, 1988
talc	$[Mg_xFe_{1-x}]_{3-y}Al_{2y}Si_{4-y}O_{10}(OH)_2$	
sapphirine	$[Mg_xFe_{1-x}]_{4-y/2}Al_9Si_{2-y/2}O_{20}$	Holland and Powell, 1998
spinel	$Mg_xFe_{1-x}Al_2O_4$	
chlorite	$[Mg_xFe_wMn_{1-x-w}]_{5-y+z}Al_{2(1+y-z)}Si_{3-y+z}O_{10}(OH)_8$, $x+w \leq 1$	Holland et al., 1998
chloritoid	$Mg_xFe_yMn_{1-x-y}Al_2SiO_5(OH)_2$, $x+y \leq 1$	White et al., 2000

Table 7.2: Selected solid solutions for petrological modelling, corresponding formulae and thermodynamic references. The thermodynamic data used by the Perple_X code are based on Holland and Powell (1998, updated in 2002). The compositional variables w, x, y, and z may vary between zero and unity and are determined in Perple_X as a function of computational variables by free-energy minimization.

eclogitization, which prescribes that eclogitization occurs between 300 and 350 km north of the MFT rather than between 0 and 80 km. Constraints on the above three conditions, together with the path of the Indian lower crust in the P–T space, are described in the following sections.
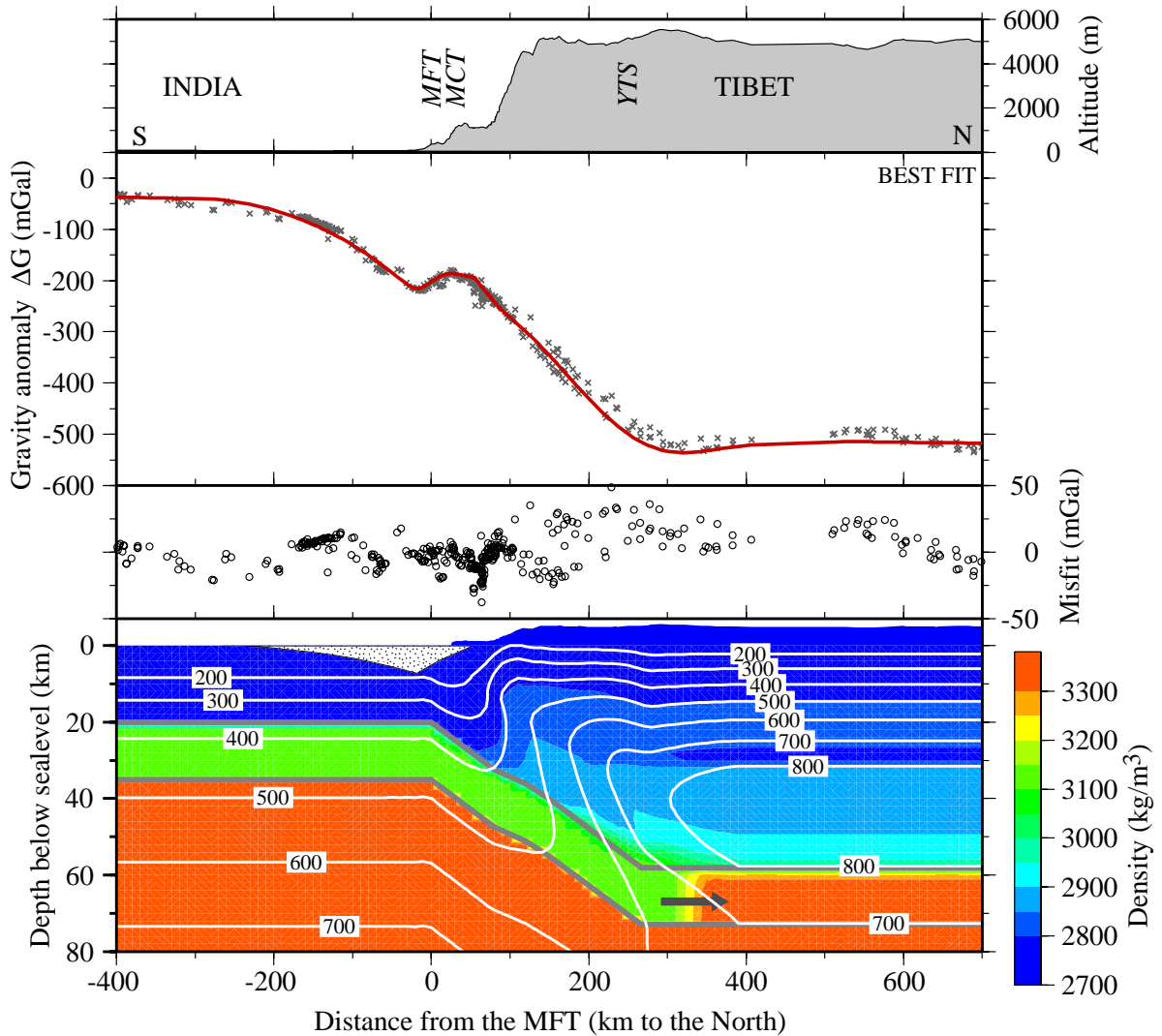
Figure 7.7: The best fit density-model (graphs as on Fig. 7.4), based on: (i) the thermal field from thermo-kinematic modelling (white contours and value in °C, $A = 2.5 \ \mu W \cdot m^{-3}$ and $q = 15 \ mW \cdot m^{-2}$); (ii) petrogenetic grids corresponding to a mafic lower crust with 1 wt.% water-content (Fig. 7.8); (iii) a delay of eclogitization until 300 km. The arrow marks the path of the Indian lower crust and the place where transformation into eclogite takes place. See Fig. 7.8 and section 6 for more details. The densities of the upper crust and the mantle are based on the petrogenetical grids of Bousquet et al.(1997).

7.6.2 Petrological constraints on the temperature field

The two criteria used to assess the temperature field of the models are the temperature at the Moho (at 35 km depth) beneath the Indian shield, T_{MI}, and the temperature of the eclogitized Indian lower crust beneath Tibet, T_{ET}. The obtained values in all tested models for both T_{MI} and T_{ET} are shown on Figure 7.8 and are discussed below.
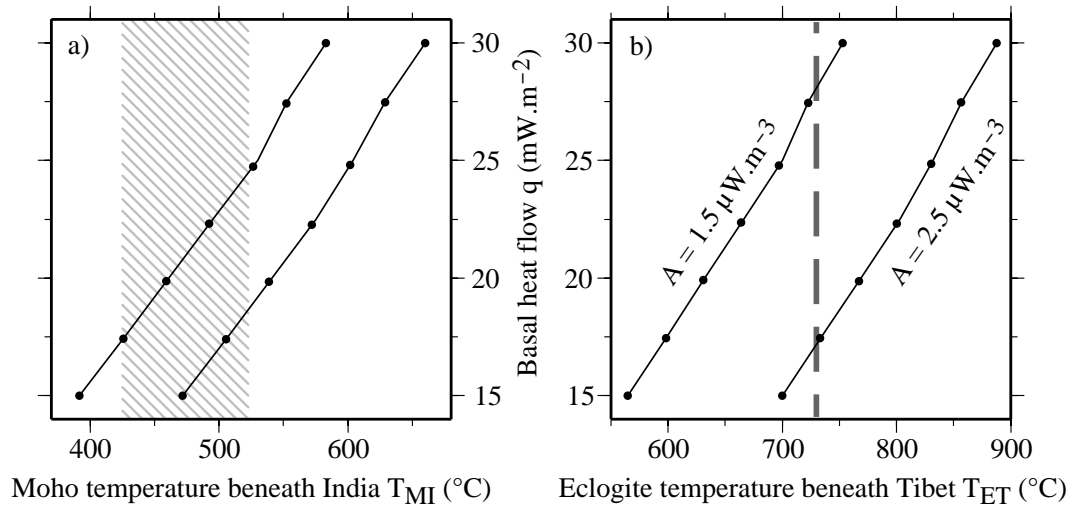
Figure 7.8: Temperature at the Moho beneath the Indian shield (T_{MI}) and within the eclogitized Indian lower crust beneath Tibet (T_{ET}), as a function of basal heat flow (q) and radiogenic heat production of the upper crust (A). In (a), the shaded region is the acceptable range of T_{MI}. In (b) the dashed line is approximate melting temperature of lowly hydrated mafic rocks.

The temperature at the Moho varies between 392 and 583°C for the "cold" ($A = 1.5$ μW·m^{-3}), and between 472 and 660°C for the "hot" ($A = 2.5$ μW·m^{-3}) thermo-kinematic models. This is equivalent to a step of about $+12.5$°C for an increase of basal heat flow of 1 mW·m^{-2} at constant A, and to an average difference of 78°C between "hot" and "cold" models of equal basal heat flow. Our best fit model uses the same thermal parameters as Bollinger *et al.* (2006), and shows a T_{MI} of 472°C. This is consistent with previous work by Henry *et al.* (1997), which favours models with T_{MI} between 417 and 463°C, and rejects models with T_{MI} of 684°C, based on heat flow measurements in the Indian shield. Putting the acceptable range of T_{MI} to around 425-525°C (shaded region in Fig. 7.8a), the basal heat flow is 15±4 mW·m^{-2} for the "hot", and 21±4 mW·m^{-2} for the "cold" models, or any equivalent combination in between.

The temperature reached by the underthrust Indian lower crust beneath Tibet provides another constraint. T_{ET} (at 350 km) varies between 565 and 753°C for the "cold",

and 700 and 888°C for the "hot" models. The temperature increase is the same for Δq = +1 mW·m^{-2} as above, but the average difference between "hot" and "cold" models at equal basal heat flow is increased to 135°C. Examples from Holsnøy Island in the Bergen Arcs complex show that the solidus is $\sim$700°C at 16-19 kbar for wet eclogites (Andersen *et al.*, 1991). Experimental studies reveal similar values: the solidus of wet mafic rocks at 20 kbar is around 700°C, and a 1% water-content rock produces about 10% melt at this temperature (Rushmer, 1991). More recently, Raimbourg *et al.* (2007) measured an average of 718°C and 20.5 kbar on samples from Holsnøy Island, without observing any sign of melting. As our model is not fully hydrated, we can expect a solidus slightly above these values (dashed line in Fig. 7.8b). Comparing the obtained values of T_{ET} with the above estimation of the solidus, we eliminate the "hot" models above q = 17 mW·m^{-2} , the "cold" models above 28 mW·m^{-2} , or any equivalent combination in between.

In summary, the best fit model with A = 2.5 μW·m^{-3} and q = 15 mW·m^{-2} is close to the highest allowed temperature without melting. This model does not change the upper crustal thermal structure of Bollinger *et al.* (2006). It therefore still satisfies both the thermochronological and peak temperature dataset available through the underplated Lesser Himalayas and its overlying crystalline nappes constraining the paleo-location of the 350°C to 550°C isotherm under the Himalayas. An uncertainty at $\pm$50°C is estimated on these mid-crustal isotherms, deduced from the uncertainty on the thermometrical (Beyssac *et al.*, 2004) and thermochronological dataset as well as on the closure temperature for Ar in muscovite and hornblende (*e.g.* McDougall and Harrison, 1999). In the meantime, other models with lower radiogenic heat production and higher basal heat flow (until A = 1.5 μW·m^{-3} and q = 21 mW·m^{-2} , "cold") are equivalent and possible. In terms of synthetic gravity anomalies, this set of solution reproduces very well the observed difference between values in India and Tibet ($\sim$500 mGal); as of the sensitivity of the solution, an increase of 4 mW·m^{-2} in a "cold" model heat flow would lower this difference by $\sim$30 mGal.

7.6.3   The choice of the petrological model

The most sensitive parameters that differentiate the three petrological models (MW, MD and MPH) are the horizontal localization of density increase, and the temperature of this zone. Based on gravity modelling in section 4.2, the highest amplitude change in the density of the lower crust is located at around 300 km north of the MFT. On the other hand, the path of the Indian lower crust in temperature–pressure space (Fig. 7.9) shows that the major increase of density is expected to occur at the transition to the blueschist facies, close to the front (between 0 and 100 km horizontal distance), irrespective of the

level of hydration (dry, partially hydrated, or wet) of the ILC. The temperature of the ILC at around 300 km is $150\pm50°C$ higher than the temperature of the zone where the density change is expected to occur from $P-T-\rho$ grids, and this is true for all thermal models. Such transformation delay clearly shows that the kinetics of the eclogitization process should be considered for the ILC, since it influences considerably its density distribution, and thus the gravity anomaly.
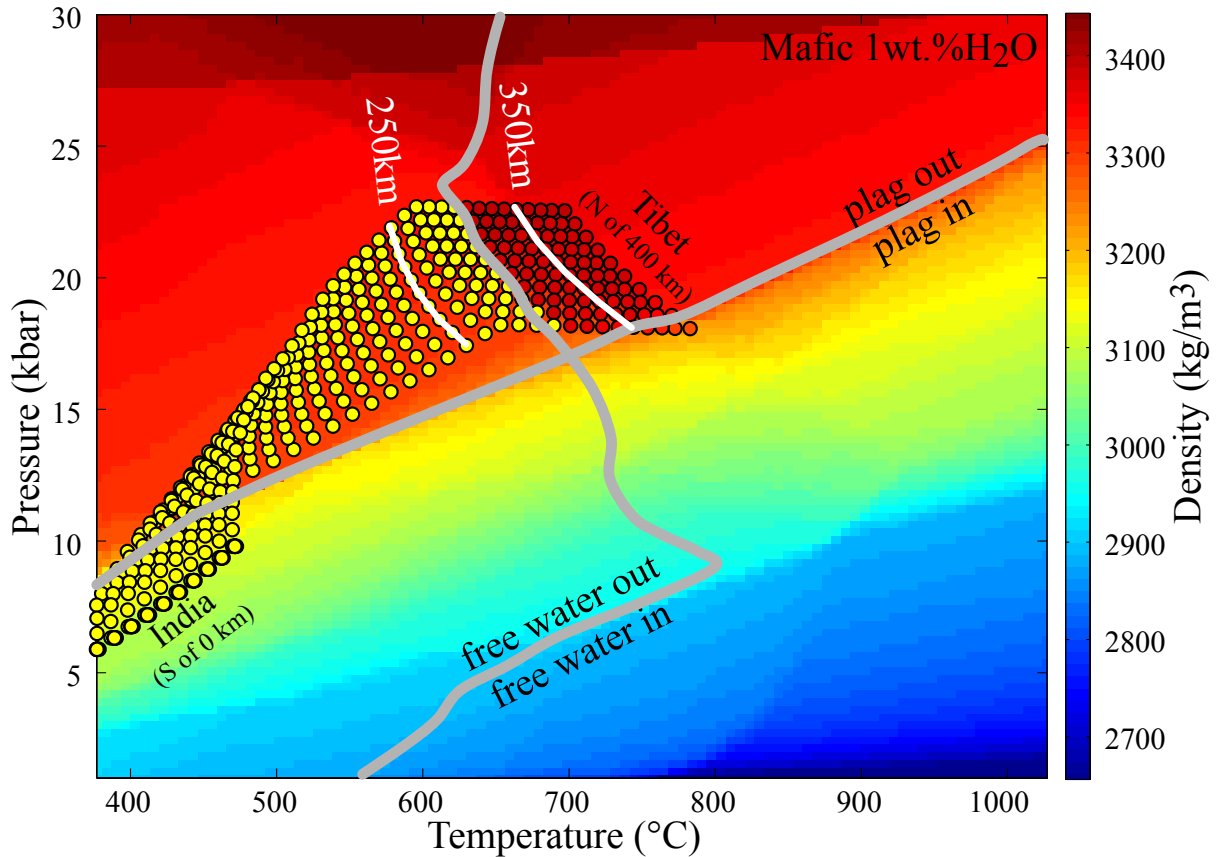
Figure 7.9: Density grid for a mafic composition with 1 wt.% water-content. Gray lines show the stability limit of plagioclase and of free water in the system. The black contoured circles show the P–T distribution for the best fit model (Fig. 7.7) with in the Indian Lower Crust during its underthrusting from South to North. The white lines delineate the position of the ILC at 250 and 350 km north of the MFT. As the disappearance of plagioclase, mainly through the breakdown of albite into jadeite +quartz, does not release water, it can be delayed (overstepped), and the ILC can keep its initial density until it crosses the dehydration line and eclogitizes rapidly. This is also represented by the colours filling the black circles, showing the actual density of the ILC (including the delay). See section 7.6.4 for more details.

Reaction overstepping by $150\pm50°C$ is unlikely in water-saturated systems since

these could not survive for geological timescales (Wood and Walther, 1983). A completely dry system is also unlikely: examples from the Bergen Arc in Norway show that a dry crust subducted into roots of continental collision zones undergoes eclogitization only if hydrous fluids are available, independently of the crossing of equilibrium boundaries (Austrheim *et al.*, 1997). Similar triggering of eclogitization in subduction zones is also known, for example in Zambia (John and Schenk, 2003). In this context, fluid is thought to infiltrate from the hydrated mantle wedge; however, in our case of underthrusting, there is no similar argument for localized fluid infiltration. These considerations lead us to favour petrological model MPH (1 wt.% H_2O) as the most realistic solution, a model for which free water is however not available along the whole ILC underthrusting path. This is in line with Henry *et al.* (1997), who discuss that, in the case of the Precambrian Indian crust, whereas the water necessary to form all hydrated minerals in the blueschist facies ($\sim$5% in the MW model) may not be available, a water-content of about 1% can probably be found.

The gravity anomalies associated to a mafic lower crust with three different hydration levels (MW, MD and MPH) are shown on Figure 7.10a. The primary point here is to reproduce the observed absolute step between the two endpoints of the profile. The synthetic anomalies corresponding to the three models actually support the petrological considerations developed above. A mafic lower crust hydrated at 1 wt.% H_2O (MPH) reproduces well the difference of $\sim$500 mGal between India and Tibet, whereas synthetic anomalies obtained by considering either the wet or the dry model are clearly off, situated about 80 mGal above and 60 mGal below the data, respectively. However, between $\sim$50 and $\sim$350 km horizontal distance, the synthetic anomalies of the MPH model follow the same gradient as the observations, but are offset by $+100$ mGal. This is due to the fact that the locus of density-change in the ILC is calculated assuming thermo-chemical equilibrium (*i.e.* no reaction overstepping).

7.6.4   Implications for the eclogitization kinetics

Figure 7.10b shows three different reaction kinetics for the eclogitization of the ILC (inset), and the corresponding gravity anomalies. The curve assuming thermochemical equilibrium, where the change in density occurs fully and exactly where it is anticipated by the MPH petrogenetic grid, is reported from Figure 7.10a. The low-kinetics case is based on the assumption that the eclogitization process is sluggish: it begins as it is expected from the petrogenetic grid, but the transformation progresses linearly with distance (thus time) until its completion at 300 km horizontal distance. We see that the synthetic gravity anomalies still fail to follow the observed data. Finally, the best fit model (see also Fig.
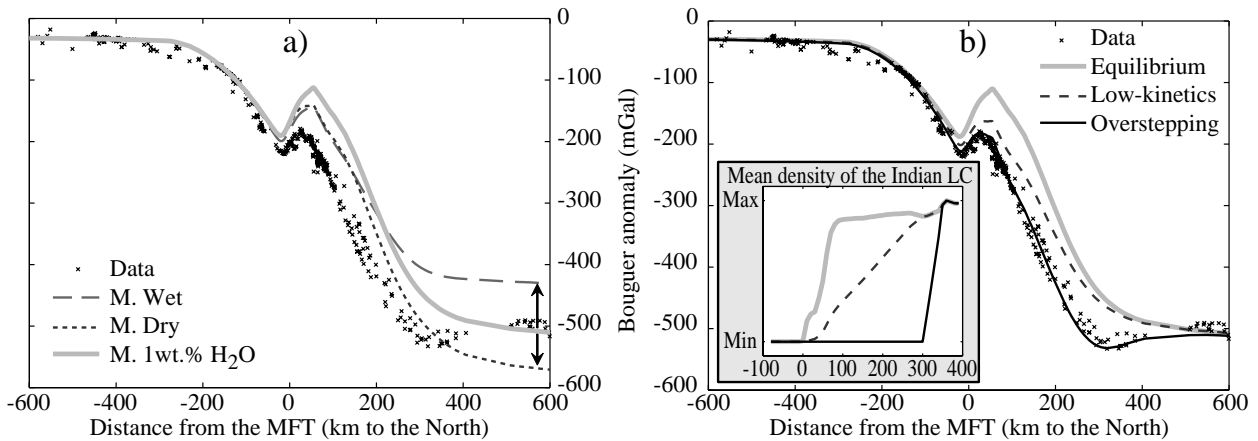
Figure 7.10: (a) The effect of the choice of hydration level on gravity anomalies (with thermal parameters of $A = 2.5 \ \mu W \cdot m^{-3}$ and $q = 15 \ mW \cdot m^{-2}$). The first step in resolving the problem is to reproduce the step of ~500 mGal in Bouguer anomalies between the two endpoints of the profile. While the 1 wt.% water-content model reproduces the observed step between India and Tibet, the wet model falls short of it, and the dry model step is too large, as it is emphasized by the arrows at ~600 km. (b) The effect of reaction kinetics on gravity anomalies, using the 1 wt.% water-content model. For the equilibrium and slowed-down (see inset) models of eclogitization, the calculated anomalies are clearly different from observations between 0 and 400 km. The best fit model is where the eclogitization is delayed to about 300 km (see inset, as well as Figs. 7.7 and 7.9).

7.7) is where the eclogitization process is delayed (overstepped) until 300 km and then occurs within 50 km. The synthetic anomaly fits very well to the observed one, included the gravity-low at ~300 km. It should be noted that other types of density evolutions can also fit the observations, provided that the transition proceeds in the 250-350 km interval and that it is monotonous. We also note that density variations due to compressibility and thermal expansion partially cancel out in the descending part of the ILC, thus the remaining effect, being less than 10% of the density change related to eclogitization, is neglected.

Figure 7.9 summarizes the non-gravimetric constraints of our models. It shows the petrogenetic grid of the MPH model, with two lines enhanced in gray: the limit of stability of plagioclase and of free water in the system (dehydration line), respectively. The circles show the path of the underthrusting Indian lower crust in the P–T field with the colours corresponding to its density. We claim that, along this path, the conversion of the plagioclase component into garnet and/or clinopyroxene, which does not release water, is kinetically hindered. The density change predicted by the petrogenetic grid (equilibrium conditions) does not actually occur. Later on, when the P–T conditions of this metastable

lower crust reach the dehydration line, free water is produced which catalyses the metamorphic reactions (water is provided under these conditions by amphibole and epidote breakdown). Eclogitization occurs then relatively quickly due to the large temperature overstep (150±50°C), and density reaches its maximum value (equilibrium assemblage).

We highlighted the position of the Indian lower crust at 250 and 350 km, which encompass the dehydration line in this pressure range (Fig. 7.9). On the one hand, they are the limits of the zone until which eclogitization is delayed, and also inside which we cannot distinguish between different densification models on the basis of gravity. On the other hand, this ±50 km zone corresponds to an uncertainty of ±50°C in temperature, which is similar to the temperature constraints obtained when assessing the thermal field (the ±4 mW·m^{-2} corresponding to ±50°C). Thus, even if a smaller trade-off is possible between eclogitization localization and the thermal structure, it is realistic to consider the two white lines as a lower and upper bound to the temperature field, and to assume that the key factor in the eclogitization process is the release of free water in the system.

We consider that the geometry used in the thermo-kinematic model is within the error-bars of profile P2, and the obtained results are roughly valid for this profile. The main difference in the geometry of profile P2 compared to profile P1 is a steeper descent of the lower crust to its maximal depth (Figure 7.5b). On the same figure, we reported the relocated microseismicity data of Monsalve *et al.* (2006). A clear cluster of events is visible between 140 and 200 km North of the MFT and at a depth of ∼60-80 km. This zone of microseismicity is located where the ILC reaches its maximum depth, *i.e.* where eclogitization is catalyzed due to water release by dehydration reactions. The observed microseismicity is therefore an additional argument for the release of free water in the eclogitization zone of the ILC; the liberated water increases pore pressure and causes failure at previously stable stress conditions.

Concerning profile P3, we have followed the same modelling steps with a more accurate geometry. The calculations are less well constrained as gravity anomaly data show more dispersion in the region of interest (between 100 and 400 km), but our results show that a delay of ∼200 km is probable, followed by a transition zone of kinetics that is longer than in the best fit model.

7.7 Conclusions

This study brings new constraints on metamorphic reaction overstepping and kinetics at field scale from petrological models, gravity anomalies and seismological data at the southern border of the Tibetan Plateau.

We compile both seismological and Bouguer anomaly data along three arc-perpendicular profiles. Forward gravity modelling based on the observed geometries and varied densities show that Airy-type isostatic compensation is unlikely to occur, as it yields unrealistic densities. This suggests that higher density eclogites are required to support the Tibetan Plateau. Multilayer models show that Indian lower crust eclogitization is completed once the ILC reaches its maximal depth.

In order to interpret these geophysical data in a petrological frame:

(i) we performed thermo-kinematic modelling to obtain the temperature field in the area;

(ii) we calculated realistic petrogenetic (pressure–temperature–density) grids;

(iii) we tested wet, dry, and partially hydrated mafic lower-crustal composition models.

This led us to probe different types of reaction kinetics for the eclogitization of the ILC. The Indian lower crust follows a blueschist–eclogite path in the temperature–pressure space. The derived density profiles were used for forward modelling of Bouguer anomalies. Comparison of the different models show that at least a small amount of water should be contained in the ILC prior to underthrusting, and that the plagioclase-consuming reactions (no water release) are overstepped, and therefore densification is delayed. This delay lasts until the attainment of the dehydration reactions where eclogitization will occur in less than 100 km horizontal distance. Considering the underthrusting rate (17 mm·yr^{-1}), the eclogitization occurs quickly (less than 6 Myr). Even when considering the uncertainties of the localization of eclogitization and of the temperature field, the appearance of free water in the system remains the key factor in the eclogitization process. The partial eclogitization of mafic compositions (gabbroic rocks from Zambia) along a blueschist-eclogite path has already been documented by John and Schenk (2003). They also reach the conclusions that large overstepping of reaction boundaries has occurred and that the gabbro-eclogite transformation was triggered by the presence of a free fluid-phase.

The derivation of mineral reaction kinetics is one of the challenges of metamorphic petrology. Even though reaction progress can be evaluated, reaction duration is difficult to assess from field-based observations. All attempts that have been made to derive reaction rates in metamorphic systems (*e.g.* Baxter and DePaolo, 2000; Carlson *et al.*, 1995; Vance

and O'Nions, 1992; Christensen *et al.*, 1989) show that reaction kinetics in nature are lower, by several orders of magnitude, than those obtained experimentally (see Baxter, 2003 for a review). Baxter (2003) suggests that water availability during metamorphism can account for this discrepancy. For example, Rubie (1986) has proposed that at deep crustal levels, fluid-present conditions could be transitory and related to relatively short dehydration events. This is in line with the interpretation of our gravity dataset in the frame of phase equilibria which strongly suggests that the water released by mineral dehydration can trigger eclogitization reactions. This result emphasizes how the sluggishness of nucleation kinetics can be a source of disequilibrium during metamorphism as already pointed out by Rubie (1998). Our new type of time-resolved constraint on the eclogitization process, which suggests that crystallization (nucleation and growth) of the stable mineral assemblage can be delayed by at least 100°C under free-fluid absent conditions, clearly prompts the investigation of the role of water on mineral nucleation kinetics.

Acknowledgements

Afterword

The current section briefly discusses a few issues related to the study presented in this chapter, completing the EPSL paper. The mentioned three density grids are presented in more detail, and the differences with earlier studies are analyzed. Finally, before starting a discussion on the implementation of metamorphic phase changes in finite element simulations in the next chapter, the possibility of linking modelled eclogites with field occurrences is investigated.

7.8.1   Further notes on petrogenetical grids

The effect of water on density grids for a mafic composition

In the study on the densification of the Indian lower crust, we have tested three petrological models with the same mafic composition: a fully hydrated case, a dry composition, and the preferred, partially hydrated model. Here the density grids for all of these models are presented and compared (Fig. 7.11).

As discussed in Section 7.5.2, wet models (such as the MW model) is the one that is most commonly used in petrology. The fact that water is not a limiting factor allows all hydrated minerals to be formed, for example amphiboles, epidotes and chlorites in the blueschist facies. This way, the petrogenetical grid presents relatively low densities at low temperatures. As these relatively light minerals disappear towards higher temperatures by dehydration reactions, sub-vertical frontiers mark the progressive densification of the rock.

The partially hydrated model differs significantly from the wet model by the limited amount or absence of those mineral phases that require more than 1 wt.% of water. This reduces the presence of the previously mentioned chlorites to lower pressures, for example, and thus affects the composition (and density) of several facies. The blueschist domain, for example, becomes significantly denser due to the stability of garnets at low temperatures. The dehydration reactions are obviously less pronounced in these grids, the only visible sub-vertical densification front being at $\sim 700°C$ and 20-25 kbar. The most prominent density variations occur along sub-horizontal lines: these correspond (1) to the breakdown of feldspars (approximately the ~ 3150 kg·m^{-3} isodensity line; see upper dashed line on Fig. 7.11) according to the water-free albite = jadeite + quartz reaction at low temperatures, and (2) to the appearance of garnets (the ~ 2900 kg·m^{-3} isodensity line, lower dashed line). The phase diagram of the MPH model from Perple_X is shown on Figure 7.12.

Finally, the dry model does not allow the formation of hydrated minerals, such as amphiboles, thus the sub-vertical densification lines are absent from the grid. The major
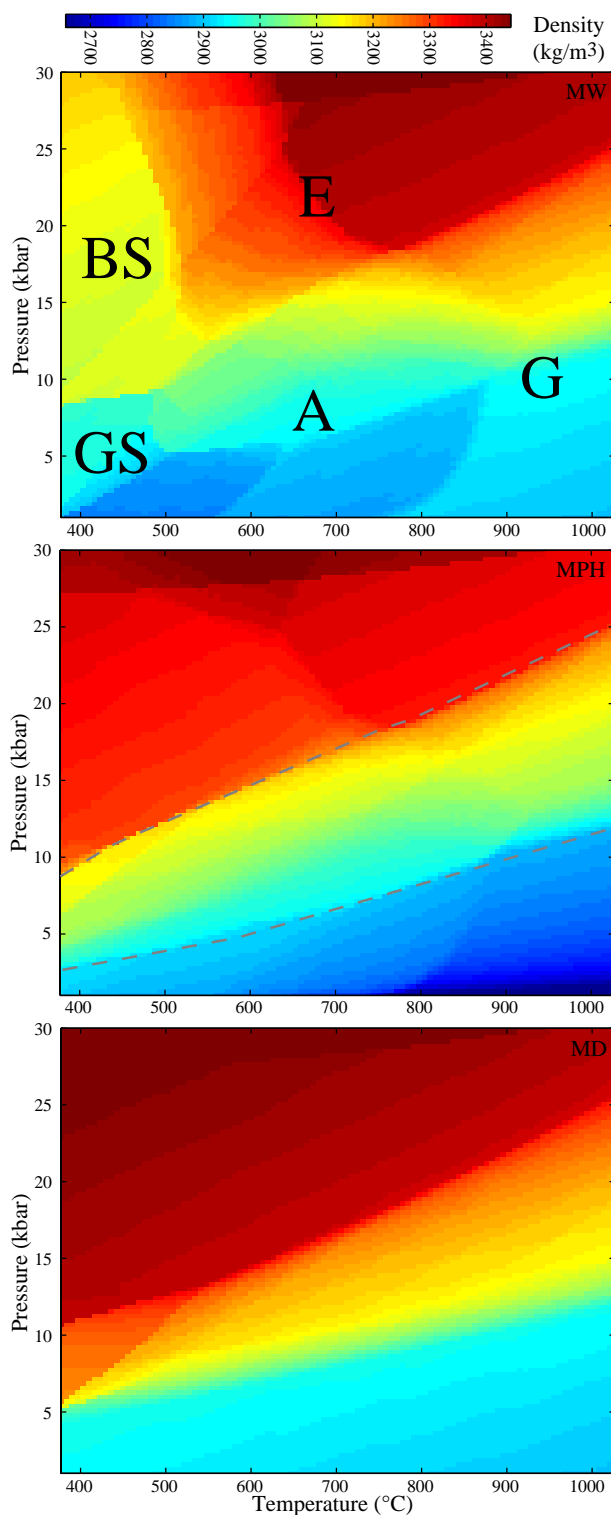
Figure 7.11: Petrogenetical grids for wet (top), partially hydrated (middle) and dry (bottom) models, yielding density as a function of temperature and pressure. On the wet model, the letters note the main metamorphic facies: GS – greenschist, BS – blueschist, A – amphibolite, E – eclogite, G – granulite. On the partially hydrated model, the lower and upper gray dashed lines represent the limit of stability of garnet and feldspar, respectively. See text for discussion.

difference in densities compared to the MPH model appears at low metamorphic grades, where 1 wt.% of water content still formed some hydrated minerals. The sub-horizontal feldspar-out and garnet-in reactions dominate in this petrogenetical grid.
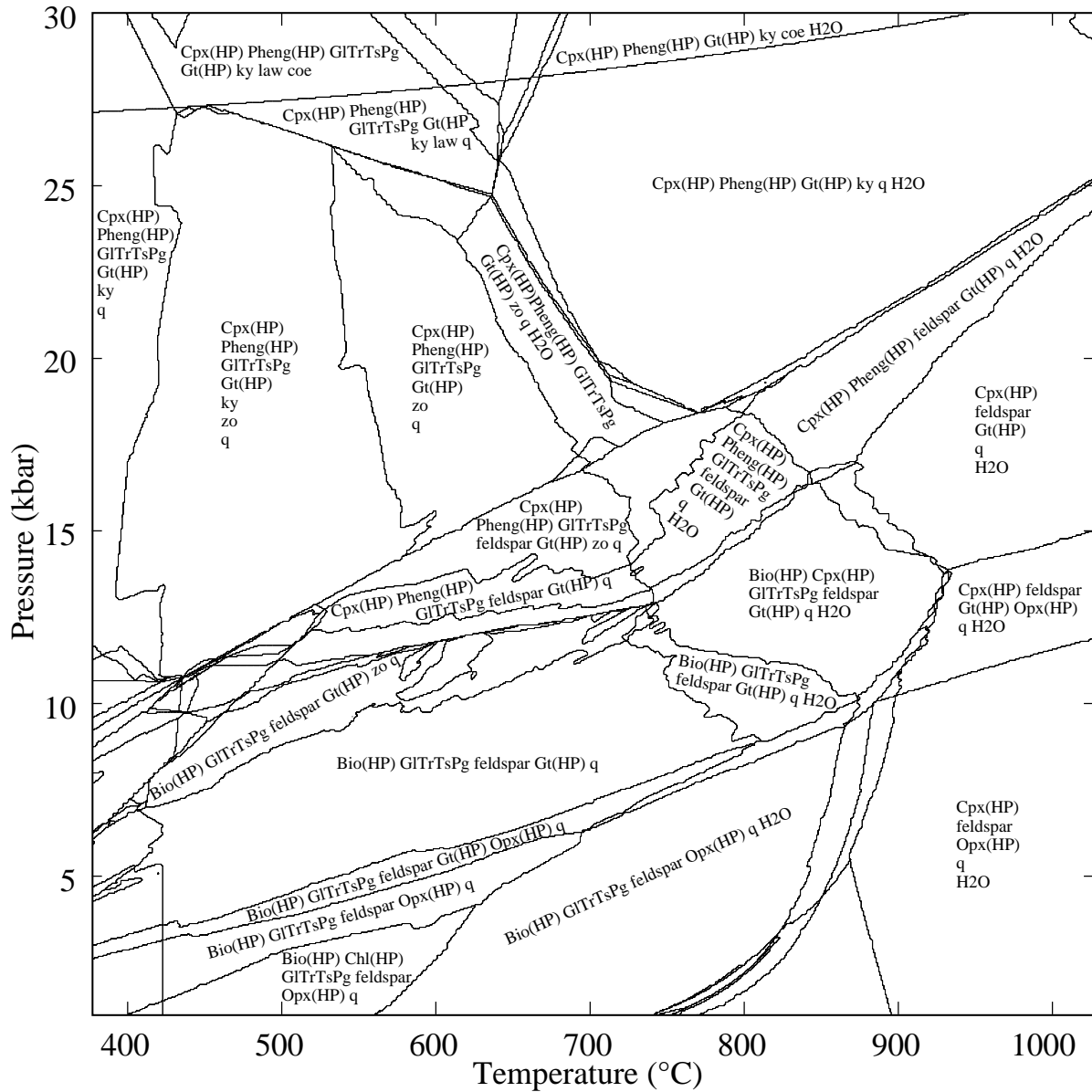
Figure 7.12: Phase diagram of the mafic, partially hydrated (MPH) model from Perple_X. Only those fields are labelled that are sufficiently large to include readable text. Abbreviations are the following: Bio (HP) – biotite; Chl (HP) chlorite; coe – coesite; Cpx(HP) – clinopyroxene; GlTrTsPg – amphibole; Gt(HP) – garnet; H2O – water; ky – kyanite; law – lawsonite; Opx(HP) – orthopyroxene; Pheng(HP) – phengites; q – quartz; zo – zoisite.

Comparison with a previous petrogenetical grid

Our study is not the first to present petrogenetical grids to investigate the density structure of an orogen. Bousquet *et al.* (1997) have calculated similar grids for three different compositions that were applied to the Alpine and Himalayan ranges, as well as to the Andean Plateau (Bousquet *et al.*, 1997; Henry *et al.*, 1997; Le Pichon *et al.*, 1997; Goffé *et al.*, 2003). Here we compare our MW model to the "andesitic" density grid of Bousquet *et al.* (1997), as it has a similar mineralogical composition, and as it was used to model the lower crust.

The two grids and their differences are shown on Figure 7.13. The one by Bousquet *et al.* (1997) includes 11 metamorphic facies of constant mineralogy (see labels on Fig. 7.13a). The difference between the andesitic and MW grids shows as much as 250 kg·m^{-3} deviation at some key locations, such as around 550-600°C and 13-15 kbar. These differences are due to the assumptions during the construction of the grids. Primarily, Perple_X accounts for compositional variations of solid solutions within the same facies, for example by the use of omphacite, while Bousquet *et al.* (1997) chose to use two clinopyroxene poles of constant composition, diopside and jadeite. This causes that the changes in density (and all physical properties is general) are more gradual on Figure 7.13b compared to Figure 7.13a, where a bulk value was assigned for the entire facies. This gradual variation *versus* constant value is also reflected in the water content of the models (Fig. 7.13 d and e), although the first order variations are similar, such as the increase of water content from greenschist to blueschist facies. Other, comparatively minor differences in density are due to (1) the difference in minerals that are allowed to form in the two models, (2) to the slight differences in the mineralogical composition of the system, and (3) to the fact that our model neglects the *Ti*-content.

Finally, the novelty in our approach is the introduction of reaction overstepping (metamorphic disequilibrium), an issue developed in Section 7.6.4. It was possible to constrain this phenomenon by the Bouguer anomalies and the density modelling, which, in turn, is based on the new images of the lithospheric boundaries, unavailable at previous studies.

7.8.2　Is there field evidence for these eclogites?

This chapter includes several large geophysical datasets, and also a significant amount of numerical modelling. The discussion is developed on rocks on that are located at ∼20-35 km depth in India, and on their transformation into eclogite at ∼60-75 km beneath Tibet.
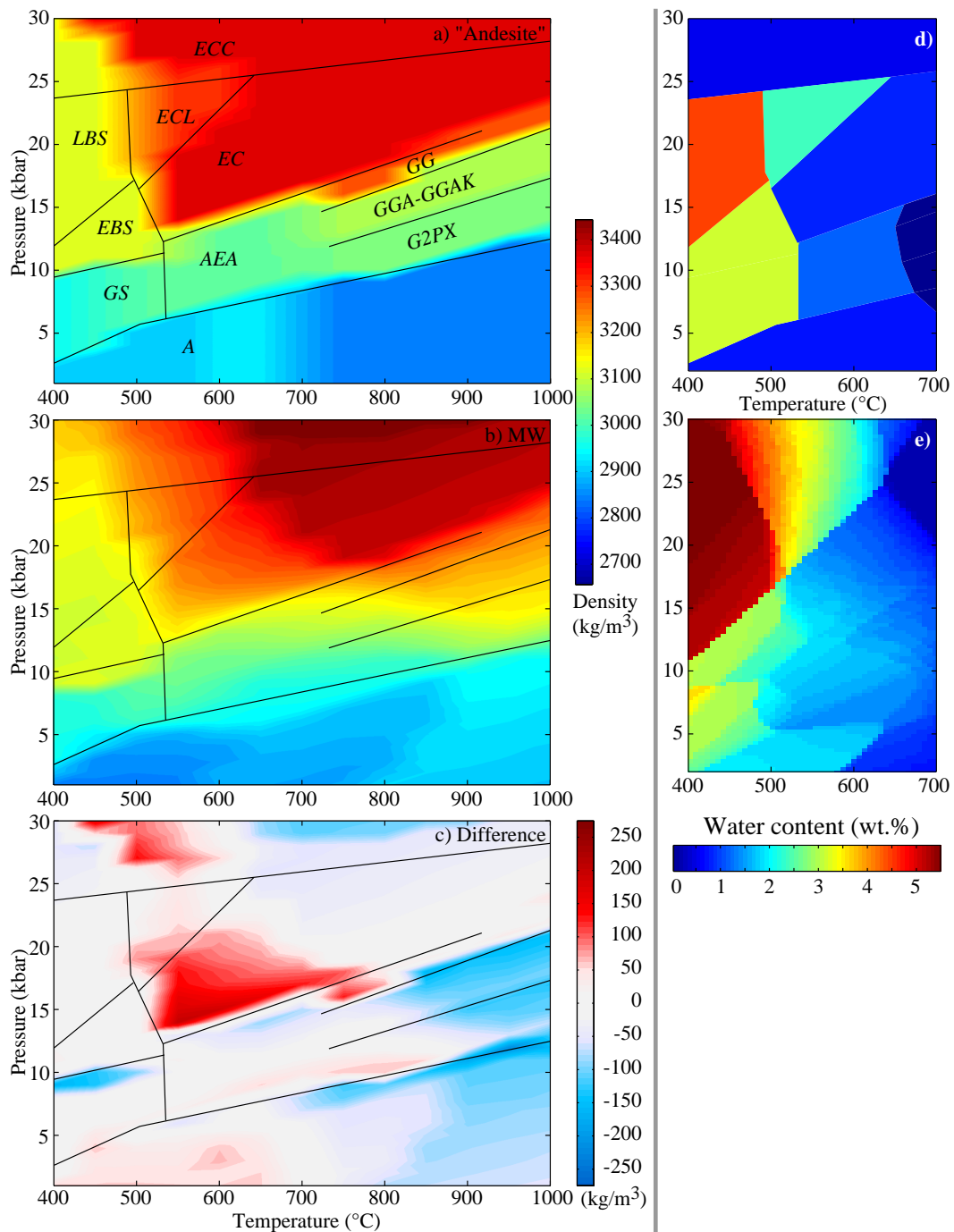
Figure 7.13: Comparison of petrogenetical grids used to model the lower crust in a fully hydrated case. (a) "Andesitic" composition from Bousquet et al.(1997). (b) "Mafic Wet" model from Perple_X. (c) Difference of (a) and (b). (d) and (e): water content of the models presented in (a) and (b), respectively. See text for discussion. The black lines mark the limits of the metamorphic facies used in Bousquet et al.(1997), with the following abbreviations: GS – greenschist; A – amphibolite; LBS – lawsonite blueschist; EBS – epidote blueschist; AEA – albite epodite amphibolite; G2PX – granulite with ortho- and clinopyroxenes; GGA – garnet granulite with plagioclase; GGAK – garnet granulite with plagioclase and kyanite; GG – plagioclase absent granulite; EC – eclogite; ECL – eclogite with lawsonite; ECC – eclogite with coesite.

Is there a link to geological observations at all?

While the lower crust in the Himalayan foreland is too far from the surface to be reached by drilling, we can count on exhumation processes to show us what can be found at depth. These reveal that there are two groups of eclogites along the Himalayan Arc, distinct in both time and space:

– The more studied locations are close to the western syntax, such as the Tso Morari region and the Kaghan valley, and also located close to the Yarlung Tsangpo Suture. The analyzed ultra-high pressure rocks of Paleocene-Eocene age (55-46 Ma) are associated to the early stage of subduction of the thinned Indian margin (upper crust and sediments). The recorded P-T conditions show UHP metamorphism accompanied by high temperatures, estimates ranging between 18.5 and 39 kbar, and 500-770°C, respectively (Guillot *et al.*, 1997; de Sigoyer *et al.*, 2000; Kaneko *et al.*, 2003; Mukherjee *et al.*, 2003).

– The second type of eclogite occurrence is in the central part of the Himalayan Arc, in the Kharta region (E-Nepal), located close to the Main Central Thrust. Hence the structural position is significantly to the South of that of the first group. The samples are in the Lesser Himalayan series, but are close to the Higher Himalayan Crystalline (Groppo *et al.*, 2007). Unfortunately, the granulite facies metamorphism almost completely erased the eclogite facies imprints (Carosi *et al.*, 1999). However, based on the analysis of a few eclogite relics, the pressure-temperature conditions of the eclogite facies could be estimated to P>15 kbar (but no UHP metamorphism) and T>580°C (and up to ∼700°C, Groppo *et al.*, 2007). The clockwise exhumation also erased the possibility of dating peak metamorphic conditions, but the mentioned granulite facies retro-morphose is estimated to have occurred in the Miocene (Lombardo and Rolfo, 2000). In summary, the second type of eclogites experienced lower pressures compared to the first group, and were generated prior to ∼25-20 Ma.

These observations suggest two different contexts for eclogite generation at two different periods of continental collision. In light of the geometries and the evolutionary scenario presented in Chapter 5, there is a possible link between the modelled eclogites (this Chapter) and the central Himalayan samples described above. The relatively low pressure conditions, together with the location of the samples, agree with the mechanism of underplating; the pre-Miocene (probably Oligocene) beginning of eclogitization would correspond to the onset of underplating. The fact that the temperatures in our thermal model (Fig. 7.7) are higher above than within the Indian Lower Crust, would explain the

granulite facies overprint during exhumation. Whether the origin of the eclogite samples is related to the top of the underplated lower crust, or to the bottom of the upper crust, is not yet constrained, and should be determined by geochemical and petrological investigations.

CHAPTER 8

Ongoing studies and future prospects

8.1 Introduction

This chapter discusses topics on which we have already advanced and will yield results in a near future, and perspectives that can be derived from the work presented in this thesis and should be addressed in the following years.

The first issue is to take into account density changes related to different metamorphic facies in numerical modelling, in a correct way. Chapter 7 showed that these variations can be larger than 10%, but existing models only impose densities based on metamorphism, without changing the volumes accordingly. Here we present our improved approach that respects mass conservation. The first results of this ongoing study are subject to a presentation at the 2007 AGU Fall Meeting[1].

A second theme is the analysis of topographic and gravity anomaly variations along the Himalayan arc. Based on oceanic examples, we investigate if a link between the above variations and seismogenic behaviour can be deduced in a continental context.

Finally, a discussion is held on the presented imaging and modelling techniques: why and in what aspect they are innovative, and what are the conditions for their application. I would also like to give an outlook to future steps to make concerning data acquisition, processing, and inversion. With increasing amount and quality of data, and/or by combining several research domains at the same time, the solution for many question can be realistically put into perspective within the next few years.

---

[1]Hetényi, G., Godard, V., Cattin, R. and Brunet, F. (2007). Role of metamorphic reactions and related density changes in mountain building. Tectonophysics section, session 23, poster T21B-0584.

8.2   Metamorphic phase changes in numerical modelling

8.2.1   Introduction and raising the problem

Studying metamorphic reactions is a large and entire field within petrology. These reactions not only provide information on past pressure and temperature conditions in a mountain range or a subduction zone, but also serve to investigate CO_2 sequestration, and explain both major discontinuities of the upper mantle. Chapter 7 presented an example of metamorphic reaction modelling, the transformation of the Indian lower crust beneath Tibet into eclogite. The petrogenetic grids emphasized the variations in density related to facies change, amounting to more than 10% volumetric decrease. Metamorphic reactions with non-negligible density change occur in the upper crust as well, both in continental and oceanic context (for example serpentinization).

The amplitude of volumetric variations related to metamorphic phase changes points to an important issue in numerical modelling. Computer simulations are aimed to reproduce geodynamic problems, such as rifting, subduction, or mountain building and plateau uplift, as discussed in Section 2.4. According to my knowledge, a major part of the numerical models does not account for density changes within different lithospheric units: the density of the elements is independent from P-T conditions (Type I model, Fig. 8.1a). However, according to the density variations pointed out by petrogenetic grids, this would be necessary: the density changes may not only affect the evolution of topography, but also modify the mass distribution at depth, thus changing the induced gravity field and the dynamics of the interior of the lithosphere.

A minor part of the numerical models accounts for metamorphism, and includes variations of density as a function of pressure and temperature (Type II model, Fig. 8.1b). However, another issue arises here, which is mass conservation. Type II models actually update the density and the related mass fields, but keep the volume of the elements unchanged. Hence an artefact appears due to the corresponding "creation" or "suppression" of mass.

The ideal solution is a numerical model that accounts for both metamorphism and mass conservation (Type III model, Fig. 8.1c). The density of the elements would be imposed using petrogenetic grids, and the occurring densification and "lightening" would be accompanied by volume decrease and increase, respectively.

The following sections present the first steps in the construction of a Type III numerical model, in which densities are imposed and volumes respect mass conservation. First a static resolution method is presented as an illustration. Then the options and the solution
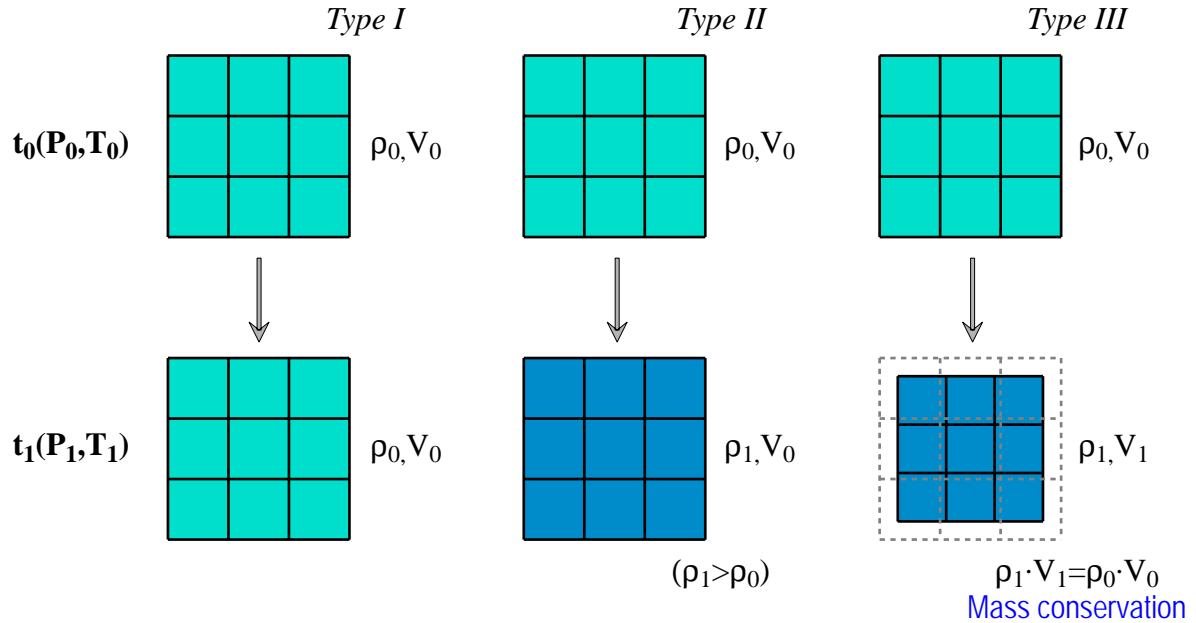
Figure 8.1: Three types of numerical model with respect to metamorphic phase changes. At the initial state t_0, the pressure and temperature conditions are P_0 and T_0, respectively, and the density and the volume of the elements are the same for all models (ρ_0 and V_0). At the final state t_1, the P-T conditions have changed (P_1, T_1), and should correspond (in this example) to an increase in density (ρ_1). While Type I *models do not take into account density changes at all,* Type II *models do, and affect ρ_1 to all concerned elements (see colour code). However, the volume of the elements remains the same (V_0). Finally,* Type III *models impose volumetric changes that correspond to the density variations and mass conservation (*i.e. *volume decrease in this example).*

for the dynamic resolution are discussed, together with stability tests. Finally, the first order results of the effect of metamorphic phase changes (MPC) on the localization of deformation in a convergent context are presented. The effects are compared to those induced by diffusive erosion, as well as those related to the considered rheological behaviours.

8.2.2   Presentation of the numerical modelling tool

`Cast3M` [2] (also known as CASTEM) is a finite element modelling tool developed for engineering purposes at the Département de Mécanique et de Technologie of the CEA. It aims to analyse structures and their behaviour in (among others) mechanical and thermal problems, offering different choices of the resolution algorithm. Being a general purpose finite element modelling (FEM) tool, it contains several modules that allow to construct

---

[2] Available at http://www-cast3m.cea.fr/

codes solving specific problems in a flexible way. The numerous ($\sim$500) pre-defined functions help to perform many operations on different type of objects, such as meshes, models, and fields. An example of operators is shown on Figure 8.2.

Figure 8.2: *An example of available operators in* `Cast3M` *. The four corners represent four physical properties:* $\underline{\underline{\varepsilon}}$ *is the deformation field,* $\underline{\underline{\sigma}}$ *is the stress field,* $\underline{F}$ *are the nodal forces, and* $\underline{u}$ *is the displacement field. The red commands show the existing operators in* `Cast3M` *that allow to perform transformations in the direction of the arrows.*
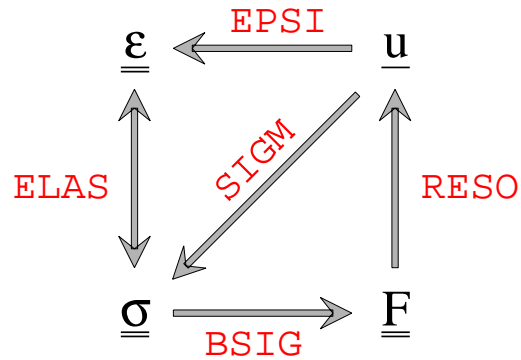
`Cast3M` is coded at two different levels. The upper, interpreted language (`gibiane`) allows to construct the resolution of a problem in a simple way, using its own coding syntax. The lower level is the source code, `esope`, similar to `Fortran`, which includes and creates the compiled codes corresponding to functions used in the upper level, such as calculating the stress field from the deformation field for a given rheological behaviour. The power of `Cast3M` lies in the available functions, their modularity, and the possibility to introduce new operators easily (no "black-box effect"). The disadvantages are the slower performances compared to an entirely compiled (but unmodifiable) code, and the specific syntax of `gibiane` that requires several months of apprenticeship to handle different operators correctly.

Geodynamic applications

The resolution of the thermomechanical problem and other advantages make `Cast3M` a suitable candidate for finite element modelling of geodynamic problems. A set of tools in this approach were developed by V. Godard during his Ph.D. thesis (Godard, 2006). These include the setup of procedures that solve the thermal and mechanical problem using a dynamic resolution scheme. Source codes in `Cast3M` were adapted to account for elastic, viscous, visco-elastic (both linear and non-linear), plastic, and visco-elasto-plastic rheology. Finally, different type of erosion laws were implemented, simulating diffusive and several river incision processes. As the geodynamic models simulate few million years in time, re-meshing was also adapted in order to stabilize rapid erosion of topography. For more details on all these aspects, I refer to Godard (2006). Finally, I note that due to the slower performance of `Cast3M` with respect to other "non-interpreted" (*i.e.* compiled)

codes, simulating large geodynamic problems and long simulations is restricted to 2-D models.

8.2.3 Static resolution of MPC

In a first approach, the introduction of metamorphic phase changes including mass conservation (Type III model on Fig. 8.1) is developed in a static mode. The resolution scheme is represented on Figure 8.3. The goal is to obtain a displacement field of the mesh nodes that reduces/stretches the elements affected by a density increase/decrease. Here we suppose that the relative change in density is entirely compensated by a relative change in volume. This volumetric change is then transformed into an isotropic deformation field. Unfortunately, there is no operator that allows to calculate the displacement in a direct manner from this point, thus we have to compute (1) the stress field, then (2) the nodal forces, and finally (3) the wanted displacement field.
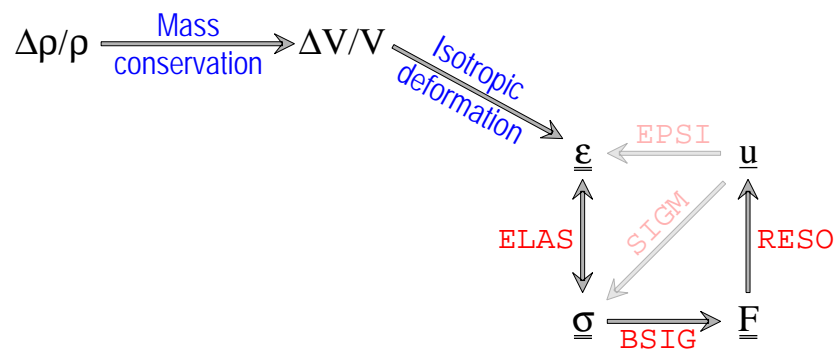
Figure 8.3: Static resolution scheme of metamorphic phase changes. See text for description.

A first test of a purely mechanical problem is performed on an elastic isotropic block model shown on Figure 8.4. The metamorphic phase change is simulated by increasing the density of five elements on the right side of the model, one by one, by 400 kg·m^{-3} , which is the same order of magnitude as the eclogitization of the lower crust. The static resolution scheme is applied after each change. Density values are imposed over the entire model, which means that the upper and lower media keep their densities, and, for the already changed small blocks, any remaining deviations from the imposed values are included in the following step. This usually concerns a few elements close to the edges, which may have up to 20% relative error between the imposed and actual density values. The amount of this error can be easily diminished if curved contours are used, and/or by applying a finer mesh.

The obtained displacement field after increasing the density of all five blocks is shown on Figure 8.5, focusing on the zone of interest. The most important effect occurs

Figure 8.4: Geometry and boundary conditions of the mechanical model used to test metamorphic phase changes with a static resolution scheme. Two media (crust and mantle) are kept at constant density, while the contoured blocks increase density one by one. Boundary conditions allow free vertical but no horizontal movement on both sides, and apply a basal pressure to support the model hydrostatically. The dashed line contours the zoomed region on Figure 8.5.
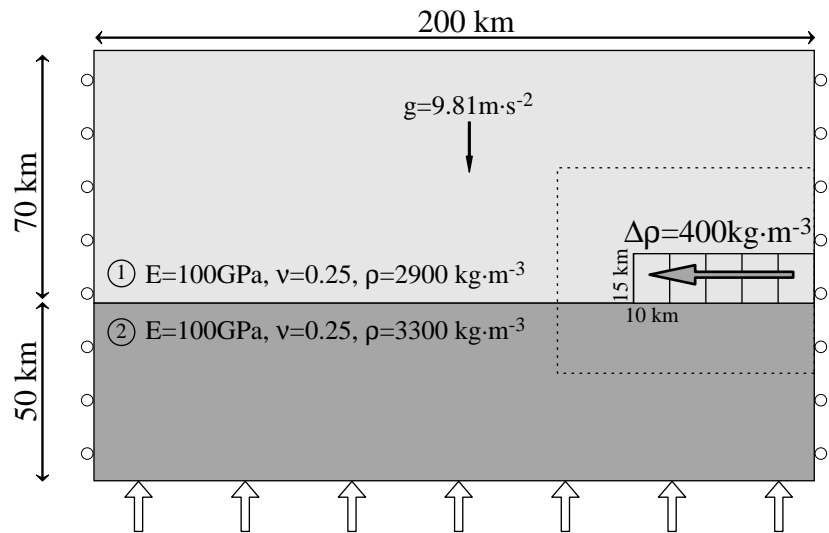
above the affected zone. Here the displacement field is close to vertical, and amounts to more than 1200 m on top of the metamorphic zone. Even if elasticity partially attenuates this effect further away, subsidence at surface can attain as much as 800 m. We note that the zone underlying the densifying region is also deformed towards the area of volumetric decrease, and the neighbouring elements to the left at the same depth do the same.

Another interesting effect to look at is the variation of the stress field related to densification. For this test, we have applied a $\Delta\rho$ of 100 kg·m^{-3} only. Figure 8.6 shows the absolute change in stress field from the initial to the final state of the density increase. The most important variations occur on the edge of the latest affected (most to the left) block, where the change in stress is between about −0.6 and 0.4 MPa. Stress changes along the top and the bottom of the affected zone are also present, but exhibit lower values, due to the stepwise densification, and possible re-equilibration during the following steps.

The amplitude of variations in the stress field due to metamorphic phase changes (MPC) points to an important issue concerning earthquakes. It has been observed, using a large number of small earthquakes, and reporting their source radius versus their seismic moment (Fig. 8.7), that the stress drop related to the earthquakes is approximately constant and independent of the event's size (Hanks, 1977; Scholz, 1990). The amplitude of stress drop is always in the 0.03–30 MPa range, but most of the events are comprised between 0.1 and 10 MPa. The stress variations related to MPC, as shown above, fall exactly within this

Displacement field (→ : 1000 m)
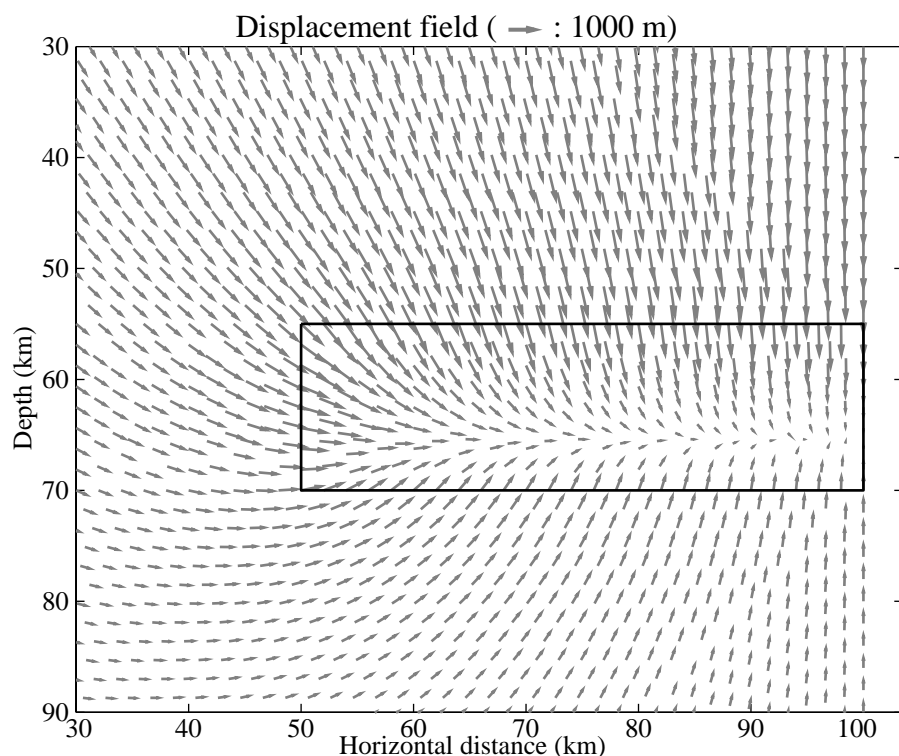
Figure 8.5: Displacement field after having changed the densities and having applied the static resolution scheme for metamorphic phase changes (zoomed view compared to Figure 8.4). The black box contours the area of density increase. No vertical exaggeration. See text for discussion.

range, even for a density change of 100 kg·m^{-3} that would correspond to 25% eclogitization with reference to the above example. Moderate size earthquakes can be caused by phase transitions, as it is suggested for deep events in the upper mantle (*e.g.* Kirby *et al.*, 1991). However, as metamorphic reactions require some time to be completed, I would not go too far by saying that phase transformations alone can cause earthquakes, and rather suggest that the related density variations may modify the stress field and trigger small events more frequently.

To conclude on tests performed by a static resolution method, I note that metamorphic phase changes were implemented in thermal models as well. In these cases, realistic petrogenetical grids were used to calculate the density of a zone as a function of the changed temperature conditions. These tests were found stable, and showed similar effects on the deformation field and subsidence of the surface than above.

Drawbacks of the static resolution method

The first inconvenience is related to the implementation of MPCs: the imposed density values are not exactly obtained after the resolution of the problem. Using a scaling parameter controlling the amount of density change compared to the prescribed one does not help the situation. Iterating towards the imposed density values, either for a certain
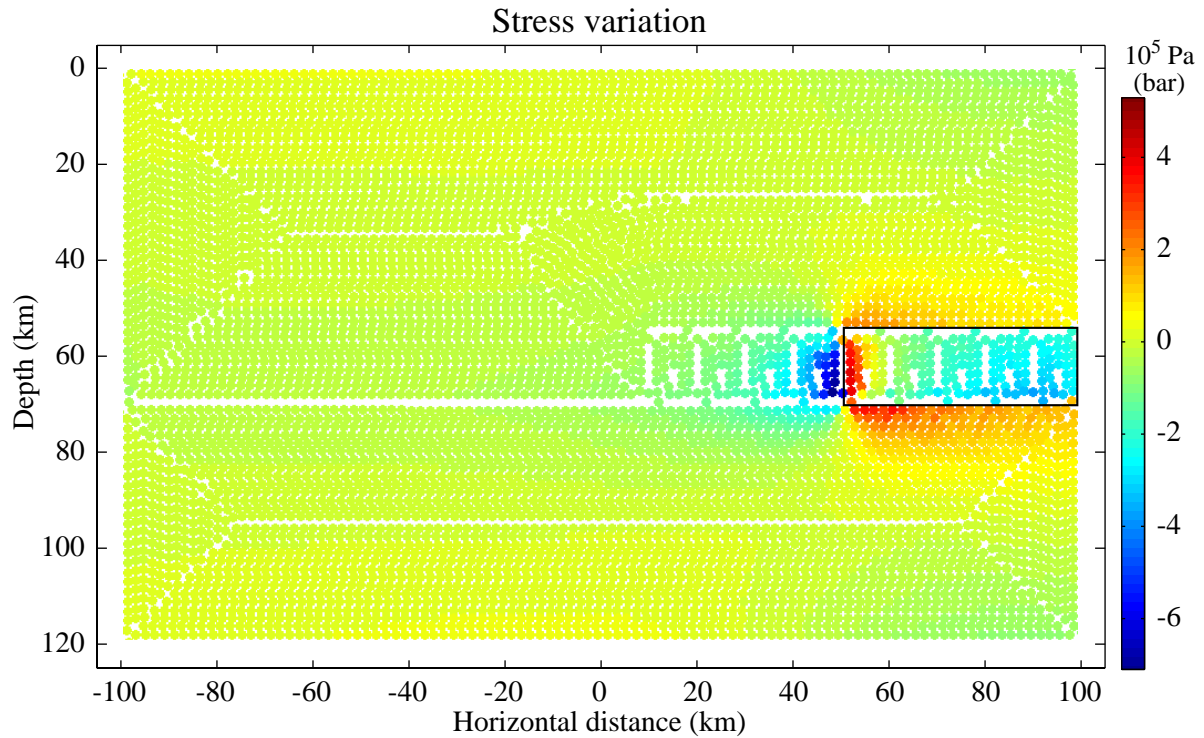
Stress variation

Figure 8.6: The variation of stress field $\Delta\underline{\underline{\sigma}}$ $(= \Delta\sigma_{xx} + \Delta\sigma_{yy} + \Delta\sigma_{zz})$ due to a density increase of 100 kg·m^{-3} within the black rectangle. No vertical exaggeration. See text for discussion.

Figure 8.7: The logarithmic relationship between source radius and seismic moment of earthquakes, showing that the range of stress drop is independent from these quantities. From Scholz (1990), based on Hanks (1977). The dashed lines correspond to constant stress drop of 1 bar and 100 bars.
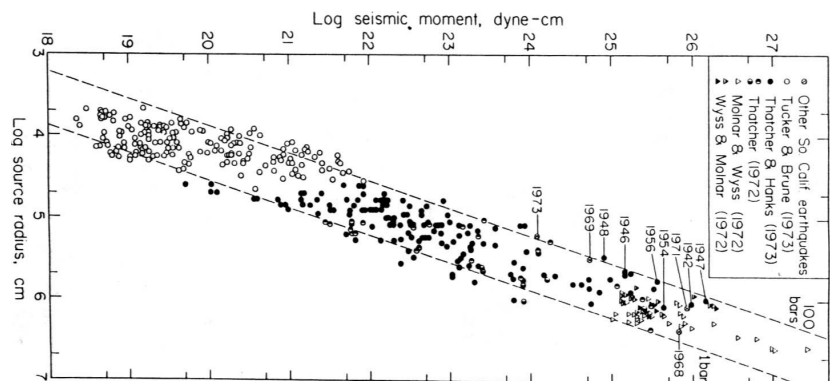
number of iterations, or until attaining a given level of precision, may take considerable time, and often diverge even if the first steps seem to be convergent.

The second drawback concerns the boundary conditions. In the presented example, we have not allowed the left and right sides of the model to move horizontally, although it was clear that MPCs generate horizontal stresses, as it was visible on the left hand side

of zone of density change (Fig. 8.5). More importantly, in the static resolution method, where the gravity forces and the hydrostatic pressure at the base of the model have to remain in equilibrium, at least one point have to be fixed (no vertical movement), in order to let `Cast3M` solve the problem[3]. In the presented example, this point was fixed far from the density changes, on the left hand side of the model, but this choice is not unique. One could argue that fixing several points, or fixing the entire base of the model would be a better solution, but all of these choices introduce long wavelength artefacts. The solution for this issue, clearly, is to implement dynamic resolution of metamorphic phase changes, where such artefacts and problems do not arise.

8.2.4   Dynamic resolution of MPC

Solving geodynamic problems using a dynamic resolution scheme is a widespread approach. It allows to follow the evolution of different systems, such as subduction zones or mountain building, for a considerable time (several millions or tens of millions of years; *e.g.* Avouac and Burov, 1996). Due to pressure and temperature variations, metamorphic phase changes also occur in these timescales, thus it seems to be a straightforward way to implement MPCs into a dynamic resolution scheme. The already coded rheological behaviour and erosion laws in `Cast3M` (Godard, 2006) provide a complete and comprehensive frame to study these geodynamic processes. The continuation of V. Godard's work allows to assess the individual effect of metamorphic phase changes, as well as its interaction with rheology and erosion.

Contrarily to the static resolution, we cannot use the displacement field to impose volumetric variations related to metamorphic phase changes in the dynamic scheme. The principal reason for this is that the dynamic scheme is based on a different logic: going by half time-steps, it updates successively the displacement field, the geometry, the stress field, the forces acting on the system, the acceleration and the velocities. Then the two latter parameters are corrected for kinematic boundary conditions (for example convergence), followed by the application of erosion processes, as well as remeshing, if needed. More details on the temporal discretization of the problem can be found in Godard (2006).

In consequence, metamorphic phase changes have to be integrated in a new manner. As the solution for this type of problem is not evident, the pioneering work presented below required considerable amount of time, including coding the sources and running numerical tests. Four options were implemented and analyzed in detail:

---

[3]If no point is fixed by the user, `Cast3M` chooses a point automatically, without any control from the user.

1. Vary the compressibility of the concerned elements;

2. Integrate other geodynamic processes by additional nodal forces;

3. Integrate other geodynamic processes by imposing a deformation field;

4. Integrate other geodynamic processes by modifying the internal stress of the system.

Compressibility   One way to accommodate volumetric variations is to vary the compressibility through the corresponding elastic moduli, and proportionally to the deviation between the actual and wanted volumes. This may be performed in an iterative manner, until a given level of precision is obtained. This approach, however, requires recalculation of the internal stress of the system at every iteration step, which is an extremely time-consuming procedure for models with a usual number of elements. Furthermore, the volumetric changes were either too slow, or of weak amplitude.

The following three options start off as the static resolution scheme, and integrate the other geodynamic processes at different points, as shown on Figure 8.8.

Figure 8.8: Options for the integration of metamorphic phase changes in the dynamic resolution scheme. The green arrows represent exit points from the outlined procedure, where the corresponding physical parameters can be transmitted to the geodynamic routine. See text for discussion.
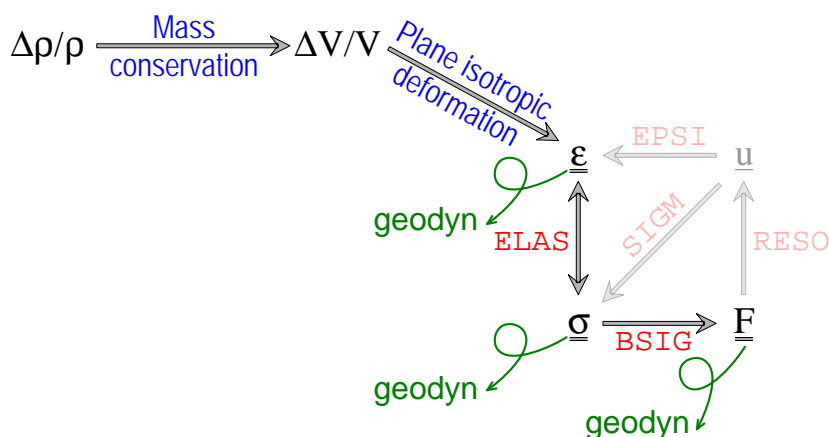
Nodal forces   The choice resembling most to the static resolution scheme is to perform all but the last steps from relative density change to displacement field, and thus stop at the calculation of nodal forces (F_{MPC}). Then this field can be added as an external force when different forces are appraised in the resolution of the geodynamic problem. Numerous attempts were performed within this group of try, with two principal conclusions. (1) If we introduce F_{MPC} to the geodynamic problem, even with a weight that increases linearly from 0 to 1 in time, the numerical scheme diverges. (2) If we apply a given fraction of F_{MPC}, and maintain F_{MPC} proportional to the difference between the expected and actual

volumes hoping to attain low deviations by internal convergence of the series with time, we find that only a fraction of the expected volume change occurs. At the same time, the internal stress of the system increases to counterbalance the effect of F_{MPC}, which is considered as an external force in the system. Hence this resolution scheme was abandoned.

Deformation field   Another way to impose volume changes to the system is to impose a deformation field ε_{MPC} that would reduce/stretch the corresponding elements. ε_{MPC} can be calculated easily according to Figure 8.8 supposing isotropic and plane deformation (in 2-D), but a problem arises when trying to integrate it to the geodynamic routine. The first, minor issue is that because the deformation field of the geodynamic routine is not cumulative, but corresponds to the deformation at the actual discretization step, the amplitude of ε_{MPC} is usually too large and should be added by small fractions during several steps. The main problem, however, is that according to the scheme on Figure 8.8, the calculation of ε_{MPC} does not take into account the boundary conditions of the system. Thus its application is not compatible with the resolution of the problem, and causes divergence.

Internal stress   The last option to integrate metamorphic phase changes is through the stress field. According to Figure 8.8, we first calculate σ_{MPC} supposing plane, isotropic deformation. Then several different integration methods were tested in order to obtain the imposed volumes for the metamorphosed elements. It would be pointless to detail all these tests with respect to scaling σ_{MPC} and its relation to σ_{INT}, the internal stress of the system, and I choose to focus on the method that works. According to this implementation, the internal stress of the system is modified directly by substracting a fraction of the stresses corresponding to metamorphic phase change:

$$\sigma_{INT} = \sigma_{INT} - \frac{\sigma_{MPC}}{\mathcal{F}} \tag{8.1}$$

where $\mathcal{F} > 1$ is a coefficient that has a double role, as discussed below. Using Equation 8.1 basically weakens the internal stress of the system in areas of density change, and forces the elements to deform in consequence. Manipulating the internal stress of a system directly seems to be pertinent choice, and can be also found in engineering applications of phase transformation (*e.g.* Moumni *et al.*, 2007). Note that σ_{MPC} is proportional to the deviation between the imposed and actual densities, thus unvarying zones will not be affected by this approach. The meaning and effects of $\mathcal{F}$, such as description of stability tests of this approach are discussed in the following section, with technical details in Note

J.

8.2.5   Characterization of the σ_{MPC} approach

The $\mathcal{F}$ **coefficient** has a double role in Equation 8.1. While a higher value for $\mathcal{F}$ allows a smoother, longer, and numerically stable equilibration process, a smaller value can be interpreted as rapid MPC, with the possibility of causing instabilities. Both aspects can be explained in terms of inertia. Numerically, the resolution of density changes is divergent if we introduce σ_{MPC} into the system all at once, even with a linearly increasing weight with time. However, convergence is satisfied when only a given fraction of σ_{MPC} is applied. In the meantime, from a more realistic point of view, metamorphic processes do not occur instantaneously in the lithosphere, thus a given value of $\mathcal{F}$ could correspond to a certain kinetics during which metamorphic reactions are completed[4]. In the presented numerical models, $\mathcal{F}$=20 was chosen (unless noted otherwise), that allowed to obtain the imposed volumes in less than 0.5% of the total calculation time.

Stability tests were performed on a block model with three tabular media representing the mantle, the lower and the upper crust, without convergence and erosion. The density of the lower crust was changed by a constant $\Delta\rho$. The results reproduced the expected subsidence related to MPC of the lower crust, and then remained in equilibrium for different values of model parameters. These included different values of the mesh size (between 5 and 20 km), of $\mathcal{F}$ (15 to 200), of $\Delta\rho$ (0 to 400 kg·m^{-3}), of the number of steps ($2 \cdot 10^3$ to $2 \cdot 10^6$), different rheologies (elastic, non-linear visco-elastic, and visco-elasto-plastic), and the presence or absence of topography. Introducing several density changes at different moments of the simulation, or introducing σ_{MPC} in a short time period (1% instead of 10%) did not affect the stability of these test. Similar tests with a horizontal convergence of 20 mm·yr^{-1} were also found stable for all the above parameters, as well as for different durations of one time step (usually 20 years, tested between 1 year and 40 years).

---

[4]This type of application would require more accurate estimates of reaction kinetics, as well as detailed testing to calibrate the corresponding value of $\mathcal{F}$.

Note J

SOME TECHNICAL NOTES ON THE IMPLEMENTATION OF MPCs IN `Cast3M`

Obtaining the correct densities as a function of P and T is performed by using petrogenetic grids created in Perple_X, presented in Chapter 7.

Affecting the density is performed at frequency given by the user, usually at every 10% of the computation. At these moments, densities are interpolated for all elements, one by one. The local pressure is determined by $P = \int \rho(z) \, dz$ rather than by taking the first invariant of the stress field, which appeared to be perturbed by shear stresses in `Cast3M`. Then the interpolated density field is affected to both the mechanical and thermal properties of the system.

Computing times. Updating the density field increases the run time of the simulations, depending on the frequency of the updates. This is mainly due to the interpolation process, which is proportional to the size of the elementary zone, and the size of the T-P-ρ file. For example:

Elem. zone	Number of elements	T-P-ρ file size	Interpolation time
Upper crust	3128	4 (ρ=const.)	282 sec
Lower crust	916	625	1493 sec
Mantle	1514	4 (ρ=const.)	67 sec

Hence updating once the entire density field for this model takes about a half hour. Taking into account MPCs (at every 10%) in a model with convergence increases the total run time from $\sim$12 hours to $\sim$18 hours (on one processor of an Intel$^{\circledR}$ Xeon$^{\mathrm{TM}}$3.06 GHz computer and using 2 GByte RAM).

In the meantime, the increase in computation time due to the calculation of σ_{MPC} proportional to the difference between imposed and actual volumes is negligible, so this operation is performed at **every time step**.

Remeshing the model when erosion processes are included may introduce instabilities. As remeshing itself induces numerical noise in the imposed density field or the actual relative error of volumes, we chose to re-define the density field immediately after remeshing, and to neglect the relative errors prior to this operation. This is not a major problem, as these errors are the same order of magnitude that the perturbations caused by convergence at each time step. However, if remeshing occurs immediately after the update of programmed densities (within 0.5% calculation time), when the MPCs are not equilibrated yet, there is a high chance that instabilities will appear, especially if $\mathcal{F}$ is small and the remeshing criterion is high (50% of an element have disappeared by erosion). In the few tested cases, a higher $\mathcal{F}$ (=100) and a lower criterion (=25%) allowed to solve the problem.

8.2.6 Preliminary results on the localization of deformation

The effect of metamorphic phase changes on the evolution of the lithosphere's deformation using a dynamic resolution scheme is presented in this section. First the model parameters, then the effects with comparison to erosion processes and rheology are discussed.

Model characteristics

The geometry and boundary conditions of the model are shown on Figure 8.9 with the thermal and mechanical parameters listed in Table 8.1. All parameters were kept constant, except for the density of the lower crust that evolved according to the partially hydrated mafic petrogenetic grid (Fig. 7.9). A basal heat flow of 15 mW·m^{-2} is applied, which induces a maximal surface heat flow of 67 mW·m^{-2} and temperatures within the model ranging between 0°C (imposed at the surface) and 1317°C. The simulation is run for 4 Myr (200'000 time steps of 20 years), and the density of the lower crust is updated at every 10% of the computation. In order to avoid numerical instabilities, the different processes are introduced gradually: σ_{MPC} between 2 and 6%, convergence between 7 and 15%, and erosion between 0 and 30% of the calculation. The $\mathcal{F}$ coefficient was set to 20, and remeshing was imposed when half of an element have disappeared by diffusive erosion.

Table 8.1: *Mechanical and thermal parameters of the model on Fig. 8.9. Equations governing rheology are as in Chapter 6. ρ is density, E is Young's modulus, ν is Poisson's ratio, γ_0 is power-law strain rate, n is power-law exponent, E_a is power-law activation energy, K is thermal conductivity, C is heat capacity, and A is radiogenic heat production.*

Parameter	Mantle	Lower crust	Upper crust
Mechanical			
ρ (kg·m^{-3})	3300	MPH-grid	2900
E (GPa)	70	20	20
ν	0.25	0.25	0.25
γ_0 (MPa^{-n}·s^{-1})	$7 \cdot 10^{-14}$	$6.31 \cdot 10^{-20}$	$6.03 \cdot 10^{-24}$
n	3.0	3.05	2.72
E_a (kJ·mol^{-1})	$510 \cdot 10^3$	$276 \cdot 10^3$	$134 \cdot 10^3$
Thermal properties			
K (W·m^{-1}·K^{-1})	2.5	2.5	2.5
C (J·kg^{-1}·K^{-1})	1200	1200	1200
A (μW·m^{-3})	0.02	0.5	1
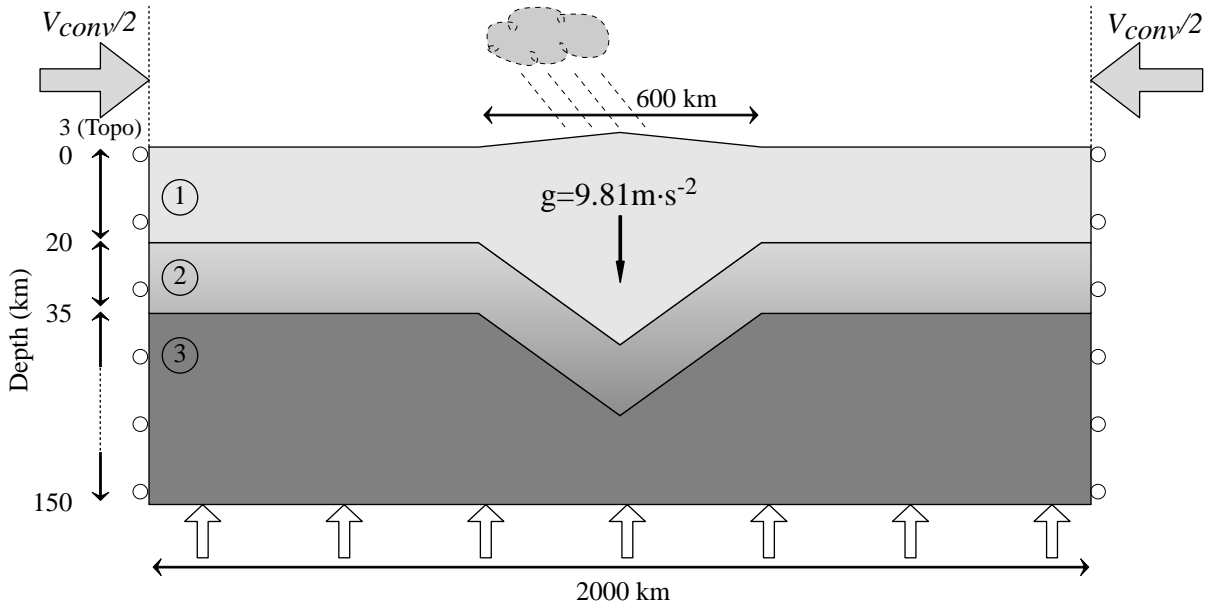
Figure 8.9: Geometry and boundary conditions of the thermomechanical model used to test metamorphic phase changes with a dynamic resolution scheme. The mechanical and thermal parameters of the three media (mantle, lower and upper crust) are summarized in Table 8.1. The 3 km high topography at the centre of the model (x=0) is isostatically compensated at the beginning of the simulation, supposing a constant lower crustal density. Boundary conditions allow free vertical movement on both sides of the model, and apply a basal hydrostatic support. Convergence rate (v_{conv}=20 mm·yr^{-1}) is symmetric, and erosion processes are diffusive. Vertical exaggeration is 10:1.

Comparing the effects of rheology, erosion, and metamorphic phase changes

Here we compare the deformation of the topography and the Moho in the convergent model presented above after 55 km ($\sim$2.75%) of horizontal shortening. In the case of topography, the relative evolution is shown by adjusting the displacements at the edge of the model to zero. For the Moho (and the base of the model), the relative displacement is shown by using the same adjustment and by substracting the original form of the interface. This way the relative deformations can be easily assessed.

First the effect of the considered rheology is analyzed (Fig. 8.10). All three curves show that for the visco-elastic rheology, the final geometries are broader compared to the elastic case, and the relative amplitudes are more important.

In a second study (Fig. 8.11) we add linear diffusive erosion, and apply an erosion coefficient of $k = 1 \cdot 10^{-4} \ m^2 \cdot s^{-1}$, which is close to the lower end of mass diffusivity used in the Himalayas (Cattin and Avouac, 2000). In consequence, the topographies found in
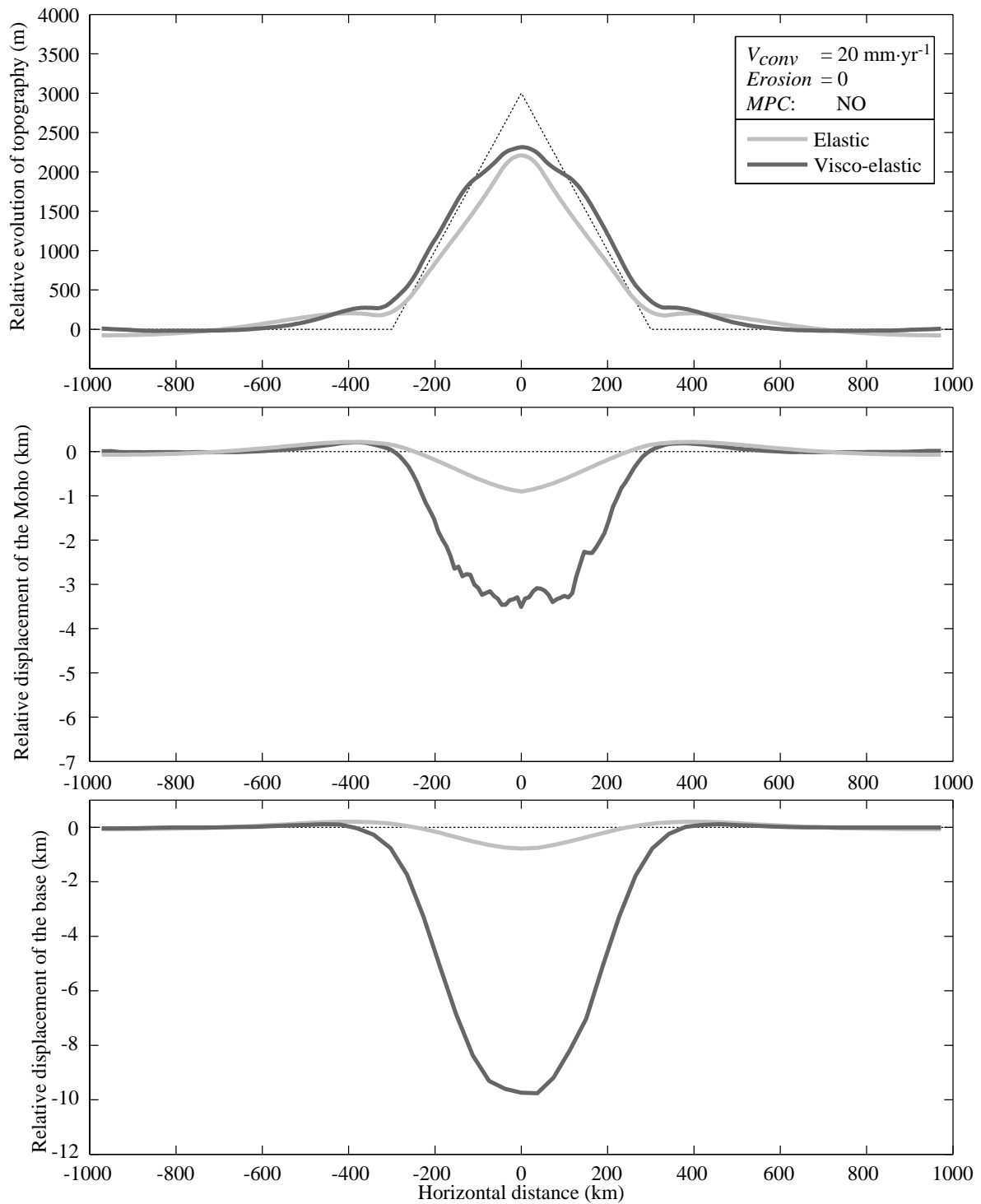
Figure 8.10: The effect of elastic and non-linear visco-elastic rheology on deformation. The gray curves show the geometry of the interfaces with respect to the dashed line (initial state for topography, 0 for the Moho and the base of the model).

the previous analysis are lowered, especially for the elastic case, and the relative deflection of the Moho is decreased. More importantly, it can be observed that the wavelength of the topography is larger than without erosion: the flanks of the mountain migrate toward the forelands, and the Moho's curve reaches near-zero relative displacement further away from the centre of the orogen.

Figure 8.11: The effect of erosion processes on topography and Moho geometry. The gray curves from Figure 8.10 are shown for reference.

In the previous two cases, the density of the lower crust was kept constant (2900 kg·m^{-3}), and metamorphic phase changes were not taken into account (*i.e.* Type I model of Figure 8.1). In this type of model, there is a discrepancy in the total mass of the system between the initial and final state: due to convergence, the elements are compressed while their densities remain constant. This type of error can be quantified by a criterion of mass conservation:

$$\delta_{MC} = \frac{\sum_i V_i^1 \rho_i^1 - \sum_i V_i^0 \rho_i^0}{\sum_i V_i^0 \rho_i^0} \tag{8.2}$$

where V and ρ denote the volume and density of the ith element at the initial (0) and final

(1) state of the model, respectively. In the previous simulations, δ_{MC} reached about –1.8% and –0.3% in the elastic and visco-elastic models, respectively, which is a considerable "loss" of mass. One could implement a numerical code where densities vary according to compression of the elements, but this way there would be no physical control of the density values, *i.e.* the densities would vary independently from geodynamic processes, such as metamorphic phase changes. In the following, we aim to respect mass conservation and eliminate errors from both sources: from the compression of the elements (Type I model) on one hand, and from the neglect of metamorphic facies (Type II model) on the other.

In the next test the density changes related to metamorphic facies are accounted for (Fig. 8.12). The curves representing deformation show a clear signal for both the topography and the Moho, and imply opposite consequences with respect to erosion. The relative displacements are increased, and the distance between the two flanks of the deformed topography (the spatial wavelength) is smaller than without MPCs. The amplitude of the effects are comparable to those of erosion processes. Thus localization of deformation is amplified by MPCs in the same way, but at a lower extent, as the difference between visco-elastic and elastic rheologies, with an additional narrowing of topography. Using this approach, mass conservation is respected at $\delta_{MC} = 5 \cdot 10^{-5}$ % and $1.5 \cdot 10^{-4}$ % for the visco-elastic and elastic case, respectively.

In a final test, both diffusive erosion and metamorphic phase changes are modelled. The density change in the lower crust between the initial and final state of the model is shown on Figure 8.13: it reaches a maximum of $\sim$30 kg·m^{-3} in the root of the mountain range, which is about 1% change compared to the average density of the crust. The combined effect of erosion and MPCs on deformation of the topography and the Moho with respect to the previous tests are shown on Figures 8.14 and 8.15 for elastic and visco-elastic rheology, respectively.

In the elastic case (Fig. 8.14), erosion still increases the width of the mountain, but metamorphic phase changes counteract in the centre of the orogen and keep a higher maximum altitude, allowing less decrease with respect to the initial state. In case of the Moho, the effects compensate each other closely, reproducing the curve without both erosion and MPCs.

In the non-linear visco-elastic case (Fig. 8.15), the combined effect of MPCs and erosion produces a topography that is in between the curves caused by individual effects. The general shape is very similar to the case where no erosion nor MPCs were taken into account, with a higher maximal altitude and slightly narrower flanks. This demonstrates that the influence of metamorphism is comparable to that of erosion for the considered
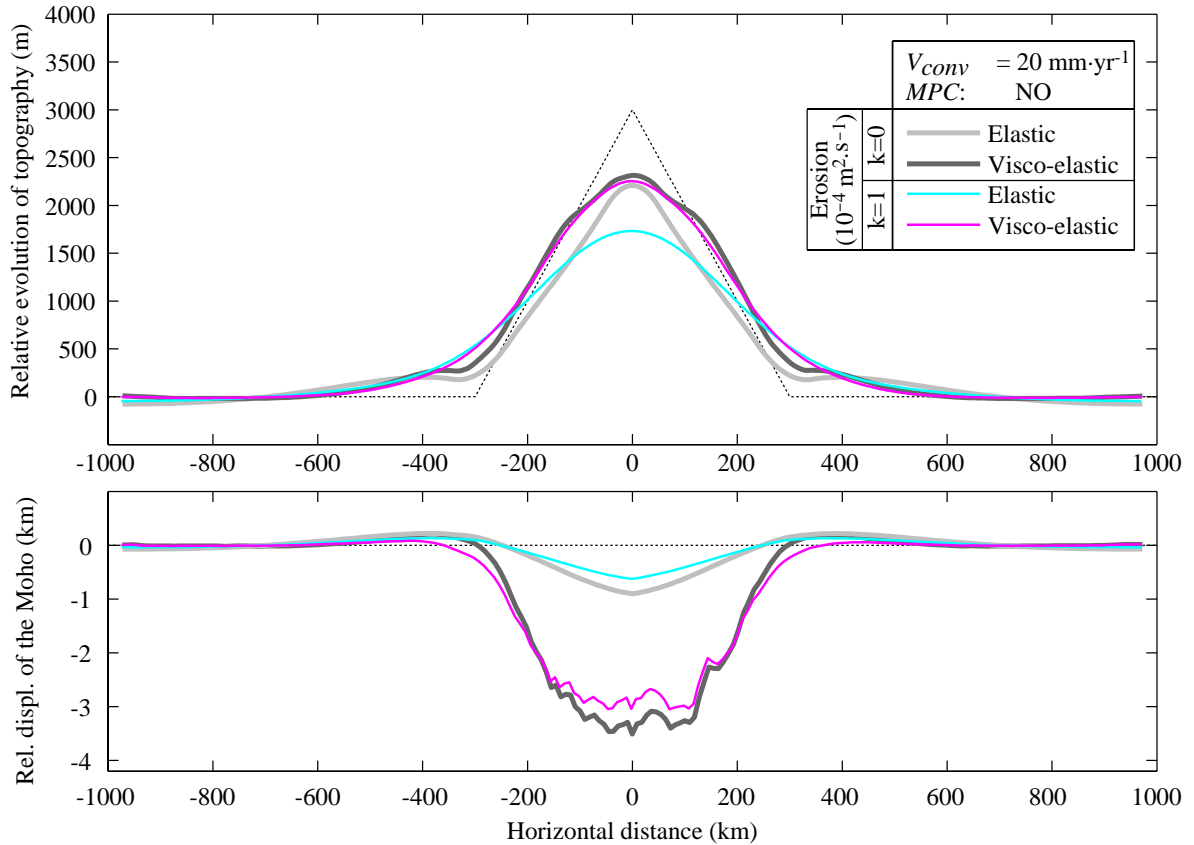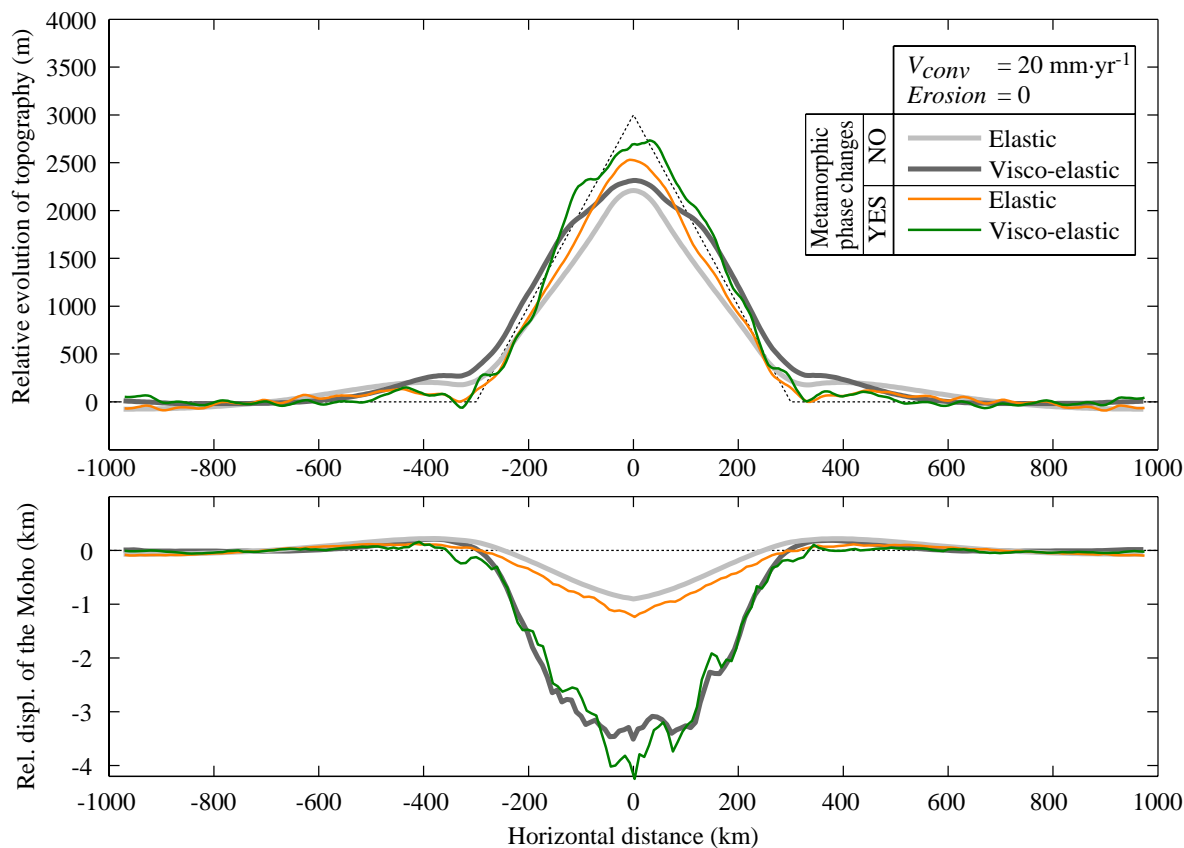
Figure 8.12: The effect of metamorphic phase changes on topography and Moho geometry. The gray curves from Figure 8.10 are shown for reference. Topography is smoothed using a 50 km wide sliding window in order to eliminate oscillations related to MPC (in all subsequent figures as well).
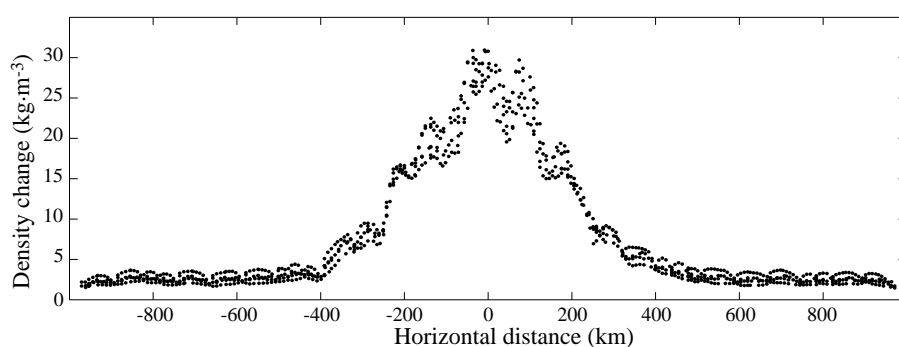
Figure 8.13: Densification of the lower crust due to metamorphic phase changes from the initial to the final state of the simulation (visco-elastic rheology, diffusive erosion).

parameters, and that their effects can potentially cancel out. For the Moho, the amplitude of the deflection is compensated between the two processes, but the width of the mountain's root is slightly increased. Adding erosion to MPCs does not affect the conservation of mass,
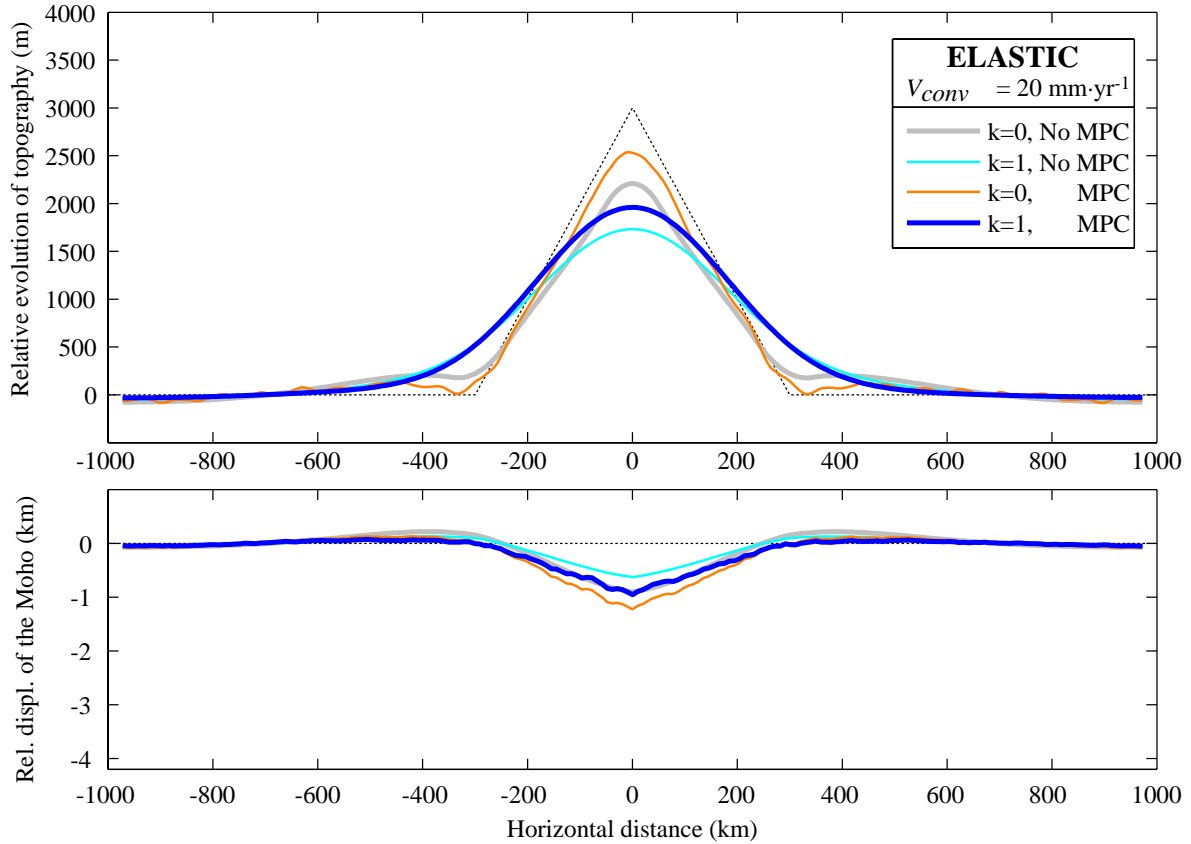
Figure 8.14: The effect of erosion and metamorphic phase changes for elastic rheology (thick curve). The gray curve with none of the processes, as well as the thin curves with one effect only, are reported from previous figures. Erosion coefficient k *is in* $10^{-4}\ m^2 \cdot s^{-1}$.

which is verified at $\delta_{MC} = 1.2 \cdot 10^{-4}$ % and $3.7 \cdot 10^{-4}$ % for the elastic and visco-elastic rheology, respectively.

In summary, the primary cause of deformation localization is the considered rheological behaviour, with visco-elasticity being more efficient than elasticity. The effects of metamorphic phase changes and erosion processes are comparable in terms of amplitude, and are both smaller with respect to that of rheology. Metamorphic phase changes increase the relative amplitude of deformations such as topography and crustal root of mountains, and tend to narrow the width of an orogen by maintaining a strong topographic gradient, even in a convergent context. In the meantime, the effects of erosion act in the opposite way and tend to lower and widen topography. The resulting deformation pattern is dependent of the relative weight of these two processes. Metamorphic phase changes are governed by the pressure-temperature conditions and the corresponding petrogenetic grids. The effect of deformation localization is linked to the absolute density differences between distant,
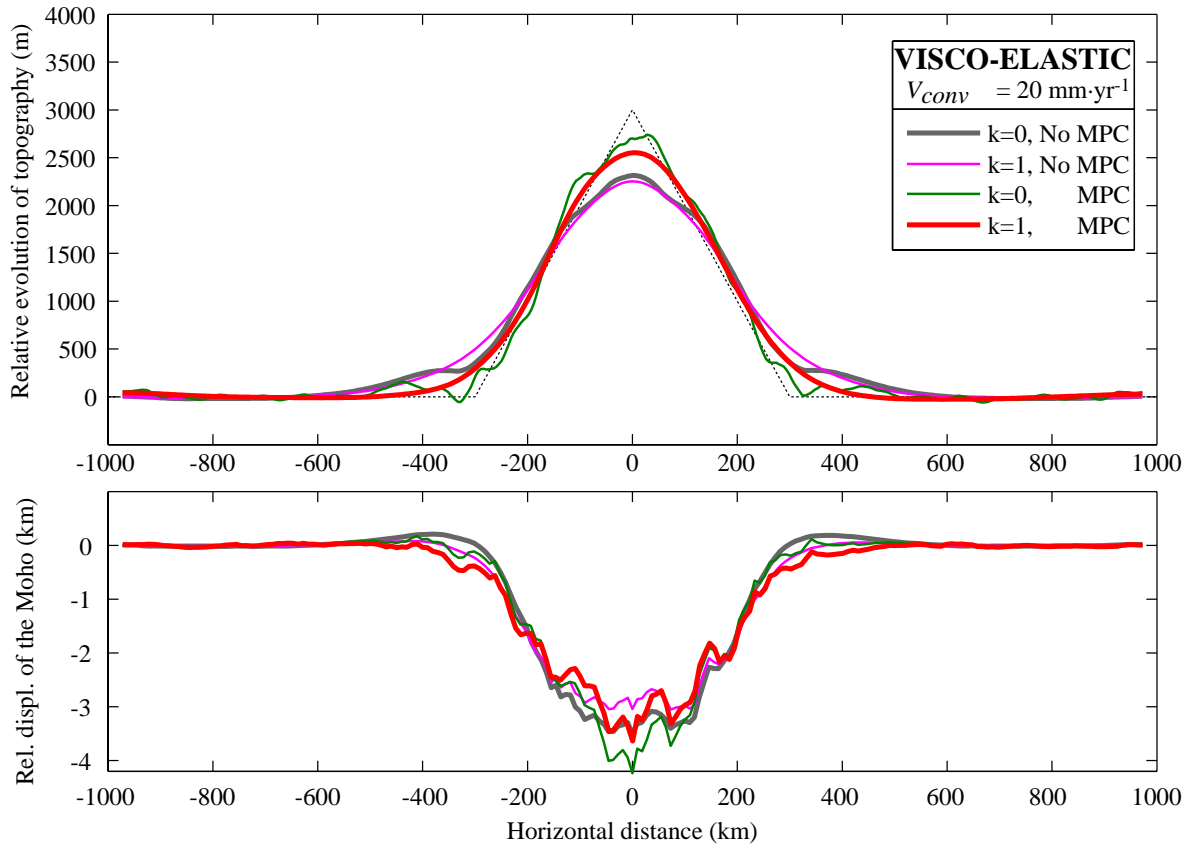
Figure 8.15: The effect of erosion and metamorphic phase changes for visco-elastic rheology (thick curve). The gray curve with none of the processes, as well as the thin curves with one effect only, are reported from previous figures. Erosion coefficient k *is in* 10^{-4} $m^2 \cdot s^{-1}$.

cold regions of an orogen and its central, thickened and warmer part. However, depending on the petrogenetical grid, warmer zones may correspond to different density values with respect to the mantle, and may affect the shape of the Moho by isostatic compensation as well. In our case, for example, higher temperatures meaning smaller densities cause a relatively higher topography due to the increased density contrast of the lower crust with the mantle. Thus even if metamorphic phase changes occur at depth and on the million year scale, they have a major effect on topography and interact closely with surface processes.

In applying numerical models to real cases, the importance and type (*e.g.* diffusive, river incision) of erosion should be calibrated based on field observations in a mountain range, and the petrogenetic grids to use should be calculated using available petrological constraints on bulk composition, and especially on water content. This way numerical modelling provides a common ground of investigation of geodynamic processes for geomorphology, petrology, and geophysical imaging (see Chapters 6 and 7).

8.2.7   Questions to ask and perspectives

The major shortcoming of the current implementation of metamorphic phase changes through modification of the stress field is the way in which σ_{MPC} is calculated. At the moment, the computation of σ_{MPC} from ε_{MPC} (Fig. 8.8) is performed by supposing an elastic behaviour. This may result in stresses that are too important for a visco-elastic, and especially for plastic rheology, and cause instabilities. In the meantime, the `COMP` operator in `Cast3M` , that allows to follow the evolution of a system using a given rheology, requires several other input fields to perform the above computation step, and may be highly time consuming. The possibility to change towards the use of this operator should be analyzed in the future.

Another (probably more philosophical) question is the assumed isotropy while transforming relative volume changes to deformation ($\Delta V/V \Rightarrow \varepsilon_{MPC}$; Fig. 8.8). This hypothesis was supposed at the beginning of our approach, but there is no evidence that metamorphic processes create isotropic stresses in reality. Tests on a layered model in convergence without erosion were found to be stable using anisotropic deformation field, but the factor of anisotropy was taken from the stress field of the system, a choice which is not more supported than using isotropy. Further discussion with petrologists and numerical modellers may bring new elements to this issue.

Concerning the perspectives, the next step is to run simulations where all elementary zones (*i.e.* mantle, lower and upper crust) evolve according to their specific petrogenetic grid. This would probably not affect too much the density structure of the mantle, but rather that of the upper crust, especially when it reaches considerable depths in a subduction zone or in the interior of a mountain range's crustal root. The needed petrogenetic grids can be easily derived from Perple_X (Connolly, 2005). At the same time, the effect of other erosion processes, such as river incision, and its interaction with metamorphic phase changes should be analyzed.

Another issue to consider is the tracking of elements in different metamorphic facies not only in terms of density, but also in terms of their mechanical properties, determining their rheology. For example, in the case of the Indian lower crust undergoing eclogitization, new elastic moduli and parameters defining rheology could be affected to the elements satisfying certain P-T conditions. This issue, however, relies on experimental data, that not always cover the entire range of pressure and temperature conditions needed for numerical modelling.

A further improvement in developing numerical models is to include reaction kinetics. Again, these laws are based on reactions observed in laboratory conditions with

usually fully water-saturated conditions. Nonetheless, in cases where kinetic slow-down or overstepping is put in evidence, numerical models could follow the temporal evolution of elements subjected to metamorphic reactions, and affect the corresponding densities and other physical properties according to given curves of reaction completion with time. The implementation of these types of delays could be performed by choosing an appropriate value for the $\mathcal{F}$ coefficient, and by adding a temporal variable to account for absolute delays.

Finally, a technically challenging task is to simulate the *initiation* of large scale geodynamic processes, such as subduction or continental collision. These require to include contact zones with the possibility of large displacements, and, due to this, to handle lithospheric layers that go beyond the boundary of adjacent layers near to the edge of the model. These aspects are difficult to implement and are not discussed in the frame of this thesis. Nonetheless, developments in this direction will certainly reveal interesting features about the early life of mountain ranges, and also about the evolution of underplating as observed in the central part of the Himalaya-Tibet region.

8.3   Looking at gravity anomalies perpendicularly

Using the compiled gravity anomaly dataset (Section 3.5), here we present an important application on along-arc variations. The original idea was developed in the oceanic domain for subduction zones, and gave new information on the seismogenic behaviour of mega-thrusts. An attempt is made to apply this method to a continental case. The conclusiveness of the results with respect to the data coverage is also discussed.

8.3.1   Trench-parallel anomalies and seismogenic behaviour

Song and Simons (2003) studied free-air gravity anomaly and topography variations along oceanic subduction zones, in relationship with the occurrence of great earthquakes. Their finding is that regions of strongly negative trench-parallel gravity anomaly (TPGA) concentrate most of the big events, while positive TPGA regions are relatively aseismic. Moreover, the TPGA anomalies correlate well with trench-parallel topography anomalies (TPTA), suggesting that over time scales up to ~1 Ma, spatial variations of seismogenic behaviour within one subduction zone are stationary and linked to the geological structure. They propose a model (Fig. 8.16) in which spatial variations in frictional properties on the plate interface control both the seismogenic behaviour and the trench-parallel anomalies.

Figure 8.16: Illustration of the observed correlation of TPGA and TPTA with seismogenic behaviour. The left panel schematically shows variations in gravity and topography due to changes in shear tractions on the plate interface (red line). Solid and dashed lines indicate gravity and topography anomalies corresponding to lower (τ_2) and higher (τ_1) shear tractions on the plate interface. The right panel schematically indicates changes in seismogenic behaviours with changes in shear tractions. Large shear tractions tend to produce stick-slip behaviour, and small shear tractions tend to produce stable sliding. (From Song and Simons, 2003)
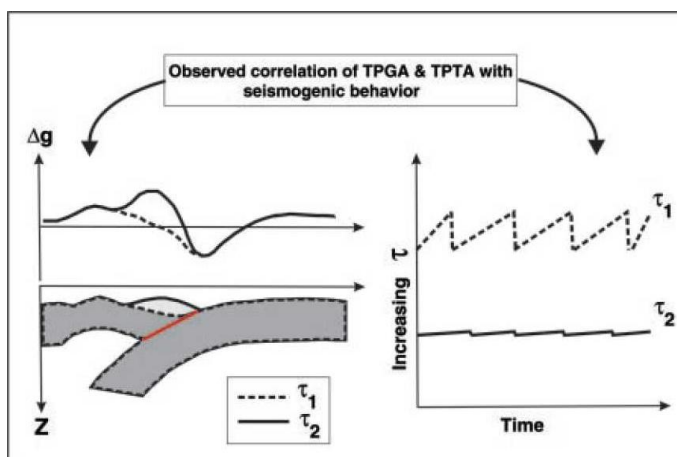
8.3.2   Continental application – processing

Based on Song and Simons (2003)'s idea, we calculate arc-parallel gravity and to-pography anomalies (APGA and APTA), and apply the above method to a continental case: the Himalayan arc.

First, the shape of the central arc is described by two arc segments, so that it follows the curve of the Himalayas at its front. Then the studied region is delimited to $\pm 2.5°$ distance inside and outside this arc, with the exception of the Shillong plateau in E-India, which is not part of the Himalayan arc but has a prominent topography. Then 10 km wide concentric arc-stripes were defined, along which the data points were averaged.
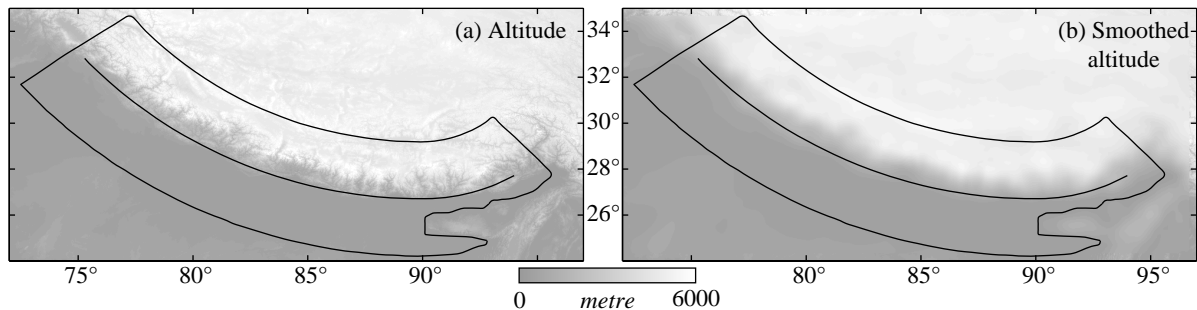
Figure 8.17: Real topography at 2 arcmin *resolution (a) and the smoothed map for used for arc-parallel topography anomaly (APTA) calculation (b). The poles of the western and eastern arcs are located at latitude 41°N and 33°N and longitude 90°E, with radii of 14.3° and 6.3°, respectively.*

Gravity data is taken from the compiled dataset presented in Chapter 3 (Fig. 3.18). The GETECH dataset in eastern Nepal is included for this study exclusively. The data points within each concentric arc-stripe were regrouped to calculate an average value that takes into account their along-arc distribution. Then, this average value was removed from the Bouguer anomaly to yield the APGA.

Topography data is taken from the SRTM[5] (Rodriguez *et al.*, 2005) at 2 *arcmin* resolution (Fig. 8.17a), yielding cells of ~ 3.7 km in width and ~ 3-3.4 km in height. As topography data at the given resolution still shows valleys and rifts, the cells are laterally smoothed with the smallest value at which these features are eliminated, that is over 10 cells (~ 30 km; Fig. 8.17b). Then, similarly to above, average values within the concentric arc-stripes are removed to provide the APTA (Fig. 8.18).

---

[5]Shuttle Radar Topography Mission
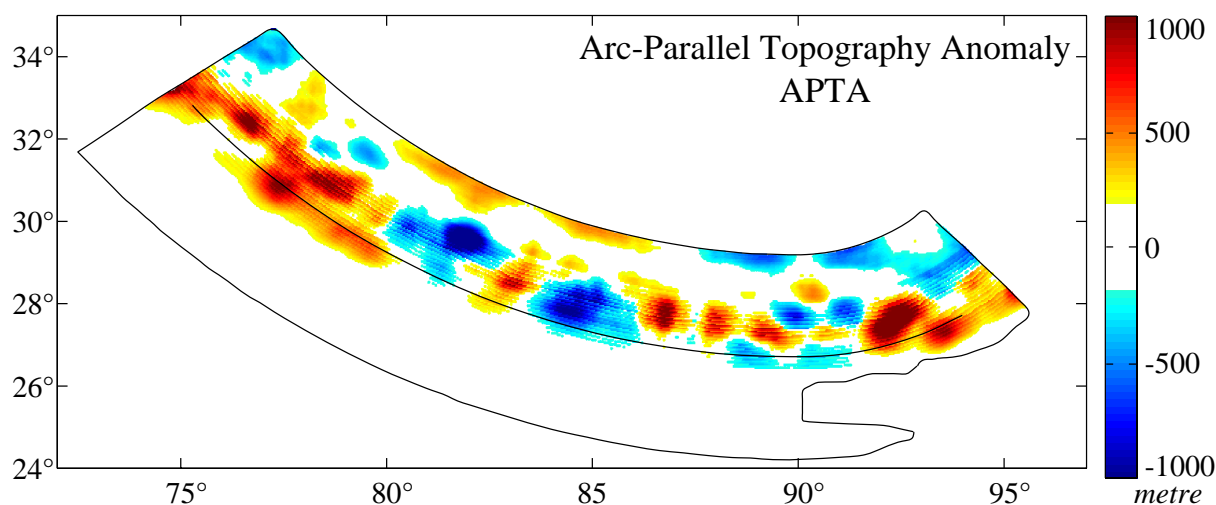
Figure 8.18: Arc-parallel topography anomaly in the Himalayan arc, represented over the entire zone of study (black contour). See text for discussion.

8.3.3   Arc-parallel anomalies – results

The arc-parallel topography anomaly (APTA) for the entire studied zone is shown on Figure 8.18. The amplitude of the anomalies is in the order of ±750-1000 m, which is about 5 times more elevated than in the oceanic cases in Song and Simons (2003). This is probably due to larger erosion rates on continents compared to oceanic trenches. The more prominent anomalies are located north of the front of the Himalayas, in the zone where India starts to underthrust along the Main Himalayan Thrust. The main negative anomalies are located between longitudes $\sim83.5°$-86°E and ~80-82.5°E, which, if spatially coincident with negative APGA, would correspond to strongly coupled zones and thus high seismic hazard. Strongly positive anomalies are located at $\sim75°$-80°E and $\sim92°$-94°E, together with some more spotty zones between $\sim86°$-90°E.

The arc-parallel gravity anomaly (APGA, Fig. 8.19) also shows negative and positive anomalies, that are about the same range as in the oceanic case (~50 mGal). The positive anomalies lie at $\sim88°$-93°E and west of $\sim78°$E, and negative anomalies occupy the space in between. However, the main difference of APGA from APTA is the gravity anomalies are located south of the Himalayan front, where the topography anomalies are zero. Actually the correlation of positive and negative APTA and APGA is suggested by the eye only. If we represent APTA only where APGA is available (Fig. 8.19), — and thus where comparison makes sense, — we see that there is no gravity measurement available where the most prominent APTA occur. The only zone where APGA and APTA cover each other along the Himalayan range is in central Nepal, at ~85-86°E, where the topography anomaly varies
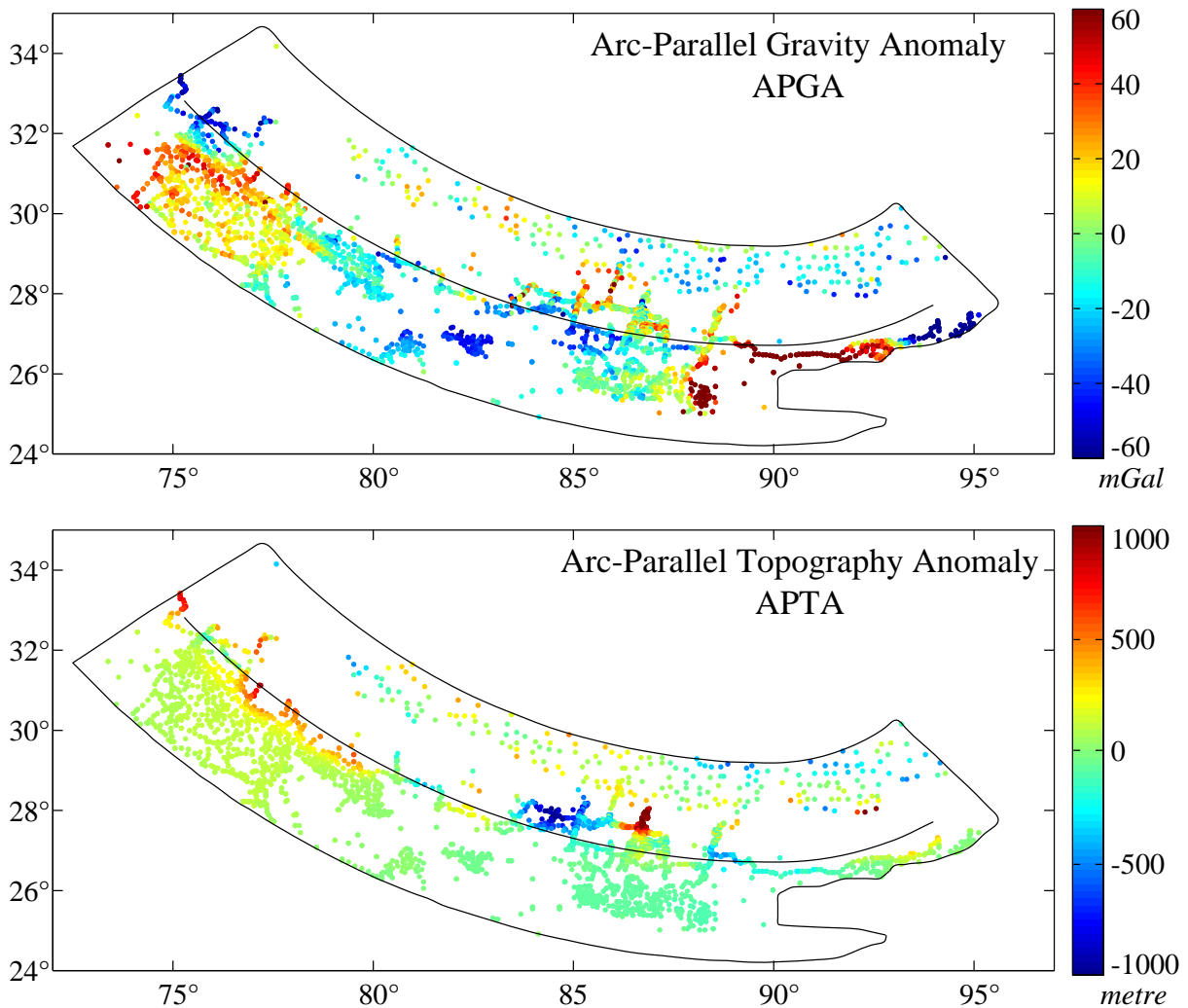
Figure 8.19: Arc-parallel topography and gravity anomaly in the Himalayan arc, represented at those locations only where gravity data was measured. See text for discussion.

from negative to positive values towards the east, but APGA — although its coverage is limited — does not show strong anomalies. The non-correlation of APGA and APTA is also illustrated on Figure 8.20.

In conclusion, there is a potential of using arc-parallel topography and gravity anomalies in continental context. Based on Song and Simons (2003)'s method, we showed that strongly negative and positive APTA regions exist along the Himalayas, but the lack of gravity anomaly measurements causes that relevant information concerning the seismo-genic behaviour cannot be inferred. Future field surveys should aim to cover the Nepali Far West, NW-India, Bhutan, and the eastern syntax of the Himalayas in order to cal-
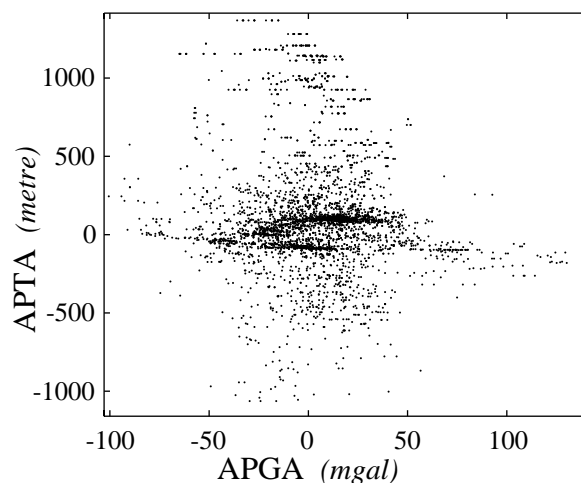
Figure 8.20: Cross-plot of APGA and APTA values. The lack of correlation is due to the poor coverage of gravity data in the Himalayan arc.

culate APGA. On a technical side, APTA should be analyzed together with topographic maps, as the spatially rapid changes of topography on continents may cause artefacts (for example deeply incised valleys, or young volcanoes). In the meantime, maps also help the interpretation: the Kathmandu Klippe, a zone of negative APTA, is known to have been destroyed by large historical earthquakes (*e.g.* Bilham, 1995), and the discussion on fluid accumulation, with the lateral variations of the Moho's plunge location (see Section 4.3.3) also points to the same elevated seismic hazard of central Nepal. Furthermore, APTA and APGA estimates can also be completed by energy balance calculations based on micro-seismicity data, as well as lateral variations of deformation rates seen by GPS (Bettinelli *et al.*, 2006).

However, we repeat that further analyses concerning APGA should be preceded by the completion of the gravity anomaly data coverage along the Himalayan arc in order to improve the quality of the image. This leads us to the issue of imaging: what are the optimal conditions to obtain a geophysical image (either in map view, along a vertical profile, or in 3-D) that has an acceptable quality?

8.4   Improved imaging

8.4.1   Conditions for making an image

Geophysical experiments in Tibet aiming to reveal the crustal and lithospheric structure have increased their resolution during the decades. Nonetheless, due to the size of the Tibetan Plateau, the relative coverage is still low. In fact, the problem here is not the amount of work put into surveying, but the extreme surface to cover. To give a more pre-

cise idea of Tibet's area, Figure 8.21 shows, at the same scale, the plateau as well as two geographic zones that may be familiar to the Reader. This comparison, combined with the increased efforts needed for access, logistics and field conditions in Tibet, illustrates well the difficulties of obtaining high data coverage all over the plateau. However, despite these difficulties, efforts must continue to obtain a homogeneous coverage at an even resolution for all geophysical datasets. These are the number one and two criteria for producing an image at depth.
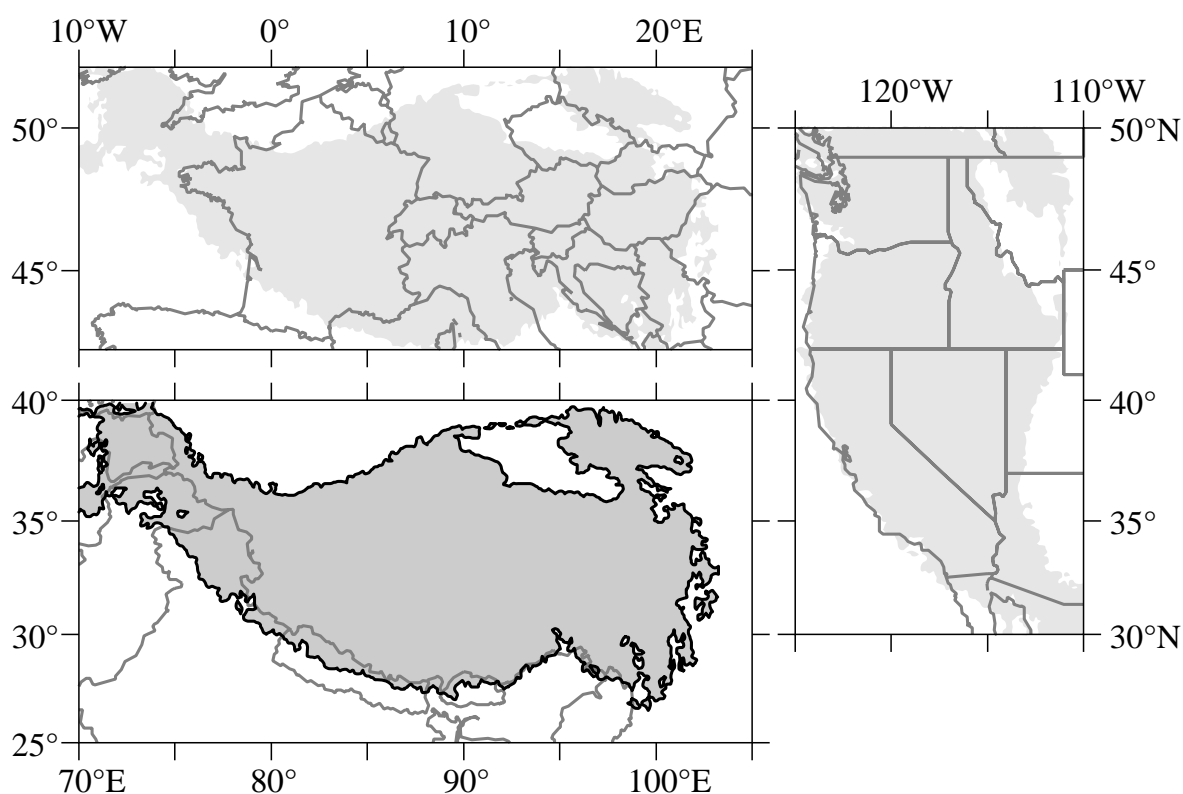
Figure 8.21: Comparing Tibet's size to Europe (at middle latitudes) and the US West Coast. For Tibet (bottom), the shaded region and the thick black line contour the zone lying above 3500 m altitude. This surface would easily encompass France, Switzerland, half of Germany and Italy, Austria, Hungary, and former Czechoslovakia and Yugoslavia (top); or California, Nevada, Oregon, Washington, Idaho and more (right).

For gravity data, Figure 3.18 presented a compilation that seems to be rather homogeneous. However, if we calculate the distance to the location of the closest gravity measurement (Fig. 8.22), it turns out that the coverage is sparser in the central and the western part of the plateau. More importantly, and unfortunately, the greatest hole in the dataset is where the gravity anomalies vary the most: along the Himalayas. With the ex-

ception of central Nepal and Sikkim, there is no data point at all in the Himalayan arc in NE India, western Nepal, all of Bhutan, and around the eastern syntax. As discussed above (Section 8.3), the acquisition of gravity data along the Himalayan arc has a key importance in the analysis of arc-parallel anomalies and seismic hazard.

For seismic and seismological data, Figure 8.22 shows that the interpretation is even more difficult. The coverage is similar to the geographic coverage about 100 years ago: a few lines run across the plateau, leaving vast unexplored areas, especially in the northern-northwestern part of Tibet. The need for better data coverage does not apply for gravity and seismological observations only: heat flow measurements are necessary to better constrain the thermal structure beneath the plateau, and magnetotelluric data at higher resolution would allow to further discuss the correlation between bright spots and extensional grabens (see Section 4.4.1).
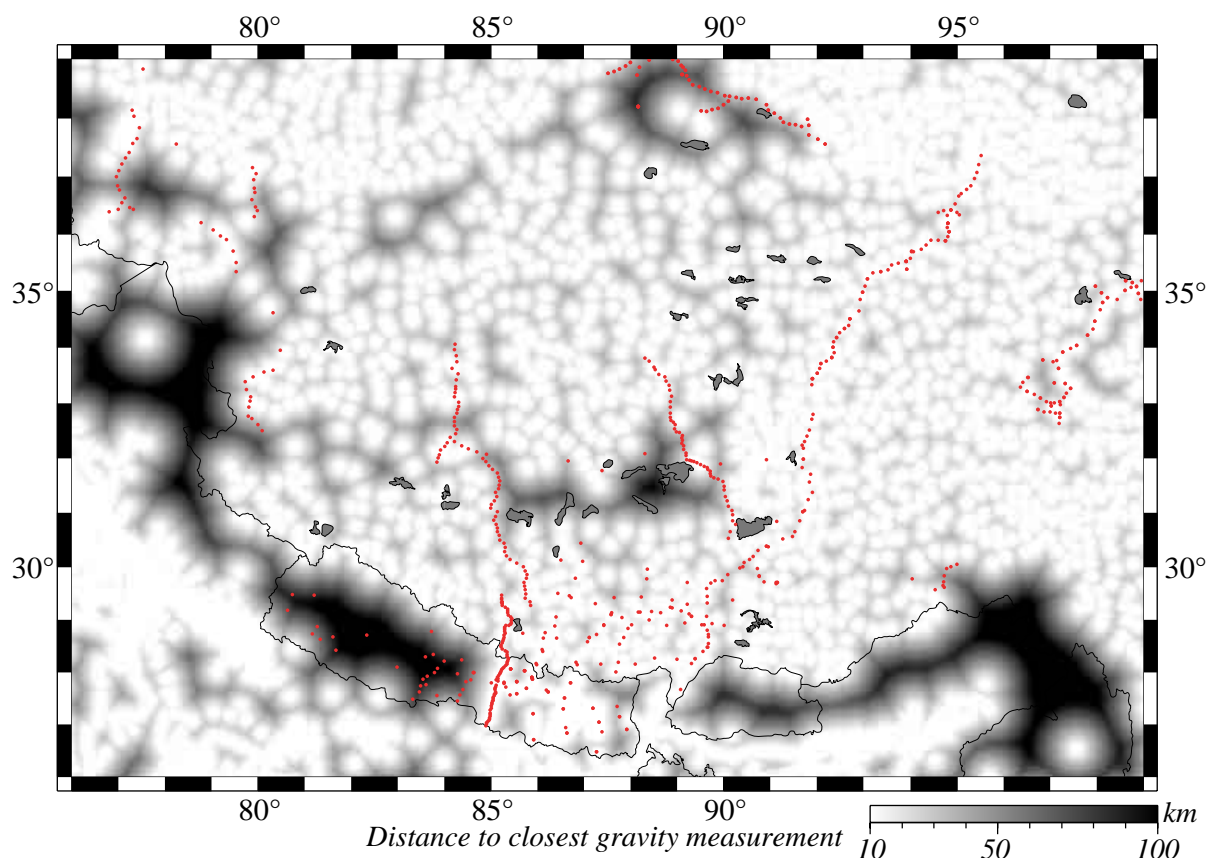
Figure 8.22: Coverage of gravity anomaly measurements in the Himalayan-Tibetan region. The colour scale represents the distance to the closest data point, revealing the gaps in coverage along the Himalayan arc. Red dots show the location of seismometers deployed in the Tibet, mostly by temporary (array) experiments.

8.4.2   Hi-CLIMB — improved seismological images

The Hi-CLIMB experiment can be regarded as the beginning of a new generation of passive seismology exploration. The number of stations and sites, the three-year duration, the amount of collected data, and the average station spacing — satisfying the above imaging condition for coverage along a profile — are only quantitative measures of the records it holds. The real difference can be illustrated by showing what the experiment would have yielded if a "classic" acquisition was deployed. By "classic", we mean a typical old "French style" Lithoscope (1992-2001) experiment with about 35 stations spaced at an average distance of 20-25 km, for a duration of a few months. All other parameters were kept the same for RF processing and migration, except that the final image has been smoothed more, in order to better connect the possible interfaces (Fig. 8.23).

The images speak for themselves. The Hi-CLIMB experiment's image is clear and shows the continuity of the interfaces at high resolution, especially within the crust. The simulated, previous generation experiment allows to pick the highest impedance contrast beneath each station (supposedly the Moho), but fails to:

– connect them without ambiguity;

– identify and delimit low velocity zones and bright spots in the upper crust;

– provide any information from the migration of multiples (double interface, Moho pick for average V_P/V_S calculation), which has been shown to be the most advantageous tool in imaging (Chapter 5).

Most of the observations and interpretations presented in this thesis, emerging from the above images obtained in structurally complex zones, could not have been made using a previous generation experiment. In fact, during migration, the close station spacing provides a large number of rays that cross each other at shallow depth, and sample the main interfaces, such as the Moho, at an increased number of times compared to the "classic" case. This is similar to the fold of a seismic shot during industrial exploration: the more geophones you put, the higher number of times you sample the same point at depth. The fold, or the number of traces crossing each cell of the migration mesh, is shown on Figure 8.24 for both migrations. For the Hi-CLIMB experiment, using the W3 selection list with $\sim 1 \cdot 10^4$ traces, and the average inter-station distance of $\sim$4 and $\sim$9 km imaging the Moho at $\sim$40 and $\sim$75-80 km depth in Nepal and in Tibet, respectively, the number of stations sampling the same point on the crust-mantle boundary is roughly 10 and 9. These numbers make the interpreters comfortable even if one or two stations are temporarily out of order, and allow stacking to suppress noise efficiently.

The key to the success, in my opinion, is not only the records mentioned above. Using
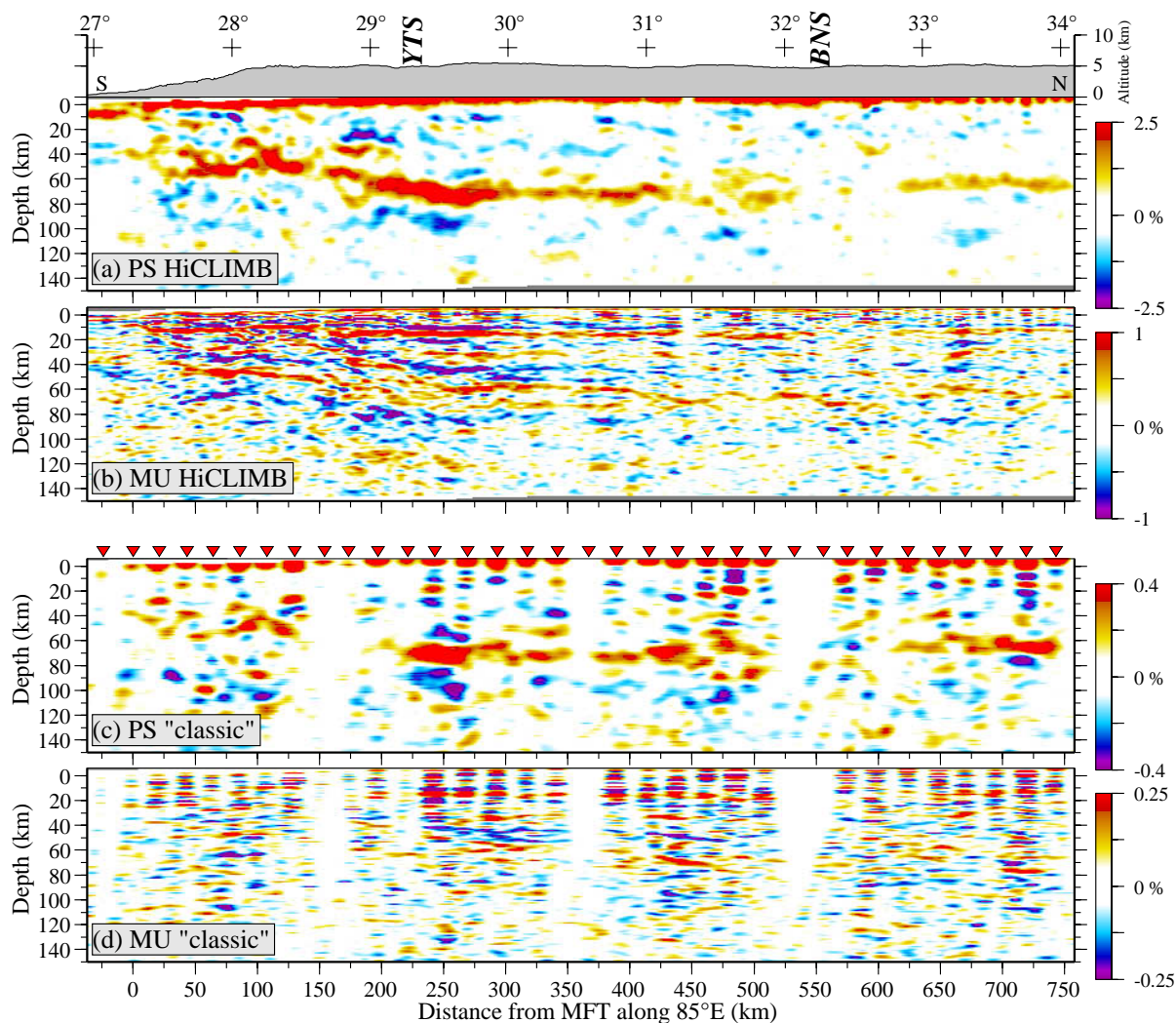
Figure 8.23: Comparison of migrated RF profiles of the complete Hi-CLIMB dataset (a and b) with a simulated "classic" acquisition using less stations deployed more sparsely (c and d, location of simulated stations of the rarified profile is marked with red triangles). All processing parameters are the same for the PS (a and c) and multiple (b and d) phases, except for horizontal smoothing which is 3 and 5 km, respectively, for the Hi-CLIMB profile and the "classic" simulation.
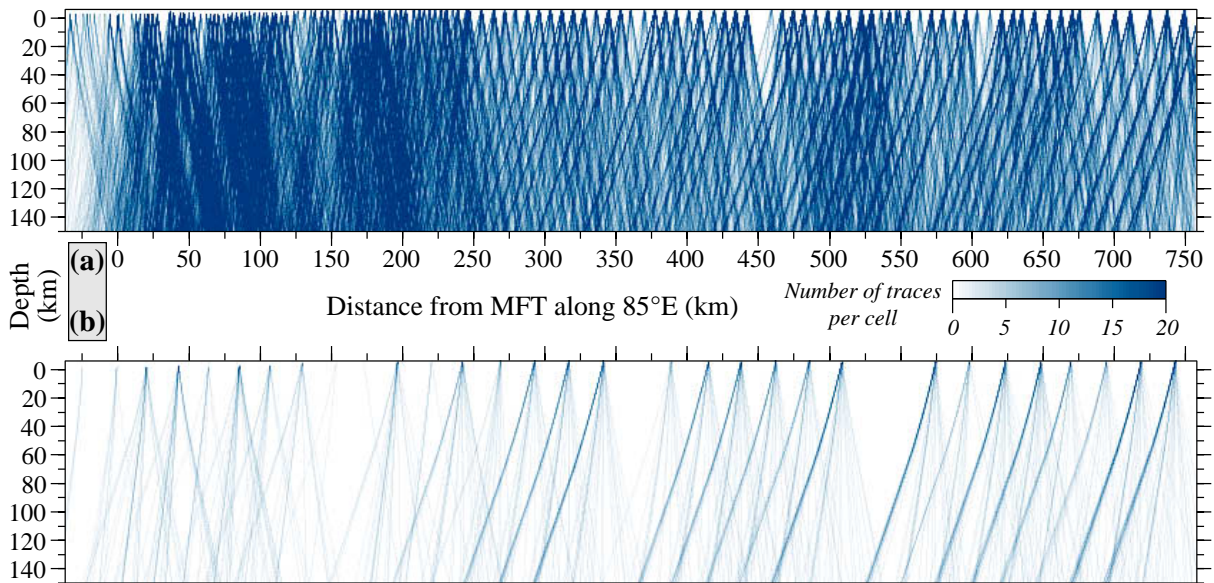
Figure 8.24: Trace count per migration cell (fold) for the full Hi-CLIMB dataset (a) and for the simulated sparse deployment (b) at the same colour scale. The coverage of the profile by a large number of traces allows to use small size cells to image fine structures and to still have several rays crossing and providing information.

a relatively homogeneous instrument park, tested and adapted to field conditions, together with continuous station verification, is also crucial. In case of the Hi-CLIMB experiment, the main array's stations, exclusively from IRIS-PASSCAL[6] showed a better performance with regard to lower atmospheric pressure, for example, than the lateral stations deployed in southern Tibet by other institutes. The regular checking and repairing, as well as efforts on recovering and organizing data, greatly contributed to the integrity of the dataset.

8.5   Improvements in interpretation

8.5.1   About the Hi-CLIMB experiment

The Hi-CLIMB broadband seismology experiment's first, "in the field" part, was running between September 2002 and September 2005. The amount of acquired data is very large, and the possibilities of seismological applications alone are numerous. This thesis presented several studies where seismological data was joint to other type of datasets and/or

---

[6]Incorporated Research Institutions for Seismology – Program for the Array Seismic Studies of the Continental Lithosphere

investigation methods. However, the more thorough processing and analysis in the domain of seismology would certainly provide further constraints. This was not my objective, and it is neither my task to enumerate what could be done in this second, "in the lab" part of the experiment, but I would like to emphasize a few points that are/would be complementary to the topics discussed in this thesis.

Reliable information on absolute velocities is of primary importance. The analysis and relocalization of local earthquakes, similarly to Monsalve *et al.* (2006) for the HIMNT experiment, would greatly improve our knowledge on P wave velocities, and would allow to construct a 2-D absolute velocity model in both V_P and V_S , improving the accuracy of RF migrations, among other things. Furthermore, the distribution of the events would also yield information about the distribution of brittle and ductile deformation zones with depth, and strengthen the constraints on the actual rheology of the lithosphere. This analysis could be completed by further continuation of solving focal mechanisms of earthquakes that occurred during the experiment (Burtin *et al.*, 2005) and by inversion for the velocity model beneath the array.

The lithospheric structure is well constrained by receiver functions using P-to-S conversions, and also by S-to-P conversions (G. Wittlinger, personal communication). However, other deconvolution methods, developed for single-component seismometers (Li and Nabelek, 1999), should be performed as well, as the results may provide further details on Moho and lithospheric features. Analysis of surface waves would certainly add more information concerning the different tectonic blocks.

Finally, the upper mantle structure, not strongly constrained in this study, should be investigated by shear-wave splitting, which would provide primary information on the existence and distribution of anisotropy. Thus deformation patterns of the lithospheric mantle could be inferred, compared to results from other approaches, and simulated by numerical modelling.

8.5.2   Inversion and modelling issues

The recovery of absolute velocities, together with receiver functions, is usually performed using joint inversions. The complementary methods are tomography (*e.g.* Vergne, 2002), and dispersion curves from surface wave measurements (*e.g.* Julià *et al.*, 2000). Since the development of the ambient noise cross-correlation method to obtain Rayleigh-wave dispersion curves (Shapiro and Campillo, 2004), the possibility to jointly invert RFs with this type of data is also open (see Section 4.3).

The advantages of using both seismological and gravity information to image the

structure of the lithosphere has been illustrated in Chapter 7. In the presented example, the contours of structures obtained by receiver function migration were directly — but separately — used as density contrasts to model Bouguer anomaly. The joint inversion of both seismologic and gravimetric data would be a powerful way to recover velocity and density perturbations together. Efforts are undertaken to apply the developed joint inversion methods to the lithosphere using appropriate laws relating densities and velocities (Zeyen and Achauer, 1997; Tiberi *et al.*, 2003; Basuyau, 2007).

Conclusions

This thesis presents high-resolution images of the lithosphere across the Himalayas and Southern Tibet using new seismological data from the Hi-CLIMB experiment, and two studies concerning the ongoing physical processes — flexure and eclogitization — across and beneath the southern margin of the Tibetan Plateau.

Improved imaging with receiver functions is accomplished due to two main factors. The first one is the close station spacing of a large number of seismometers, that allow to cross seismic wave's ray-path (and thus information) starting from shallow depths, and to constrain intra-crustal and lithospheric interfaces at an increased coverage. The second factor is related to the imaging technique: receiver functions are first selected using quality control criteria, and then migrated as direct conversions and as multiple phases. The use of multiple conversions clearly helps to focus the image by pointing out those zones where interferences are potentially blurring the migrated profiles. As a result of the exceptional field deployment and the thorough analysis, the presented images show many details and new information within the crust and on the Mohorovičić discontinuity. Despite the complexities, our understanding of the lithospheric structure have advanced. The images draw the major faults in Nepal near the surface, shallow bright spots in the Tibetan upper crust in correlation with extensional grabens, the Main Himalayan Thrust from its surface expression to its deeper ductile part, and the Indian lower crust underplated beneath Lhasa block. The northward propagation of India's lithosphere (except its upper crust) extends up to 31.3°N, ~100 km south of the Banggong-Nujiang Suture. In this zone the crust-mantle boundary is undefined, suggesting a mixing zone of Indian and Eurasian material, the latter being identified by a more simple lithospheric structure beneath Qiangtang block.

Based on the available new information on geometry, earlier studies investigating physical processes of the collision zone can be re-appraised. The flexure of India was modelled since a quarter of a century, using gravity anomalies and thermomechanical modelling. However, as precise estimates of crustal thickness and flexural curvature were not available, the analyses were not well-defined. The results show that while the lithospheric layers decouple from south to north, and the subsequent loss of strength of the upper and lower crust decreases the effective elastic thickness of the India plate, mechanical support of the topography by the upper mantle resists and prevails. This, together with the fact that geometries induced by a weak-mantle rheology ("crème brûlée") are unambiguously different from observations, favours a strong-mantle rheology ("jelly sandwich").

The seismological image of lithospheric contours also allows to map density variations within the crust, and especially in the underplated Indian lower crust. A localized and significant (>10%) increase in density is constrained to occur close to the Yarlung Tsangpo Suture on three different profiles, and is interpreted as eclogitization. Petrological modelling using a mafic composition and different assumptions on water content suggest partial hydration of the lower crust. Furthermore, in order to fit the gravity anomalies, a kinetic hindrance of metamorphic reactions have to be introduced. Based on modelling results, this overstepping is possible for reactions that does not involve free water. Rapid eclogitization of the lower crust occurs when pressure-temperature conditions reach dehydration reaction curves.

Taking into account density variations related to metamorphic reactions, accompanied by volumetric variations in order to respect mass conservation, is an important aspect in numerical modelling, as the corresponding effects on the evolution of mountain building can be significant.

The presented results emphasize the importance of resolution of geophysical surveys. The new information are significant not only from a seismological and structural point of view, but also provide new elements on the evolution of the collision zone, on the matter of regional isostasy, and on the importance of metamorphic reactions in mountain building.

In the meantime, answering open questions always raise new issues. While the main crustal features and the Moho are clearly imaged and well constrained by receiver function migrations, the primary seismological method used in this work, question marks appear concerning the role and the advance of the lithospheric mantle. Other seismological investigations should be performed to infer further and more robust results, especially in light of the new dataset's potential (size and quality).

The obtained results on the crust should be completed by methods yielding absolute velocities, such as joint inversion with tomography or surface wave dispersion curves,

as well as S-to-P receiver functions. Local seismicity analysis would provide information not only on P wave velocities but also on the strength on the lithospheric layers. Mapping anisotropy by shear-wave splitting would certainly contribute to the understanding of dynamic processes.

Finally, I need to emphasize that the presented high-resolution images constrain the geometry of the structures along a single line only. Although the first order lateral variations of the Moho and the Main Himalayan Thrust are mapped in southern Tibet, there are still large areas that have remained unexplored by most geophysical methods, including seismology, magnetotellurics and heat flow measurement. In lack of these, and the subsequent modelling approaches, the 3-D pattern of the plateau's structure cannot be discussed in further detail, and large scale lateral processes such as extrusion cannot be better constrained. Future field experiments should gather both scientific and political efforts, and aim to obtain a sufficient coverage at an even resolution that will allow to discuss the evolution of deformation of the entire Tibetan Plateau. In the meantime, application of the imaging and modelling methods to other regions, such as the Altiplano or Anatolia, would contribute to further develop joint approaches and to improve our understanding of collisional contexts and plateau formation.
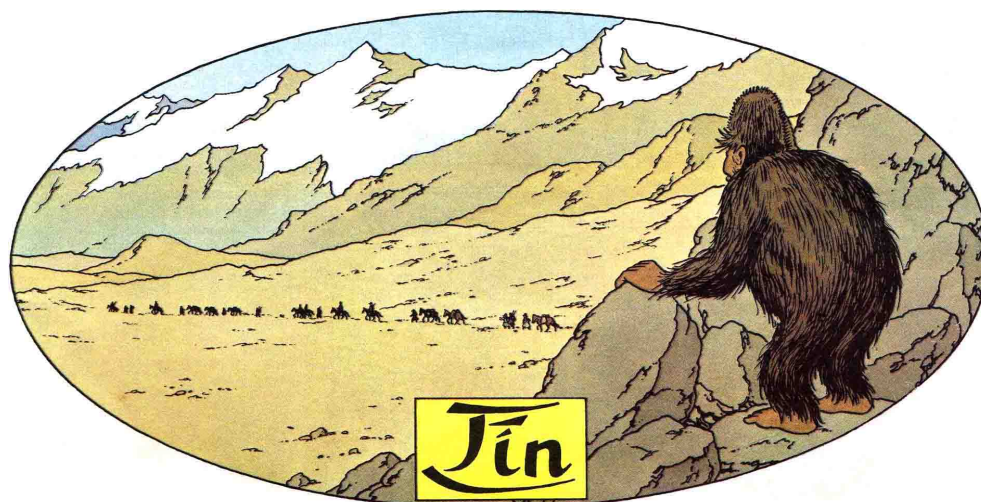
APPENDIX A

List of abbreviations

ANSS	Advanced National Seismic System
BGI	Bureau Gravimétrique International
BNS	Banggong-Nujiang Suture
CAGS	Chinese Academy of Geological Sciences
CCP	Common Conversion Point
CEA	Commissariat à l'Énergie Atomique
CNRS	Centre National de la Recherche Scientifique
DMG	Department of Mines and Geology (Nepal)
DyETI	Dynamique et Évolution de la Terre Interne
EET	Effective Elastic Thickness
ENS	École Normale Supérieure
GPS	Global Positioning System
GSN	Global Seismographic Network
Hi-CLIMB	Himalayan-Tibetan Continental LIthosphere during Mountain Building
HIMNT	HIMalayan Nepal Tibet earthquake seismic experiment
ILC	Indian Lower Crust
INDEPTH	INternational Deep Profiling of Tibet and the Himalayas
INSU	Institut National des Sciences de l'Univers
IPGP	Institut de Physique du Globe de Paris
LVZ	Low Velocity Zone

MBT	Main Boundary Thrust
MCT	Main Central Thrust
MD	Mafic and Dry
MFT	Main Frontal Thrust
MHT	Main Himalayan Thrust
Moho	Mohorovičić discontinuity
MPC	Metamorphic Phase Change
MPH	Mafic and Partially Hydrated
MT	Magnetotellurics
MW	Mafic and Wet
NA	Neighbourhood Algorithm
OSU	Oregon State University
RF	Receiver Function
RRF	Radial Receiver Function
TRF	Tangential Receiver Function
YTS	Yarlung Tsangpo Suture

APPENDIX B

Station information

The Hi-CLIMB experiment deployed a large number of stations between September 2002 and September 2005. The closely spaced main array concentrated most of the stations, but two small profiles to its west (Nepal), and lateral sites to its east (Tibet) acquired useful data that allowed to investigate 3-D variations of crustal structure. Also in Nepal, to the east, 15 stations from the HIMNT experiment were made available. The following table summarizes the stations' name, geographical co-ordinates, the deployed type of sensor and data acquisition system (DAS). When a sensor was replaced by another type, the date of change is noted in *year.julian day* format.

Station ID	Latitude (°)	Longitude (°)	Altitude (m)	Sensor	DAS
Hi-CLIMB main array, Phase1 (76 stations)					
H0010	26.9833	84.8932	22	CMG3T	RT72A
H0020	27.0176	84.9050	24	CMG3T	RT72A
H0030	27.0408	84.9074	27	CMG3ESP	RT72A
H0040	27.0665	84.9373	33	CMG3T	RT72A
H0050	27.0871	84.9533	38	CMG3T	RT72A
H0060	27.1079	84.9671	42	CMG3ESP	RT72A
H0070	27.1344	84.9699	51	CMG3T	RT72A
H0080	27.1661	84.9840	75	CMG3T	RT72A
H0090	27.2018	84.9793	113	CMG3ESP	RT72A
H0100	27.2305	84.9872	162	CMG3T	RT72A
H0120	27.2829	84.9885	267	CMG3ESP	RT72A
H0130	27.3152	85.0081	523	STS2	RT72A
Followed on next page					

Station ID	Latitude (°)	Longitude (°)	Altitude (m)	Sensor	DAS
Continued ...					
H0150	27.3698	85.0137	647	CMG3ESP	RT72A
H0160	27.3953	85.0221	461	STS2	RT72A
H0170	27.4196	85.0251	396	STS2	RT72A
H0180	27.4514	85.0328	475	CMG3ESP	RT72A
H0190	27.4717	85.0422	505	STS2	RT72A
H0200	27.4990	85.0450	563	STS2	RT72A
H0210	27.5287	85.0470	809	CMG3ESP	RT72A
H0220	27.5583	85.0697	1883	STS2	RT72A
H0230	27.5800	85.0733	2316	STS2	RT72A
H0240	27.6078	85.1070	2153	CMG3ESP	RT72A
Replaced: CMG3T (on 03.095)					
H0250	27.6312	85.1009	1737	STS2	RT72A
H0260	27.6733	85.0928	1854	CMG3T	RT72A
H0270	27.6957	85.0902	1597	CMG3ESP	RT72A
H0280	27.7270	85.0961	1289	STS2	RT72A
H0290	27.7565	85.1119	1162	STS2	RT72A
H0310	27.8005	85.0049	512	CMG3ESP	RT72A
H0320	27.8367	85.1510	937	STS2	RT72A
H0330	27.8613	85.1168	494	CMG3ESP	RT72A
H0340	27.8864	85.1507	545	STS2	RT72A
Replaced: CMG3T (on 03.043)					
Replaced: CMG3ESP (on 03.228)					
H0350	27.9112	85.1396	525	STS2	RT72A
H0360	27.9445	85.1645	618	CMG3ESP	RT72A
Replaced: CMG40T (on 03.298)					
H0370	27.9725	85.1863	595	STS2	RT72A
H0380	27.9950	85.2069	1448	STS2	RT72A
H0390	28.0251	85.2217	1965	CMG3ESP	RT72A
H0400	28.0572	85.2267	1932	STS2	RT72A
H0410	28.0798	85.2568	1989	STS2	RT72A
H0420	28.1070	85.2883	2005	CMG3ESP	RT72A
H0430	28.1379	85.3206	1837	STS2	RT72A
H0440	28.1661	85.3416	1442	STS2	RT72A
H0450	28.1946	85.3505	1488	CMG3ESP	RT72A
H0460	28.2151	85.3574	1693	STS2	RT72A
H0470	28.2515	85.3676	1757	STS2	RT72A
H0480	28.2708	85.3793	1789	STS2	RT72A
H0490	28.3059	85.3466	1912	CMG3T	RT72A
H0500	28.3411	85.3524	2243	CMG3T	RT72A
H0510	28.3863	85.3487	2698	CMG3T	RT72A
Followed on next page					

Continued ...					
Station ID	Latitude (°)	Longitude (°)	Altitude (m)	Sensor	DAS
H0520	28.4085	85.3128	2868	CMG3T	RT72A
			Replaced: CMG40T (on 03.345)		
			Replaced: CMG3T (on 03.347)		
H0530	28.4537	85.2448	3035	CMG3T	RT72A
H0540	28.4920	85.2224	3199	STS2	RT72A
H0550	28.5168	85.2161	3334	CMG3T	RT72A
H0560	28.5620	85.2464	3612	CMG3T	RT72A
H0570	28.5948	85.2598	3714	CMG3ESP	RT72A
H0580	28.6318	85.2697	3739	CMG3T	RT72A
H0590	28.6691	85.2808	3810	CMG3T	RT72A
H0600	28.7112	85.2803	3887	CMG3T	RT72A
			Replaced: CMG40T (on 03.345)		
			Replaced: CMG3T (on 03.347)		
H0610	28.7484	85.3037	3985	CMG3T	RT72A
H0620	28.7859	85.2959	3989	CMG3T	RT72A
H0630	28.8196	85.2939	4042	CMG3T	RT72A
H0640	28.8430	85.2945	4028	CMG3T	RT72A
H0641	28.8562	85.2939	4106	STS2	RT72A
H0650	28.8955	85.3274	4288	STS2	RT72A
H0655	28.8953	85.3824	5113	STS2	RT72A
H0660	28.9169	85.4189	4829	STS2	RT72A
H0670	28.9431	85.4383	4728	STS2	RT72A
H0680	28.9838	85.4410	4662	STS2	RT72A
H0690	29.0234	85.4550	4701	STS2	RT72A
H0700	29.0559	85.4215	4706	STS2	RT72A
H0710	29.0859	85.3756	4731	STS2	RT72A
H0720	29.1367	85.3643	4685	STS2	RT72A
H0730	29.1720	85.3647	4708	STS2	RT72A
H0740	29.2015	85.3564	4620	STS2	RT72A
H0750	29.2348	85.3141	4659	STS2	RT72A
H0760	29.2713	85.2431	4626	STS2	RT72A
H0770	29.3070	85.2432	4470	STS2	RT72A
Hi-CLIMB main array, Phase2 (76 stations)					
H0780	29.3414	85.2371	4678	STS2	RT72A
H0790	29.3802	85.2271	4764	STS2	RT72A
H0800	29.4119	85.2313	4785	CMG3T	RT72A
H0810	29.4669	85.2323	4891	CMG3T	RT72A
H1000	29.2672	85.8576	4560	CMG3T	RT72A
H1010	29.3354	85.8363	4753	CMG3T	RT72A
H1020	29.4130	85.7369	5039	STS2	RT72A
Followed on next page					

Station ID	Latitude (°)	Longitude (°)	Altitude (m)	Sensor	DAS
Continued ...
H1030	29.4830	85.7546	5012	CMG3T	RT72A
H1040	29.5614	85.7398	5115	CMG3T	RT72A
H1050	29.6387	85.7244	5219	CMG3T	RT72A
H1060	29.7066	85.7081	5232	CMG3T	RT72A
H1070	29.7767	85.7634	5261	CMG3T	RT72A
H1071	29.7701	85.7749	5340	CMG3T	RT72A
H1080	29.8502	85.7826	5403	CMG3T	RT72A
H1090	29.9221	85.7329	5260	CMG3T	RT72A
H1100	29.9936	85.6974	5315	CMG3T	RT72A
H1110	30.0664	85.5525	5435	CMG3T	RT72A
H1120	30.1380	85.4146	5479	STS2	RT72A
H1130	30.2058	85.3283	5078	STS2	RT72A
H1140	30.2802	85.2967	5185	STS2	RT72A
H1150	30.3579	85.3130	5120	STS2	RT72A
H1160	30.4340	85.2885	5217	STS2	RT72A
H1170	30.4954	85.1974	4846	STS2	RT72A
H1180	30.5812	85.1759	4974	STS2	RT72A
H1190	30.6494	85.1376	4831	STS2	RT72A
H1200	30.7151	85.1410	4828	STS2	RT72A
H1210	30.7821	85.1094	4874	STS2	RT72A
H1220	30.8598	85.0687	4776	STS2	RT72A
H1230	30.9320	85.0989	4778	STS2	RT72A
H1240	31.0198	85.1341	4731	CMG3ESP	RT72A
Replaced: CMG40T (on 04.332)
H1250	31.0841	84.9978	4850	CMG3T	RT72A
H1260	31.1549	85.0120	4992	CMG3T	RT72A
H1270	31.2252	85.0720	4726	CMG3ESP	RT72A
H1280	31.3016	85.1299	4732	CMG3T	RT72A
H1290	31.3782	85.1029	4822	CMG3T	RT72A
H1300	31.4454	85.1600	5050	CMG3ESP	RT72A
H1310	31.5152	85.1828	5218	CMG3T	RT72A
H1320	31.5837	85.1893	5225	STS2	RT72A
H1330	31.6558	85.1704	5132	CMG3ESP	RT72A
H1340	31.7319	85.1403	5064	CMG3T	RT72A
H1350	31.8029	85.0323	4973	CMG3T	RT72A
H1360	31.8622	84.9536	4988	STS2	RT72A
H1370	31.9453	84.8929	4736	CMG3T	RT72A
H1380	32.0039	84.8227	4638	CMG3ESP	RT72A
H1390	32.0723	84.9051	4586	CMG40T	RT72A
H1400	32.1187	84.6944	4488	CMG40T	RT72A
Followed on next page

Station ID	Latitude (°)	Longitude (°)	Altitude (m)	Sensor	DAS
		Continued ...			
H1405	32.1805	84.5130	4636	CMG40T	RT72A
H1410	32.2360	84.3739	4561	CMG40T	RT72A
H1415	32.3078	84.2188	4616	CMG40T	RT72A
H1420	31.9347	83.8425	4955	STS2	RT72A
H1421	32.0088	83.8713	4792	STS2	RT72A
H1422	32.0638	83.8992	4620	STS2	RT72A
H1423	32.1586	83.9242	4854	CMG3ESP	RT72A
H1424	32.2175	84.0048	4568	STS2	RT72A
H1425	32.2815	84.0637	4489	CMG40T	RT72A
H1430	32.3815	84.1311	4485	STS2	RT72A
H1440	32.4544	84.2395	4554	STS2	RT72A
H1450	32.5241	84.2715	4652	CMG3ESP	RT72A
H1460	32.5980	84.2235	4665	STS2	RT72A
H1470	32.6666	84.2157	4687	CMG3T	RT72A
H1480	32.7467	84.2163	4655	STS2	RT72A
H1490	32.8216	84.2668	4818	CMG3ESP	RT72A
H1500	32.8946	84.2863	5075	STS2	RT72A
H1510	32.9489	84.3047	4964	STS2	RT72A
H1520	33.0270	84.3147	4865	CMG3ESP	RT72A
H1530	33.1190	84.2209	4660	STS2	RT72A
H1540	33.1934	84.2277	4824	STS2	RT72A
H1550	33.2644	84.2456	4683	CMG3ESP	RT72A
H1560	33.3071	84.2464	4584	STS2	RT72A
H1570	33.4219	84.2629	4700	STS2	RT72A
H1580	33.5325	84.2913	4947	CMG3ESP	RT72A
H1590	33.6278	84.1707	4830	STS2	RT72A
H1600	33.7501	84.2694	4678	STS2	RT72A
H1610	33.8583	84.2628	4809	CMG3ESP	RT72A
H1620	33.9663	84.2233	5100	STS2	RT72A
H1630	34.0653	84.2274	5342	STS2	RT72A
		Hi-CLIMB, Tibetan laterals (37 stations)			
T0010	28.0117	87.6816	4647	CMG3ESP	RT130
T0020	28.1673	85.9685	3819	TRIL40	Q330
T0030	28.1501	86.8483	5154	STS2	RT72A
T0040	28.1645	87.3562	3700	STS2	RT72A
T0050	28.1926	87.7420	4283	CMG3ESP	RT130
T0060	28.1560	88.0987	4424	CMG3ESP	RT130
T0070	28.2790	88.5150	4614	CMG3ESP	RT130
T0080	28.2569	88.9912	4634	CMG3ESP	RT130
T0090	28.2686	89.3918	4450	CMG3ESP	RT130
		Followed on next page			

Station ID	Latitude (°)	Longitude (°)	Altitude (m)	Sensor	DAS
Continued ...					
T0100	28.4319	86.0969	4487	TRIL40	Q330
T0110	28.6492	86.1308	4727	TRIL40	Q330
T0130	28.5804	87.0703	4400	STS2	RT72A
T0140	28.5364	87.7575	4240	CMG3ESP	RT130
T0150	28.8883	86.3772	4464	STS2	RT72A
T0160	28.9003	87.4244	5113	STS2	RT72A
T0170	28.8384	87.9500	4649	CMG3ESP	RT130
T0180	28.9928	88.3919	3953	CMG3ESP	RT130
T0190	28.8933	88.7809	4326	CMG3ESP	RT130
T0200	28.9369	89.1619	4094	CMG3ESP	RT130
T0210	28.9027	89.5764	4050	CMG3ESP	RT130
T0230	29.0558	86.3978	4738	STS2	RT72A
T0240	29.1052	87.5753	4041	2Hz	HAT
T0250	29.1449	88.1589	4100	CMG3ESP	RT130
T0255	29.0705	89.3026	3891	2Hz	HAT
T0260	29.4491	86.6845	4613	STS2	RT72A
T0270	29.4229	87.6518	4062	STS2	RT72A
T0280	29.4300	88.2304	4011	CMG3ESP	RT130
T0290	29.3705	88.8856	3852	2Hz	HAT
T0300	29.3986	89.6250	3845	2Hz	HAT
T0310	29.7867	86.8140	5439	STS2	RT72A
T0320	29.7695	88.3495	5044	CMG3ESP	RT130
T0330	29.7048	89.2132	4070	2Hz	HAT
T0340	29.6882	89.7184	4386	STS2	RT72A
T0350	30.1259	86.5077	4934	STS2	RT72A
T0360	30.1005	86.9646	5168	TRIL40	Q330
T0370	29.9547	88.3552	4892	CMG3ESP	RT130
T0380	30.4419	86.9306	4950	STS2	RT72A
Hi-CLIMB, Nepal Pokhara profile (15 stations)					
NP010	27.4948	83.3181	40	CMG3T	RT72A
NP020	27.6274	83.4605	68	CMG3T	RT72A
NP030	27.7504	83.4963	283	CMG3T	RT72A
NP035	27.8090	83.5222	774	CMG3T	RT72A
NP040	27.8713	83.5368	1364	CMG3T	RT72A
NP050	27.9361	83.6395	752	CMG3T	RT72A
NP060	27.9971	83.7869	707	CMG3T	RT72A
NP070	28.0784	83.8606	897	CMG3T	RT72A
NP071	28.0822	83.8371	821	CMG3T	RT72A
NP075	28.1487	83.8741	1098	CMG3ESP	RT72A
NP080	28.2147	84.0025	811	CMG3T	RT72A
Followed on next page					

Station ID	Latitude (°)	Longitude (°)	Altitude (m)	Sensor	DAS
Continued ...					
NP082	28.2786	83.9377	1241	CMG3ESP	RT72A
NP085	28.3531	83.9548	1257	CMG3ESP	RT72A
NP090	28.2942	83.5948	1038	CMG3T	RT72A
NP100	28.7796	83.7191	2735	STS2	RT72A
Hi-CLIMB, Nepal Gumba profile (6 stations)					
NG010	27.4614	84.2799	114	CMG3T	RT72A
NG020	27.5702	84.3292	110	CMG3T	RT72A
NG030	27.6797	84.4037	136	CMG3T	RT72A
NG040	27.8243	84.4638	197	STS2	RT72A
NG050	27.8606	84.5640	325	STS2	RT72A
NG060	28.0016	84.6235	1097	STS2	RT72A
Hi-CLIMB, Nepal – from HIMNT (15 stations)					
NBENS	28.2379	84.3712	735	CMG3T	RT72A
NBIRA	26.4840	87.2670	12	STS2	RT72A
NBUNG	27.8771	85.8909	1191	STS2	RT72A
NDOML	27.9753	84.2820	352	STS2	RT72A
NGUMB	27.5562	83.8391	530	CMG3T	RT72A
NHILE	27.0482	87.3242	2088	STS2	RT72A
NJANA	26.7106	85.9242	11	STS2	RT72A
NJIRI	27.6342	86.2303	1866	STS2	RT72A
NNAMC	27.8027	86.7146	3523	STS2	RT72A
NPHAP	27.5150	86.5842	2488	STS2	RT72A
NRUMJ	27.3038	86.5482	1319	STS2	RT72A
NSIND	27.2107	85.9088	465	STS2	RT72A
NSUKT	27.7057	85.7611	745	STS2	RT72A
NTHAK	27.5996	85.5566	1551	STS2	RT72A
NTUML	27.3208	87.1950	360	STS2	RT72A
HIMNT experiment (29 stations)					
BIRA	26.4840	87.2670	12	STS2	RT72A
BUNG	27.8771	85.8909	1191	STS2	RT72A
DINX	28.6646	87.1157	4374	STS2	RT72A
GAIG	26.8380	86.6318	166	STS2	RT72A
HILE	27.0482	87.3242	2088	STS2	RT72A
ILAM	26.9102	87.9227	1181	STS2	RT72A
JANA	26.7106	85.9242	11	STS2	RT72A
JIRI	27.6342	86.2303	1866	STS2	RT72A
LAZE	29.1403	87.5922	4011	STS2	RT72A
MAZA	28.6713	87.8553	4367	STS2	RT72A
MNBU	28.7558	86.1610	4500	STS2	RT72A
NAIL	28.6597	86.4126	4378	STS2	RT72A
Followed on next page					

Station ID	Latitude (°)	Longitude (°)	Altitude (m)	Sensor	DAS
Continued ...
NAMC	27.8027	86.7146	3523	STS2	RT72A
NLMU	28.1548	85.9777	3889	STS2	RT72A
ONRN	29.3020	87.2440	4350	STS2	RT72A
PHAP	27.5150	86.5842	2488	STS2	RT72A
PHID	27.1501	87.7645	1176	STS2	RT72A
RBSH	28.1955	86.8280	5100	STS2	RT72A
RC14	29.4972	86.4373	4756	STS2	RT72A
RUMJ	27.3038	86.5482	1319	STS2	RT72A
SAGA	29.3292	85.2321	4524	STS2	RT72A
SAJA	28.9093	88.0209	4351	STS2	RT72A
SIND	27.2107	85.9088	465	STS2	RT72A
SSAN	29.4238	86.7290	4585	STS2	RT72A
SUKT	27.7057	85.7611	745	STS2	RT72A
THAK	27.5996	85.5566	1551	STS2	RT72A
TUML	27.3208	87.1950	360	STS2	RT72A
XIXI	28.7409	85.6904	4660	STS2	RT72A
YALA	28.4043	86.1133	4434	STS2	RT72A
Global Seismographic Network (2 stations)					
LSA	29.7000	91.1500	3774	STS1	Qgsn
KMI	25.1233	102.740	1940	STS1	Qgsn
End					

APPENDIX C

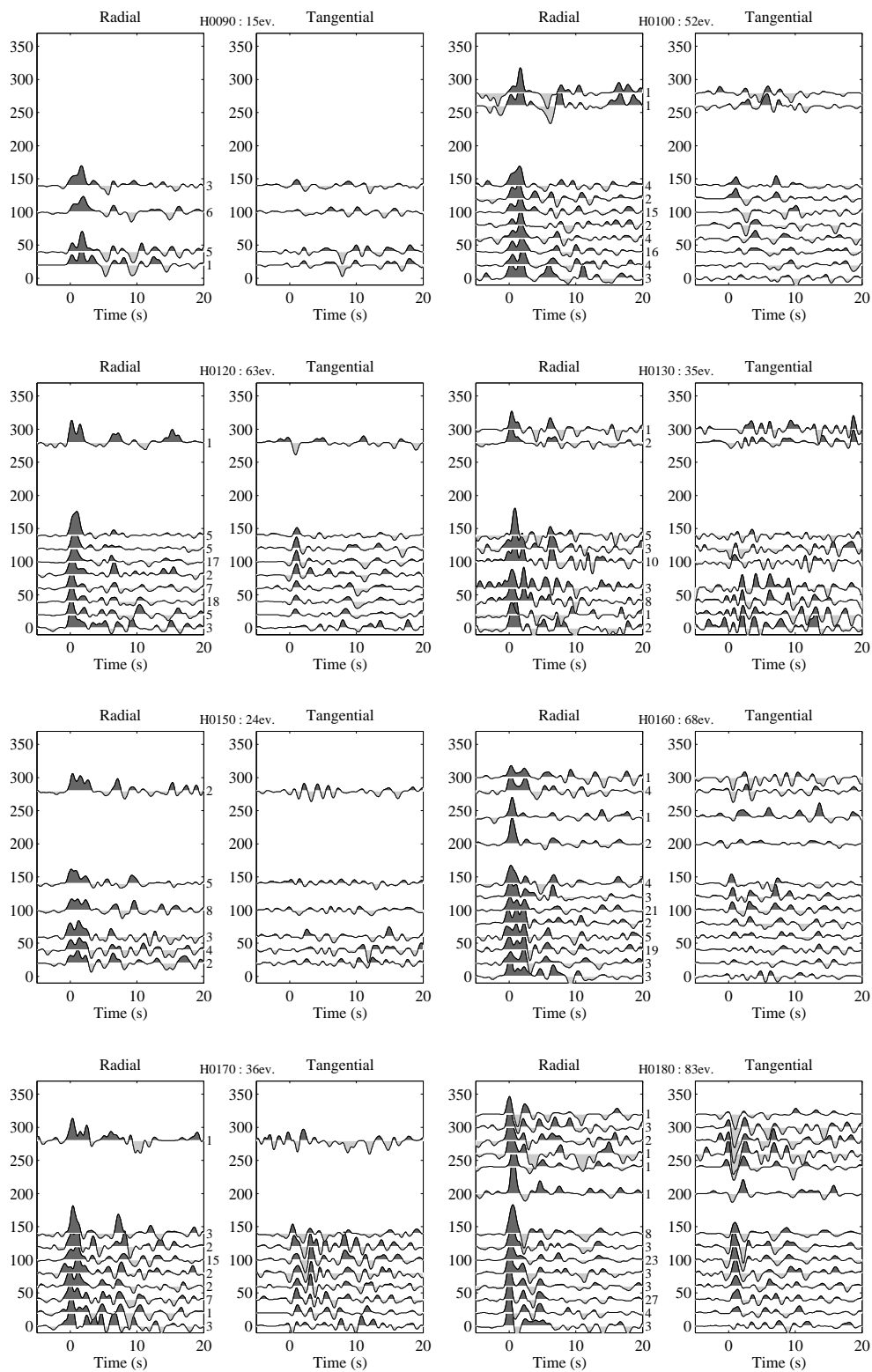## Computed receiver functions

The amount of data acquired during the Hi-CLIMB experiment, and also because of the scope of this thesis, there is no possibility to discuss the individual observations made at all deployed stations.

However, the computed receiver functions are presented here for all stations of the Hi-CLIMB experiment, showing back-azimuthal variation (on the ordinate) of the radial and tangential components. Here we use traces that have passed the second quality control (see Section 3.4.1) on list W3, and events M$\geq$5.5. The number of total events and their back-azimuthal distribution is noted between the radial and tangential component graphs.
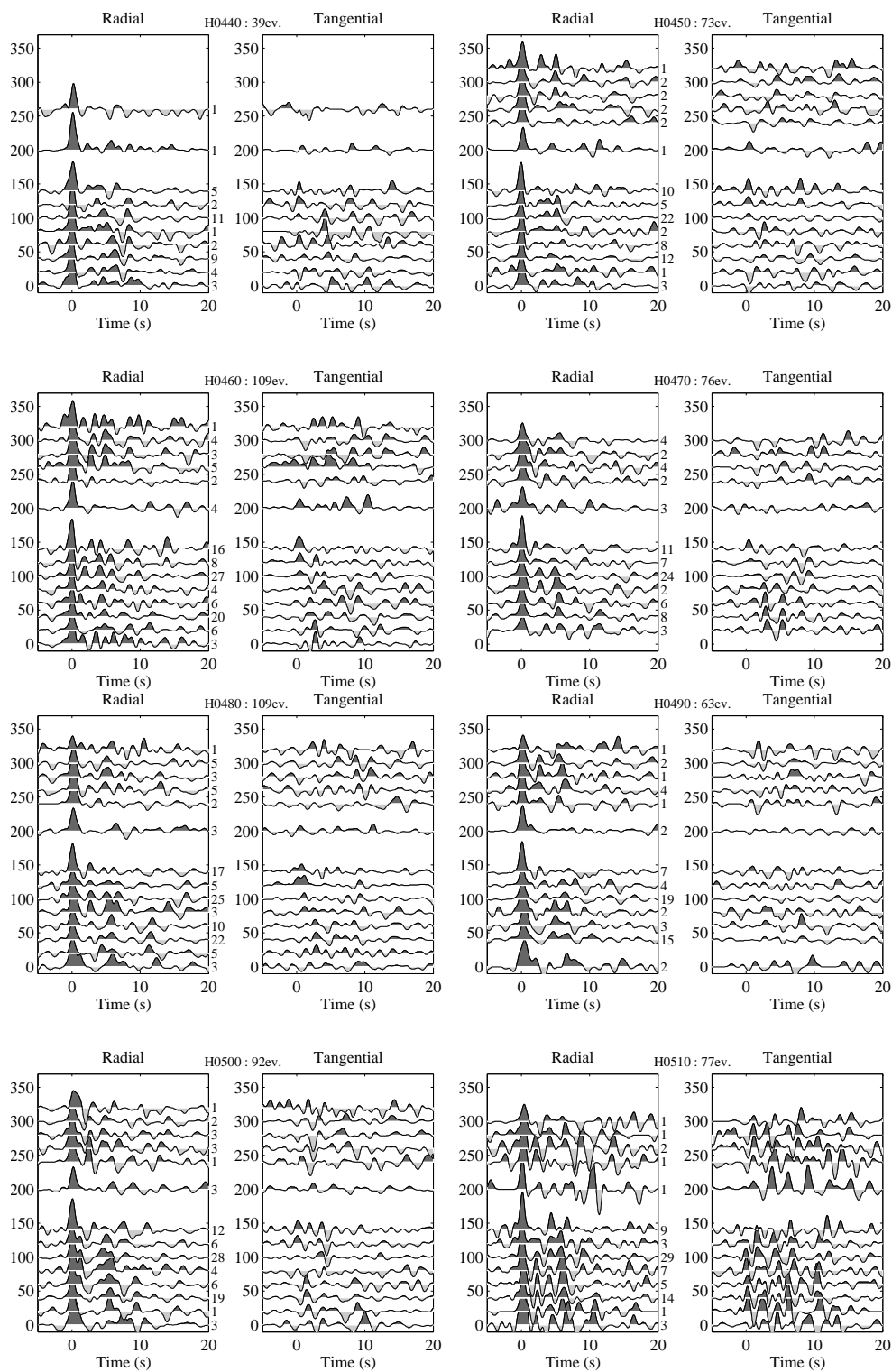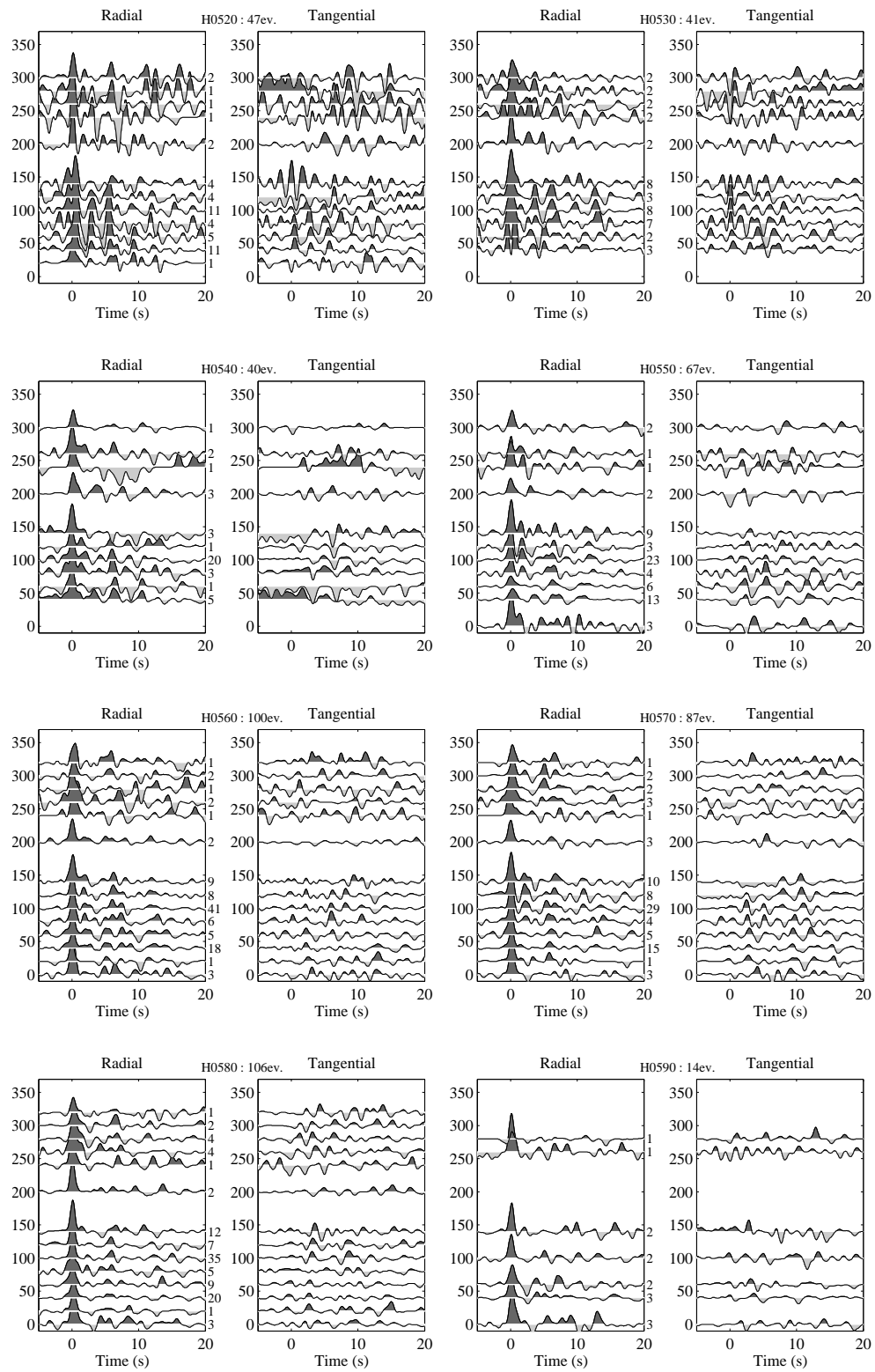
Main array, Phase1
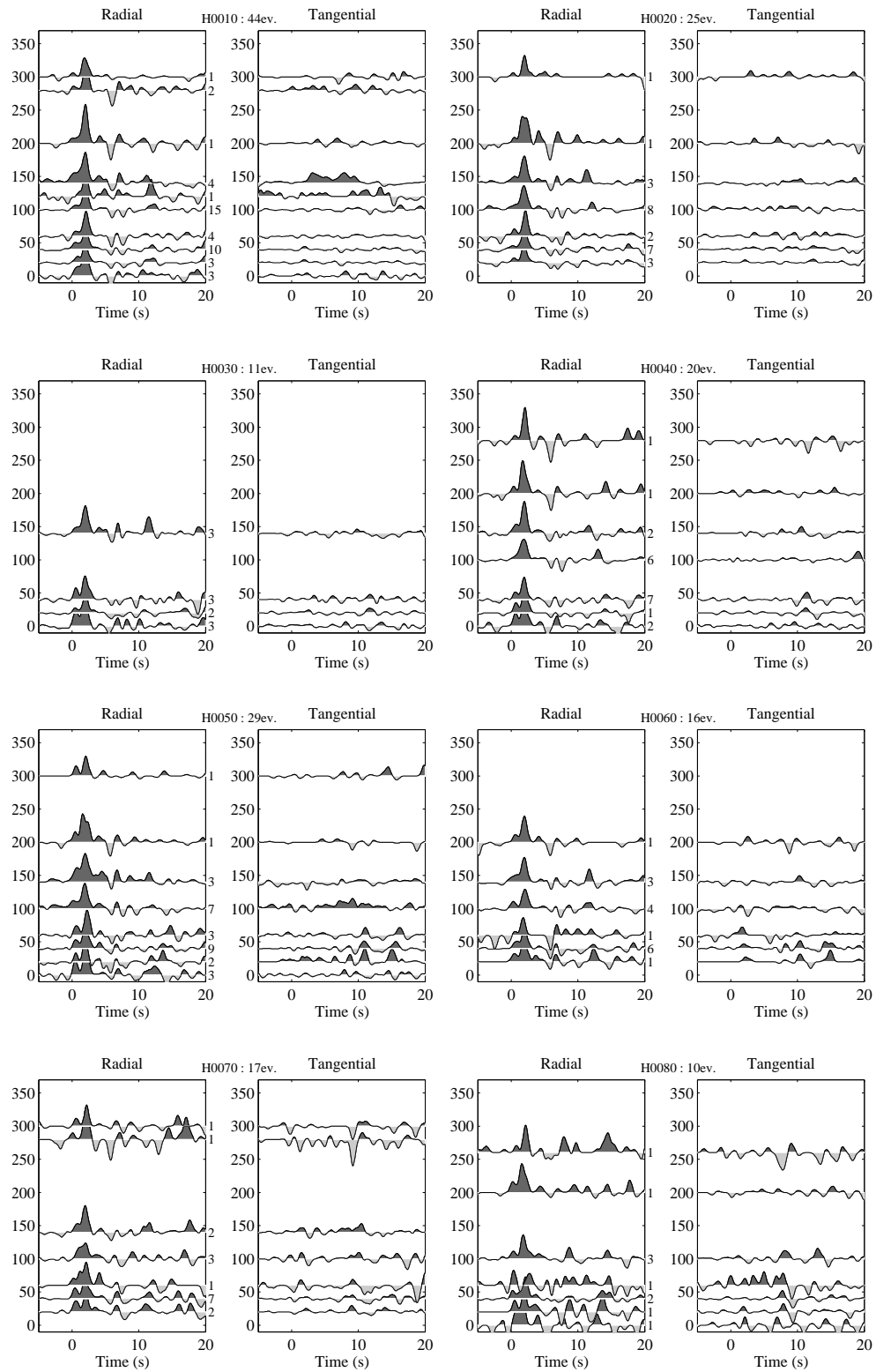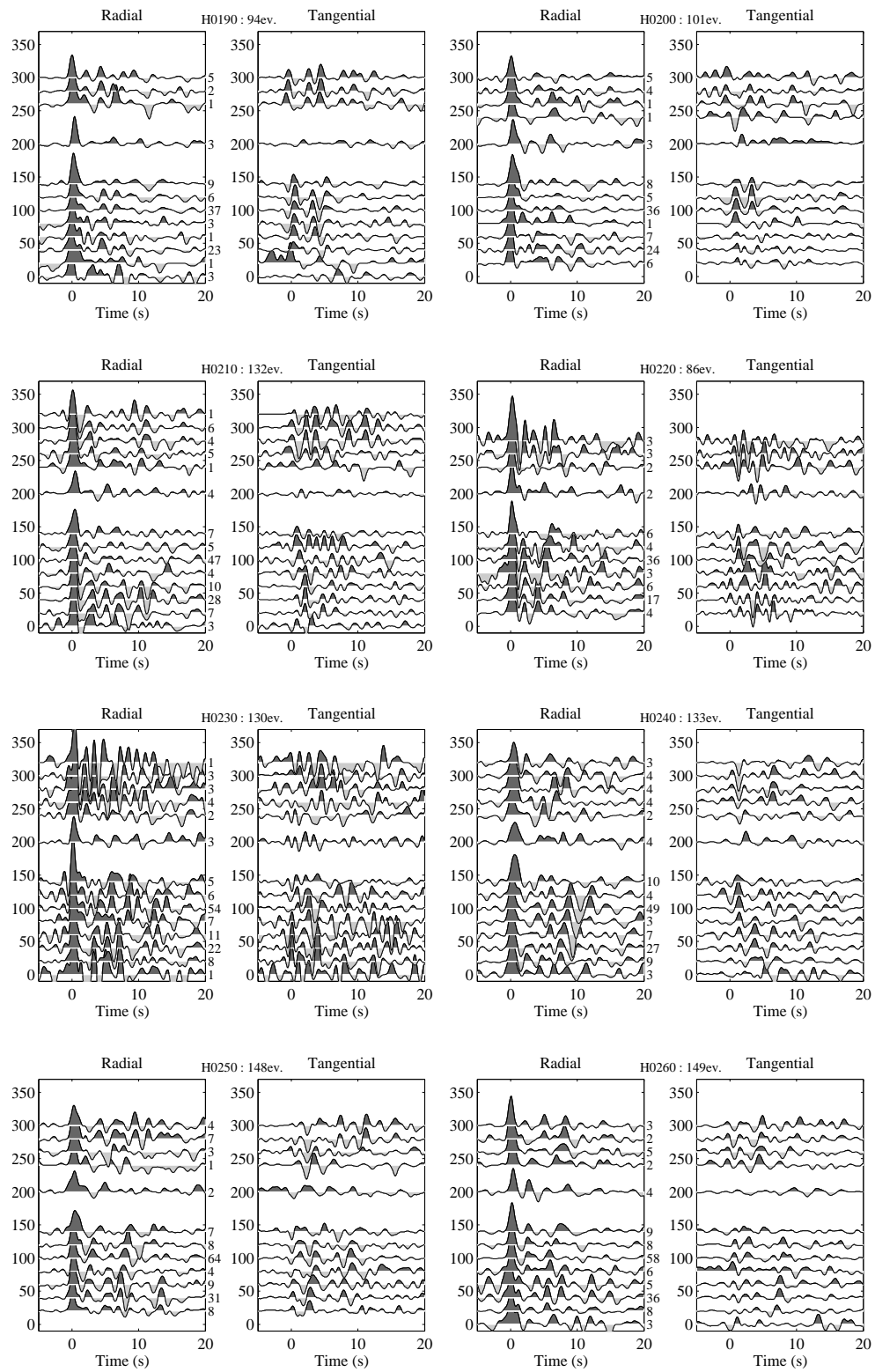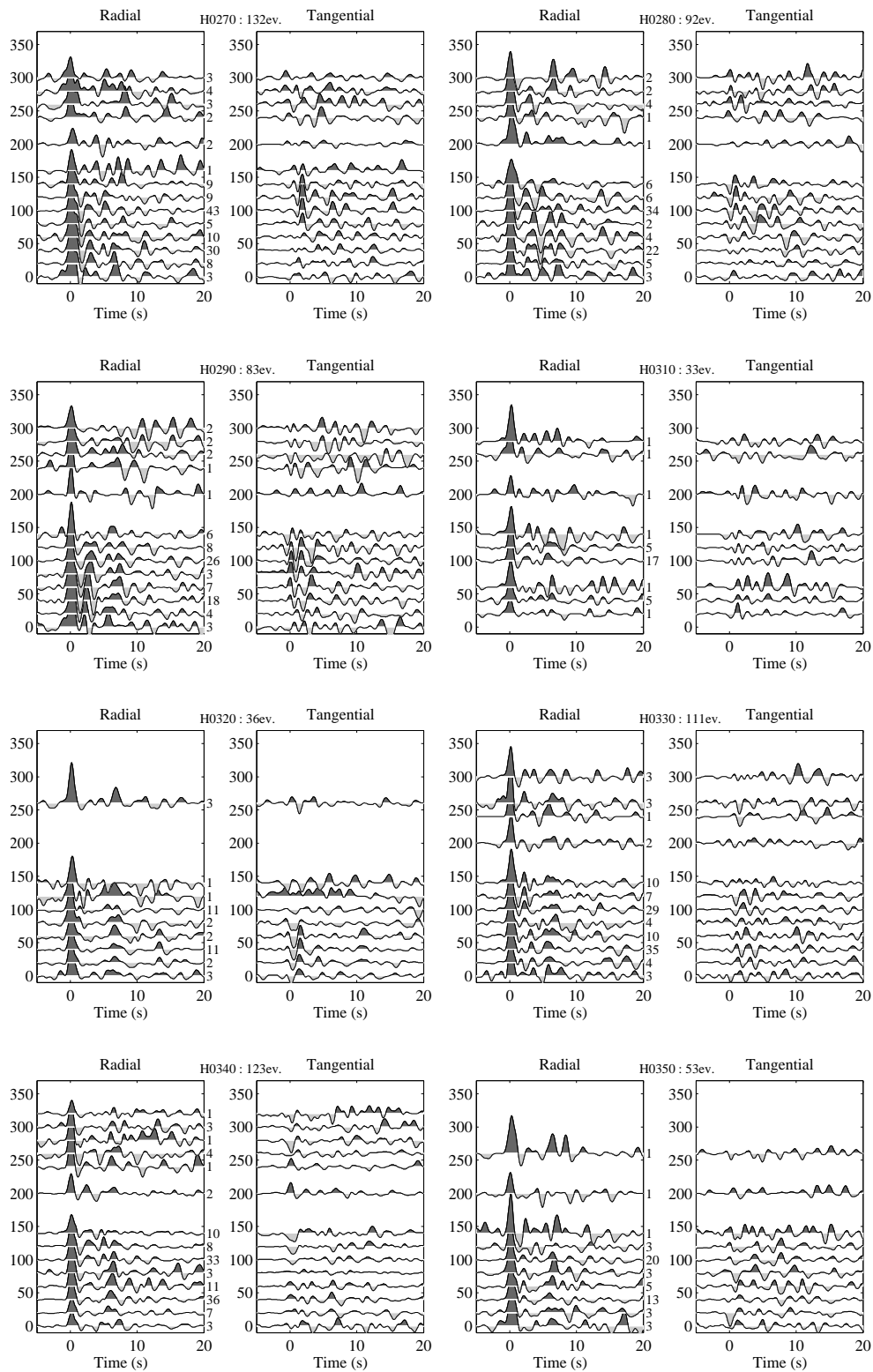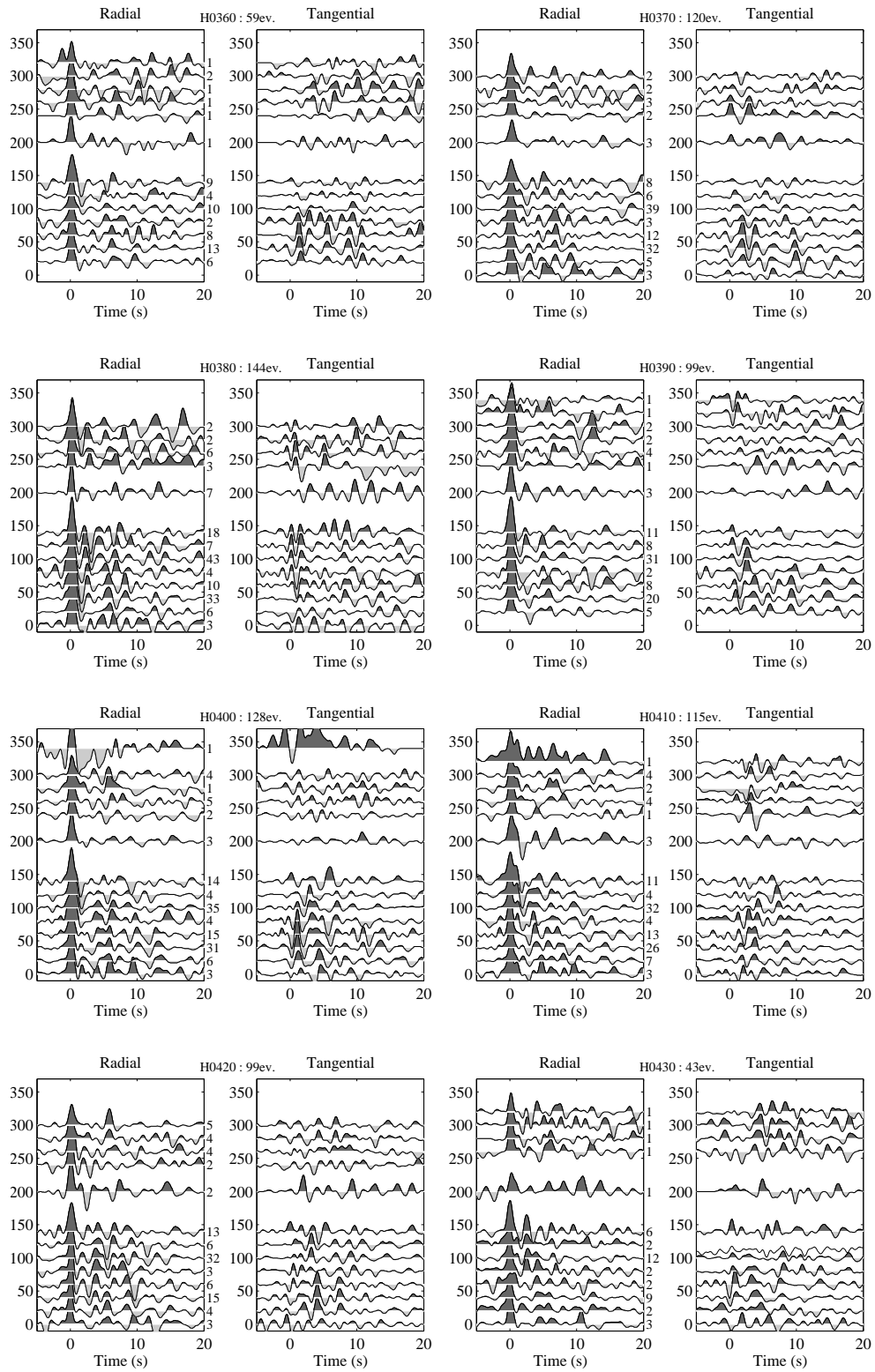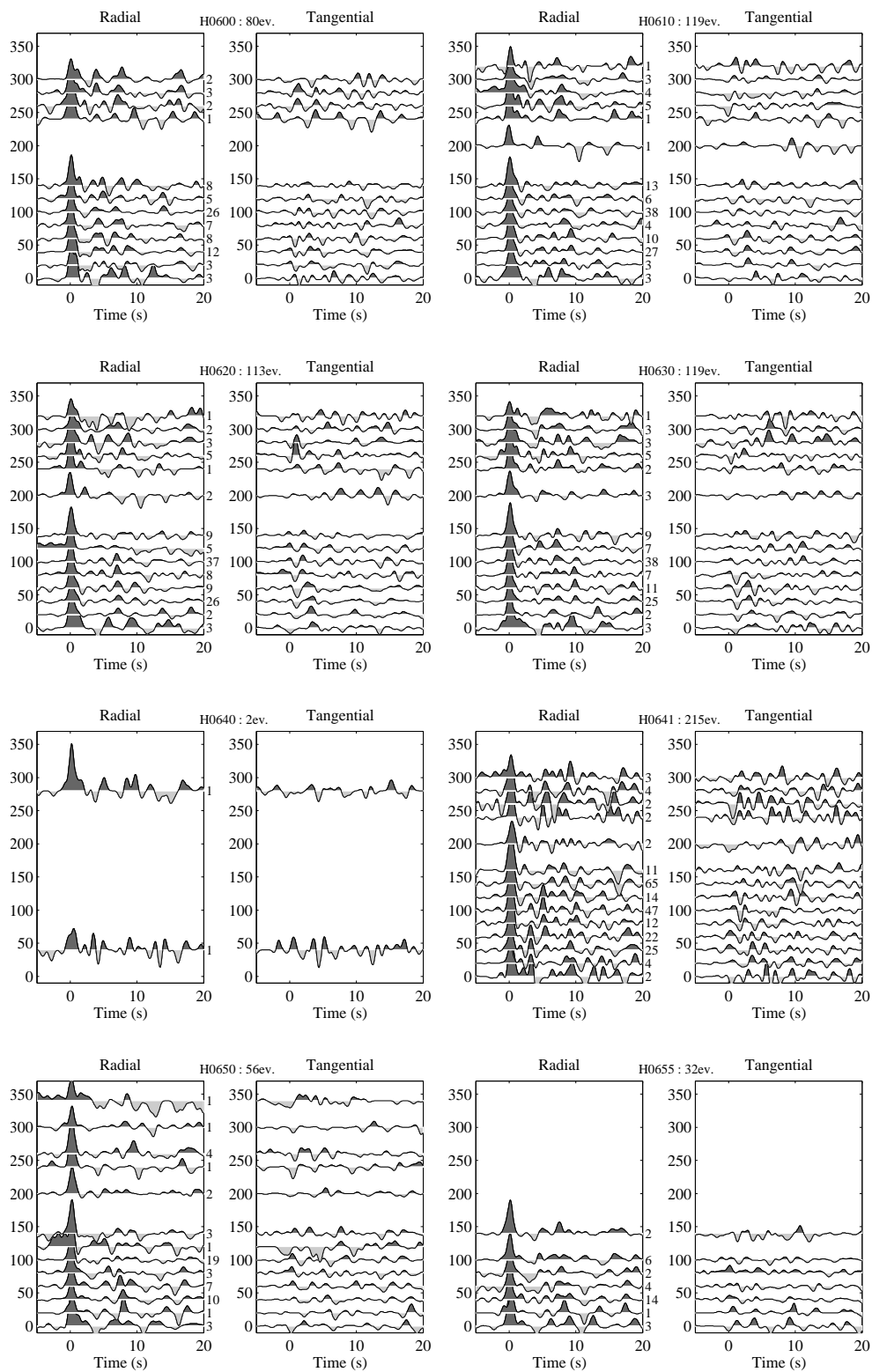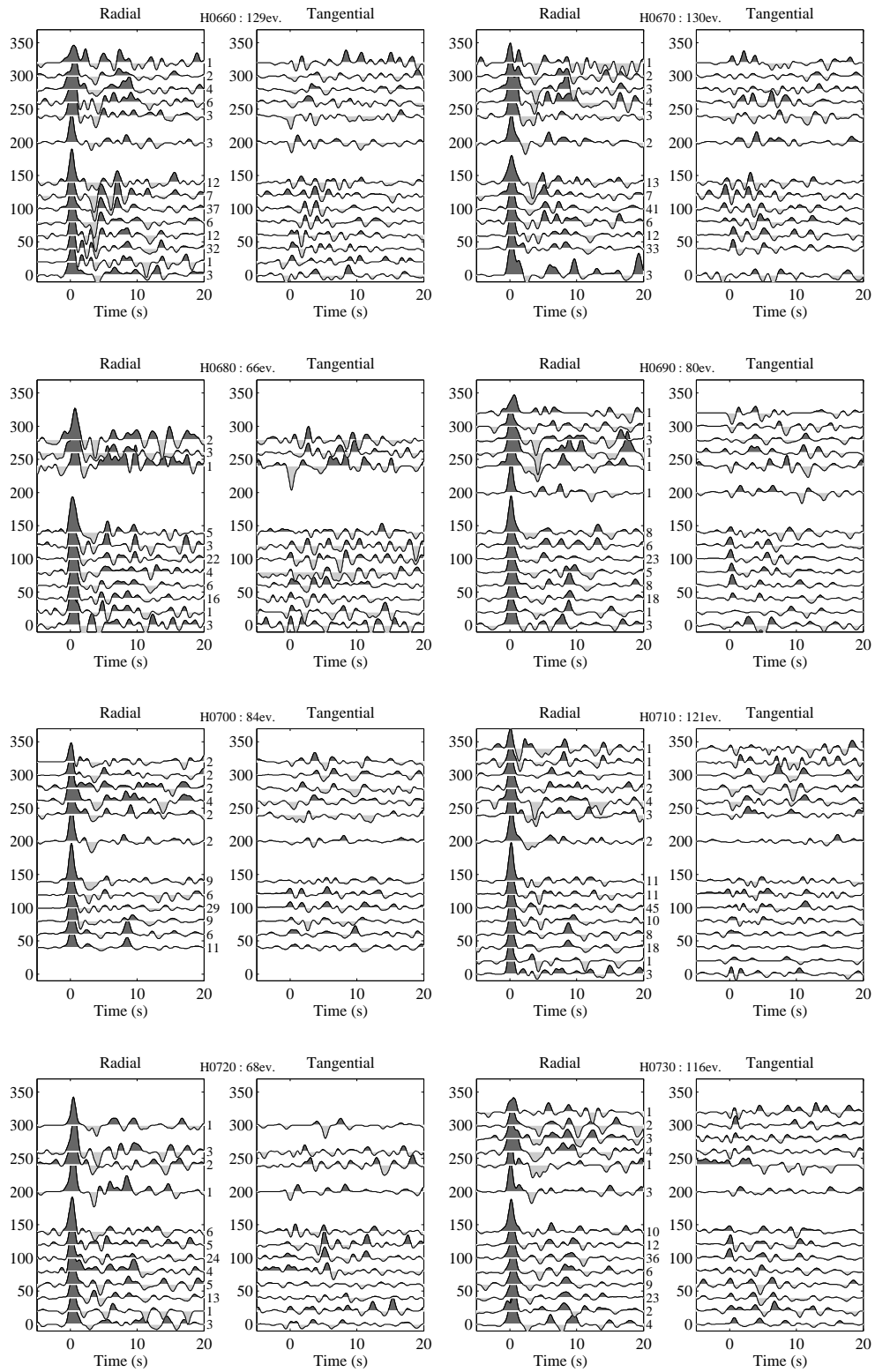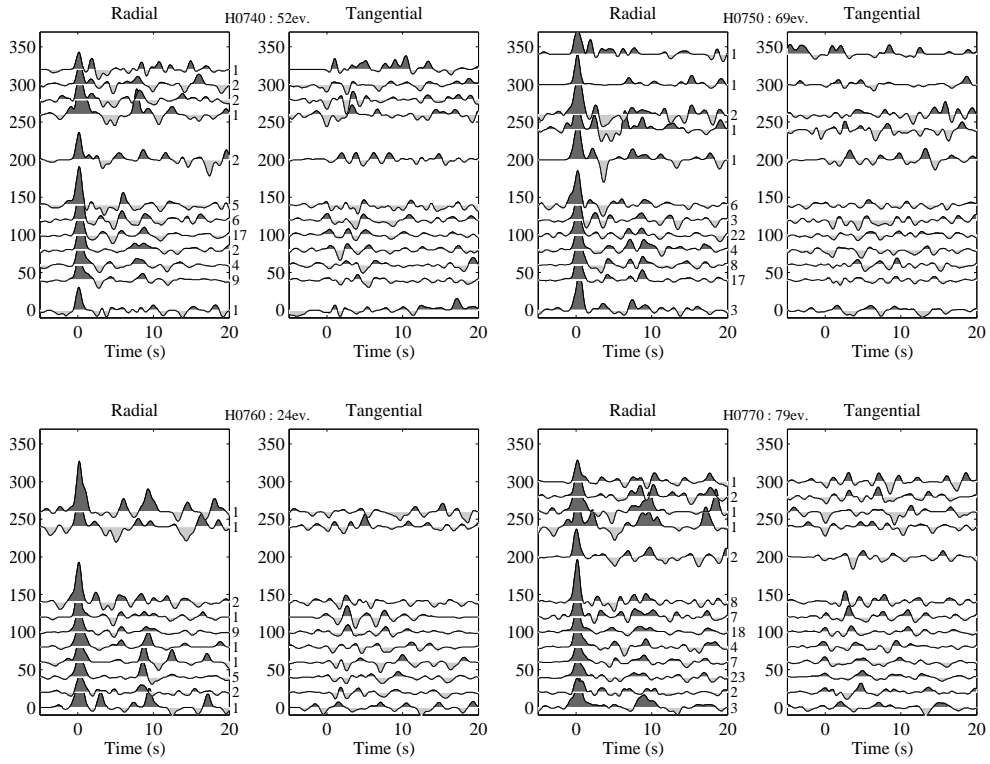
Main array, Phase2
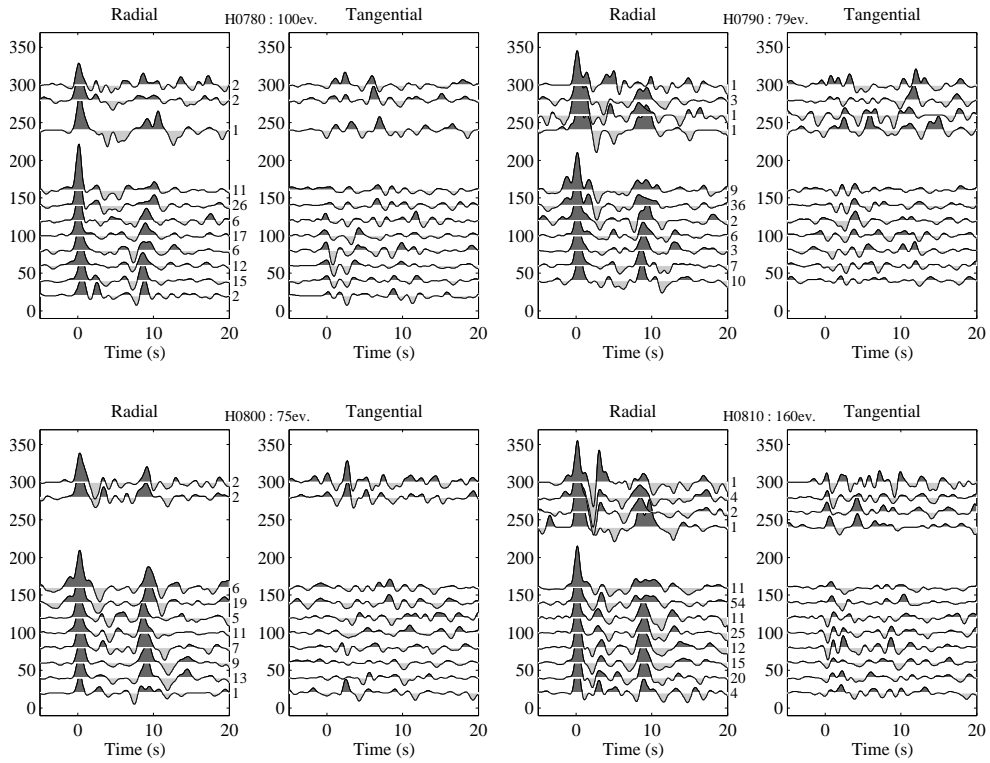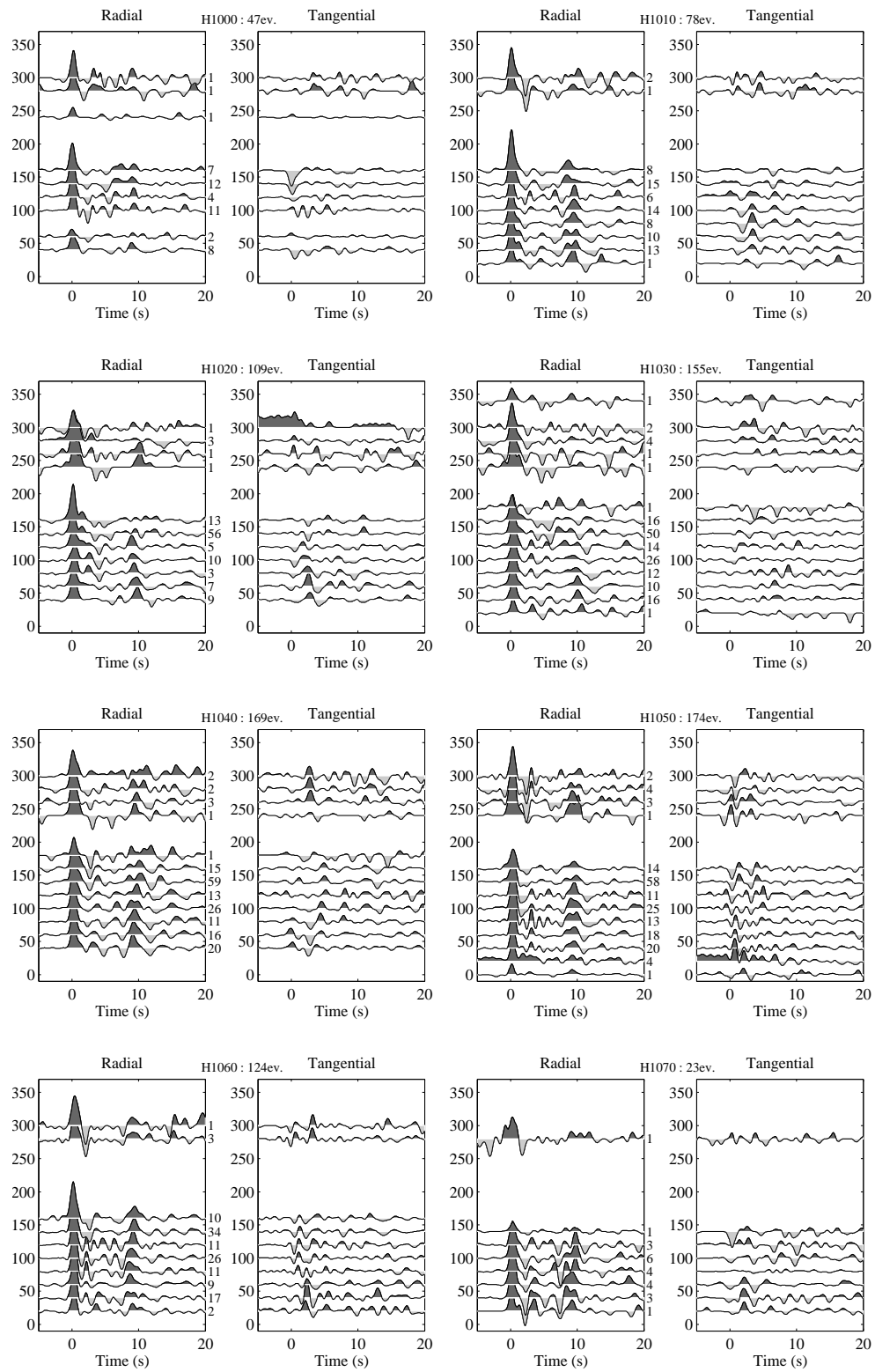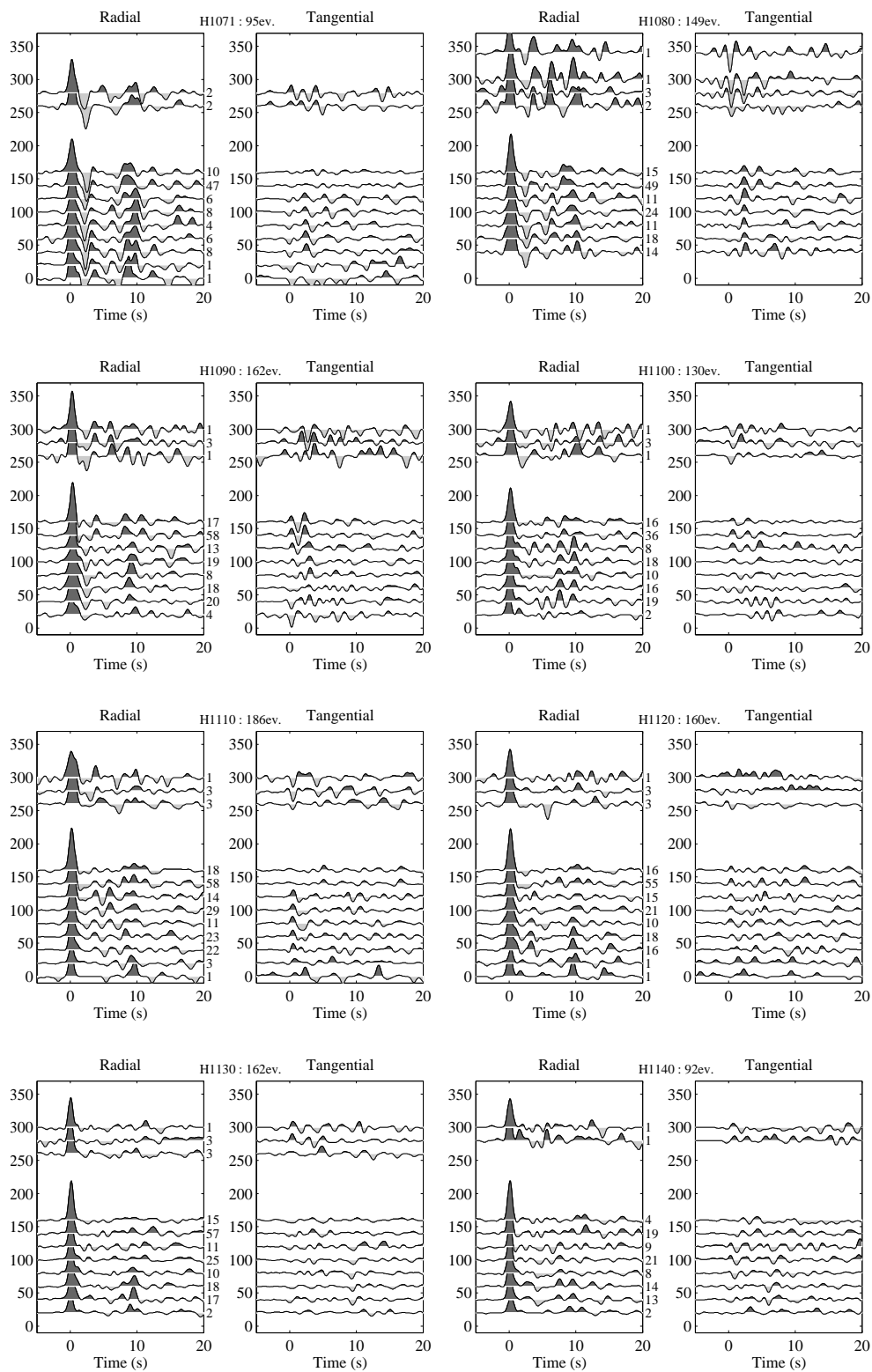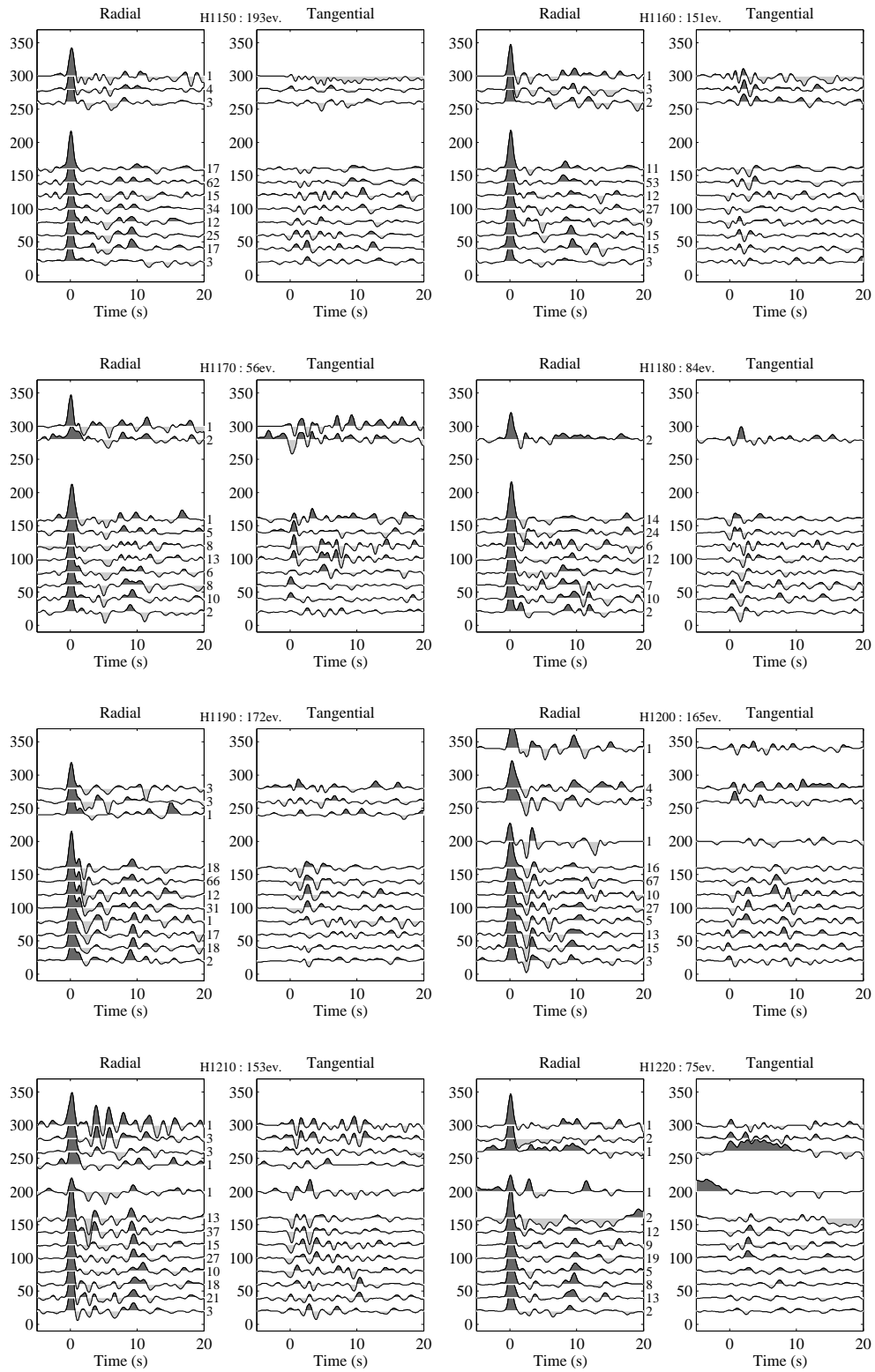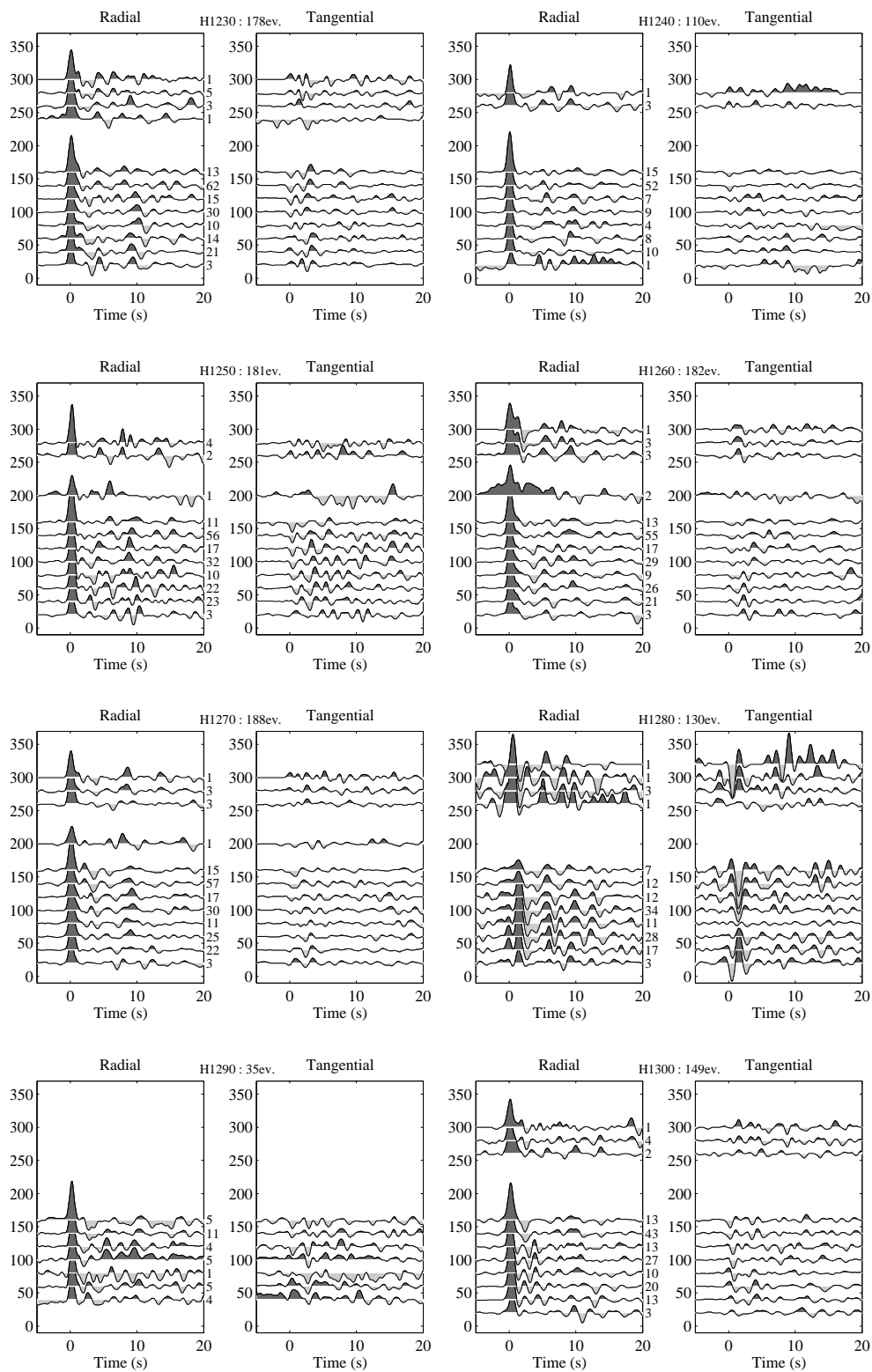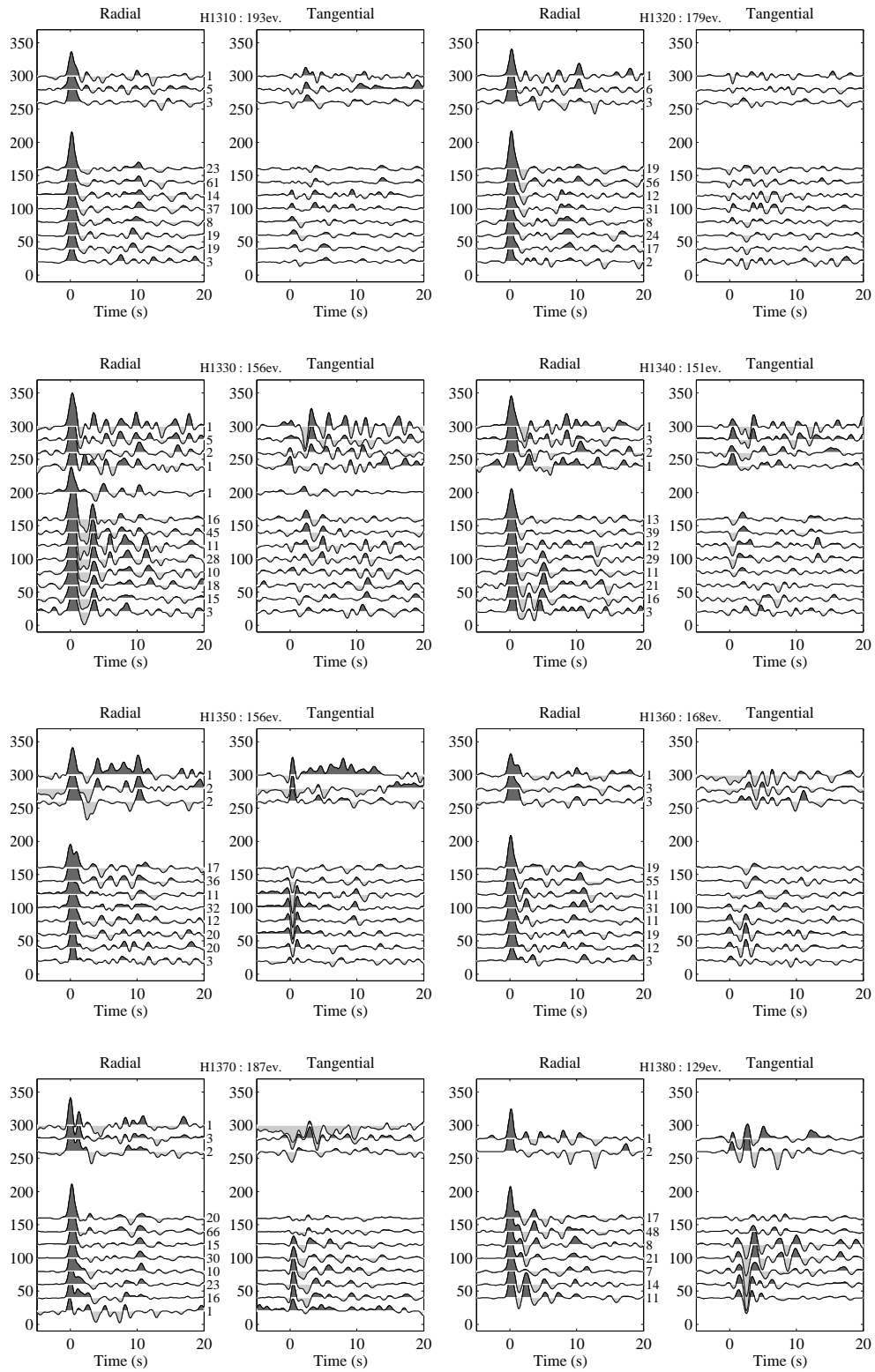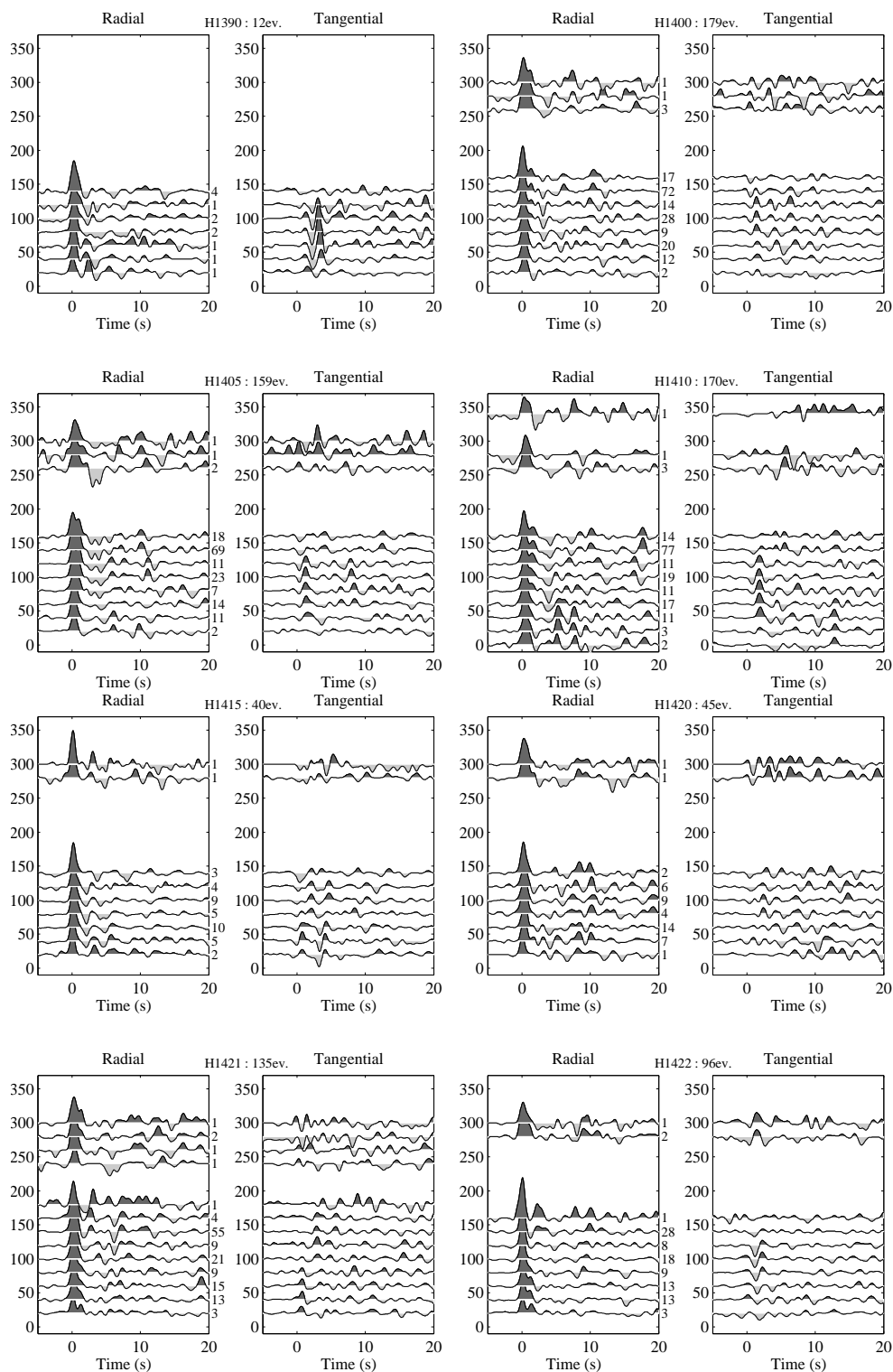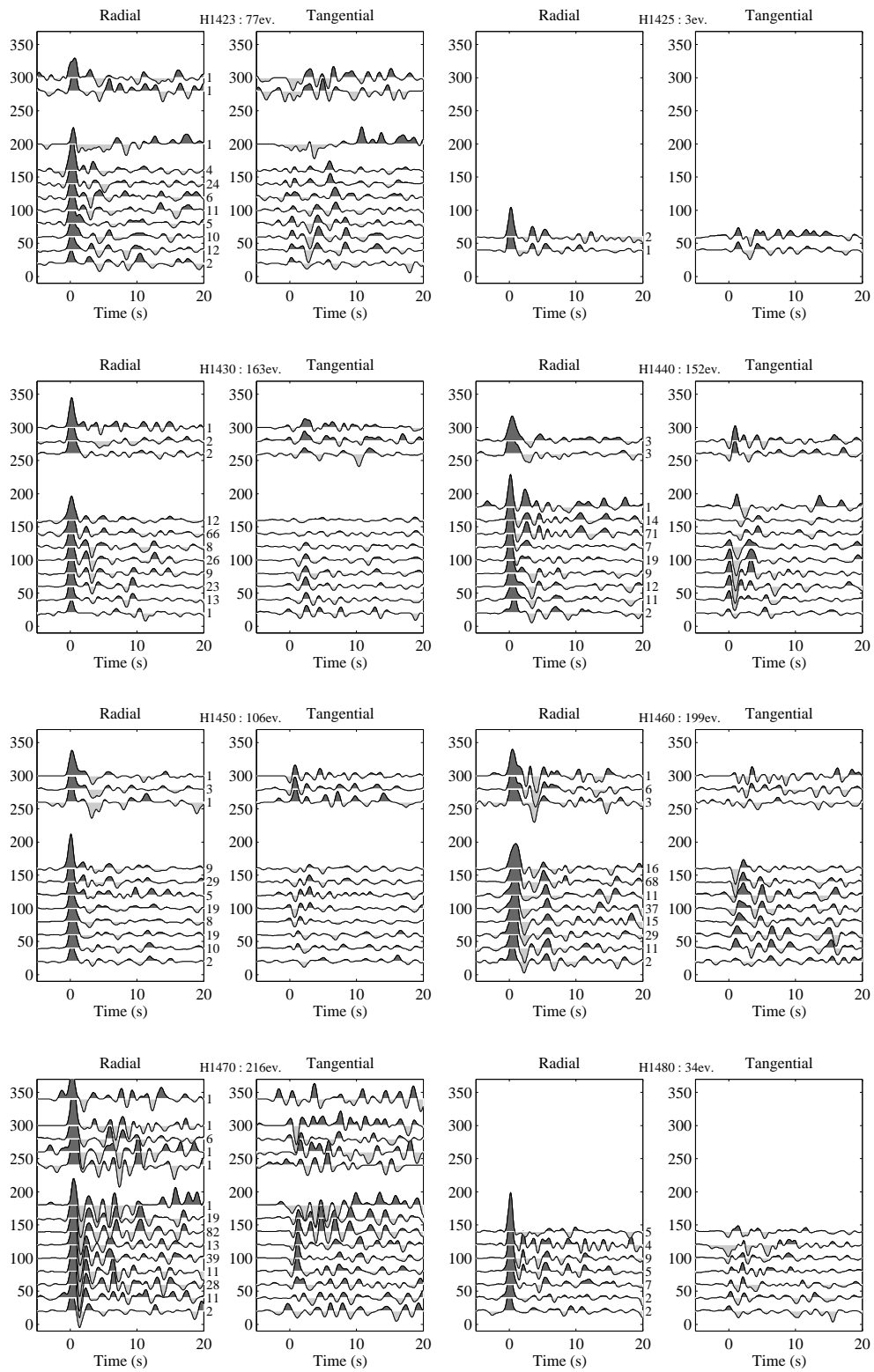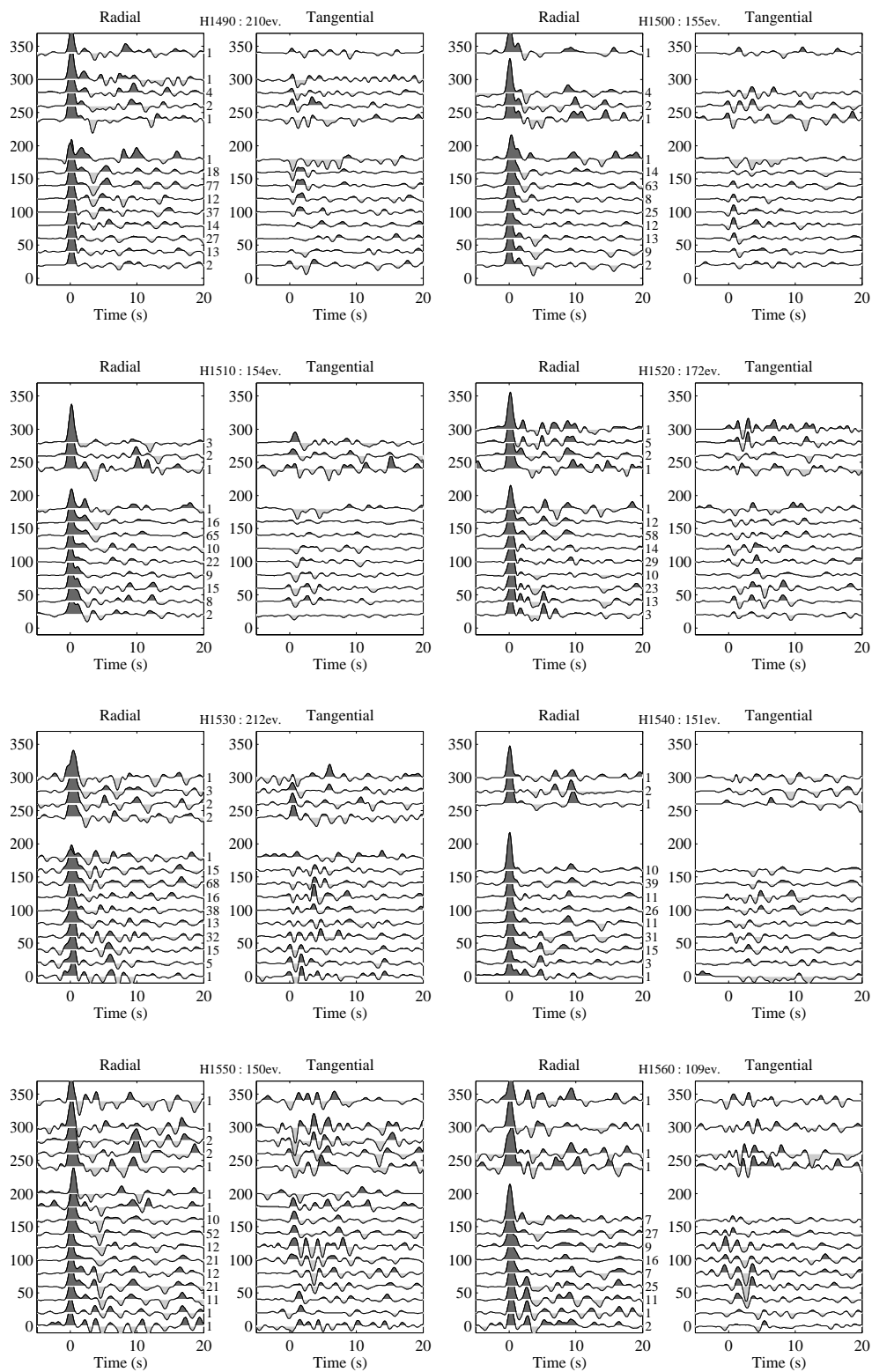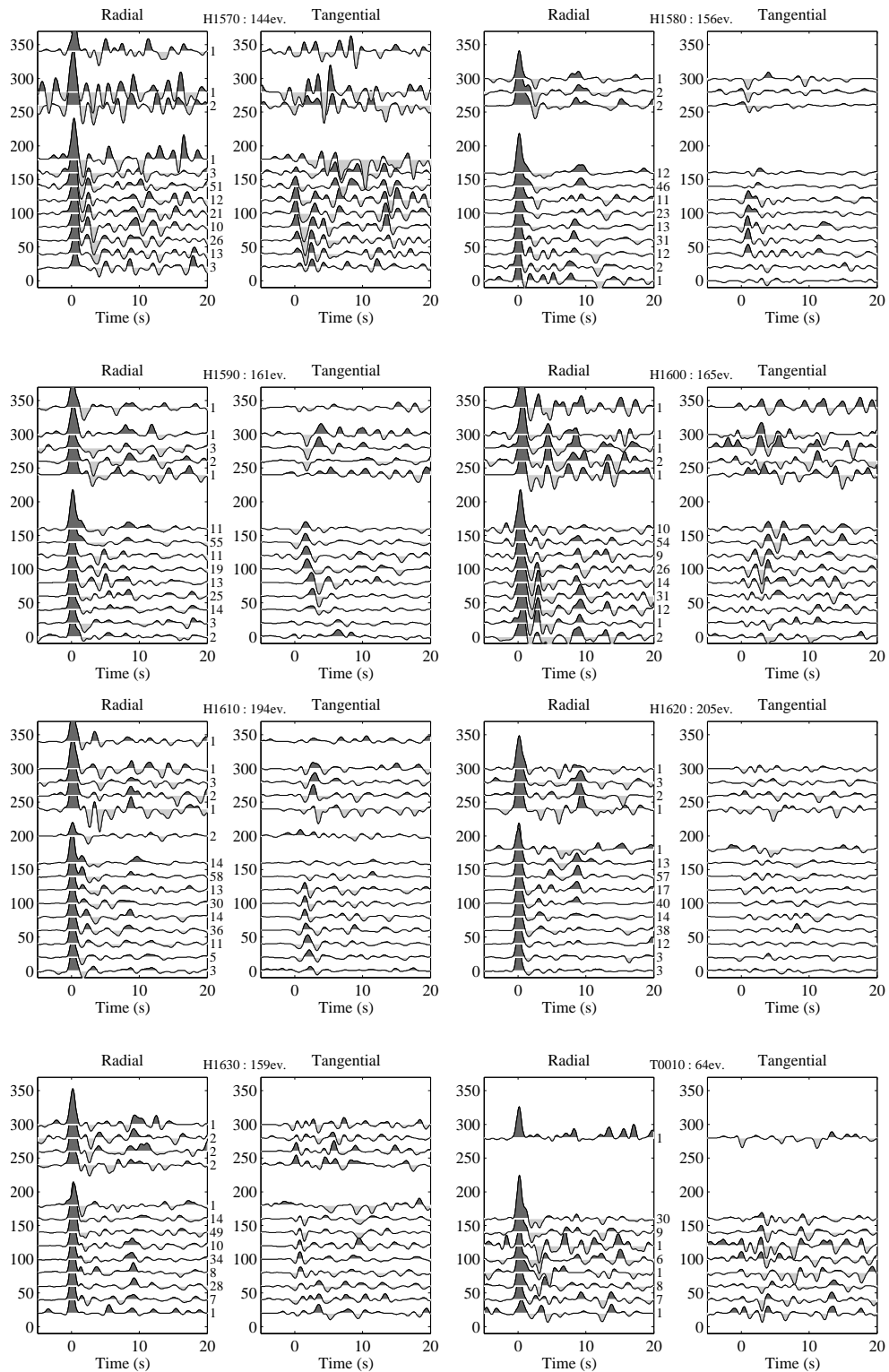
↪ **Lateral stations, Tibet**
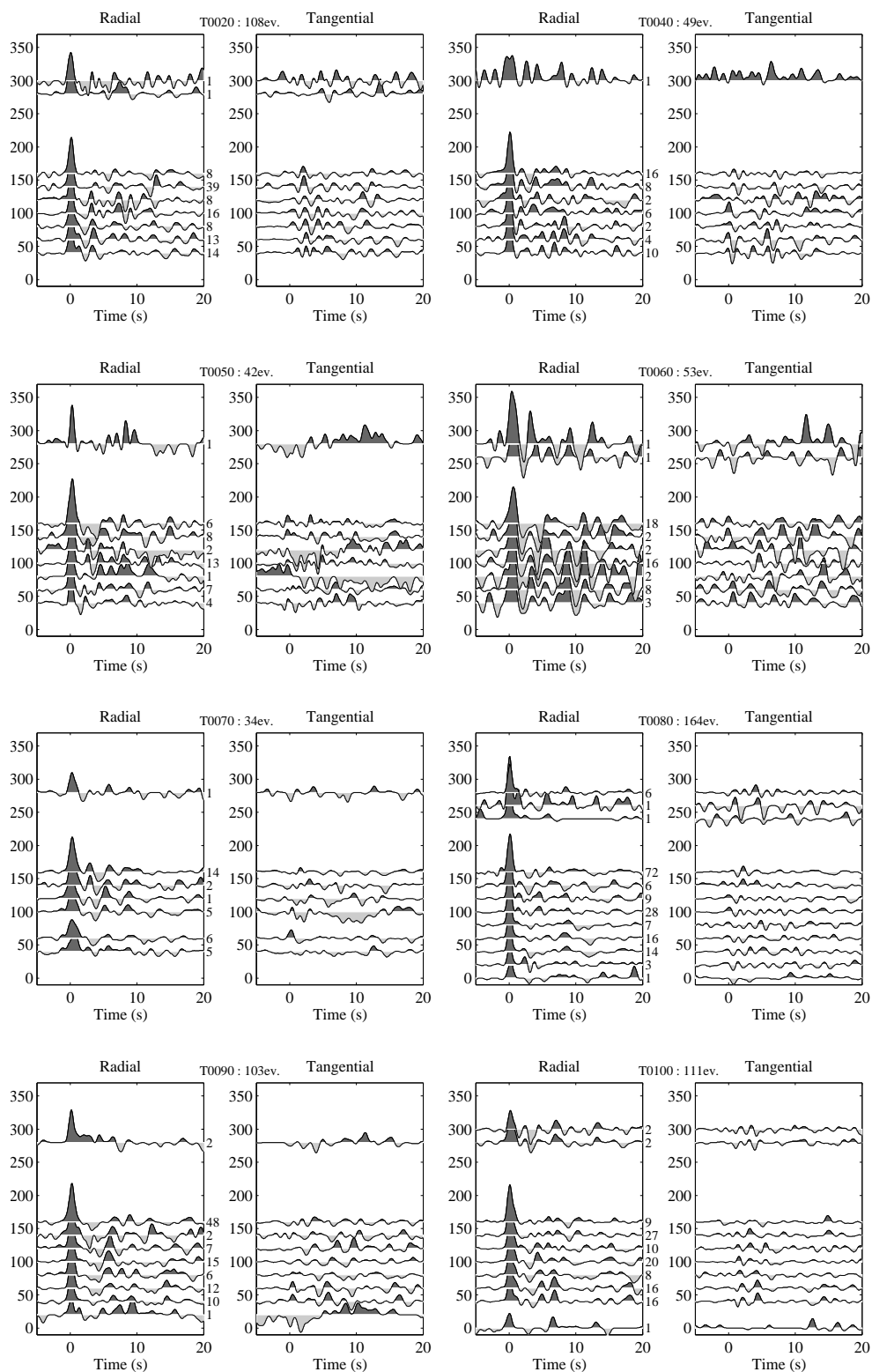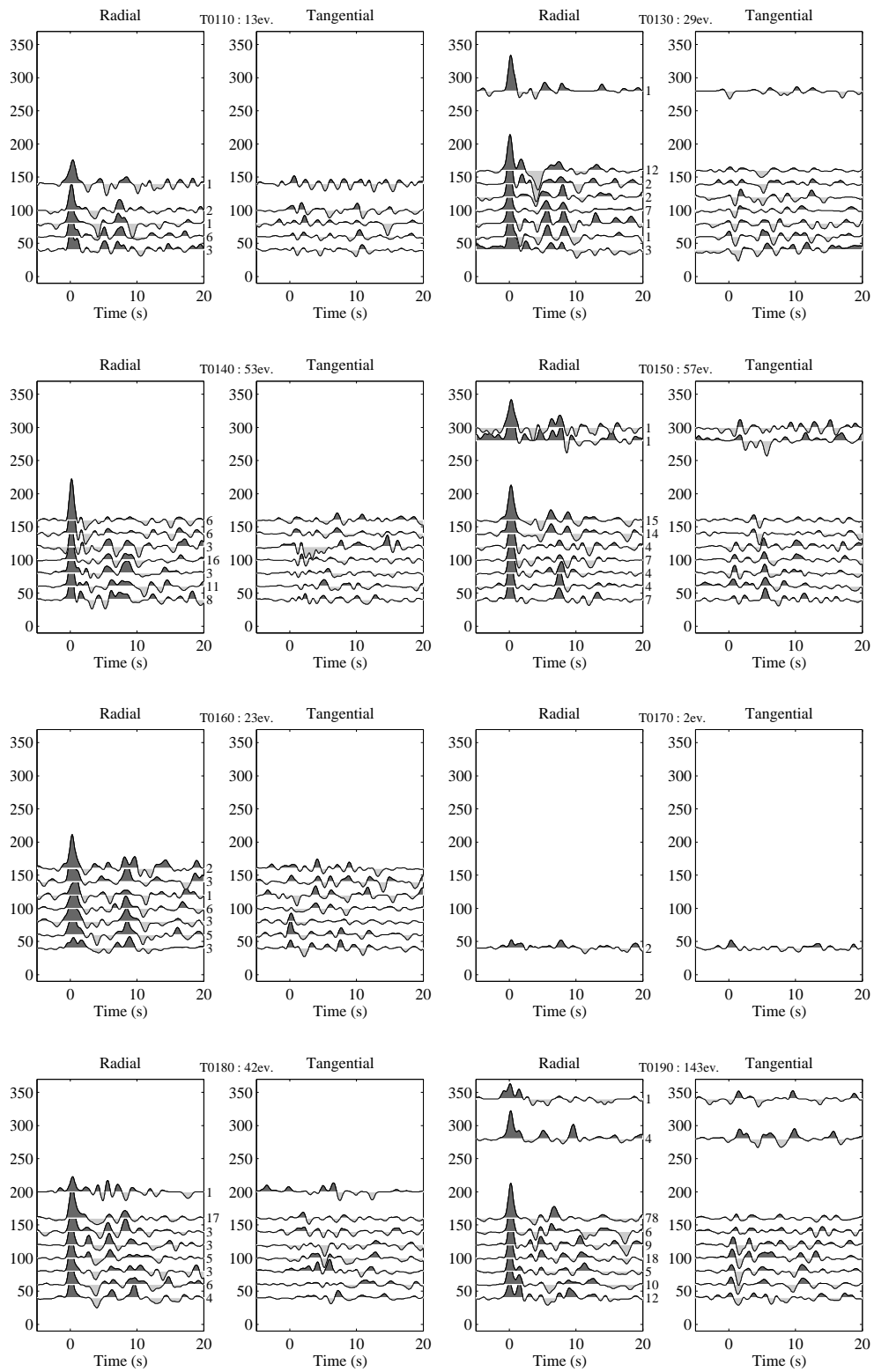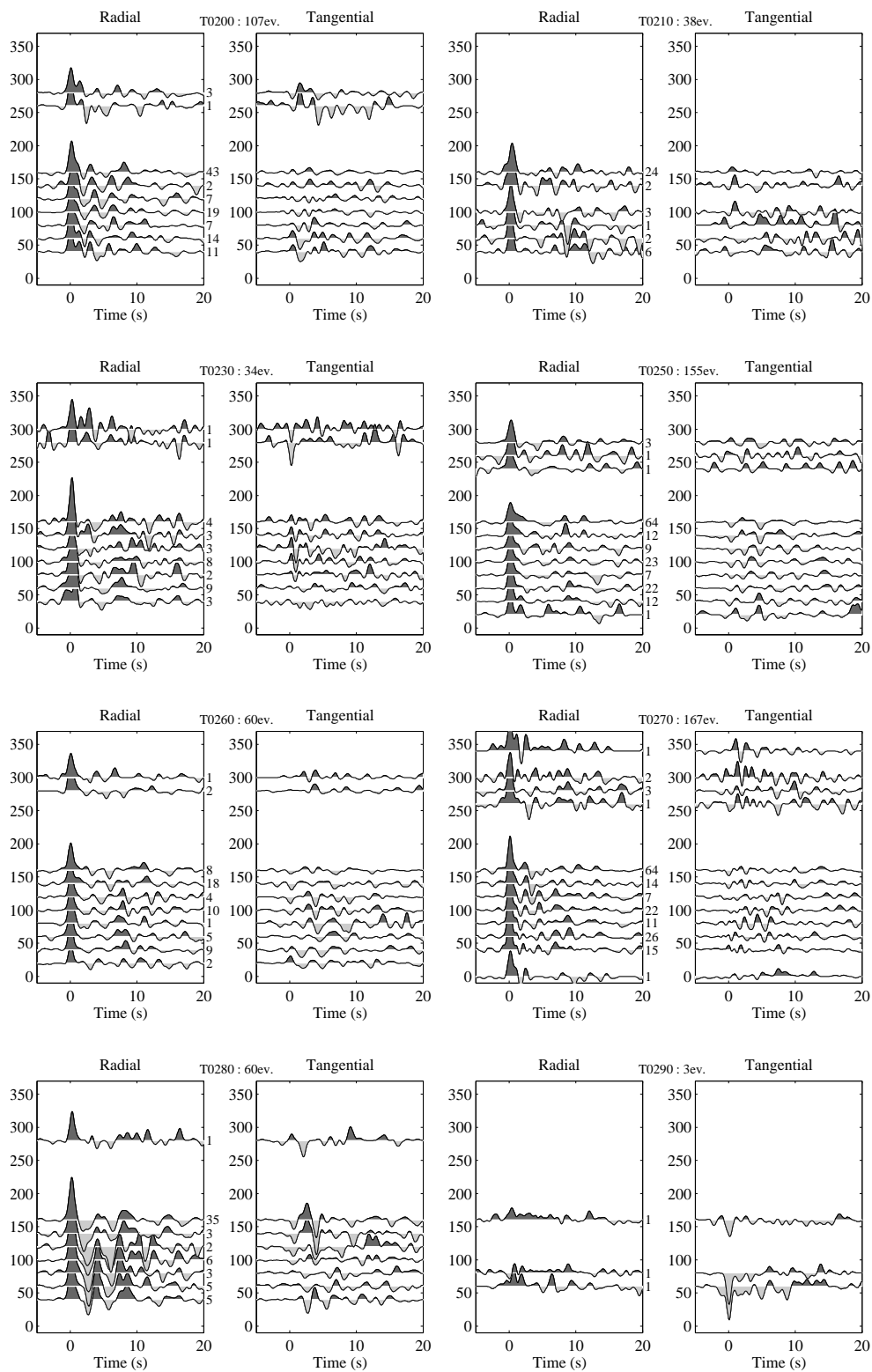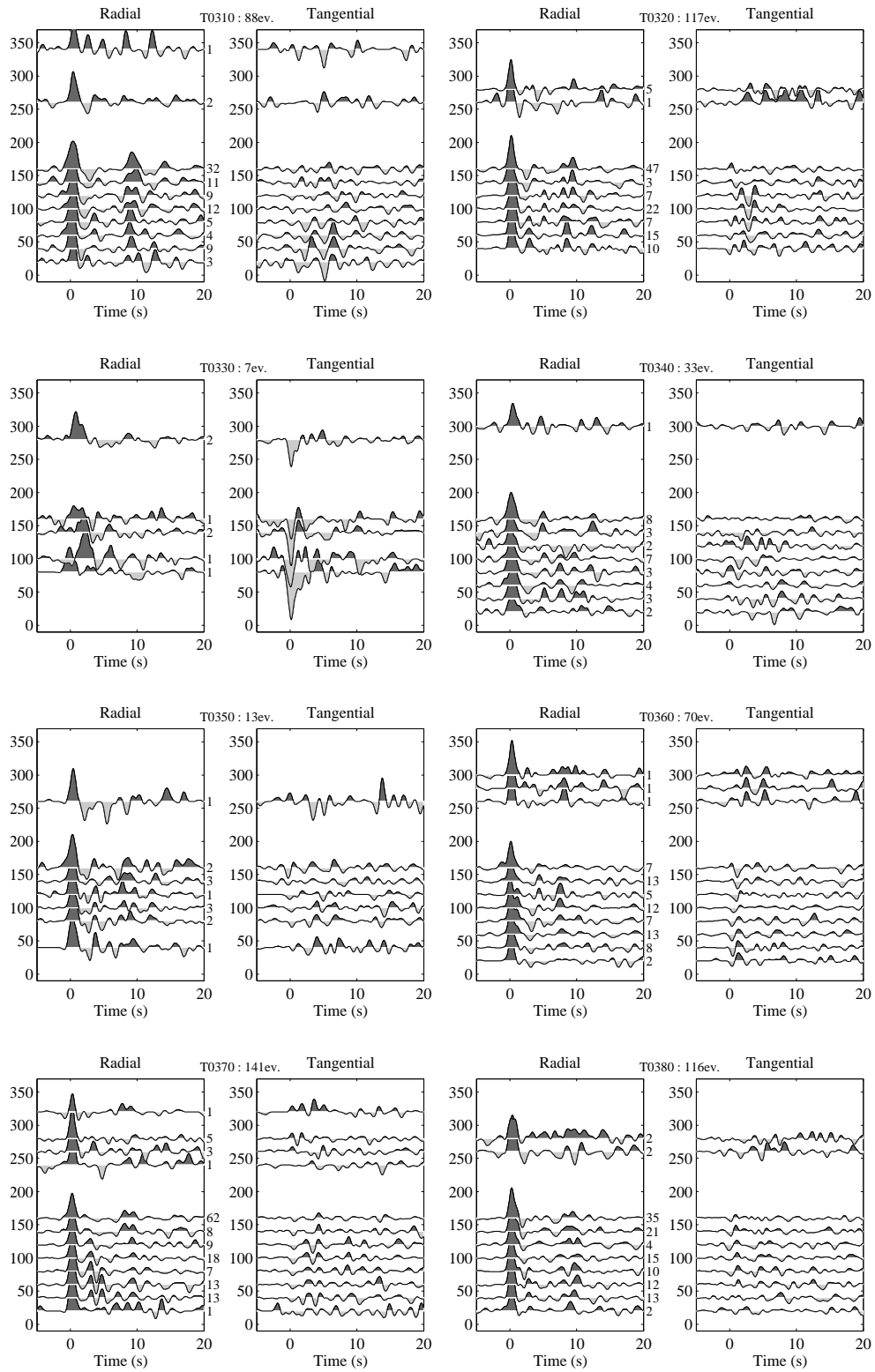
Lateral stations, Nepal
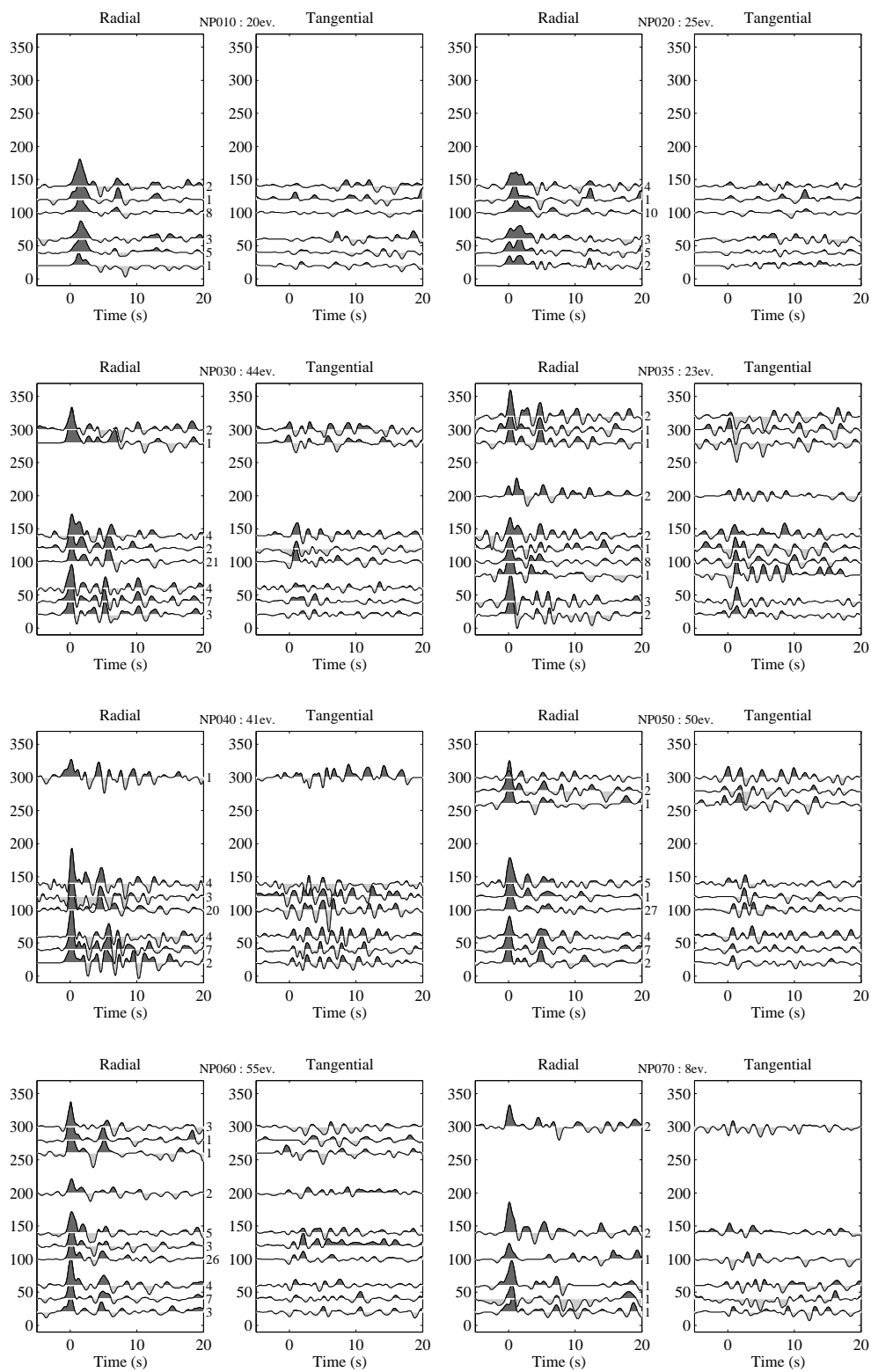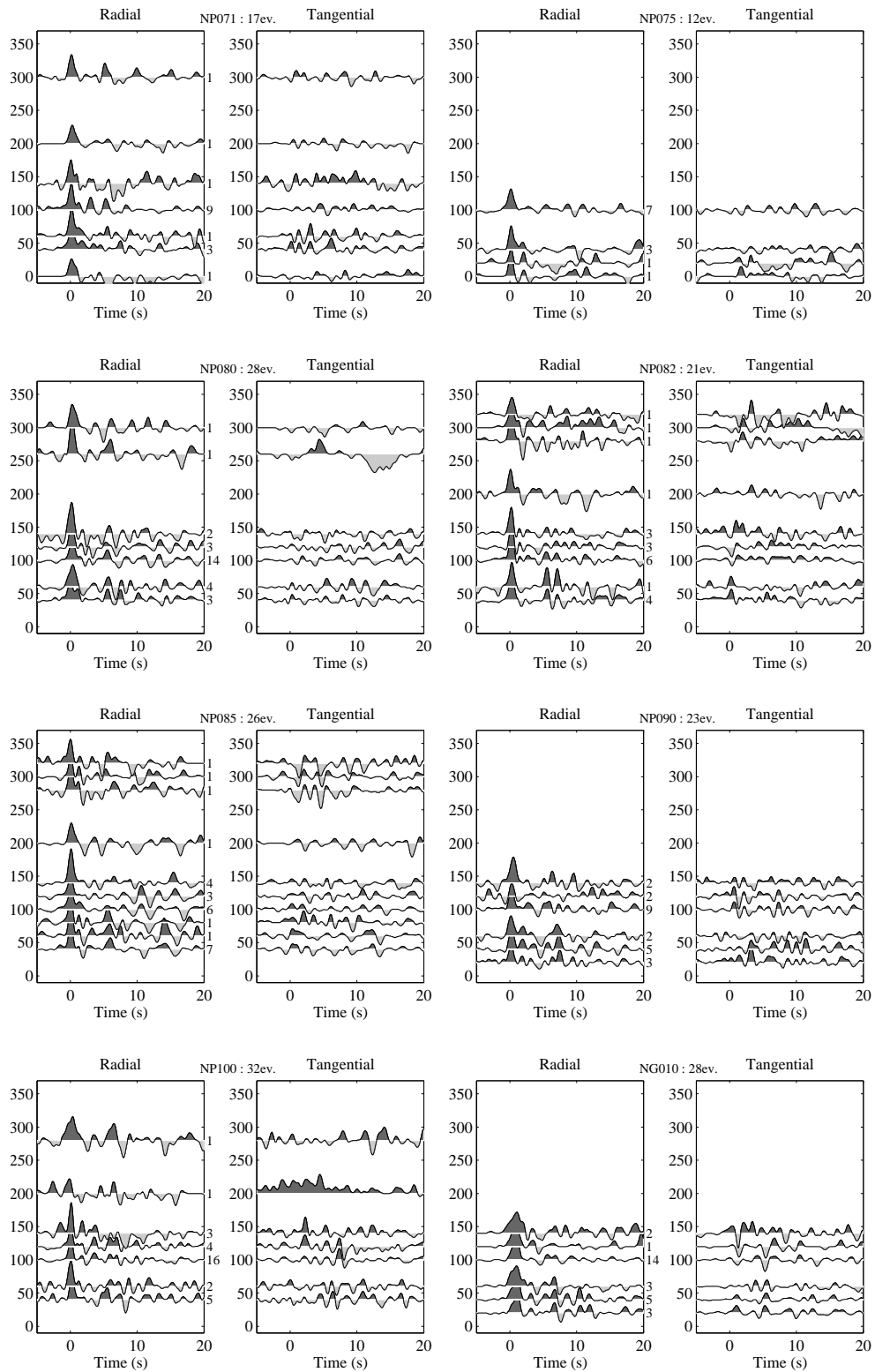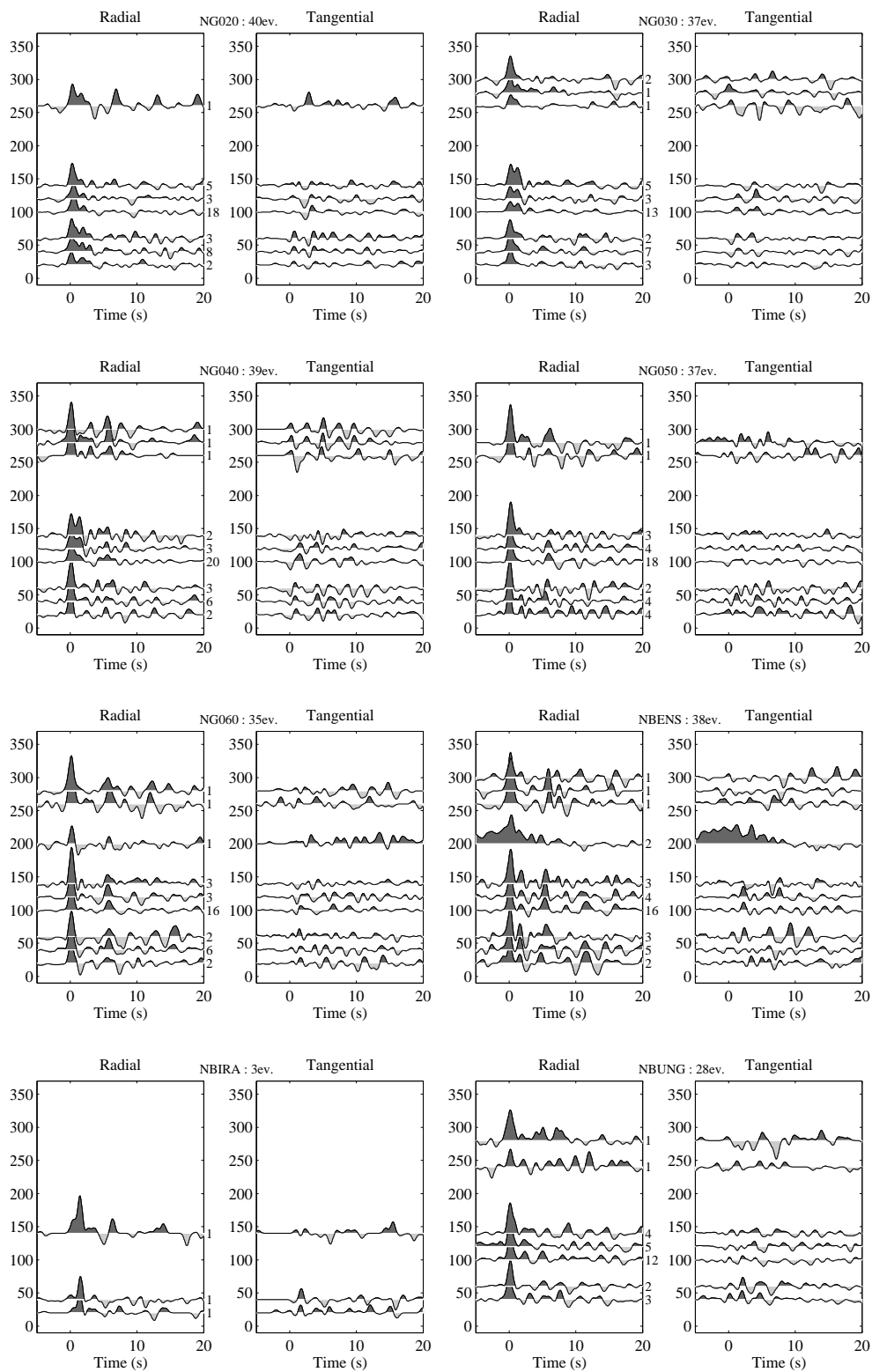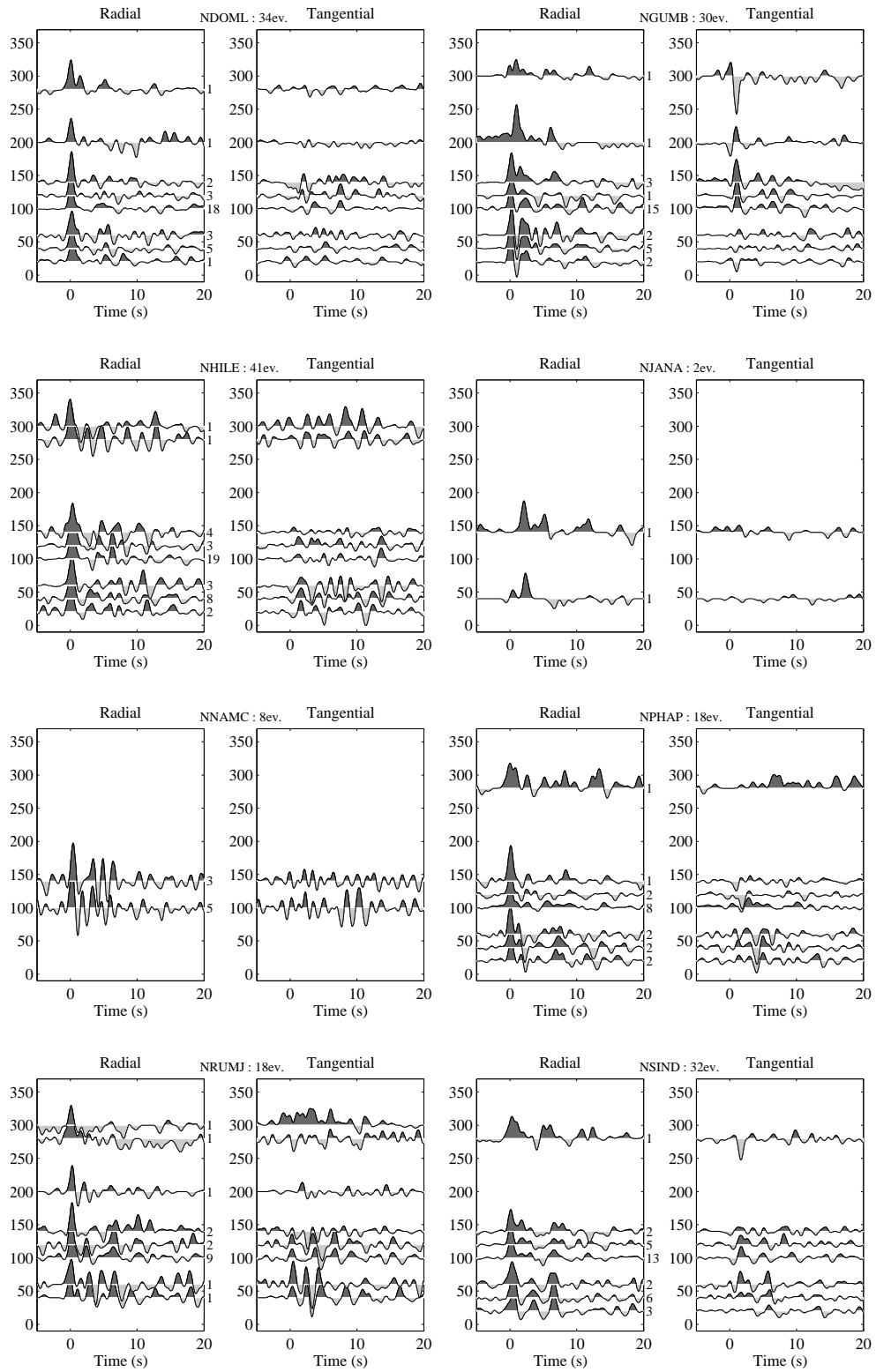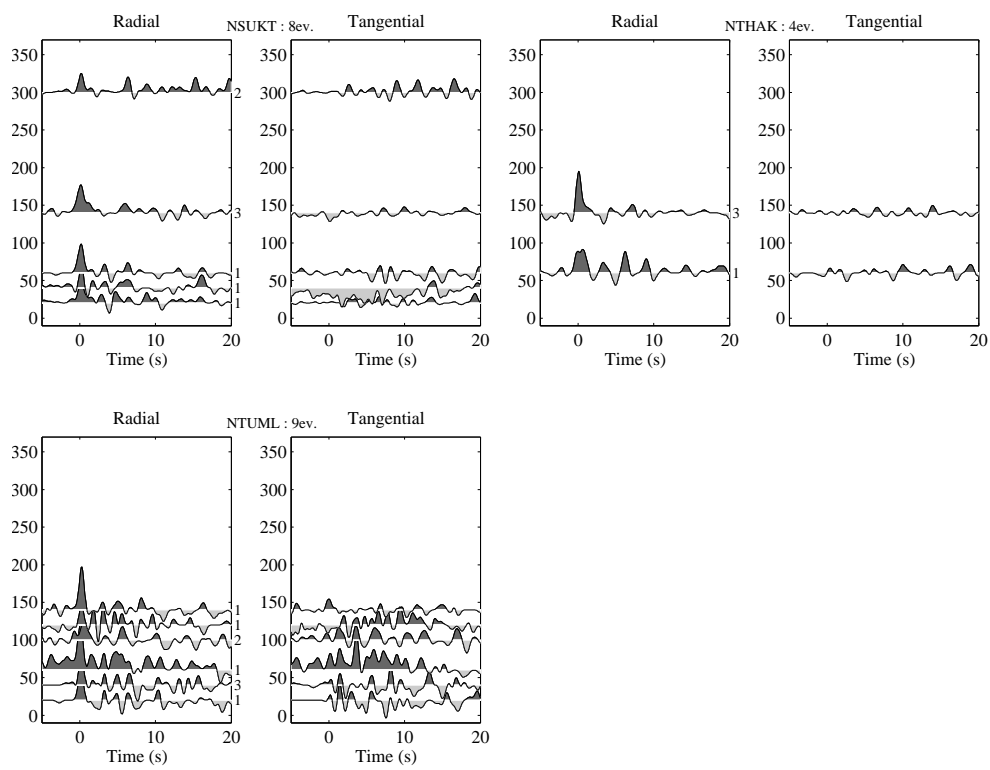
Examples of RF inversion

Receiver function inversion in theory has been summarized in Chapter 3, and the applications to the Hi-CLIMB data has been mentioned in Section 4. This appendix presents in some more detail the parameters of the inversion procedure, as well as a few examples of stations where both the semi-linearized and the NA method were applied.

Semi-linearized inversion

First, high quality traces were selected for the inversion. The selection was similar to the quality control described in Section 3.4.1, and yielded between 1 and 27 traces per station. The inverse problem was solved in a step-like procedure, starting from low frequency RFs and a few thick layers, and ending at high frequency RFs and many thin layers, according to Table D.1. For the first round of inversion, the same initial velocity model was used for all stations with 10 km thick layers and linearly increasing velocities with depth. The following steps took the best velocity model resulting from the previous round as an input.

At the end of the inversion steps, three criteria was analyzed in order to characterize the robustness of the results. First, the velocity model from the last round of inversion was used to produce a low-frequency RF, which was compared to the observed data filtered similarly. Second, the evolution of the misfit between the observed and the modelled RFs was checked from the first to the last inversion step, expecting a decrease. Third: the consistency of the velocity models issued from the 6 rounds of the inversion was visually

Inversion step	Frequency (sec)	Layer thickness (km)
1	20	10
2	10	10
3	10	5
4	5	5
5	5	2.5
6	2	2.5

Table D.1: Maximum frequency content and layer thicknesses of the velocity model in the 6 steps of the semi-linearized inversion procedure.

evaluated. In summary: while the misfits were not always monotonously decreasing from steps 1 to 6, there was a good correlation between stations with coherent velocity models during the iteration, and those that reproduced the low frequency RFs with the fine scale velocity model. Based on these criteria, about one third of the inversions were graded as bad quality, about half as medium, and $\sim 20\%$ as good quality. The major drawback of the inversion procedure here was the automated process that precluded visual selection of divergent iterations, and the application of a constant V_P/V_S -ratio for all models.

For those $\sim 20\%$ of the stations where the semi-linearized inversion process was of good quality, we also applied the Neighbourhood Algorithm.

NA inversion

This non-linear inversion scheme was applied to 34 stations. The initial velocity models were based on the results of the semi-linear inversions, which were approximated by linear segments to produce 2- to 5-layer crustal models overlying a half-space. The V_P/V_S of the layers was allowed to vary between 1.70 and 1.90, except for the mantle, fixed to 1.80. The inversions were performed on receiver functions filtered at 2 s (0.5 Hz). The NA inversion ran with 100 iterations with 100 velocity models each, of which 80 were re-sampled from one iteration step to the following one. The misfit function comparing the observed and synthetic waveforms was calculated using a cross-correlation based norm.

In evaluating the results, the *velocity–depth* curves resulting from the NA inversion were compared to those from the semi-linearized one (see the examples below). Also, the best 1% of the tested models is represented in V_P , V_S and V_P/V_S : their coherency or dispersion is representative of the uniqueness of the solution.

Examples and results

Here we show a few examples of inversion results at stations where both the semi-linearized and the NA method were applied. Figure D.1 shows three stations where the inversion provided robust results: the semi-linear and NA velocity profiles match well, and the dispersion of V_P/V_S with depth is small. The fourth station illustrates well the forces and the weaknesses of RF inversions alone: the velocity models recover the relative variations by both methods, however, the absolute values differs by as much as 0.5 km·s^{-1} in V_S . Furthermore, the V_P/V_S -ratio is not constrained in the NA inversion.
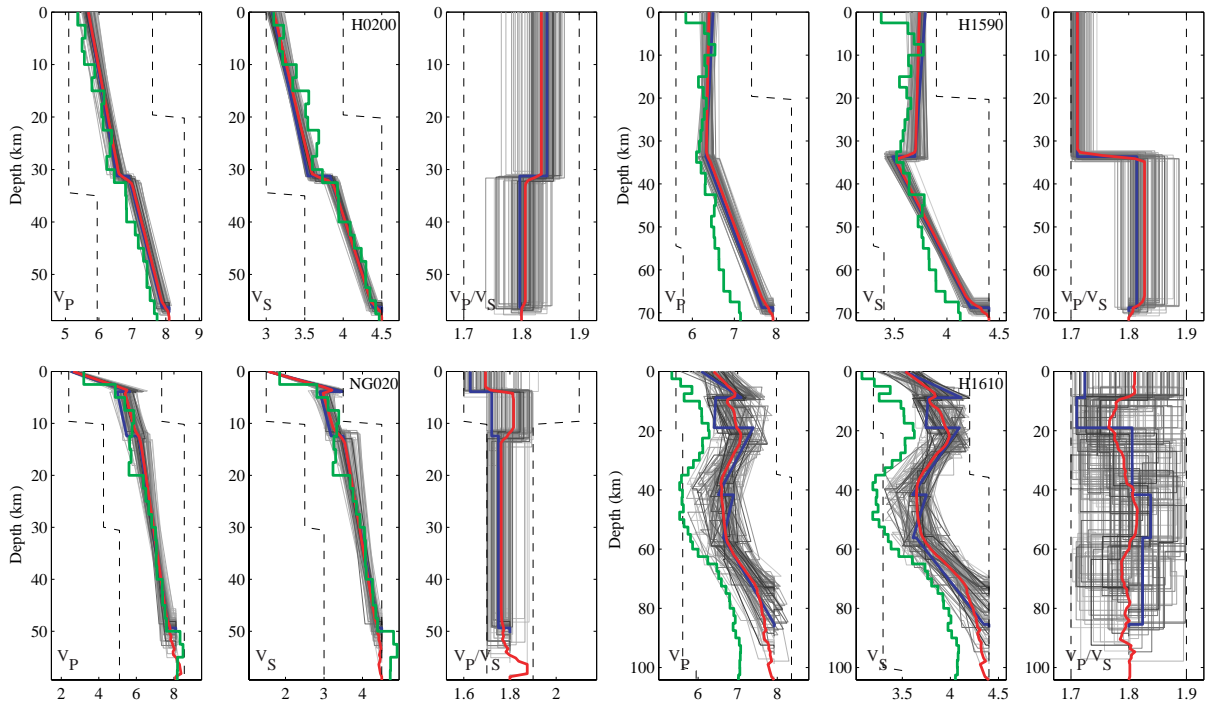
Figure D.1: Inversion results for four stations illustrating stable (H0200, H1590, NG020) and unstable (H1610) cases. Velocities are in km·s^{-1} . The green line is from the semi-linearized method, assuming constant V_P/V_S . The blue, gray and red curves are the best velocity model, the best 1% of all tested velocity models, and the average of these latters, respectively, from the NA.

We also present a few stations where the presence of an upper crustal low velocity zone was clear (Fig. D.2). These LVZs were also imaged by migration along the main array. Stations H0280 and H0420 are above the LVZ1 associated to aqueous fluids accumulated at the MHT from dewatering of sediments during metamorphic reactions. Station H1080 is located in the Tak Kyel Co graben in southern Lhasa block, above a bright spot, similarly to station H1200. Stations H1310 and H1320 clearly show the presence of a low velocity zone

beneath Dawa Co graben. Finally, stations T0320 and T0370 from the lateral deployment in southern Tibet also show the LVZ signature.
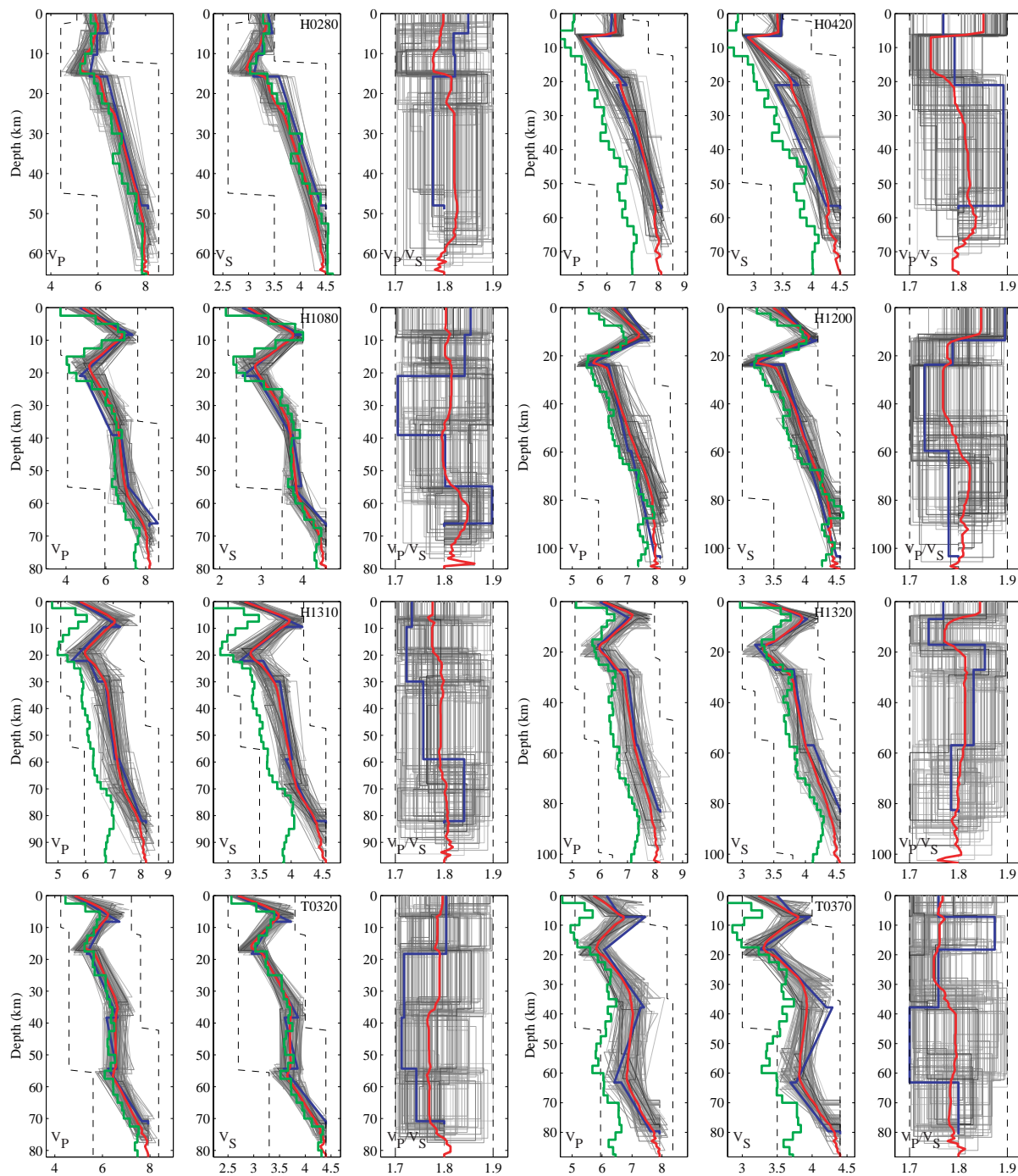
Figure D.2: Inversion results showing eight examples on the presence of low velocity zones in Nepal (first row) and southern Tibet (second to fourth row). Colour code is as on Figure D.1.

The presence of low velocity zones, constrained by the inversions, is also visible on the stacked receiver functions (Fig. D.3). The negative amplitude arrivals within a few seconds after the P wave indicate a significant decrease of velocity in the upper crust. The inversion procedure basically quantifies the thickness and the velocity decrease in these LVZs, and the propagation properties across the crust. However, the provided image and values have to be handled carefully. First, the inversion of RFs alone does not provide absolute velocities, hence only the relative velocity changes can be considered (Chapter 3). Second, inverting RFs alone is not the more robust method that exists: joint inversions with surface waves or other type of data should be performed (Chapter 8). This is especially true in an active convergent context, where the structures are complexified by both dipping boundaries and anisotropic layers, causing diffraction, attenuation, and strong back-azimuthal dependence of the RFs. Finally, while searching for absolute velocities, correct densities should be considered, as pointed out in Section 5.3.1.
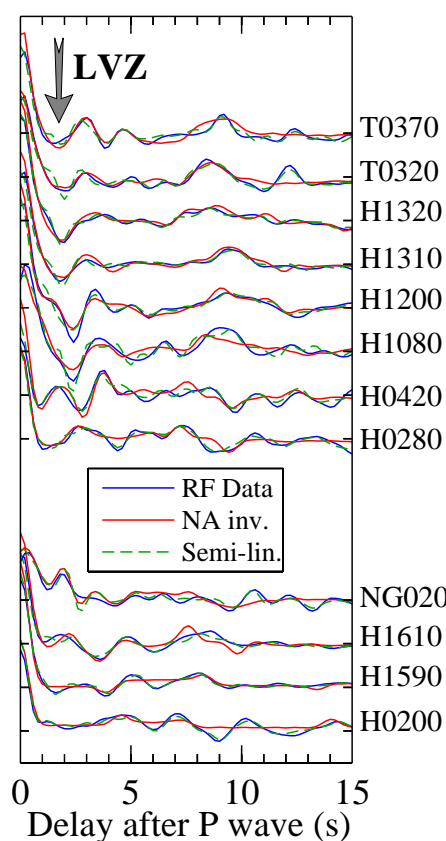
Figure D.3: Comparison of the observed and inverted receiver functions at the stations shown in this Appendix (see Fig. D.1 for the lower, Fig. D.2 for the upper group). The inverted traces are derived from the final step of the inversion procedure, at 0.5 Hz maximum frequency. On the above group of traces, the bright spots can be inferred from the negative amplitudes marked by the arrow.

A guide to GRANOM

GRANOM

Δg_z

GRAvity ANOMaly calculator

ρ_3 ρ_1

ρ_2

Author : György HETÉNYI
Ecole Normale Supérieure, Paris, France
hetenyi@geologie.ens.fr

With contributions from: R. Cattin, M. Guyomard & M. Denolle

© *György Hetényi 2006–2007*

Last update: *February 5th, 2007 (Version 1.2)*
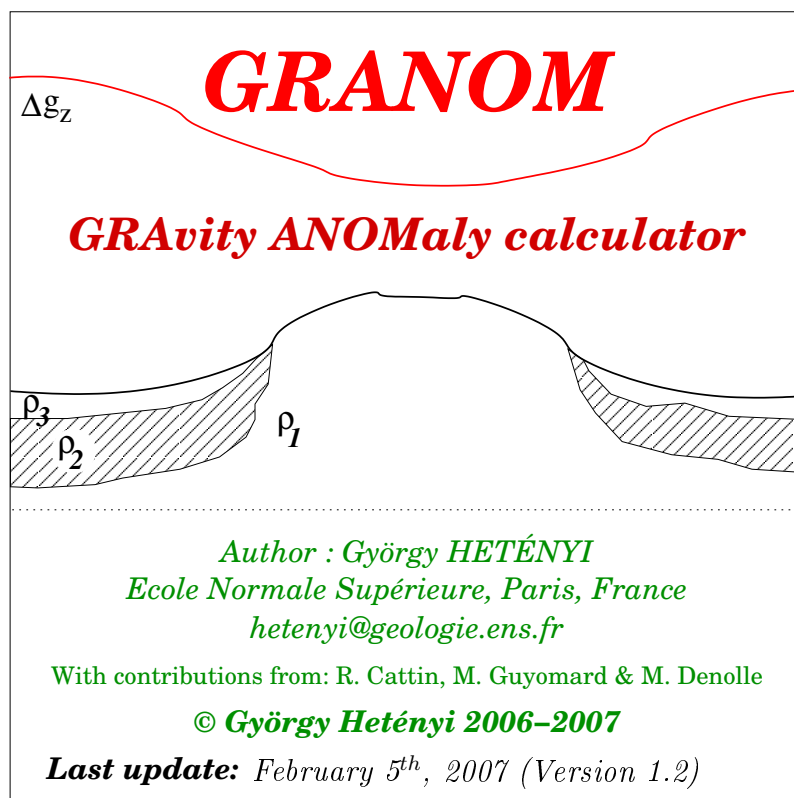
Summary

GRANOM is an interactive tool to work with gravity anomaly data. It calculates the gravity anomaly associated to the provided geometries and densities, and compares calculated and observed data. It allows to add, modify and delete bodies or vertex-points of bodies. There is also a one-button output of a complete study as an `.eps` figure or a text file, a direct output to a GMT-script, as well as the possibility to backup and reload different models tried in a same study.

Installation

The only technical requirement to use GRANOM is to have MATLAB installed on your computer. No special toolbox is required.

At this moment, GRANOM is in a β-version. Just type `tar -xzf granom.v1.2beta.tgz` in the folder where you want to install the program. Then launch `matlab -nodesktop` in the same folder, and type `granom`. A graphic window will appear (see below), but keep the terminal window handy as messages appear there. You can of course launch and use GRANOM from other folders: in this case you should add a path in MATLAB which points to the folder where you have installed GRANOM (*e.g.* `addpath /home/myself/Granom/`).

Input data structure

The input data consists of two types of files.

The first one is the `.data.`-file. It describes the field measurements point by point and should contain four columns:

- the x-coordinate along profile (in metres, positive to the right);

- the altitude above sea-level (in metres, positive upwards);

- Δg_x, the horizontal gravity anomaly (in mGal);

- Δg_z, the vertical gravity anomaly (in mGal).

The second type of file is the `.geom.`-file. It describes the geometry of one body and should contain:

- on the first line: the density-anomaly of the body (in kg/m^3);

- from the second line and on: the coordinates of the vertexes of the body in two columns:

– the x-coordinate along profile (in kilometres, positive to the right),

– and the depth below sea-level (in kilometres, positive downwards).

Please preferentially use a clock-wise order for the vertex points.

The bodies should be continuous, without holes or loops (or even overlying segments) in their contour. The contours may be left open as GRANOM closes them automatically

One `.data.`-file describes one dataset, and `.geom.`-file describes one body only. To use several datasets and bodies in the same study, start your filenames with the same name, followed by `.data.` and `.geom.`, respectively, and then any name you wish. A good idea would be to gather all these files to the same directory, such as in the sample set of files provided with GRANOM in the `Sample/` directory, with the common study-name `test`.

Calculations

The gravity anomaly calculations are based on the algorithm of Won and Bevis (1987).

Note that calculations are performed in a common coordinate-system where x is positive to the right, z is positive downwards, and units are in SI (distance in metres, density in kg/m^3), except for gravity anomalies (1 mGal = 10^{-5} m/s^2).

Getting started: main graphic window

Once you have typed `granom` in MATLAB, the main graphic window appears (Fig. E.1). Buttons are mostly activated when they can be used, except for the red ones at the bottom:

- **RESTART**: clears the current study and restarts GRANOM .

- **QUIT**: quits GRANOM and erases all variables.

- **GO HOME**: quits MATLAB.

- **About...**: information about GRANOM .

- **Guide**: opens this guide (in .pdf) with `acroread`.

    You can get a hint for each active button or text-box if you move the cursor over it. Let's explore the functions by going through examples!

    Enter the study-directory and -name (`Sample/test`) into the text-box,and press 'Enter'. Push the **READ DATA** button to read the input files. This also checks if they are
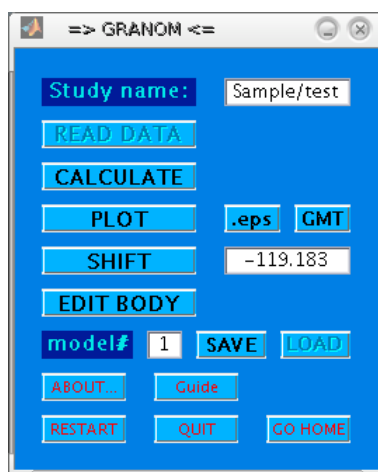
Figure E.1: The main window

in the correct format: if bodies are defined counter-clockwise, GRANOM automatically turns them around and warns you (as for `.geom.1` and `.geom.2` in the example); if there is a loop in the contour, or if there are overlapping segments, the body is ignored (as `.geom.5`) and a respective message ('CROSS' or 'OVERLIE') is shown.

   Press **CALCULATE** to calculate the gravity anomaly corresponding to the entire study (*i.e.* the effect of all correctly defined bodies at all data points).

   Push **PLOT** to get figure 'A' (for anomalies) with, from top to bottom (Fig. E.2):

- the topography;

- the observed and calculated gravity anomaly;

- their difference;

- the geometry of the bodies.

   The **.eps** button next to the **PLOT** button creates a `.eps`-file of this figure with a name composed of the study name, of `.figA.`, and the model number (see below).

   The **GMT** button next to the **.eps** button is a direct output towards GMT. It creates a folder in your study-folder, containing a `fig.gmt`-file and all the complementary files to produce a figure. Just enter the model number when asked in GRANOM , and then launch `fig.gmt` in the new folder. **NOTE1**: You need to have GMT installed on your computer for this to work. **NOTE2**: this button first creates a `.par` file in the study folder, which contains information that helps to create the `fig.gmt`-file. If you wish to modify the GMT-script, you can either do it directly in `fig.gmt`, or modify the `.par`-file (`Sample/test.par` in the example) and type `granom2gmt` in MATLAB.
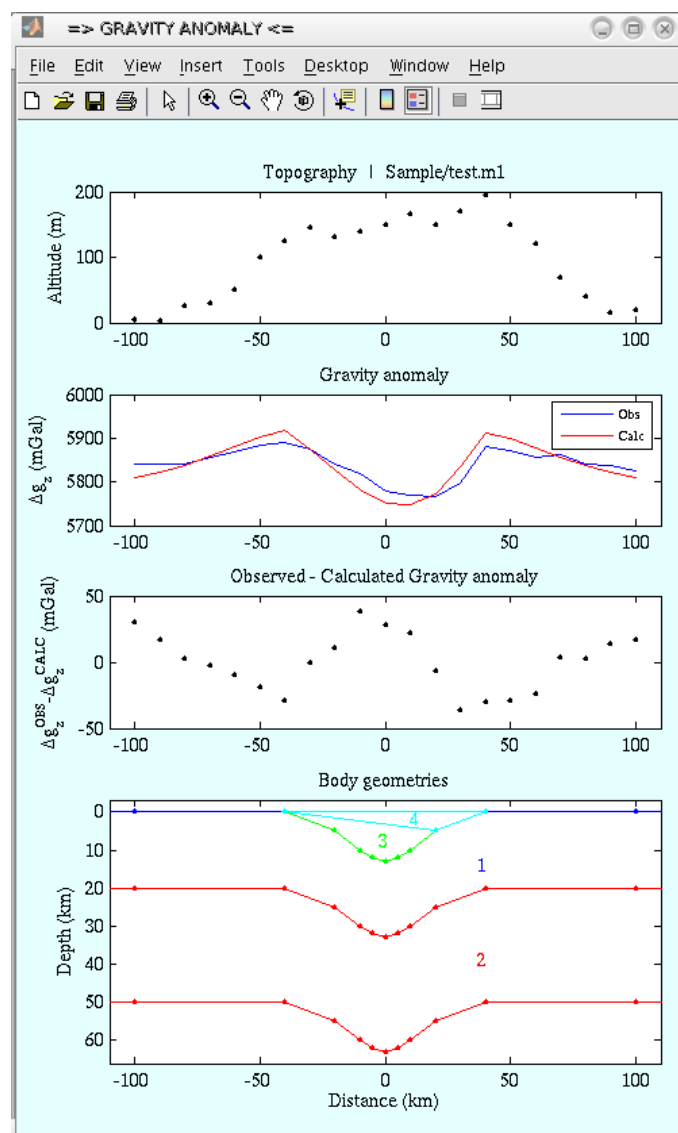
Figure E.2: The anomaly figure

When you push the **PLOT** button, GRANOM automatically calculates the best constant shift to apply to the calculated gravity anomaly in order to fit the observed values, based on an $\mathcal{L}_2$-norm difference. This value appears next to the **SHIFT** button (here -119.183) and the data appears shifted already. If you are not happy with this shift, or want to try other values, you can enter any value into the text-box (let's try -130) and the press **SHIFT**. Now the shifted calculated anomalies appear on the 2nd subfigure, and so does the new difference (3rd subfigure). The cumulative difference (or "error") according to the $\mathcal{L}_2$-norm is visible in the figure title, and is shown also in the terminal window along

with the χ^2-value, the semblance value, and the standard deviation of the difference (SIG) between observed and (shifted) calculated data:

$$\mathcal{L}_2 = \sqrt{\sum_i^N (Obs_i - Cal_i)^2}; \tag{E.1}$$

$$\chi^2 = \frac{\sum_{i=1}^N ((Obs_i - Cal_i)/\sigma_i)^2}{N}; \tag{E.2}$$

$$semblance = \exp(-\chi^2); \tag{E.3}$$

$$SIG = std(Obs - Cal); \tag{E.4}$$

where σ is the is the estimated uncertainty. It is either read from the `.sigma`-file (`Sample/test.sigma` in this example), which should contain two columns (first is the x-coordinate of the data and the second is the estimated uncertainty), or, in lack of the above file, σ is automatically set to 1.

The **EDIT BODY** button opens a second window that manages the geometry of the bodies; this is detailed in a following section.

Saving and loading backups

On the last line before the bottom red buttons, you can save backups of your study, labeled by the model numbers (model#s). When you start your study, the model# is automatically set to 0, and a first `.anom.`-file is created(`Sample/test.anom.m0.out`). The `.anom.`-files are sort of auxiliary files for GRANOM , but you can also use them for your own purposes. They contain six columns: the x-coordinate, the altitude, the calculated horizontal and vertical, and then the observed horizontal and vertical gravity anomaly, all in units of the common coordinate-system.

At each time you perform a calculation, the model# is updated to the become the highest existing (*i.e.* saved) model number plus one, and GRANOM creates the corresponding `.anom.`-file. At the point where you want to save your entire model (let's say model number 1), press **SAVE**, which creates two `.full.`-files. First is `Sample/test.full.m1.out` is an ASCII-file containing the name of the study, the date, all information on bodies, anomalies, the used shift and the obtained error. It also creates `Sample/test.full.m1.mat` which serves to reload this model any time you need. Then the model# is set to 2, 3, etc... and future files will be named `.m2.`, `.m3.`, etc...

To reload a saved model, enter its number into the text-box and press 'Enter' (or move the mouse out of the window). If the file exists, the **LOAD** button becomes active

and you just need to push it. If it does not, the existing model#s are shown in the terminal window so you can easily choose another model number.

Note: the **SAVE** button does not overwrite existing files. If you enter an existing model# and inadvertently press the **SAVE** button, it shows all existing model#s in the terminal window and sets current one in the text-box to the highest one plus one.

The editing window

This second command window (Fig. E.3) offers options to edit the geometries of the study with the help of a fourth, interactive 'B'-window (for body) which is opened at the same time (Fig. E.4). The latter window displays all bodies in the study along with their numbers using different colours.
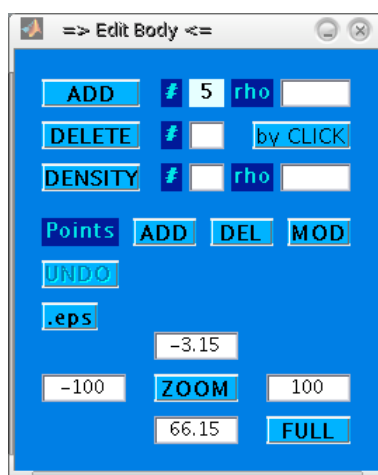
Figure E.3: The editing window

At the bottom of this editing window, you can choose to visualize the full study area by clicking on the **FULL** button, or to zoom onto a region by specifying the left, right, lower and upper limits and by pressing the **ZOOM** button (Fig. E.4a and b). Note that once you have set up your region of interest, pressing the **FULL** button will not erase them so you can zoom there again as long as you do not change the values.

Similarly to the first one, the **.eps** button right above allows the user to save the 'B'-figure into a .eps-file with a name composed of the study name, of .figB., and the model number (see above).
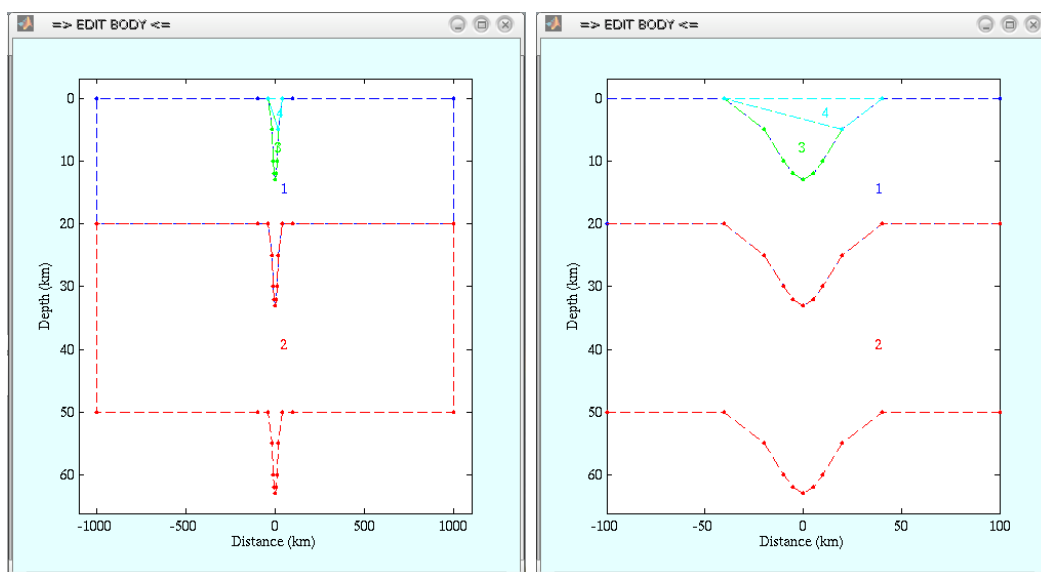
Figure E.4: The body window. (a) Full zoom. (b) Zoom of interest.

Edit a body

The first three rows of this editing window allow to manipulate entire bodies.

To add a body (its number appears in the middle of the first row), first enter its density to the right, and then push **ADD**. The cursor becomes active on the 'B'-figure, and you can click the vertexes of your new body. The technique is the following:

- add a point with the *left* button of your mouse;

- erase the previously added point with the *right* or *center* button of your mouse;

- cancel the whole adding process by pressing 'c' on the keyboard;

- finish the adding process by pressing 'Enter' on the keyboard.

Once you have finished adding the vertexes, the new geometry is tested as the originals (clockwise-orientation, no hole, no crossing contour), and is added to the study only if it was found to be correct.

NOTE *(about a trick on zooming):* If you need to zoom while adding a body, you should enter the zooming limits and click 2(!) times on the **ZOOM** button. Then you can come back to the 'B'-figure, and continue to click. One bothering (but yet unexplained) effect: the first new click in the 'B'-figure does not appear at the correct place, so you have to erase with the *right* or *CENTER* button of your mouse...

To delete a body, there are two ways. In case you know its number, you can enter it into the text-box of the second line, and then press the **DELETE** button. The 'B'-figure is automatically updated. The other way of deleting is by pushing the **by CLICK** button

which activates the cursor of the mouse over the 'B'-figure, and then you can click <u>inside</u> the body you want to erase. If several bodies overlie each other where you click, GRANOM offers you the choice in the terminal window to erase all, none, or the specified ones (enter `a`, `n` or the corresponding numbers, respectively).

To modify a body's density-anomaly, first you have to enter its number into the text-box in the middle of the third line, and press 'Enter'. The body's density-anomaly appears in the other text-box in this line, where you can edit it. You validate your choice by pressing the **DENSITY** button, and the change is confirmed in the terminal window.

Edit a vertex

The vertexes of all bodies appear as dots on their contour in the 'B'-window. You may add, modify and delete a vertex using the three buttons in the fourth line, to the right of 'Points'. As all three modes use the existing vertex which is closest to your clicking; try to click as precise as possible.

To add a vertex, press the **ADD** button and select the place in the 'B'-window where you want to add your vertex. Note that the new point will be added to the body to which the closest existing vertex belongs. If this point is shared by several bodies, GRANOM offers you the choice to add this new vertex to all, none, or the specified ones (enter `a`, `n` or the corresponding numbers in the terminal window, respectively). Note that the new vertex will be inserted between the closest and the second closest vertexes.

To delete a vertex, press the **DEL** button and select the vertex in the 'B'-window that you want to delete. If this point is shared by several bodies, GRANOM offers you the choice to delete this vertex from all, none, or the specified ones (enter `a`, `n` or the corresponding numbers in the terminal window, respectively). The chosen vertex will then appear as a yellow disk, and you should press 'd' on the keyboard to confirm its deletion.

To modify the position of a vertex, press the **MOD** button and follow the same procedure. Once the vertex appears in yellow, click its new position.

What if I made a mistake?

Good news: If you made a bad editing operation, you can correct it! You just need to push the **UNDO** button in red, which comes back to the previous stage of the geometries.

Bad news: This button UNDOes one and only one step...

Good news: Don't worry! That's why there is the **SAVE** and **LOAD** button on the main window so you can try, backup and reload different models...

Note: **UNDO** uses the `tmp.mat`-file in the directory you work in, so for your own calmness, do not erase it during your work...

Some details and advanced features - description of variables

This section details the name of the principal variables so that users can manipulate data *in-line*, within MATLAB. (**NOTE**: If you decide to modify values *in-line*, be aware that the **UNDO** button becomes useless for your operations.) A good example is to set a vertex at a given, precise position; or to translate an entire body.

- **G** is a structure that is used by the `granom2gmt.m` script, and contains information about the GMT-output of GRANOM . The used values are determined in the `prep_granom2gmt.m` script and are written in the `.par`-file.

- **H** is a structure array that contains all the handles and button callbacks. Some variables handle the figures (such as the used font's type and size, the displayed curves' colour, symbol- and line-type), these can be found in `SUB/personals.m` and can be modified by the user. At this point of the software development, it is not recommended to modify other fields of **H**.

- **X** is the x-coordinate of the data points in kilometres (column vector).

- **anomaly** is the calculated gravity anomaly corresponding to the current bodies and densities. It has two components x and z in fields `.x` and `.z` (row vectors).

- **anomaly0** is the same as **anomaly** but for the original bodies and densities (*i.e.* the ones in the files).

- **azoom** are the x- and z-limits of the zooming button.

- **datapts** are the x- and z-coordinates of the data points in the common coordinate system (row vectors).

- **densanom** are the density anomalies of the bodies (row vector).

- **geometry** is a cell array, containing the x- and z-coordinates (column vectors) of the bodies (one per cell) in the common coordinate system.

- **gravdata** is the observed gravity anomalies Δg_x and Δg_z in mGals (row vectors).

- **imodel** is the current model number.

- **result_file** is the current output-filename and **result_file0** is the original output-filename.

- **shift0** and **shift0n** are the best shift determined for the original case and the current modified case, respectively, and **shift** is the shift specified by the user.

- **study** is the studyname including the folder-names from the current directory, and **studyrep** is the folder where the study is located.

Example: Translating body #2 10 km deeper and 5 km to the right would be this simple:

```
geometry{2}.x=geometry{2}.x+5000;
geometry{2}.z=geometry{2}.z+10000;
```

More to come...

Comments are welcome!

References

Agocs, W. B. (1957). Aeromagnetic survey of Indo-Gangetic Plains and Rajasthan. Oil Nat. Gas. Comm., unpublished report.

Airy, G. B. (1855). On the computation of the effect of the attraction of mountain-masses, as disturbing the apparent astronomical latitude of stations in geodetic surveys. *Phil. Trans. Roy. Soc. London*, **145**, 101–104.

Aitchison, J. C., Ali, J. R. and Davis, A. M. (2007). When and where did India and Asia collide? *J. Geophys. Res. 112*(B5), B05423.

Allègre, C. J., Courtillot, V., Tapponnier, P., Hirn, A., Mattauer, M., Coulon, C., Jaeger, J. J., Achache, J., Schaerer, U., Marcoux, J., Burg, J. P., Girardeau, J., Armijo, R., Gariepy, C., Goepel, C., Li, T., Xiao, X., Chang, C., Li, G., Lin, B., Teng, J. W., Wang, N., Chen, G., Han, T., Wang, X., Den, W., Sheng, H., Cao, Y., Zhou, J., Qiu, H., Bao, P., Wang, S., Wang, B., Zhou, Y. and Ronghua, X. (1984). Structure and evolution of the Himalaya-Tibet orogenic belt. *Nature 307*(5946), 17–22.

Alsdorf, D., Makovsky, Y., Zhao, W., Brown, L. D., Nelson, K. D., Klemperer, S., Hauck, M., Ross, A., Cogan, M., Clark, M., Che, J. and Kuo, J. (1998). INDEPTH (International Deep Profiling of Tibet and the Himalaya) multichannel seismic reflection data: description and availability. *J. Geophys. Res. 103*(B11), 26993–26999.

Ammon, C. J. (1991). The isolation of receiver effects from teleseismic P waveforms. *Bull. Seismol. Soc. Am.*, **81**, 2504–2510.

Ammon, C. J., Randall, G. E. and Zandt, G. (1990). On the nonuniqueness of receiver function inversions. *J. Geophys. Res.*, **95**, 15303–15318.

Andersen, T., Austrheim, H. and Burke, E. A. J. (1991). Mineral fluid melt interactions in high-pressure shear zones in the Bergen Arcs Nappe Complex, Caledonides of W Norway: implications for the fluid regime in Caledonian eclogite-facies metamorphism. *Lithos 27*(3), 187–204.

Anderson, D. L. (1989). *Theory of the Earth*. Blackwell Scientific Publications, 366 pp.

Argand, E. (1924). La tectonique de l'Asie. In *Congrès Géologique Internationale, Bruxelles, Compte rendus de la XIIIe session*, Volume 1, pp. 171–372. Vaillant-Carmanne, Liège.

Armijo, R., Tapponnier, P., Mercier, J. L. and Han, T. L. (1986). Quaternary extension in Southern Tibet – field observations and tectonic implications. *J. Geophys. Res. 91*(B14), 13803–13872.

Austrheim, H., Erambert, M. and Engvik, A. K. (1997). Processing of crust in the root of the Caledonian continental collision zone: The role of eclogitization. *Tectonophysics 273*(1-2), 129–153.

Avouac, J. P. (2003). Mountain building, erosion, and the seismic cycle in the Nepal Himalaya. *Advances in Geophysics*, **46**, 1–80.

Avouac, J. P. and Burov, E. B. (1996). Erosion as a driving mechanism of intracontinental mountain growth. *J. Geophys. Res. 101*(B8), 17747–17769.

$\mathcal{B}$annister, S., Yu, J., Leitner, B. and Kennett, B. L. N. (2003). Variations in crustal structure across the transition from West to East Antarctica, Southern Victoria Land. *Geophys. J. Int. 155*(3), 870–884.

Barazangi, M. and Ni, J. (1982). Velocities and propagation characteristics of Pn and Sn beneath the Himalayan Arc and Tibetan plateau: possible evidence for underthrusting of Indian continental lithosphere beneath Tibet. *Geology 10*(4), 179–185.

Bascou, J., Barruol, G., Vauchez, A., D., M. and Egydio-Silva, M. (2001). EBSD-measured lattice-preferred orientations and seismic properties of eclogites. *Tectonophysics*, **342**, 61–80.

Basuyau, C. (2007). Imagerie des structures lithosphériques d'une jeune marge continentale: inversion conjointe gravimétrie–sismologie dans le golfe d'Aden. Master's thesis, Université Pierre et Marie Curie, 73 pp.

Baxter, E. (2003). Natural constraints on metamorphic reactions rates. In D. Vance, W. Müller, and I. Villa (Eds.), *Geochronology, Linking the isotopic record with petrology and textures*. Geol. Soc., London, Spec. Publ.

Baxter, E. F. and DePaolo, D. J. (2000). Field measurement of slow metamorphic re-
action rates at temperatures of 500 degrees to 600 degrees C. *Science 288*(5470),
1411–1414.

Beaumont, C., Jamieson, R. A., Nguyen, M. H. and Lee, B. (2001). Himalayan tectonics
explained by extrusion of a low-viscosity crustal channel coupled to focused surface
denudation. *Nature 414*(6865), 738–742.

Beaumont, C., Jamieson, R. A., Nguyen, M. H. and Medvedev, S. (2004). Crustal channel
flows: 1. Numerical models with applications to the tectonics of the Himalayan-
Tibetan orogen. *J. Geophys. Res. 109*(B6), B06406.

Beck, R. A., Burbank, D. W., Sercombe, W. J., Riley, G. W., Barndt, J. K., Berry, J. R.,
Afzal, J., Khan, A. M., Jurgen, H., Metje, J., Cheema, A., Shafique, N. A., Lawrence,
R. D. and Khan, M. A. (1995). Stratigraphic evidence for an early collision between
northwest India and Asia. *Nature 373*(6509), 55–58.

Benoit, M. H., Nyblade, A. A., VanDecar, J. C. and Gurrola, H. (2003). Upper mantle
P wave velocity structure and transition zone thickness beneath the Arabian Shield.
Geophys. Res. Lett. 30(10), 1531.

Besse, J. and Courtillot, V. (1988). Paleogeographic maps of the continents bordering
the Indian Ocean since the Early Jurassic. *J. Geophys. Res. 93*(B10), 11791–11808.

Besse, J., Courtillot, V., Pozzi, J. P., Westphal, M. and Zhou, Y. X. (1984). Palaeomag-
netic estimates of crustal shortening in the Himalayan thrusts and Zangbo suture.
Nature, **311**, 621–626.

Bettinelli, P., Avouac, J. P., Flouzat, M., Jouanne, F., Bollinger, L., Willis, P. and
Chitrakar, G. R. (2006). Plate motion of India and interseismic strain in the Nepal
Himalaya from GPS and DORIS measurements. *J. of Geodesy 80*(8-11), 567–589.

Beyssac, O., Bollinger, L., Avouac, J. P. and Goffe, B. (2004). Thermal metamorphism in
the lesser Himalaya of Nepal determined from Raman spectroscopy of carbonaceous
material. *Earth Planet. Sci. Lett. 225*(1-2), 233–241.

Bilham, R. (1995). Location and magnitude of the 1833 Nepal earthquake and its re-
lation to the rupture zones of contiguous Great Himalayan earthquakes. *Current
Science 69*(2), 101–128.

Birch, F. (1961). The velocity of compressional waves in rocks to 10 kilobars, part 2. *J.
Geophys. Res.*, **66**, 2199–2224.

Bollinger, L., Avouac, J. P., Beyssac, O., Catlos, E. J., Harrison, T. M., Grove, M., Goffe, B. and Sapkota, S. (2004). Thermal structure and exhumation history of the Lesser Himalaya in central Nepal. *Tectonics 23*(5), TC5015.

Bollinger, L., Avouac, J. P., Cattin, R. and Pandey, M. R. (2004). Stress buildup in the Himalaya. *J. Geophys. Res. 109*(B11), B11405.

Bollinger, L., Henry, P. and Avouac, J. P. (2006). Mountain building in the Nepal Himalaya: Thermal and kinematic model. *Earth Planet. Sci. Lett. 244*(1-2), 58–71.

Bousquet, R., Goffé, B., Henry, P., Le Pichon, X. and Chopin, C. (1997). Kinematic, thermal and petrological model of the Central Alps: Lepontine metamorphism in the upper crust and eclogitisation of the lower crust. *Tectonophysics 273*(1-2), 105–127.

Brown, L. D., Zhao, W. J., Nelson, D. K., Hauck, M., Alsdorf, D., Ross, A., Cogan, M., Clark, M., Liu, X. W. and Che, J. K. (1996). Bright spots, structure, and magmatism in southern Tibet from INDEPTH seismic reflection profiling. *Science 274*(5293), 1688–1690.

Brunel, M. (1986). Ductile thrusting in the Himalayas: shear sense criteria and stretching lineations. *Tectonics 5*(2), 247–265.

Budweg, M., Bock, G. and Weber, M. (2006). The Eifel Plume – imaged with converted seismic waves. *Geophys. J. Int. 166*(2), 579–589.

Burdick, L. J. and Helmberger, D. V. (1974). Time functions appropriate for the deep earthquakes. *Bull. Seismol. Soc. Am.*, **56**, 1419–1428.

Burov, E. and Watts, A. (2006). The long-term strength of the continental lithosphere: "jelly sandwich" or "crème brûlée"? *GSA Today 16*(1), 4–10.

Burov, E. B. and Diament, M. (1992). Flexure of the continental lithosphere with multi-layered rheology. *Geophys. J. Int.*, **109**, 449–468.

Burov, E. B. and Diament, M. (1995). The effective elastic thickness (T_e) of continental lithosphere – What does it really mean? *J. Geophys. Res. 100*(B3), 3905–3927.

Burtin, A., Bollinger, L., Vergne, J., Cattin, R. and Nábělek, J. (2007). Spectral analysis of seismic noise induced by rivers: A new tool to monitor spatio-temporal changes in stream hydrodynamics. *J. Geophys. Res.*, **submitted**, .

Burtin, A., Nábělek, J., Baur, J. and Vergne, J. (2005). Evidence for the Decoupling of Stress Above and Beneath the Main Himalayan Thrust. In *EoS Trans. AGU, 86(52), Fall Meet. Suppl., Abstract T43A-1379B.*

$\mathcal{C}$alkins, J. A., Zandt, G., Gilbert, H. J. and Beck, S. L. (2006). Crustal images from San Juan, Argentina, obtained using high frequency local event receiver functions. *Geophys. Res. Lett. 33*(7), L07309.

Carlson, W. D., Denison, C. and Ketcham, R. A. (1995). Controls on the nucleation and growth of porphyroblasts: Kinetics from natural textures and numerical models. *Geological Journal 30*(3-4), 207–225.

Carosi, R., Lombardo, B., Musumeci, G. and Pertusati, P. C. (1999). Geology of the Higher Himalayan Crystallines in Khumbu Himal (Eastern Nepal). *J. of Asian Earth Sci. 17*(5-6), 785–803.

Carozzi, A. E. (1977). *Tectonics of Asia, by Emile Argand*. Hafner Press, New York, 218 pp.

Cassidy, J. F. (1992). Numerical experiments in broad-band receiver function-analysis. *Bull. Seismol. Soc. Am. 82*(3), 1453–1474.

Cattin, R. and Avouac, J.-P. (2000). Modeling mountain building and the seismic cycle in the Himalaya Nepal. *J. Geophys. Res. 105*(B6), 13389–13407.

Cattin, R., Martelet, G., Henry, P., Avouac, J. P., Diament, M. and Shakya, T. R. (2001). Gravity anomalies, crustal structure and thermo-mechanical support of the Himalaya of Central Nepal. *Geophys. J. Int. 147*(2), 381–392.

Chen, L., Wen, L. X. and Zheng, T. Y. (2005). A wave equation migration method for receiver function imaging: 1. Theory. *J. Geophys. Res. 110*(B11), B11309.

Chen, Q. Z., Freymueller, J. T., Wang, Q., Yang, Z. Q., Xu, C. J. and Liu, J. N. (2004). A deforming block model for the present-day tectonics of Tibet. *J. Geophys. Res. 109*(B1), B01403.

Chen, W. P. and Yang, Z. H. (2004). Earthquakes beneath the Himalayas and Tibet: Evidence for strong lithospheric mantle. *Science 304*(5679), 1949–1952.

Christensen, J. N., Rosenfeld, J. L. and Depaolo, D. J. (1989). Rates of tectonometamorphic processes from rubidium and strontium isotopes in garnet. *Science 244*(4911), 1465–1469.

Christensen, M. I. and Mooney, W. D. (1995). Seismic velocity structure and composition of the continental-crusta global view. *J. Geophys. Res. 100*(B6), 9761–9788.

Chung, S. L., Lo, C. H., Lee, T. Y., Zhang, Y. Q., Xie, Y. W., Li, X. H., Wang, K. L. and Wang, P. L. (1998). Diachronous uplift of the Tibetan plateau starting 40 Myr

ago. *Nature 394*(6695), 769–773.

Clark, M. K., Bush, J. W. M. and Royden, L. H. (2005). Dynamic topography produced by lower crustal flow against rheological strength heterogeneities bordering the Tibetan Plateau. *Geophys. J. Int. 162*(2), 575–590.

Clark, M. K. and Royden, L. H. (2000). Topographic ooze: Building the eastern margin of Tibet by lower crustal flow. *Geology 28*(8), 703–706.

Clayton, R. W. and Wiggins, R. A. (1976). Source shape estimation and deconvolution of teleseismic body waves. *Geophys. J. R. Astron. Soc.*, **47**, 151–177.

Clitheroe, G., Gudmundsson, O. and Kennett, B. L. N. (2000). Sedimentary and upper crustal structure of Australia from receiver functions. *Austr. J. of Earth Sci.*, **47**, 209–216.

Connolly, J. A. D. (2005). Computation of phase equilibria by linear programming: A tool for geodynamic modeling and its application to subduction zone decarbonation. *Earth Planet. Sci. Lett. 236*(1-2), 524–541.

Copeland, P. and Harrison, T. M. (1990). Episodic rapid uplift in the Himalaya revealed by Ar40/Ar39 analysis of detrital H-feldspar and muscovite, Bengal fan. *Geology 18*(4), 354–357.

*D*e la Torre, T. L. and Sheehan, A. F. (2005). Broadband seismic. noise analysis of the Himalayan Nepal Tibet Seismic Experiment. *Bull. Seismol. Soc. Am. 95*(3), 1202–1208.

de Sigoyer, J., Chavagnac, V., Blichert-Toft, J., Villa, I. M., Luais, B., Guillot, S., Cosca, M. and Mascle, G. (2000). Dating the Indian continental subduction and collisional thickening in the northwest Himalaya: Multichronology of the Tso Morari eclogites. *Geology 28*(6), 487–490.

DMG (1990). Exploration opportunities in Nepal. Technical report, Department of Mines and Geology.

*E*ndrun, B., Meier, T., Bischoff, M. and Harjes, H. P. (2004). Lithospheric structure in the area of Crete constrained by receiver functions and dispersion analysis of Rayleigh phase velocities. *Geophys. J. Int. 158*(2), 592–608.

England, P. and Houseman, G. (1986). Finite strain calculations of continental deformation. 2. Comparison with the India-Asia collision zone. *J. Geophys. Res. 91*(B3), 3664–3676.

England, P. and Houseman, G. (1989). Extension during continental convergence, with application to the Tibetan Plateau. *J. Geophys. Res. 94* (B12), 17561–17579.

England, P., Lefort, P., Molnar, P. and Pecher, A. (1992). Heat-sources for tertiary metamorphism and anatexis in the Annapurna-Manaslu region Central Nepal. *J. Geophys. Res. 97* (B2), 2107–2128.

England, P. and Molnar, P. (2005). Late Quaternary to decadal velocity fields in Asia. *J. Geophys. Res. 110* (B12), B12401.

$\mathcal{F}$erris, A., Abers, G. A., Christensen, D. H. and Veenstra, E. (2003). High resolution image of the subducted Pacific (?) plate beneath central Alaska, 50-150 km depth. *Earth Planet. Sci. Lett. 214* (3-4), 575–588.

Fielding, E., Isacks, B., Barazangi, M. and Duncan, C. (1994). How flat is Tibet? *Geology 22* (2), 163–167.

Fielding, E. J. (1996). Tibet uplift and erosion. *Tectonophysics 260* (1-3), 55–84.

Fort, M. (1996). Late Cenozoic environmental changes and uplift on the northern side of the central Himalaya: A reappraisal from field data. *Palaeogeography Palaeoclimatology Palaeoecology 120* (1-2), 123–145.

Francheteau, J., Jaupart, C., Shen, X. J., Kang, W. H., Lee, D. L., Bai, J. C., Wei, H. P. and Deng, H. Y. (1984). High heat-flow in southern Tibet. *Nature 307* (5946), 32–36.

Frederiksen, A. W. (2000). *Seismic imaging of the Canadian upper mantle.* Ph. D. thesis, University of British Columbia.

Fuhrman, M. L. and Lindsley, D. H. (1988). Ternary-feldspar modeling and thermometry. *American Mineralogist 73* (3-4), 201–215.

$\mathcal{G}$alvé, A., Hirn, A., Mei, J. A., Gallart, J., de Voogd, B., Lepine, J. C., Diaz, J., Wang, Y. X. and Hui, Q. A. (2002). Modes of raising northeastern Tibet probed by explosion seismology. *Earth Planet. Sci. Lett. 203* (1), 35–43.

Galvé, A., Sapin, M., Hirn, A., Diaz, J., Lepine, J. C., Laigle, M., Gallart, J. and Jiang, M. (2002). Complex images of Moho and variation of Vp/Vs across the Himalaya and South Tibet, from a joint receiver-function and wide-angle-reflection approach. *Geophys. Res. Lett. 29* (24), 2182.

Gan, W., Zhang, P., Shen, Z.-K., Niu, Z., Wang, M., Wan, Y., Zhou, D. and Cheng, J. (2007). Present-day crustal motion within the Tibetan Plateau inferred from GPS measurements. *J. Geophys. Res.*, **112**, B08416.

Gansser, A. (1964). *Geology of the Himalayas.* Wiley Interscience Publications, London, 289 pp.

Gansser, A. (1991). Facts and theories on the Himalayas. *Eclogae Geol. Helv.*, **84 (1)**, 33–59.

Godard, V. (2006). *Couplage érosion-tectonique en contexte de convergence intracontinentale. Étude comparée de la chaîne Himalayenne et des Longmen Shan (est-Tibet).* Ph. D. thesis, Ecole Normale Supérieure – Paris XI. 243 pp.

Goffé, B., Bousquet, R., Henry, P. and Le Pichon, X. (2003). Effect of the chemical composition of the crust on the metamorphic evolution of orogenic wedges. *J. Metam. Geol. 21*(2), 123–141.

Groppo, C., Lombardo, B., Rolfo, F. and Pertusati, P. (2007). Clockwise exhumation path of granulitized eclogites from the Ama Drime range (Eastern Himalayas). *J. Metam. Geol. 25*(1), 51–75.

Guillot, S., de Sigoyer, J., Lardeaux, J. M. and Mascle, G. (1997). Eclogitic metasediments from the Tso Morari area (Ladakh, Himalaya): evidence for continental subduction during India-Asia convergence. *Contrib. Mineral. Petro. 128*(2-3), 197–212.

Guillot, S., Garzanti, E., Baratoux, D., Marquer, D., Mahéo, G. and de Sigoyer, J. (2003). Reconstructing the total shortening history of the NW Himalaya. *Geochem. Geophy. Geosys.*, **4**, 1064.

Gupta, M. L. (1993). Is the Indian shield hotter than other Gondwana shields. *Earth Planet. Sci. Lett. 115*(1-4), 275–285.

Guéguen, Y. and Palciauskas, V. (1992). *Introduction à la physique des roches.* Hermann, Paris, 299 pp.

*H*acker, B. R. and Abers, G. A. (2004). Subduction Factory 3: An Excel worksheet and macro for calculating the densities, seismic wave speeds, and H2O contents of minerals and rocks at pressure and temperature. *Geochem. Geophy. Geosys.*, **5**, Q01005.

Haines, S. S., Klemperer, S. L., Brown, L., Jingru, G. R., Mechie, J., Meissner, R., Ross, A. and Zhao, W. J. (2003). INDEPTH III seismic data: From surface observations to deep crustal processes in Tibet. *Tectonics 22*(1), 1001.

Hanks, T. (1977). Earthquake stress-drops, ambient tectonic stresses, and stresses that drive plates. *Pure Appl. Geophys.*, **115**, 441–458.

Harrison, T. M., Copeland, P., Kidd, W. S. F. and Lovera, O. M. (1995). Activation of the Nyainqentanghla Shear Zone: Implications for uplift of the southern Tibetan Plateau. *Tectonics 14*(3), 658–676.

Harrison, T. M., Lovera, O. M. and Grove, M. (1997). New insights into the origin of two contrasting Himalayan granite belts. *Geology 25*(10), 899–902.

Hassani, R., Jongmans, D. and Chéry, J. (1997). Study of plate deformation and stress in subduction processes uding two-dimensional finite element models. *J. Geophys. Res.*, **102**, 17951–17965.

Hauck, M. L., Nelson, K. D., Brown, L. D., Zhao, W. and Ross, A. R. (1998). Crustal structure of the Himalayan Orogen at approximately 90 degrees east longitude from Project INDEPTH deep reflection profiles. *Tectonics 17*(4), 481–500.

Heim, A. and Gansser, A. (1939). Central Himalaya: Geological observations of the Swiss expedition 1936. *Denksch. Schweizer. Naturf. Ges.*, **73 (1)**, 245.

Helffrich, G., Asencio, E., Knapp, J. and Owens, T. (2003). Transition zone structure in a tectonically inactive area: 410 and 660 km discontinuity properties under the northern North Sea. *Geophys. J. Int. 155*(1), 193–199.

Henry, P., Le Pichon, X. and Goffé, B. (1997). Kinematic, thermal and petrological model of the Himalayas: Constraints related to metamorphism within the underthrust Indian crust and topographic elevation. *Tectonophysics 273*(1-2), 31–56.

Hetényi, G., Cattin, R., Vergne, J. and Nábělek, J. L. (2006). The effective elastic thickness of the India Plate from receiver function imaging, gravity anomalies and thermomechanical modelling. *Geophys. J. Int. 167*(3), 1106–1118.

Hetényi, M. (1946). *Beams on elastic foundation.* University of Michigan Press, Ann Arbor.

Hirn, A., Lepine, J. C., Jobert, G., Sapin, M., Wittlinger, G., Xu, Z. X., Gao, E. Y., Wang, X. J., Teng, J. W., Xiong, S. B., Pandey, M. R. and Tater, J. M. (1984). Crustal structure and variability of the Himalayan border of Tibet. *Nature 307*(5946), 23–25.

Hirn, A., Nercessian, A., Sapin, M., Jobert, G., Xu, Z. X., Gao, E. Y., Lu, D. Y. and Teng, J. W. (1984). Lhasa block and bordering sutures, a continuation of a 500-km Moho traverse through Tibet. *Nature 307*(5946), 25–27.

Hirn, A. and Sapin, M. (1984). The Himalayan zone of crustal interaction: suggestions from explosion seismology. *Annales Geophysicae 2*(2), 123–130.

Hofstetter, A. and Bock, G. (2004). Shear-wave velocity structure of the Sinai subplate from receiver function analysis. *Geophys. J. Int. 158*(1), 67–84.

Holland, T., Baker, J. and Powell, R. (1998). Mixing properties and activity-composition relationships of chlorites in the system MgO-FeO-Al2O3-SiO2-H2O. *European Journal of Mineralogy 10*(3), 395–406.

Holland, T. and Powell, R. (1996). Thermodynamics of order-disorder in minerals .2. Symmetric formalism applied to solid solutions. *American Mineralogist 81*(11-12), 1425–1437.

Holland, T. J. B. and Powell, R. (1998). An internally consistent thermodynamic data set for phases of petrological interest. *J. Metam. Geol. 16*(3), 309–343.

Holt, W. E., Chamot-Rooke, N., Le Pichon, X., Haines, A. J., Shen-Tu, B. and Ren, J. (2000). Velocity field in Asia inferred from Quaternary fault slip rates and Global Positioning System observations. *J. Geophys. Res. 105*(B8), 19185–19209.

Holt, W. E., Li, M. and Haines, A. J. (1995). Earthquake strain rates and instantaneous relative motions within Central and Eastern Asia. *Geophys. J. Int. 122*(2), 569–593.

Hu, S. B., He, L. J. and Wang, J. Y. (2000). Heat flow in the continental area of China: a new data set. *Earth Planet. Sci. Lett. 179*(2), 407–419.

Huang, J. L. and Zhao, D. P. (2006). High-resolution mantle tomography of China and surrounding regions. *J. Geophys. Res. 111*(B9), B09305.

Huang, W. C., Ni, J. F., Tilmann, F., Nelson, D., Guo, J. R., Zhao, W. J., Mechie, J., Kind, R., Saul, J., Rapine, R. and Hearn, T. M. (2000). Seismic polarization anisotropy beneath the central Tibetan Plateau. *J. Geophys. Res. 105*(B12), 27979–27989.

Huc, R. P. (1854). *Souvenirs d'un voyage dans la Tartarie, le Thibet et la Chine, II: Dans le Thibet.* Plon-Nourrit, Paris. 2nd edition, 1926. 318 pp.

$\mathcal{J}$ackson, J. (2002). Strength of the continental lithosphere: time to abandon the jelly sandwich? *GSA Today 12*(9), 4–10.

Jackson, M. E. and Bilham, R. (1994). 1991-1992 GPS measurements across the Nepal Himalaya. *Geophys. Res. Lett. 21*(12), 1169–1172.

James, D. E., Niu, F. L. and Rokosky, J. (2003). Crustal structure of the Kaapvaal craton and its significance for early crustal evolution. *Lithos 71*(2-4), 413–429.

Jamieson, R. A., Beaumont, C., Medvedev, S. and Nguyen, M. H. (2004). Crustal channel flows: 2. Numerical models with implications for metamorphism in the Himalayan-Tibetan orogen. *J. Geophys. Res. 109*(B6), B06407.

Jamieson, R. A., Beaumont, C., Nguyen, M. H. and Lee, B. (2002). Interaction of metamorphism, deformation and exhumation in large convergent orogens. *J. Metam. Geol. 20*(1), 9–24.

Jiang, X. D., Hin, Y. and McNutt, M. K. (2004). Lithospheric deformation beneath the Altyn Tagh and West Kunlun faults from recent gravity surveys. *J. Geophys. Res. 109*(B5), B05406.

Jin, Y., McNutt, M. K. and Zhu, Y. S. (1996). Mapping the descent of Indian and Eurasian plates beneath the Tibetan Plateau from gravity anomalies. *J. Geophys. Res. 101*(B5), 11275–11290.

John, T. and Schenk, V. (2003). Partial eclogitisation of gabbroic rocks in a late precambrian subduction zone (Zambia): prograde metamorphism triggered by fluid infiltration. *Contrib. Mineral. Petro. 146*(2), 174–191.

Johnson, M. R. W. (2002). Shortening budgets and the role of continental subduction during the India-Asia collision. *Earth-Science Reviews 59*(1-4), 101–123.

Jordan, T. A. and Watts, A. B. (2005). Gravity anomalies, flexure and the elastic thickness structure of the India-Eurasia collisional system. *Earth Planet. Sci. Lett. 236*(3-4), 732–750.

Jouanne, F., Mugnier, J., Pandey, M. R., Gamond, J. F., Le Fort, P., Serrurier, L., Vigny, C., Avouac, J.-P. and members, I. (1999). Oblique convergence in the Himalayas of Western Nepal deduced from preliminary results of GPS measurements. *Geophys. Res. Lett. 26*(13), 1933–1936.

Julià, J., Ammon, C. J., Herrmann, R. B. and Correig, A. M. (2000). Joint inversion of receiver function and surface wave dispersion observations. *Geophys. J. Int. 143*(1), 99–112.

Julià, J., Ammon, C. J. and Nyblade, A. A. (2005). Evidence for mafic lower crust in Tanzania, East Africa, from joint inversion of receiver functions and Rayleigh wave dispersion velocities. *Geophys. J. Int. 162*(2), 555–569.

Jull, M. and Kelemen, P. B. (2001). On the conditions for lower crustal convective instability. *J. Geophys. Res. 106*(B4), 6423–6446.

$\mathcal{K}$anasewich, E. (1973). *Time sequence analysis in geophysics.* The University of Alberta Press, 364 pp.

Kaneko, Y., Katayama, I., Yamamoto, H., Misawa, K., Ishikawa, M., Rehman, H. U., Kausar, A. B. and Shiraishi, K. (2003). Timing of Himalayan ultrahigh-pressure metamorphism: sinking rate and subduction angle of the Indian continental crust beneath Asia. *J. Metam. Geol. 21* (6), 589–599.

Karner, G. D. and Watts, A. B. (1983). Gravity-anomalies and flexure of the lithosphere at mountain ranges. *J. Geophys. Res. 88* (NB12), 449–477.

Kennett, B. L. N. and Engdahl, E. R. (1991). Traveltimes for global earthquake location and phase identification. *Geophys. J. Int. 105* (2), 429–465.

Kind, R., Ni, J., Zhao, W. J., Wu, J. X., Yuan, X. H., Zhao, L. S., Sandvol, E., Reese, C., Nabelek, J. and Hearn, T. (1996). Evidence from earthquake data for a partially molten crustal layer in southern Tibet. *Science 274* (5293), 1692–1694.

Kind, R., Yuan, X., Saul, J., Nelson, D., Sobolev, S. V., Mechie, J., Zhao, W., Kosarev, G., Ni, J., Achauer, U. and Jiang, M. (2002). Seismic images of crust and upper mantle beneath Tibet: Evidence for Eurasian plate subduction. *Science 298* (5596), 1219–1221.

Kirby, S. H., Durham, W. B. and Stern, L. A. (1991). Mantle phase-changes and deep-earthquake faulting in subducting lithosphere. *Science 252* (5003), 216–225.

Klootwijk, C. T., Conaghan, P. J. and Powell, C. M. (1985). The Himalayan Arc: large-scale continental subduction, oroclinal bending and back-arc spreading. *Earth Planet. Sci. Lett. 75* (2-3), 167–183.

Kosarev, G., Kind, R., Sobolev, S. V., Yuan, X., Hanka, W. and Oreshin, S. (1999). Seismic evidence for a detached Indian lithospheric mantle beneath Tibet. *Science 283* (5406), 1306–1309.

Kumar, M. R., Saul, J., Sarkar, D., Kind, R. and Shukla, A. K. (2001). Crustal structure of the Indian Shield: New constraints from teleseismic receiver functions. *Geophys. Res. Lett. 28* (7), 1339–1342.

Kumar, P., Yuan, X. H., Kind, R. and Ni, J. (2006). Imaging the colliding Indian and Asian lithospheric plates beneath Tibet. *J. Geophys. Res. 111* (B6), B06308.

$\mathcal{L}$angston, C. (1977a). Corvallis, Oregon, crustal and upper mantle receiver structure from teleseismic P-waves and S-waves. *Bull. Seismol. Soc. Am. 67* (3), 713–724.

Langston, C. (1977b). Effect of planar dipping structure on source and receiver responses for constant ray parameter. *Bull. Seismol. Soc. Am. 67*(4), 1029–1050.

Langston, C. (1979). Structure under Mount Rainier, Washington, inferred from teleseismic body waves. *J. Geophys. Res. 84*(B9), 4749–4762.

Larson, K. M., Bürgmann, R., Bilham, R. and Freymueller, J. T. (1999). Kinematics of the India-Eurasia collision zone from GPS measurements. *J. Geophys. Res. 104*(B1), 1077–1093.

Lavé, J. and Avouac, J.-P. (2000). Active folding of fluvial terraces across the Siwaliks Hills, Himalayas of central Nepal. *J. Geophys. Res. 105*(3), 5735–5770.

Le Pichon, X. (2007). Mouvements gravitaires crustaux. In *Cours du Collège de France*.

Le Pichon, X. and Chamot-Rooke, N. (1991). Extension of continental crust. In D. W. Müller, J. A. McKenzie, and H. Weissert (Eds.), *Controversies in modern geology: evolution of geological theories in sedimentology, earth history and tectonics*, pp. 313–318. Harcourt Brace Jovanovich, London.

Le Pichon, X., Henry, P. and Goffé, B. (1997). Uplift of Tibet: From eclogites to granulites: Implications for the Andean Plateau and the Variscan belt. *Tectonophysics 273*(1-2), 57–76.

LeFort, P. (1986). Metamorphism and magmatism during the Himalayan collision. In *Collision Tectonics*. Geol. Soc. Spec. Publ., 19, 159-172.

Lemonnier, C., Marquis, G., Perrier, F., Avouac, J. P., Chitrakar, G., Kafle, B., Sapkota, S., Gautam, U., Tiwari, D. and Bano, M. (1999). Electrical structure of the Himalaya of Central Nepal: high conductivity around the mid-crustal ramp along the MHT. *Geophys. Res. Lett. 26*(21), 3261–3264.

Levin, V. and Park, J. (1997). P-SH conversions in a flat-layered medium with anisotropy of arbitrary orientation. *Geophys. J. Int. 131*(2), 253–266.

Li, S. H., Unsworth, M. J., Booker, J. R., Wei, W. B., Tan, H. D. and Jones, A. G. (2003). Partial melt or aqueous fluid in the mid-crust of Southern Tibet? Constraints from INDEPTH magnetotelluric data. *Geophys. J. Int. 153*(2), 289–304.

Li, X. Q., Kind, R., Yuan, X. H., Wolbern, I. and Hanka, W. (2004). Rejuvenation of the lithosphere by the Hawaiian plume. *Nature 427*(6977), 827–829.

Li, X. Q. and Nabelek, J. L. (1999). Deconvolution of teleseismic body waves for enhancing structure beneath a seismometer array. *Bull. Seismol. Soc. Am. 89*(1), 190–201.

Ligorría, J. and Ammon, C. J. (1999). Iterative deconvolution and receiver-function estimation. *Bull. Seismol. Soc. Am. 89* (5), 1395–1400.

Lóczy, L. (1876). Az Alpesek keletkezése. (The birth of the Alps). *Természettudományi Közlöny*, **VIII (82)**, 225–236.

Lóczy, L. (1880a). Földrajz és geológia. (Geography and geology). *Földtani Értesítő*, **I (6)**, 113–119.

Lóczy, L. (1880b). A földrengésröl. (About the earthquake). *Természettudományi Közlöny*, **137**, 3–19.

Lóczy, L. (1880c). Gróf Széchenyi Béla utazásából: I. Kuku-nor, II. Keleti Tibet. (From Count Béla Széchenyi's travel: I. Kuku-nor II. East Tibet). *Földrajzi Közlemények*, **VIII**, 321–345.

Lóczy, L. (1883). A keleti Himalájába tett kirándulásról. (On the excursion made in the Eastern Himalayas). *Földtani Közlöny*, **XIII**, 211–212.

Lóczy, L. (1886). *A khinai birodalom természeti viszonyainak és országainak leírása. (Description of natural relations and countries of the Chinese Empire).* Kir. M. Természettudományi Társ., Budapest, 865 pp.

Lóczy, L. (1890). *A geológiai megfigyelések leírásai és eredményei gróf Széchenyi Béla keletázsiai útjából 1877-1880. (The description of geological observations and their results from Count Béla Széchenyi's East-Asian travel 1877-1880). Különlenyomat a "Gróf Széchenyi Béla keletázsiai útjának tudományos eredményei" címü munkából.* Kilián, Budapest, 428 pp.

Lóczy, L. (1898). Gróf Széchenyi Béla kelet-ázsiai utazásának földrajzi és földtani eredményei (Kivonat akadémiai székfoglalójából). (Geographical and geological results of Count Béla Széchenyi's travel to East-Asia (Extract from his inaugural speech in the Academy)). *Földrajzi Közlemények*, **XXVI**, 184–192.

Lóczy, L. (1907). Megfigyelések a Keleti-Himalájában. (Observations in the Eastern Himalayas). With German summary: Beobachtungen im östlichen Himalaya. *Földrajzi Közlemények*, **XXXV (6–7)**, 227–243, 293–310.

Lóczy, L. (1919). Gróf Széchenyi Béla emlékezete. (The memory of Count Béla Széchenyi). *Földrajzi Közlemények*, **XLVII**, 1–14.

Lombardo, B. and Rolfo, F. (2000). Two contrasting eclogite types in the Himalayas: implications for the Himalayan orogeny. *J. of Geodyn. 30* (1-2), 37–60.

Lyon-Caen, H. and Molnar, P. (1983). Constraints on the structure of the Himalaya from an analysis of gravity anomalies and a flexural model of the lithosphere. *J. Geophys. Res. 88*(B10), 8171–8191.

Lyon-Caen, H. and Molnar, P. (1985). Gravity anomalies, felxure of the Indian plate, and the structure, support and the evolution of the Himalaya and the Ganga basin. *Tectonics 4*(6), 513–538.

$\mathcal{M}$aggi, A., Jackson, A., Priestley, K. and Baker, C. (2000). A re-assessment of focal depth distributions in southern Iran, the Tien Shan and northern India: do earthquakes really occur in the continental mantle? *Geophys. J. Int.*, **143**, 629–661.

Mahéo, G., Fayoux, X., Guillot, S., Garzanti, E., Capiez, P. and Mascle, G. (2006). Relicts of an intra-oceanic arc in the Sapi-Shergol melange zone (Ladakh, NW Himalaya, India): implications for the closure of the Neo-Tethys Ocean. *Journal Of Asian Earth Sciences 26*(6), 695–707.

Mahéo, G., Guillot, S., Blichert-Toft, J., Rolland, Y. and Pêcher, A. (2002). A slab breakoff model for the Neogene thermal evolution of South Karakorum and South Tibet. *Earth Planet. Sci. Lett. 195*(1-2), 45–58.

Makovsky, Y. and Klemperer, S. L. (1999). Measuring the seismic properties of Tibetan bright spots: Evidence for free aqueous fluids in the Tibetan middle crust. *J. Geophys. Res. 104*(B5), 10795–10825.

Makovsky, Y., Klemperer, S. L., Huang, L. Y. and Lu, D. Y. (1996). Structural elements of the southern Tethyan Himalaya crust from wide-angle seismic data. *Tectonics 15*(5), 997–1005.

Makovsky, Y., Klemperer, S. L., Ratschbacher, L., Brown, L. D., Li, M., Zhao, W. J. and Meng, F. L. (1996). INDEPTH wide-angle reflection observation of P-wave-to-S-wave conversion from crustal bright spots in Tibet. *Science 274*(5293), 1690–1691.

Mallett, F. R. (1875). On the geology of the Dárjíling district and the Western Duárs. *Memoirs of the Geol. Survey of India*, **XI**, 1 − 96.

Martelet, G., Sailhac, P., Moreau, F. and Diament, M. (2001). Characterization of geological boundaries using 1-Dwavelet transform on gravity data: Theory and application to the Himalayas. *Geophysics 66*(4), 1116–1129.

Masek, J. G., Isacks, B. L., Gubbels, T. L. and Fielding, E. J. (1994). Erosion and tectonics at the margins of continental plateaus. *J. Geophys. Res. 99*(B7), 13941–13956.

McDougall, I. and Harrison, T. M. (1999). *Geochronology and Thermochronology by the 40Ar/39Ar Method.* Oxford Univ. Press, New York, 269 pp.

McKenzie, D. and Fairhead, D. (1997). Estimates of the effective elastic thickness of the continental lithosphere from Bouguer and free air gravity anomalies. *J. Geophys. Res. 102*(B12), 27523–27552.

McNamara, D. E., Owens, T. J., Silver, P. G. and Wu, F. T. (1994). Shear-wave anisotropy beneath the Tibetan Plateau. *J. Geophys. Res. 99*(B7), 13655–13665.

McNamara, D. E., Owens, T. J. and Walter, W. R. (1995). Observations of regional phase propagation across the Tibetan Plateau. *J. Geophys. Res. 100*(B11), 22215–22229.

McNamara, D. E., Walter, W. R., Owens, T. J. and Ammon, C. J. (1997). Upper mantle velocity structure beneath the Tibetan Plateau from Pn travel time tomography. *J. Geophys. Res. 102*(B1), 493–505.

Meade, B. J. (2007). Present-day kinematics at the India-Asia collision zone. *Geology 35*(1), 81–84.

Mechie, J., Sobolev, S. V., Ratschbacher, L., Babeyko, A. Y., Bock, G., Jones, A. G., Nelson, K. D., Solon, K. D., Brown, L. D. and Zhao, W. (2004). Precise temperature estimation in the Tibetan crust from seismic detection of the alpha-beta quartz transition. *Geology 32*(7), 601–604.

Mellman, G. (1980). A method of body-wave waveform inversion for determination of earth structure. *Geophys. J. R. Astron. Soc.*, **62**, 481–504.

Menon, R., Kumar, P. S., Reddy, G. K. and Srinivasan, R. (2003). Radiogenic heat production of Late Archaean bundelkhand granite and some Proterozoic gneisses and granitoids of central India. *Current Science 85*(5), 634–638.

Métivier, F., Gaudemer, Y., Tapponnier, P. and Klein, M. (1999). Mass accumulation rates in Asia during the Cenozoic. *Geophys. J. Int.*, **137**, 280–318.

Miyashiro, A. (1982). *Orogeny.* John Wiley & Sons.

Molnar, P. and Chen, W. P. (1983). Focal depths and fault plane solutions of earthquakes under the Tibetan Plateau. *J. Geophys. Res. 88*(NB2), 1180–1196.

Molnar, P., England, P. and Martinod, J. (1993). Mantle dynamics, uplift of the Tibetan Plateau, and the Indian monsoon. *Reviews of Geophysics 31*(4), 357–396.

Molnar, P. and Tapponnier, P. (1975). Cenozoic tectonics of Asia: effects of a continental collision. *Science 189*(4201), 419–426.

Monsalve, G., Sheehan, A., Schulte-Pelkum, V., Rajaure, S., Pandey, M. R. and Wu, F. (2006). Seismicity and one-dimensional velocity structure of the Himalayan collision zone: Earthquakes in the crust and upper mantle. *J. Geophys. Res. 111*(B10), B10301.

Moumni, Z., Zaki, W. and Nguyen, Q. S. (2007). Theoretical and numerical modeling of solid–solid phase change: Application to the description of the thermomechanical behavior of shape memory alloys. *Int. J. of Plasticity*, **in press**, .

Mugnier, J. L. and Huyghe, P. (2006). Ganges basin geometry records a pre-15 Ma isostatic rebound of Himalaya. *Geology 34*(6), 445–448.

Mukherjee, B. K., Sachan, H. K., Ogasawara, Y., Muko, A. and Yoshioka, N. (2003). Carbonate-bearing UHPM rocks from the Tso-Morari region, Ladakh, India: Petrological implications. *Int. Geol. Rev. 45*(1), 49–69.

𝒩ábělek, J., Vergne, J. and Hetényi, G. (2005). Project Hi-CLIMB: A synoptic view of the Himalayan collision zone and Southern Tibet. In *EoS Trans. AGU, 86(52), Fall Meet. Suppl., Abstract T52A-02.*

Nelson, K. D., Zhao, W. J., Brown, L. D., Kuo, J., Che, J. K., Liu, X. W., Klemperer, S. L., Makovsky, Y., Meissner, R., Mechie, J., Kind, R., Wenzel, F., Ni, J., Nabelek, J., Chen, L. S., Tan, H. D., Wei, W. B., Jones, A. G., Booker, J., Unsworth, M., Kidd, W. S. F., Hauck, M., Alsdorf, D., Ross, A., Cogan, M., Wu, C. D., Sandvol, E. and Edwards, M. (1996). Partially molten middle crust beneath southern Tibet: Synthesis of project INDEPTH results. *Science 274*(5293), 1684–1688.

Ni, J. and Barazangi, M. (1983). High-frequency seismic-wave propagation beneath the Iindian Shield, Himalayan Arc, Tibetan Plateau and surrounding regions: high uppermost mantle velocities and efficient Sn propagation beneath tibet. *Geophys. J. R. Astron. Soc. 72*(3), 665–689.

Nicholson, T., Bostock, M. and Cassidy, J. F. (2005). New constraints on subduction zone structure in northern Cascadia. *Geophys. J. Int. 161*(3), 849–859.

𝒪ldham, F. R. S. R. D. (1914). On the effect of the Gangetic alluvium on the plumb-line in Northern India. *Proc. Roy. Soc., A*, **90**, 32–41.

Oreshin, S., Vinnik, L., Peregoudov, D. and Roecker, S. (2002). Lithosphere and asthenosphere of the Tien Shan imaged by S receiver functions. *Geophys. Res. Lett. 29*(8), 1191.

Owens, T. J. (1987). Crustal structure of the Adirondacks determined from broad-band teleseismic wave-form modeling. *J. Geophys. Res. 92*(B7), 6391–6401.

Owens, T. J. and Zandt, G. (1997). Implications of crustal property variations for models of Tibetan plateau evolution. *Nature 387*(6628), 37–43.

Owens, T. J., Zandt, G. and Taylor, S. R. (1984). Seismic evidence for an ancien rift beneath the Cumberland Plateau, Tennessee : A detailed analysis of broadband teleseismic P waveforms. *J. Geophys. Res. 89*(B9), 7783–7795.

Özalaybey, S., Savage, M. K., Sheehan, A. F., Louie, J. N. and Brune, J. N. (1997). Shear-wave velocity structure in the northern Basin and Range province from the combined analysis of receiver functions and surface waves. *Bull. Seismol. Soc. Am. 87*(1), 183–199.

$\mathcal{P}$ark, J. and Levin, V. (2000). Receiver functions from multiple-taper spectral correlation estimates. *Bull. Seismol. Soc. Am. 90*(6), 1507–1520.

Patriat, P. and Achache, J. (1984). India-Eurasia collision chronology has implications for crustal shortening and driving mechanism of plates. *Nature*, **311**, 615–621.

Paul, J., Bürgmann, R., Gaur, V. K., Bilham, R., Larson, K. M., Ananda, M. B., Jade, S., Mukal, M., Anupama, T. S., Satyal, G. and Kumar, D. (2001). The motion and active deformation of India. *Geophys. Res. Lett. 28*(4), 647–650.

Peterson, J. (1993). *Observations and modelling of seismic background noise.* US Geological Survey Open-File Report 93-322, Albuquerque, NM, 94 pp.

Pinet, C., Jaupart, C., Mareschal, J. C., Gariepy, C., Bienfait, G. and Lapointe, R. (1991). Heat-flow and structure of the lithosphere in the Eastern Canadian shield. *J. Geophys. Res. 96*(B12), 19941–19963.

Powell, C. M. A. and Conaghan, P. J. (1973). Plate tectonics and Himalayas. *Earth Planet. Sci. Lett. 20*(1), 1–12.

Powell, R. and Holland, T. (1999). Relating formulations of the thermodynamics of mineral solid solutions: Activity modeling of pyroxenes, amphiboles, and micas. *American Mineralogist 84*(1-2), 1–14.

Pratt, J. H. (1855). On the attraction of the Himalaya Mountains and of the elevated regions beyond them, upon the plumb line in India. *Philos. Trans. R. Soc. London*, **145**, 53–100.

Pêcher, A. (1978). *Déformations et métamorphisme associés à une zone de cisaillement. Exemple du grand chevauchement central himalayen (M.C.T), transversale des Annapurnas et du Manaslu, Népal.* Ph. D. thesis, Univ. Grenoble.

$\mathcal{R}$aimbourg, H., Goffé, B. and Jolivet, L. (2007). Garnet reequilibration and growth in the eclogite facies and geodynamical evolution near peak metamorphic conditions. *Contrib. Mineral. Petro. 153*(1), 1–+.

Raiverman, V., Kunte, S. V. and Mukherjea, A. (1983). Basin geometry, Cenozoic sedimentation and hydrocarbon peospects in north western Himalaya and Indo-Gangetic Plains. *Petroleum Asia Journ.*, **11**, 67–92.

Rao, R. U. M., Rao, G. V. and Narain, H. (1976). Radioactive heat-generation and heat-flow in Indian shield. *Earth Planet. Sci. Lett. 30*(1), 57–64.

Rapine, R., Tilmann, F., West, M., Ni, J. and Rodgers, A. (2003). Crustal structure of northern and southern Tibet from surface wave dispersion analysis. *J. Geophys. Res. 108*(B2), 2120.

Replumaz, A., Karason, H., vanderHilst, R. D., Besse, J. and Tapponnier, P. (2004). 4-D evolution of SE Asia's mantle from geological reconstructions and seismic tomography. *Earth Planet. Sci. Lett. 221*(1-4), 103–115.

Rodgers, A. T. J. and Schwartz, S. Y. (1997). Low crustal velocities and mantle lithospheric variations in southern Tibet from regional Pnl waveforms. *Geophys. Res. Lett. 24*(1), 9–12.

Rodriguez, E., Morris, C., Belz, J., Chapin, E., Martin, J., Daffer, W. and Hensley, S. (2005). An assessment of the SRTM topographic products. Technical Report Technical Report JPL D-31639, Jet Propulsion Laboratory, Pasadena, California, 143 pp.

Rowley, D. B., Pierrehumbert, R. T. and Currie, B. S. (2001). A new approach to stable isotope-based paleoaltimetry: implications for paleoaltimetry and paleohypsometry of the High Himalaya since the Late Miocene. *Earth Planet. Sci. Lett. 188*(1-2), 253–268.

Royden, L. (1996). Coupling and decoupling of crust and mantle in convergent orogens: Implications for strain partitioning in the crust. *J. Geophys. Res. 101*(B8), 17679–17705.

Royden, L. H. (1993). The steady-state thermal structure of eroding orogenic belts and accretionary prisms. *J. Geophys. Res.*, **98**, 4487–4507.

Rubie, D. (1998). Disequilibrium during metamorphism: the role of nucleation kinetics. In P. Treloar and P. O'Brien (Eds.), *What drives metamorphism and metamorphic reactions?* Geol. Soc., London, Spec. Publ. 138, pp. 199–214.

Rubie, D. C. (1986). The catalysis of mineral reactions by water and restrictions on the presence of aqueous fluid during metamorphism. *Mineralogical Magazine 50*(357), 399–415.

Rudnick, R. and Gao, S. (2003). The composition of the continental crust. In H. D. Holland and K. Turekian (Eds.), *Treatise on Geochemistry, Vol. 3, The Crust (Ed. Rudnick, R. L.).* 1–64: Elsevier-Pergamon, Oxford.

Rudnick, R. L. and Fountain, D. M. (1995). Nature and composition of the continental-crust: a lower crustal perspective. *Reviews of Geophysics 33*(3), 267–309.

Rushmer, T. (1991). Partial melting of 2 amphibolites: contrasting experimental results under fluid-absent conditions. *Contrib. Mineral. Petro. 107*(1), 41–59.

Rychert, C. A., Fischer, K. M. and Rondenay, S. (2005). A sharp lithosphere-asthenosphere boundary imaged beneath eastern North America. *Nature 436*(7050), 542–545.

Saltus, R. W. and Blakely, R. J. (1995). *HYPERMAG: An interactive, 2- and 2.5-dimensional gravity and magnetic modelling program, version 3.5.* US Geological Survey Open-File Report 93-287. Reston, VA, 39 pp.

Sambridge, M. (1999a). Geophysical inversion with a neighbourhood algorithm - I. Searching a parameter space. *Geophys. J. Int.*, **138**, 479–494.

Sambridge, M. (1999b). Geophysical inversion with a neighbourhood algorithm - II. Appraising the ensemble. *Geophys. J. Int.*, **138**, 727–746.

Sastri, V. V., Bhandari, L. L., Raju, A. T. R. and Datta, A. K. (1971). Tectonic framework and subsurface stratigraphy of the Ganga basin. *Journal of the Geological Society of India 12*(3), 222–233.

Saul, J., Kumar, M. R. and Sarkar, D. (2000). Lithospheric and upper mantle structure of the Indian Shield, from teleseismic receiver functions. *Geophys. Res. Lett. 27*(16), 2357–2360.

Savage, M. K. (1998). Lower crustal anisotropy or dipping boundaries? Effects on receiver functions and a case study in New Zealand. *J. Geophys. Res. 103*(B7), 15069–15087.

Savage, M. K., Park, J. and Todd, H. (2007). Velocity and anisotropy structure at the Hikurangi subduction margin, New Zealand from receiver functions. *Geophys. J. Int. 168*(3), 1034–1050.

Schelling, A. (1992). The tectonostratigraphy and structure of the eastern Nepal Himalaya. *Tectonics 11*(5), 925–943.

Schelling, D. and Arita, K. (1991). Thrust tectonics, crustal shortening, and the structure of the far-eastern Nepal Himalaya. *Tectonics 10*(5), 851–862.

Scholz, C. (1990). *The mechanics of earthquakes and faulting.* Cambridge University Press, 439 pp.

Schulte-Pelkum, V., Monsalve, G., Sheehan, A., Pandey, M. R., Sapkota, S., Bilham, R. and Wu, F. (2005). Imaging the Indian subcontinent beneath the Himalaya. *Nature 435*(7046), 1222–1225.

Shapiro, N. M. and Campillo, M. (2004). Emergence of broadband Rayleigh waves from correlations of the ambient seismic noise. *Geophys. Res. Lett. 31*(7), L07614.

Sheehan, A. F., Abers, G. A., Jones, C. H. and Lernerlam, A. L. (1995). Crustal thickness variations across the Colorado Rocky-Mountain from teleseismic receiver functions. *J. Geophys. Res. 100*(B10), 20391–20404.

Shen, F., Royden, L. H. and Burchfiel, B. C. (2001). Large-scale crustal deformation of the Tibetan Plateau. *J. Geophys. Res. 106*(B4), 6793–6816.

Shen, Z. K., Lu, J. N., Wang, M. and Burgmann, R. (2005). Contemporary crustal deformation around the southeast borderland of the Tibetan Plateau. *J. Geophys. Res. 110*(B11), B11409.

Shi, D., Zhao, W. J., Brown, L., Nelson, D., Zhao, X., Kind, R., Ni, J., Xiong, J. Y., Mechie, J., Guo, J., Klemperer, S. and Hearn, T. (2004). Detection of southward intracontinental subduction of Tibetan lithosphere along the Bangong-Nujiang suture by P-to-S converted waves. *Geology 32*(3), 209–212.

Shin, Y. H., Xu, H., Braitenberg, C. and Fang, J. Wang, Y. (2007). Moho undulations beneath Tibet from GRACE-integrated gravity data. *Geophys. J. Int.*, **170**, 971–985.

Solon, K. D., Jones, A. G., Nelson, K. D., Unsworth, M. J., Kidd, W. F., Wei, W., Tan, H., Jin, S., Deng, M., Booker, J. R., Li, S. and Bedrosian, P. (2005). Structure of the crust in the vicinity of the Banggong-Nujiang suture in central Tibet from INDEPTH magnetotelluric data. *J. Geophys. Res. 110*(B10), B10102.

Song, T. R. A. and Simons, M. (2003). Large trench-parallel gravity variations predict seismogenic behavior in subduction zones. *Science 301* (5633), 630–633.

Suess, E. (1875). *Die Entstehung der Alpen*. Wien, IV+168 pp.

Sun, W. (1989). *Bouguer gravity anomaly map of the People's Republic of China*. Chin. Acad. Geoexplor., Beijing.

Szafián, P. and Horváth, F. (2006). Crustal structure in the Carpatho-Pannonian region: insights from three-dimensional gravity modelling and their geodynamic significance. *Int. J. of Earth Sci. 95* (1), 50–67.

T alwani, M., Worzel, J. L. and Landisman, M. (1959). Rapid gravity computations for 2-dimensional bodies with application to the Mendocino submarine fracture zone. *J. Geophys. Res. 64* (1), 49–59.

Tapponnier, P., Xu, Z. Q., Roger, F., Meyer, B., Arnaud, N., Wittlinger, G. and Yang, J. S. (2001). Oblique stepwise rise and growth of the Tibet plateau. *Science 294* (5547), 1671–1677.

Taylor, M. and Peltzer, G. (2006). Current slip rates on conjugate strike-slip faults in central Tibet using synthetic aperture radar interferometry. *J. Geophys. Res. 111* (B12), B12402.

Telegdi-Roth, K. (1949). A geológus Lóczy Lajos születésének 100 éves évfordulója alkalmával tartott elöadás. (Including French summary: Louis Lóczy le géologue). *Földtani Közlöny*, **79 (1–4)**, 311–319.

Thatcher, W. (2007). Microplate model for the present-day deformation of Tibet. *J. Geophys. Res. 112* (B1), B01401.

Tiberi, C., Diament, M., Déverchère, J., Petit-Mariani, C., Mikhailov, V., Tikhotsky, S. and Achauer, U. (2003). Deep structure of the Baikal rift zone revealed by joint inversion of gravity and seismology. *J. Geophys. Res. 108* (B3), 2133.

Tiberi, C., Leroy, S., d'Acremont, E., Bellahsen, N., Ebinger, C., Al-Lazki, A. and Pointu, A. (2007). Crustal geometry of the northeastern Gulf of Aden passive margin: localization of the deformation inferred from receiver function analysis. *Geophys. J. Int. 168* (3), 1247–1260.

Tilmann, F., Ni, J. and Team, I. I. S. (2003). Seismic imaging of the downwelling Indian lithosphere beneath central Tibet. *Science 300* (5624), 1424–1427.

Tiwari, V. M., Rao, M. B. S. V., Mishra, D. C. and Singh, B. (2006). Crustal structure across Sikkim, NE Himalaya from new gravity and magnetic data. *Earth Planet. Sci. Lett. 247*(1-2), 61–69.

Toussaint, G., Burov, E. and Avouac, J. P. (2004). Tectonic evolution of a continental collision zone: A thermomechanical numerical model. *Tectonics 23*(6), TC6003.

Turcotte, D. and Schubert, G. (1982). *Geodynamics, application of continuum physics to geological problems*. John Wiley & Sons, New York, 450 pp.

Turner, S., Arnaud, N., Liu, J., Rogers, N., Hawkesworth, C., Harris, N., Kelley, S., Van-Calsteren, P. and Deng, W. (1996). Post-collision, shoshonitic volcanism on the Tibetan plateau: Implications for convective thinning of the lithosphere and the source of ocean island basalts. *J. of Petrology 37*(1), 45–71.

Turner, S., Hawkesworth, C., Liu, J. Q., Rogers, N., Kelley, S. and Vancalsteren, P. (1993). Timing of Tibetan uplift constrained by analysis of volcanic-rocks. *Nature 364*(6432), 50–54.

𝒰nsworth, M. J., Jones, A. G., Wei, W., Marquis, G., Gokarn, S. G. and Spratt, J. E. (2005). Crustal rheology of the Himalaya and Southern Tibet inferred from magnetotelluric data. *Nature 438*(7064), 78–81.

𝒱an der Voo, R., Spakman, W. and Bijwaard, H. (1999). Tethyan subducted slabs under India. *Earth Planet. Sci. Lett. 171*(1), 7–20.

Vance, D. and O'Nions, R. K. (1992). Prograde and retrograde thermal histories from the central Swiss Alps. *Earth Planet. Sci. Lett. 114*(1), 113–129.

Vergne, J. (2002). *Imagerie des structures et dynamique de la lithosphère de la marge nord-est du Tibet*. Ph. D. thesis, Université Louis Pasteur – Strasbourg I. 244 pp.

Vergne, J., Cattin, R. and Avouac, J. P. (2001). On the use of dislocations to model interseismic strain and stress build-up at intracontinental thrust faults. *Geophys. J. Int. 147*(1), 155–162.

Vergne, J., Nábělek, J. L. and the Hi-CLIMB Team (2005). Geometry and characteristics of the Main Himalayan Thrust in Nepal/Tibet revealed by the Hi-CLIMB seismological experiment. In *Eos Trans. AGU, 86 (52), Fall Meet. Suppl., Abstract T52A-03*.

Vergne, J., Wittlinger, G., Hui, Q. A., Tapponnier, P., Poupinet, G., Mei, J., Herquel, G. and Paul, A. (2002). Seismic evidence for stepwise thickening of the crust across the NE Tibetan plateau. *Earth Planet. Sci. Lett. 203*(1), 25–33.

Waddell, L. A. (1910). *Lhasa and Its Mysteries, with a Record of the Expedition of 1903-1904. (Hungarian translation by A. Schwalm: A rejtelmes Lhassza; Ed. L. Lóczy)*. Lampel, Budapest, 288 pp.

Wang, C. S., Li, X. H., Hu, X. M. and Jansa, L. F. (2002). Latest marine horizon north of Qomolangma (Mt Everest): implications for closure of Tethys seaway and collision tectonics. *Terra Nova 14*(2), 114–120.

Watanabe, T. (1993). Effects of water and melt on seismic velocities and their application to characterization of seismic reflectors. *Geophys. Res. Lett. 20*(24), 2933–2936.

Watts, A. B. and Burov, E. B. (2003). Lithospheric strength and its relationship to the elastic and seismogenic layer thickness. *Earth Planet. Sci. Lett.*, **213**, 113–131.

Watts, A. B. and Zhong, S. (2000). Observations of flexure and the rheology of oceanic lithosphere. *Geophys. J. Int. 142*(3), 855–875.

Wei, C. J. and Powell, R. (2003). Phase relations in high-pressure metapelites in the system KFMASH (K2O-FeO-MgO-Al2O3-SiO2-H2O) with application to natural rocks. *Contrib. Mineral. Petro. 145*(3), 301–315.

Wei, W. B., Unsworth, M., Jones, A., Booker, J., Tan, H. D., Nelson, D., Chen, L. S., Li, S. H., Solon, K., Bedrosian, P., Jin, S., Deng, M., Ledo, J., Ray, D. and Roberts, B. (2001). Detection of widespread fluids in the Tibetan crust by magnetotelluric studies. *Science 292*(5517), 716–718.

Wessel, P. and Smith, W. (1991). Free software helps map and display data. *EoS Trans. AGU*, **72**, 441 and 445–446.

Westaway, R. (1995). Crustal volume balance during the India-Eurasia collision and altitude of the Tibetan Plateau: A working hypothesis. *J. Geophys. Res. 100*(B8), 15173–15192.

White, R. W., Powell, R., Holland, T. J. B. and Worley, B. A. (2000). The effect of TiO2 and Fe2O3 on metapelitic assemblages at greenschist and amphibolite facies conditions: mineral equilibria calculations in the system K2O-FeO-MgO-Al2O3-SiO2-H2O-TiO2-Fe2O3. *J. Metam. Geol. 18*(5), 497–511.

White, R. W., Powell, R. and Phillips, G. N. (2003). A mineral equilibria study of the hydrothermal alteration in mafic greenschist facies rocks at Kalgoorlie, Western Australia. *J. Metam. Geol. 21*(5), 455–468.

Willett, S. D. and Beaumont, C. (1994). Subduction of Asian lithospheric mantle beneath Tibet inferred from models of continental collision. *Nature 369*(6482), 642–645.

Wilson, C. K., Jones, C. H. and Gilbert, H. J. (2003). Single-chamber silicic magma system inferred from shear wave discontinuities of the crust and uppermost mantle, Coso geothermal area, California. *J. Geophys. Res. 108*(B5), 2226.

Wilson, D. and Aster, R. (2005). Seismic imaging of the crust and upper mantle using regularized joint receiver functions, frequency-wave number filtering, and multimode Kirchhoff migration. *J. Geophys. Res.*, **110**, B05306.

Wittlinger, G., Farra, V. and Vergne, J. (2004). Lithospheric and upper mantle stratifications beneath Tibet: New insights from Sp conversions. *Geophys. Res. Lett. 31*(19), L19615.

Wittlinger, G., Vergne, J., Tapponnier, P., Farra, V., Poupinet, G., Jiang, M., Su, H., Herquel, G. and Paul, A. (2004). Teleseismic imaging of subducting lithosphere and Moho offsets beneath western Tibet. *Earth Planet. Sci. Lett. 221*(1-4), 117–130.

Won, I. J. and Bevis, M. (1987). Computing the gravitational and magnetic-anomalies due to a polygon - algorithms and fortran subroutines. *Geophysics 52*(2), 232–238.

Wood, B. J. and Walther, J. V. (1983). Rates of hydrothermal reactions. *Science 222*(4622), 413–415.

$\mathcal{X}$i, Y. E. (1985). *Atlas of the Palaeogeography of China*. Cartographic Publishing House, Beijing.

$\mathcal{Y}$in, A. and Harrison, T. M. (2000). Geologic evolution of the Himalayan-Tibetan orogen. *Annual Review of Earth and Planetary Sciences*, **28**, 211–280.

$\mathcal{Z}$aman, H. and Torii, M. (1999). Palaeomagnetic study of Cretaceous red beds from the eastern Hindukush ranges, northern Pakistan: palaeoreconstruction of the Kohistan-Karakoram composite unit before the India-Asia collision. *Geophys. J. Int. 136*(3), 719–738.

Zandt, G. and Ammon, C. J. (1995). Continental crust composition constrained by measurements of crustal Poisson's ratio. *Nature*, **374**, 152–154.

Zeyen, H. and Achauer, U. (1997). Joint inversion of teleseismic delay times and gravity anomaly data for regional structures: Theory and synthetic examples. In K. Fuchs (Ed.), *Upper Mantle Heterogeneities From Active and Passive Seismology, NATO workshop*, pp. 155–168. Kluwer Acad., Norwell, Mass.

Zhang, P. Z., Shen, Z., Wang, M., Gan, W. J., Burgmann, R. and Molnar, P. (2004). Continuous deformation of the Tibetan Plateau from global positioning system data.

Geology 32(9), 809–812.

Zhao, W., Nelson, K. D. and Project INDEPTH Team (1993). Deep seismic reflection evidence for continental underthrusting beneath southern Tibet. *Nature*, **366**, 557–559.

Zheng, T. Y., Zhao, L. and Chen, L. (2005). A detailed receiver function image of the sedimentary structure in the Bohai Bay Basin. *Phys. Earth Planet. Inter. 152*(3), 129–143.

Zhisheng, A., Kutzbach, J. E., Prell, W. L. and Porter, S. C. (2001). Evolution of Asian monsoons and phased uplift of the Himalayan Tibetan plateau since Late Miocene times. *Nature 411*(6833), 62–66.

Zhu, L. P. (2000). Crustal structure across the San Andreas Fault, southern California from teleseismic converted waves. *Earth Planet. Sci. Lett. 179*(1), 183–190.

Zhu, L. P. and Kanamori, H. (2000). Moho depth variation in southern California from teleseismic receiver functions. *J. Geophys. Res.*, **105**, 2969–2980.

Zienkiewicz, O. and Taylor, R. (1989). *The finite element method*. McGraw-Hill, New York.